THE GEOCHRONOLOGY AND RADIOGENIC ISOTOPE SYSTEMATICS OF THE OLYMPIC DAM COPPER-URANIUM-GOLD-SILVER DEPOSIT, SOUTH AUSTRALIA.

James Patrick Johnson

A thesis submitted for the degree of Doctor of Philosophy
of The Australian National University.

February, 1993

All data presented in this thesis are my own unless otherwise acknowledged. XRF analyses were performed by Bruce Chappell of the Geology Department, ANU, and by John Pyke of the Australian Geological Survey Organisation. Neutron activation analyses were performed by Bruce Chappell, and by Becquerel Laboratories, Sydney. XRD analyses were carried out by the Western Mining Corporation laboratory in Kalgoorlie. With the exception of support samples collected by Ken Cross at Olympic Dam, all sample collection, processing and analytical work was performed by the author. Technical instruction was provided by laboratory staff at ANU. The interpretations and conclusions presented were formulated by the author, but have benefitted from discussions with colleagues who are duly acknowledged.

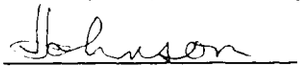

James Patrick Johnson

Dedicated to the memory of Robert Hill.

TABLE OF CONTENTS

LIST OF TABLES

N.B. Page numbers below refer either to the page on which the table occurs, or to the page immediately preceeding the table.

LIST OF FIGURES

N.B. Page numbers below refer either to the page on which the table occurs, or to the page immediately preceeding the table.

LIST OF COLOUR PLATES

N.B. Page numbers below refer to the page immediately preceeding the plate.

ACKNOWLEDGEMENTS

This study was conducted with the coopération of Olympic Dam Operations joint venture partners, Western Mining Corporation Limited and the BP Group. I am grateful to both for financial and logistical support. I would particularly like to thank Ken Cross, the Senior Research Geologist at Olympic Dam, for his guidance, patience, friendship and support, and the ability to impart some of his considerable knowledge of earth sciences in general and the deposit in particular. I am grateful to Jeff Gresham for bringing the project to my attention and for his enthusiasm in getting it started. Many Western Mining personnel provided logistical support and/or stimulating discussion during the course of the project: thanks to Olympic Dam Chief Geologist Rob Smith, Douglas Haynes, Roy Woodall, Hamish Paterson, Richard Barratt, the mine geologists who continually brought new underground exposures or drill intersections to my attention, Rob Scott, Ian Burgan and other members of the drafting department, John Burwell and his core farm crew for their efficient and cheerful assistance whenever it was required, Chris Charman and Jackie Haddock for their assistance.

Ian Campbell supervised this study, and Robert Hill, Malcolm McCulloch and Chris Heinrich were advisors. Their guidance, encouragement and support were valuable and appreciated. I am grateful to Bill Compston and Malcolm McCulloch for providing generous access to their laboratories (SHRIMP and isotopes lab. respectively) without which this work could not have been accomplished. Many people have offered their thoughts and opinions in discussions which helped to refine the ideas presented in this thesis; David Compston, Lynton Jaques, Adam Kent, Sue Kesson, Bob Loucks, Shen-Su Sun and Lesley Wyborn are gratefully acknowledged.

Assistance and instruction in laboratory procedures were provided by Bill Compston, Robert Dabrowski, Robert Hill, Peter Kinny and Ian Williams (SHRIMP operation and data processing), Mark Fanning, Les Kinsley, Malcolm McCulloch, Graham Mortimer, Andrea Thom, Frank Volker and Gael Watson (isotope lab), Harri Kokonnen, John Mya and Richard Rudowski (mineral separation), Audrey Chapman, Marc Norman and Mike Shelley (ICP), Pam Scowen and Nick Ware (electron probe), and Roy Doyle (XRF-Geology department). Thanks to Bruce Chappell for providing XRF trace element and INAA analyses and advice regarding the data. I thank Keith Massey for preparing polished thin sections and ion probe mounts, especially the difficult samples.

I am grateful to Steve Eggins, Mark Fanning, John Foden, Kathy Stewart, Shen-Su Sun and Christine Wawryk for kindly making unpublished data available. Lesley Wyborn, John Pyke and Bill Pappas of the Australian Government Geological Survey Organisation are gratefully acknowledged for providing XRF data. Sue Daly and John

Parker of the South Australian department of Mines and Energy were generous with their time and their knowledge of South Australian regional geology.

Jan Bitmead helped me out of many sticky computer-related problems and has been a good friend throughout. I thank Adam Kent and Jackie Windh for their constructive comments on earlier thesis drafts. Karen Connors helped with typing, and Michael Pocock with collating. I am grateful to the friends who provided support throughout and made some of the problems seem a little smaller, especially Poe, Adam, Leesa, David, Idunn, Roger, Pam, Jeremy and Jackie. My sincere thanks to my parents, brothers and sisters who have given me enormous encouragement and moral support. Special thanks to Karen for keeping the light at the end of the tunnel.

This study was carried out under receipt of an Australian Postgraduate Research Award.

Errata

A) On page 14, paragraph 2, sentence 3: At the end of the sentence there should be a reference ...(Roberts and Hudson, 1983).

B) In Chapter 5 and in Appendix 6 all graphs that present TiO_2-normalised chemical data for trace elements should have axes labelled with "*Element* ppm/TiO_2%" rather than the labels in the format "*Element*/ TiO_2.

ABSTRACT

The Olympic Dam Cu-U-Au-Ag deposit is a syngenetic orebody hosted by the Olympic Dam Breccia Complex, a high level, hematite-rich hydrothermal breccia system. The breccia complex occurs entirely within, and clearly post-dates, the Roxby Downs Granite. Cu-Fe sulphide distribution within the deposit is zoned from pyrite-rich assemblages at depth, upwards to chalcopyrite-rich ores, ultimately to bornite-chalcocite ores. Minor proportions of paragenetically early magnetite are widely distributed. Felsic and mafic/ultramafic dykes are broadly coeval with ore deposition.

The Roxby Downs Granite has an age of 1588 ± 4 Ma. Prior to this study the age of the breccia complex was unclear. SHRIMP U-Pb isotopic data for zircons from three igneous rock units constrain the minimum age for the bulk of the mineralisation. Two autobrecciated felsic dykes that intrude hematite-rich sedimentary rocks and hydrothermal breccias have ages of 1592 ± 8 Ma and 1584 ± 20 Ma respectively. An ashfall tuff horizon from within a diatreme that cross-cuts hematite-quartz breccias contains zircons with an age of 1597 ± 8 Ma. These three minimum age constraints are within error of the age of the host granite, meaning that the breccia complex has an age of ~1590 Ma. This age determination allows confident correlation of ore deposition with a major regional magmatic episode, the Gawler Range/ Hiltaba volcano-plutonic event.

Pb isotopic measurements of hydrated U-Th-Y-REE-rich hydrothermal zircon-xenotime overgrowths on magmatic zircons yielded evidence of complex Pb mobility histories, and provided no strong evidence regarding the age of the deposit. SHRIMP analyses of Olympic Dam pitchblende indicate that U and Pb mobility has reset isotopic systematics heterogeneously, even on a microscopic scale. This open system behaviour is also apparent from the data of earlier workers. An earlier U-Pb concordia upper intercept "age" of 1400 Ma for Olympic Dam pitchblende, calculated by regression analysis of averaged isotopic analyses, should therefore be regarded with caution.

Sm-Nd isotopic data indicate that the different hematite-sulphide assemblages share an initial εNd signature of -2.5. This suggests that these ore types are cogenetic at 1590 Ma. This signature also indicates that ore fluids received contributions of Nd from crustal rocks such as the host granite (εNd -5) and from rocks or magmas derived from the mantle at 1590 Ma. In contrast, the volumetrically minor magnetite-rich assemblages have the same initial Nd signature as the host granite, suggesting that they are possibly cogenetic. The hematitic ores and breccias yield a fourteen point Sm-Nd isochron age of 1572 ± 99 Ma consistent with the age constraints provided by zircon geochronology. The least altered mafic/ultramafic dykes within the deposit have an initial isotopic signature of εNd +4 and are therefore a plausible source of the primitive Nd component in the hematitic rocks. With progressive alteration, these dykes have become depleted in

several of the elements that are enriched in the Olympic Dam ores and breccias, particularly Cu, Cr, Ni, V, Mn, Nb and Y. The trace element and Nd isotopic relationships strongly implicate the mafic/ultramafic dykes, or their plutonic or extrusive equivalents, as metal sources. Interpreted primary enrichments in incompatible elements suggest a strongly alkaline affinity for the mafic/ultramafic rocks.

Rb-Sr isotopic systematics of the Olympic Dam breccias and mafic/ultramafic dykes show evidence of open system behaviour after ore deposition. No firm conclusions regarding ore genesis are drawn from these data.

In view of the data presented, plausible hypotheses of ore genesis include: a) fluid mixing involving a hypogene, granite-related fluid, and a saline meteoric fluid transporting metals of economic interest that have been leached from the Gawler Range volcanic pile, and b) the sequential activity of a granite-related fluid that produced magnetite-rich mineralisation, and a fluid derived by late-stage exsolution of magmatic volatiles from an alkaline mafic or ultramafic pluton.

1 INTRODUCTION

1.1 Rationale

The Olympic Dam copper-uranium-gold-silver deposit is located in central South Australia approximately 520 km NNW of Adelaide (lat.30° 27'S, long.136° 53'E). It is approximately 30 km west of Andamooka and is situated on the Andamooka 1:250,000 and the Mattaweara 1:100,000 scale map sheets. The deposit contains in excess of 30 million tonnes of Cu, 1 million tonnes of U, 1200 tonnes of Au and 7000 tonnes of Ag, making it one of the largest concentrations of these metals in the world (see ore reserves, table 1.1). No other deposit is known to have the same metal association and similar grades. Consequently there has been much curiosity and speculation regarding possible genetic models for forming "Olympic Dam-type" deposits, mainly with a view to developing exploration strategies.

Table 1.1 Resource and reserve statement for Olympic Dam (after Reeve et al., 1990).

	Million tonnes	Cu %	U_3O_8 kg/t	Au g/t	Ag g/t
Inferred resource	2000	1.6	0.6	0.6	3.5
Measured and indicated resource	450	2.5	0.8	0.6	6.0

The mineralisation at Olympic Dam is hosted by the hematite-rich Olympic Dam Breccia Complex which occurs entirely within the Roxby Downs Granite. The spatial relationship between hematite breccias and the host granite suggests a genetic link, and partially comparable Proterozoic ironstones in other continents also share a spatial association with alkalic felsic igneous rocks. However, beyond noting the empirical associations it has previously not been possible to establish the role of the granite, i.e. whether it is a source of metals, a necessary geochemical trap for metals sourced elsewhere, or even if there is a temporal link between granite emplacement and ore genesis.

Within the Olympic Dam deposit there are several different Cu-Fe sulphide associations (pyrite ± chalcopyrite, chalcopyrite, bornite ± chalcocite, chalcocite) some of which appear to be paragenetically later than others. There are also widely varying lithological

facies represented, including the predominant subvolcanic breccias whose clast population may be dominated by hematite or granite, volcanogenic rocks in diatreme zones, finely laminated sedimentary rocks deposited in a quiescent lacustrine environment, autobrecciated felsic and mafic dikes, and coherent dolerite intrusives. Lithological and mineralogical complexity have hitherto made it difficult to establish which are the requisite features for forming this type of deposit, and which features are of purely local and perhaps lesser significance. It is important to understand which geological features are essential to primary ore genesis, and which may represent later modifying events. For example, if there is no temporal link between the host granite and the hematite breccias, then the role of the host granite may be only as a trap for ore metals. Similarly, if the paragenetically later sulphides appear to represent a much later modifying event affecting a lower grade "protore", then ore genesis models would need to account for two developmental stages. Clearly the importance of understanding which hydrothermal products are temporally linked with which rock units cannot be overstated for developing a genetic model.

In order to address these problems an investigation of the geochronology and radiogenic isotope systematics of various deposit rock types has been undertaken. The first aim of the study has been to establish the age of the Olympic Dam Breccia Complex and several key regional rock units regarded as potential metal sources. This aim has been achieved, with U-Pb zircon ages showing the breccias have an age of ~1590 Ma which correlates with the Gawler Range Volcanics, the products of a major regional volcanic event on the Gawler Craton. Having erected the geochronological framework, the second aim has been to use radiogenic isotopes to correlate between the various mineralogical subgroups within the deposit in order to establish groups of rock types which appear to be cogenetic. Sm-Nd isotopes have been particularly useful in this regard, having enabled the recognition of; a) linked geneses for ores and hematitic breccias, and b) isotopic differences between hematitic ores, the host granite and magnetite breccias. The third aim has been to use isotopic characteristics of the ore to trace sources of the fluids and/ or metals. These studies have strongly implicated the involvement in ore genesis of mafic/ ultramafic rocks produced during the Gawler Range Volcanic event.

Field work was carried out in part during ten months of employment as a mine geologist at Olympic Dam during 1988, and subsequently during visits to the mine in July 1989, March 1990 and July 1991. The sampling strategy was aimed at collecting geographically separate samples of each of the lithological and mineralogical subgroups discerned on the basis of macroscopic observations. Seventy seven samples were taken from the Olympic Dam deposit and a further ten samples from relevant regional rock units. The petrographic and geochemical work undertaken has been primarily directed at characterising the samples as support for the isotopic work. The nature of the sampling strategy was governed by the aim of identifying isotopic groupings rather than to provide

comprehensive geochemical coverage. This study should therefore not be viewed as an attempt at a detailed geochemical study of Olympic Dam. Indeed the isotopic work described establishes which of the lithological groups can be regarded as cogenetic, and in so doing erects a suitable framework within which a later detailed geochemical study may be conducted.

Over 100 regular and polished thin sections were made and 80 whole-rock samples were crushed for geochemical analysis. Mineral separations were carried out for 9 samples for U-Pb zircon geochronological studies, and 39 samples were dissolved and prepared for isotope dilution analysis of Rb-Sr and Sm-Nd isotopes.

1.2 Previous work

Roberts and Hudson (1983) published the first geological description of the Olympic Dam deposit. Their work took place at an early stage in the commercial development of the deposit and is based on relatively sparsely spaced surface drilling. They interpreted the host breccias to be of sedimentary origin and the introduction of ore metals to be related to local volcanism. Reeve et al. (1990), with the relatively recent availability of a large volume of detailed information obtained from underground exposures and close-spaced drilling, reinterpreted the geology and favour a subvolcanic magmatic/ hydrothermal origin for both the host breccias and the mineralisation. Oreskes and Einaudi (1990), who concentrated on the rare earth element (REE) mineralogy and distribution of the REE within the deposit, concluded that the brecciation and introduction of metals resulted from hypogene hydrothermal fluids venting at the palaeosurface.

Haynes (1979), Lalor (1984, 1986), Esdale et al. (1987) and O'Driscoll (1985) described various aspects of the discovery and evaluation of the deposit. General similarities between the mineralisation and/ or the geological setting of Olympic Dam and other Middle Proterozoic iron oxide-rich deposits have been noted by Hauck and Kendall (1984), Meyer (1988), Hagni and Brandom (1988, 1989), Kisvarsanyi and Kisvarsanyi (1989), Hauck (1989), Einaudi and Oreskes (1989), Hitzman et al. (1990), Philpotts et al. (1991) and Hitzman et al. (1992). Oreskes (1990) discussed the U content of Olympic Dam hematite, focussing on the implications of the linked transport and precipitation of Fe and U for fluid chemistry and depositional mechanisms. The geological implications of a preliminary assessment of the U-Pb zircon data presented in Chapter 3 have been summarised by Johnson and Cross (1991a, b). Johnson and Cross (1991b) also discussed the significance of Nd isotopic analyses of various Olympic Dam rock types. Oreskes and Einaudi (1992) discussed fluid inclusion and stable isotope constraints on the temperatures of formation for various ore types at Olympic Dam. Haynes et al. (submitted) have used geochemical modelling to assess the viability of several ore genesis models. These workers favour a model in which ore

deposition results from the mixing of a hypogene fluid, possibly of magmatic derivation, with a metal-bearing meteoric fluid which has interacted with basaltic rocks. Discussion of aspects of the models proposed by earlier workers is included through the text.

1.3 Thesis structure

This thesis is divided into eight chapters. Chapter 2 describes the regional geology and the main geological features of the deposit. After describing the deposit, the specific aims of the project and the sampling strategy are discussed. Chapter 3 documents the U-Pb zircon geochronology of the deposit, discussing analyses of igneous zircons and hydrothermal mantles around magmatic zircons. In Chapter 4, attempts at dating pitchblende by ion probe are discussed. This work explains the discrepancy between the ~1400 Ma deposit age postulated by Trueman et al. (1988) on the basis of pitchblende dating, and the ~1590 Ma age proposed in Chapter 3. The geochemistry of the Olympic Dam breccias is examined in Chapter 5 with particular attention to elemental gains and losses for the deposit during ore deposition. In Chapter 6 the geochemistry of the altered mafic/ ultramafic dykes is investigated to assess their petrogenetic affinities. The dykes appear to have alkaline characteristics and are therefore a plausible source for many of the deposit's elemental enrichments described in Chapter 5. Sm-Nd isotopic studies of the deposit are documented in Chapter 7, revealing that ore genesis probably involved fluids which had interacted with mafic or ultramafic rocks at 1590 Ma. The evidence of the preceding chapters is summarised in Chapter 8, and the ore genesis models consistent with the new data are discussed.

2 GEOLOGICAL SETTING

2.1 Regional Geology

Olympic Dam is located in the northeast of the Gawler Craton (Figure 2.1), an Archaean and Proterozoic terrain onlapped to the west by the Tertiary Eucla Basin, the north by Mesozoic sedimentary rocks of the Ackaringa Basin, and bounded to the east by the Torrens Hinge Zone, a major northerly trending fault zone separating the Gawler Craton from the Late Proterozoic-Cambrian Adelaide Geosyncline. Archaean rocks are known in the Sleaford Complex to the west, and the Mulgathing Complex in the south of the craton (Creaser, 1989). The deposit occurs in Middle Proterozoic basement rocks beneath an incomplete sequence of undeformed Late Proterozoic and Cambrian sedimentary rocks of the Stuart Shelf (Figure 2.1). The stratigraphy of the Stuart Shelf sequence has been described by Mason et al. (1978), Preiss (1987), Parker (1990) and Reeve et al. (1990). At Olympic Dam the lowermost units of Stuart Shelf stratigraphy are not present, the deposit being directly overlain by members of the Wilpena Group. The Adelaidean sedimentary rocks of the Stuart Shelf are thought to be the undeformed equivalents of the metasedimentary rocks of the Adelaide Geosyncline to the east. Together these sedimentary provinces have been interpreted to represent the fill of a Late Proterozoic intracontinental rift where extension was followed by partial closure (von der Borch, 1980) which resulted in compressional deformation within the Adelaide Geosyncline.

To the southwest of the Stuart Shelf, deformed granitic rocks and metasedimentary rocks of the of the Early Proterozoic Lincoln Complex and Hutchison Group are intruded by undeformed granitic rocks of the Hiltaba supersuite (Reeve et al., 1990). The Hiltaba granitoids are thought to be cogenetic with the felsic rocks of the Gawler Range Volcanics (Giles, 1988 and Creaser, 1989; Figure 2.1), an enormous outpouring of predominantly felsic magmas covering an area of at least 25,000 km^2. The rocks are mainly welded ashflow tuffs with lesser airfall tuffs and lavas. They comprise an assemblage of dacites, rhyodacites and rhyolites, with subsidiary potassic andesites and tholeiitic basalts (Blisset et al., 1989), and were extruded at ~1590 Ma (Fanning et al, 1988; Creaser, 1989). The combined volume of the volcanics and the Hiltaba supersuite granites has led a number of workers to conclude that crustal underplating and/ or mantle diapirism triggered extensive crustal melting to give rise to the felsic magmas (Giles, 1988; Wyborn et al., 1987). Geophysical evidence supports this view indicating the presence of large volumes of mafic material in the lower crust beneath the Gawler Range Volcanics (Stewart and Foden, 1990). The volcano-plutonic event is interpreted as an episode of incipient intracontinental rifting (Reeve et al., 1990).

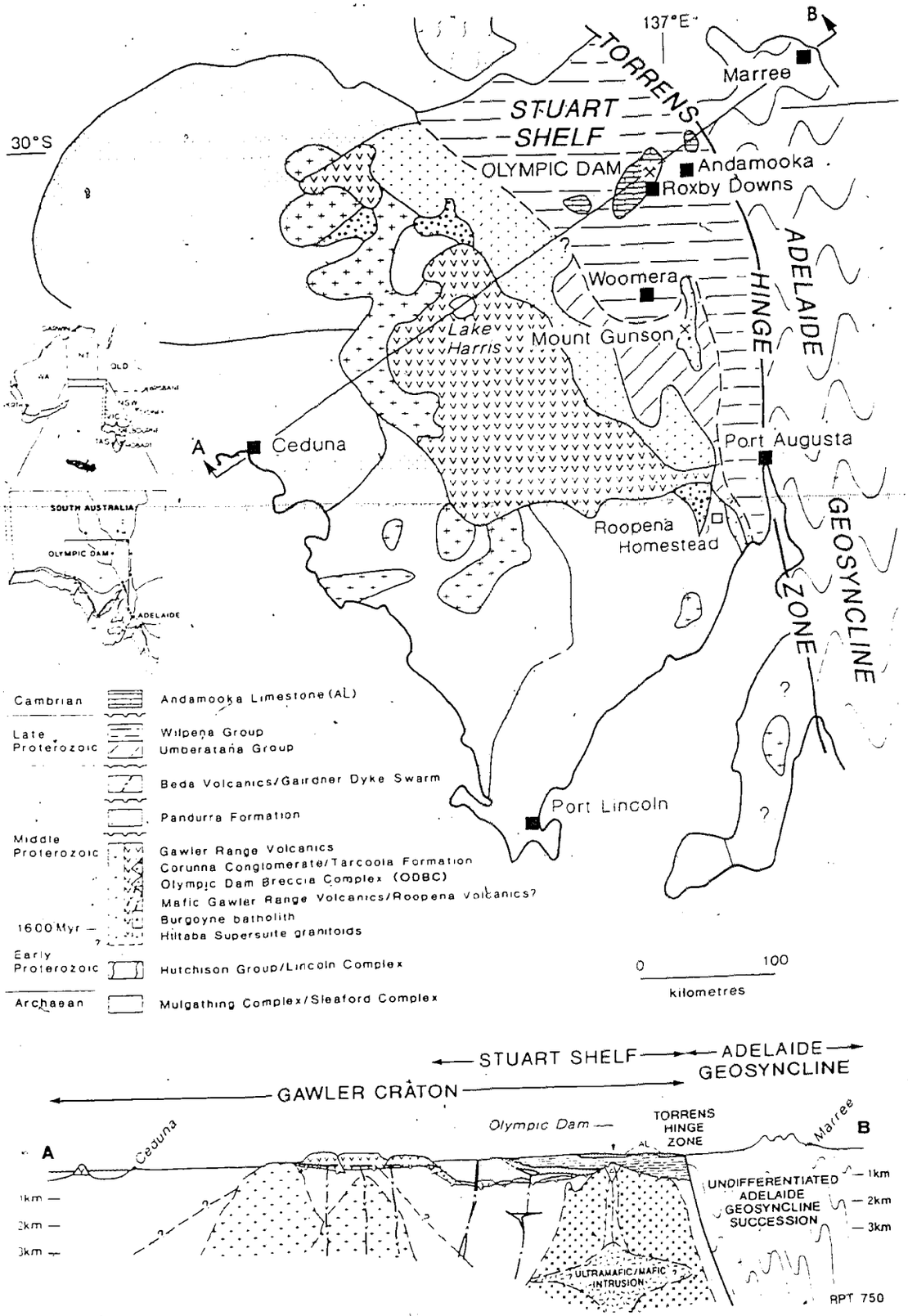

Figure 2.1 Regional geology and schematic regional cross section of the Gawler Craton. Olympic Dam lies in the northeast of the craton beneath the sedimentary rocks of the Stuart Shelf. (modified after Reeve et al., 1990)

The Gawler Range Volcanics include a relatively minor proportion of basaltic rocks (Giles, 1988; Blisset et al., 1989) and these probably represent samples of magma which caused crustal melting. The basaltic rocks of the Roopena Volcanics (~40 km southwest of Port Augusta; Figure 2.1) have been correlated with the basalts of the Gawler Range Volcanics on the basis of their geochemistry (Giles and Teale, 1979), and zircon dating of a tuff associated with the Roopena Volcanics (this study; Chapter 3) indicates that they are indeed correlatives of the Gawler Range Volcanics. This correlation increases the amount of known basaltic magmatism associated with the Gawler Range volcanic event.

Beneath the sedimentary rocks of the Stuart Shelf similar geological relationships are evident in the basement rocks. Deformed Early Proterozoic equivalents of the Hutchison Group and Lincoln Complex are intruded by the post-orogenic Hiltaba supersuite granitoids. In the vicinity of Olympic Dam these granitoids form a complex of plutons which Reeve et al. (1990) referred to as the Burgoyne batholith. The Burgoyne batholith consists of at least two suites of granitoids, the White Dam Suite to the east near Andamooka, and the Wirrda Suite to the west near Olympic Dam (Creaser, 1989). Plutons range in composition from quartz monzodiorite to granite and have A-type geochemical characteristics (cf. Collins et al., 1982). The Roxby Downs Granite which hosts the Olympic Dam deposit is an evolved pluton, and is a member of the Wirrda Suite. The entire Burgoyne batholith was emplaced at 1585 to 1600 Ma (Creaser, 1989; Mortimer et al., 1988a).

2.2 Geology of the Olympic Dam deposit

2.2.1 The Roxby Downs Granite

The Olympic Dam mineralisation is restricted to the Olympic Dam Breccia Complex (Reeve et al., 1990), which occurs wholly within the Roxby Downs Granite (formerly the Olympic Dam Granite). Where unaltered, the Roxby Downs Granite is a pink-red, medium to coarse grained rock which by the Streckeisen (1976) classification scheme is a quartz-poor syenogranite. Its approximate modal composition is 50% alkali feldspar, 20-25% sodic plagioclase, 20-25% quartz, 5-8% amphibole+biotite, accessory magnetite, zircon, sphene, apatite and trace fluorite, allanite and uranothorite (Reeve et al., 1990). Alkali feldspar commonly displays rapakivi textures (K-feldspar rimmed by albite). Geochemically the granite displays an A-type signature (high contents of K_2O, REE, Zr, Y, U, Th and F). The most detailed work to date on the Roxby Downs Granite is that of Creaser (1989), who concluded that the granite is the product of fractional crystallisation of a quartz-monzonite melt derived from partial melting of a deep-crustal tonalitic source. The granite has been precisely dated at 1588 ± 4 Ma (Creaser, 1989) by conventional U-Pb zircon techniques.

2.2.2 Host Breccias

The most complete account of the Olympic Dam Breccia Complex is that of Reeve et al. (1990). Much of the following description of the deposit is adapted from that source, although most of the features have also been observed by the author during employment as a mine geologist in 1988. The breccia complex consists of a variety of breccia types with the main components being granite and hematite. There is a broad concentric lithological zonation from pristine granite surrounding the deposit, through fractured granite, granite-dominant breccias, heterolithic breccias, hematite-dominant breccias, through to hematite-quartz breccias in the core of the deposit. Figure 2.2 shows a schematic plan view of the deposit at the main development level of the mine; Figure 2.3 shows a schematic cross section. The breccia complex can be divided into two general compositional varieties, granite-rich and hematite-rich breccias. Reeve et al. (1990) stressed that any subdivisions are arbitrary and that there is a continuum of compositional variability between granitic and hematitic end members.

Granite-rich breccias vary from matrix-poor types showing crackle or jigsaw textures, to more matrix-rich types where such textures are absent. Matrix consists of granite-derived fragments and/ or hematite.

Hematite-rich breccias are widespread and are the most important host rocks for mineralisation. Their compositional variability encompasses: a) Heterolithic breccias with abundant hematite and granite clasts in a hematite matrix; b) Hematite breccias with dominantly hematite clasts in a hematite matrix; and c) Hematite-quartz breccias with clasts of hematite and granite-derived quartz in a hematite-quartz matrix. Clasts in all breccia types are generally angular and approximately equidimensional. They are highly variable in size from less than 0.5 cm up to blocks several metres across. Generally clasts are less than 20 cm across (Reeve et al., 1990).

Figure 2.2 (overleaf). Simplified geological plan of Olympic Dam at the main development level of the mine (modified after Reeve et al., 1990). Note the lithological zonation from the host granite at the margins to progressively more hematite-rich lithologies in the centre of the breccia complex.

Figure 2.3 (overleaf). Mine-scale cross section of the Olympic Dam deposit (after Reeve et al., 1990). Note the zonation from granite and granite-dominant breccias at the margins of the deposit, to progressively more hematite-rich breccias near the centre. The bornite-chalcopyrite interface is shown as a convolute dotted line. A diatreme structure (V1 from Figure 2.2) is represented in the centre of the section.

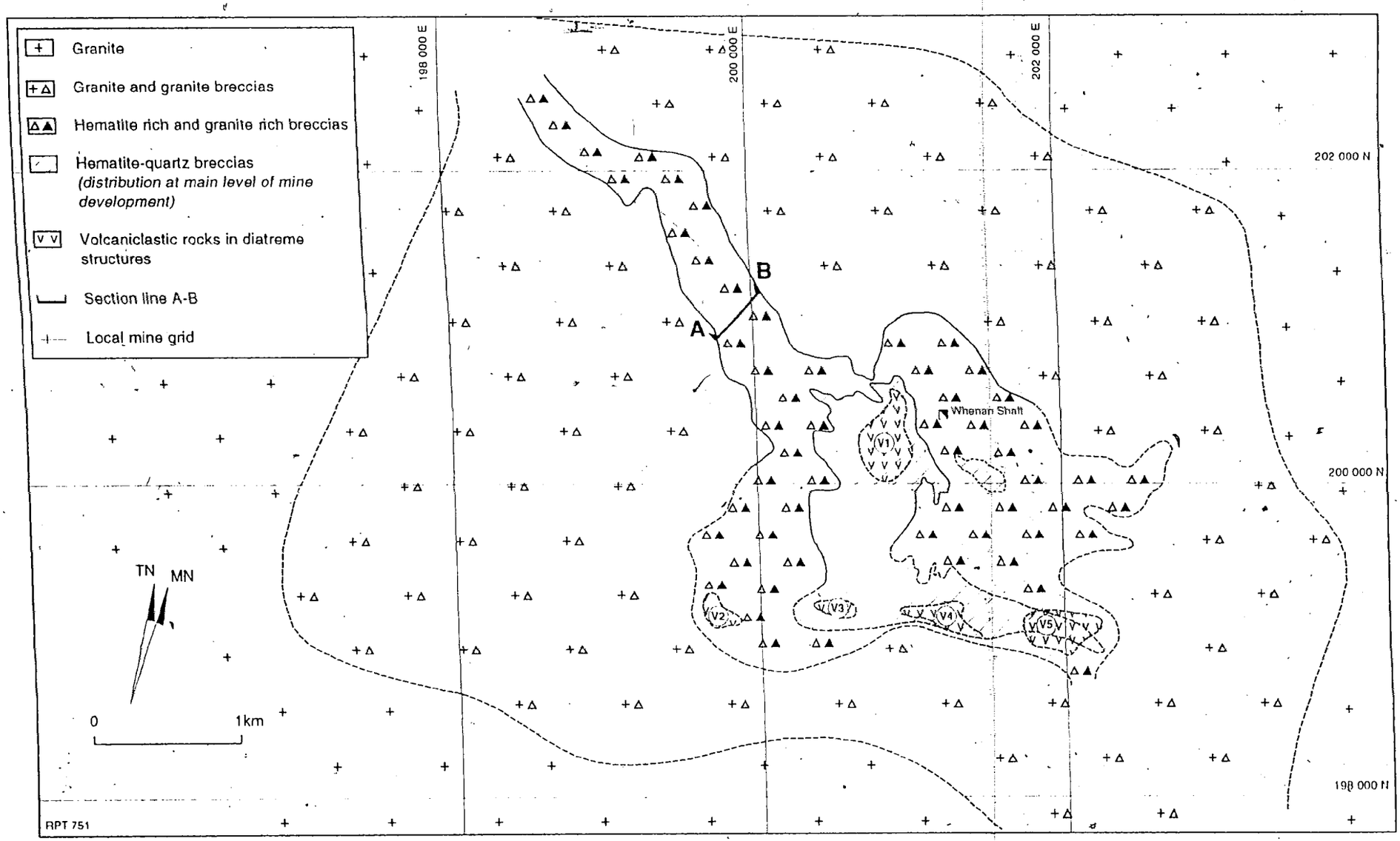
Granite
Granite and granite breccias
Hematite rich and granite rich breccias
Hematite-quartz breccias
(distribution at main level of mine development)
Volcaniclastic rocks in diatreme structures
Section line A-B
Local mine grid
198 000 E
200 000 E
202 000 E
202 000 N
200 000 N
198 000 N
A
B
Whenan Shaft
V1
V2
V3
V4
V5
TN
MN
0
1km
RPT 751

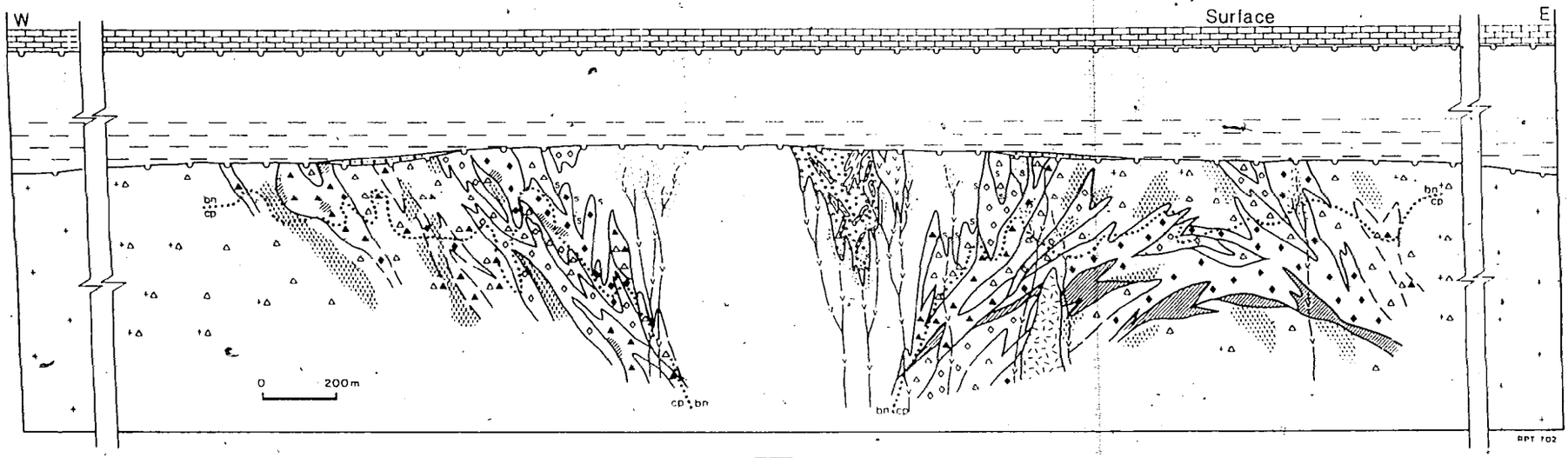

CAMBRIAN

LATE PROTEROZOIC

COVER SEQUENCE

WILPENA GROUP

Andamooka Limestone

Tent Hill Formation
Arcoona Quartzite Member
Corraberra Sandstone Member
Tregolana Shale Member (localised basal dolomite)

Local pebble conglomerate

MIDDLE PROTEROZOIC

BASEMENT

ODBC

Granite rich breccias
Hematite rich matrix
Heterolithic granitic breccias

Granite and granite breccias

Roxby Downs Granite

Granite rich and hematite rich breccias

Hematite rich breccias
Hematite breccias
Hematite-quartz breccias
Heterolithic hematitic breccias

Dolerite

Laminated fine grained tuffs
Volcaniclastic conglomerate
Peperite, tuffisite
Mafic and felsic dykes

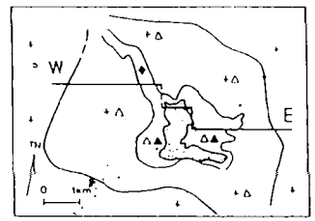

bn / cp Bornite-chalcopyrite (bn-cp) interface

Silicified zones

The described zonation from outermost granite breccias to the hematite-quartz breccia core applies on a deposit scale (Figures 2.2 and 2.3). However, the deposit cannot be viewed as a single breccia pipe representing a single brecciation episode. There is abundant evidence for multiple brecciation events. For example, hematite clasts probably represent broken vein or matrix hematite from earlier breccias; metre-scale clasts are commonly observed to be fragments of pre-existing breccias. These in turn may contain clasts of earlier breccias. The evidence for overprinting of multiple brecciation episodes suggests that the complex is a set of nested breccia pipes which are commonly transgressive to each other. The breccias probably formed dominantly by hydrothermal brecciation of the Roxby Downs Granite, in contrast to the diatremes in the deposit (described below) which are thought to have formed by explosive interaction of mafic/ ultramafic magmas with wet surficial rocks after the main brecciation event(s).

Minor components occurring as dicrete clasts in the breccias include fluorite, barite, siderite, and sulphides ± pitchblende.

2.2.3 Surficial rock types

2.2.3.1 Laminated hematite-quartz sandstone

Finely laminated hematite-quartz rocks occur locally as a ~200 m thick sequence truncated above by the unconformable base of the Late Proterozoic Adelaidean sedimentary rocks. Clasts of hematite-quartz sandstone occur in many of the breccias. Reeve et al. (1990) interpret these rocks as sediments deposited in a maar lake environment. Roberts and Hudson (1983) suggested a lake environment with fumarolic input of iron. These sediments and the interpretation of their environment of formation are particularly important to this study. A felsic dyke which intrudes them has provided a date which is crucial to inferring the age of the breccia complex (Section 3.3.1).

2.2.3.2 Diatremes

Surficial rocks are also localised in several distinctive zones which have been interpreted by Krcmarov (1987), Bradbury (1988) and Reeve et al. (1990) as diatreme structures. These zones are labelled V1 to V5 in Figure 2.2. However, Oreskes and Einaudi (1990) described one of these zones as a down-faulted package of volcaniclastic rocks which they interpret as being ~200 million years older than the breccia complex. The central "diatreme" (V1, Figure 2.2) has been exposed by underground development and has been the subject of extensive mapping prior to the commencement of this project.

Lorenz (1985) provided a detailed review of the processes and products of diatreme formation. Diatremes are subvolcanic structures which occur below small explosive

volcanoes ("maars"). Diatremes form by phreatomagmatic processes i.e. an interaction of magma and external water (mostly groundwater) giving rise to powerful vapour explosions, or by explosive degassing of rapidly ascending, volatile-rich magma (e.g. kimberlites; Mitchell, 1986). They are typically cone-shaped, constricting downwards to a root zone which is usually a dyke or dyke swarm. Diatremes are predominantly filled with pyroclastic rocks which are well-bedded in the upper levels but disrupted by collapse structures and fluidisation fabrics at lower levels. Narrow pyroclastic vents may cut the pyroclastic rocks. Slabs of country rock may occur near the diatreme walls. Reworked surficial eruptives may be deposited on the crater floor and subside into the diatreme during or following subsequent eruptions (Lorenz, 1985).

All of the diatreme features listed above have been observed in the zones of volcaniclastic rocks at Olympic Dam. The exposed "diatreme" (V1, Figure 2.2) is elliptical in plan, measuring 500 m x 200 m at the unconformity surface. The upper parts are dominated by subaerial volcanics which taper rapidly downwards into two terminations. At the apices of these two inverted cone structures there are altered mafic/ ultramafic dykes and tuffisites (intrusive tuffs) of subvertical orientation. If the diatreme interpretation is correct, then these two dyke zones would represent root zones. The surficial rock types within the "diatreme" consist of a chaotically disrupted sequence of volcanogenic cobble conglomerates, lapilli tuffs and laminated ash-fall tuffs. All of these rock types are sericitised and/ or hematitised. Cobbles are predominantly porphyritic felsic rocks, although vesicular mafic/ ultramafic cobbles also occur. Ash-fall tuffs show soft-sediment deformation fabrics e.g. slump folds and abundant small-scale faults of variable offset, attitude and sense of movement. Fragments of basaltic material (Krcmarov, 1987; Bradbury, 1988) up to 10 cm across are interspersed with the surficial rock types. They have wispy shapes, very fine grainsize and pervasive sericite and chlorite alteration (Plate 1). Krcmarov (1987), Bradbury (1988) and Reeve et al. (1990) interpret the wispy basaltic fragments as juvenile pyroclasts i.e. fragments of the magma which was explosively emplaced to produce the diatreme. Their fine grainsize would thus result from their origin as quench-fragments of basaltic glass. These fragments commonly occur concentrated in subvertical zones around the margins of relatively coherent blocks of surface rock types. Such zones may represent the "narrow pyroclastic vents" of Lorenz (1985).

If the zones of surficial rocks described above are not diatremes, the only plausible alternative is that they are down-faulted packages of the surface rocks which overlay the deposit. This interpretation has been advocated by Oreskes and Einaudi (1990). It could explain the various tuffs and the rounded cobbles within these zones, but it does not explain the presence of the wispy basaltic fragments, which cannot be interpreted as epiclastic when their delicate fabrics are considered. Nor can it explain the overall conical

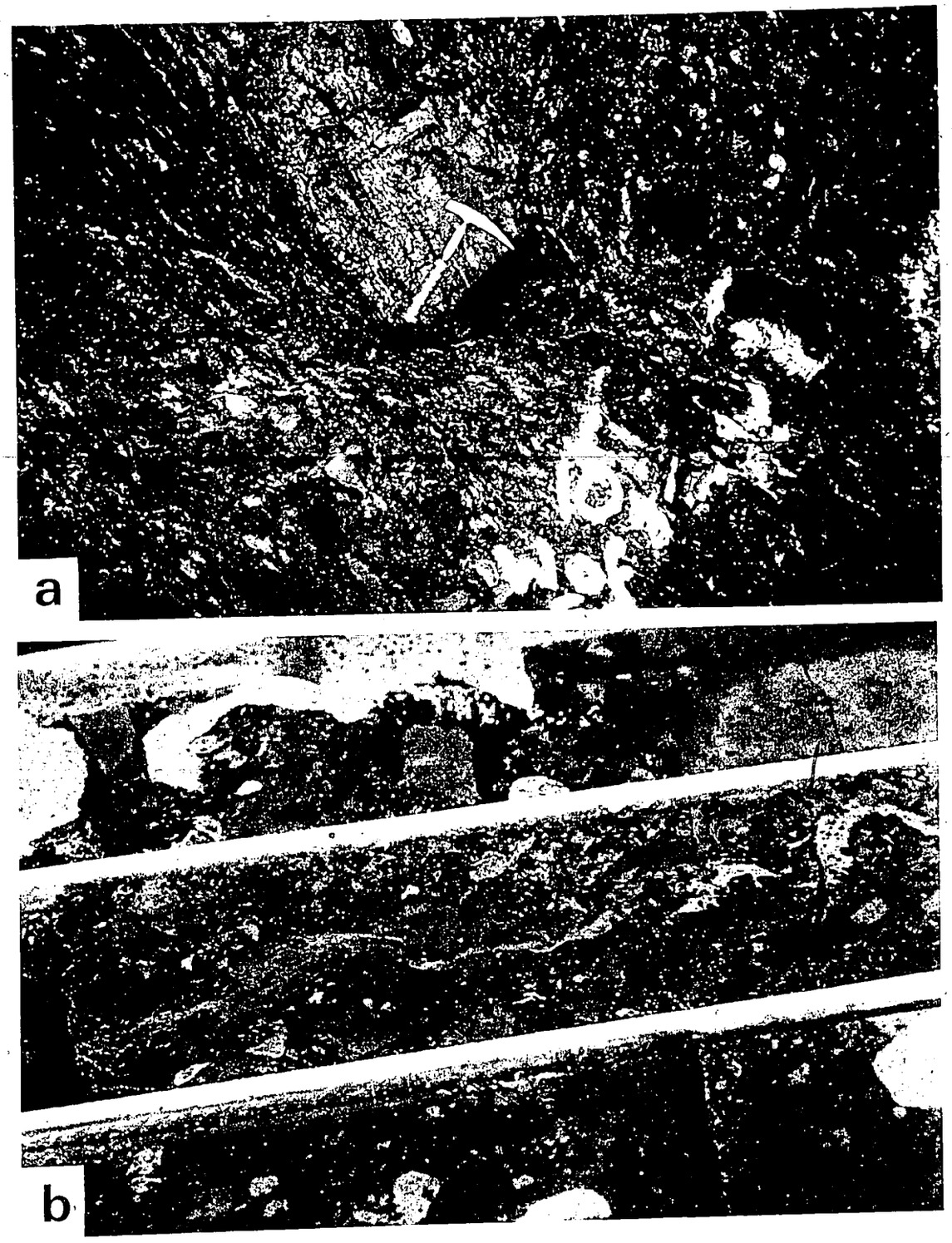

Plate 1 Diatreme lithologies. **a)** Zone of volcaniclastic diatreme-fill. Rounded brown cobbles at lower left are sericitised felsic volcanics, clasts in a volcanogenic conglomerate. Elongate yellow-green fragments are juvenile mafic/ultramafic intrusive pyroclasts which form streaming fabrics from lower right to upper left, interpreted to result from the explosive intrusion of the mafic/ultramafic melt. A large block of laminated ash-fall tuff occurs behind the hammer. **b)** Drillcore sample through diatreme. The delicate textures of the mafic/ultramafic pyroclasts (yellowish-green) indicate *in situ* quenching. Rounded brown felsic cobbles present in upper section of photograph.

shape of the structure, and the presence of basaltic dykes immediately below the structure. Collapse of crater-fill could account for the faulted contacts reported by Oreskes and Einaudi (1990), but it is also likely that late-stage faults (Sugden and Cross, 1991) nucleated on the margins of volcaniclastic units because of the competency contrast between these and the hard hematite wallrocks.

In view of the abundant similarities to documented diatreme characteristics, the diatreme interpretation is favoured in this work. Zircons from a tuff within this diatreme have provided a date which is believed to represent the age of the active diatreme. As such it represents an important minimum age constraint on the rocks intruded by the diatreme (Section 3.3.3).

2.2.4 Igneous Intrusions

The driving force of the diatremes was the explosive intrusion of mafic/ ultramafic magmas, probably into wet unconsolidated near-surface units. The igneous intrusive rocks evident from this event are the juvenile mafic pyroclasts described above, and the coherent dykes interpreted as feeder dykes in the diatreme root zones. There are other coherent mafic/ ultramafic dykes locally abundant near the diatremes. They are invariably strongly altered to sericite + chlorite ± serpentine ± hematite assemblages. Their general mafic affinity can be discerned by the presence of chromian spinels and olivine pseudomorphs, and by their Cr and Ni contents which can be up to ~2400 ppm and ~1900 ppm respectively (Appendix 2). This study illustrates the importance of these rocks in ore genesis at Olympic Dam. The dykes are therefore discussed in detail in Chapter 6.

Medium grained dolerite has been intersected in drillcore in the eastern part of the breccia complex. Its relative lack of alteration suggests it is much younger than the breccias, and a Rb-Sr mineral-whole rock isochron indicates it has an age of 1059 ± 69 Ma (Creaser, 1989).

Felsic intrusive rocks are largely restricted to the southern parts of the breccia complex where they are observed only in drillcore. They occur as sericite altered fragmental dykes emplaced into hematitic sediments and breccias. Their fragmental nature is interpreted to be due to the intrusion of felsic magma into wet unconsolidated material with consequent autobrecciation and quenching of the felsic fragments. Two such dykes have been dated as part of this study and a more detailed description of their mode of occurrence is presented in Chapter 3.

2.2.5 *Alteration*

Sericite, hematite, chlorite and silica are the main alteration phases. Sericitisation occurs throughout the deposit whereas hematitisation is more abundant near the centre of the deposit. Chlorite alteration is patchy but tends to be more abundant at depth. Silicification occurs in discrete zones with irregular shapes. Minor carbonate alteration affects the northeastern part of the deposit (Reeve et al., 1990). Much of the hematite in the deposit is thought to have replaced pre-existing minerals including those of granitic and secondary hydrothermal origin.

2.2.6 *Veins*

Hematite, sericite, chlorite and barite veinlets are common. Larger barite-fluorite veins are also widespread. Veinlets of copper sulphides ± pitchblende are locally abundant but are not an important form of economic mineralisation on a deposit scale.

2.2.7 *Mineralisation*

The Olympic Dam deposit contains anomalous concentrations of Fe, Cu, U, Au, Ag, Ba, F and light rare earth elements (LREE). When normalised to the bulk composition of the continental crust (Taylor and McLennan, 1985) the enrichment factors of the anomalous metals are†: Fe 3-6; Cu 333; U 745; Au 267; Ag 75; La 125; Ce 91. The most anomalous concentration in the deposit is that of uranium. Weak mineralisation is widespread in most breccia types outside of ore zones. Background levels in non-ore breccias can be up to 0.5% Cu, 200 ppm U, 0.5 ppm Au and 1 ppm Ag (Reeve et al., 1990).

Ore zones are generally within hematitic breccias, although they are absent from the hematite-quartz breccias at the centre of the deposit. Copper generally occurs with uranium, with minor and variable gold and silver. Gold ore occurs in separate zones hosted by either granitic or hematitic breccias.

2.2.7.1 Copper

The main copper minerals are the sulphides chalcopyrite ($CuFeS_2$), bornite (Cu_5FeS_4) and chalcocite (Cu_2S). These are most common as disseminated grains intergrown with

---

† Enrichment factors calculated using the "measured and indicated resource" grades (Table 1.1) for Cu, U, Au and Ag, 30-60% Fe, 2000 ppm La and 3000 ppm Ce (see text).

matrix hematite. On a deposit scale the sulphide mineralisation displays a broadly vertical zonation from pyrite at depth, upwards to chalcopyrite, then bornite and chalcocite (Oreskes and Einaudi, 1990; Reeve et al., 1990). Comparatively minor, essentially sulphide-free zones containing native copper or gold occur locally above or adjacent to the chalcocite-bearing zones. Because mineralogical boundaries and, to a lesser extent, lithological boundaries within the breccia complex are highly irregular and locally convoluted, the above-mentioned zonation is also developed laterally on scales of metres to hundreds of metres. The interface between chalcopyrite- and bornite-bearing zones is typically sharp and readily mappable (e.g. Figure 2.3 and 5.18; see also Figure 2.b of Reeve et al., 1990). At the interface, bornite + chalcopyrite may coexist over short intervals (<5m); however, chalcocite + chalcopyrite is never seen. The sulphide abundance is generally similar on either side of the interface, but copper grades in the bornite-chalcocite zones are typically 2 to 3 times higher than those in adjacent chalcopyrite (-pyrite) zones (4- 6% and <3% respectively). Copper minerals occur as disseminations, microveinlets and fragments. Contrary to the claims of Oreskes and Einaudi (1992), fragments of sulphide and sulphide-bearing rock fragments are conspicuous and widespread throughout many of the hematitic and (to a lesser extent) granitic breccias.

Oreskes and Einaudi (1990) interpret the bornite/ chalcopyrite interface as the result of weathering and supergene enrichment of a primary chalcopyrite + pyrite ore. However, Roberts and Hudson (1983) and Reeve et al. (1990) argue that the gross zonation pattern is of primary hypogene origin with only minor localised areas of supergene enrichment. They cite the absence of typical supergene textures (e.g. chalcocite rims on the other sulphides), the absence of any leached zone near the unconformity, and sulphide textures indicative of high temperature crystallisation (symplectic intergrowths of bornite and chalcocite) to support their case. The origin of the sulphide interface is discussed further in Chapters 5 and 7.

2.2.7.2 Uranium

Uranium is present at above background levels in all copper mineralised zones. In many areas in the deposit uranium is concentrated in a relatively narrow zone associated with the upper portions of the bornite-chalcocite zones. However, there are also some zones of high grade U which are transgressive to the sulphide interface, demonstrating that the sulphide species is not the sole control on high grade U mineralisation. This point raises the possibility that uranium and copper sulphide mineralisation may be temporally distinct in some cases.

In general, chalcopyrite-pyrite mineralisation is of low to medium U content (~250 to 700 ppm U). There are also zones in which rich chalcocite-bornite ore contains relatively low

U concentrations. In some cases sericite-altered granite breccias with only low hematite contents may contain significant U concentrations.

Most of the U occurs as pitchblende (U_3O_8; partially oxidised and hydrated uraninite, UO_2). It usually occurs as fine grained (less than 5 μm to tens of μm) disseminations, or as aggregates of fine grains. This form of U is probably syngenetic with the hematite and sulphides. Other forms include colloform and crustiform cavity-filling textures and veinlets. These are interpreted as indicating remobilisation of U. Pitchblende may occur as rims to, and replacements of, other breccia components such as hematite and sulphides. Other U minerals which have been observed include coffinite [$U(SiO_4)_{1-x}(OH)_{4x}$] and brannerite [$(U,Ca,Ce)(Ti,Fe)_2O_6$] (Reeve et al., 1990; Trueman et al., 1988).

2.2.7.3 Gold

Gold occurs in low to moderate concentrations (0.3 to 1 ppm) in all Cu-U mineralisation but does not show a clear correlation with Cu or U content (Reeve et al., 1990). Gold also occurs in higher grade zones (several ppm) which are spatially distinct from the Cu-U zones. Cu sulphide inclusions and sericite intergrowths have been observed with gold, demonstrating their contemporaneous growth. Gold inclusions in hydrothermal rims on zircon grains have also been observed (see Plate 3).

2.2.7.4 Silver

Silver occurs with all Cu mineralisation, mostly within Cu sulphides. The silver content of gold grains is generally <3 wt% (Reeve et al., 1990).

2.2.7.5 Other elements

The Olympic Dam deposit is strongly enriched in the LREE, with abundances of ~2000 ppm La and ~3000 ppm Ce common for mineralised zones. The hematite-quartz breccias at the centre of the deposit, although essentially barren of Cu-U mineralisation, contain higher LREE concentrations than the surrounding breccias. Fluorine occurs predominantly as fluorite in the form of disseminated grains, clasts and veins. Fluorite-

---

Figure 2.4 (overleaf). Gravity and magnetic contours superimposed on the deposit geology. Olympic Dam is situated on coincident positive anomalies in gravity and magnetic signatures (slightly offset). The mass of dense hematite can account for the gravity anomaly, but the magnetic anomaly remains a matter for speculation.

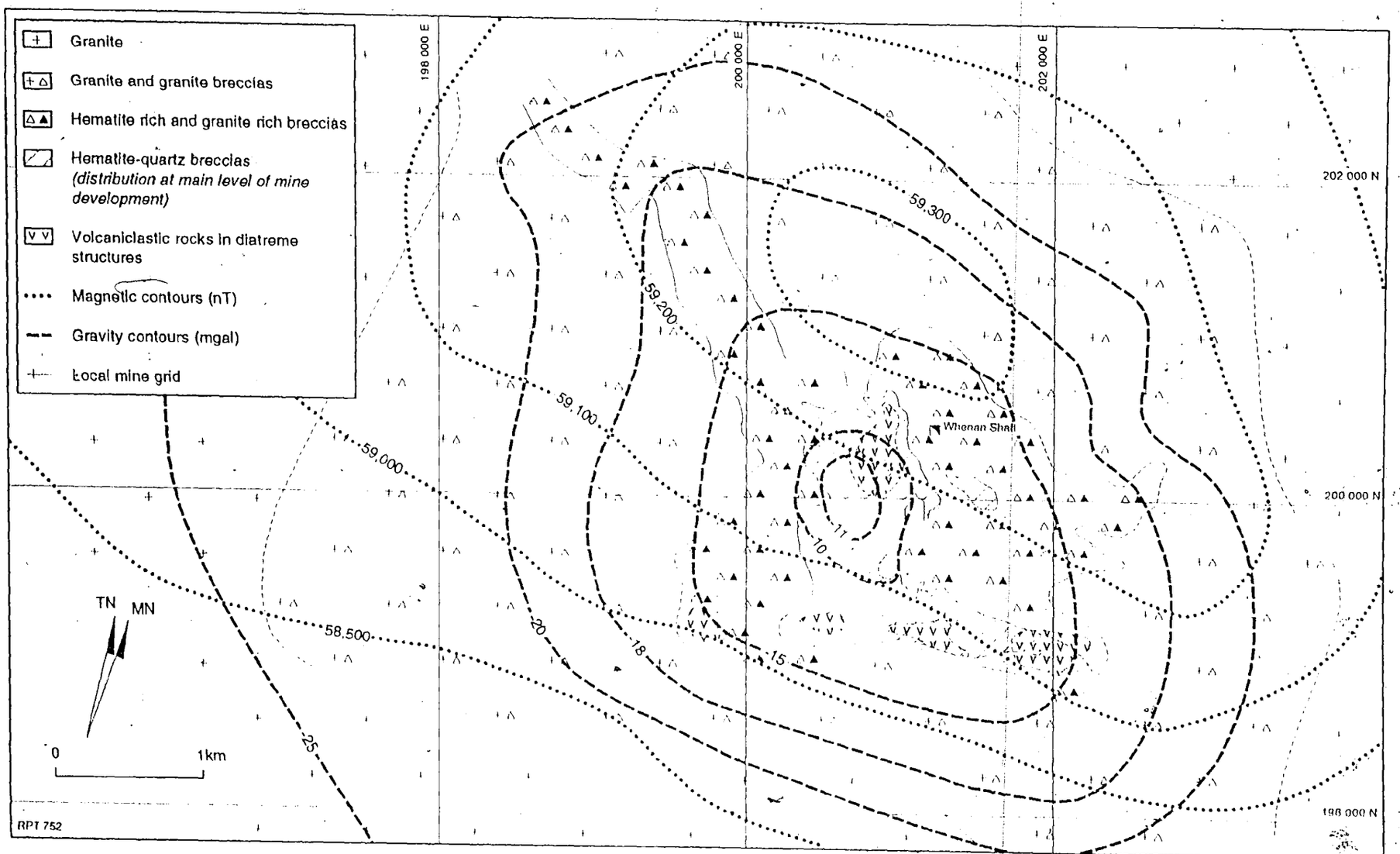
Granite
Granite and granite breccias
Hematite rich and granite rich breccias
Hematite-quartz breccias
(distribution at main level of mine development)
Volcaniclastic rocks in diatreme structures
Magnetic contours (nT)
Gravity contours (mgal)
Local mine grid
198 000 E
200 000 E
202 000 E
202 000 N
200 000 N
198 000 N
59,300
59,200
59,100
59,000
58,500
Whenan Shaft
11
10
20
18
15
25
TN
MN
0
1km
RPT 752

rich ore zones may contain up to ~2% F (Reeve et al., 1990). Sericite is also enriched in fluorine (up to 1%). Most hematite breccias are rich in Ba (0.5 to 5 wt%), present as disseminated barite grains and as barite veins.

2.3 Olympic Dam geophysical characteristics

The location of Olympic Dam coincides with positive anomalies in both the gravity and magnetic data (Figure 2.4). The gravity anomaly can be attributed to the dense hematite-rich breccias within the deposit (Roberts and Hudson, 1983). However, the magnetic anomaly cannot be accounted for by the rocks within the deposit, and presumably results from a large magnetic body beneath the current depth of drilling. Magnetite-rich breccias are present in minor quantities within the deposit, but may be more prevalent at depth. This suggestion provides a plausible explanation for the magnetic anomaly. It may also be caused by a large mafic/ ultramafic pluton beneath the deposit, as was suggested by Reeve et al. (1990). Mafic/ ultramafic dykes within the deposit, which appear to be coeval with formation of the breccias, may have been sourced from such a pluton. In Section 3.4 a firm correlation is established between the age of the Olympic Dam Breccia Complex and the age of the Gawler Range Volcanics. In this regard it is interesting to note that the Gawler Range Volcanic province is also underlain by a positive gravity anomaly (Creaser, 1989; Stewart and Foden, 1990). This suggests the presence of a major mafic intrusive at depth. Stewart and Foden (1990) interpret the inferred large mass of mafic rock to be the cause of the large scale crustal melting manifested by the Gawler Range Volcanics. Indeed gabbros contemporaneous with the Gawler Range Volcanics have been intersected in drill holes on the margins of the positive gravity anomaly (Stewart and Foden, 1990). The positive magnetic anomaly at Olympic Dam and the inference that it may represent an underlying mafic pluton is important to this study because there is strong independent evidence from Sm-Nd isotopic systematics (Chapter 7) that mafic/ ultramafic rocks or magmas played an integral part in ore genesis.

2.4 Problems to be addressed

From the description of the deposit it is clear that radiogenic isotope studies can help to solve some of the problems associated with deriving a genetic model for Olympic Dam. The first of these problems is unravelling the geochronology of the deposit. At the commencement of this project the age of brecciation was poorly constrained. A maximum age of ~1590 Ma is indicated by U-Pb zircon dating of the Roxby Downs Granite which hosts the breccias (Creaser,1989; Mortimer et al., 1988a). A minimum age of 676 ± 200 Ma is indicated by Rb-Sr dating of the Woomera Shale (Webb et al.,1983), a correlative of the Tregolana Shale which directly overlies the deposit. Sericite from hydrothermally altered granite wallrock has yielded Rb-Sr dates from ~1520

Ma down to 1315 Ma (Gustafson and Compston, 1979; Creaser, 1989). Rb-Sr ages for altered volcanics in the deposit range from ~1360 to 750 Ma (Gustafson and Compston, 1979).

Trueman et al. (1988) calculated a 1390 ± 100 Ma U-Pb discordia age from ion microprobe analyses of Olympic Dam pitchblende and interpreted this as a primary age for U mineralisation. I disagree with this interpretation because there is abundant evidence in the data of Trueman et al. (1988) and from this project that there has been a prolonged history (~1 Ga) of U/Pb mobility after primary mineralisation was emplaced. This calls into question the methods of data treatment employed by Trueman et al. (1988). Examination of this age calculation is important because the reported age led Oreskes and Einaudi (1990) to suggest that ore formation occurred 200 Ma after emplacement of the host granite. The pitchblende data are discussed in detail in Chapter 4.

Clearly, there were no precise constraints on the minimum age of the brecciation event, or whether economic mineralisation is temporally associated with the emplacement or brecciation of the host granite. Thus the specific geochronological questions to be answered in this project are:

1) What is the age of the Olympic Dam Breccia Complex? A minimum age can be obtained by dating felsic dykes (mentioned above) which intrude the complex.

2) What are the ages of Cu-U-Au-Ag mineralising events; i.e. is economic mineralisation coeval with the main brecciation episodes? This problem can be addressed by attempting to date hydrothermal minerals e.g. pitchblende and hydrothermal mantles around zircons by U-Pb methods, and by generating Sm-Nd and Rb-Sr isochron ages for ore and non-ore rock types.

3) What are the ages of the various intrusive bodies within the deposit e.g. diatremes, dolerites and felsic dykes? Do their ages imply any association with ore-forming or ore-modifying processes?

4) Which rock units from the regional geology have ages appropriate for their consideration as potential sources for Olympic Dam metals?

With the geochronology of the deposit established, the framework is in place for Sm-Nd and Rb-Sr studies. The specific problems investigated in this part of the project are:

1) What are the isotopic signatures of the different ore and alteration types? The ore and alteration types with similar isotopic signatures are interpreted as cogenetic, whereas different signatures imply different modes of origin or different modification processes.

This approach enables the identification of those rock types which are an integral part or product of the ore-forming process, and those rocks which are not necessarily involved in ore genesis.

2) Isotopic tracing of ore provenance. The isotopic signatures of various regional rock units which are thought to be plausible source rocks are compared with Olympic Dam ores. This enables the identification of the possible metal sources for Olympic Dam.

2.5 Sampling strategy

The sampling strategy undertaken to address these problems was to take ~5 geographically separate samples of each broad category of ore mineralogy and alteration mineralogy (see sample location map, Figure 2.5). The categories sampled are: pyrite-rich ore, chalcopyrite-rich ore, bornite/ chalcocite ore, barren hematite breccia, hematite-quartz breccia, leached hematite, sericitised granite, hematite altered granite, magnetite-rich breccias, and laminated hematite-quartz sediments. These rock types were sampled for geochemical comparisons and subsequent sample selection for isotopic analysis. The program of analysis for the ore types described is designed to test whether any given category may represent a modified version of a different (perhaps primary) category, or whether all categories are coeval.

The intrusive and intrusion-related rocks sampled are: altered mafic/ ultramafic dykes, dolerite dykes, ash-fall tuff from a diatreme zone, and felsic dykes. These were sampled for chemical analysis and dating. The regional samples taken for isotopic tracing work and dating are from the Roopena Volcanics, Pandurra Formation sandstone, magnetite mineralisation from the Acropolis prospect, and a post-deformation anorthositic gabbro from about 30 km east of the deposit. Each of these rock units is discussed in more detail in later sections of the thesis.

Figure 2.5 (overleaf). Mine scale sample location map. Symbols used for sample rock type are the same as used in figures pertaining to geochemistry of the deposit (Chapters 5 and 7).

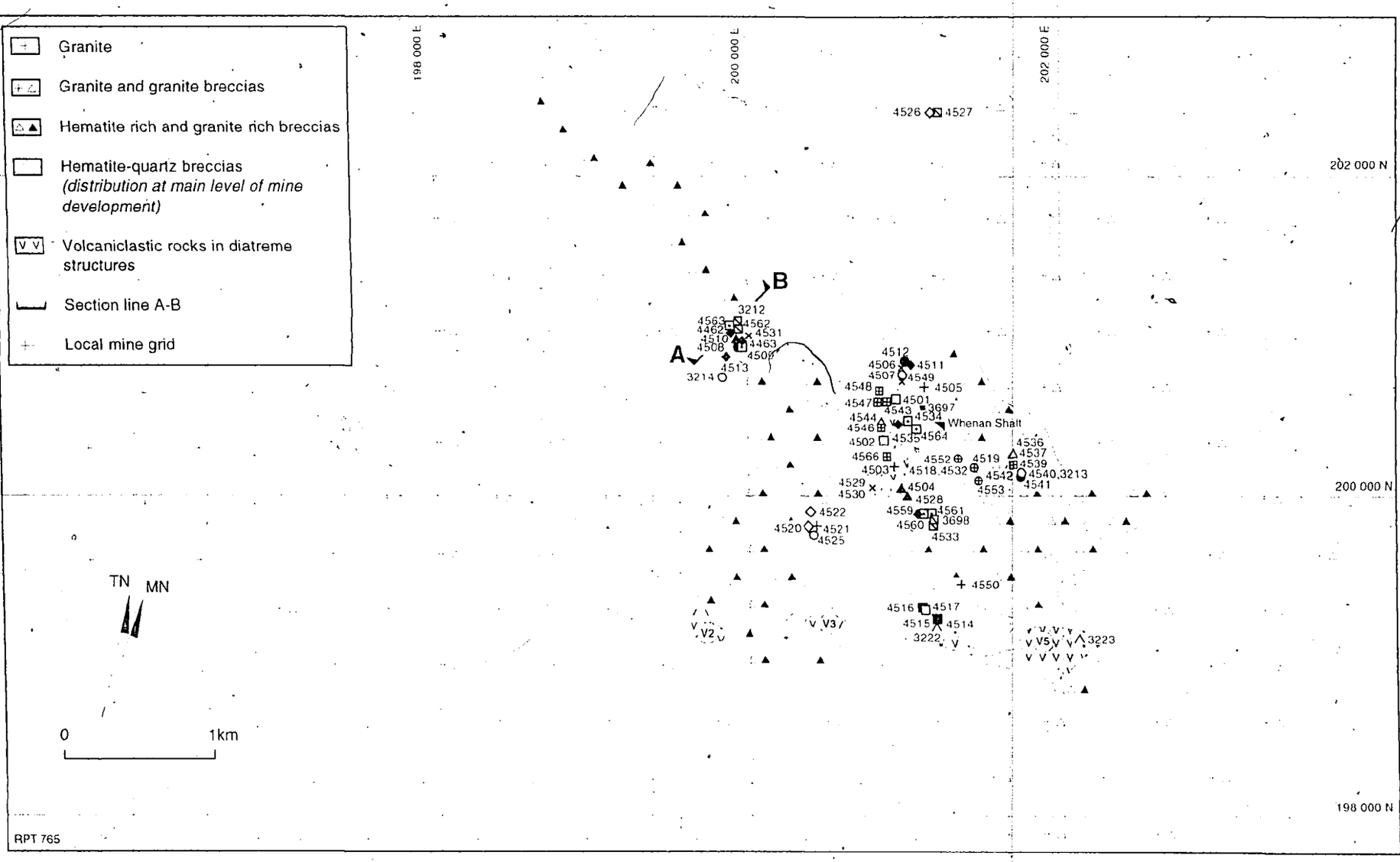
Granite
Granite and granite breccias
Hematite rich and granite rich breccias
Hematite-quartz breccias
(distribution at main level of mine development)
Volcaniclastic rocks in diatreme structures
Section line A-B
Local mine grid
198 000 E
200 000 E
202 000 E
202 000 N
200 000 N
198 000 N
A
B
Whenan Shaft
TN
MN
0
1km
RPT 765

3 U-Pb ZIRCON GEOCHRONOLOGY

3.1 Importance of the age of the deposit

Among recent workers there has been some consensus on the genesis of the Olympic Dam breccias and mineralisation. The models of Reeve et al. (1990) and Oreskes and Einaudi (1990, 1992) both invoke hydrothermal circulation associated with magmatism as the cause of brecciation and the precipitation of hematite and ore minerals. However, there are significant geochronological differences between the models of these workers and these have important implications for ore genesis. Reeve et al. (1990) proposed that the deposit formed in a subvolcanic environment as an integral part of a major regional magmatic event, the Gawler Range/ Hiltaba volcano-plutonic event. Oreskes and Einaudi (1990) suggested a magmatic heat source for the hydrothermal system but argued that the deposit formed approximately 200 Ma after the Gawler Range/ Hiltaba event, indeed at a time for which no magmatic events are known on the Gawler Craton. It is important to recognise the age relationships between the deposit and the rocks in which it occurs. The model of Reeve et al. (1990) implies that the tectonic setting giving rise to large scale crustal melting (the Gawler Range Volcanics/ Hiltaba supersuite granitoids) is the requisite environment for metallogenesis. In contrast, if the deposit is 200 Ma younger than its host rocks (Oreskes and Einaudi, 1990) the implication is that the host rocks are incidental to ore genesis except perhaps in a role as a trap for ore mineral precipitation. This would mean that the occurrence of Olympic Dam-type deposits need not be limited to the tectonic environments indicated by the rocks which host the Olympic Dam deposit itself.

The purpose of this chapter is to establish the age of the Olympic Dam Breccia Complex. It includes SHRIMP (Sensitive High Resolution Ion Microprobe) U-Pb dates on zircons extracted from igneous rocks which constrain the age of the breccia complex. These dates allow definite correlation between the deposit and regional events thereby more firmly establishing the tectonic environment of ore genesis. Knowledge of the age of the deposit also allows age corrections to be applied to data obtained from other radiogenic isotope systems (Rb-Sr and Sm-Nd; see Chapter 7) enabling their use as tracers of ore metal provenance.

This chapter also reports SHRIMP analyses of zircons from strongly altered samples of the host granite. The age determined for the granite from these samples agrees with that determined previously from samples of fresh granite (Creaser, 1989). Pb isotopic ratios from hydrothermal mantles around granitic zircons provide evidence of Pb and/ or U mobility throughout the history of deposit until recent times. Several rim analyses are interpreted as indicating an age for hydrothermal activity consistent with the constraints obtained from igneous zircons.

All of the Olympic Dam rocks dated in this study are strongly hydrothermally altered. This study shows that such rocks can be dated using the ion microprobe, as this tool allows identification of zircon grains with disturbed isotopic systematics and rejection of analyses of those grains from age calculations.

3.2 SHRIMP analytical procedures

Zircons were separated from ~1 kg samples using a combination of heavy-liquid and magnetic separation methods. Hand-picked zircons were mounted in epoxy and sectioned by polishing. U-Th-Pb analyses were performed on the ion microprobe SHRIMP at the Australian National University. The details of the method are set out in Compston et al. (1984) and Compston et al. (1986). A primary O_2^- beam is used to sputter material from a ~30 μm diameter area on the polished and carbon or gold-coated zircon. Each analysis is the mean of seven cycles through the Pb, Th and U masses. Pb/U ratios are referenced to a value of $^{206}Pb/^{238}U = 0.0928$ (equivalent to an age of 572 Ma) for the standard zircon SL3. Reproducibility of Pb/U for the standard analyses varied from 0.5 to 2.8%, and is combined with errors calculated from counting statistics to give the errors quoted in the data tables. Ages were calculated using radiogenic $^{207}Pb/^{206}Pb$ ratios weighted according to analytical precision and as such they are insensitive to uncertainties in Pb/U. The contribution of the hydride ^{206}PbH to the $^{207}Pb/^{206}Pb$ ratio was corrected where necessary by monitoring discrepancies between the $^{207}Pb/^{206}Pb$ ratio measured for the standard zircon and its known value. In most cases no correction was necessary and, where made, the corrections are small (e.g. 0.3% or a difference of ~0.0003 in $^{207}Pb/^{206}Pb$ ratio). Similarly, small excesses in ^{204}Pb counts, which affect common Pb corrections, were monitored by comparing the measured and expected ^{204}Pb counts for the standard zircon. Where necessary, corrections were applied to the analyses for the sample zircons. Quoted errors are at 95% confidence limits unless otherwise stated. In general, analyses showing evidence of ancient Pb loss are rejected in age calculations. Any further analyses which appear to be statistical outliers (with $^{207}Pb/^{206}Pb$ ratios more than two standard deviations from the mean) are rejected iteratively. The justification for this is that they represent analyses of grains which have undergone small amounts of ancient lead-loss. Ratios of radiogenic isotopes have been corrected for common Pb using the measured abundance of ^{204}Pb. The common Pb fraction (f206%; see data Tables) is generally low, with the exception of those zircons formed or altered by hydrothermal processes. Decay constants used are those recommended by Steiger and Jäger (1977).

3.3 Minimum age constraints

133 analyses of 114 grains were obtained from seven samples from Olympic Dam. The analyses are listed in Tables 3.1 to 3.9. Three samples are rocks which, according to

field relationships, provide minimum age constraints on the formation of the Olympic Dam Breccia Complex. In each case the field relationships and a brief rock description are included with the results. In addition, analyses of zircons obtained from three samples of altered Roxby Downs Granite are reported. These confirm the granite age of 1588 ± 4 Ma reported by Creaser (1989). This is a maximum age constraint for the formation of the breccias. The altered granite samples were analysed primarily in an attempt to directly date hydrothermal overgrowths on magmatic zircons. Although these rims do not yield unambiguous age information, their Pb isotopic ratios provide information about Pb, U and Th mobility, and about common Pb compositions. They also provide some direct evidence that the hydrothermal overgrowths formed at approximately the same time as is indicated for the brecciation event.

3.3.1 Felsic dykes

Samples RX3222 and RX3223 consist of sericite-altered porphyritic felsic fragments hand-picked from matrix-poor (<5%) intervals of volcaniclastic breccias intersected in vertical diamond drill holes RD32 and RD647 respectively. Sample localities are shown in Figure 2.5. Fragments were carefully inspected to avoid contamination by matrix material.

3.3.1.1 RX3222 (RD32, 364-367m)

Volcanic fragments were collected from the central zone of a 7 m interval of volcaniclastic breccia occurring within laminated hematite-quartz sandstones in the southeastern-central part of the deposit (Figure 2.5). The zone sampled is a matrix-poor shatter breccia with fragment sizes predominantly less than 5 cm, ranging up to ~10 cm. Towards the margins of the unit the volcanic fragments tend to be more dispersed and matrix-supported. The matrix consists of sericite-hematite altered granular felsic microclasts variably mixed with hematite-quartz sandstone in which layering has been disturbed or destroyed. In the volcanic fragments, original tabular plagioclase phenocrysts have been replaced by fine-grained sericite. Zircons occur as discrete euhedra in the groundmass which consists of fine-grained intergrowths of sericite + quartz ± hematite, probably the alteration products of a primary glassy groundmass. Many volcanic fragments, especially those dispersed in sandy matrix, have ragged and delicate outlines with numerous millimetre-scale apophyses.

This volcaniclastic unit lies approximately 50 m below the unconformity between the breccia complex and the overlying Tregolana Shale. It is the uppermost of three such units occurring within a several hundred metre thick disrupted sequence of finely laminated hematite-quartz sandstones underlain by intraformational rubble breccias. The hematite-quartz sandstones are interpreted to represent the surficial (crater-lake) product of the venting hydrothermal system at Olympic Dam (Reeve et al., 1990). They contain

Plate 2 Felsic dykes. **A)** RD32, 380m. Sericitised porphyritic fragmental felsic rock occurs in the left of the photograph. Finely laminated hematite-quartz sandstone occupies the right three metres of drillcore. The central metre (right of pen) contains a sheet-like zone of felsic fragments which is transgressive to the laminae in the hematite-quartz sandstone, illustrating the intrusive nature of the felsic rocks. The laminae are disturbed immediately around the felsic fragments but are coherent within centimetres of this zone.

B) Sericitised felsic fragmental dyke (central metre of drillcore) emplaced into heterolithic breccias. Elongate delicately shaped fragments attest to *in situ* quench fragmentation. "Inclusions" of hematite breccia within zones of jigsaw fit of felsic fragments (centre-left) also indicate an intrusive origin for the felsics. The dykes in A) and B) are interpreted to result from the emplacement of felsic magma into wet unconsolidated hematitic sediments and breccias, causing autobrecciation and quench fragmentation of the magma.

A

B

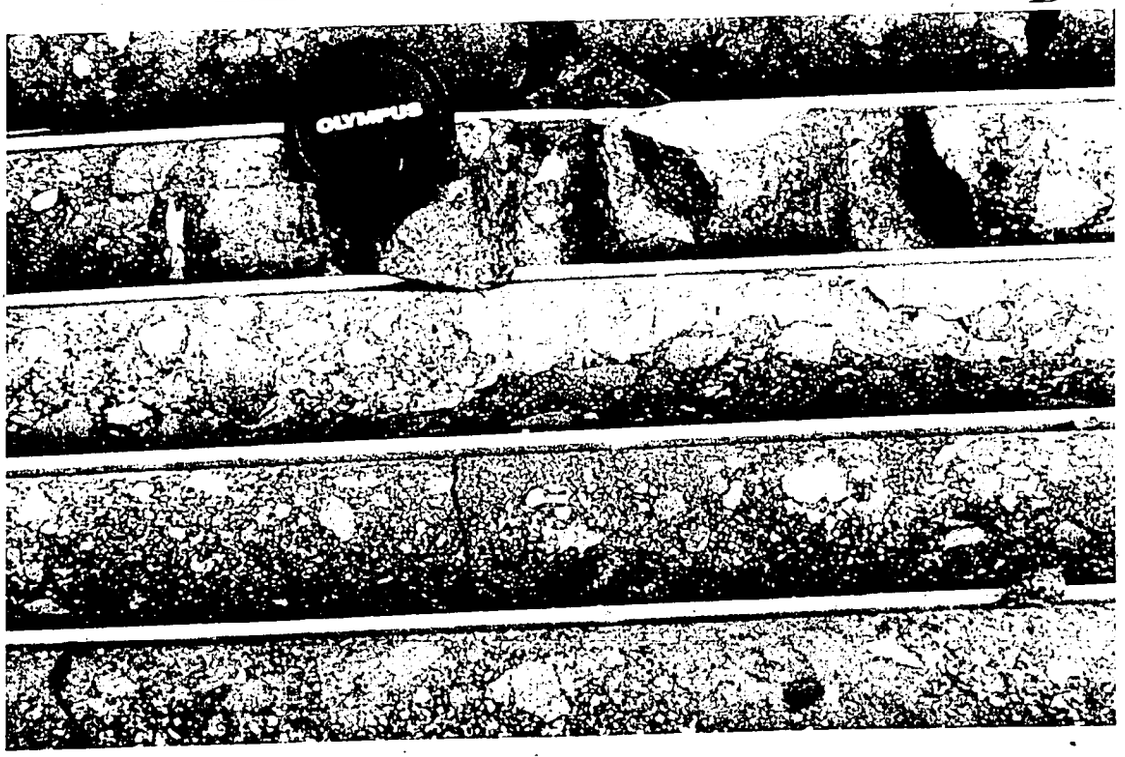

both clastic hematite and interstitial microlaths of hematite indicative of in situ precipitation. The latter are consistent with the hydrothermal input of iron to the crater lake. Trace element and Nd isotopic data provide evidence to support the interpretation that these sedimentary rocks are an integral part of the Olympic Dam system (Johnson and Cross, 1991b; Chapter 7). The underlying rubble breccias and similar rocks elsewhere within the Olympic Dam Breccia Complex have been interpreted by Reeve et al. (1990) to be subsided remnants of the crater-lake deposits.

It is unlikely that the delicate outlines of the felsic fragments would have been preserved if the volcaniclastic units were emplaced by mass transport processes, so an epiclastic origin for these rocks is considered implausible. Significantly, sandstone in the marginal facies of these volcanic units has been reworked, largely homogenised, and thoroughly mixed with volcanic fragments, but beyond the limits of volcanic fragment dispersal the sandstone is well bedded and comparatively undisrupted (although locally contorted or microfaulted). Dilational fabrics, other than late-stage crackle veining, are restricted to the volcaniclastic zones. This rules out the possibility that the felsic rocks were fragmented as part of the main brecciation episodes at Olympic Dam. The volcaniclastic zones show no evidence of significant particle attrition or cataclasis, so selective fault-related brecciation of felsic dykes is also an implausible explanation for their origin.

The fragment morphologies and general fabrics of the volcaniclastic units are distinctively hydroclastic. Locally, narrow sheet-like zones of fragmental felsics cross-cut sandstones in which bedding is preserved (Plate 2), supporting an intrusive mechanism of emplacement. The overall characteristics of these felsic rocks suggest that they formed by autobrecciation of feldspar-phyric magmas as they intruded (and locally fluidised) wet unconsolidated sediments. Intrusive volcaniclastics (fragmental dykes) of this type have been referred to as peperites (see Fisher and Schmincke, 1984; and Cas and Wright, 1987 for brief reviews, and Thornton, 1989 for a concise definition), and this term was adopted for Olympic Dam felsic fragmental dykes by Reeve et al. (1990). The emplacement of these peperites prior to the lithification of some of the reworked surficial ejecta of the Olympic Dam hydrothermal system provides a minimum age constraint for the onset of the hematite-producing hydrothermal activity.

About ninety zircon grains were prepared in Mount Z-737. Most of the grains are clear euhedral crystals typically ~100 μm long by ~50 μm across. Many show weak internal zoning. Twenty-one analyses were made on eighteen grains and these are presented in Table 3.1. All have very low levels of common Pb (f206 generally <0.4%; see Table 3.1) and are therefore insensitive to the common Pb composition chosen. In this case average crustal Pb (Cumming and Richards, 1975) of 1590 Ma was used. All analyses combined yield a weighted mean $^{207}Pb/^{206}Pb$ age of 1593 ± 7 Ma with scatter in excess of that expected from analytical uncertainties alone. Analyses 18-1 and 26-1 have

Table 3.1. Ion microprobe data for dyke sample RX3222.

Analysis No.	U (ppm)	Th (ppm)	^{204}Pb (ppb)	f206[a] (%)	$^{204}Pb/^{206}Pb$	$^{208}Pb/^{206}Pb$	$^{206}Pb/^{238}U$	$^{207}Pb/^{235}U$	$^{207}Pb/^{206}Pb$	$^{207}Pb/^{206}Pb$ age ± 1σ (Ma)
9.1	266	167	15	0.41	0.000257	0.184	0.2510 ± 48	3.35 ± 0.08	0.0969 ± 11	1566 ± 21
10.1	205	136	12	0.40	0.000250	0.199	0.2699 ± 52	3.61 ± 0.09	0.0970 ± 15	1567 ± 29
11.1	378	315	10	0.18	0.000113	0.250	0.2705 ± 51	3.69 ± 0.08	0.0990 ± 7	1605 ± 13
12.1	195	124	4	0.14	0.000088	0.189	0.2583 ± 50	3.48 ± 0.08	0.0977 ± 11	1581 ± 21
13.1	169	112	5	0.20	0.000122	0.200	0.2634 ± 51	3.55 ± 0.08	0.0977 ± 11	1580 ± 22
14.1	169	125	3	0.13	0.000079	0.210	0.2544 ± 41	3.45 ± 0.08	0.0984 ± 13	1594 ± 25
15.1	406	562	23	1.00	0.000626	0.258	0.1056 ± 20	1.38 ± 0.03	0.0948 ±13	1524 ± 27
16.1	185	115	6	0.24	0.000153	0.185	0.2661 ± 51	3.59 ± 0.08	0.0978 ± 10	1583 ± 20
17.1	228	147	18	0.47	0.000295	0.187	0.3062 ± 21	4.14 ± 0.06	0.0980 ± 11	1587 ± 21
18.1	210	130	18	0.53	0.000331	0.182	0.3000 ± 20	3.97 ± 0.05	0.0960 ± 10	1548 ± 19
19.1	190	117	10	0.30	0.000188	0.184	0.3159 ± 22	4.35 ± 0.05	0.0998 ± 10	1620 ± 18
17.2	270	181	5	0.14	0.000085	0.193	0.2724 ± 55	3.71 ± 0.08	0.0988 ± 6	1601 ± 11
19.2	200	128	8	0.27	0.000169	0.184	0.2645 ± 53	3.59 ± 0.08	0.0985 ± 9	1595 ± 17
20.1	213	137	6	0.18	0.000110	0.183	0.2874 ± 58	3.87 ± 0.09	0.0977 ± 7	1581 ± 14
21.1	212	162	4	0.12	0.000072	0.217	0.3014 ± 61	4.10 ± 0.09	0.0987 ± 7	1599 ± 13
22.1	166	111	5	0.19	0.000121	0.196	0.3006 ± 60	4.05 ± 0.09	0.0977 ± 7	1580 ± 13
9.2	330	261	3	0.06	0.000038	0.233	0.2935 ± 18	3.97 ± 0.03	0.0981 ± 4	1588 ± 9
23.1	169	113	5	0.17	0.000107	0.195	0.2908 ± 19	3.98 ± 0.04	0.0992 ± 8	1609 ± 16
24.1	273	179	0	0.01	0.000004	0.196	0.2967 ± 18	4.03 ± 0.03	0.0984 ± 5	1594 ± 9
25.1	124	71	6	0.29	0.000179	0.170	0.3027 ± 119	4.10 ± 0.18	0.0981 ± 13	1589 ± 25

Table 3.1 continued

Analysis No.	U (ppm)	Th (ppm)	^{204}Pb (ppb)	f206[a] (%)	$^{204}Pb/^{206}Pb$	$^{208}Pb/^{206}Pb$	$^{206}Pb/^{238}U$	$^{207}Pb/^{235}U$	$^{207}Pb/^{206}Pb$	$^{207}Pb/^{206}Pb$ age ± 1σ (Ma)
26.1	172	116	4	0.13	0.000081	0.196	0.2998 ± 118	4.13 ± 0.17	0.0999 ± 7	1623 ± 13
14.2	154	107	3	0.13	0.000081	0.203	0.2996 ± 118	4.07 ± 0.17	0.0985 ± 9	1595 ± 18

[a] Denotes percentage of common ^{206}Pb in the total measured ^{206}Pb

$^{207}Pb/^{206}Pb$ values which lie more than 2σ away from the weighted mean. When these points are rejected the excess scatter is removed and an age of 1592 ± 8 Ma results. This is the preferred age for this sample.

Figure 3.1 is a concordia plot displaying the analyses for RX3222. The reverse discordant points were analysed in a separate session to those showing slight normal discordance, which suggests that the reverse discordance may be an artifact of run conditions and may relate to the different conductive coatings on the standard (carbon then gold, with a carbon-coated sample) between the two days of data collection. The $^{207}Pb/^{206}Pb$ ratios are unaffected by uncertainties in the Pb/U calibration.

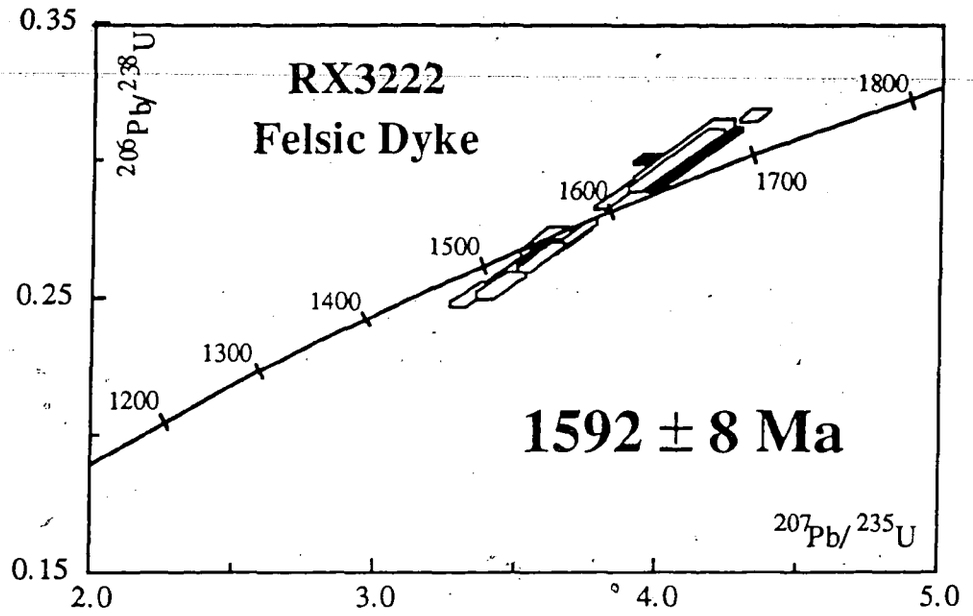

Figure 3.1 Concordia diagram for dyke sample RX3222. Analyses rejected from the age calculation are shaded black (one sigma error boxes). 1592 ± 8 Ma (weighted mean $^{207}Pb/^{206}Pb$, 95% confidence) is a minimum age constraint on the hematite-quartz sandstone unit intruded by the dyke. As such, this date constrains the age of the onset of hematite deposition at Olympic Dam (see text).

Blocks of hematite-quartz sandstone similar to the sandstone intruded by the felsic dyke are found locally within some of the main breccia bodies of the deposit. Some of these blocks contain chalcopyrite-mineralised, altered granitic bombs which deform the sedimentary laminae below them. The surrounding hematite-quartz sandstone is unmineralised. If it is assumed that the hematite-quartz sandstone observed as blocks was deposited contemporaneously with the sequence of apparently identical sedimentary rocks intruded by the felsic dyke from which RX3222 was obtained, then 1592 ± 8 Ma may also represent a minimum age constraint for the onset of chalcopyrite mineralisation.

This supports the proposition that the metals of economic interest were introduced at the same time as the iron.

3.3.1.2 RX3223 (RD647, 474-478m)

These volcanic fragments were collected from the central part of a 30 m interval of volcaniclastics occurring within Cu (-U-Au-Ag) mineralised hematitic breccias approximately 900 m east of RX3222 (Figure 2.5). In general they show more intense hydrothermal alteration than fragments comprising RX3222. They are commonly more brownish (weakly hematitic), contain less groundmass quartz, and sericite ± hematite replacement of plagioclase is more conspicuous. Some fragments also have narrow (<5 mm) bleached rinds. Otherwise they are petrographically and geochemically similar to RX3222 fragments, and are believed to belong to the same magmatic suite.

The unit sampled is the central one of five prominent volcaniclastic units intersected in diamond drill hole RD647, and it lies approximately 120 m below the breccia complex-Tregolana Shale unconformity. It is directly overlain by 15 m of medium-grained hematite breccia containing bornite-chalcocite + minor chalcopyrite mineralisation averaging approximately 2.5% Cu. A 6 m transition zone of heterolithic hematite-volcanic breccia contains 1 m intervals assaying from 1500 to 2000 ppm Cu, and 0.3 to 1.6 ppm Au, whereas the matrix-poor zones sampled are only slightly anomalous in Cu (~50-100 ppm). The heterolithic and/or matrix-rich margins of several other volcaniclastic units are more strongly mineralised, with assays for 1 m intervals ranging from 0.2 to 4% Cu, and from 0.03 to 0.1% U (typical Olympic Dam Cu-U ore contains 0.06 to 0.08% U).

All of the principal volcaniclastic units in RD647 have fabrics and clast morphologies comparable to those described for volcaniclastics in RD32 (e.g. RX3222). Granitic breccias overlying, intercalated with, and underlying the volcaniclastics show extreme disaggregation and patchy fluidal layering of varying orientations. Similar wispy and diffuse layering occurs in the associated hematitic breccias, and the matrix in framework-supported granite breccias completely underlying the volcaniclastics also exhibits highly irregular fluidal layering.

The volcaniclastics themselves are interpreted to be peperites, i.e. dykes which underwent quench fragmentation as they intruded and mixed with wet, unconsolidated, fine- to medium-grained hydrothermal breccias (Plate 2 illustrates peperite fabric). The host breccias were locally fluidised and/or further disaggregated by this phreatomagmatic activity. A significant proportion of the finer-grained hematite-sericite matrix in the heterolithic parts of the peperites, and especially that within the framework-supported volcanic-rich parts, is sulphide-poor. Gradational textures with granulated margins of larger (pyro-)clasts suggest that this matrix material is probably hydroclastic ash, rapidly

Table 3.2. Ion microprobe data for felsic dike sample RX3223

Analysis No.	U (ppm)	Th (ppm)	^{204}Pb (ppb)	f206[a] (%)	$^{204}Pb/^{206}Pb$	$^{208}Pb/^{206}Pb$	$^{206}Pb/^{238}U$	$^{207}Pb/^{235}U$	$^{207}Pb/^{206}Pb$	207Pb/206Pb age ± 1σ (Ma)
1.1	177	153	10	0.41	0.000256	0.256	0.2488 ± 48	3.30 ± 0.08	0.0963 ± 14	1554 ± 27
2.1	283	173	15	0.44	0.000277	0.195	0.2211 ± 42	2.90 ± 0.07	0.0951 ± 10	1529 ± 20
3.1	230	197	8	0.26	0.000160	0.259	0.2516 ± 48	3.38 ± 0.08	0.0975 ± 12	1577 ± 23
4.1	269	215	10	0.27	0.000168	0.237	0.2524 ± 48	3.44 ± 0.08	0.0988 ± 13	1601 ± 19
5.1	222	172	13	0.53	0.000334	0.194	0.1981 ± 38	2.60 ± 0.06	0.0953 ± 13	1535 ± 25
6.1	268	220	7	0.25	0.000158	0.256	0.1836 ± 35	2.46 ± 0.06	0.0972 ± 11	1570 ± 21
7.1	234	155	7	0.25	0.000157	0.195	0.2240 ± 43	2.94 ± 0.07	0.0953 ± 14	1533 ± 27
8.1	189	160	11	0.47	0.000295	0.252	0.2366 ± 45	3.20 ± 0.08	0.0982 ± 13	1591 ± 25
27.1	213	149	17	0.54	0.000338	0.203	0.2684 ± 47	3.60 ± 0.12	0.0973 ± 24	1573 ± 48
28.1	216	150	10	0.31	0.000191	0.196	0.2736 ± 50	3.67 ± 0.27	0.0973 ± 67	1573 ± 135
29.1	380	294	21	0.40	0.000253	0.236	0.2488 ± 41	3.25 ± 0.07	0.0947 ± 11	1521 ± 22
30.1	196	123	13	0.46	0.000286	0.182	0.2658 ± 46	3.53 ± 0.09	0.0963 ± 17	1554 ± 33
31.1	384	325	4	0.07	0.000041	0.254	0.2805 ± 47	3.85 ± 0.07	0.0995 ± 8	1615 ± 15
32.1	205	158	15	0.48	0.000299	0.228	0.2764 ± 49	3.65 ± 0.10	0.0958 ± 17	1543 ± 34
33.1	191	135	13	0.47	0.000293	0.204	0.2763 ± 48	3.60 ± 0.10	0.0944 ± 18	1516 ± 36
34.1	301	365	25	0.58	0.000362	0.262	0.2685 ± 46	3.51 ± 0.09	0.0948 ± 17	1523 ± 34
36.1	267	177	18	0.43	0.000270	0.194	0.2849 ± 50	3.87 ± 0.11	0.0985 ± 20	1597 ± 39
37.1	204	124	9	0.31	0.000193	0.186	0.2650 ± 48	3.68 ± 0.11	0.1006 ± 22	1635 ± 42

[a] Denotes the percentage of common ^{206}Pb in the total measured ^{206}Pb

altered during the phreatomagmatic activity accompanying peperite emplacement. In the hematite breccias, copper sulphides occur both in the clasts and disseminated throughout the matrix. Thin bornite rims have also been observed on several hematite clasts in breccias adjacent to the peperites. In the heterolithic peperites, sulphides tend to be confined to the hematite clasts and hematitic matrix. These features, and the Cu-U grade distribution described above, strongly suggest that the RD647 peperites intruded pre-existing Cu-U mineralisation.

If the interpretation that these peperites are fragmental intrusives is valid, and they do indeed postdate the Cu-U(-Au) mineralisation in their host breccias, then their age provides a definitive minimum age for the onset of Olympic Dam ore genesis. The altered nature of the this sample and RX3222 suggests that they do not post-date circulation of hydrothermal fluids at Olympic Dam and therefore should probably be regarded as coeval with the hydrothermal system.

Ninety zircons from RX3223 were prepared in Mount Z-737. They are similar in morphology to those in RX3222, but show a pale brown colour in many of the grains in contrast to the very clear grains in the previous sample. Single analyses were made of eighteen grains (Table 3.2).

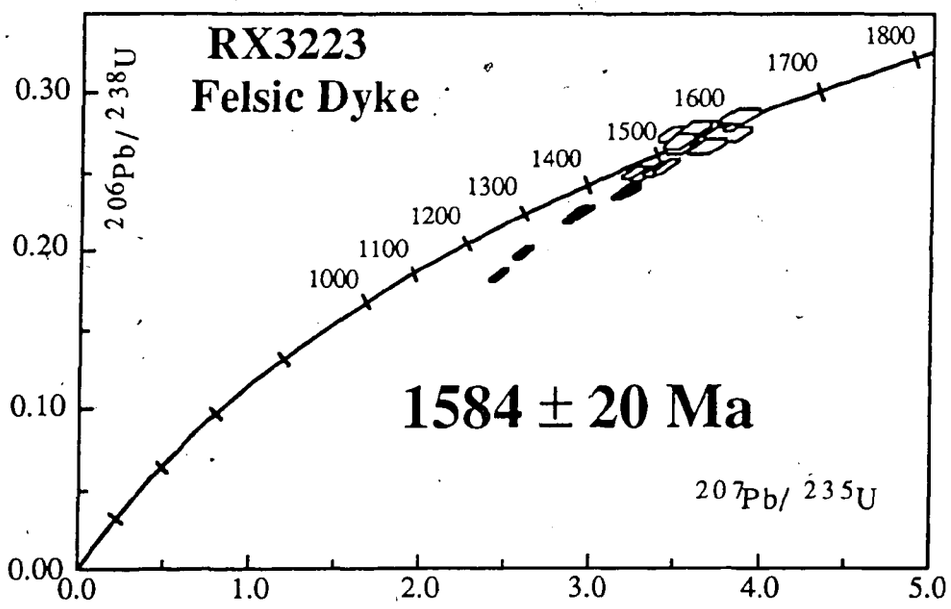

Figure 3.2 Concordia diagram for dyke sample RX3223. Analyses rejected from the age calculation are shaded black (one sigma error boxes). 1584 ± 20 Ma (weighted mean $^{207}Pb/^{206}Pb$, 95% confidence) constrains the minimum age of the hematitic breccias which the dyke intrudes, and possibly also the Cu-U mineralisation hosted by the breccias (see text).

Figure 3.2 (concordia diagram) shows that several analyses having a moderate degree of discordance have lower $^{207}Pb/^{206}Pb$ ratios than the main group of concordant or near-concordant analyses. The zircons from RX3223 also have higher levels of common Pb than RX3222 (f206%, see Tables 3.1 and 3.2). These features indicate that the zircons from RX3223 have more disturbed isotopic systematics than those from RX3222, and this correlates with the observation that this sample is more strongly altered than RX3222. The weighted mean $^{207}Pb/^{206}Pb$ age for this sample, excluding the four most discordant points (2.1, 5.1, 6.1 and 7.1) on the criterion of ancient Pb loss, is 1577 ± 16 Ma. This age has scatter well in excess of that expected from analytical error, and much of the scatter rests with point 29.1 for which the $^{207}Pb/^{206}Pb$ value lies more than 2σ away from the weighted mean ratio. If this analysis is rejected, the calculated age is 1584 ± 20 Ma. This age still has scatter slightly in excess of that expected from analytical uncertainties although no further points warrant deletion as outliers. The excess scatter is assumed to result from small amounts of ancient disturbance. The preferred age for this sample is therefore 1584 ± 20 Ma (n=13). This age is indistinguishable from that of the other dyke sample RX3222 (1592 ± 8 Ma).

3.3.2 Diatreme tuff

A third minimum age constraint for the Olympic Dam breccias is provided by a date from two samples (RX2820 and RX4544) taken from a tuff horizon within the diatreme designated as V1 in Figure 2.2. The same zone was described by Oreskes and Einaudi (1990) as a down-faulted package of volcaniclastic rocks which they interpret as being older than the breccia complex. The interpretation of the sampled horizon as a tuff within a diatreme is critical to the significance of the date obtained for these samples. The reasons for interpreting these rocks as a diatreme have been discussed in detail in Section 2.2.3.2.

Samples RX2820 and RX4544 were taken from a band of well-sorted ash-fall tuff approximately 20 cm thick occurring within volcanogenic conglomerates. The ash fragments are angular, have irregular shapes, and generally range in size from 0.5 to 1 mm. Clear, unstrained, apparently volcanic quartz grains are abundant. They are typically subhedral fragments, perhaps of larger euhedral grains. The non-quartz fragments are strongly altered, with sericite the dominant alteration phase, and lesser chlorite and hematite. Accessory zircon is also present within these fragments. Tabular sericite aggregates (50 to 100 μm long by ~10 μm across), probably pseudomorphing plagioclase, are common. They display intersertal textures reminiscent of those commonly found in the groundmass of volcanic rocks. A small proportion of the clasts appear to be lithic fragments of sericite-altered granite. The volcanic quartz fragments and the relict fine-grained igneous texture within many of the other fragments, coupled

with the angular margins of the fragments, are the criteria used to classify this rock as a tuff.

Zircons obtained from two samples of the tuff were mounted and analysed separately. The preferred age quoted below is derived by combining the data from the duplicate samples.

3.3.2.1 RX2820

Twenty-one analyses of sixteen grains yielded Proterozoic ages; five analyses of morphologically distinctive zircon gave Archaean (2880 Ma) ages. The Proterozoic grains analysed are euhedral, clear and unzoned, or pale brown and weakly zoned. They range in size and shape from squat grains ~50 to 100 μm by 200 μm, to more elongate grains ~100 by 300 μm. Analytical data are presented in Table 3.3. Analyses 6.1, 20.2 and 21.1 were rejected from the age calculation due to ancient Pb loss, resulting in a weighted mean $^{207}Pb/^{206}Pb$ age of 1597 ± 9 Ma.

The Archaean grains are brown, strongly zoned and rounded, and are never observed with clear Proterozoic rims. Consequently contamination during mineral processing, rather than zircon inheritance, was suspected. RX2820 was the only sample received in prepared form, having been crushed in an industrial laboratory. Sample RX4544 was collected from precisely the same locality to resolve the question of whether the Archaean grains are a contaminant in RX2820, or are inherited from an older source. Results for RX4544 (below) indicate that these Archaean grains are a contaminant, and for this reason the analyses with Archaean ages are not included in Table 3.3.

3.3.2.2 RX4544

RX4544 was processed entirely in the sample preparation laboratories at the Australian National University. Thirteen analyses were made on eleven grains, primarily to check whether the Archaean grains analysed in RX2820 represent contamination during sample processing. All zircons from RX4544 are similar in morphology and size to the Proterozoic grains described for RX2820. A disproportionate number of dark, strongly zoned zircons were analysed because these most closely resembled the Archaean grains observed in RX2820. None yielded Archaean ages; their brown colour presumably results from metamictisation due to their relatively high U contents (Table 3.3). The absence of Archaean zircons in this sample confirms that the Archaean grains in RX2820 represent a contaminant.

Analyses 2.1, 3.1, 4.1 and 10.1 were rejected from age calculation because of evidence for ancient Pb loss. The remaining nine analyses yield a weighted mean $^{207}Pb/^{206}Pb$ age of 1599 ± 19 Ma and therefore verify that the 1597 ± 9 Ma date obtained from RX2820 is

Table 3.3. Ion microprobe data for diatreme tuff samples RX2820 and RX4544

Analysis No.	U (ppm)	Th (ppm)	^{204}Pb (ppb)	f206[a] (%)	$^{204}Pb/^{206}Pb$	$^{208}Pb/^{206}Pb$	$^{206}Pb/^{238}U$	$^{207}Pb/^{235}U$	$^{207}Pb/^{206}Pb$	$^{207}Pb/^{206}Pb$ age ± 1σ (Ma)
Diatreme tuff sample RX2820										
1.1	149	94	5	0.25	0.000159	0.191	0.2471 ± 52	3.30 ± 0.10	0.0969 ± 21	1564 ± 40
2.1	296	161	4	0.10	0.000062	0.165	0.2604 ± 55	3.51 ± 0.16	0.0977 ± 38	1581 ± 74
2.2	296	213	6	0.16	0.000101	0.217	0.2419 ± 50	3.27 ± 0.08	0.0979 ± 10	1585 ± 19
3.1	395	621	4	0.08	0.000053	0.505	0.2288 ± 47	3.09 ± 0.07	0.0981 ± 8	1588 ± 15
4.1	380	220	5	0.09	0.000054	0.177	0.2554 ± 53	3.47 ± 0.08	0.0984 ± 7	1594 ± 12
4.2	549	402	0	0.00	0.000000	0.226	0.2334 ± 48	3.20 ± 0.07	0.0995 ± 4	1614 ± 8
5.1	163	100	0	0.02	0.000014	0.185	0.2539 ± 53	3.49 ± 0.09	0.0996 ± 12	1617 ± 22
6.1	394	193	44	1.26	0.000792	0.219	0.1622 ± 33	2.24 ± 0.06	0.1000 ± 13	1623 ± 23
10.1	263	127	1	0.04	0.000024	0.148	0.2510 ± 52	3.40 ± 0.10	0.0981 ± 19	1588 ± 37
11.1	302	174	1	0.02	0.000011	0.175	0.2581 ± 53	3.47 ± 0.08	0.0975 ± 9	1578 ± 17
12.1	209	131	5	0.19	0.000118	0.197	0.2555 ± 53	3.48 ± 0.09	0.0989 ± 13	1603 ± 25
13.1	202	109	1	0.05	0.000032	0.163	0.2644 ± 55	3.58 ± 0.12	0.0983 ± 25	1592 ± 47
14.1	457	327	3	0.04	0.000026	0.219	0.2575 ± 53	3.45 ± 0.08	0.0971 ± 8	1568 ± 16
15.1	315	173	6	0.14	0.000087	0.175	0.2478 ± 51	3.36 ± 0.08	0.0983 ± 7	1591 ± 13
15.2	324	212	6	0.12	0.000077	0.203	0.2610 ± 54	3.58 ± 0.09	0.0995 ± 11	1615 ± 20
16.1	159	68	1	0.06	0.000035	0.126	0.2680 ± 57	3.58 ± 0.15	0.0968 ± 32	1564 ± 63
17.1	198	116	1	0.05	0.000033	0.175	0.2502 ± 52	3.40 ± 0.12	0.0984 ± 26	1595 ± 50
18.1	442	333	3	0.05	0.000033	0.227	0.2361 ± 49	3.16 ± 0.12	0.0970 ± 28	1567 ± 54

Table 3.3 continued

Analysis No.	U (ppm)	Th (ppm)	^{204}Pb (ppb)	f206[a] (%)	$^{204}Pb/^{206}Pb$	$^{208}Pb/^{206}Pb$	$^{206}Pb/^{238}U$	$^{207}Pb/^{235}U$	$^{207}Pb/^{206}Pb$	$^{207}Pb/^{206}Pb$ age ± 1σ (Ma)
20.1	242	135	2	0.06	0.000035	0.168	0.2602 ± 54	3.52 ± 0.12	0.0981 ± 23	1588 ± 45
20.2	315	216	10	0.28	0.000177	0.225	0.2037 ± 42	2.65 ± 0.06	0.0942 ± 9	1512 ± 18
21.1	4377	1049	529	1.72	0.001080	0.142	0.1284 ± 26	1.21 ± 0.03	0.0685 ± 4	884 ± 13
Diatreme tuff sample RX4544										
1.1	221	154	4	0.13	0.000078	0.210	0.2838 ± 81	3.86 ± 0.19	0.0985 ± 37	1596 ± 72
2.1	690	281	29	0.42	0.000261	0.188	0.1866 ± 52	2.33 ± 0.07	0.0905 ± 8	1436 ± 17
3.1	1223	419	63	1.06	0.000664	0.183	0.0895 ± 25	0.97 ± 0.03	0.0784 ± 9	1157 ± 23
4.1	367	160	13	0.28	0.000173	0.145	0.2428 ± 68	3.16 ± 0.10	0.0944 ± 12	1515 ± 24
4.2	193	94	1	0.02	0.000013	0.145	0.3026 ± 86	4.14 ± 0.13	0.0992 ± 9	1608 ± 17
5.1	222	167	13	0.40	0.000249	0.223	0.2727 ± 77	3.62 ± 0.17	0.0963 ± 31	1553 ± 62
5.2	205	137	2	0.07	0.000042	0.199	0.2852 ± 81	3.87 ± 0.13	0.0983 ± 14	1592 ± 27
6.1	193	123	9	0.32	0.000200	0.186	0.2780 ± 79	3.72 ± 0.13	0.0969 ± 15	1565 ± 29
7.1	203	165	0	0.00	0.000000	0.239	0.3006 ± 85	4.12 ± 0.12	0.0994 ± 8	1613 ± 15
8.1	281	202	2	0.05	0.000034	0.208	0.3020 ± 85	4.07 ± 0.13	0.0977 ± 14	1581 ± 26
9.1	181	109	2	0.08	0.000048	0.172	0.2869 ± 81	3.91 ± 0.14	0.0989 ± 19	1603 ± 35
10.1	719	341	18	0.22	0.000136	0.182	0.2106 ± 59	2.58 ± 0.08	0.0888 ± 7	1399 ± 14
11.1	169	148	2	0.08	0.000047	0.255	0.2881 ± 82	3.91 ± 0.13	0.0985 ± 13	1596 ± 24

[a] Denotes the percentage of common ^{206}Pb in the total measured ^{206}Pb

an age of the tuff rather than an age for contaminant grains. On the basis that the two samples are duplicates and that their ages are statistically identical, it is reasonable to pool the data from these samples.

3.3.2.3 Pooled data: RX2820 and RX4544

When the data are pooled and the same analyses deleted as for the individual dates, the twenty-seven points yield a weighted mean $^{207}Pb/^{206}Pb$ age of 1597 ± 8 Ma. Data for the two samples are presented in Figure 3.3.

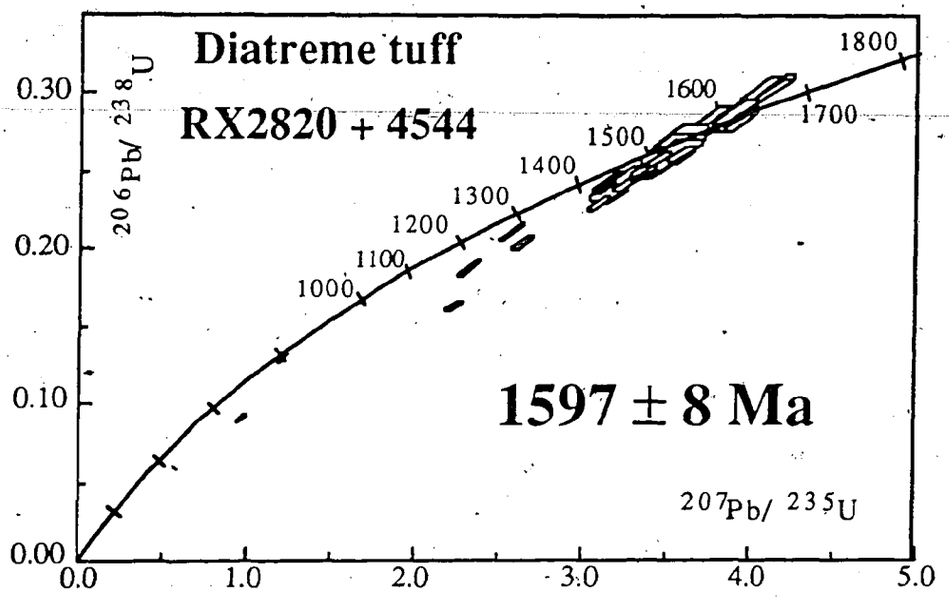

Figure 3.3 Concordia diagram for the pooled data from duplicate diatreme tuff samples RX2820 and RX4544. Analyses rejected from the age calculation are shaded black (one sigma error boxes). Field relationships suggest that 1597 ± 8 Ma (weighted mean $^{207}Pb/^{206}Pb$, 95% confidence) is the age of diatreme activity, and therefore represents a minimum age constraint for the hematite-quartz breccias intruded by the diatreme (see text).

It is possible that some of the zircons analysed were derived from the relatively uncommon granitic fragments in this tuff. However, zircons ***are*** present within volcanic fragments in the tuff, and such zircons are expected to dominate in the sample. Any analysed zircons derived from the granitic fragments have ages not resolvably different from the main (volcanic-derived) population and their inclusion will not adversely affect the calculation of an age for the tuff. 1597 ± 8 Ma is therefore the preferred age of the diatreme tuff. Given the diatreme interpretation, the tuff must have been deposited on the crater floor of the active diatreme before its collapse, consequent soft-sediment deformation, and emplacement at its present relative level. 1597 ± 8 Ma is therefore a date on diatreme activity. As such it represents a minimum age constraint on the rocks

which the diatreme intrudes, namely the hematite-quartz breccias in the core of the deposit. It may also constrain the minimum age of a bornite-chalcocite ore zone which appears to be cross-cut by the northern part of the diatreme.

There is a superficial discrepancy between the age for the diatreme tuff (1597 ± 8 Ma) and the age of the Roxby Downs Granite (1588 ± 4 Ma). Although the ages appear distinct at the 1σ level, they are unresolvable at the 95% confidence level. The apparent age discrepancy may relate to a hydride contribution to elevated ^{207}Pb counts during analysis, although the data for the zircon standard are ambiguous in this regard. Field relationships indicate that the diatreme cannot be older than the granite, and the zircon age of 1597 ± 8 Ma demonstrates that the diatreme is not considerably younger than the granite. Therefore, while it is acknowledged that there may be an unresolved hydride contribution to increasing the calculated $^{207}Pb/^{206}Pb$ age, it is apparent that the geological meaning of the age is not in question and that it does constrain the minimum age of the main brecciation event at Olympic Dam.

3.3.3 Summary

The three ages discussed above (RX3222, RX3223, RX2820+4544) each provide a minimum age for the hematite-producing hydrothermal system. Two of the samples (RX3223, RX2820+4544) clearly post date the onset of brecciation, and probably also provide minimum age constraints for Cu sulphide mineralisation. The third sample (RX3222) provides a minimum age for epiclastic reworking of the surficial parts of the Olympic Dam Breccia Complex (producing the hematite-quartz sandstones). The three dates, 1592 ± 8 Ma, 1584 ± 20 Ma and 1597 ± 8 Ma are the same within error. Moreover these three minimum age constraints cannot be resolved from the age of the host granite, 1588 ± 4 Ma, which provides a maximum age for the deposit. The Olympic Dam Breccia Complex therefore has an age of ~1590 Ma.

3.4 Zircons in hydrothermally altered granite

Some Olympic Dam zircons have narrow (generally 10-50 μm) irregular to euhedral overgrowths of optically distinctive "zircon" (see below). The distribution of these mantled zircons is not well understood. They have been observed in some hematite-rich ore zones, and in zones of sericitised granite and granitic breccia.

The petrographic characteristics of the zircon overgrowths strongly suggest that they are hydrothermal precipitates on magmatic primary grains. An ion- and electron microprobe study of these overgrowths was undertaken to:

(1) see if the compositions of core and overgrowth pairs are consistent with magmatic and hydrothermal origins respectively, and

(2) obtain U-Pb isotopic ages which might be inferred to directly date Olympic Dam Breccia Complex hydrothermal activity.

To facilitate microprobe work, mixed populations of mantled and unmantled zircons were extracted from three samples of intensely sericitised granite microbreccia (RX3698, RX3212, and RX4533). A single in situ mantled zircon grain occurring in a chalcocite-bornite mineralised breccia (RX066) was also analysed. The isotopic data for these zircons are listed in Tables 3.4 to 3.7. As a whole, these data are considerably complex. It is advantageous to first describe and discuss the comparatively straightforward subset of the data obtained from the unmantled zircons and the cores of mantled zircons. These are simply termed granitic zircons in the following section. The populations in each of the three samples display similar size distributions and optical characteristics. They include grains with obvious core-overgrowth textures (Plates 3 and 4), clear and unzoned grains without overgrowths, and clear to brown grains exhibiting regular growth zone patterns. The grains are euhedral to subhedral, equant to elongate, and range in size from 100 μm across (equant), to 100 μm by 200 μm (elongate). The darker brown grains appear to be metamict, showing many fine cracks and an overall opacity. Granitic zircons from all three samples are similar in size and appearance.

3.4.1 Granitic zircons

3.4.1.1 RX3698

Seventeen analyses were obtained from zircon grains interpreted to be of magmatic origin. The concordia plot for RX3698 (Figure 3.4) shows four analyses which are strongly discordant (2.3, 5.2, 9.1, 13.2). These points are therefore rejected from age calculation, giving a weighted mean $^{207}Pb/^{206}Pb$ age of 1573 ± 9 Ma. However, this date includes scatter well in excess of that expected from analytical error, with probable outliers having low apparent ages interpreted to result from ancient lead loss. Iterative deletion of outliers yields an age of 1595 ± 11 Ma (95% confidence) based on nine analyses (7.1, 4.2, 8.1 and 10.1 deleted). This is the preferred age for this sample.

3.4.1.2 RX3212

Twenty four analyses of cores or unrimmed grains were collected from a total of eleven grains. The concordia plot (Figure 3.5) shows many discordant analyses. When these are deleted the weighted mean $^{207}Pb/^{206}Pb$ age is 1549 ± 9 Ma (95% confidence; deleting 1.1, 3.1, 3.2, 3.4, 4.2, 5.2, 5.3, 6.1, 11.1 and 6.6). This calculation results in excessive scatter about the mean $^{207}Pb/^{206}Pb$ ratio. Deleting analyses 4.1, 8.1 and 9.1 removes this scatter and yields an age of 1598 ± 14 Ma based on 11 analyses. This is the preferred age for this sample.

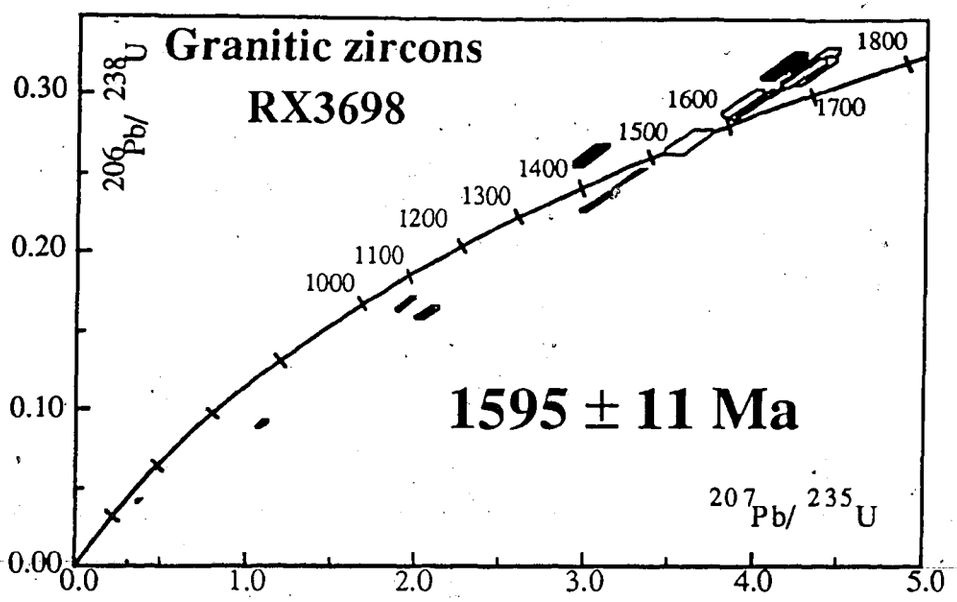

Figure 3.4 Concordia diagram for zircon cores and unmantled grains from RX3698, a sample of intensely sericite altered granite breccia (one sigma error boxes). Analyses rejected from the age calculation are shaded black (one sigma error boxes).

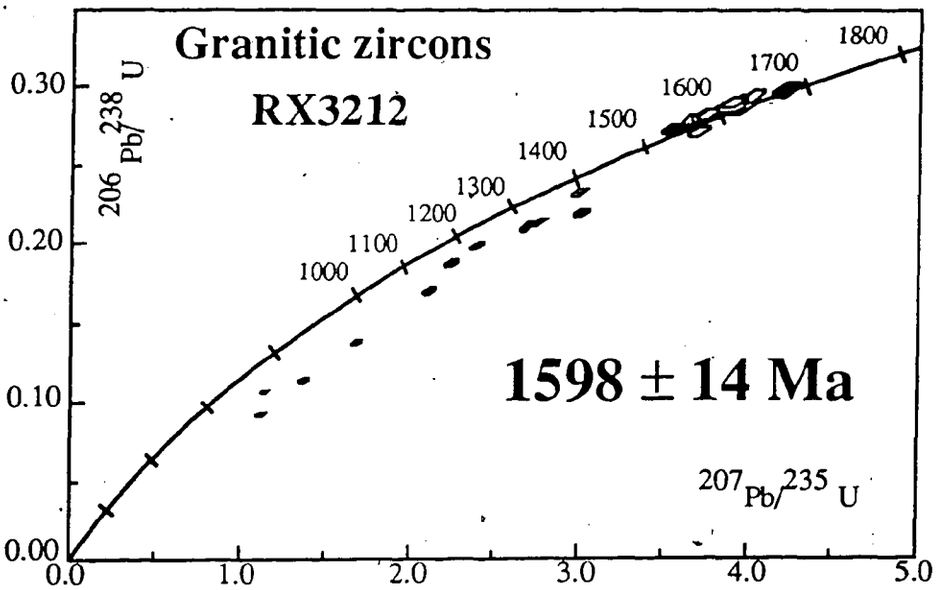

Figure 3.5 Concordia diagram for zircon cores and unmantled grains from RX3212, a sample of altered granite breccia. Analyses rejected from the age calculation are shaded black (one sigma error boxes). The preferred ages for this sample and RX3698 are in agreement with the more precise age of 1588 ± 4 Ma (Creaser, 1989) determined from relatively unaltered granite.

3.4.1.3 RX4533

Although six cores were analysed, it appears that the setting used to monitor the ^{204}Pb background was inappropriate, introducing an unnecessarily large uncertainty into the measurement of ^{204}Pb at low abundances. For this reason the ^{204}Pb corrected

Table 3.4. Ion microprobe data for granitic zircons from altered Roxby Downs Granite samples

Analysis No.	U (ppm)	Th (ppm)	^{204}Pb (ppb)	f206[a] (%)	$^{204}Pb/^{206}Pb$	$^{208}Pb/^{206}Pb$	$^{206}Pb/^{238}U$	$^{207}Pb/^{235}U$	$^{207}Pb/^{206}Pb$	$^{207}Pb/^{206}Pb$ age ± 1σ (Ma)
Altered granite breccia RX3698										
1.1	88	127	10	0.80	0.000499	0.426	0.2708 ± 78	3.61 ± 0.14	0.0967 ± 21	1561 ± 41
2.3	664	1450	71	1.22	0.000766	0.217	0.1614 ± 45	2.07 ± 0.07	0.0931 ± 15	1490 ± 31
4.2	494	366	28	0.42	0.000264	0.192	0.2466 ± 69	3.25 ± 0.10	0.0954 ± 19	1537 ±12
5.2	1652	2208	450	5.36	0.003360	0.250	0.0896 ± 25	1.10 ± 0.04	0.0893 ± 13	1410 ± 40
7.1	2317	3557	3081	8.63	0.005413	0.362	0.2619 ± 74	3.03 ± 0.10	0.0839 ± 13	1289 ± 30
8.1	390	351	17	0.35	0.000219	0.193	0.2325 ± 66	3.07 ± 0.09	0.0957 ± 7	1541 ± 14
9.1	6763	7070	2004	12.00	0.007529	0.471	0.0404 ± 11	0.38 ± 0.01	0.0685 ± 16	884 ± 50
10.1	157	115	23	0.87	0.000543	0.215	0.3189 ± 91	4.16 ± 0.14	0.0947 ± 13	1523 ± 26
11.1	439	426	18	0.26	0.000164	0.285	0.2957 ± 83	4.00 ± 0.12	0.0981 ± 5	1588 ± 10
12.1	233	181	8	0.20	0.000126	0.236	0.3156 ± 90	4.28 ± 0.13	0.0984 ± 7	1594 ± 13
13.1	371	237	9	0.14	0.000091	0.196	0.3072 ± 87	4.20 ± 0.12	0.0991 ± 5	1607 ± 9
13.2	745	496	101	1.49	0.000936	0.221	0.1672 ± 47	1.93 ± 0.06	0.0839 ± 9	1290 ± 22
14.1	140	109	12	0.48	0.000302	0.236	0.3163 ± 91	4.35 ± 0.14	0.0996 ± 11	1617 ± 20
14.2	229	187	25	0.67	0.000421	0.225	0.2952 ± 84	3.93 ± 0.12	0.0965 ± 10	1557 ± 20
15.1	160	110	3	0.12	0.000077	0.215	0.3147 ± 90	4.29 ± 0.13	0.0988 ± 8	1602 ± 16
16.1	233	158	10	0.26	0.000165	0.194	0.2927 ± 83	3.96 ± 0.12	0.0982 ± 8	1590 ± 15
16.3	163	83	17	0.59	0.000369	0.147	0.3215 ± 92	4.36 ± 0.14	0.0983 ± 12	1592 ± 23

Table 3.4 continued

Analysis No.	U (ppm)	Th (ppm)	^{204}Pb (ppb)	f206[a] (%)	$^{204}Pb/^{206}Pb$	$^{208}Pb/^{206}Pb$	$^{206}Pb/^{238}U$	$^{207}Pb/^{235}U$	$^{207}Pb/^{206}Pb$	$^{207}Pb/^{206}Pb$ age ± 1σ (Ma)
Altered granite breccia RX3212										
1.1	358	216	10	0.26	0.000160	0.232	0.2127 ± 28	2.76 ± 0.05	0.0943 ± 8	1513 ± 15
2.2	339	193	36	0.72	0.000451	0.176	0.2702 ± 36	3.71 ± 0.07	0.0996 ± 12	1616 ± 22
3.1	501	398	20	0.45	0.000279	0.320	0.1697 ± 22	2.12 ± 0.04	0.0905 ± 9	1436 ± 20
3.2	499	395	6	0.11	0.000066	0.298	0.1978 ± 26	2.39 ± 0.04	0.0878 ± 7	1378 ± 15
3.3	264	271	3	0.07	0.000042	0.303	0.2856 ± 39	3.91 ± 0.06	0.0992 ± 7	1609 ± 13
3.4	806	447	24	0.49	0.000309	0.268	0.1129 ± 15	1.38 ± 0.03	0.0887 ± 11	1398 ± 25
4.1	44	42	0	0.002	0.000001	0.289	0.2979 ± 47	4.22 ± 0.09	0.1028 ± 14	1676 ± 25
4.2	277	204	6	0.47	0.000292	0.243	0.0916 ± 12	1.12 ± 0.03	0.0890 ± 17	1403 ± 36
5.1	88	95	3	0.25	0.000156	0.316	0.2854 ± 41	3.95 ± 0.08	0.1003 ± 14	1630 ± 26
5.2	258	177	17	0.65	0.000409	0.256	0.1870 ± 25	2.25 ± 0.04	0.0871 ± 11	1363 ± 25
5.3	260	184	3	0.13	0.000083	0.300	0.1363 ± 18	1.68 ± 0.03	0.0895 ± 9	1416 ± 20
5.4	118	128	2	0.12	0.000076	0.338	0.2931 ± 42	4.02 ± 0.08	0.0995 ± 12	1614 ± 22
6.1	515	493	16	0.28	0.000174	0.378	0.2101 ± 28	2.69 ± 0.04	0.0928 ± 8	1484 ± 16
6.2	349	494	6	0.12	0.000073	0.414	0.2902 ± 39	3.93 ± 0.06	0.0983 ± 6	1591 ± 12
6.3	285	321	0	0.004	0.000003	0.331	0.2871 ± 39	3.92 ± 0.06	0.0990 ± 6	1605 ± 11
7.1	229	143	22	0.66	0.000416	0.182	0.2724 ± 32	3.57 ± 0.09	0.0951 ± 19	1529 ± 37
8.1	356	183	28	0.52	0.000325	0.151	0.2786 ± 31	3.66 ± 0.07	0.0954 ± 12	1536 ± 24

Table 3.4 continued

Analysis No.	U (ppm)	Th (ppm)	^{204}Pb (ppb)	f206 (%)	$^{204}Pb/^{206}Pb$	$^{208}Pb/^{206}Pb$	$^{206}Pb/^{238}U$	$^{207}Pb/^{235}U$	$^{207}Pb/^{206}Pb$	$^{207}Pb/^{206}Pb$ age ± 1σ (Ma)
Altered granite breccia RX3212 contd.										
9.1	415	209	21	0.40	0.000253	0.165	0.2319 ± 25	3.00 ± 0.05	0.0939 ± 10	1505 ± 21
10.1	258	192	18	0.45	0.000282	0.224	0.2858 ± 33	3.88 ± 0.09	0.0984 ± 17	1595 ± 33
10.2	318	207	18	0.36	0.000226	0.194	0.2894 ± 33	3.90 ± 0.07	0.0979 ± 11	1584 ± 22
11.1	721	138	27	0.66	0.000412	0.117	0.1061 ± 11	1.14 ± 0.02	0.0782 ± 11	1152 ± 28
6.4	216	251	13	0.39	0.000241	0.339	0.2809 ± 33	3.75 ± 0.07	0.0967 ± 14	1562 ± 27
6.5	245	225	9	0.25	0.000154	0.269	0.2811 ± 32	3.76 ± 0.06	0.0971 ± 11	1568 ± 22
6.6	385	453	12	0.27	0.000168	0.394	0.2185 ± 24	3.01 ± 0.05	0.1000 ± 11	1625 ± 20
Altered granite breccia RX4533										
1.1	185	90	1	0.02	0.000012	0.146	0.2710 ± 22	3.74 ± 0.05	0.1001 ± 10	1626 ± 19
2.1	136	116	3	0.16	0.000103	0.257	0.2623 ± 23	3.60 ± 0.10	0.0996 ± 26	1617 ± 50
3.1	286	214	5	0.13	0.000081	0.231	0.2590 ± 20	3.58 ± 0.04	0.1002 ± 8	1628 ± 14
4.1	117	83	6	0.33	0.000204	0.205	0.2711 ± 36	3.67 ± 0.37	0.0981 ± 95	1589 ± 194
1.2	234	124	1	0.04	0.000024	0.149	0.2692 ± 22	3.68 ± 0.05	0.0992 ± 10	1609 ± 18
4.3	148	96	14	0.62	0.000386	0.171	0.2832 ± 27	3.67 ± 0.12	0.0939 ± 29	1506 ± 60
7.1	231	132	1	0.04	0.000027	0.165	0.2722 ± 22	3.69 ± 0.04	0.0982 ± 7	1590 ± 13
8.2	190	149	12	0.44	0.000277	0.222	0.2606 ± 21	3.41 ± 0.06	0.0948 ± 14	1525 ± 28

[a] Denotes the percentage of common ^{206}Pb in the total measured ^{206}Pb

$^{207}Pb/^{206}Pb$ ratios cannot be used for the cores, and no age has been calculated. The $^{204}Pb/^{206}Pb$ ratios of the hydrothermal overgrowths are not significantly affected by the high background because their ^{204}Pb counts are very much higher than those for the zircon cores. The uncertainty introduced into the $^{204}Pb/^{206}Pb$ ratios for the overgrowth analyses as a result of the high background has a maximum value of ~5%, but is generally less than 1%. This small degree of uncertainty does not adversely affect the Pb-Pb isotopic arguments made below.

The two determinations of the age of the Roxby Downs Granite reported above, *viz* 1595 ± 11 Ma and 1598 ± 14 Ma, agree within error. They are also both within error of the more precise age of 1588 ± 4 Ma determined by Creaser (1989) and Creaser and Cooper (in press) on samples of relatively unaltered Roxby Downs Granite.

3.4.2 Overgrowths mantling granitic zircons

Many of the inferred magmatic zircons extracted from RX3698, RX3212 and RX4533 were enclosed in ~10 to 50 μm wide mantles of a clear to pale yellow translucent mineral with slightly lower reflectance than the zircon cores (e.g. Plates 3. and 4). These overgrowths are composed of a material intermediate in composition between zircon and xenotime (YPO_4) - a mineral which is isostructural with zircon (Deer et al., 1966). Electron microprobe analyses presented in Table 3.5 show that, relative to the magmatic zircon cores, the overgrowths contain anomalously high concentrations of ThO_2, UO_2, Y_2O_3, P_2O_5, Yb_2O_3, CaO and BaO. Analysis totals are generally low, typically around 90%, indicating that the overgrowths contain significant water, either as OH^- substituting in the zircon structure or as adsorbed molecular water in metamict grains (Mumpton and Roy, 1961). Pupin (1980) discussed the formation of "hydrozircon" rims rich in U, Th and Y in the late stages of crystallisation of hydrous granitic magmas. These typically have a "distinctive zoned structure" similar in appearance to many of the overgrowths observed in this study (e.g. Plates 3 and 4; cf. Figure 6a of Pupin, 1980). Rubin et al. (1989) also described hydrothermal zircons with relatively high concentrations of U, Th and Y, and low totals (by electron microprobe) which they attributed to the water content of the grains. Cyrtolite, an altered form of zircon, is known to contain appreciable water (Deer et al., 1966), along with U, Y, and "other rare elements" (Dana, 1932). Compston et al. (1984) reported enrichments of U, Th, Y, Yb, and P in metamict zircon.

The zircon cores observed in this study are chemically distinct from the overgrowths. By contrast with the latter, the cores contain only a few hundred ppm U and Th (Table 3.6; cf. Table 3.4), no appreciable Y, P, Yb, Ca or Ba, and electron microprobe analyses of them have totals very close to 100% (see Table 3.5). These differences, and the dissimilarities in optical properties, indicate that the overgrowths had a substantially

a

b

Plate 3 Photomicrographs of granitic zircon with hydrothermal overgrowth, from sericitised granite breccia sample RX45533 (grain 4; cf. data in Tables 3.4 and 3.6). **a)** Plane polarised light. Clear granitic zircon core contains less than 150 ppm U, in contrast to the translucent yellow overgrowth which contains over 5000 ppm U.
b) Reflected light. Hydrothermal overgrowths typically have lower reflectance than the granitic zircon cores. Note inclusion of gold and pits made by ion probe analysis. Width of frame is 325 μm.

Table 3.5. Selected electron probe analyses of magmatic zircon cores and hydrothermal rims.

	Cores		Overgrowths			
Oxides (Wt%)	RX3698 5.3	RX3212 5.1	RX3698 5.1	RX4533 8.1	RX4533 9.2	RX3212 9.3
P_2O_5	<0.03	<0.02	1.96	0.06	0.05	1.12
SiO_2	32.73	32.88	25.91	31.36	29.9	31.86
ZrO_2	66.31	65.70	45.50	63.78	59.6	51.97
HfO_2	1.20	1.47	1.03	1.73	1.55	1.09
ThO_2	0.06	<0.06	2.15	0.12	<0.07	0.13
UO_2	0.07	<0.05	1.72	0.39	0.36	2.23
Y_2O_3	<0.05	<0.04	8.54	1.8	0.64	2.03
Yb_2O_3	0.04	0.02	0.5	0.18	0.04	0.15
CaO	<0.01	<0.01	1.26	0.1	0.21	1.05
BaO	<0.03	<0.03	0.21	<0.03	0.04	0.24
Total	100.41	100.07	88.78	99.53	92.39	91.87

different mode of origin to that of the cores. The habits, chemical signature, and geological setting of the overgrowths clearly point to a hydrothermal origin, whereas most of the cores are essentially identical to magmatic zircons observed in the Roxby Downs Granite. Some that are not identical contain patches of "zircon" with comparatively lower reflectance and higher U and Th than the host magmatic zircon. These patches occur adjacent to cracks - consistent with an origin by alteration of magmatic zircon in contact with a hydrothermal fluid. The zircons with such patchy alteration zones frequently lack overgrowths, which is somewhat surprising given that the zircon exterior must have been at least partially exposed to the fluids which penetrated the cracks. This observation argues against any suggestion that the zircon mantles formed by alteration of magmatic zircon rims. The fact that the magmatic zircons do display some alteration effects raises the possibility that some zircon mantles formed by a combination of new mineral growth and alteration of pre-existing zircon.

An age for the hydrothermal overgrowths should date the hydrothermal event. However, the compositional differences between these overgrowths and the standard zircon (SL3) allow the possibility of different matrix effects during ion probe analysis. This means that it cannot be assumed that the relative ion yields for Pb, U and Th will be the same for unknowns and standard. Accordingly little weight is given to the Pb/U ratios and the Pb, U and Th concentrations listed for overgrowths in Table 3.6. Where comparisons are available for U and Th determinations by electron probe and ion probe, they are found to differ by 5 to 25%of the ion probe total for U, and by 12 to 100% for Th. However, the

Table 3.6. Ion microprobe data for hydrothermal overgrowths around magmatic zircons from samples of altered Roxby Downs Granite

Analysis No.	U (ppm)	Th (ppm)	^{204}Pb (ppb)	$f206^a$ (%)	$^{204}Pb/^{206}Pb$	$^{208}Pb/^{206}Pb$	$^{206}Pb/^{238}U$	$^{207}Pb/^{235}U$	$^{207}Pb/^{206}Pb$	$^{207}Pb/^{206}Pb$ age ± 1σ (Ma)
Altered granite breccia RX4533										
2.2	5068	294	115	1.23	0.000768	0.098	0.0341 ± 2	0.406 ± 0.005	0.0864 ± 8	1347 ± 19
3.2	9910	326	96	1.41	0.000882	0.110	0.0126 ± 1	0.128 ± 0.002	0.0737 ± 11	1034 ± 29
4.2	5552	353	427	3.24	0.002030	0.277	0.0428 ± 3	0.628 ± 0.008	0.1064 ± 10	1739 ± 18
4.2	5604	379	921	7.02	0.004401	0.288	0.0405 ± 3	0.425 ± 0.010	0.0761 ± 17	1099 ± 45
4.4	6815	403	1400	9.09	0.005698	0.318	0.0383 ± 3	0.349 ± 0.009	0.0662 ± 15	811 ± 48
5.1	1659	121	85	2.35	0.001471	0.154	0.0399 ± 3	0.422 ± 0.009	0.0766 ± 15	1111 ± 38
6.1	5966	286	141	1.79	0.001120	0.092	0.0242 ± 2	0.206 ± 0.003	0.0616 ± 9	660 ± 31
8.1	3187	979	16949	16.30	0.010210	0.618	0.5087 ± 36	6.520 ± 0.079	0.0930 ± 8	1487 ± 17
8.3	3491	1019	1310	11.68	0.007320	0.467	0.0528 ± 4	0.601 ± 0.016	0.0825 ± 21	1257 ± 50
9.1	7859	256	253	3.45	0.002158	0.133	0.0168 ± 1	0.150 ± 0.003	0.0650 ± 13	774 ± 43
4.5	5217	297	12680	17.89	0.011207	0.669	0.2078 ± 15	2.808 ± 0.036	0.0980 ± 10	1586 ± 18
Altered granite breccia RX3212										
1.2	8031	2250	2310	1.56	0.000976	0.182	0.3385 ± 46	4.33 ± 0.10	0.0928 ± 16	1484 ± 34
2.1	3974	307	169	1.07	0.000671	0.112	0.0732 ± 10	0.72 ± 0.01	0.0717 ± 6	978 ± 18
8.2	10602	1133	214	0.71	0.000446	0.089	0.0524 ± 5	0.46 ± 0.01	0.0638 ± 5	736 ± 15
9.2	6007	655	141	0.71	0.000447	0.086	0.0607 ± 6	0.54 ± 0.01	0.0649 ± 5	772 ± 16
9.3	3300	216	140	0.86	0.000537	0.078	0.0917 ± 9	0.85 ± 0.01	0.0677 ± 6	858 ± 18

Table 3.6 continued

Analysis No.	U (ppm)	Th (ppm)	^{204}Pb (ppb)	f206[a] (%)	$^{204}Pb/^{206}Pb$	$^{208}Pb/^{206}Pb$	$^{206}Pb/^{238}U$	$^{207}Pb/^{235}U$	$^{207}Pb/^{206}Pb$	$^{207}Pb/^{206}Pb$ age ± 1σ (Ma)
Altered granite breccia RX3698										
2.1	3045	3011	607	6.30	0.003953	0.383	0.0551 ± 16	0.57 ± 0.02	0.0747 ± 16	1059 ± 45
2.2	8365	10911	1187	5.93	0.003720	0.405	0.0419 ± 12	0.41 ± 0.01	0.0705 ± 13	942 ± 37
3.1	6482	82781	7376	15.19	0.009530	0.669	0.1182 ± 33	1.19 ± 0.04	0.0728 ± 12	1007 ± 35
4.1	6878	8970	3451	13.63	0.008547	0.774	0.0592 ± 17	0.57 ± 0.02	0.0694 ± 14	910 ± 43
5.1	16088	21393	2966	12.63	0.007925	0.735	0.0237 ± 7	0.21 ± 0.01	0.0629 ± 16	703 ± 53
6.1	6175	5693	990	8.46	0.005309	0.506	0.0323 ± 9	0.29 ± 0.01	0.0658 ± 15	801 ± 50
16.2	6314	7395	1070	8.13	0.005102	0.544	0.0356 ± 10	0.30 ± 0.01	0.0601 ± 15	608 ± 55

[a] Denotes the percentage of common ^{206}Pb in the total measured ^{206}Pb

Pb isotopic ratios of the overgrowths are unaffected by problems in calibrating Pb to U and Th, and these are discussed below.

3.4.2.1 RX4533

Measured ratios of $^{207}Pb/^{206}Pb$ versus $^{204}Pb/^{206}Pb$ for granitic zircon cores and hydrothermal zircon overgrowths from RX4533 are plotted in Figure 3.6a. The shaded area is the field of permissible lead compositions for a system formed at 1590 Ma and containing common Pb of an average crustal composition (Cumming and Richards, 1975). The lower bound is limited by the composition of radiogenic lead formed from present-day uranium decay. All of the analyses for RX4533 plot within this field. When viewed together, the hydrothermal overgrowths do not adhere to a single mixing array, and it is likely that the grain-to-grain variations in Pb isotopic compositions represent closure to Pb mobility at different times during the deposit's history. This is not surprising considering the likelihood of groundwater circulation through the deposit as a result of thermal convection generated by in situ uranium decay.

Comparatively more order is apparent among the data for samples with $^{204}Pb/^{206}Pb$ ratios lower than 0.004. Figure 3.6b shows that all except two analyses of the magmatic zircons lie on a mixing line between 1590 Ma crustal Pb and radiogenic Pb of 1590 Ma age. The other two magmatic zircon analyses plot on a possible mixing trend along with analyses of three of the hydrothermal overgrowths (2.2, 5.1, 9.1). These three analyses each include a proportion of magmatic zircon core; ~25% of the spot in 2.2, ~60% in 5.1, and ~10% in 9.1. The isotopic compositions measured therefore have contributions of common and radiogenic Pb from magmatic zircon adjacent to the hydrothermal overgrowth. However, the overgrowths contain ~5000, ~1600 and ~7800 ppm U respectively, in contrast to ~200 ppm U in the cores. The dominant influence on the measured Pb isotopic composition is therefore the radiogenic Pb contributed from the overgrowths. The observed trend is the result of mixing of at least three different components of Pb. They are: a) Pb with a $^{207}Pb/^{206}Pb$ ratio of approximately 0.1; b) a common Pb equivalent to a 1590 Ma Cumming and Richards (1975) crustal Pb; c) Pb with a radiogenic $^{207}Pb/^{206}Pb$ subcomponent possibly as low as ~0.06. The fact that such highly radiogenic Pb (U contents up to ~8000 ppm in the hydrothermal overgrowths) has a $^{207}Pb/^{206}Pb$ component of approximately 0.1 is permissive of the interpretation that the hydrothermal rims formed at approximately 1600 Ma. The low $^{207}Pb/^{206}Pb$ component is consistent with an origin as radiogenic Pb introduced into the zircons after about 600 Ma, probably in the Phanerozoic. This component may represent isotopic disturbance well after mineral formation.

The plot of measured $^{208}Pb/^{206}Pb$ versus $^{204}Pb/^{206}Pb$ (Figure 3.7a) shows the hydrothermal overgrowth analyses lying on a mixing trend between a common Pb

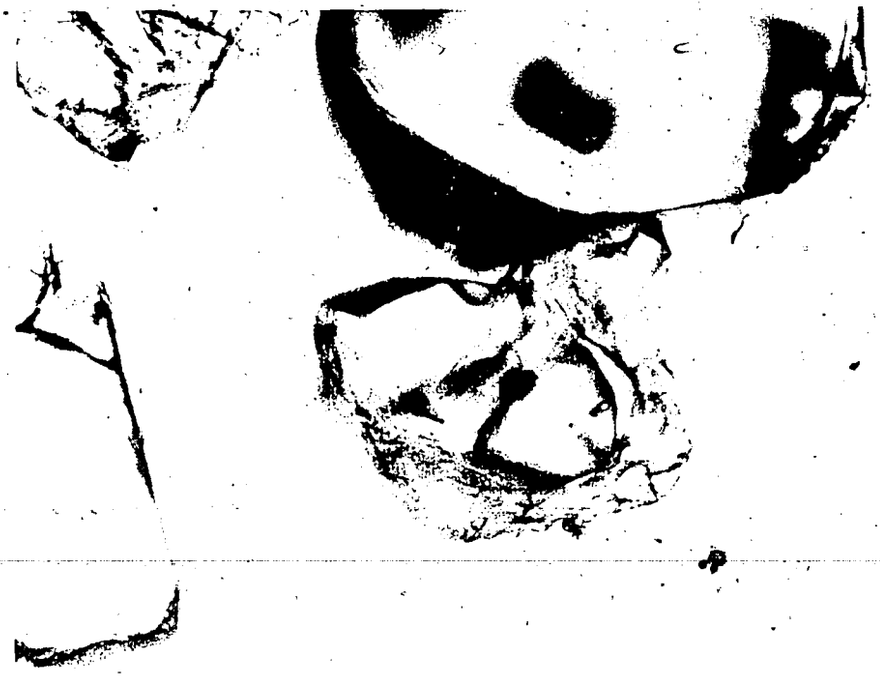

a

b

Plate 4 Photomicrographs of granitic zircons with hydrothermal overgrowths from sericitised granite breccia sample RX4533. a) Grain 2, plane polarised light. b) Grain 9 (central zircon), plane polarised light; width of frame is 325 μm for both. Analyses of the hydrothermal rims on these grains and grain 5, together with analyses of two magmatic zircons, yielded a linear array in $^{207}Pb/^{206}Pb$ versus $^{204}Pb/^{206}Pb$-space. The radiogenic end-member of the mixing line is permissive of an interpretation of an age of approximately 1590 Ma.

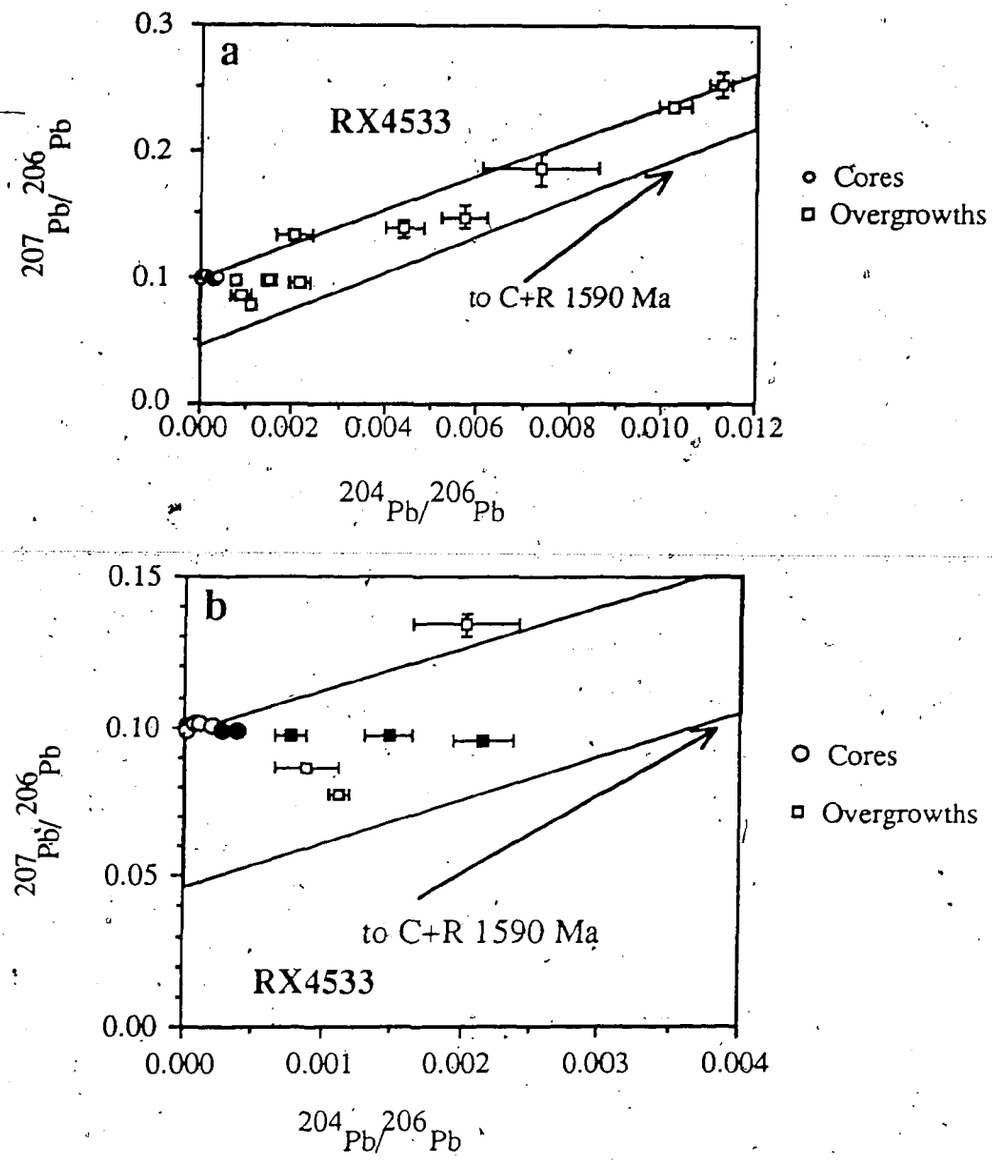

Figure 3.6 Isotopic ratios for magmatic zircons and their hydrothermal overgrowths from altered granite sample RX4533 (gold ore). (a) $^{207}Pb/^{206}Pb$ versus $^{204}Pb/^{206}Pb$ (one sigma error bars). The stippled area represents the field of permissible lead compositions for a mineral formation age of 1590 Ma with common Pb of average crustal composition at 1590 Ma ("C+R" denotes Cumming and Richards [1975] model for crustal Pb isotopic evolution). (b) The analyses with lower $^{204}Pb/^{206}Pb$ from (a). Three hydrothermal overgrowth analyses (2.2, 5.1, 9.1; see plate 4) and two altered magmatic cores (shaded black) form a possible mixing array between 3 components: i) Pb with a $^{207}Pb/^{206}Pb$ ratio of ~0.1; ii) crustal Pb of 1590 Ma (Cumming and Richards, 1975); iii) Phanerozoic Pb (low $^{207}Pb/^{206}Pb$). The high $^{207}Pb/^{206}Pb$ component in such highly radiogenic Pb is permissive of the interpretation that the hydrothermal overgrowths formed at approximately 1600 Ma. However, the data are far from conclusive.

---

component with a higher $^{208}Pb/^{206}Pb$ (more thorogenic) signature than 1590 Ma crustal Pb, and a radiogenic end-member which is dominated by uranogenic (^{206}Pb) lead. The

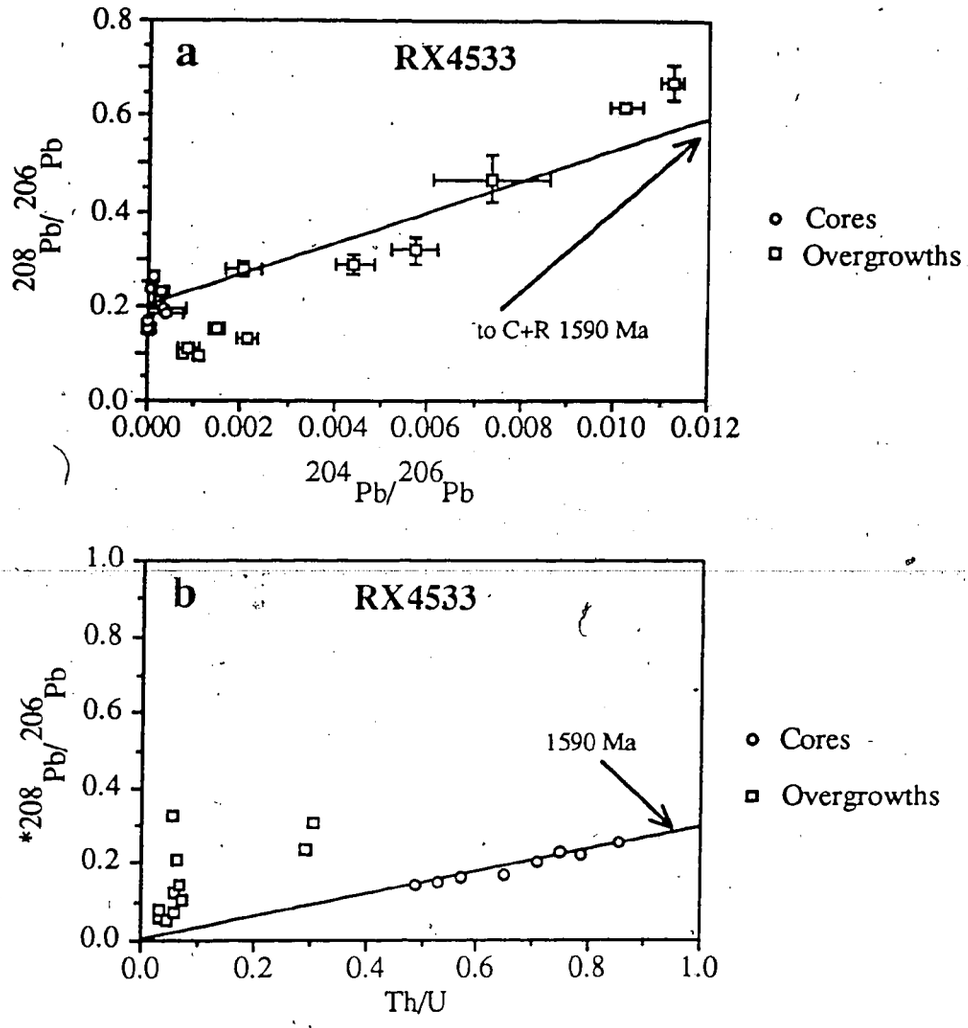

Figure 3.7 a) Plot of measured $^{208}Pb/^{206}Pb$ versus $^{204}Pb/^{206}Pb$ for altered granite sample RX4533, with reference line to 1590 Ma average crustal lead ("C+R" denotes Cumming and Richards, 1975 model for crustal Pb isotopic evolution). Possible origins of the trend are discussed in the text (one sigma error bars). **b)** Th/U versus radiogenic $^{208}Pb/^{206}Pb$ isochron diagram showing the good fit of data from core analyses to the theoretical isochron for 1590 Ma. This indicates closed system isotopic behaviour in these granitic zircons. The converse is true for the overgrowths.

---

low $^{208}Pb/^{206}Pb$ radiogenic end-member is consistent with local derivation (from within the deposit). The high $^{208}Pb/^{206}Pb$ "common" Pb end-member may have been derived from the breakdown, during hydrothermal alteration, of uranothorite, a primary accessory phase in the Roxby Downs Granite (Creaser, 1989). The trend may result from a post-1590 Ma isotopic disturbance which incompletely mixed lead from the above two sources.

The plot of radiogenic $^{208}Pb/^{206}Pb$ versus Th/U (Figure 3.7b) illustrates that the analyses of RX4533 hydrothermal overgrowths plot well away from the theoretical isochron, indicating either Pb mobility, or differential mobility of U and Th, or both. This is

probably a function of their degree of metamictisation due to their high U and Th contents. In contrast, the magmatic zircons conform more closely to the 1590 Ma isochron, indicating closed system behaviour since crystallisation.

3.4.2.2 RX3212

The magmatic cores and hydrothermal overgrowths analysed from sample RX3212 show relatively low levels of common Pb in the $^{207}Pb/^{206}Pb$ versus $^{204}Pb/^{206}Pb$ diagram (Figure 3.8a). All analyses plot within the field of permissible Pb compositions for grains of 1590 Ma age having average crustal common Pb. The hydrothermal overgrowths plot along a trend from a point on the 1590 Ma crustal common Pb mixing line towards a zero-age radiogenic end-member. This indicates that these grains have been open systems with respect to Pb mobility in recent times. Recent Pb mobilization within the deposit has been confirmed by Guthrie (1991) and workers from the Commonwealth Scientific and Industrial Research Organisation (CSIRO; unpublished data). Their analyses of whole-rock samples from the breccia complex indicate that, on a local scale, the deposit is not in secular equilibrium with respect to U, Th and Pb isotopes. However, the average isotopic make-up of all samples analysed approximates to an equilibrium composition, suggesting that groundwaters have not flushed Pb from the breccia complex as a whole in geologically recent times.

On the $^{208}Pb/^{206}Pb$ versus $^{204}Pb/^{206}Pb$ diagram (Figure 3.8b), the overgrowths form a mixing array, from an indeterminate common Pb end-member to a radiogenic end-member with very low $^{208}Pb/^{206}Pb$ (~0.02). When viewed in conjunction with the evidence for mixing with recent or present day Pb (above), it appears that the recent Pb component has a low $^{208}Pb/^{206}Pb$ ratio. This suggests that the source of the recent Pb is rich in U relative to Th, which is consistent with it having been derived locally from the uranogenic Pb of the Olympic Dam deposit. This suggestion is consistent with the findings of the CSIRO study (above).

The magmatic zircons plotted in Figure 3.8b show an overall negative correlation between $^{208}Pb/^{206}Pb$ and $^{204}Pb/^{206}Pb$. They form a mixing trend from a radiogenic end-member with a relatively high $^{208}Pb/^{206}Pb$ ratio (~0.4), to common Pb compositions which coincide with the trend defined by the hydrothermal overgrowths (which is interpreted to result from recent Pb mobility). This in turn suggests that the negative correlation observed for the magmatic grains in $^{208}Pb/^{206}Pb$-$^{204}Pb/^{206}Pb$ space is also a manifestation of recent Pb mobility. The $^{208}Pb/^{206}Pb$ (radiogenic) versus Th/U plot (Figure 3.8c) shows that several of the magmatic zircons conform to the theoretical 1590 Ma isochron, indicating that they have remained closed systems with respect to Th, U

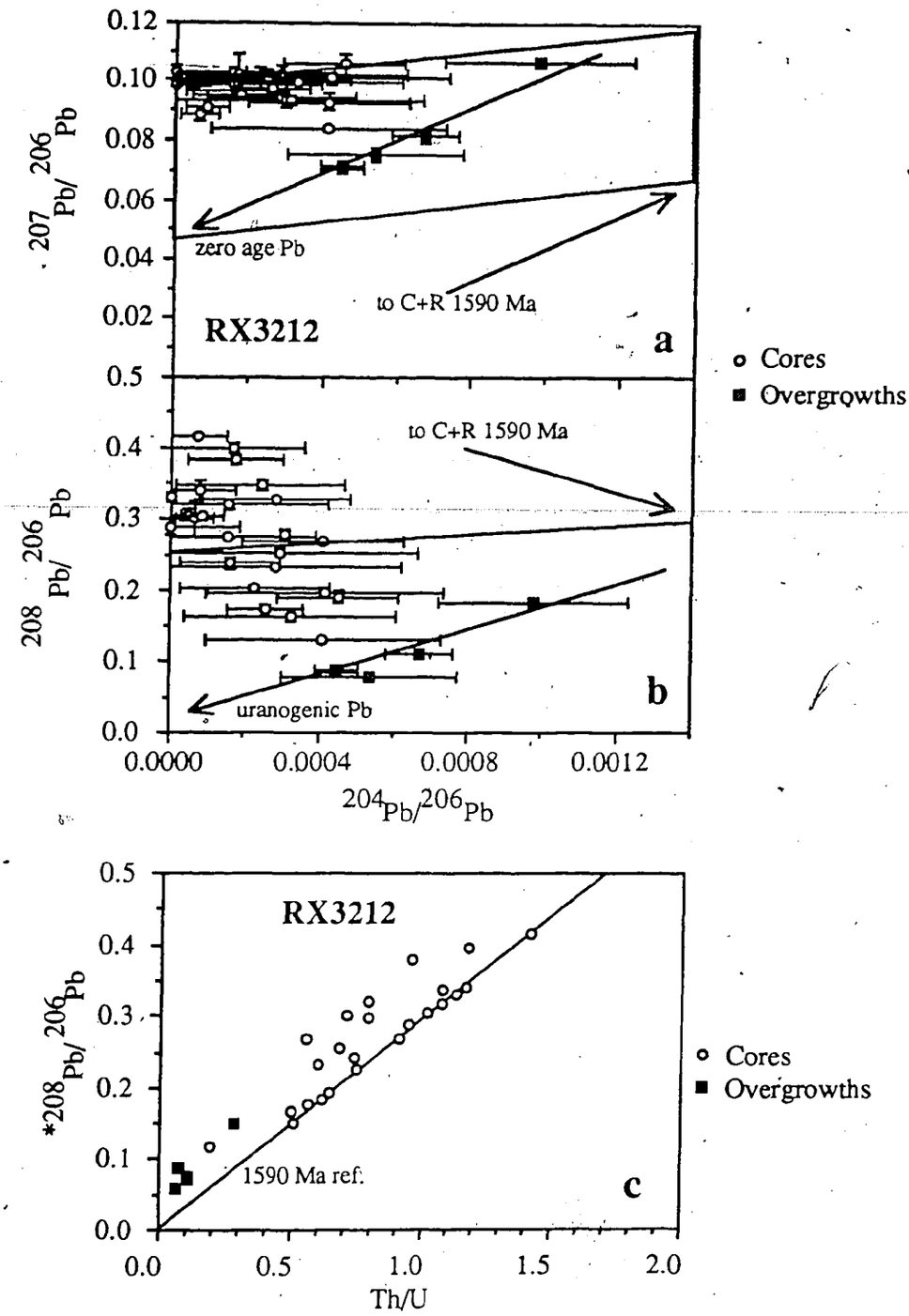

Figure 3.8 Isotopic ratios for granitic zircons and hydrothermal overgrowths from altered granite sample RX3212. (a) Measured $^{207}Pb/^{206}Pb$ versus $^{204}Pb/^{206}Pb$ (one sigma error bars); shaded area is the field of permissible lead compositions for a mineral formation age of 1590 Ma with the same age common Pb of average crustal composition ("C+R" denotes Cumming and Richards, 1975 model for crustal Pb isotopic evolution). Overgrowth analyses form a mixing array (see arrow) between a common Pb end-member close to the 1590 Ma common Pb - radiogenic Pb trend, and a zero-age radiogenic Pb. This indicates Pb mobility until recent times. (b) Measured $^{208}Pb/^{206}Pb$ versus $^{204}Pb/^{206}Pb$ with reference line to 1590 Ma average crustal lead. Overgrowth analyses form a trend showing that the zero-age Pb end-member observed in (a) is

Figure 3.8 contd. strongly uranogenic (low $^{208}Pb/^{206}Pb$). This is consistent with its derivation locally (within the ore deposit) rather than from an exotic source. The magmatic cores form a trend toward the rim array of recent origin, indicating that they too have suffered "zero-age" isotopic disturbance. (c) Th/U versus radiogenic $^{208}Pb/^{206}Pb$ isochron diagram. The poor fit of data to the theoretical 1590 Ma isochron attests to Pb, U or Th mobility in this sample, consistent with evidence from the Pb-Pb plots (a and b).

---

and Pb. However, the hydrothermal grains and many of the other magmatic grains show evidence of differential movement of U, Th and/or Pb. For the hydrothermal grains this evidence of isotopic disturbance is consistent with that from Figures 3.8a and b. For the magmatic grains it is consistent with the discordance shown by many of the grains on the concordia plot (Figure 3.5) and provides further justification for deleting low concordance points from the age calculation (above).

3.4.2.3 RX3698

The Pb isotopic data for RX3698 magmatic zircons and hydrothermal overgrowths are plotted in Figures 3.9a and 3.9b. The $^{207}Pb/^{206}Pb$ versus $^{204}Pb/^{206}Pb$ diagram (Figure 3.9a) indicates that all of the zircons analysed have isotopic compositions within the permissible field of leads for zircons of 1590 Ma age with common Pb of average crustal composition. Most of the magmatic grains form a tight cluster with low common Pb, but three have relatively high $^{204}Pb/^{206}Pb$ ratios indicating that they are isotopically disturbed. The overgrowth compositions do not conform to a tight mixing trend. Assuming that the hydrothermal overgrowths in all grains are penecontemporaneous, the lack of linearity may represent evidence for different times of closure to Pb and/or U mobility since mineral formation. For the hydrothermal overgrowths, if the $^{207}Pb/^{206}Pb$ composition is extrapolated back to zero $^{204}Pb/^{206}Pb$ (parallel to the common Pb extrapolation field), the y-intercept is at $^{207}Pb/^{206}Pb$ values as low as ~0.06. This indicates a radiogenic Pb component of an age younger than approximately 600 Ma and supports interpretations of a long and complex history of Pb mobility. Alternatively the lack of linearity of the data in Figure 3.9 a) could be interpreted as evidence for a poorly mixed common Pb from a single isotopic disturbance episode. The $^{208}Pb/^{206}Pb$ versus $^{204}Pb/^{206}Pb$ data (Figure 3.9b) are consistent with both of the above interpretations. The data indicate incomplete mixing of a variety of Pb sources, namely:

a) A ^{204}Pb-rich 1590 Ma crustal Pb component.

b) A strongly thorogenic component, possibly from Th-rich Roxby Downs Granite minerals such as uranothorite or monazite.

c) A uranogenic Pb component consistent with local derivation from within the deposit.

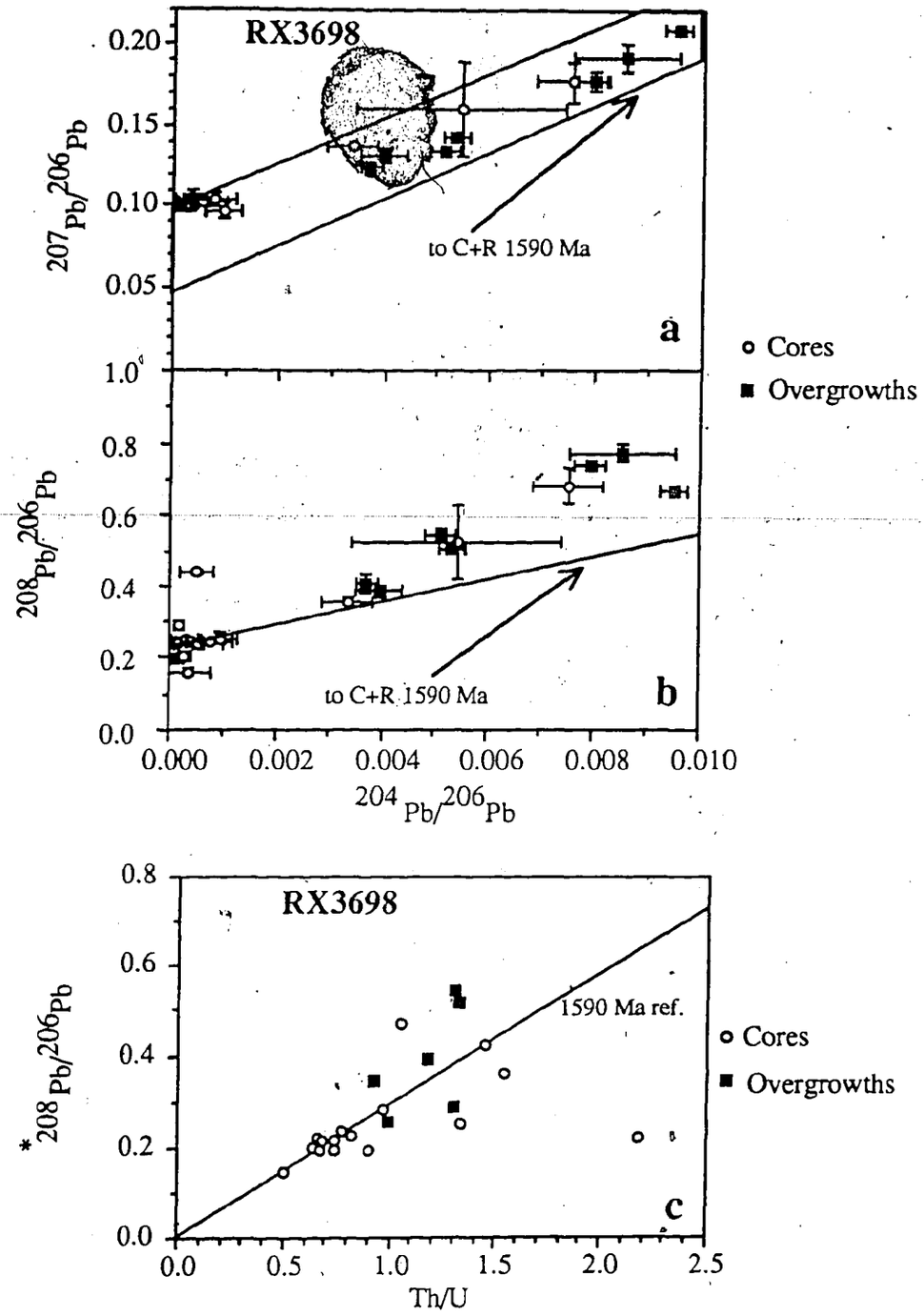

Figure 3.9 Isotopic ratios for magmatic zircons and hydrothermal overgrowths from altered granite sample RX3698. (a) Measured $^{207}Pb/^{206}Pb$ versus $^{204}Pb/^{206}Pb$ (one sigma error bars); shaded area is the field of permissible lead compositions for a mineral formation age of 1590 Ma with the same age common Pb of average crustal composition ("C+R" denotes Cumming and Richards, [1975] model for crustal Pb isotopic evolution). Overgrowths do not form a discrete mixing array, which suggests they have had different ages of closure to Pb and U mobility. (b) Measured $^{208}Pb/^{206}Pb$ versus $^{204}Pb/^{206}Pb$. The spread of data indicates poor mixing of Pb from a variety of sources (see text). (c). Th/U versus radiogenic $^{208}Pb/^{206}Pb$ isochron diagram. The poor fit of data to the theoretical 1590 Ma isochron attests to Pb, U or Th mobility in this sample, consistent with evidence from a and b.

Figure 3.9c shows a poor fit of the data to the theoretical 1590 Ma radiogenic $^{208}Pb/^{206}Pb$ - Th/U isochron for analyses of both cores and overgrowths. This attests to differential mobility of U and Th, and/or mobility of Pb in these grains, and is consistent with the degree of isotopic disturbance indicated for the magmatic zircons on the concordia plot (Figure 3.4).

3.4.2.4 RX066

Nine spot analyses were collected from within a single mantled zircon grain in a polished thin section of this sample of hematitic ore breccia. Plate 5 shows the zircon which displays three distinct zones; a homogeneous core, a patterned overgrowth on the core, and a discontinuous outer overgrowth. The analyses are listed in Table 3.7.

The homogeneous core of the grain probably represents magmatic zircon derived from the Roxby Downs Granite, although analyses 1-1, 1-2, 1-3, and 1-9 show higher concentrations of U and Th than are typical for the granitic zircons analysed from other samples (see Table 3.7; cf. Table 3.4). If the core is indeed magmatic, its high U and Th contents suggest that it has been affected by hydrothermal alteration. Analyses 1-6, 1-7 and 1-8 are from the patterned overgrowth and these show even higher U contents (2100 ppm, 7900 ppm and 3050 ppm respectively) indicating an origin from either hydrothermal precipitation or from intense alteration of magmatic zircon. For either mode of origin, their Pb isotopic signatures are likely to be dominated by radiogenic Pb derived from hydrothermally introduced uranium. The same applies to analyses 1-4 and 1-5 from the outer overgrowth; these have U contents of 6700 ppm and 8800 ppm respectively.

In a plot of $^{207}Pb/^{206}Pb$ versus $^{204}Pb/^{206}Pb$ (Figure 3.10a) the analyses all fall within the field of permissible lead compositions for a mineral forming at 1590 Ma with common Pb of average crustal composition, but they do not conform to a single mixing array. This indicates closure to Pb and U mobility at different times for the different subdomains analysed. Assuming that the core zircon is derived from the Roxby Downs Granite, three factors indicate that the core analyses are within domains which have disturbed isotopic systematics:

1) They have $^{204}Pb/^{206}Pb$ ratios in the range of 0.0004 to 0.0012, considerably higher than the range typical for the granitic zircons (0.00015 to 0.0003; see Table 3.4).

2) Although inconsistent, all of the core analyses have $^{207}Pb/^{206}Pb$ apparent ages well below the age of the granite (~1590 Ma).

3) The core has U and Th contents well above the typical range for the granite but below the concentrations in what is interpreted to be purely hydrothermal zircon - consistent with alteration of pristine zircon low in U and Th by fluids enriched in U and Th.

A

B

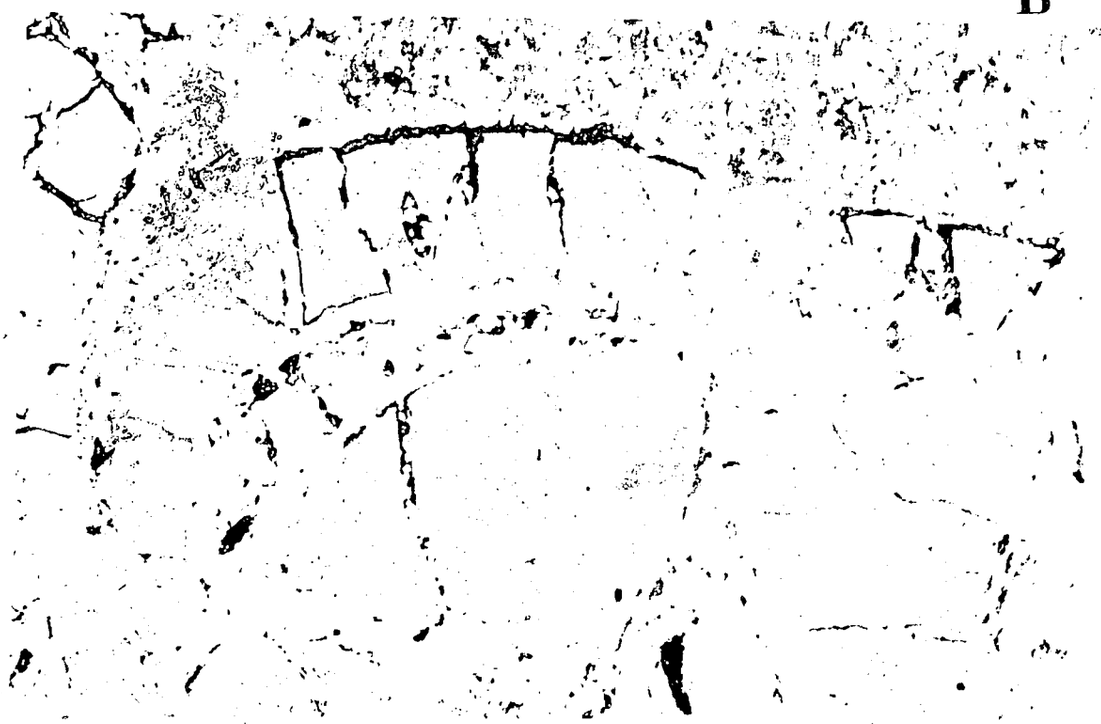

Plate 5. Reflected light photomicrographs. **A)** RX066, a single zircon grain analysed *in situ*. The grain is 100 μm long and has three distinct zones; a homogeneous core (C), a patterned overgrowth (O) and a discontinuous outer rim (R). The core is probably granitic; the other two zones are interpreted as of hydrothermal origin. The grain occurs within fluorite (dark) intergrown with hematite (light). Analyses discussed in text.
B) refer Chapter 4. RX3642-1; Pitchblende (grey) intergrown with chalcopyrite (yellow) from the innermost zone of concentric mineral growth in vug sample RX3642. Large pitchblende grains afford inclusion-free zones for ion microprobe analysis. Interlocking hematite grains at upper right. Width of frame is 1.3 mm.

Table 3.7. Ion microprobe data for single *in situ* zircon sample RX066

Analysis No.	U (ppm)	Th (ppm)	^{204}Pb (ppb)	f206[a] (%)	$^{204}Pb/^{206}Pb$	$^{208}Pb/^{206}Pb$	$^{206}Pb/^{238}U$	$^{207}Pb/^{235}U$	$^{207}Pb/^{206}Pb$	$^{207}Pb/^{206}Pb$ age ± 1σ (Ma)
1.1	953	953	158	1.09	0.000680	0.124	0.2815 ± 27	3.15 ± 0.05	0.0811 ± 8	1224 ± 19
1.2	872	872	58	0.58	0.000364	0.161	0.2127 ± 21	2.53 ± 0.04	0.0864 ± 9	1348 ± 21
1.3	826	826	41	0.67	0.000423	0.169	0.1357 ± 13	1.56 ± 0.03	0.0835 ± 10	1281 ± 23
1.4	6660	6660	1923	1.91	0.001200	0.079	0.2755 ± 26	2.62 ± 0.04	0.0690 ± 6	899 ± 18
1.5	8766	8766	3346	1.52	0.000951	0.112	0.4611 ± 45	4.81 ± 0.07	0.0757 ± 8	1086 ± 20
1.6	2070	2070	137	1.23	0.000772	0.082	0.0991 ± 10	0.99 ± 0.01	0.0725 ± 8	999 ± 21
1.7	7896	7896	237	0.98	0.000613	0.060	0.0566 ± 5	0.47 ± 0.01	0.0606 ± 5	624 ± 19
1.8	3046	3046	90	0.66	0.000412	0.089	0.0834 ± 8	0.78 ± 0.01	0.0682 ± 7	874 ± 22
1.9	1381	1381	103	0.72	0.000454	0.129	0.1911 ± 19	2.18 ± 0.04	0.0829 ± 11	1267 ± 25

[a] Denotes the percentage of common ^{206}Pb in the total measured ^{206}Pb

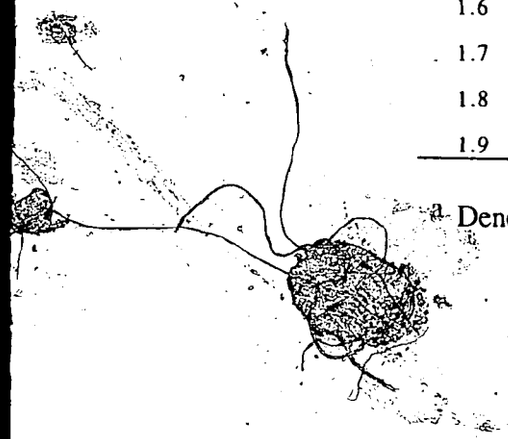

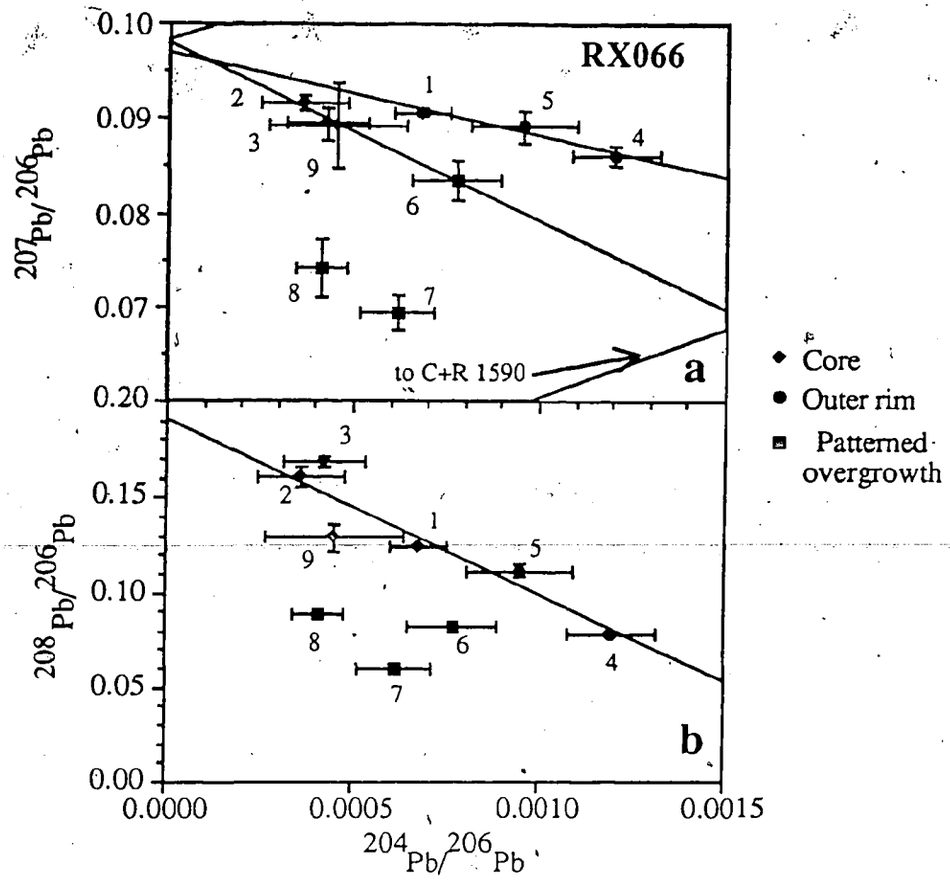

Figure 3.10. Isotopic data for sample RX066, a single zircon with three distinct growth zones analysed *in situ* (see plate 5). (a) Measured $^{207}Pb/^{206}Pb$ versus $^{204}Pb/^{206}Pb$ (one sigma error bars); shaded area is the field of permissible lead compositions for a mineral formation age of 1590 Ma with the same age common Pb of average crustal composition ("C+R" denotes Cumming and Richards, 1975 model for crustal Pb isotopic evolution). The two possible mixing trends shown are discussed in the text. (b) Measured $^{208}Pb/^{206}Pb$ versus $^{204}Pb/^{206}Pb$ with best fit line for core and outer rim analyses only. The colinearity of core and outer rim analyses is consistent with the core having been altered by the same hydrothermal fluids which produced the outer rim. The analyses of the patterned overgrowth (6, 7 and 8) illustrate open system behaviour of Pb and/ or U and Th.

These factors indicate that the zircon has undergone ancient isotopic disturbance. In $^{207}Pb/^{206}Pb$-$^{204}Pb/^{206}Pb$ space (Figure 3.10a) two possible mixing trends are apparent. One comprises three of the zircon core analyses (1-2, 1-3 and 1-9) and one analysis of the patterned overgrowth (1-6). This trend indicates mixing between radiogenic Pb with a $^{207}Pb/^{206}Pb$ value of approximately 0.1 and a component which consists of a common Pb subcomponent (high $^{204}Pb/^{206}Pb$) plus a radiogenic component with a distinctly lower $^{207}Pb/^{206}Pb$ (possibly around 0.07). The low $^{207}Pb/^{206}Pb$ radiogenic Pb indicates that this trend is the result of Pb mixing at a time much later than 1590 Ma, probably later than ~900 Ma.

The second possible mixing trend (Figure 3.10b) is formed by core analysis 1-1 and two analyses of the discontinuous outer rim, 1-4 and 1-5. This trend indicates mixing between radiogenic Pb with a $^{207}Pb/^{206}Pb$ value of about 0.95 and a Pb component which again comprises a high $^{204}Pb/^{206}Pb$ common Pb subcomponent and radiogenic Pb with a value of 0.07 to 0.08. This trend also indicates complex isotopic disturbance at an age much younger than 1590 Ma. Both trends support the interpretation that the isotopic systematics were strongly disturbed at a time later than approximately 900 Ma. The data also are permissive of the interpretation that hydrothermal zircon/ xenotime growth and alteration of magmatic zircon occurred at approximately 1600 Ma. If this is the case it would be consistent with the age of the ore depooist as determined by dating magmatic zircons (above). However, it is important to reinforce that the data from the hydrothermal zircon/ xenotime are complex, ambiguous, and ultimately inconclusive.

The remaining two analyses (1-7 and 1-8) are of the patterned overgrowth rimming the zircon core. On the $^{207}Pb/^{206}Pb$ versus $^{204}Pb/^{206}Pb$ plot (Figure 3.10a) these analyses lie well below the others, and probably represent areas of the zircon grain which have undergone disturbance much later in the deposit's history than is apparent for the other analyses.

The plot of $^{208}Pb/^{206}Pb$ versus $^{204}Pb/^{206}Pb$ (Figure 3.10b) shows a trend between the core analyses and those of the discontinuous outer overgrowth. The trend is from low $^{204}Pb/^{206}Pb$ - high $^{208}Pb/^{206}Pb$ for the core, toward high common Pb (high $^{204}Pb/^{206}Pb$), - low $^{208}Pb/^{206}Pb$ values for the overgrowth. The colinearity of the overgrowth analyses and the core analyses is consistent with the core having been altered by the fluids which produced the rim, as is suggested above on the basis of elevated U and Th concentrations in the core.

3.4.2.5 Summary

The hydrothermal overgrowths mantling relict magmatic zircons, and the hydrothermally altered magmatic zircon populations, have yielded information on several points of interest.

1) Although some of the data permit the interpretation of formation of hydrothermal zircon/ xenotime at ~1590 Ma (the age of the deposit indicated from magmatic zircon dates), the data are far from conclusive in this regard. The possible mixing arrays that permit this interpretation indicate major isotopic disturbance at ages of about 900 Ma or younger.

2) Most of the analyses of zircon overgrowths indicate Pb and/or U and Th mobility since formation, with closure to mobility of these elements at varying times from 1590 Ma to the present.

3) RX3212 zircon overgrowths show evidence of mixing involving " zero-age" Pb which has a strongly uranogenic composition, consistent with local derivation (within the deposit). Magmatic zircons from the same sample also show evidence for recent Pb mobility, consistent with the Pb-loss trend displayed on the concordia plot.

3.5 Discussion

Geochemical correlations between hematite content of breccias and REE concentrations (Oreskes and Einaudi,1990), REE and Cu concentrations in pyrite and chalcopyrite ores (Johnson and Cross, 1991b; Chapter 5), Cu and U concentrations (Roberts and Hudson, 1983; Oreskes and Einaudi, 1990; Reeve et al. 1990; Chapter 5), and U concentrations in hematite (Oreskes, 1990), all suggest that Cu, U and REE were introduced contemporaneously with Fe (hematite). Nd isotopic data (Johnson and Cross, 1991b; Chapter 7) support this conclusion. Therefore the implication of the minimum age constraints provided by the zircon dates for the hematite-producing hydrothermal system, is that primary economic mineralisation was also introduced at ~1590 Ma. Textural relationships and metal distributions in RD647 support this interpretation.

In a regional perspective, the dates reported here are the same within error as the age of the Gawler Range Volcanics, (1592 ± 2 Ma ; Fanning et al., 1988), an enormous outpouring of predominantly felsic magmas which form an extensive volcanic province covering an area of at least 25,000 km^2 (see Chapter 2). Thus the brecciation (and possibly the mineralisation) event at Olympic Dam can be correlated with a major thermal event that affected much of the Gawler Craton. This provides strong evidence in support of the genetic model of Reeve et al. (1990) who argued that the deposit formed as an integral part of the Gawler Range Volcanic event. Indeed, despite their altered nature, the dykes dated in this study bear trace element geochemical similarities to the Gawler Range Volcanics (Figure 3.11 overleaf).

The dated peperite dykes are representatives of the volcanic rocks thought by Oreskes and Einaudi (1990) to show evidence for "emplacement during hydrothermal activity", and Hitzman et al. (1992) suggest that these dykes may represent "...a direct magmatic affiliation" for the deposit. I agree with these geological interpretations. However, the correlation in age between the Olympic Dam Breccia Complex and the Gawler Range Volcanics does not agree with the age of brecciation as suggested by Oreskes and Einaudi (1990, 1992). These workers interpret the ~1400 Ma pitchblende date determined by

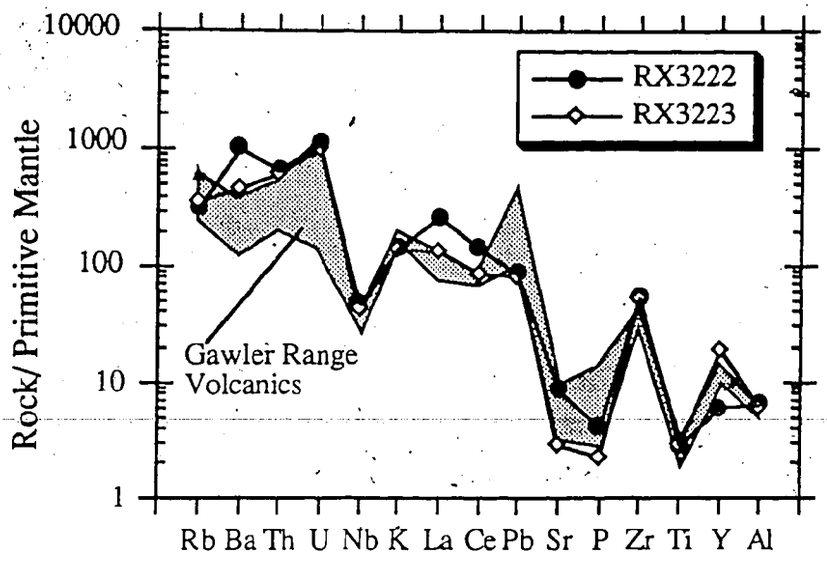

Figure 3.11 Comparison of incompatible element chemistry of the dated dyke samples RX3222 and RX3223 with felsic variants of the Gawler Range Volcanics (shaded field). The similar geochemistry coupled with the age correlation (see text) indicates that the dykes are correlatives of the Gawler Range Volcanics. Data for Gawler Range Volcanics after Blisset et al. (1989); mantle normalising values of Ringwood (1991).

Trueman et al. (1988) as the actual age of formation of the breccia complex, in contrast to the present interpretation of this date as a minimum age for ore formation (Chapter 4). The genetic model of Oreskés and Einaudi (1990) which follows from their acceptance of this age as being that of mineralisation, and which cannot relate the formation of the deposit to any know regional geological events, needs revision in light of the new age constraints reported here. They suggested that the large-scale hydrothermal activity at Olympic Dam probably required a magmatic heat source. I agree with this interpretation and suggest that the magmatic heat source is related to the Gawler Range volcanic event. Other evidence used by Oreskes and Einaudi (1990) and Einaudi and Oreskes (1989) to support the proposition that there was a long time interval between granite emplacement and ore deposition includes the coarse-grained nature of the host granite, coupled with the interpretation that the deposit formed in a near-surface environment. They suggest that a long interval is required to allow time for the uplift and unroofing of the plutonic body. However, the geochronological data now show that the Olympic Dam brecciation event occurred soon after emplacement of the Roxby Downs Granite, thus implying that the granite was emplaced at a high crustal level. The Roxby Downs Granite is a member of the Hiltaba supersuite of granitoids and these have been described as high level intrusives (Webb et al., 1986; Fanning et al., 1988; Giles, 1988; Mortimer et al., 1988a; Creaser, 1989; Reeve et al., 1990) on the basis of their intrusive relationships with volcanic rocks

regarded as cogenetic using geochemical criteria (Giles, 1988; Creaser, 1989). The Roxby Downs Granite, as a member of this suite, can therefore reasonably be postulated as a high level intrusive. Qualitative hornblende geobarometry indicates that the granitoids of the Burgoyne batholith crystallised at pressures less than 200 MPa, i.e. a maximum depth of approximately 7 km (Creaser, 1989). The granite may have crystallised at considerably shallower depths. If the granite magma intruded its own hot ejecta blanket the thermal gradient between the magma and the country rocks could be sufficiently low to allow the development of the coarsely crystalline texture now observed (e.g. Giles, 1988). The rounded dacitic cobbles preserved in the diatreme structures within the deposit may be remnants of such an overlying volcanic pile. Reeve et al. (1990) suggested that the hydrothermal system may even have vented through both the Roxby Downs Granite and some overlying volcanics (Gawler Range Volcanics equivalents).

3.6 Conclusions regarding Olympic Dam

The application of the ion microprobe SHRIMP to the geochronology of the Olympic Dam deposit has advanced our understanding of the genesis of the orebody. The dates reported here allow a confident age correlation between the deposit and regional magmatism, thereby establishing the tectono-magmatic environment of ore formation. Three minimum age constraints from intrusive rocks at Olympic Dam agree within error with the age of the granite which hosts the deposit, thereby constraining the age of the Olympic Dam Breccia Complex to be ~1590 Ma. Brecciation occurred in a near-surface environment, probably within a few million years (<8) of emplacement of the host granite. This implies that the granite was emplaced at a high crustal level, possibly intruding a comagmatic volcanic pile.

Analyses of zircons from hydrothermally altered granite provide two separate confirmations of the ~1590 Ma age of the granite determined by Creaser (1989). The hydrothermal zircon/ xenotime rims analysed have very complex isotopic systematics dominated by evidence for disturbance hundreds of millions of years after 1590 Ma. Some rims indicate disturbance in geologically recent times. The data are permissive of the interpretation that growth of hydrothermal zircon/ xenotime and alteration of magmatic zircon occurred at 1590 Ma, the age of the deposit indicated by igneous zircons. However, the data are too tenuous to be construed as strongly supporting this interpretation.

The Olympic Dam Breccia Complex can be correlated in age with the Gawler Range/ Hiltaba volcano-plutonic event. Indeed the two dykes dated in this study share trace element and petrographic similarities with felsic rocks of the Gawler Range Volcanics,

indicating that they are direct correlatives. The age correlation provides support for the interpretation of Reeve et al. (1990) who suggested that the deposit formed in a subvolcanic environment as an integral part of the Gawler Range/ Hiltaba event. It is inconsistent with the geochronological framework proposed by Oreskes and Einaudi (1990, 1992).

The age of the deposit clearly relates metallogenesis to a particular tectonic setting i.e. an environment of large scale crustal melting caused by the emplacement into the crust of large volumes of hot mantle-derived melts, probably an intracontinental rift setting (Reeve et al., 1990).

3.7 Regional lithologies dated

Two rock units which occur well outside the limits of the Olympic Dam deposit have been dated as part of this project. The first is an anorthositic gabbro which occurs in the Proterozoic basement beneath the Stuart Shelf sedimentary rocks near Andamooka (see Figure 2.1). The second is a tuff which according to field relationships and geochemical correlations (below) is interpreted to be contemporaneous with the basalts of the Roopena Volcanics, which crop out ~40 km southwest of Port Augusta (Figure 2.1). Both were dated in order to constrain the age of mafic rocks considered as potential analogues for sources of heat and/ or metals for Olympic Dam.

3.7.1 "Bill's Lookout" gabbro (RX4567)

RX4567 was sampled from Western Mining Corporation drillhole BLD1, drilled at the "Bill's Lookout" locality which lies northeast of the Andamooka Opal Field adjacent to Lake Torrens (Figure 2.1). The hole was drilled to test coincident gravity and magnetic anomalies, and intersected gabbro, the likely cause of the geophysical anomalies, at about 550 m depth. The gabbro is a dark green medium to coarse grained rock containing relatively minor anorthositic zones. It is only weakly deformed and hence is interpreted to have been relatively little affected by the Kimban Orogeny (1850 –1700 Ma; Fanning et al., 1988; Creaser, 1989; Parker, 1990), possibly even emplaced after the Kimban Orogeny. Indeed Creaser (1989; p.41) was unsure whether to classify the gabbro as belonging to "Suite 2" (older, deformed intrusives) or to "Suite 3" (undeformed Hiltaba supersuite intrusives). With regard to this project, it was therefore considered possible that the gabbro was emplaced at the same time as the post-orogenic Hiltaba supersuite granitoids and the Gawler Range Volcanics. If this was the case then the gabbro, as a contemporaneous mafic intrusion, would have warranted investigation as possibly being related to ore genesis at Olympic Dam.

RX4567 was taken from one of the anorthositic zones because these were thought to be the most likely to contain zircon. The anorthosite consists essentially of ~70% (by

Table 3.8 Ion probe data for RX4567; anorthositic gabbro from Bill's Lookout prospect

Analysis No.	U (ppm)	Th (ppm)	^{204}Pb (ppb)	f206[a] (%)	$^{204}Pb/^{206}Pb$	$^{208}Pb/^{206}Pb$	$^{206}Pb/^{238}U$	$^{207}Pb/^{235}U$	$^{207}Pb/^{206}Pb$	$^{207}Pb/^{206}Pb$ age ± 1σ
1.1	113	116	7	0.39	0.000248	0.300	0.2858 ± 88	4.30 ± 0.17	0.1092 ± 21	1786 ± 36
2.1	345	254	10	0.18	0.000118	0.215	0.2958 ± 90	4.38 ± 0.14	0.1075 ± 9	1757 ± 15
3.1	240	236	12	0.31	0.000197	0.292	0.3036 ± 92	4.50 ± 0.15	0.1074 ± 13	1756 ± 22
4.1	113	96	5	0.29	0.000189	0.253	0.2993 ± 92	4.47 ± 0.15	0.1083 ± 14	1771 ± 23
5.1	472	200	7	0.09	0.000055	0.121	0.2999 ± 91	4.49 ± 0.14	0.1085 ± 6	1774 ± 10
6.1	247	269	1	0.02	0.000010	0.275	0.3015 ± 92	4.52 ± 0.15	0.1088 ± 11	1780 ± 18
7.1	208	209	4	0.12	0.000078	0.292	0.2966 ± 90	4.37 ± 0.15	0.1068 ± 11	1745 ± 19
8.1	160	101	5	0.18	0.000115	0.187	0.3250 ± 99	4.83 ± 0.17	0.1078 ± 13	1763 ± 22
8.2	89	50	3	0.17	0.000111	0.157	0.3028 ± 94	4.34 ± 0.17	0.1040 ± 20	1696 ± 37
9.1	215	221	18	0.48	0.000311	0.277	0.3088 ± 94	4.41 ± 0.16	0.1035 ± 16	1688 ± 28
10.1	126	128	3	0.14	0.000090	0.286	0.3053 ± 95	4.48 ± 0.26	0.1065 ± 47	1740 ± 84
9.2	174	189	3	0.12	0.000076	0.287	0.3004 ± 93	4.49 ± 0.16	0.1083 ± 15	1772 ± 25
11.1	140	126	1	0.06	0.000036	0.264	0.3065 ± 94	4.51 ± 0.16	0.1067 ± 16	1744 ± 27

[a] Denotes the percentage of common ^{206}Pb in the total measured ^{206}Pb

volume) plagioclase and 30% relict clinopyroxene. Grains of clinopyroxene are euhedral and tabular, up to 5 mm long, and are extensively altered to hornblende around the grain margins and along cleavage traces. Plagioclase grains are euhedral, up to 10 mm long, and have undergone extensive alteration to sericite. Cracks within plagioclase grains are occasionally filled by secondary amphibole. The anorthosite contains accessory magnetite (martite), pyrite and zircon. Zircons are observed as individual, equant euhedra up to ~50 μm across, and as clusters of subhedral grains ~150 by 100 μm. They generally occur within plagioclase grains but are also present within some clinopyroxenes. The rock is weakly deformed, with a foliation defined mainly by veinlets of secondary amphibole. Cleavage traces in relict clinopyroxene commonly display kinks where the foliation is transgressive to the mineral cleavage.

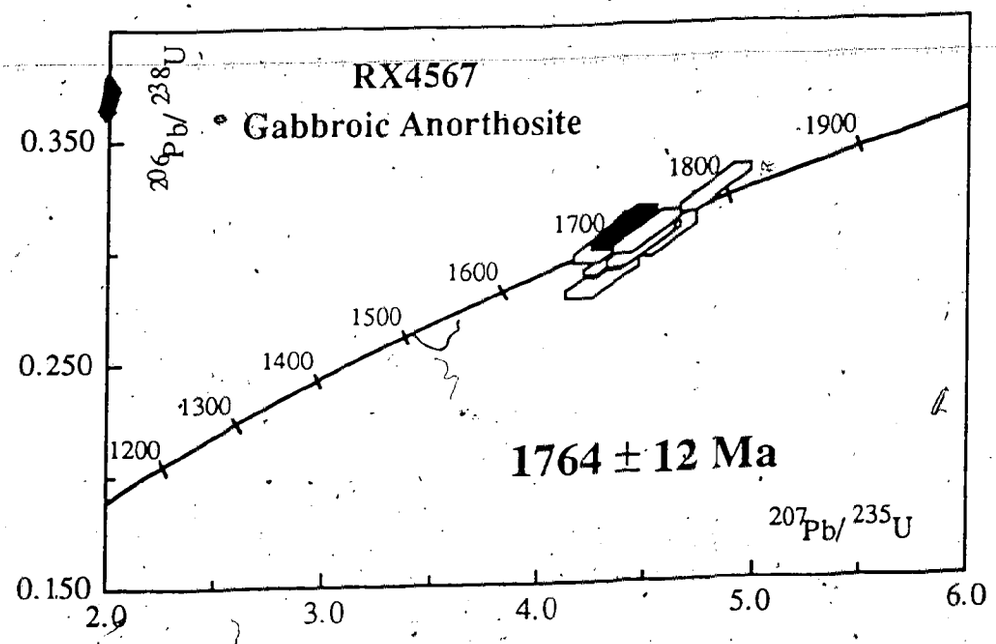

Figure 3.12 Concordia diagram for sample RX4567, a gabbroic anorthosite from the "Bill's Lookout" prospect near Andamooka (drillhole BLD1). Analysis 9-1, rejected from the age calculation, is shaded black (one sigma error boxes). At 1764 ± 12 Ma, the age of the gabbro demonstrates that it is too old to be considered a plausible source of heat or fluids for Olympic Dam ore genesis.

About 200 zircons were extracted and prepared in mount Z-904. The grains are mostly fragments of larger grains measuring up to ~150 μm wide and ~300 μm long. They are clear and generally unzoned. Thirteen analyses were made on eleven grains (see Table 3.8 and Figure 3.12). All analyses together yield an age of 1761 ± 12 Ma, but this has scatter in excess of that expected from analytical uncertainty. The scatter rests with analysis 9-1 and when this is deleted the resulting age is 1764 ± 12 Ma with no excess scatter. This is the preferred age for the anorthositic gabbro.

The calculated age can be correlated with the discordia upper intercept age of 1755 ± 12 Ma calculated by Fanning et al. (1988) for the McGregor Volcanics, a bimodal suite of acid tuffs and basaltic lavas exposed in the Moonabie Range southwest of Whyalla (Fanning et al., 1988). The deformation and alteration of the gabbro may be due to the effects of the late stages (D_3) of the Kimban Orogeny, or to the thermal and stress regime imposed during the ~1590 Ma emplacement of the adjacent Opal Fields Suite (Burgoyne batholith/ Hiltaba supersuite) granitoids. The "Bill's Lookout" gabbro age is ~170 m.y. older than the Olympic Dam Breccia Complex and it is therefore not a plausible source of heat or fluids for ore genesis at Olympic Dam. For this reason the gabbro has not been investigated further in this study.

3.7.2 Roopena Tuff

The Roopena Volcanics are a sequence of basalts which occur on and around Roopena Station (Figure 2.1). The main area of basalt outcrop is an erosional remnant lying in a palaeotopographic low in the unconformably underlying Moonabie Formation (Figure 3.13). Basalts are confined to the area between the Roopena Fault to the west, the Moonabie Formation to the south, and to the north and east by the sandstones of the Pandurra Formation which unconformably overlie the volcanics (Figure 3.13). There are numerous smaller areas of basalt outcrop occurring west of the Roopena Fault near Iron Knob and these may also belong to the Roopena Volcanics (Blisset et al., 1989, Gawler Range Volcanics map sheet).

In the past there has been some confusion over the age relationships of the rocks in this area. The Roopena Volcanics have been dated by Rb-Sr methods yielding ages of 1317 ± 30 Ma (Compston et al., 1966) and 1256 ± 120 Ma (Webb et al., 1982). However, these ages were called into question by an indicated Rb-Sr age of 1424 ± 51 Ma for shale interbeds in the overlying Pandurra Formation (Fanning et al., 1983), and by a geochemical correlation made between the Roopena Volcanics and basalts of the seemingly older Gawler Range Volcanics (Giles and Teale, 1979). Blisset et al. (1989) also equated the Roopena Volcanics with the Gawler Range Volcanics.

Sample RX4574 was taken as part of this study in order to provide further age constraints on the Roopena Volcanics. It is a sample of a tuff horizon that occurs at a depth of 94m in drillhole "Roopena DDH6" (drilled by the South Australian Department of Mines and Energy; see Figure 3.14). This drillhole is collared in the basalts of the Roopena Volcanics (e.g. sample RX4576), passes through an apparently conformable sequence consisting of ~70 m of siltstones and volcaniclastic sandstones, the sampled tuff horizon, and a second basalt horizon at ~106 m depth. The lower basalt horizon (e.g. sample RX4573) is similar in appearance to the basalt at the surface. Both are dark green, strongly altered, amygdaloidal rocks consisting originally of plagioclase and

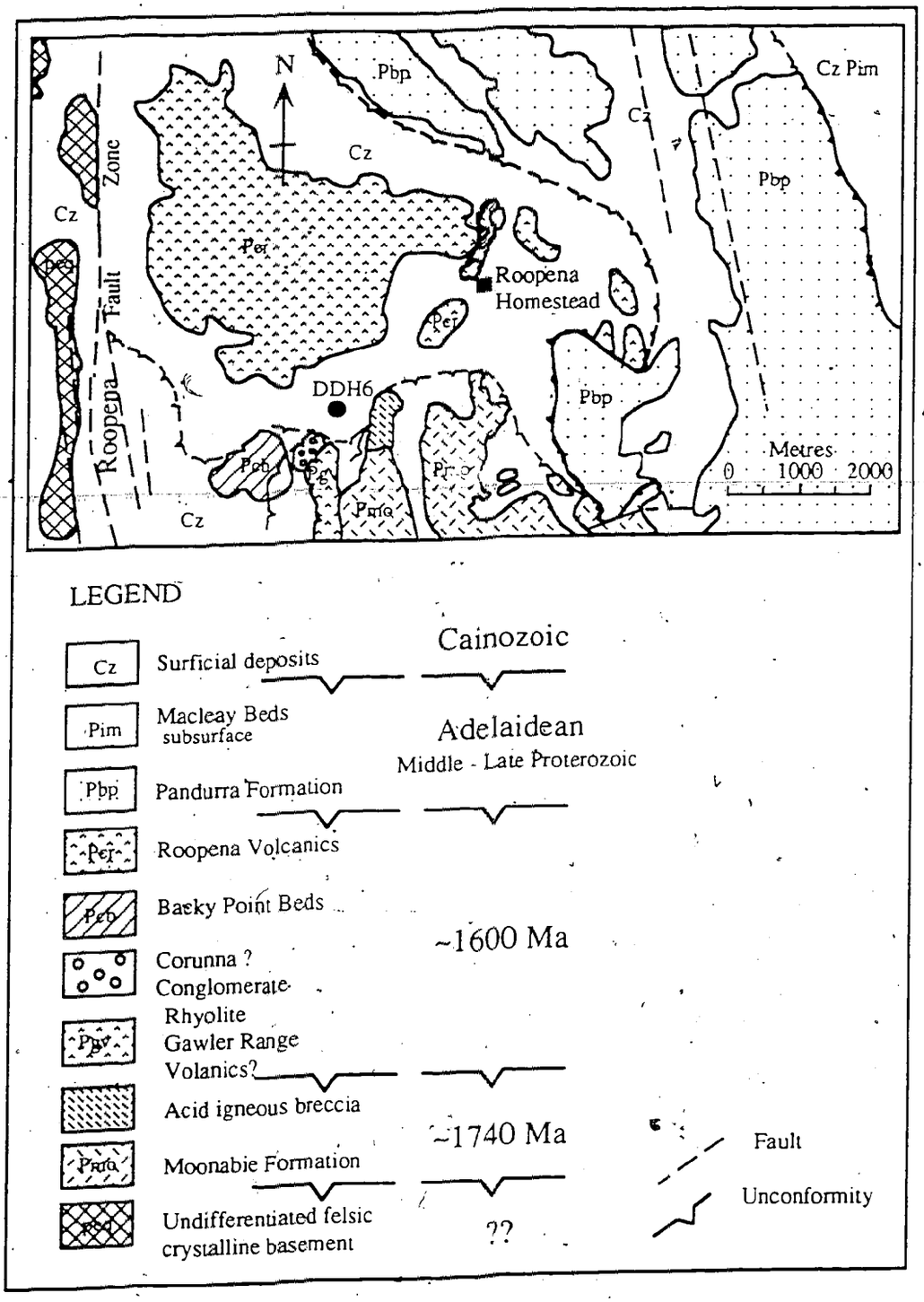

Figure 3.13. Geology of the Roopena area. Note location of Roopena DDH6 from which the dated tuff sample RX4574 was obtained. (Modified after Thomson et al., 1976; Figure 14)

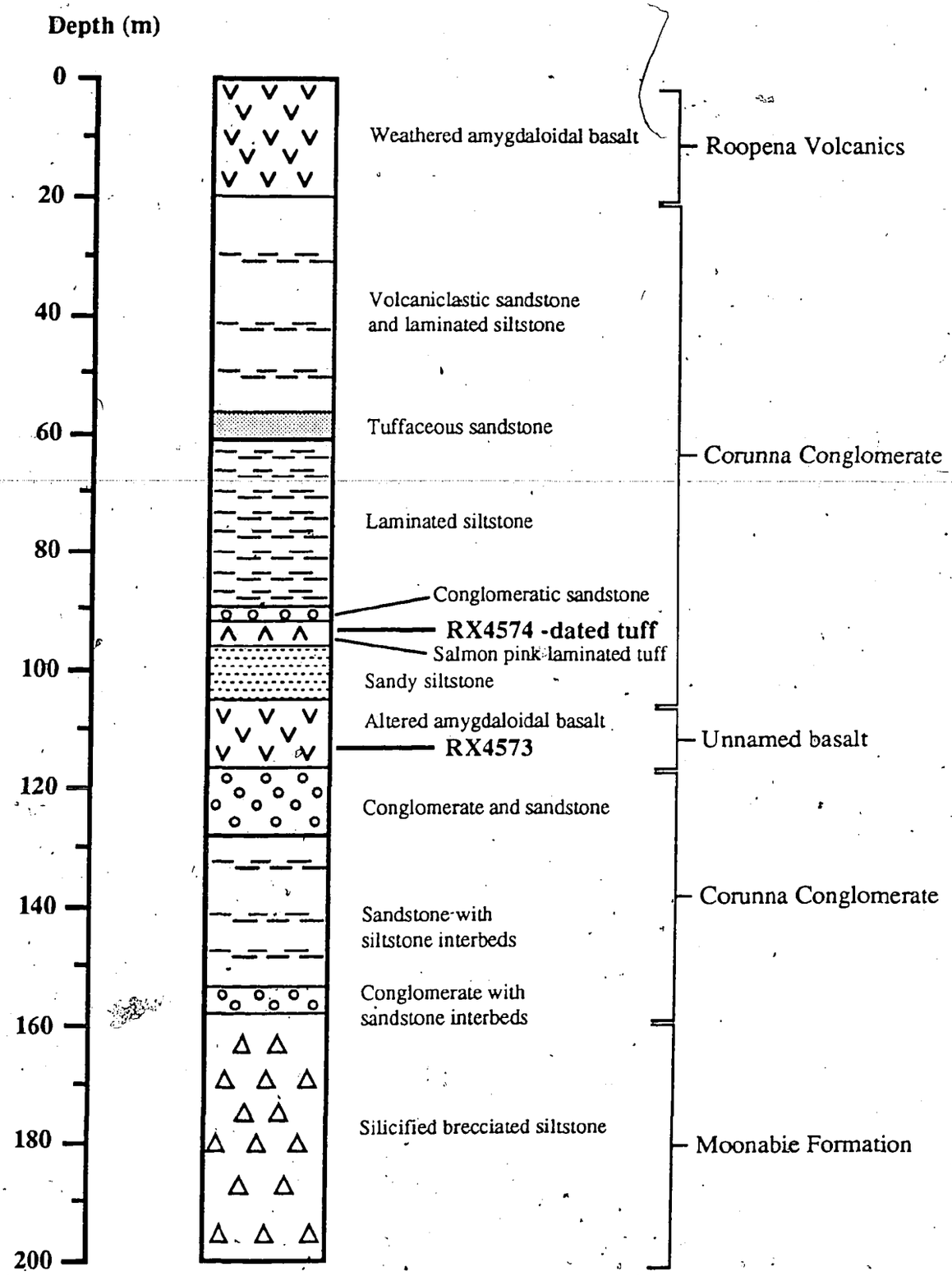

Figure 3.14 Summary log of Roopena DDH6 (South Australian Department of Mines and Energy). Basalt horizons at the surface and at 106-116m are geochemically correlated (RX4576 and RX4573; cf. Figure 3.15). Dated rhyolitic tuff sample RX4574 from 94m.

clinopyroxene with an intergranular texture. Plagioclase has been extensively altered to sericite, and pyroxene and rare olivine phenocrysts have been altered to chlorite, serpentine and hematite. The only obvious petrographic differences between RX4576 (surface basalt) and RX4573 (basalt at 106 m depth) are the presence of octahedral hematite after magnetite grains in RX4576, the presence of silicification in RX4576, and the presence of carbonate alteration in RX4573.

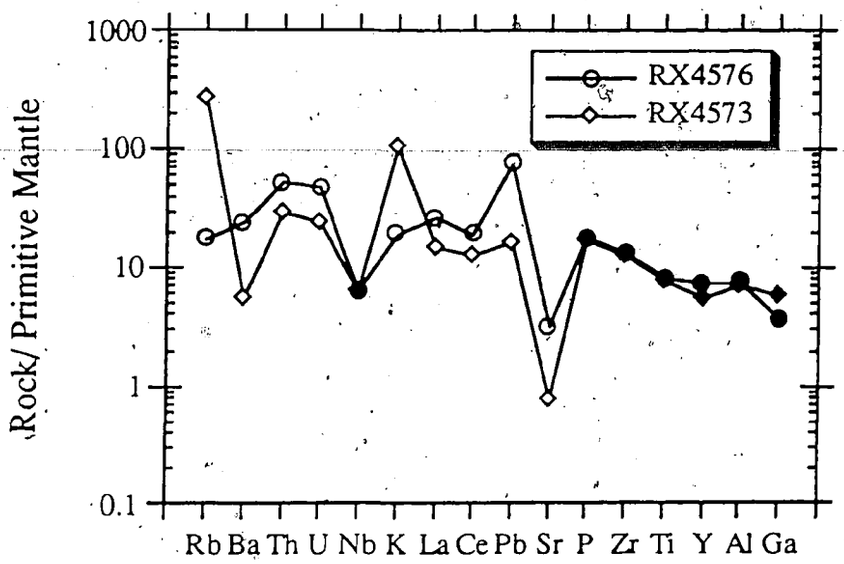

Figure 3.15 Geochemical comparison between altered basalt samples RX4576 (surface sample of Roopena Volcanics) and RX4573 (Roopena DDH6, 106m). Note the similarity of signatures for relatively immobile elements (closed symbols) suggesting that the two basalt horizons are genetically related. The differences in signature for the other elements (open symbols) are interpreted to result from element mobility during alteration (mantle normalising values of Ringwood, 1991).

The geochemistry of the two basalt horizons is compared in Figure 3.15. This diagram illustrates that the elements generally regarded as relatively immobile (Nb, P, Zr, Ti, Y and Al; shown by closed symbols) have similar signatures in both samples. The elements which show differences in signature (open symbols in Figure 3.15) are more mobile and are likely to have been disturbed during the extensive alteration experienced by these rocks. The geochemical signatures therefore suggest that the two basalt horizons are genetically related.

Given the geochemical correlation between the basalt unit below the tuff horizon with the surface basalts of the Roopena Volcanics, and the fact that the sequence of volcanics and volcanogenic sediments in which the tuff occurs appears to be conformable, it is reasonable to regard the lower basalts as being cogenetic with the Roopena Volcanics,

i.e. having formed in different pulses of essentially the same volcanic event. The lower basalt and the felsic tuff dated should therefore be regarded as part of the Roopena Volcanics. This means that the zircon age reported below represents the age of the Roopena Volcanics.

The dated sample (RX4574) is a salmon-pink, rhyolitic tuff displaying fine laminations and graded bedding. In thin section it displays a vitroclastic to eutaxitic texture and consists almost entirely of devitrified glass shards and angular fragments of volcanic quartz. The shards are moderately flattened parallel to the bedding plane but cannot have been intensely compacted because they show remnant cuspate shapes and no evidence of deformation around the angular quartz grains. Shards vary in size up to 500 μm long by 50 μm wide and are invariably altered to sericite. Shard rims are clearly defined by narrow zones of opaque oxide dusting. The interstices between larger shards are filled with microcrystalline aggregates of quartz and sericite, probably devitrified quartzo-feldspathic glass. The chemical composition of the (rhyolitic) tuff is listed in appendix 2. Figure 3.16 shows that the geochemical signature of RX4574 is similar to the felsic rocks of the Gawler Range Volcanics for some elements (Rb, Th, U, Nb, K, P, Zr, Ti, Al), but shows a marked contrast for others (Ba, La, Ce, Pb, Sr, Y).

Approximately 150 zircons were extracted from the tuff and prepared in Mount Z-905. Most of the zircons are clear and unzoned but there is evidence for an inherited zircon component, with several grains displaying clear unzoned rims around brown zoned cores. The grains are generally euhedral, equant and typically 50 to 100 μm across, although they range in size up to 200 μm by 100 μm.

Thirty-nine analyses were made on thirty-one zircon grains, and three age populations of zircons are recognised (Table 3.9). Figure 3.17 is a concordia diagram of these data and illustrates the three age populations. The principal zircon population has an age of 1587 ± 15 Ma (n=31; analyses 6-1 and 31-1 deleted on the grounds of ancient Pb loss). This is the same age as the Gawler Range Volcanics (1592 ± 2 Ma; Fanning et al., 1988) and confirms that this tuff is properly regarded as a correlative of these volcanics. This correlation suggests that the differences in geochemical signature between the tuff sample RX4574 and the felsic rocks of the Gawler Range Volcanics (Figure 3.16) may reflect the altered nature of the sample.

Four zircon grains analysed appear to be inherited from pre-existing rocks, with five analyses (20-1, 20-2, 22-1, 22-2 and 25-1) providing a pooled age of 1741 ± 40 Ma. The observed standard error on the mean $^{207}Pb/^{206}Pb$ ratio is greater than that expected from analytical uncertainties and is probably a result of variable disturbance of the isotopic systematics of these grains when they were assimilated into the rhyolitic magma

Table 3.9. Ion microprobe data for RX4574, a rhyolitic tuff from the Roopena Volcanics succession

Analysis No.	U (ppm)	Th (ppm)	^{204}Pb (ppb)	f206[a] (%)	$^{204}Pb/^{206}Pb$	$^{208}Pb/^{206}Pb$	$^{206}Pb/^{238}U$	$^{207}Pb/^{235}U$	$^{207}Pb/^{206}Pb$	$^{207}Pb/^{206}Pb$ age ± 1σ[b]
1.1	130	95	2	0.08	0.000052	0.158	0.2844 ± 52	3.89 ± 0.11	0.0992 ± 18	1610 ± 35
2.1	81	60	7	0.59	0.000367	0.225	0.2905 ± 54	3.86 ± 0.12	0.0963 ± 21	1554 ± 41
3.1	110	51	8	0.46	0.000288	0.142	0.2753 ± 51	3.69 ± 0.12	0.0972 ± 22	1572 ± 44
4.1	114	46	1	0.07	0.000043	0.119	0.2873 ± 53	3.97 ± 0.15	0.1002 ± 32	1627 ± 60
4.2	157	67	10	0.41	0.000256	0.129	0.2915 ± 53	3.88 ± 0.11	0.0966 ± 18	1559 ± 36
5.1	325	339	8	0.18	0.000115	0.178	0.2514 ± 44	3.45 ± 0.08	0.0995 ± 12	1615 ± 22
6.1	1216	3247	403	7.29	0.004572	0.301	0.0785 ± 14	0.89 ± 0.03	0.0820 ± 27	1244 ± 65
7.1	168	132	5	0.20	0.000126	0.199	0.2774 ± 50	3.69 ± 0.09	0.0964 ± 14	1555 ± 28
8.1	131	82	3	0.14	0.000086	0.180	0.2961 ± 54	4.02 ± 0.09	0.0985 ± 13	1596 ± 24
9.1	129	63	2	0.11	0.000070	0.149	0.2899 ± 52	3.93 ± 0.10	0.0983 ± 14	1592 ± 27
10.1	128	75	2	0.12	0.000072	0.184	0.2773 ± 39	3.78 ± 0.18	0.0990 ± 43	1605 ± 82
11.1	104	56	13	0.78	0.000490	0.170	0.3017 ± 92	3.77 ± 0.39	0.0907 ± 86	1440 ± 191
12.1	264	162	16	0.43	0.000272	0.196	0.2592 ± 73	3.41 ± 0.15	0.0953 ± 30	1534 ± 61
12.2	138	65	7	0.35	0.000217	0.142	0.2670 ± 71	3.49 ± 0.15	0.0948 ± 31	1525 ± 62
13.1	67	48	1	0.09	0.000057	0.217	0.2722 ± 74	3.72 ± 0.12	0.0990 ± 16	1605 ± 31
14.1	94	52	6	0.46	0.000286	0.168	0.2790 ± 75	3.77 ± 0.17	0.0981 ± 33	1589 ± 65
15.1	160	256	7	0.39	0.000246	0.223	0.2027 ± 54	2.70 ± 0.13	0.0965 ± 37	1558 ± 75
16.1	76	82	2	0.23	0.000143	0.283	0.2216 ± 135	3.26 ± 0.30	0.0980 ± 81	1586 ± 163
17.1	165	89	9	0.38	0.000241	0.154	0.2413 ± 68	3.62 ± 0.82	0.0954 ± 208	1536 ± 479
18.1	113	72	3	0.19	0.000119	0.184	0.2753 ± 94	3.62 ± 0.14	0.0949 ± 22	1526 ± 44

Table 3.9 continued

Analysis No.	U (ppm)	Th (ppm)	^{204}Pb (ppb)	f206[a] (%)	$^{204}Pb/^{206}Pb$	$^{208}Pb/^{206}Pb$	$^{206}Pb/^{238}U$	$^{207}Pb/^{235}U$	$^{207}Pb/^{206}Pb$	$^{207}Pb/^{206}Pb$ age ± 1σ
19.1	125	162	11	0.58	0.000362	0.378	0.2770 ± 74	3.66 ± 0.14	0.0961 ± 24	1549 ± 47
3.2	164	81	0	0.00	0.000002	0.138	0.2762 ± 74	3.98 ± 0.12	0.1003 ± 11	1630 ± 20
21.1	181	96	9	0.34	0.000212	0.151	0.3049 ± [illegible]	3.62 ± 0.14	0.0963 ± 24	1553 ± 47
21.2	132	77	10	0.50	0.000311	0.168	0.2386 ± 63	3.54 ± 0.23	0.0948 ± 53	1524 ± 109
23.1	131	83	23	1.13	0.000711	0.188	0.2880 ± 76	3.54 ± 0.21	0.0906 ± 44	1439 ± 95
24.1	165	73	4	0.16	0.000100	0.130	0.2729 ± 72	3.85 ± 0.13	0.1005 ± 19	1633 ± 35
27.1	191	180	59	2.17	0.001362	0.201	0.2708 ± 73	3.59 ± 0.16	0.1003 ± 31	1630 ± 59
27.2	116	93	3	0.19	0.000120	0.162	0.3123 ± 82	3.82 ± 0.45	0.0986 ± 110	1598 ± 224
28.1	118	63	11	0.59	0.000373	0.154	0.3119 ± 83	3.73 ± 0.14	0.0943 ± 21	1514 ± 42
29.1	125	133	2	0.11	0.000066	0.190	0.2835 ± 76	3.67 ± 0.14	0.1003 ± 23	1629 ± 44
30.1	139	76	13	0.59	0.000373	0.165	0.2778 ± 73	3.78 ± 0.14	0.0955 ± 23	1537 ± 46
31.1	147	84	21	0.92	0.000577	0.165	0.2352 ± 61	3.64 ± 0.14	0.0924 ± 23	1475 ± 48
Inherited zircons										
20.1	146	90	12	0.47	0.000300	0.179	0.2597 ± 69	4.50 ± 0.16	0.1070 ± 22	1749 ± 37
20.2	246	859	17	0.51	0.000326	0.268	0.2811 ± 81	3.51 ± 0.11	0.1068 ± 16	1746 ± 27
22.1	234	203	4	0.10	0.000065	0.244	0.2866 ± 76	4.67 ± 0.14	0.1085 ± 14	1773 ± 24
22.2	151	109	12	0.46	0.000289	0.184	0.2652 ± 71	4.48 ± 0.18	0.1041 ± 27	1698 ± 48
25.1	377	515	96	1.98	0.001241	0.272	0.2870 ± 76	3.33 ± 0.12	0.1028 ± 21	1675 ± 38
26.1	418	547	15	0.35	0.000222	0.070	0.2854 ± 75	2.97 ± 0.09	0.1130 ± 14	1847 ± 23

[a] Denotes percentage of common ^{206}Pb in the total measured ^{206}Pb

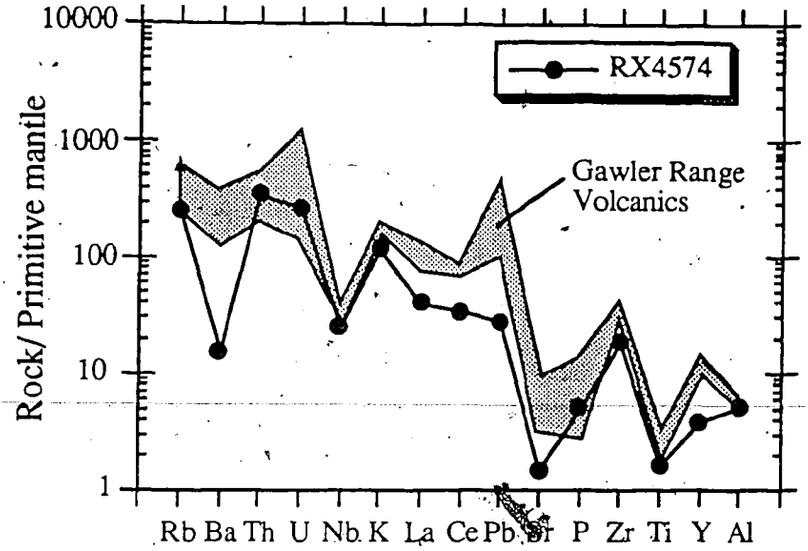

Figure 3.16 Comparison of chemical signatures of rhyolitic tuff sample RX4574 from Roopena (DDH6, 94m), and the felsic rocks of the Gawler Range Volcanics (data from Blisset et al., 1989). The signatures are similar for Rb, Th, U, Nb, K, P, Ti, and Al. Other elements (excluding Ba) show similarity in pattern shape but differ in degree of enrichment. Mantle normalising values of are those of Ringwood (1991).

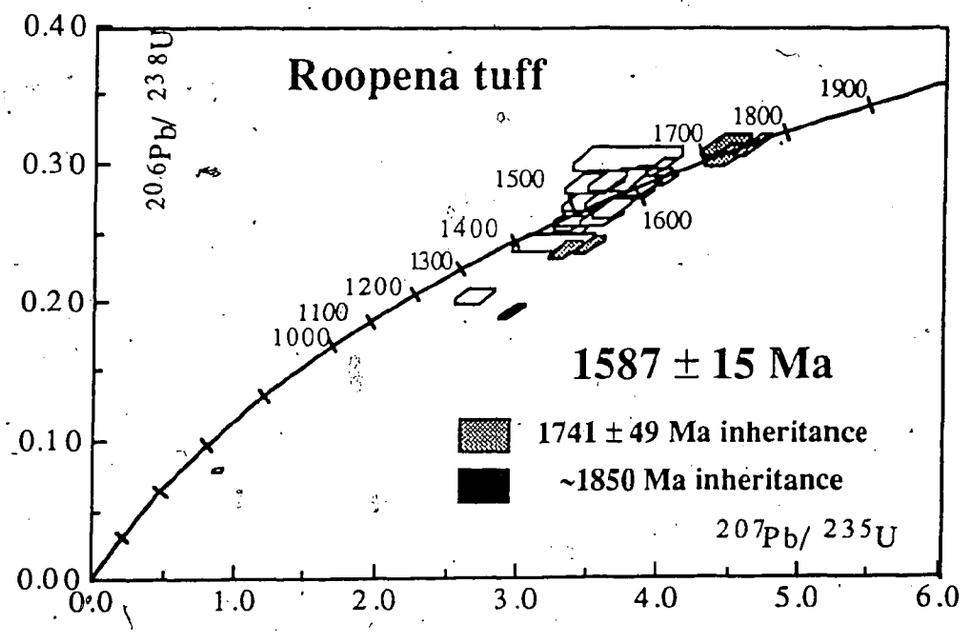

Figure 3.17 Concordia diagram for sample RX4574, a rhyolitic tuff from a conformable sequence of the Roopena Volcanics (Roopena DDH6, 94m). The age of the tuff (1587 ± 15) is indistiguishable from that of the Gawler Range Volcanics (1592 ± 2; Fanning et al., 1988), thereby cofirming the correlation between the Roopena Volcanics and basalts of the Gawler Range Volcanics proposed by Giles and Teale (1979).

at ~1590 Ma. The inheritance age of 1741 ± 40 Ma is within error of the age of the McGregor Volcanics (~1740 Ma; Fanning et al., 1988). The Moonabie Formation, which underlies the Roopena Volcanics, is interlayered with the McGregor Volcanics in the Moonabie Range (Webb et al., 1986). The McGregor Volcanics are therefore a probable source of much of the volcanogenic detritus in the Moonabie Formation, and possibly are the ultimate source of the 1741 ± 40 Ma inherited zircons in the Roopena tuff.

A single discordant analysis (26-1) has an apparent age of 1848 ± 23 Ma ($^{207}Pb/^{206}Pb$ age, 1σ error). This age can be correlated with the age of the Tidnamurka Volcanics (1806 ± 27 Ma) in the Peake and Denison Inlier in the northeast of the Gawler Craton (Fanning et al., 1988), rhyodacites of the Bosanquet Formation near Kimba (1845 ± 9 Ma; Rankin et al., 1988), and with the granitoids of the Donington Suite (1843 ± 2 Ma; Mortimer et al., 1988b).

As mentioned above, the main age population of zircons from the Roopena tuff (1587 ± 15 Ma) shows that the tuff can be correlated with the Gawler Range Volcanics. The similarity of geochemical signatures of the two basalt horizons, above and below the tuff, suggests that they are genetically related and therefore that the magma chamber from which they emanated existed through the time interval in which the dated tuff was deposited. It is therefore concluded that the age of the rhyolitic tuff effectively constrains the age of the Roopena Volcanics.

The age correlation between the Roopena Volcanics and the Gawler Range Volcanics confirms the geochemical correlation of basalts made by Giles and Teale (1979) and Blisset et al. (1989). It is significant because it represents recognition of the largest areal extent of mafic volcanism yet observed to be associated with the Gawler Range Volcanic event. The other exposures of basalts (e.g. near Kokatha) occur low in the Gawler Range Volcanics stratigraphy, whereas the Roopena Volcanics are stratigraphically higher than the Corunna Conglomerate, a unit thought to be contemporaneous with the later stages of the Gawler Range Volcanic event (Blisset et al., 1989). This demonstrates a continuing input of mafic magmas through the duration of the Gawler Range volcanic event. The existence of chronostratigraphically late basaltic volcanism in the Roopena Volcanics also illustrates that the late stage mafic/ ultramafic magmatism in the Olympic Dam deposit, evident as dykes and diatremes, is not a unique occurrence in the Gawler Range event. This point has implications for models of ore genesis because it more clearly illustrates the availability at high crustal levels of a source of intense heat which would be able to drive hydrothermal circulation.

4 U-Pb PITCHBLENDE GEOCHRONOLOGY

4.1 Introduction

The main uranium mineral in the Olympic Dam deposit is pitchblende which, as mentioned in Chapter 2, occurs in a variety of forms. Fine grained disseminations in hematitic breccias may be primary forms, whereas cavity-filling colloform, crustiform and vein occurrences in both hematitic and altered granitic rocks are probably secondary. Pitchblende at Olympic Dam also has a variety of mineralogical associations, with high grade U frequently concentrated in a narrow (10-20 m) zone within bornite-chalcocite ore zones. However, it can also occur in zones of continuous high U concentration which are transgressive to the chalcopyrite-bornite sulphide interface. The variety of modes of occurrence of pitchblende and particularly the presence of secondary styles of mineralisation, suggest that U has undergone at least localised remobilisation after the primary mineralisation event at ~1590 Ma (probable primary mineralisation age established in Chapter 3). This raises questions about the importance of remobilisation processes in forming economic concentrations of U at Olympic Dam. Remobilisation of U may have been episodic and related to regional geological events which provided anomalous heat and fluid fluxes, e.g. the emplacement of the Gairdner Dyke Swarm dolerites at ~1060 Ma, the sealing of the unconformity above the deposit in the Late Proterozoic, or perhaps deformational events in the nearby Adelaide Fold Belt (early Palaeozoic; von der Borch, 1980).

It is also possible that U remobilisation has been more or less continuous, perhaps with U dissolving in oxidised groundwaters as complexes of U^{6+} and reprecipitating in more reduced microenvironments e.g. in contact with sulphide minerals. The heat generated by radioactive decay of U in the deposit may have been sufficient to drive low-level fluid circulation throughout the deposit's history, thus facilitating the semi-continuous mobilisation of U. The uranium series disequilibrium observed by Guthrie (1991) indicates that U has been mobile even in recent times at Olympic Dam, which is consistent with the "semi-continuous" remobilisation model. The question of which U-remobilisation model is more applicable at Olympic Dam can be addressed by dating the different forms of uranium mineralisation. An ion microprobe study of Olympic Dam pitchblende was initiated for this purpose and to attempt to date the primary mineralisation event. Recognition of major remobilisation events would illustrate potentially important events in upgrading the deposit, and would lend support to age interpretations based on the U-Pb discordia regression approach (e.g. Trueman et al., 1988). On the other hand, recognition of continual microscale Pb and U remobilisation events in pitchblendes would indicate that the assumption of episodic Pb loss implicit in the discordia regression of Pb-

U data is not justified, and that age interpretations would be better based on apparent $^{207}Pb/^{206}Pb$ ages as minimum age constraints.

Previous attempts to date uranium mineralisation using the ion microprobe include that described by Shimizu and Hart (1982) in which the Pb isotopic compositions of inclusions of galena within uraninite were used to place minimum age constraints on uraninite formation. Hinthorne et al. (1979) dated uraninite from the Witwatersrand Reefs by ion microprobe. These workers noted variable common Pb and obtained dates which were slightly lower than the accepted ages for the uraninites in the region. Reed et al. (1987) and Trueman et al. (1988) provided further descriptions of dating pitchblende directly using an ion probe, and both contributions refer to dating of the same samples from Olympic Dam. These workers did not use a uraninite standard to calibrate Pb/U ratios internally, but rather measured Pb and U concentrations by electron probe analysis in the ion probe pits and converted Pb/U atomic ratios to isotopic ratios using the Pb/Pb isotopic data. In deriving a discordia through means of ion probe analyses they implicitly assumed that all of the pitchblendes analysed and used in the regression shared a common age of precipitation, and that Pb loss for all samples occurred in a single event. They therefore tentatively proposed that the discordia upper intercept age of ~1400 Ma represents the age of the primary mineralisation event at Olympic Dam. It is important to assess the validity of this age calculation because it has been used by Oreskes and Einaudi (1990, 1992) to erect an ore genesis model which postulates that ore deposition occurred ~200 Ma after emplacement of the Roxby Downs Granite. The key issue in the credibility of the 1400 Ma discordia age is the nature of U remobilisation, whether it is episodic, or more-or-less continuous. The data presented in this study indicate that mobility of U and/ or Pb has affected the U mineralisation for over one billion years and therefore suggest that the use of the discordia approach is inappropriate (see section 4.6.2 below). This provides a simple explanation for the discrepancy between the interpreted primary mineralisation age of ~1400 Ma presented by Trueman et al. (1988) and the primary mineralisation age of ~1590 Ma interpreted from the zircon geochronological work presented in Chapter 3.

In zircon geochronological studies using SHRIMP, $^{206}Pb/^{238}U$ ratios of unknowns are calibrated using the correlated ion yields of Pb^+, U^+ and UO^+ from a standard zircon for which the $^{206}Pb/^{238}U$ ratio is known from Thermal Ionisation Mass Spectrometry (TIMS). No such standard was in use for uraninite/ pitchblende at the commencement of this study. Although use of such a standard would have been the ideal way to approach ion probe studies of pitchblende, it was recognised that developmental work for a uraninite standard would represent a substantial investment of time and effort. In order to assess the merits, with regard to the Olympic Dam pitchblende application, of investing the time on developing a uraninite standard, a reconnaissance ion probe study was undertaken. In view of the preliminary nature of this study, the criterion used for sample

selection was ease of sample preparation and analysis. Consequently five samples of the coarsest pitchblende available were selected, including a traverse of three samples from the outer to the inner growth bands of a vug filled by chalcopyrite and pitchblende (RX3642, 1-3), a vein of pitchblende + chalcocite within sericite-altered granite (RX3700), and a coarse-grained pitchblende + bornite/chalcocite intergrowth (RX4569). All of these samples are probably secondary forms of mineralisation.

4.2 Samples

RX3642 was taken from the "37 DNW Green 5 Undercut" locality and is a sample of a vug filled with concentric layers of chalcopyrite, silty black hematite and crustiform pitchblende. Three samples representing different chronostratigraphic layers were cored from a polished thin section of this sample and mounted in a single ion probe mount. In each of the three vug-samples the pitchblende is coarse grained and relatively free of visible inclusions, with individual grains up to ~500 µm providing large areas of pure pitchblende for analysis (see Plate 5).

RX3700 was sampled from drill hole RD 783 at 675m depth and is a sample of a 3mm wide vein of pitchblende + chalcocite which cuts sericitised granite. The pitchblende has colloform habit with individual grains up to ~150 µm across, and is intimately intergrown with chalcocite. The pitchblende has a "dirty" appearance with ubiquitous microscopic inclusions which could not be avoided during analysis (see Plate 6). The inclusions are generally less than 1 µm in size and, although they have not been definitely identified, the electron probe in Energy Dispersive Spectrum (EDS) mode showed a copper peak for scans of this sample, suggesting that the inclusions may also be chalcocite.

RX4569 was sampled from the"" DNW Green 3" stope and is a sample of coarsely intergrown pitchblende and bornite/ chalcocite. It is from an ore zone which Oreskes and Einaudi (1990) suggested has a supergene origin i.e. secondary enrichment, in a weathering environment, of a primary chalcopyrite-rich ore . Although the pitchblende + bornite intergrowths are coarse (zones up to 3 cm wide), the colloform pitchblende invariably has micron-scale inclusions of bornite ± chalcocite (EDS scans on the electron probe showed the presence of copper) and hematite such that it is impossible to analyse a ~30 µm diameter spot without analysing inclusions along with the pitchblende (see Plate 6). The fact that pitchblende occurs as inclusions within sulphide grains in the same sample as sulphide inclusions within pitchblende suggests that the two minerals precipitated contemporaneously. This in turn suggests that a reliable date on the pitchblende in this sample would represent a date on the bornite/ chalcocite mineralisation in this locality and may be of relevance to the question of supergene enrichment.

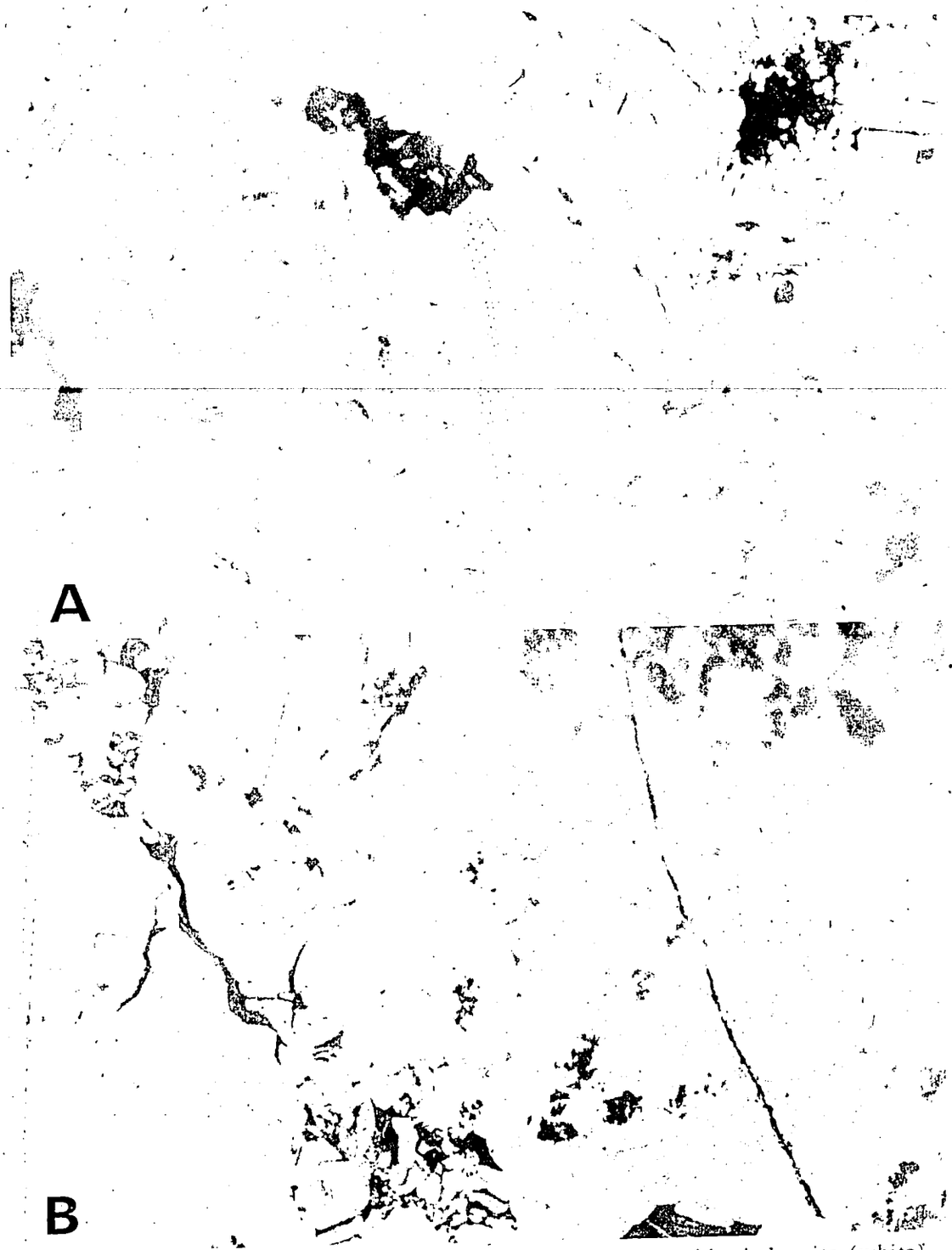

Plate 6. A) RX3700. Pitchblende (light grey) intergrown with chalcocite (white). Mottled appearance of pitchblende is due to evenly distributed inclusions (many < 1μm) of a Cu-mineral, probably chalcocite (see text).

B) RX4569. Pitchblende (mid-grey) intergrown with chalcocite (white) and bornite (pink). Sulphide inclusions within pitchblende, and vice versa within the same sample, indicate contemporaneous growth for these minerals. Chalcocite infilling polygonal cracks (right) may represent remobilisation of sulphides after pitchblende precipitation. Width of frame is 325 μm for A) and B).

4.3 Analytical Methods

Analysis was carried out using SHRIMP at the Australian National University. Each analysis consists of the mean of four scans through the masses ^{204}Pb, ^{206}Pb, ^{207}Pb, ^{208}Pb, ^{238}U, $^{248}(ThO)$, $^{254}(UO)$ and $^{270}(UO_2)$, with respective count times of 10s, 5s, 10s, 10s, 1s, 5s, 1s, and 1s. The Pb/Pb isotopic ratios are accepted as measured and common lead corrections are made based on the abundance of ^{204}Pb using average crustal Pb compositions (Cumming and Richards, 1975) appropriate to the $^{207}Pb/^{206}Pb$ ages indicated for each analysis. No allowance was made for the contribution of Pb hydrides to the Pb peaks measured because of the reconnaissance nature of the study. However, it is recognised that this would be necessary for routine analysis of unknowns, and that monitoring of hydrides would be facilitated by the use of a standard uraninite with known isotopic ratios.

Determination of Pb/U ratios is more complex than Pb/Pb ratios. During ion probe analysis the sputtering process does not yield Pb^+ and U^+ ionic species in the same relative abundance as the Pb/U elemental ratio in the sample. The $^{206}Pb/^{238}U$ ratio therefore has to be determined indirectly and this can be done by two methods: (A) The method used by Trueman et al. (1988) and Reed et al. (1987) in which electron probe measurements of Pb and U are used in conjunction with the Pb isotopic composition to calculate $^{206}Pb/^{238}U$, or (B) The method described by Compston et al. (1984, 1986) for zircon analysis in which $^{206}Pb/^{238}U$ is determined by calibrating the correlated yields of Pb and U ionic species for a mineral standard with known $^{206}Pb/^{238}U$. Method (B) is regarded as preferable because it relies on one analysis technique only and in so doing avoids the possibility that the Pb/U ratio determined from the relatively narrow beam of the electron probe is not representative of the Pb/U ratio over the whole volume analysed by the ~30 μm beam of the ion probe. In view of the unavailability of a uraninite/pitchblende standard at the commencement of this study, the internal $^{206}Pb/^{238}U$ calibration method could not be employed immediately. One of the aims of the reconnaissance study was to ascertain whether pitchblende would yield well-correlated abundances of Pb and U ionic species in a similar manner to zircons because, if this were the case, it would suggest that routine ion probe analysis of pitchblende would be feasible if a standard uraninite was developed. Consequently, $^{206}Pb/^{238}U$ ratios were determined by a modified internal calibration method which allowed for the absence of a mineral standard. For comparison, they were also determined by using electron probe Pb/U determinations. The calibration method is discussed in detail in Section 4.4 and the results of the two methods are listed in Table 4.1.

4.4 Lead - Uranium calibration

The standard procedure for the calibration of Pb/U ratios for SHRIMP analyses of zircon is to derive a calibration curve which relates the measured ionic ratios of $^{206}Pb^+/^{238}U^+$ and $^{254}(UO^+)/^{238}U^+$ for a standard zircon with known $^{206}Pb/^{238}U$. The $^{206}Pb/^{238}U$ ratio for the unknowns is then calculated from the following equation:

$$^{206}Pb/^{238}U_{sample} = {}^{206}Pb/^{238}U_{std.} \cdot \frac{(^{206}Pb^+/^{238}U^+_{meas.})}{(^{206}Pb^+/^{238}U^+_{calc.})} \quad (1)$$

where $^{206}Pb^+/^{238}U^+_{meas.}$ represents the measured ionic ratio for the sample, and $^{206}Pb^+/^{238}U^+_{calc.}$ is the ionic ratio calculated by applying the equation of the calibration curve to the measured UO^+/U^+ for the sample. In the absence of a uraninite/ pitchblende standard the calibration curve was derived by a modified version of the method described above. With a standard, the calibration curve would be derived from the correlated $^{254}(UO^+)/^{238}U^+$ and $^{206}Pb^+/^{238}U^+$, or $^{270}(UO_2^+)/^{254}(UO^+)$ and $^{206}Pb^+/^{254}(UO^+)$ ionic ratios, with the assumption that the standard has a homogeneous Pb/U elemental ratio. This assumption cannot be made in the present study because the analyses are on different pitchblende grains. To circumvent this problem, the Pb/U calibration was derived by the following procedure:

(i) One ion probe analysis (3642-3.2), which had also been analysed by electron probe, was arbitrarily designated as a standard analysis to which all others would be related.

The atomic weight of the Pb analysed by this spot was calculated;

$$\text{At. Wt. Pb} = \frac{\{206+(207.^{207}Pb/^{206}Pb)+(208.^{208}Pb/^{206}Pb)+(204.^{204}Pb/^{206}Pb)\}}{1+^{207}Pb/^{206}Pb+^{208}Pb/^{206}Pb+^{204}Pb/^{206}Pb} \quad (2)$$

The atomic weight was used to convert the PbO_2 wt% value from electron probe analysis into molecular proportions which, when divided by the molecular proportions of UO_2, yields the Pb/U elemental ratio for the standard analysis. The $^{206}Pb/^{238}U$ isotopic ratio was then calculated using the Pb/U elemental ratio, the Pb isotopic data, and the constancy of the isotopic proportions of U.

The use of this analysis as a standard with "known" $^{206}Pb/^{238}U$ assumes that the Pb/U ratio as determined from electron probe analysis is representative of the whole volume analysed by the larger beam of the ion probe. This assumption may not be valid and, if incorrect, will cause a systematic error in all of the Pb/U isotopic ratios calculated from this "standard" analysis. However, this will not detract from the value of the reconnaissance calibration exercise because its aim is to test the method rather than the

Table 4.1 Data used in the calibration of $^{206}Pb/^{238}U$ ratios (method described in text).

	Measured ion probe ratios					Electron probe		Calculated values					
Analysis No.	$^{204}Pb/^{206}Pb$	$^{207}Pb/^{206}Pb$	$^{208}Pb/^{206}Pb$	$^{206}Pb/UO$	UO_2/UO	Wt% PbO_2	Wt% UO_2	Atom..Wt. Pb	Pb/U. atomic	$^{206}Pb/^{238}U$ ep	$^{206}Pb/UO$ norm.	$^{206}Pb/UO$ calib.	$^{206}Pb/^{238}U$ calib.
Vug samples- chalcopyrite + pitchblende													
3642-1.1	0.000097	0.059093	0.005035	0.0740	1.6376			206.0648				0.3014	0.0490
3642-1.2	0.000091	0.060237	0.004859	0.0952	1.6131	4.84	83.74	206.0655	0.0655	0.0620	0.3133	0.2872	0.0661
3642-1.3	0.000105	0.059125	0.005346	0.1181	1.7409	4.5	82.55	206.0654	0.0618	0.0585	0.4121	0.3643	0.0647
3642-1.4	0.000130	0.057792	0.006160	0.0668	1.6763	3.16	81.79	206.0656	0.0438	0.0415	0.3288	0.3245	0.0411
3642-1.5	0.000106	0.058487	0.005042	0.0647	1.7148			206.0643				0.3480	0.0371
3642-1.5	0.000100	0.058342	0.004840	0.0579	1.5629			206.0638				0.2587	0.0447
3642-2.1	0.000095	0.057634	0.005034	0.0451	1.5163	1.63	42.31	206.0635	0.0437	0.0414	0.2227	0.2332	0.0386
3642-2.2	0.000139	0.057459	0.005800	0.0441	1.4938	1.7	35.9	206.0647	0.0537	0.0509	0.1771	0.2212	0.0398
3642-2.3	0.000118	0.056196	0.005006	0.0450	1.5613	2.58	83.48	206.0622	0.0350	0.0333	0.2771	0.2578	0.0348
3642-2.4	0.000077	0.056551	0.004441	0.0417	1.4671	3.05	84.04	206.0615	0.0412	0.0391	0.2187	0.2072	0.0402
3642-2.5	0.000100	0.056945	0.004852	0.0270	1.3036	2.79	83.78	206.0626	0.0378	0.0358	0.1542	0.1281	0.0420
3642-3.1	0.000067	0.086299	0.003093	0.3994	1.7393	15.27	75.64	206.0848	0.2289	0.2117	0.3764	0.3633	0.2194
3642-3.2	0.000069	0.085586	0.003373	0.4618	1.9256	14.43	75.85	206.0847	0.2157	0.1995	0.4618	0.4877	0.1889
3642-3.3	0.000069	0.085432	0.003284	0.3734	1.7903	13.97	75.99	206.0844	0.2085	0.1929	0.3864	0.3959	0.1882
3642-3.4	0.000072	0.084819	0.003217	0.4124	1.841			206.0837				0.4294	0.1916
3642-3.5	0.000069	0.085725	0.003346	0.3850	1.7642			206.0847				0.3791	0.2027

Table 4.1 contd.

Analysis No.	Measured ion probe ratios $^{204}Pb/^{206}Pb$	$^{207}Pb/^{206}Pb$	$^{208}Pb/^{206}Pb$	$^{206}Pb/UO$	UO_2/UO	Electron probe Wt% PbO_2	Wt% UO_2	Atom. Wt. Pb	Pb/U atomic	Calculated values $^{206}Pb/^{238}U$ ep	$^{206}Pb/UO$ norm.	$^{206}Pb/UO$ calib.	$^{206}Pb/^{238}U$ calib.
Vug samples- chalcopyrite + pitchblende													
3642-3.6	0.000080	0.063672	0.004311	0.0554	1.4614	4.49	80.14	206.0675	0.0635	0.0599	0.1880	0.2043	0.0541
3642-3.7	0.000067	0.081796	0.003640	0.2161	1.5695	14.27	74.61	206.0819	0.2169	0.2013	0.2149	0.2624	0.1643
3642-3.8	0.000084	0.078706	0.003909	0.0874	1.3746	6.87	71.29	206.0798	0.1093	0.1017	0.1725	0.1611	0.1082
3642-3.9	0.000070	0.083838	0.003132	0.1076	1.3676	11.36	76.4	206.0828	0.1686	0.1562	0.1377	0.1578	0.1361
3642-3.10	0.000060	0.085403	0.002821	0.1186	1.3536	13	75.17	206.0835	0.1961	0.1815	0.1305	0.1511	0.1566
3642-3.11	0.000102	0.060127	0.004867	0.0410	1.3753	3.88	80.13	206.0654	0.0549	0.0519	0.1609	0.1615	0.0506
Bornite-chalcocite-pitchblende													
4569.1	0.000143	0.061372	0.006632	0.1240	1.5461	5.92	72.5	206.0696	0.0926	0.0873	0.2888	0.2494	0.0992
4569.2	0.000189	0.061771	0.009909	0.1131	1.5558	6.06	74.12	206.0758	0.0927	0.0871	0.2633	0.2547	0.0886
4569.3	0.000168	0.061404	0.008412	0.1261	1.634	6.06	77.35	206.0728	0.0888	0.0836	0.3063	0.2993	0.0841
4569.4	0.000155	0.061559	0.007454	0.0916	1.491	5.79	68.2	206.0712	0.0963	0.0907	0.2053	0.2197	0.0832
4569.5	0.000282	0.063052	0.013804	0.0870	1.4534	5.64	64.91	206.0836	0.0985	0.0921	0.1904	0.2002	0.0867
4569.6	0.000135	0.060855	0.006345	0.0773	1.4626	5.95	71.84	206.0687	0.0939	0.0886	0.1775	0.2049	0.0753
4569.7	0.000249	0.062161	0.011551	0.0740	1.4592			206.0789				0.2032	0.0727

Table 4.1 contd.

Analysis No.	Measured ion probe ratios					Electron probe		Calculated values					
	$^{204}Pb/^{206}Pb$	$^{207}Pb/^{206}Pb$	$^{208}Pb/^{206}Pb$	$^{206}Pb/UO$	UO_2/UO	Wt% PbO_2	Wt% UO_2	Atom. Wt. Pb	Pb/U atomic	$^{206}Pb/^{238}U$ ep	$^{206}Pb/UO$ norm.	$^{206}Pb/UO$ calib.	$^{206}Pb/^{238}U$ calib.
Chalcocite-pitchblende vein													
3700.1	0.000091	0.080112	0.004610	0.2887	1.416	8.59	78.34	206.0822	0.1243	0.1155	0.5009	0.1813	0.3177
3700.2	0.000088	0.078814	0.004901	0.2659	1.3952	11.86	73.53	206.0816	0.1829	0.1700	0.3136	0.1711	0.3101
3700.3	0.000093	0.080731	0.004836	0.3060	1.4001	12.94	73.47	206.0831	0.1997	0.1853	0.3305	0.1735	0.3520
3700.4	0.000103	0.079871	0.005011	0.2652	1.3903	10.35	74.05	206.0827	0.1585	0.1471	0.3610	0.1687	0.3137
3700.5	0.000080	0.079831	0.004182	0.2866	1.4274	11.3	75.49	206.0812	0.1697	0.1577	0.3643	0.1870	0.3058
3700.6	0.000086	0.081821	0.004371	0.2097	1.3801	9.69	77.11	206.0832	0.1425	0.1321	0.3175	0.1638	0.2555
3700.7	0.000094	0.074274	0.005348	0.1293	1.3139	5.06	76.79	206.0785	0.0747	0.0697	0.3734	0.1328	0.1944
3700.8	0.000080	0.077581	0.004287	0.1718	1.2698			206.0795				0.1131	0.3030
3700.9	0.000066	0.075481	0.004991	0.1408	1.2335	7.48	76.7	206.0790	0.1106	0.1031	0.2747	0.0976	0.2880

"ep." denotes use in calculation of Pb/U ratio determined by electron probe

"norm." denotes ratio which has been normalised to designated standard analysis 3642-3.2

"calib." denotes ratio obtained using calibration curve (see Figure 4.1)

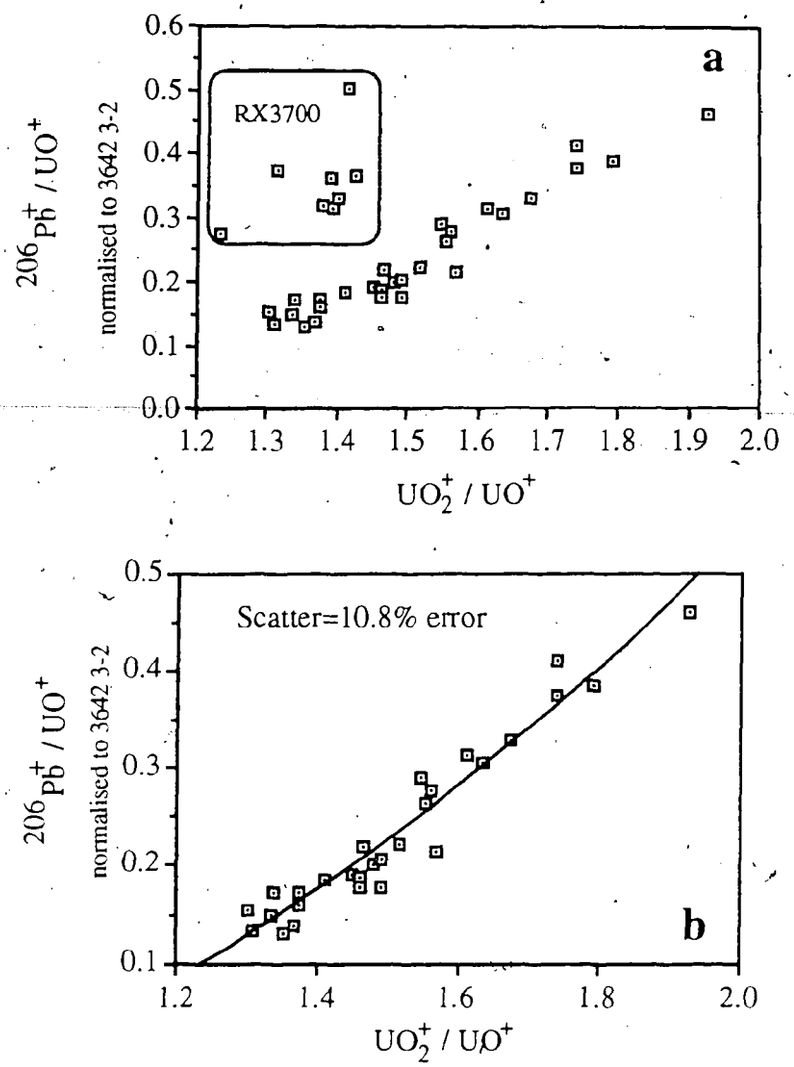

Figure 4.1 Calibration of Pb/U ratios for ion probe pitchblende analyses: **a)** $^{206}Pb^+/^{254}(UO)^+$ covaries with $^{270}(UO_2)^+/^{254}(UO)^+$ for all of the Olympic Dam samples except RX3700 (see text). **b)** Similar plot to a) but without the data for RX3700; the covariation of ionic ratios approximates a curve which can be expressed by the quadratic

$$Pb^+/UO^+ = 0.20559.(UO_2/UO)^2 - 0.085795.(UO_2/UO) - 0.10941.$$

Scatter about the curve results in an uncertainty of 10.8% in Pb/U calibration (see text).

---

absolute values of the ratios. In routine analysis, a standard uraninite with known $^{206}Pb/^{238}U$ would be used and thereby remove the above assumption.

(ii) For each unknown the $^{206}Pb^+/UO^+$ measured was normalised to the standard analysis using equation (3) in order to enable plotting of the values of $^{206}Pb^+/UO^+$ and UO_2^+/UO^+ for a constant Pb/U (that of the standard).

$$^{206}Pb^+/UO^+_{norm.} = {}^{206}Pb^+/UO^+_{meas.} \times \frac{Pb/U_{ep}\ std.}{Pb/U_{ep}\ sample} \qquad (3)$$

Subscript "ep" indicates values determined by electron probe.

(iii) The normalised Pb^+/UO^+ values are then plotted against the measured UO_2^+/UO^+ values (Figure 4.1) and the two variables are observed to be related by the quadratic

$$Pb^+/UO^+ = 0.20559.(UO_2/UO)^2 - 0.085795.(UO_2/UO) - 0.10941 \quad (4)$$

This curve excludes the data for sample RX3700 because this sample yielded anomalously high Pb^+/UO^+ relative to the other samples, which may be due to radiogenic Pb accumulated within the Cu sulphide inclusions unavoidably analysed with the pitchblende (above). The scatter about the curve equates to an uncertainty of 10.8% in the calibration of the Pb/U ratio and this error has been incorporated in the uncertainties in isotopic ratios quoted in Table 4.2. This uncertainty is unacceptably high for routine analysis but may be an artifact of the use of different pitchblendes with different Pb/U ratios normalised to a standard Pb/U value. The calibration uncertainty is significantly reduced by derivation of the calibration curve from a single standard uraninite (see Appendix 1). An analogous calibration curve was derived for the correlated ratios $^{206}Pb^+/U^+$ and UO^+/U^+ (Figure 4.2) but this calibration was not used because the scatter about the curve was equivalent to a greater uncertainty of 17%.

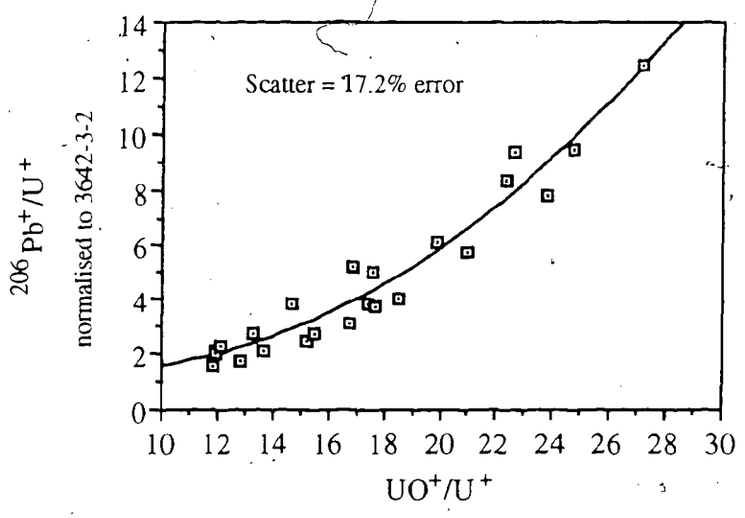

Figure 4.2 Covariation of $^{206}Pb^+/^{238}U^+$ with $^{254}(UO)^+/^{238}U^+$. The data show more scatter about the curve (17%) than in Figure 4.1. This curve was therefore not used to calibrate Pb/U ratios.

(iv) Having derived the calibration curve, the calculation of $^{206}Pb/^{238}U$ for the unknowns is analogous to the method used for zircons:

$$^{206}Pb/^{238}U_{unknown} = {}^{206}Pb/^{238}U_{std.} \times \frac{(^{206}Pb^+/UO^+_{meas.})}{(^{206}Pb^+/UO^+_{calc.})} \quad (5)$$

where "$^{206}Pb^{+}/UO^{+}_{calc.}$" is the value calculated by processing the UO_2^{+}/UO^{+} of the unknown through the calibration equation (4). Table 4.1 lists the data necessary to follow the calibration procedure.

Figure 4.3 shows a comparison between the $^{206}Pb/^{238}U$ values calculated using the UO_2/UO-Pb/UO calibration curve, and the "true" values calculated using the electron probe PbO_2 and UO_2 concentration data.

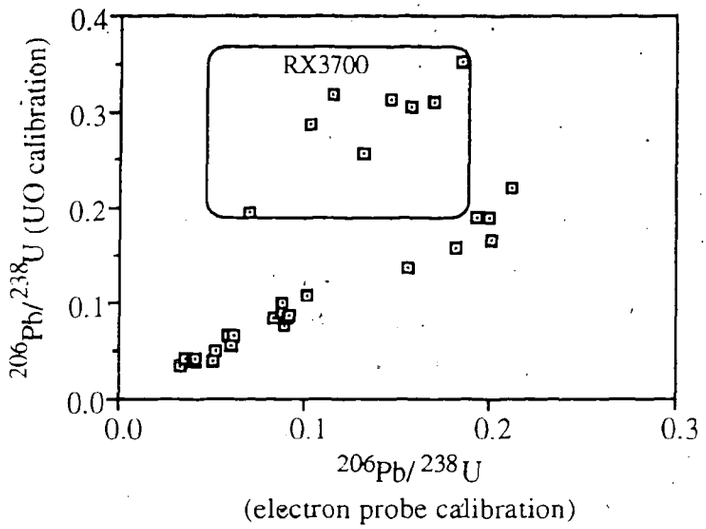

Figure 4.3 Comparison between $^{206}Pb/^{238}U$ ratios calculated using the UO_2/UO-Pb/UO calibration curve and values calculated using electron probe Pb/U elemental ratios. Excluding the data for RX3700 (see text) there is an approximate 1:1 relationship indicating that the internal Pb/U calibration method is successful.

With the exception of RX3700, in which sulphide inclusions in pitchblende were unavoidably analysed, there is an approximate 1:1 relationship between the values calculated by the two different methods. This suggests that the UO_2/UO-Pb/UO calibration technique is capable of correctly calibrating Pb/U ratios for pitchblende. The small differences between the values calculated by the different methods probably result from heterogeneities in Pb/U ratio within the areas analysed by the ion probe beam, thus rendering non-representative the Pb/U ratio calculated from the relatively small beam of the electron probe. The achievement of successful internal Pb/U calibration provides justification for pursuing the development of a uraninite standard. Work was initiated on a coarse crystalline uraninite, which had previously been analysed by thermal ionisation mass spectrometry (TIMS), from the Musoshi copper deposit in Zaire (Richards et al., 1988). The developmental work, and the reason it was ceased, is discussed in Appendix 1.

4.5 Results

The results of each analysis are listed in Table 4.2 and plotted on a concordia diagram in Figure 4.4, the most striking feature of the which is the long narrow error boxes. These result from the large (10.8%) Pb/U calibration uncertainty contrasted with the $^{207}Pb/^{206}Pb$ error which is small because of the low errors from counting statistics on the large Pb peaks.

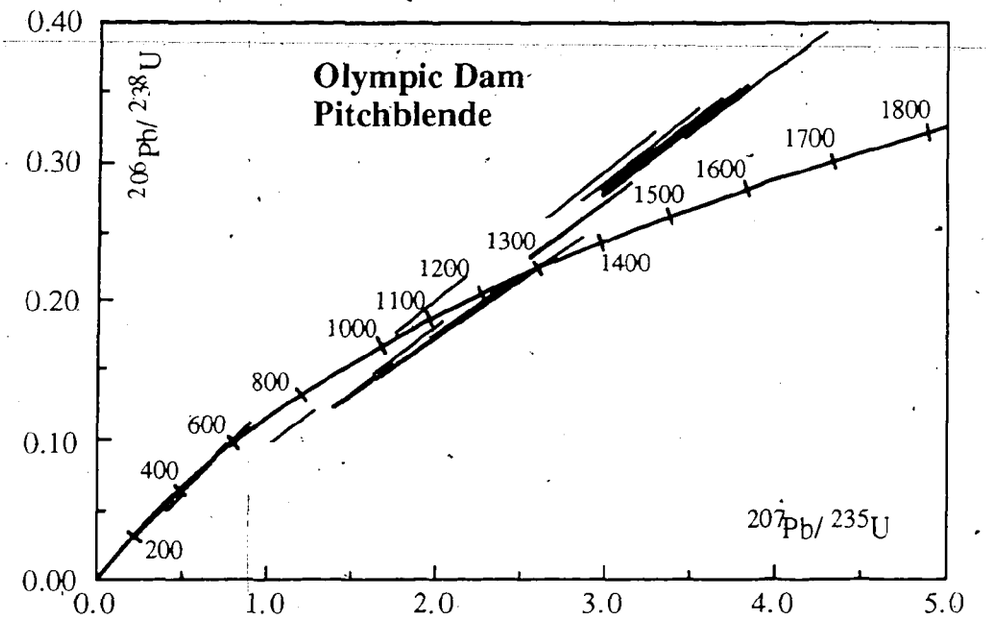

Figure 4.4 Concordia diagram for Olympic Dam pitchblende analyses showing the broad scatter of apparent ages. The long narrow error boxes result from the large uncertainty in Pb/U calibration (10.8%) and the very small uncertainty in $^{207}Pb/^{206}Pb$ ratios due to very high Pb counts. The reverse discordant points are for RX3700 (see text).

The data for each sample were processed by regression analysis in order to ascertain which samples had been subjected to ancient Pb loss, and at what time. Where ancient Pb loss is indicated from the lower intercept of discordia, the upper intercept is regarded as the best estimate of the age of formation of pitchblende in that sample. Where the lower intercept is within error of the origin and the errors on the intercept are large, it is not clear whether Pb loss is recent or ancient. In such cases the weighted mean $^{207}Pb/^{206}Pb$ age is used as a minimum age estimate. If the points are relatively concordant this estimate will be close to the true age of mineral formation. Results for the individual samples are discussed below.

RX3642-1: This sample is the innermost of the traverse of three taken across the concentric bands of a vug filled with chalcopyrite, pitchblende and hematite. The six

Table 4.2 Ion microprobe data for Olympic Dam pitchblende

	Measured ratios			Radiogenic ratios			
Sample No.	$^{204}Pb/^{206}Pb$	$^{208}Pb/^{206}Pb$	f206 %	$^{206}Pb/^{238}U$	$^{207}Pb/^{235}U$	$^{207}Pb/^{206}Pb$	$^{207}Pb/^{206}Pb$ age ± 1σ
Vug samples - chalcopyrite + pitchblende							
3642-1.1	0.000097	0.0050	0.17	0.0494 ± 53	0.39 ± 0.04	0.0577 ± 2	518 ± 7
3642-1.2	0.000091	0.0049	0.16	0.0667 ± 72	0.54 ± 0.06	0.0589 ± 2	564 ± 7
3642-1.3	0.000105	0.0053	0.18	0.0652 ± 70	0.52 ± 0.06	0.0576 ± 2	515 ± 6
3642-1.4	0.000130	0.0062	0.23	0.0414 ± 45	0.32 ± 0.03	0.0559 ± 2	448 ± 9
3642-1.5	0.000106	0.0050	0.19	0.0374 ± 40	0.29 ± 0.03	0.0570 ± 2	489 ± 8
3642-1.5a	0.000100	0.0048	0.18	0.0450 ± 48	0.35 ± 0.04	0.0569 ± 2	487 ± 9
3642-2.1	0.000095	0.0050	0.17	0.0389 ± 42	0.30 ± 0.03	0.0563 ± 3	462 ± 10
3642-2.2	0.000139	0.0058	0.25	0.0400 ± 43	0.31 ± 0.03	0.0554 ± 3	429 ± 11
3642-2.3	0.000118	0.0050	0.21	0.0351 ± 38	0.26 ± 0.03	0.0545 ± 3	391 ± 11
3642-2.4	0.000077	0.0044	0.14	0.0405 ± 44	0.31 ± 0.03	0.0554 ± 3	429 ± 10
3642-2.5	0.000100	0.0049	0.18	0.0424 ± 46	0.32 ± 0.04	0.0555 ± 3	432 ± 13
3642-3.1	0.000067	0.0031	0.11	0.2212 ± 238	2.60 ± 0.28	0.0854 ± 1	1324 ± 2
3642-3.2	0.000069	0.0034	0.11	0.1905 ± 205	2.22 ± 0.24	0.0846 ± 1	1307 ± 2
3642-3.3	0.000069	0.0033	0.11	0.1898 ± 204	2.21 ± 0.24	0.0845 ± 1	1303 ± 2
3642-3.4	0.000072	0.0032	0.12	0.1932 ± 208	2.23 ± 0.24	0.0838 ± 1	1288 ± 2
3642-3.5	0.000069	0.0033	0.11	0.2044 ± 220	2.39 ± 0.26	0.0848 ± 1	1310 ± 2
3642-3.6	0.000080	0.0043	0.14	0.0545 ± 59	0.47 ± 0.05	0.0625 ± 2	692 ± 8
3642-3.7	0.000067	0.0036	0.11	0.1657 ± 178	1.85 ± 0.20	0.0808 ± 1	1218 ± 3
3642-3.8	0.000084	0.0039	0.14	0.1091 ± 117	1.17 ± 0.13	0.0775 ± 2	1134 ± 5
3642-3.9	0.000070	0.0031	0.11	0.1372 ± 148	1.57 ± 0.17	0.0829 ± 2	1266 ± 5
3642-3.10	0.000060	0.0028	0.10	0.1580 ± 170	1.84 ± 0.20	0.0846 ± 2	1305 ± 4
3642-3.11	0.000102	0.0049	0.18	0.0510 ± 55	0.41 ± 0.04	0.0586 ± 3	554 ± 10
Bornite-chalcocite-pitchblende intergrowth							
4569.1	0.000143	0.0066	0.25	0.0999 ± 108	0.82 ± 0.09	0.0593 ± 2	578 ± 6
4569.2	0.000189	0.0099	0.33	0.0892 ± 96	0.73 ± 0.08	0.0590 ± 2	568 ± 8
4569.3	0.000168	0.0084	0.29	0.0846 ± 91	0.69 ± 0.07	0.0590 ± 2	566 ± 7
4569.4	0.000155	0.0075	0.27	0.0838 ± 90	0.69 ± 0.07	0.0593 ± 2	578 ± 9
4569.5	0.000282	0.0138	0.49	0.0871 ± 94	0.71 ± 0.08	0.0590 ± 3	566 ± 10
4569.6	0.000135	0.0063	0.24	0.0758 ± 82	0.62 ± 0.07	0.0589 ± 2	563 ± 9
4569.7	0.000249	0.0116	0.43	0.0730 ± 79	0.59 ± 0.06	0.0585 ± 3	550 ± 11
Chalcocite-pitchblende vein							
3700.1	0.000091	0.0046	0.15	0.3203 ± 345	3.48 ± 0.38	0.0788 ± 1	1168 ± 3
3700.2	0.000088	0.0049	0.15	0.3126 ± 336	3.34 ± 0.36	0.0776 ± 1	1136 ± 3
3700.3	0.000093	0.0048	0.15	0.3548 ± 382	3.88 ± 0.42	0.0794 ± 1	1182 ± 3

Table 4.2 continued

Sample No.	Measured ratios $^{204}Pb/^{206}Pb$	$^{208}Pb/^{206}Pb$	f206 %[a]	Radiogenic ratios $^{206}Pb/^{238}U$	$^{207}Pb/^{235}U$	$^{207}Pb/^{206}Pb$	$^{207}Pb/^{206}P$ b age ± 1σ
Chalcocite-pitchblende vein							
3700.4	0.000103	0.0050	0.17	0.3161 ± 340	3.42 ± 0.37	0.0784 ± 1	1157 ± 3
3700.5	0.000080	0.0042	0.13	0.3083 ± 332	3.35 ± 0.36	0.0787 ± 1	1164 ± 3
3700.6	0.000086	0.0044	0.14	0.2576 ± 277	2.86 ± 0.31	0.0806 ± 1	1212 ± 3
3700.7	0.000094	0.0053	0.16	0.1959 ± 211	1.97 ± 0.21	0.0729 ± 2	1012 ± 5
3700.8	0.000080	0.0043	0.13	0.3055 ± 329	3.22 ± 0.35	0.0765 ± 1	1107 ± 2
3700.9	0.000066	0.0050	0.11	0.2904 ± 313	2.98 ± 0.32	0.0745 ± 2	1056 ± 5

[a] f206% denotes percentage of ^{206}Pb that is common Pb

analyses made on this sample have undergone varying degrees of ancient Pb loss and form a discordia with an upper intercept indicating an age of 574 ± 85 Ma and a lower intercept indicating Pb loss at 101 ± 76 Ma (MSWD 0.171, Model 1; see Figure 4.5a).

RX3642-2: This sample is from a band of pitchblende + chalcopyrite between the outermost and innermost bands in the traverse of three samples across the vug. Five analyses were made in what appears to be the same generation of crustiform pitchblende. A poorly defined discordia can be derived, with an upper intercept of 594 ± 568Ma and a lower intercept of 135 ± 299 Ma (Figure 4.5b). The errors are so large as to render these intercept ages effectively meaningless, and the only age information derived from these analyses is the minimum age of 439 ± 27 Ma indicated by the weighted mean $^{207}Pb/^{206}Pb$ ratio.

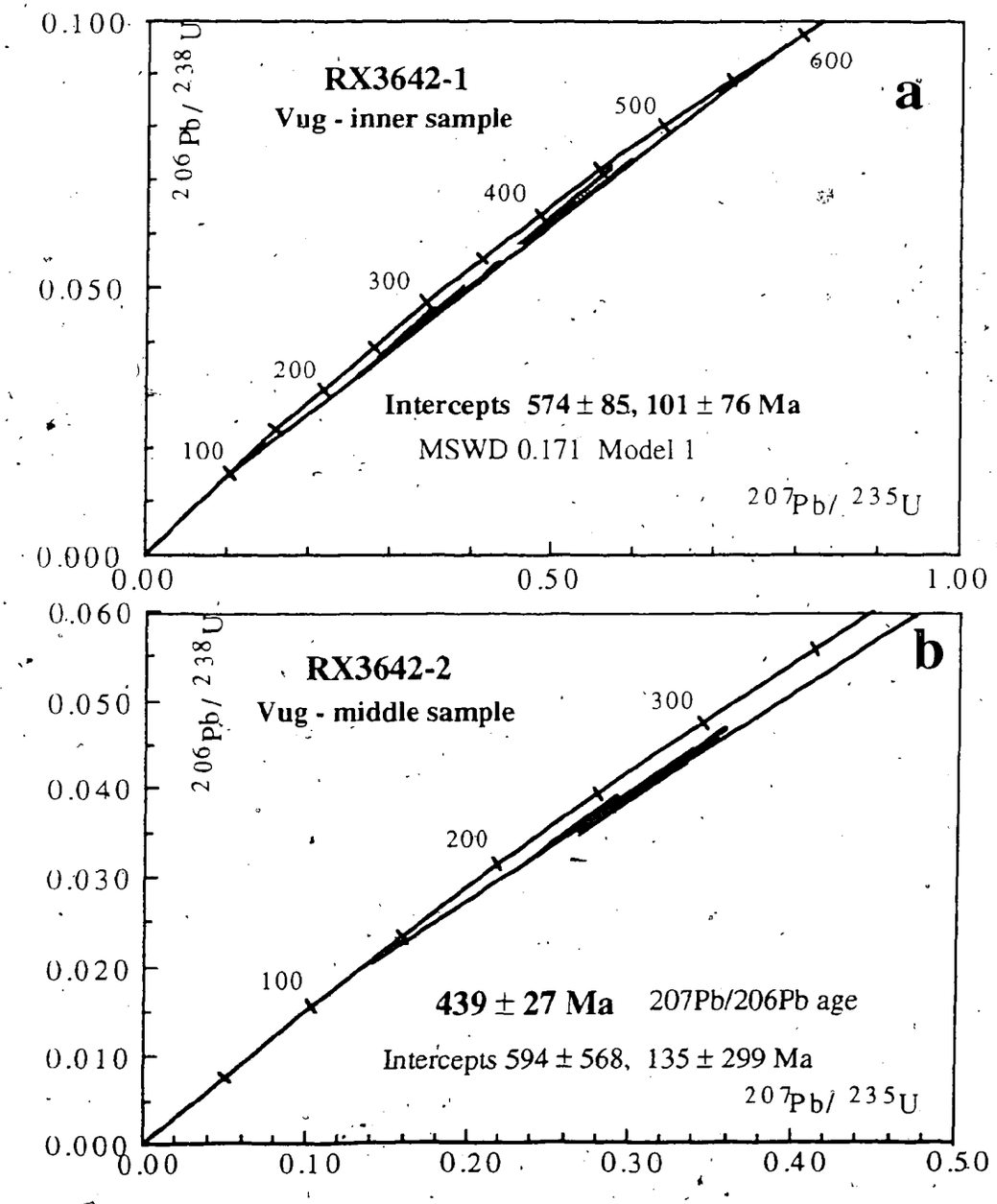

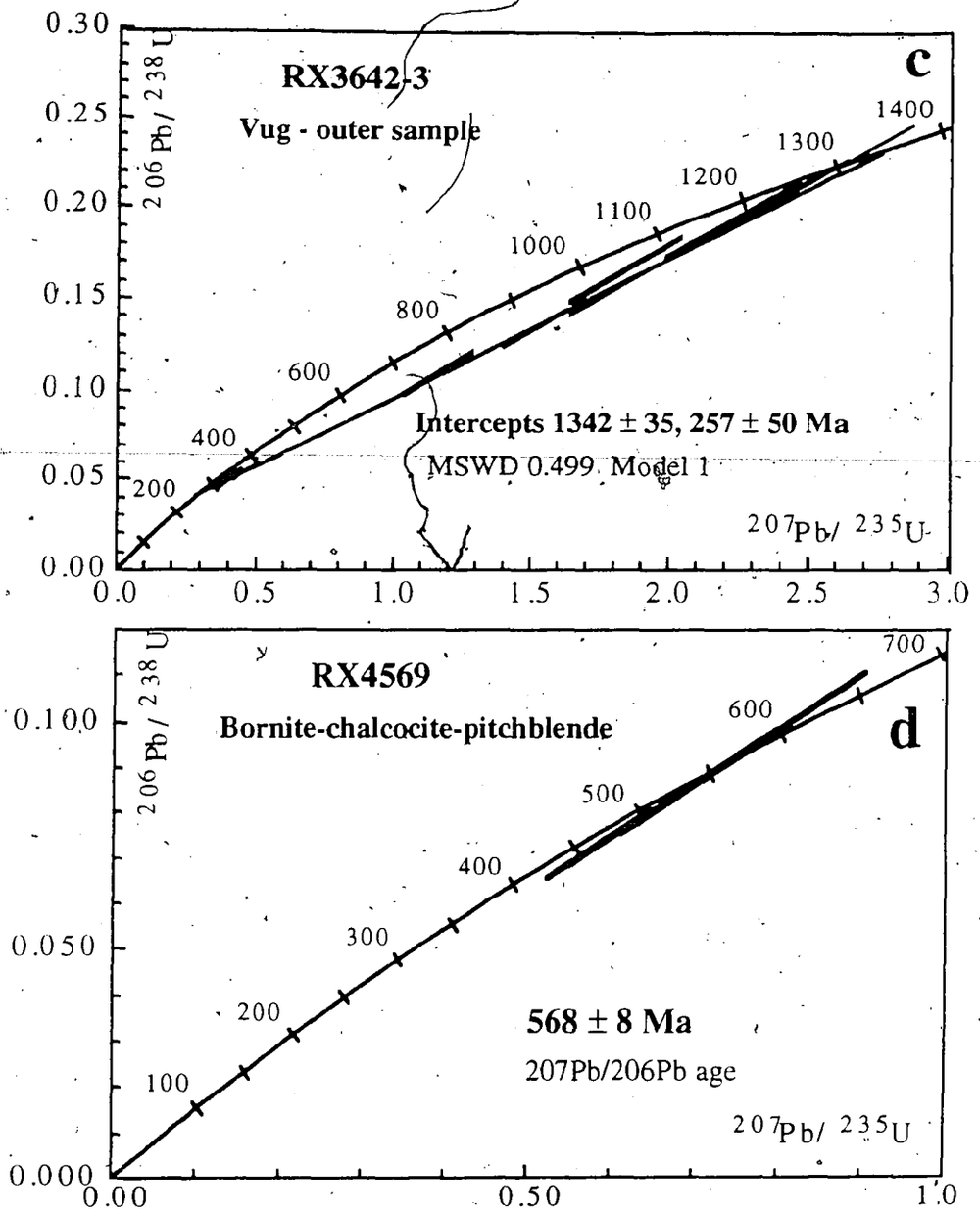

Figure 4.5 Concordia diagrams for individual samples of Olympic Dam pitchblende. **a) b)** and **c)** are RX3642-1, -2, and -3, the innermost , middle, and outermost samples respectively of a traverse across pitchblende+chalcopyrite growth layers filling a vug. The apparent ages from **a)** and **c)** show a chronostratigraphy across the vug; **b)** provides only a minimum age estimate. **d)** RX4569 yielded seven near-concordant analyses which indicate an age of 568 ± 8 Ma. The significance of the data is discussed in the text.

RX3642-3: This sample is the outermost in the traverse of three vug-samples. Eleven analyses were made from what appears to be the same growth band of pitchblende. They show highly variable degrees of ancient Pb loss and form a discordia with an upper intercept of 1342 ± 35 Ma and a lower intercept of 257 ± 50 Ma (MSWD 0.499, Model 1; see Figure 4.5c).

Within each of the three samples, RX3642-1, 2 and 3 the variable levels of discordance, even from analyses only hundreds of microns apart, provide evidence for microscale heterogeneous disturbance of the Pb-U isotopic systematics. When the larger scale is examined by comparing the data for the three samples, some order is apparent. As would be expected the oldest age calculated (1342 ± 35 Ma) is from the outermost band of pitchblende in the vug. The innermost sample, RX3642-1, yielded an apparent age of pitchblende formation of ~570 Ma. Ignoring the middle vug-sample for which the data provide only a meaningful minimum age estimate (~440Ma), the analyses demonstrate a real chronostratigraphy of pitchblende growth from the outer layer of the vug (~1340 Ma) to the inner layer (~570 Ma). If one assumes episodic Pb loss, the lower intercept ages suggest that Pb loss has occurred at ~260 and ~100 Ma, and possibly in recent times. Considering the fact that the three samples are from within centimetres of each other it is noteworthy that they do not indicate the same Pb loss age. This is consistent with multiple, perhaps many, very localised Pb loss "events" which may have affected all of the samples such that the observed isotopic signatures are the result of many overprinted Pb losses. This therefore suggests that the discordia regression approach may be yielding "ages" of no geological significance save for a crude minimum age estimate. The true age of the pitchblende in the vug is of minor geological importance because it is obviously a secondary form of mineralisation. The main importance of these "age" determinations is the contribution made to the understanding of U and Pb remobilisation processes in pitchblende.

RX4569: This sample of coarse pitchblende intergrown with bornite yielded the most coherent age data of any of the pitchblende samples analysed. The seven analyses are near concordant and all apparent $^{207}Pb/^{206}Pb$ ages agree at the two standard deviation level, yielding a weighted mean $^{207}Pb/^{206}Pb$ age of 568 ± 8 Ma (Figure 4.5d). This indicates that any Pb loss from this sample has occurred in recent times. A plot of the uncorrected $^{207}Pb/^{206}Pb$ ratio versus $^{204}Pb/^{206}Pb$ (Figure 4.6) illustrates the consistency of the data showing an apparent mixing line between a common Pb of unknown composition and the radiogenic $^{207}Pb/^{206}Pb$ composition corresponding to an age of ~570 Ma. The coherence of these data suggests that this zone of pitchblende has not undergone ancient Pb loss and that this age may be geologically meaningful as an age of formation of bornite+chalcocite+pitchblende in this locality.

RX3700: Nine analyses were made in this sample taken from a vein of pitchblende + chalcocite in sericitised granite. As mentioned earlier, anomalously high $^{206}Pb^+/UO^+$ ratios (relative to UO_2^+/UO^+), possibly due to excess radiogenic Pb in chalcocite inclusions in the sample, led to the omission of these data from the derivation of the calibration curve. The same anomalously high radiogenic Pb content is manifest as reverse discordance for these analyses on the concordia diagram (Figure 4.4). This

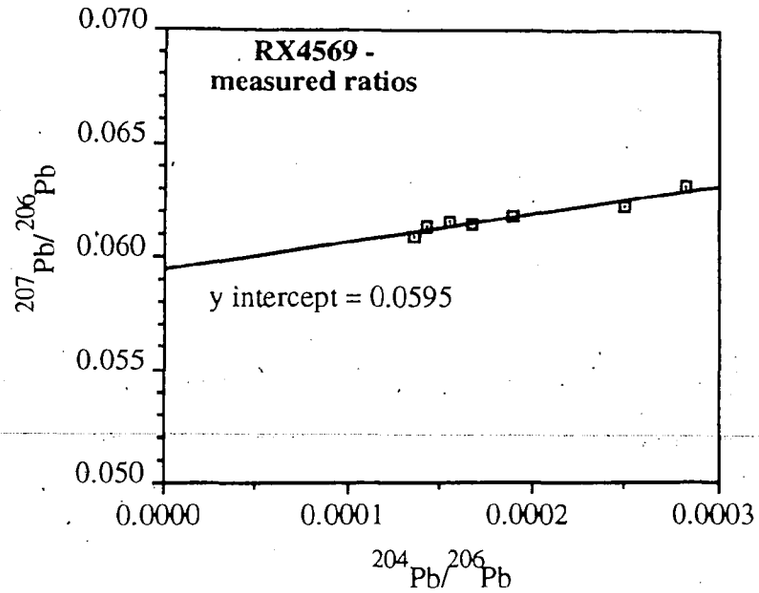

Figure 4.6 Regular mixing array between a common Pb of indeterminate composition and radiogenic Pb. The coherence of the data suggest that the subdomains analysed have undergone the same Pb and U mobility history. Y-intercept $^{207}Pb/^{206}Pb$ corresponds to an age of approximately 570 Ma.

indicates that in the analysed areas there is insufficient U to support the amount of radiogenic Pb analysed and this is may result from migration of Pb into sulphide inclusions from outside the volume analysed. An alternative interpretation is that the sample has undergone U loss. With such Pb and/ or U mobility likely, the $^{207}Pb/^{206}Pb$ ages can only be interpreted as minimum estimates of the age of pitchblende formation, and these range from 1212 ± 3 to 1012 ± 5 Ma. Regression analysis was not performed for these analyses because of their reverse discordance.

4.6 Geological implications

4.6.1 Data from this study

The major feature of the above results is the abundant evidence for disturbance of the Pb-U isotopic systematics in each of the samples except RX4569. The range of apparent pitchblende formation ages (~1340, ~570 Ma) and Pb loss ages (~260, ~100 Ma and possibly recent) indicate that these samples have not had simple isotopic histories. Even allowing for the possibility of multiple events of pitchblende growth, if the Pb-loss was episodic one would expect some evidence of the same Pb-loss "events" from all of the samples, particularly those taken within centimetres of each other (RX3642-1, 2 and 3). This is not observed. In all probability these samples have experienced multiple intermittent Pb-loss events which implies that the upper intercept pitchblende "formation ages" have no geological meaning because multiple Pb-loss events would have rotated the

discordia towards artificially high "age" upper intercepts. The information gained about the *primary* mineralisation age from these data is therefore limited. The only valid conclusion is that primary mineralisation was emplaced before 1320 Ma, the oldest apparent $^{207}Pb/^{206}Pb$ age measured (3642-3.1; see Table 4.2).

Amid the abundant evidence for easily reset isotopic systematics, the analyses of the bornite-chalcocite rich sample RX4569 are remarkable for the consistency of their $^{207}Pb/^{206}Pb$ ages . The pitchblende in this sample has a mean $^{207}Pb/^{206}Pb$ age of ~570 Ma and, given the uniformity of the $^{207}Pb/^{206}Pb$ ratios, is unlikely to have undergone any isotopic disturbance until recent times. The analyses also show this sample to contain higher levels of common Pb than the other samples (f206%, Table 4.2) and common Pb compositions indicating a well-defined mixing array (Figure 4.6). This is consistent with RX4569 having formed from modification of a protore with relatively low common Pb, by the introduction of a fluid with an exotic common Pb component, and lends support to the supergene hypothesis of Oreskes and Einaudi (1990). Although from this sample alone it could be argued that the 570 Ma age represents the age of a major Cu and U supergene remobilisation event, data from the study of Trueman et al. (1988) are inconsistent with this interpretation. Bornite-chalcocite-pitchblende ores from nearby localities which would logically also be categorised as supergene if the supergene hypothesis of Oreskes and Einaudi (1990) is correct, have apparent ages of ~1220, ~1830 and ~1360 Ma, considerably older than the 570 Ma age for sample RX4569 (see Table 4.2).

It is interesting to compare the data of Trueman et al. (1988) with those of this study. The analyses of both studies are displayed together on a concordia diagram in Figure 4.7 and for clarity the errors on the analyses are shown as uniform. This diagram illustrates the range of the ratios measured and the impossibility of fitting a single discordia through all of the data, a point noted by Trueman et al. (1988 p.38). However, these workers derived a single discordia through means of the analyses shown in Figure 4.7 (with the exception of the data denoted as "this study") and tentatively interpreted an upper intercept formation age of ~1400 Ma and a lower intercept Pb loss age from the discordia. The assumptions implicit in this treatment of the data are that all of the pitchblende samples share the same age of formation and that all have only lost Pb in a single Pb loss event. The data from the present study indicate that these assumptions do not necessarily apply at Olympic Dam (see data above) and therefore suggest that they are questionable for the data of Trueman et al. (1988). Indeed Trueman et al. (1988, p.29) recognised the problems raised by these assumptions and expressed doubts about the

---

Figure 4.7 (overleaf) Concordia diagram showing all analyses from this study and those of Trueman et al. (1988). Errors are shown as a uniform proportion of the isotopic ratios for clarity. The data indicate apparent ages of mineral growth and Pb loss which span a range of over one billion years.

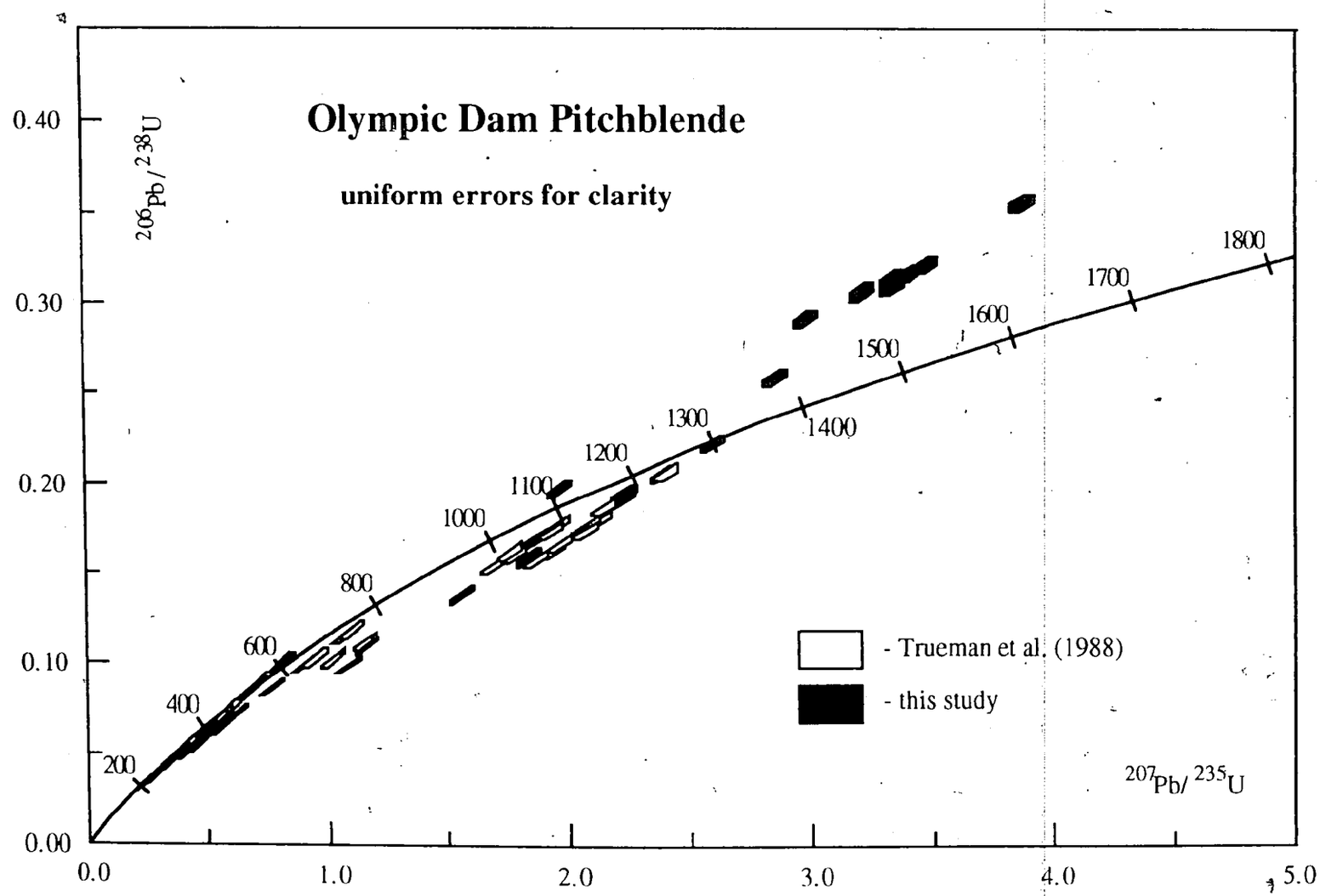
Olympic Dam Pitchblende
uniform errors for clarity
$^{206}Pb/^{238}U$
$^{207}Pb/^{235}U$
0.00
0.10
0.20
0.30
0.40
0.0
1.0
2.0
3.0
4.0
5.0
200
400
600
800
1000
1100
1200
1300
1400
1500
1600
1700
1800
- Trueman et al. (1988)
- this study

validity of averaging their data. It is possible to test the above assumptions by plotting and examining the distribution of the data for all of the analyses on separate concordia diagrams for the individual samples. If the assumptions are valid then each of the samples should display an array of analyses which yield approximately the same upper and lower intercepts of discordia as the other samples. The data of Trueman et al. (1988) have here been examined by regression analysis using the program "Isoplot" (Ludwig, 1992). Regressions were performed using 1σ absolute errors and an error correlation of 0.99. The data are plotted in 4.8 a) to f), summarised in Table 4.3 and discussed below. All ages are quoted at the 95% level of confidence.

4.6.2 Data of Trueman et al. (1988)

RD398W1/ 554.6m. The four analyses for this sample show ancient Pb loss and form a discordia with intercepts of 1414 ± 79 and 633 ± 246 Ma (MSWD 0.738, Model 1; Figure 4.8a).

RD481/ 369.5m. The six analyses from this sample form a cluster of points rather than a well defined discordia with a range of $^{206}Pb/^{238}U$ and $^{207}Pb/^{235}U$ ratios (Figure 4.8b). Regression analysis yields intercepts of 1242 ± 107 and 227 ± 447 Ma (MSWD 0.197, Model 1). The lower intercept has an extremely large uncertainty which suggests that Pb loss could have occurred at any time from ~675 Ma to recent times. The weighted mean $^{207}Pb/^{206}Pb$ age is 1224 ± 20 Ma and, considering the fact that the data are ~80% concordant, this is thought to be close to the true formation age of the pitchblende in this sample.

RD481/ 370.8m. Regression of the analyses for this sample yields intercepts of 917 ± 288 and 228 ± 364 Ma (MSWD 0.104, Model 1; see Figure 4.8c), although the actual uncertainties may be significantly greater because there are only three analyses involved (Ludwig, 1992). In view of these large uncertainties the intercept ages are not used. However, considering the linearity of these analyses on the concordia diagram, and the near-concordance of the uppermost point, the minimum age of 828 ± 97 Ma indicated by the weighted mean $^{207}Pb/^{206}Pb$ ratio is probably close to the age of formation of the pitchblende in this sample.

RD481/ 371.1m. The six analyses for this sample form a cluster of points and have statistically identical $^{207}Pb/^{206}Pb$ ratios indicating that Pb loss for this sample is recent (Figure 4.8d). The minimum age estimate, 1356 ± 13 Ma (weighted mean $^{207}Pb/^{206}Pb$ age), is therefore probably close to the true age of pitchblende growth in this sample.

RD327/ 509.1m. The six analyses for this sample display varying degrees of ancient Pb loss (Figure 4.8e) and form a discordia with intercepts of 1163 ± 270 and 273 ± 152 Ma

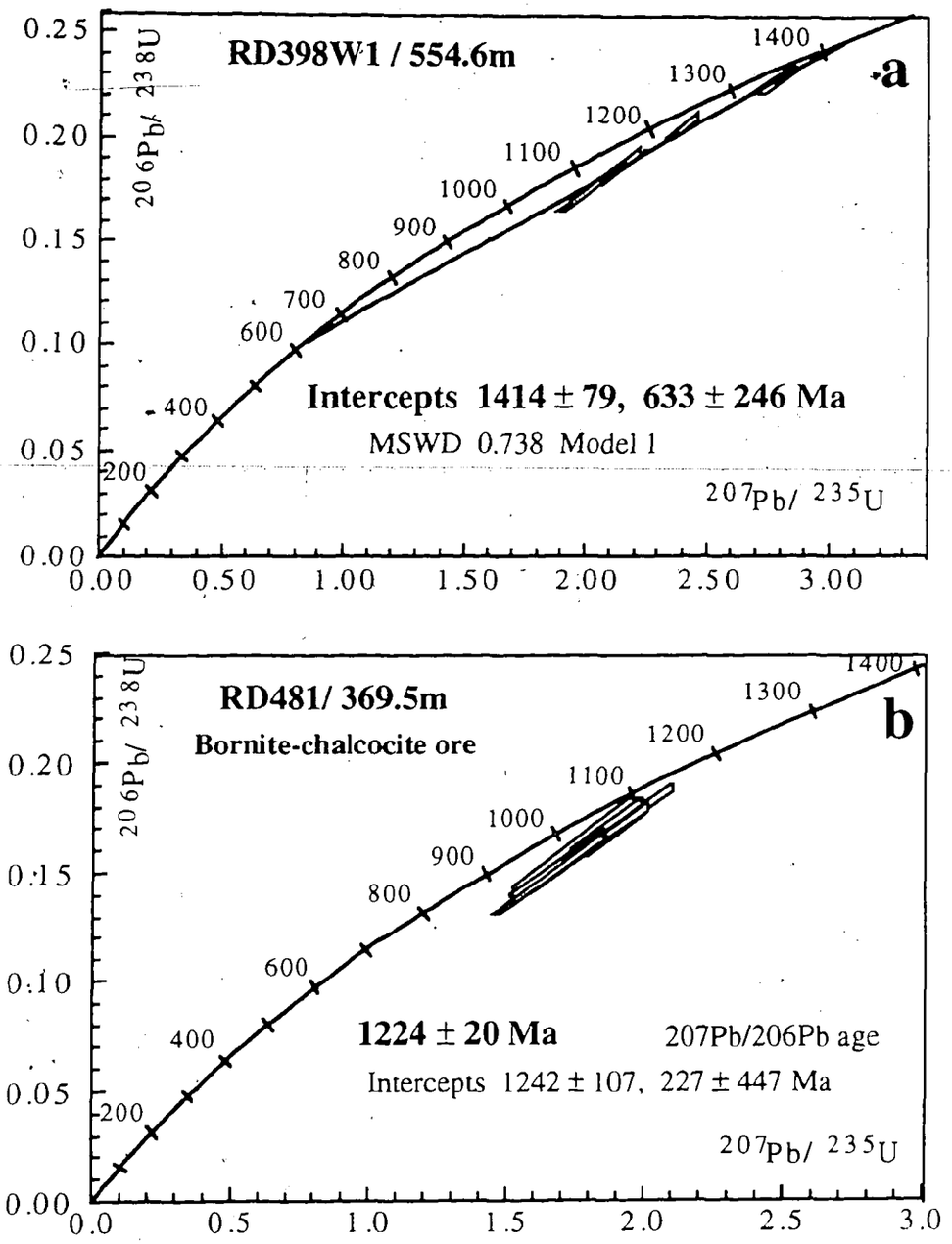

Figure 4.8 Concordia diagrams of for the data from the individual samples of Trueman et al. (1988). The indicated ages of mineral growth and Pb loss are discussed in the text.(MSWD 6.42, Model 2). The analyses plot in two groups of three and it is possible that the two groups have different ages of formation (~800 and ~600 Ma) and have undergone recent Pb loss. This may explain the relatively poor fit of the six point discordia.

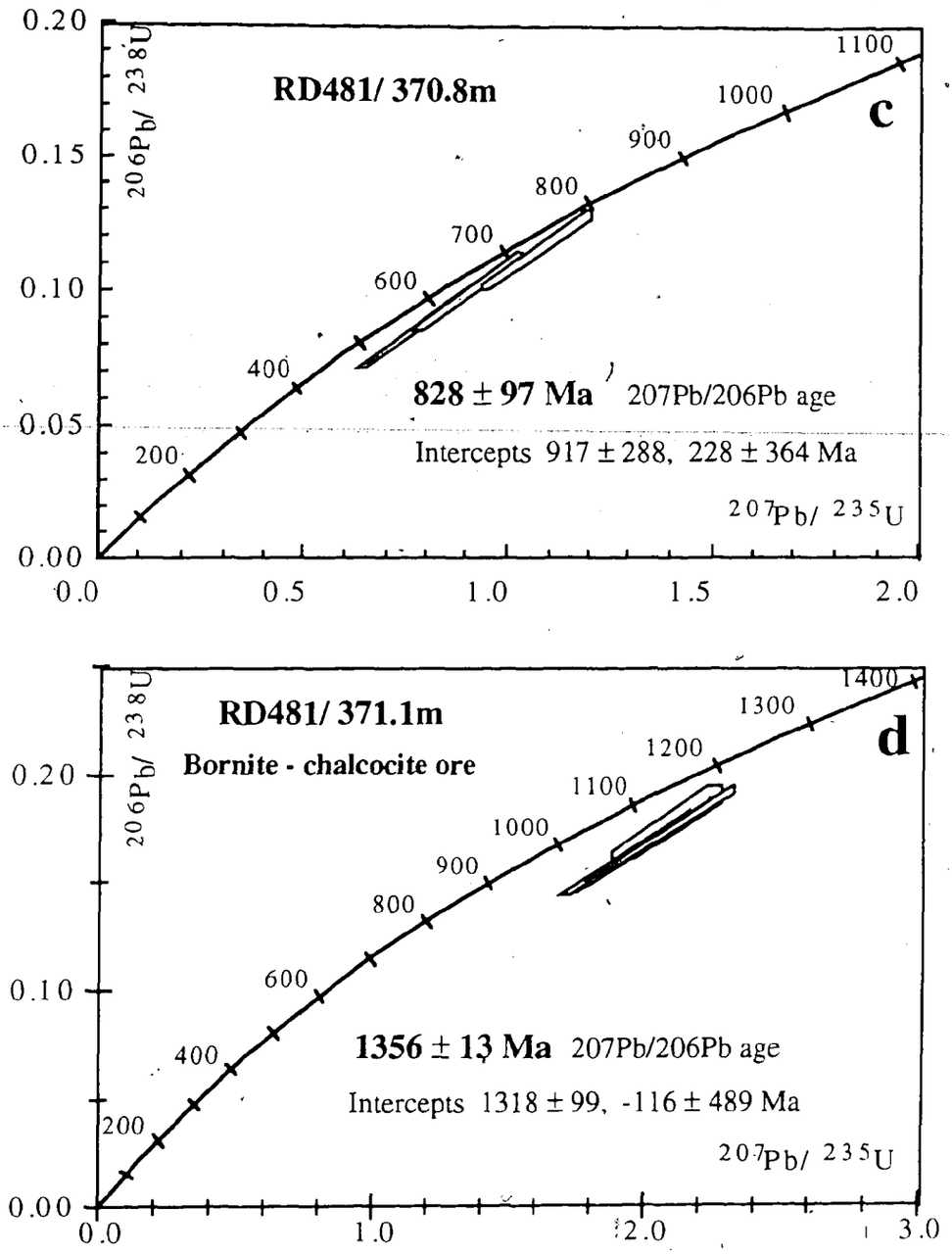

Figure 4.8 continued Concordia diagrams of for the data from the individual samples of Trueman et al. (1988). The indicated ages of mineral growth and Pb loss are discussed in the text.

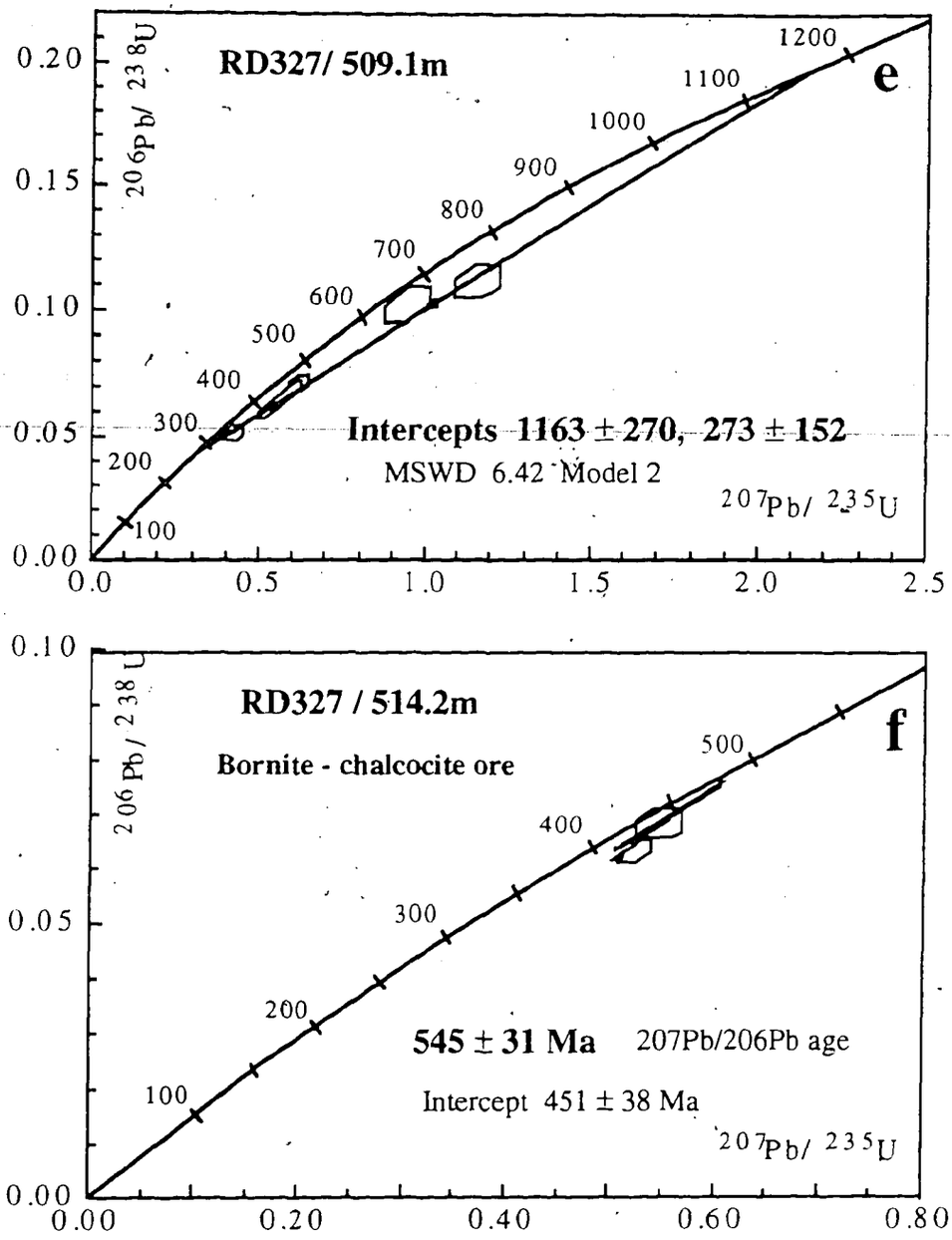

Figure 4.8 continued Concordia diagrams of for the data from the individual samples of Trueman et al. (1988). The indicated ages of mineral growth and Pb loss are discussed in the text.

RD327/ 514.2m. The five analyses for this sample yield an upper intercept age of 451 ± 38 Ma and a lower intercept with infinite error (Figure 4.8f). Considering the fact that the data are ~80% concordant, the minimum age estimate of 545 ± 31 Ma provided by the weighted mean $^{207}Pb/^{206}Pb$ ratio is probably close to the true age of pitchblende growth for this sample.

Table 4.3 Summary of age information gained from regression analysis and weighted mean $^{207}Pb/^{206}Pb$ calculations for Olympic Dam pitchblendes. Data from this study and from Trueman et al. (1988). $^{207}Pb^{206}Pb$ ages have been calculated where data are concordant or indicate recent Pb loss.

Sample No.	Sample type[d]	Upper intercept[a]	Lower intercept[a]	MSWD	Model	Weighted mean $^{207}Pb/^{206}Pb$ age[c]
This study						
RX3642-1	Vug cpy + pitch.	574 ± 85	101 ± 76	0.171	1	
RX3642-2	"	594 ± 568	135 ± 299			439 ± 27
RX3642-3	"	1342 ± 35	257 ± 50	0.499	1	
RX4569[b]	bn-cc ore					568 ± 8
Trueman et al.(1988)						
RD398W1/554.6m	pitch.+bn-cc veins	1414 ± 79	633 ± 246	0.738	1	
RD481/369.5m	bn-cc ore	1242 ± 107	227 ± 447	0.197	1	1224 ± 20
RD481/371.1m	vein pitch.	1318 ± 99	-116 ± 489	0.166	1	1356 ± 13
RD327/509.1m	pitch.+bn veins	1163 ± 270	273 ± 152	6.42	2	
RD327/514.2m	pitch.+bn-cc	451 ± 38		1.53	1	545 ± 31
RD481/370.8m	pitch.veins	917 ± 288	228 ± 364	0.104	1	828 ± 97

a. All regressions calculated using "Isoplot" version 2.50 with an error correlation of 0.99; intercept errors are quoted at 95% confidence level
b. Not regressed because analyses are concordant and near concordant
c. Weighted mean $^{207}Pb/^{206}Pb$ age errors quoted at 95% confidence level
d "pitch." = pitchblende; "bn" = bornite; "cc" = chalcocite; "cpy" = chalcopyrite

When all of the samples analysed in this study, and those analysed by Trueman et al. (1988) and are considered, eight yield ages which can be interpreted as approximating the time of precipitation of pitchblende for the respective samples. From those eight samples (RX3642-1 and 3, RX4569, RD398W1/554.6m, RD481/369.5m, 370.8m, 371.1m, and RD327/514.2m), four distinct ages of pitchblende growth have been determined; ~1350-1400 Ma, ~1220 Ma, ~830 Ma and ~570 Ma. Four distinct Pb-loss ages can be determined from the same eight samples; recent times, 101 ± 76 Ma, 257 ± 50 Ma, and 633 ± 246 Ma. The remaining samples have lower intercept errors greater than 100% (except RD327/509.1 which is ignored because it is not clear that a single regression of the six points for this sample is the appropriate treatment). There are therefore at least four distinct ages of Pb loss documented, only one of which (633 ± 246 Ma) overlaps

with any pitchblende growth ages (~570 Ma, ~830 Ma). None of the pitchblende growth ages correlates closely with any known regional geological events. Of the apparent Pb-loss ages, 633 ± 246 Ma overlaps with the interpreted age of deposition of the Tregolana Shale which overlies the deposit (676 ± 200 Ma; Webb et al., [1986] date on Woomera Shale, a correlative of the Tregolana Shale).

The range of ages of pitchblende growth and Pb loss shown by the individual samples data (Table 4.3, Figure 4.8) is open to two interpretations:

a) The samples have a geologically real range of formation and disturbance ages, which may reflect the ease with which U is dissolved and reprecipitated, or

b) The pitchblende in the samples all formed at the same time but the samples have undergone widely varied Pb-loss histories.

In either case the assumptions implicit in the taking of means of the multiple analyses of different samples and plotting these for regression analysis appear to be violated. For this reason the ~1400 Ma "primary mineralisation age" of Trueman et al. (1988) is regarded as the result of a questionable treatment of data.

The variety of apparent ages for pitchblende growth and Pb loss events calculated above attests to the ease with which pitchblende is isotopically disturbed. This is not surprising when the near-surface environment of ore formation is considered (Reeve et al., 1990; Oreskes and Einaudi, 1990). Uranium is easily mobilised as complexes of U^{6+} in oxidised environments, as is illustrated by the occurrence of "roll-front" and "unconformity-type" U deposits (Hoeve and Quirt, 1987; Adler, 1964). Moreover the radioactive decay of the U within the deposit would have provided a low-level heat source for the duration of the history of the deposit, and this would be capable of driving continuous circulation of groundwaters. It is therefore likely that interpretation "A" (above) is correct, i.e. that pitchblende at Olympic Dam has undergone varying degrees of dissolution and reprecipitation with each flux of oxidised groundwaters through the deposit. This makes it unlikely that any isotopically undisturbed primary uranium mineralisation will be found within the deposit. There is certainly no reason to believe that any of the samples analysed in this study or those of Trueman et al. (1988) listed above represent primary mineralisation. Indeed the interpretation by Oreskes and Einaudi (1990) of the 1400 Ma age of Trueman et al. (1988) as the age of ore formation is perplexing in this regard. These workers are the strongest proponents of the supergene enrichment hypothesis for forming the bornite-chalcocite ore zones at Olympic Dam. Yet it is the same "secondary" ore zones which have been sampled and analysed by Trueman et al. (1988) to yield the 1400 Ma age which Oreskes and Einaudi interpret as the age of primary mineralisation.

Whether some remobilisation took the form of a major supergene enrichment event has not been resolved by the ion probe studies of pitchblende. However, considering the range of ages of bornite-chalcocite ores which could be classified as supergene (~1360 Ma, ~1220 Ma, 830 Ma, 570 Ma) it is apparent that the isotopic data show no evidence of a single supergene event. The data indicate that if a supergene event has occurred it was prior to ~1360 Ma, in which case the ages measured for these samples have recorded localised resetting "events". The main conclusion from the totality of data is that there has been a protracted history of intermittent U mobility at Olympic Dam.

4.7 Analytical implications

The main contribution made by the reconnaissance ion probe study of Olympic Dam pitchblende is that it has demonstrated that Pb and U ionic species are sputtered in a correlated manner amenable to methods of internally calibrating $^{206}Pb/^{238}U$ ratios to a standard of known $^{206}Pb/^{238}U$. This provides justification for developmental work on a uraninite standard in order to establish ion probe analysis of uraninite/ pitchblende as a routine procedure. The developmental work was commenced as part of this study but was not completed because complications in its pursuit exceeded the scope of the study. A description of the work including reasons for its cessation can be found in Appendix 1.

Another contribution of the reconnaissance study is the recognition of the susceptibility of pitchblende to microscopically variable isotopic disturbance as evidenced by the heterogeneous isotopic signatures measured within pitchblendes which appear from field relationships to have the same age of formation. This has implications for the usefulness of the method. The apparent ease of isotopic disturbance suggests that primary mineralisation ages cannot be measured by ion probe for uraninite unless there has been an anhydrous environment since mineral formation. It also suggests that ion probe analysis may assist in the interpretation of conventional TIMS analyses of pitchblende/ uraninite by identifying isotopic disturbance (perhaps evident as microscopic heterogeneity). One would be disinclined to interpret a TIMS age calculation as a primary age if ion probe analyses demonstrated that the isotopic ratios measured by TIMS were averages of isotopically disturbed subdomains. Ion probe analysis of pitchblende also has potential to identify remobilisation events which have not affected the U-Pb systematics of more resistant minerals such as zircon.

5 GEOCHEMISTRY OF THE OLYMPIC DAM BRECCIAS

5.1 Introduction

The entire volume of the Olympic Dam Breccia Complex is believed to have been originally occupied by the Roxby Downs Granite, which subsequently underwent hydrothermal brecciation and iron-metasomatism. Many elements in addition to Fe (e.g. Cu, U, Au, Ag, REE, Ba, F) were introduced or remobilised during this hydrothermal activity. Within the metasomatised rocks Roberts and Hudson (1983) noted positive correlations between Cu, U and LREE, and a more poorly defined correlation between these elements and F. These workers also noted that U and REE can occur in high concentrations without high concentrations of Cu, but that the reverse is not usually observed. Oreskes and Einaudi (1990) noted the increase in LREE content which accompanied sericite alteration of granite and introduction of iron, and Oreskes (1990) discussed evidence from back-scattered electron imagery that Olympic Dam hematite is uraniferous, suggesting that U and hematite were co-precipitated. Reeve et al. (1990) discussed the anomalous concentrations of the ore metals, and REE, Ba and F mainly from the perspective of mineralogical mode of occurrence.

Fluid inclusion and stable isotopic data (Oreskes and Einaudi, 1992) suggest that ore formation involved the mixing of two fluids. Nd isotopic data (Chapter 7) indicate the input of REE from two or more distinct sources during ore formation, consistent with the above suggestion. Recent work by Haynes et al. (submitted) investigated Olympic Dam ore genesis using computer-aided geochemical modelling. They simulated fluid-rock and fluid-fluid reactions in an attempt to test the plausibility of different mineralisation hypotheses. Their results indicate that the observed ore-mineral assemblages are most closely "reproduced" in modelling by the mixing of two fluids:

A) A hot, saline, relatively reduced magmatic or deeply circulated crustal water, and

B) A cooler, saline, relatively oxidised meteoric water.

The geochemical data gathered in the present study are considered in the light of this model.

To date, no geochemical studies of Olympic Dam breccias have focussed on comparisons between the various ore and breccia types based on the premise that their differences may reflect origins by different processes or different stages of hydrothermal evolution. One purpose of this chapter therefore, is to examine the geochemistry of different Olympic Dam breccias and ores classified according to macroscopic features which indicate origins by possibly distinct processes. The sampling strategy for the project as a whole was

primarily aimed at assessing the *isotopic* characteristics of the different lithological categories, in keeping with the main emphasis of this thesis. The sample suite therefore cannot be viewed as suitable for a comprehensive geochemical study of the deposit. Nevertheless the limited database available for each rock type does allow new insights into the elemental gains and losses during hydrothermal activity. The following lithological categories are used in the study: 1) "fresh" Roxby Downs Granite, 2) chlorite-altered granite breccias, 3) sericite-altered granite breccias, 4) hematite-altered granite breccias, 5) "barren" hematitic and heterolithic breccias, i.e. those with no visible Cu sulphide mineralisation; 6) hematitic breccias whose textures suggest they have undergone leaching (vuggy breccias ± oxidised sulphides); 7) silicified breccias, 8) magnetite-rich breccias; 9) hematite-quartz sediments; 10) hematite-quartz breccias; 11) pyrite-rich ores; 12) chalcopyrite-rich ores; 13) bornite/chalcocite-rich ores. There is unavoidable overlap between some of these lithological categories, e.g. the magnetite-rich breccias are overprinted by chalcopyrite mineralisation and therefore could also be classified as chalcopyrite ores. The classification scheme is therefore somewhat artificial.

5.2 Paragenetic considerations

5.2.1 Magnetite/ hematite

Magnetite has been described as a paragenetically early phase at Olympic Dam (Reeve et al., 1990; Oreskes and Einaudi, 1992; Haynes et al., submitted). On the eastern side of the deposit there is a relatively small (~30 m) zone of breccias containing highly irregular patches of magnetite-rich assemblages. Two samples were taken this zone as part of this study. RX4536 contains ~40% magnetite and ~25% hematite (XRD data; Appendix 4), with hematite occurring predominantly as replacement of magnetite, and with minor late chalcopyrite replacing pyrite and magnetite. RX4537 shows a greater degree of hematite replacement of magnetite, and chalcopyrite replacement of pyrite (petrographic descriptions in Appendix 4; sample locations shown in Figure 2.5). In these examples the hematite-chalcopyrite assemblage is clearly overprinting a primary magnetite-pyrite assemblage (Plate 7). No other comparable zones of magnetite-rich breccias are known in the deposit, although many of the hematitic rocks within the deposit (excluding hematite-quartz breccias) have very fine (<5 μm) inclusions of magnetite within hematite grains (e.g. RX4529, RX4531, RX4513, RX4510, RX4549; see Plate 7). There is therefore evidence that magnetite may have been a widespread precursor to hematite at Olympic Dam. However, the observation that magnetite is paragenetically early at Olympic Dam does not necessarily imply that a widespread magnetite-dominant protore was replaced by hematite, because the same replacement effect could be created by an *in situ* evolution of hydrothermal fluid chemistry and/ or redox conditions in an essentially continuous sequence of mineral precipitation (Haynes et al., submitted).

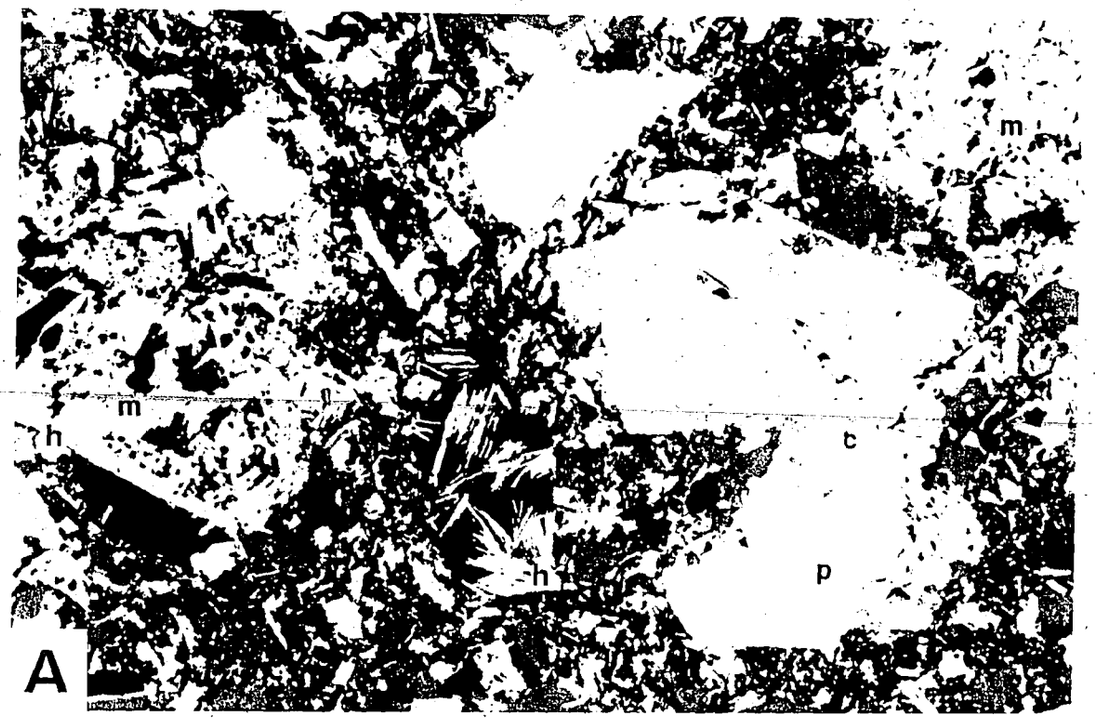

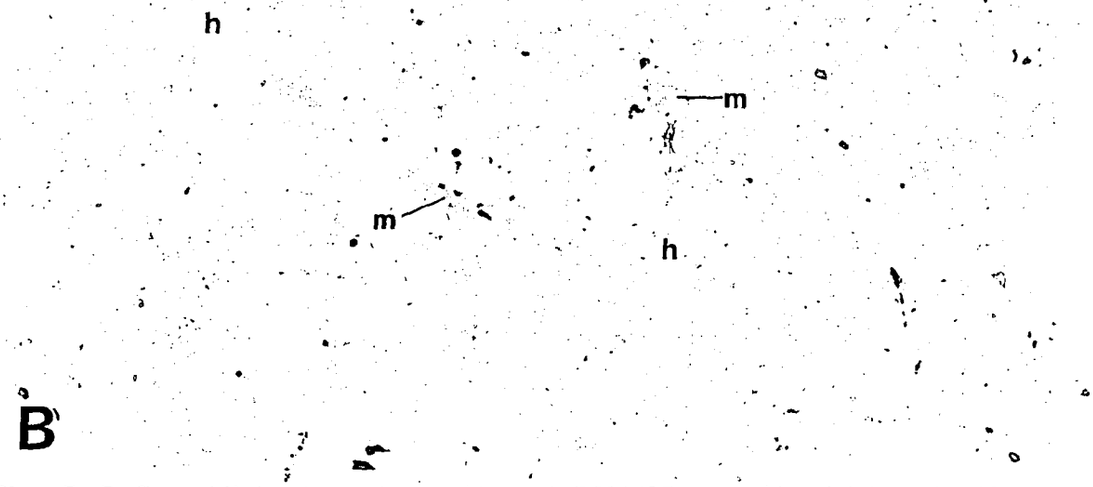

Plate 7. Reflected light photomicrographs. **A)** RX4537, magnetite-rich breccia. Note paragenetic relationships; hematite (h, pale grey) occurs as fine elongate grains and as replacement of magnetite (m, pale brown). Chalcopyrite (c) replaces pyrite (p). Gangue is predominantly siderite. Width of frame is 650 μm.

B) RX4529, hematitic breccia. Inclusions of magnetite (m) ranging in size from 10 μm to <1μm occur throughout hematite (h) grains, suggesting a more complete replacement of magnetite than is illustrated in A). Width of frame is 325 μm.

5.2.2 *Pyrite/ chalcopyrite*

Pyrite is the paragenetically earliest sulphide mineral observed at Olympic Dam. It occurs with relatively minor replacement by chalcopyrite in the magnetite dominant breccias and also in some hematitic ores (e.g. RX4529, RX4531). Pyrite is more completely replaced by chalcopyrite in many Cu-ores, which often contain chalcopyrite with remnant inclusions of pyrite (e.g. RX4508, RX4512). Monomineralic grains of chalcopyrite are also common. The paragenetic sequence described attests to temporal changes in fluid chemistry in the localities where chalcopyrite is replacing pyrite. It is not immediately apparent whether this represents an evolution in fluid chemistry during the same overall hydrothermal event, or a two stage ore genesis in which a pyrite- (and perhaps magnetite) bearing precursor assemblage was overprinted by a Cu-bearing hydrothermal fluid unrelated to the system which produced the pyritic rocks. Trace element and isotope geochemical comparisons (Chapter 7) are therefore made to test which of these models is the more likely.

5.2.3 *Bornite-chalcocite ore*

As described in Chapter 2 there is a sulphide zonation pattern at Olympic Dam from pyrite-rich ores at depth, upwards into chalcopyrite ± pyrite, through an abrupt boundary between chalcopyrite and bornite, into the bornite±chalcocite assemblage above the bornite/ chalcopyrite interface. There are two main morphological types of bornite-chalcocite ore zone; those with a narrow (10-30m) vertical extent which form a covering zone above the chalcopyrite ores, and ore zones with large (>50m) vertical extent and "flame-like" morphology. Although chalcopyrite is seen to be replaced by bornite over a short (metre-scale) interval near the bornite-chalcopyrite interface, chalcopyrite remnants are rarely observed within the higher level bornite-chalcocite ores. Bornite is often observed to be intimately intergrown with chalcocite in vermicular textures. However where bornite occurs without chalcocite, it commonly contains parallel submicron exsolution lamellae of chalcopyrite.

Two models for the origin of the bornite-chalcocite ores have been put forward. Oreskes and Einaudi (1990) proposed that these ores represent the product of supergene enrichment of a primary chalcopyrite + pyrite ore, whereas Reeve et al. (1990) and Haynes et al. (submitted) suggested that the sulphide zonation pattern could be the product of geochemical fronts in a system in which hypogene fluids mixed with meteoric fluids. The temporal differences between these models have important exploration implications. Trace element data for the bornite-chalcocite ores are therefore compared with the data for the other ores and breccias with the aim of ascertaining which of the above two models is more likely to be valid.

5.3 Analytical methods

Major and trace element data are listed in Appendix 2. Major element concentrations for 53 samples of Olympic Dam breccias, sedimentary rocks and variably altered granites were analysed in duplicate by X-ray fluorescence (XRF; Philips PW-1450 equipment) at the Australian Bureau of Mineral Resources using Li-tetraborate glass fusion discs (method after Norrish and Hutton, 1969). Sample powders were prepared using a tungsten-carbide mill. Iron-rich samples (>50 wt% total Fe) were diluted with pure silica prior to fusion in order to approximate the analysis conditions for a silicate rock. Trace elements were analysed by XRF at the Department of Geology, ANU, using pressed powder pellets (Chappell, 1991). Major and trace element results were calibrated against synthetic and standard rock samples. Analyses are accurate to 1% of the concentration of each major element oxide with the exception of Na_2O (±2% relative). H_2O+/- and CO_2 were determined by microabsorption. FeO concentrations were determined by titration. The presence in many samples of both sulphide and sulphate minerals (barite) necessitated the calculation of SO_3 and S totals. In samples containing no fresh K-feldspar (all except RX4523, RX4524 and RX4527) Ba was assumed to be present as barite, and sufficient sulphur was calculated as SO_3 to account for the Ba total. The remaining sulphur was allocated as S (sulphide).

Many samples have high concentrations (1% up to ~15%) of elements generally regarded as trace elements e.g. Cu, Ba, and less commonly La, Ce. All of these elements have been analysed as trace elements (i.e. as pressed powder pellets), assuming no absorption of the primary X-Ray beam by the elements concerned. At high concentrations (>1%) this assumption is not valid, and this has contributed to several analyses having totals which differ by more than 1% from 100% (trace element totals expressed as oxides are included in the rock total; see Appendix 2). Where this occurs, the only element totals in error are those "trace elements" for which the concentration is very high (percent levels). The data for the other elements are not affected.

The precision for trace elements is typically 1 to 4% relative (95% confidence) for concentrations greater than 100 ppm (Chappell, 1991). For concentrations below 100 ppm, the relative precision percentage increases from the above values to a maximum of ~30% at the lowest levels of detection. The lowest level of detection is 0.5 to 1ppm for most elements, 5 ppm for La and Ce, and 2 ppm for Ba. For most elements, at a concentration of ~10 ppm, the relative error is 5 to 10%.

Rare earth element (REE) concentrations were determined for 43 samples by instrumental neutron activation (INAA) according to the methods of Chappell and Hergt (1989). The data are listed in Appendix 3. Where discrepancies exist between INAA data and XRF determinations of La and Ce, the former are regarded as more reliable. INAA data are

used in the discussion of full REE patterns for a subset of the samples in Section 5.8. However, the XRF data are used in a general discussion of La and Ce distribution (Section 5.6) because more samples were analysed by this method, and this enables examination of trends for the entire sample suite.

5.4 Data treatment

The origin of the Olympic Dam Breccia Complex by hydrothermal brecciation and iron metasomatism of the host granite, and the result that the breccias comprise a spectrum with variable proportions of two major components, granite and hematite, means that total iron content is a useful variable by which to compare the major and trace element distributions within the deposit. However, the concentrations of the two metals of most economic interest, Cu and U, do not correlate with total Fe content, but do correlate with each other (Figure 5.1; U vs total Fe plotted in Appendix 6). These geochemical features and the paragenetic differences described in Section 5.2 for Fe oxides and Cu-Fe sulphides, suggest that Cu and U may have been introduced to the deposit in a separate fluid from Fe. For this reason, some of the elements discussed below are compared to Cu content, particularly where no correlation with Fe is evident.

The introduction of iron to the deposit was accompanied by extreme mobility of many elements. In breccia systems, the precipitation of hydrothermal matrix minerals can cause an apparent net depletion of elements present in a given volume of the protolith, even though they may have behaved in a geochemically immobile manner. To examine the geochemistry of the Olympic Dam Breccia Complex in terms of element mobility and the net gains and losses of elements, it is therefore necessary to identify at least one element which appears to have been immobile and by which the relative mobility of other elements can be gauged (e.g Gresens, 1966; Grant, 1986). This approach allows measurement of dilution of elements due to the introduction of hydrothermal matrix minerals, which is very large especially in the breccias.

Of the elements commonly regarded as relatively immobile (Ti, P, Zr, Y, Nb, Al), the only two from the Olympic Dam data for which the concentrations demonstrate a good correlation are Ti and Zr (Figure 5.2). It is assumed that this correlation results from the relative immobility of these elements during hydrothermal processes, rather than a remarkably fortuitous constancy of proportion of these elements had they been hydrothermally transported in significant amounts. In Chapter 3 evidence is presented for at least limited mobility of Zr (hydrothermal zircon overgrowths) and this is probably the cause of some of the scatter in Figure 5.2. TiO_2 has therefore been selected as the least mobile element.

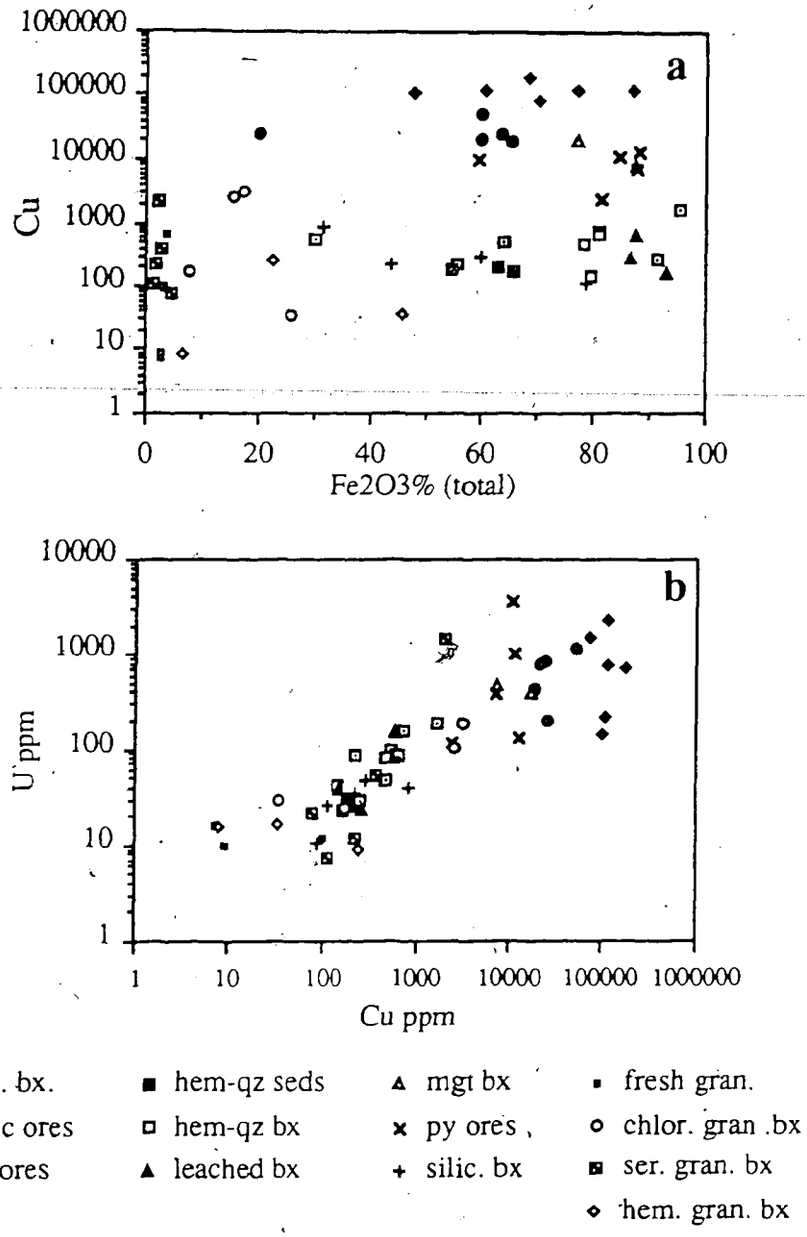

Figure 5.1 Variation diagrams for Cu, Fe_2O_3 (total) and U. **a)** Cu and Fe_2O_3 (total) concentrations are not correlated; **b)** In contrast, Cu and U concentrations are.

The discussion of the geochemistry of the breccias (below) investigates the relative mobility of the various elements by examining the changes in element/TiO_2 ratios which accompany increases in total Fe and, in some cases, Cu. Enrichment factors have been calculated for each element by normalising the element/TiO_2 ratio to the corresponding ratio for pristine granite (sample SS-87 of Creaser, 1989). This approach assumes that the TiO_2 measured in the samples under discussion is derived from the Roxby Downs Granite. The enrichment factors are listed in full in Appendix 5 and are presented in summary form in Tables 5.1 and 5.2. Figures 5.3 and 5.7 display the range and mean enrichment factor for each lithological category for major and trace elements respectively.

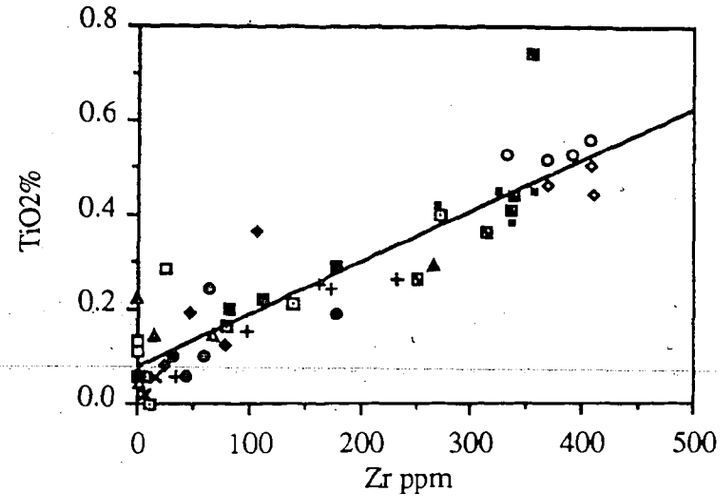

Figure 5.2 Correlated concentrations of TiO_2 and Zr are interpreted as evidence of the relatively immobile behaviour of these elements during hydrothermal processes at Olympic Dam.

The validity of the enrichment factors is dependent on the immobility of Ti. Confident resolution of one enrichment factor from another (to determine relative enrichments) depends on the degree of uncertainty in the immobility of Ti. An approximation of this uncertainty can be obtained from Figure 5.2 which shows a regression through the TiO_2 and Zr data. For the purposes of calculating an estimate of maximum uncertainty, all scatter in the data has been arbitrarily attributed to mobility of Ti. The residuals of the data have been calculated as a percentage of the corresponding TiO_2 concentration. Most samples have residual/TiO_2 ratios less than 50% (eight samples with low TiO_2 concentrations have higher ratios). This means that for most samples, the maximum amount that a TiO_2 concentration could have differed from the measured value (prior to any limited hydrothermal Ti mobility leading to the present concentration) is 50% of its present value. The element/TiO_2 ratios for most samples are confidently estimated to lie between 0.67 and 2 times their calculated values. This approach breaks down at low TiO_2 values, where residuals expressed as percentages become very high even though the absolute value of the residual may be no higher than for the other data plotted. On the basis that the majority of the data have residuals less than 50%, and because there are no obvious outliers at low TiO_2 concentrations, 50% is the figure applied to all of the data as an estimate of maximum scatter. Use of this figure means that it is reasonable to regard any calculated enrichment factors (listed in Table 5.1) between ~0.7 and 2 as not resolvable from 1, and this field is indicated on all plots in Figures 5.3 and 5.7. Only values falling outside this range are interpreted as demonstrating significant mobility of that element.

Table 5.1. Summary of major element enrichment factors (see text for method of calculation).

	"Fresh" granite	Chloritised granite	Sericitised granite	Hematitised granite	Barren hematite breccia	Pyrite-rich ores	Chalcopyrite-rich ores	Bornite-chalcocite ores	Magnetite breccias	Hematite -quartz sst.	Hematite-quartz breccia	Leached hematite breccia	Silicified breccia
SiO2	0.8-1	0.5-0.7	0.5-1.6	0.6-0.9	0.3-1	0.04-1.3	0.4-1.3	0.02-0.9	0.1, 0.2	0.5-0.6	0.2	0.01-0.2	1-1.9
Al2O3	0.8-1	0.5-0.8	0.7-1.6	0.01-0.8	0.1-1.8	0.1-0.7	0.6-2.5	0.3-1.7	0.3, 0.6	0.4-0.8	0.02-0.1	0.02-0.5	0.1-0.4
Fe2O3	1-2.7	1.5-14	0.7-2	4.2-37	28-565	401-1619	35-398	39-378	144, 527	69-119	103-268	119-228	5.1-486
FeO	0.2-1	2.5-5.4	0.1-1.3	0.1-0.5	0.2-2.1	2.8-100	2.5-10	6.8-38	41, 191	0.7-2.4	0.4-1	0.3-3.3	0.2-5.5
MnO	0.3-2	0.9-1.5	0-1.4	0.6-4.4	0.9-8.4	8.4-209	1.3-7.6	0.7-8.4	63, 275	0.9-2.5	3.9-4.6	3.5-6.1	0.5-8.4
MgO	0.4-1.1	0.7-5.3	0.4-1.5	0.04-1.6	0.4-2.2	2.4-6.5	1.1-2.6	0.4-4.6	4, 11	1.6-7.8	0.5-1.4	0.4-2.8	0.3-1.5
CaO	0.2-1	0.1-0.6	0-1.9	0-1	0-0.5	2.5-39	0.5-22	0.04-15	2, 2.8	0.1-0.3	0.3-12	0.03-1.5	0.04-0.7
Na2O	0.1-1	0.04-0.05	0.06-0.1	0.05-0.07	0.04-0.7	0.5-1.2	0.2-0.6	0.1-0.7	0.2, 0.7	0.2	0.1-0.4	0.1-0.4	0.1-0.7
K2O	0.8-1.3	0.2-0.5	0.4-1.1	0-1	0.01-0.9	0-0.4	0-1.7	0-0.8	0, 0.1	0.2-0.5	0.01-0.03	0-0.1	0-0.1
P2O5	1-1.1	1.1-5.2	0.7-7.9	0.6-1.4	4.2-21	19-52	11-39	3.2-56	9.5, 11	6.3-8.6	5.9-18	4-17	3.7-26

The following section is an examination of the geochemical behaviour of the elements analysed, in terms of their relative mobility during hydrothermal processes, net enrichments and depletions, and controls on element distribution. The elements are grouped according to the conventional classification of "Major" and "Trace" elements, even though members of the latter group may occur in percent level concentrations. The discussion of the data is on an element by element basis and relates the data to the lithological categories mentioned above. A summary of the principal enrichments and depletions with interpretation follows in the Section 5.7. Reliable determinations of Au and Ag concentrations for the present sample suite were not available at the time of writing. It is therefore not possible to determine the enrichments or depletions of these elements in the various ore types, and they are not discussed in the following geochemical overview.

5.5 Major elements

SiO_2. The scatter in the plot of SiO_2/TiO_2 vs total Fe (Appendix 6) and petrographic observations indicate that SiO_2 has been mobile during hydrothermal processes at Olympic Dam. SiO_2 has been lost from rocks within all of the rock categories except the silicified breccias (Figure 5.3 a-l). The rock categories which show only loss of SiO_2 (rather than both gains and losses) are: chloritised granitic breccias, magnetite breccias, hematite-quartz sandstones, and hematite-quartz breccias. In general SiO_2 appears to have had limited mobility and been weakly depleted relative to the host granite.

TiO_2. As mentioned above, TiO_2 appears to have been the least mobile element during hydrothermal processes at Olympic Dam (see TiO_2 correlation with Zr; Figure 5.2). The decrease of TiO_2 concentration with increasing total Fe (Figure 5.4) is therefore believed to result from dilution of granitic TiO_2 concentrations as Fe is added as matrix and replacement minerals.

Al_2O_3. Hematite replacement of alkali feldspar in rocks which preserve a granitic texture (e.g.RX4520) provides mineralogical evidence for loss of Al_2O_3 during ore genesis at Olympic Dam, which is supported by analytical data (Figure 5.3 c, d, e, f, j, k, l). In contrast, alteration of granitic feldspar to sericite appears to have occurred with no discernible Al_2O_3 mobility. Only minor Al_2O_3 was lost during chloritic alteration (Figure 5.3 a and b). The chalcopyrite-rich and bornite-chalcocite ores have higher ranges of Al_2O_3 enrichment factors than the other hematite-rich rock categories. This may result from a lesser degree of Al_2O_3 depletion during mineralisation. However, it is also possible that the paragenetically late introduction of Cu (Section 5.2) was accompanied by an enrichment in Al_2O_3. As expected, the geochemically similar trace element Ga, shows the same relative enrichment in the Cu sulphide bearing ores (below).

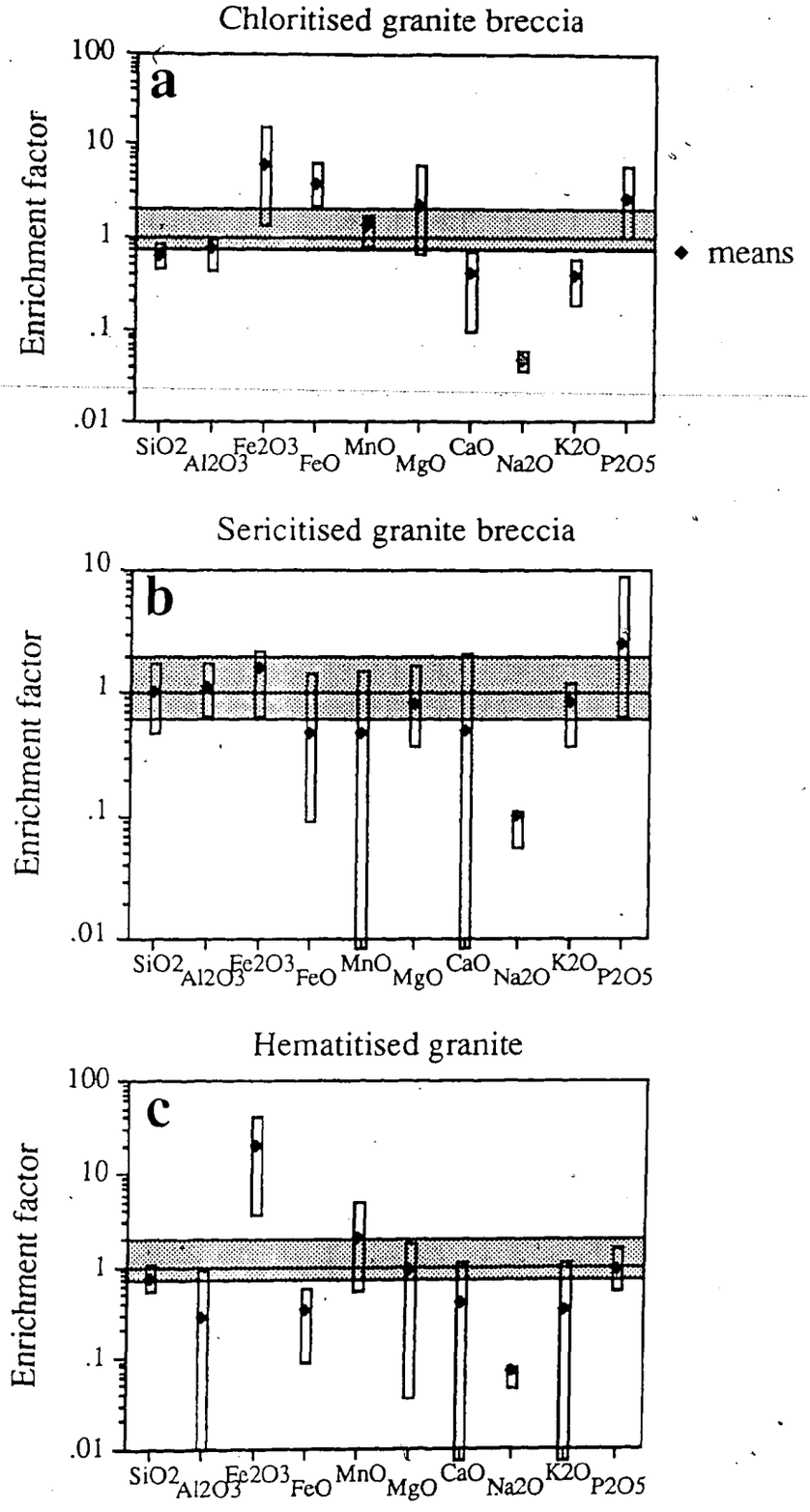

Figure 5.3 Enrichment factors for major elements in Olympic Dam breccias calculated as element/TiO_2 of sample divided by the same ratio for unaltered granite (sample SS-87), assuming immobility of TiO_2. Shaded area is field for which enrichment factors are not resolvable from 1 due to uncertainty in TiO_2 immobility (see text). Bars represent range of enrichment factors for each element; diamonds are means. Where bar crosses X-axis the range minimum is zero.

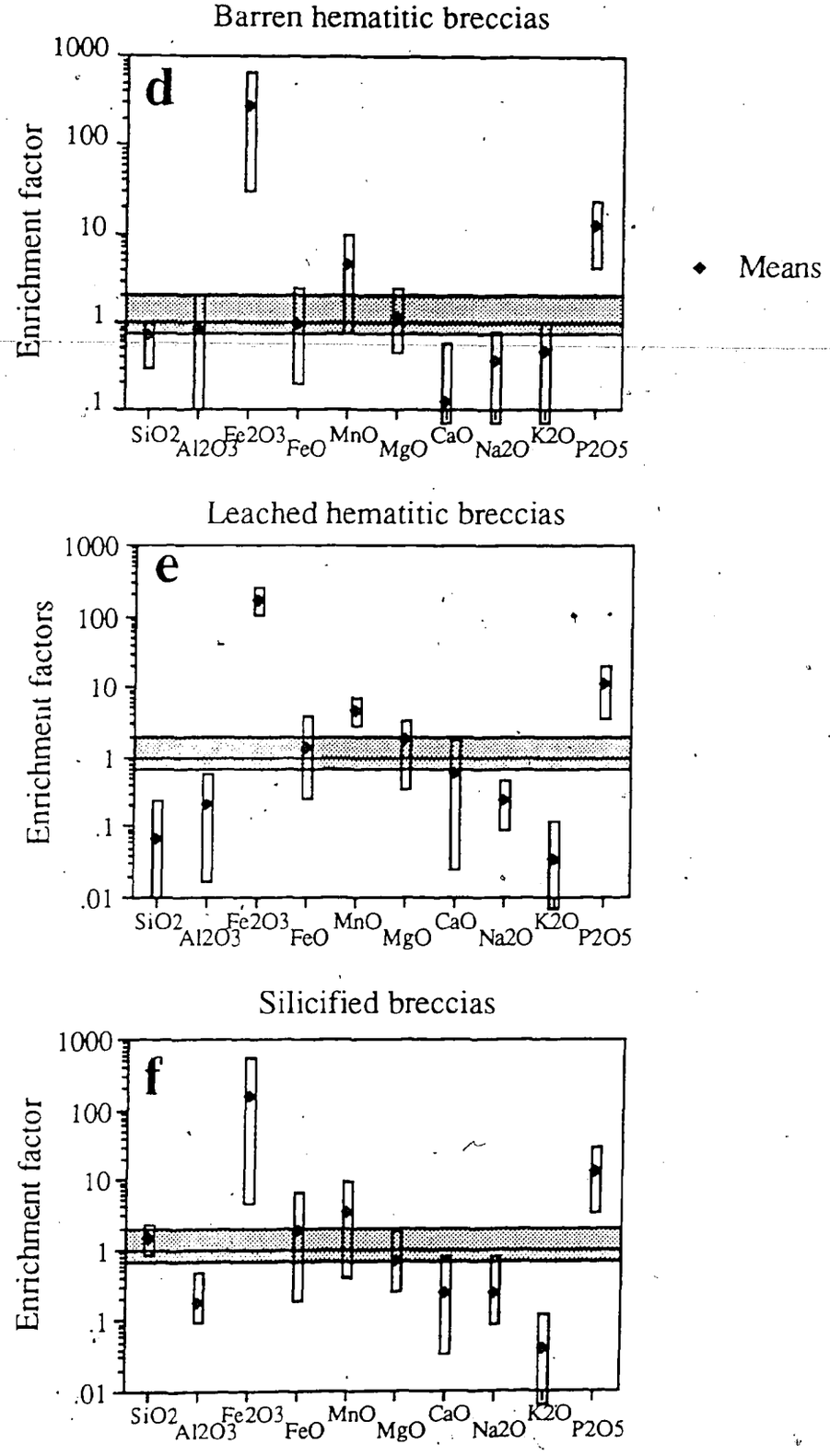

Figure 5.3 continued.

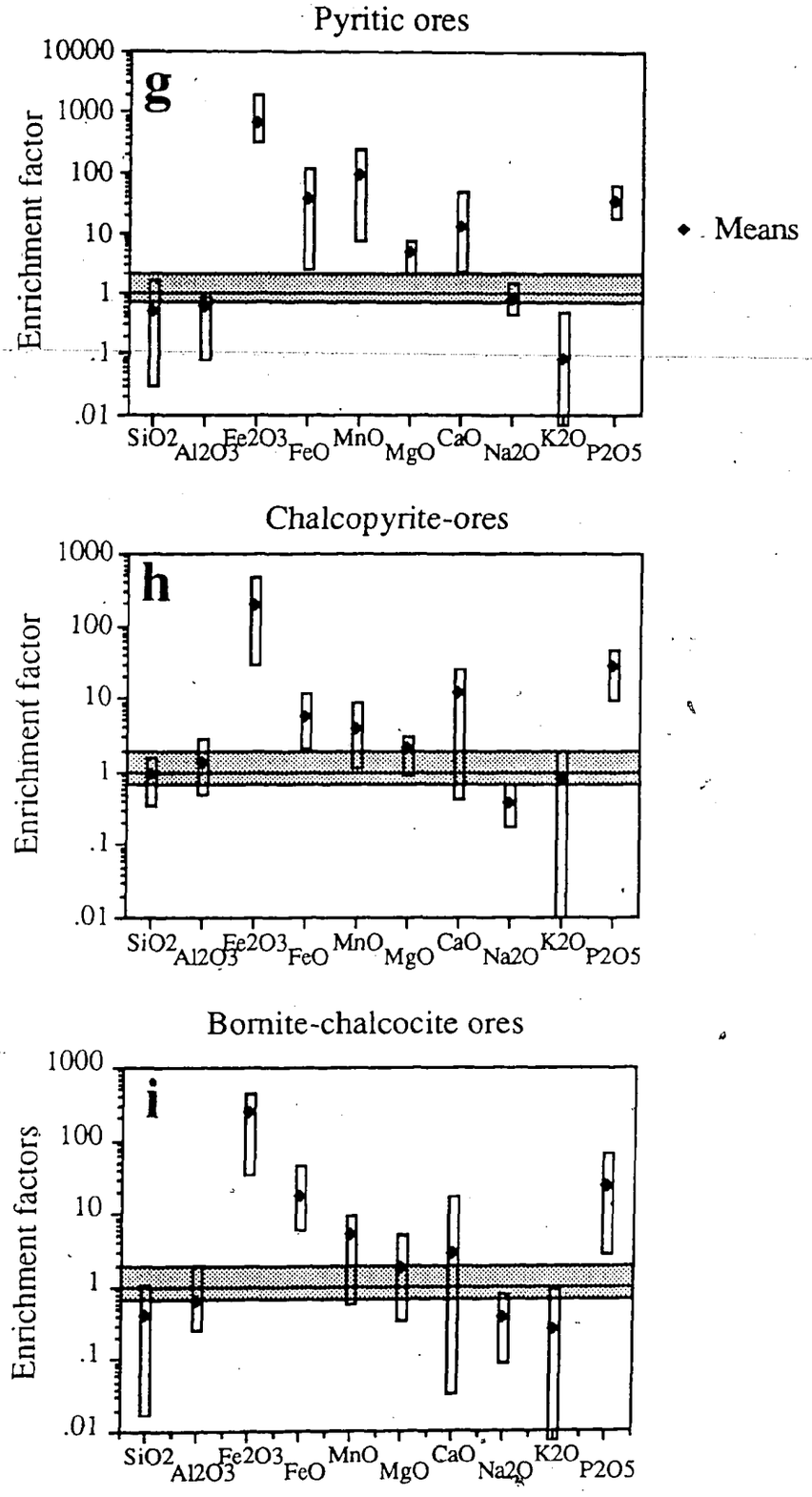

Figure 5.3 continued.

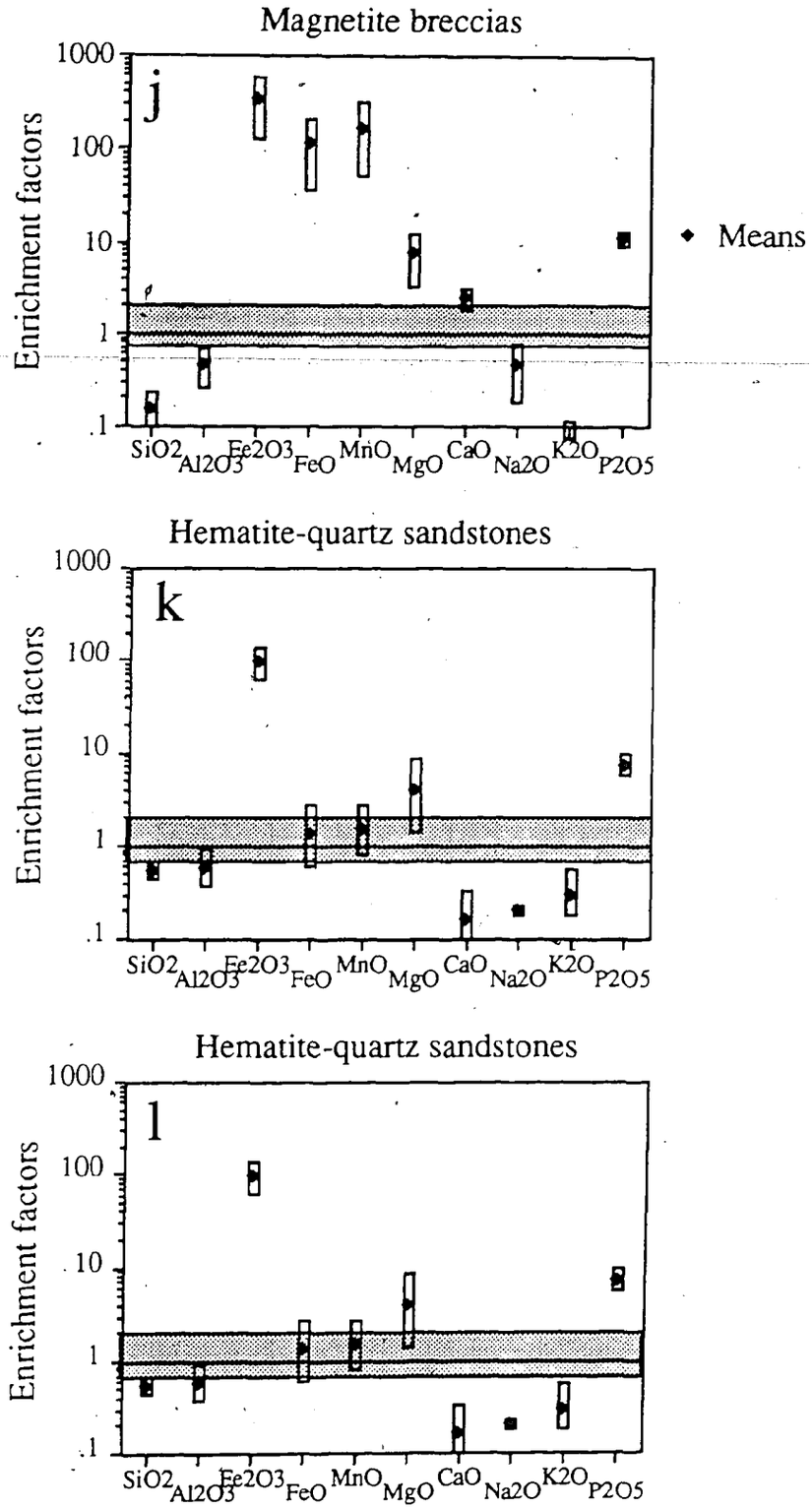

Figure 5.3 continued.

Fe_2O_3. All rock categories except sericitised granite breccias show significant enrichments in Fe_2O_3 (Figure 5.3 a-l). [Sericitised granite breccia samples have enrichment factors not resolvable from unity (i.e. range from 0.7 to 2) indicating minimal gain or loss of Fe_2O_3 during this style of alteration].

FeO. The highest enrichment factors for FeO are evident for the magnetite breccias and sulphide-bearing ores (Figure 5.3 j, g, h, i), reflecting Fe^{2+} present in magnetite, siderite and the various Cu-Fe sulphides. The ratio of FeO/TiO_2 in fresh granite (sample SS-87) is 3.65. The ratio is lower for hematite-altered and sericite-altered granitic breccias (Figure 5.3 b and c), consistent with alteration by an oxidised fluid (oxidising Fe^{2+} to Fe^{3+}). In contrast, the chloritised granitic breccias have been enriched in FeO (Figure 5.3 a) suggesting that they may have been altered in reduced conditions, possibly by a separate fluid to that which effected hematite alteration. This style of alteration may be related to the relatively reduced fluids responsible for magnetite precipitation.

MnO. All rock categories except for sericitised granite breccias show a net gain in MnO (Figure 5.3; Table 5.1); sericitised granite breccias appear to have lost MnO. The highest enrichment factors occur for the magnetite breccias and pyritic ores (Figure 5.3 j and g) and this may reflect a mineralogical control on MnO concentration, due to a rhodochrosite component in siderite which is common in these rock types. Notwithstanding the siderite-rich assemblages, there is a scattered positive correlation between MnO/TiO_2 and total Fe (Figure 5.4b). This suggests that Mn and Fe precipitation mechanisms were linked, implying a redox-controlled precipitation.

MgO. The plot of MgO/TiO_2 vs total Fe (Appendix 6) shows considerable scatter in the data indicating that MgO has been mobile during hydrothermal processes at Olympic Dam (immobility would reveal a flat trend of unchanging MgO/TiO_2). However, all of the rock categories except magnetite breccias, hematite-quartz sandstone and pyritic ores contain samples with apparent gains in MgO and samples with apparent losses (Figure 5.3). This is interpreted to mean that although MgO has been mobile, it has neither been introduced or removed on a large scale during ore formation. Chloritised granite samples are more enriched in MgO than sericitised and hematitised granite breccias (Figure 5.3 a, b and c) which is consistent with chlorite alteration being caused by different fluids to those responsible for sericite and hematite alteration.

CaO. Calcium is a relatively mobile element and has previously been observed to be depleted in even weakly altered samples of Roxby Downs Granite (Creaser, 1989). The diagrams showing enrichment factors for chloritised, sericitised, and hematitised granite breccias (Figure 5.3 a, b and c) each show net losses for CaO, consistent with the above observation. The hematitic rock categories, with the exception of the sulphide-mineralised breccias and the hematite-quartz breccias, all have CaO enrichment factors

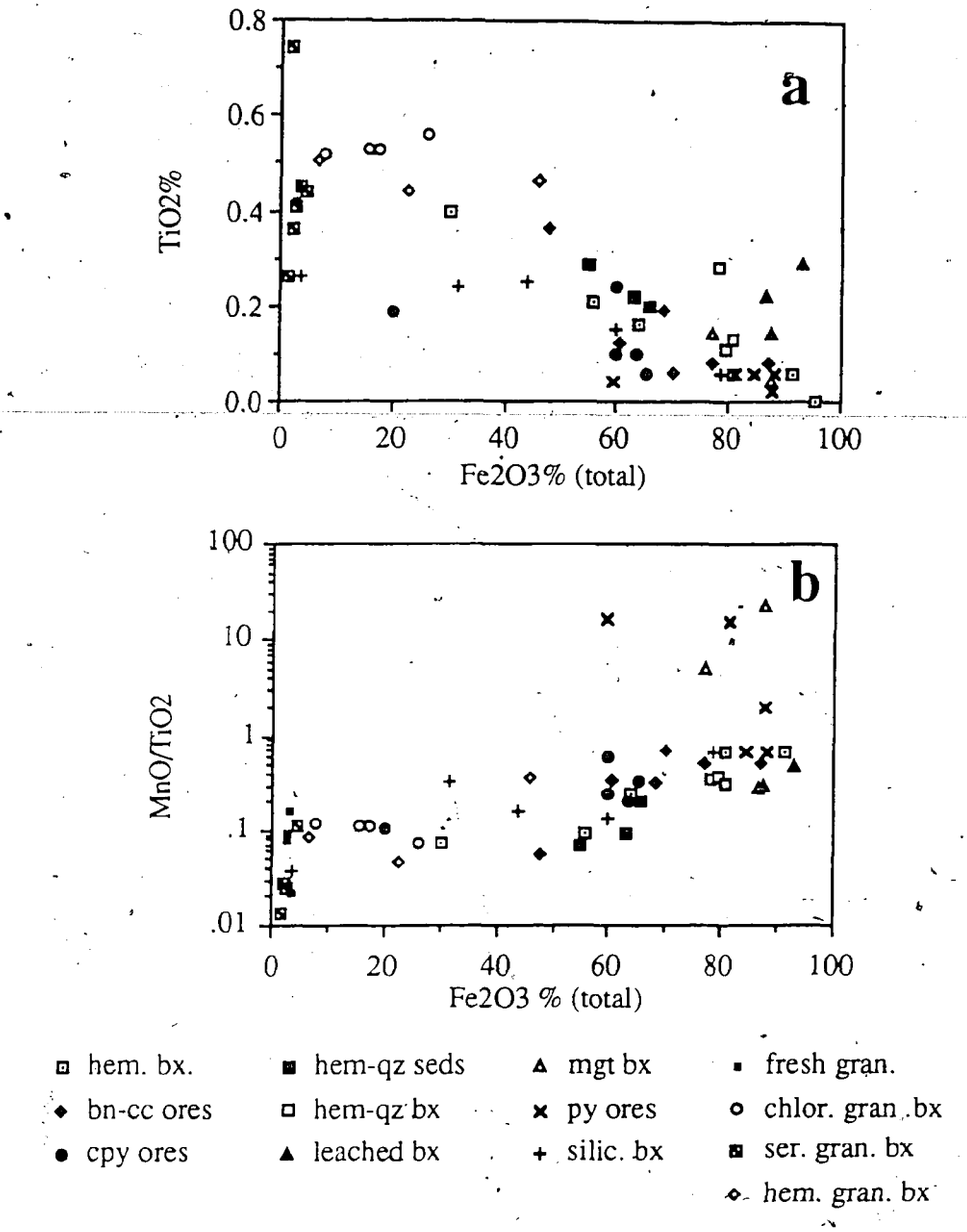

Figure 5.4 **a)** Decreasing TiO_2 with increasing Fe_2O_3 (total) is probably due to dilution of relatively immobile TiO_2 as Fe is added during brecciation. **b)** MnO/TiO_2 increases with increasing Fe_2O_3 (total) indicating addition of MnO during hydrothermal activity.

---

below 1 (Figure 5.3), indicating loss of CaO. In contrast, the pyritic, chalcopyrite-rich and bornite-chalcocite ores, and the hematite-quartz breccias have been enriched in CaO. The relatively high CaO concentrations for members of these rock categories (~2 to ~6 wt%) generally reflect the abundance of fluorite (CaF_2) and/or barite into which Ca can substitute to a limited extent (Deer et al., 1966).

Na_2O. All of the rock-types except pyrite-rich ores have had a net-depletion in Na_2O relative to the host granite composition (Figure 5.3 a-l). This is consistent with the evidence of Creaser (1989) who observed that Na_2O has been lost from even weakly

altered Roxby Downs Granite. It is not clear why the pyrite-rich ores contain relatively more sodium than other ore types. The plot of Na_2O/TiO_2 vs total Fe (Figure 5.5) illustrates the considerably lower Na_2O contents of the altered granite breccias relative to the analyses of fresh granite. It also shows an increase in Na_2O/TiO_2 for samples with more than ~50 wt% total Fe. This may reflect the saline nature of the fluids transporting Fe.

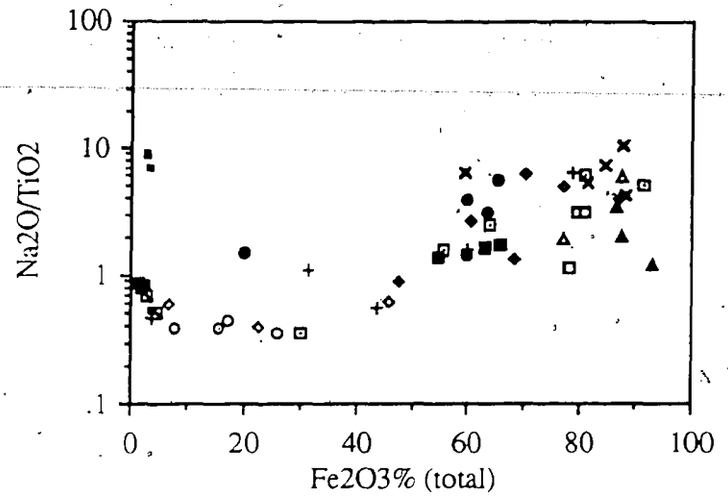

Figure 5.5 Na_2O/TiO_2 versus total iron showing that Na has been lost relative to fresh granite compositions, but has been reintroduced in samples with Fe_2O_3 (total) greater than 50%.

K_2O. Potassium has been highly mobile with K_2O/TiO_2 ratios varying over two orders of magnitude (Appendix 6). The majority of the samples examined have enrichment factors which indicate loss of K_2O (Figure 5.3). Some examples of sericitised granite (RX4527, RX3698), hematitised granite (RX4526), barren hematitic breccia (RX4563, RX4564), bornite-chalcocite ore (RX4462), and chalcopyrite-rich ore (RX4508, RX4512, RX4578) have enrichment factors not resolvable from 1 indicating no net enrichment or depletion in K_2O. None of the present samples have been enriched in K_2O. Creaser (1989) observed minor K_2O enrichments in relatively weakly altered granite samples. However, in view of the overall evidence for K_2O loss from most of the Olympic Dam breccia samples in this study, it is believed that Creaser's samples probably represent localised enrichments due to redistribution of granite-derived K_2O, rather than the introduction of metasomatic (exotic) potassium. K_2O concentrations

decrease with increasing total Fe content, suggesting that K_2O abundance reflects the relative proportion of (sericitised) granitic fragments in the breccias.

P_2O_5. The scattered trend of increasing P_2O_5/TiO_2 with increasing total iron (Figure 5.6a) indicates that phosphorus has been introduced during ore genesis. Hematite-altered granite is the only rock category to show no net gain in P_2O_5 (Figure 5.3 c). All of the other rock categories analysed have P_2O_5 enrichment factors ranging well above 2 (Figure 5.3). P_2O_5 concentrations correlate with Ce content (Figure 5.6b) which suggests that P is present dominantly in REE minerals (e.g. florencite, monazite and xenotime).

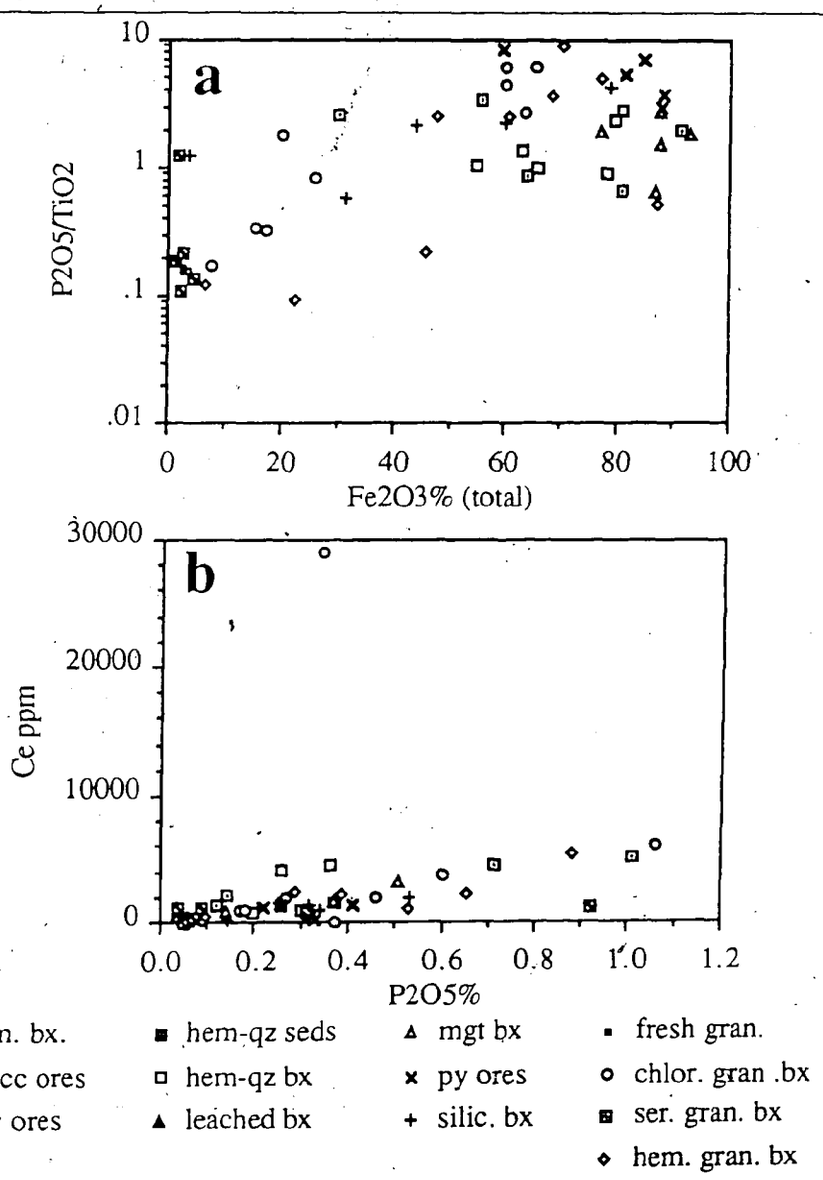

Figure 5.6 **a)** Scattered positive correlation indicates that Phosphorus has been introduced to the deposit during hydrothermal activity. **b)** Correlation between Ce and P_2O_5 suggests that P is present dominantly in REE minerals. High Ce point is for RX4578, a chalcopyrite-rich ore with the highest REE concentrations recorded at

Figure 5.6 continued. Olympic Dam. As an outlier in b), this sample probably has REE dominantly contained in bastnaesite, a carbonate, rather than the phosphates florencite, monazite or xenotime.

5.6 Trace elements

Copper. All of the rock categories analysed have been enriched in Cu (Figure 5.7). Cu concentrations range from 9 ppm (RX4524, "fresh" granite) to 176,500 ppm (i.e.~18%; RX4463, bornite-chalcocite ore). The plots of Cu vs total Fe (Figure 5.1) and Cu/TiO_2 vs total Fe (Appendix 6) show that Cu and Fe are not correlated. This suggests that precipitation mechanisms for Cu and Fe were not closely linked and implies that these elements may have been introduced to the deposit in separate fluids.

Uranium. All of the rock categories analysed show some evidence of U enrichment (Figure 5.7) although some individual samples are depleted. U concentrations range from less than 1 ppm to 3650 ppm in the present sample suite. They also correlate with Cu concentrations (Figure 5.1b). This trend indicates a relative constancy of proportion of these two elements suggesting linked mechanisms of deposition. Two samples of altered granite breccias (RX4533 and RX4522) have undergone depletion in U which suggests that some of the U present in the ores may have been derived from the host granite. U/TiO_2 ratios do not correlate with total Fe (Appendix 6) and this implies that U was not deposited by the same mechanisms as Fe, and may not have been introduced in the same fluids as Fe.

Rubidium. The calculated enrichment factors for Rb indicate that it has been depleted in the majority of the samples analysed (Table 5.2; Appendix 6; Figure 5.7 a to l). The chalcopyrite-rich ores are the only group to show no evidence of Rb depletion. The near-linear correlation between Rb and K_2O concentration (Figure 5.8) illustrates that these elements have behaved in a coherent manner. Rb abundances are therefore probably controlled by the distribution of sericite, the main potassic phase within the deposit.

Strontium. Strontium has been introduced to the deposit during ore genesis, as is illustrated by the increase in Sr/TiO_2 with increasing total Fe (Figure 5.9a). Only hematite-altered granite breccias have experienced a net Sr depletion (Figure 5.7 c). The overall addition of Sr is important because it suggests that Sr isotopes may be useful as tracers of ore fluid provenance; this subject is discussed in Chapter 7. One sample (RX4533) has an extremely high Sr concentration (5370 ppm), well above all of the other samples. RX4533 is a sericite-altered granite breccia and its high Sr concentration is consistent with the geochemical modelling of Haynes et al. (submitted) which predicts that strontianite ($SrCO_3$) will be precipitated when the ore fluid reacts with granite at relatively low water/rock ratios (i.e with a large proportion of granite). Although

Table 5.2. Summary of trace element enrichment factors (see text for method of calculation).

	Fresh granite	Chloritised granite	Sericitised granite	Hematitised granite	Barren hematite breccia	Pyrite-rich ores	Chalcopyrite-rich ores	Bornite-chalcocite ores	Magnetite breccias	Hematite -quartz sst.	Hematite-quartz breccia	Leached hematite breccia	Silicified breccia
Rb	0.7-1	0.2-0.4	0.3-0.9	0.01-0.8	0.03-1		1-1.8	0.07-1.1		0.3-0.5	0.03, 0.07	0.01-0.18	0.01-0.1
Sr	0.7-1.7	0.7-1.5	0.3-32	0.1-0.4	8-210	1.9-12	14-51	2.2-25	3.5, 7.6	7.4-11	11-38	3-10	1.2-15
Pb	0.9-2.2	0.2-0.8	0.5-11	0.3-1.7	4.8-24	18-417	10-39	11-52	11, 34	7-10	10-23	7.8-12	0.8-51
Th	0.5-0.8	0.4-1.1	0.5-1.9	0.4-0.9	0.8-2.4	1.1-12	0.8-2.4	0.3-6	1, 1.6	0.5-0.9	0.1-0.5	0.2-2.2	0.5-3
U	0.6-4.1	1.1-8.6	0.4-96	0.5-0.8	7-64	47-2223	26-283	10-577	69, 282	2.6-2.9	7-16	2.5-25	1-10
Zr	0.7-1	0.7-0.8	0.5-1.1	0.9-1.1	0.1-0.8	0-0.3	0.3-1.1	0.1-0.8	0.1, 0.5	0.5-0.7	0-0.1	0-1	0.7-1
Nb	0.8-1	0.8-1.2	0.9-2.5	0.8-1.1	1.8-62	30-248	7.7-31	3.6-178	18, 38	1.1-1.6	1.4-5.6	3.7-58	1.1-8
Y	0.7-1	0.3-0.7	0.4-1.4	0.3-1.6	0.6-8.2	3.4-18	3-18	0.5-61	4.6, 22	0.2-0.6	0.7-3.4	0.3-15	0.2-3.7
Ni	1-1.4	2.2-17	0.5-1.4	0.9-1.7	2.9-51	38-3776	0-44	0-114	26, 52	3.9-7.8	2.7-14	5.2-35	1.5-41
Cu	1-77	3.4-324	9.5-321	0.9-31	61-688	2226-19217	7133-28598	16020-77737	7049,10722	36-50	74-271	28-239	18-200
Zn	1-1.8	4-13	0.4-3.1	0.3-1.5	1.3-150	16-1900	2.4-27	1.8-53	61, 137	21-24	2.9-3.5	2.4-27	0.9-9.5
Ga	0.8-1	0.8-0.9	0.8-2.5	0.004-0.7	0.4-3.9	0.8-6.6	1.1-3	0.4-3.1	2.7, 5.4	0.7-1.9	0	0-1.3	0-1.2
V	0.8-1	0.8-1.7	0.4-1.5	0.3-1	1.9-21	8-89	5.7-8.8	2.8-37	4.8, 13	1.7-2.4	2.7-7.2	2.4-7.7	0.8-15
Cr	0.8-1	1.8-12	0.9-4.9	1.5-8.7	26-86	19-86	40-70	19-69	35, 48	22-29	44-92	34-125	4.4-73
Ba	0.8-3.4	0.01-2.1	0.4-3	0.002-0.5	5.5-375	0-4.3	0.1-182	1.8-38	0.2, 0.2	62-77	87-192	1-55	4-31
La	0.8-2.5	0.7-14	1.6-9.7	0.9-3	19-75	7.2-63	61-545	3.9-82	23, 29	13-17	18-109	11-45	3.2-99
Ce	0.7-1.9	0.5-7.5	1.2-6.7	0.7-1.8	14-52	6-49	1.7-330	4.2-56	20, 21	6-10	10-81	8.6-23	2-60

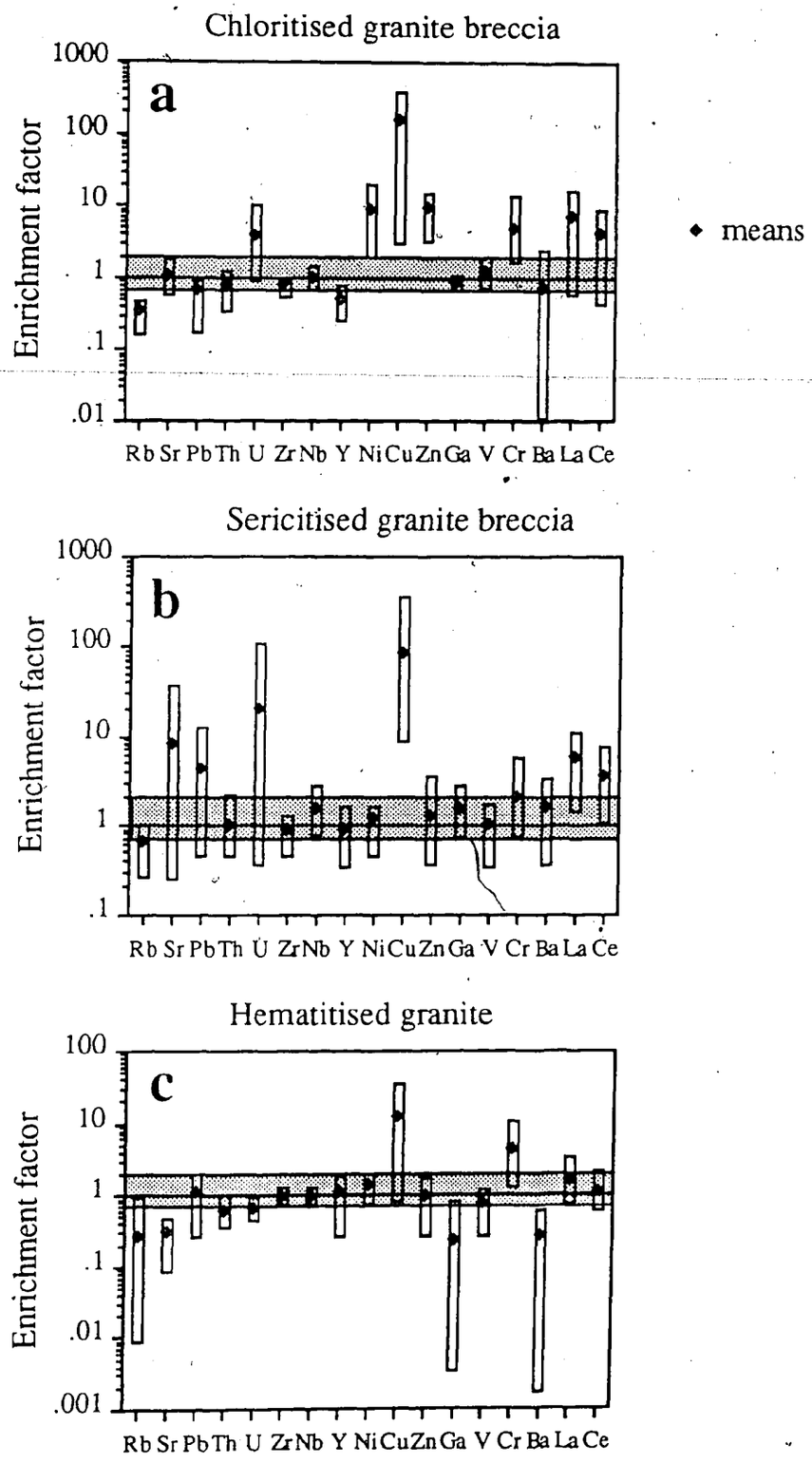

Figure 5.7 Enrichment factors for trace elements in Olympic Dam breccias calculated as element/TiO_2 of sample divided by the same ratio for unaltered granite (sample SS-87), assuming immobility of TiO_2. Shaded area is the field for which enrichment factors are not resolvable from 1 due to uncertainty in TiO_2 immobility (see text). Bars represent range of enrichment factors for each element; diamonds are means. Where bar crosses X-axis the range minimum is zero.

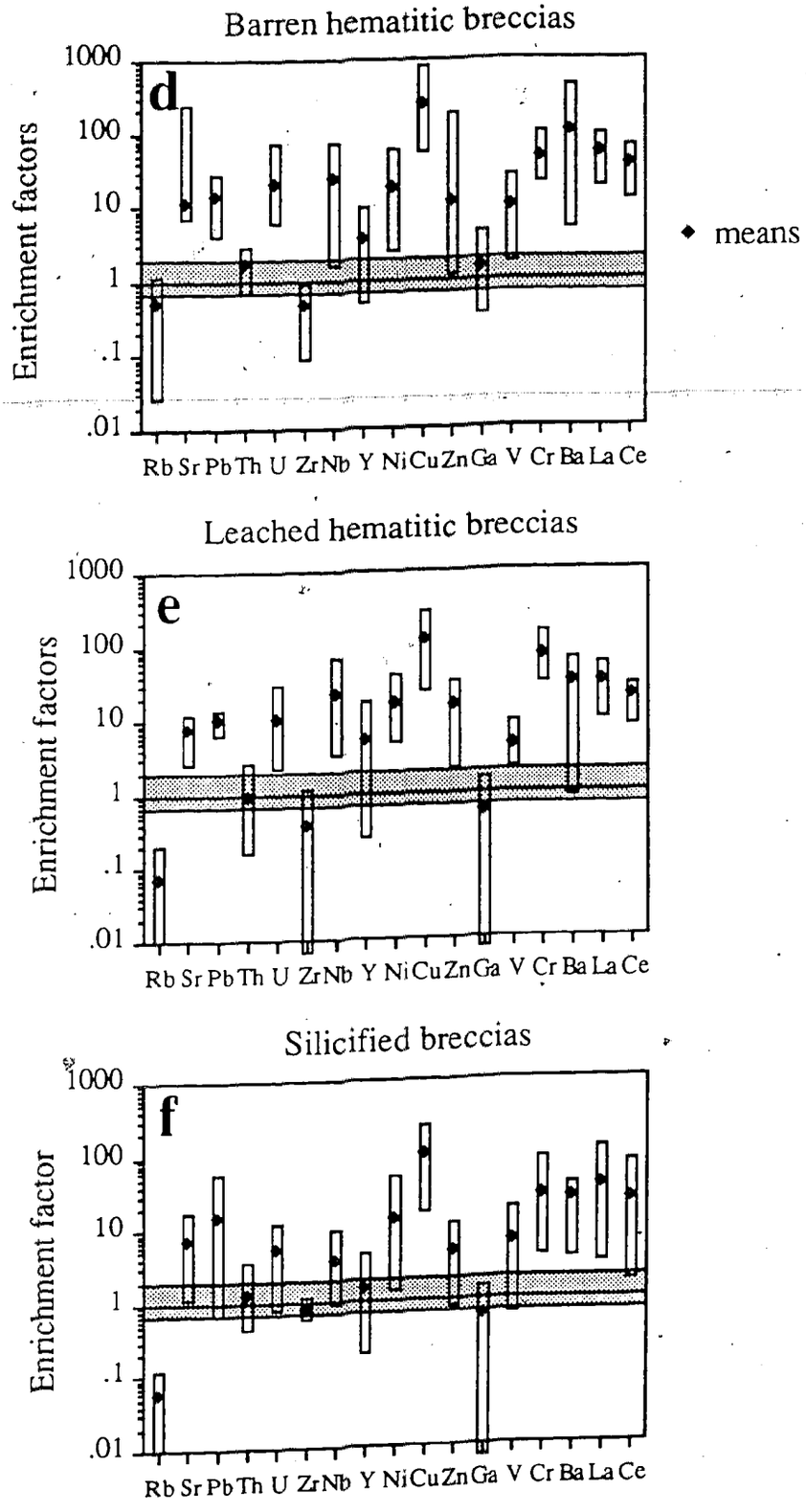

Figure 5.7 continued.

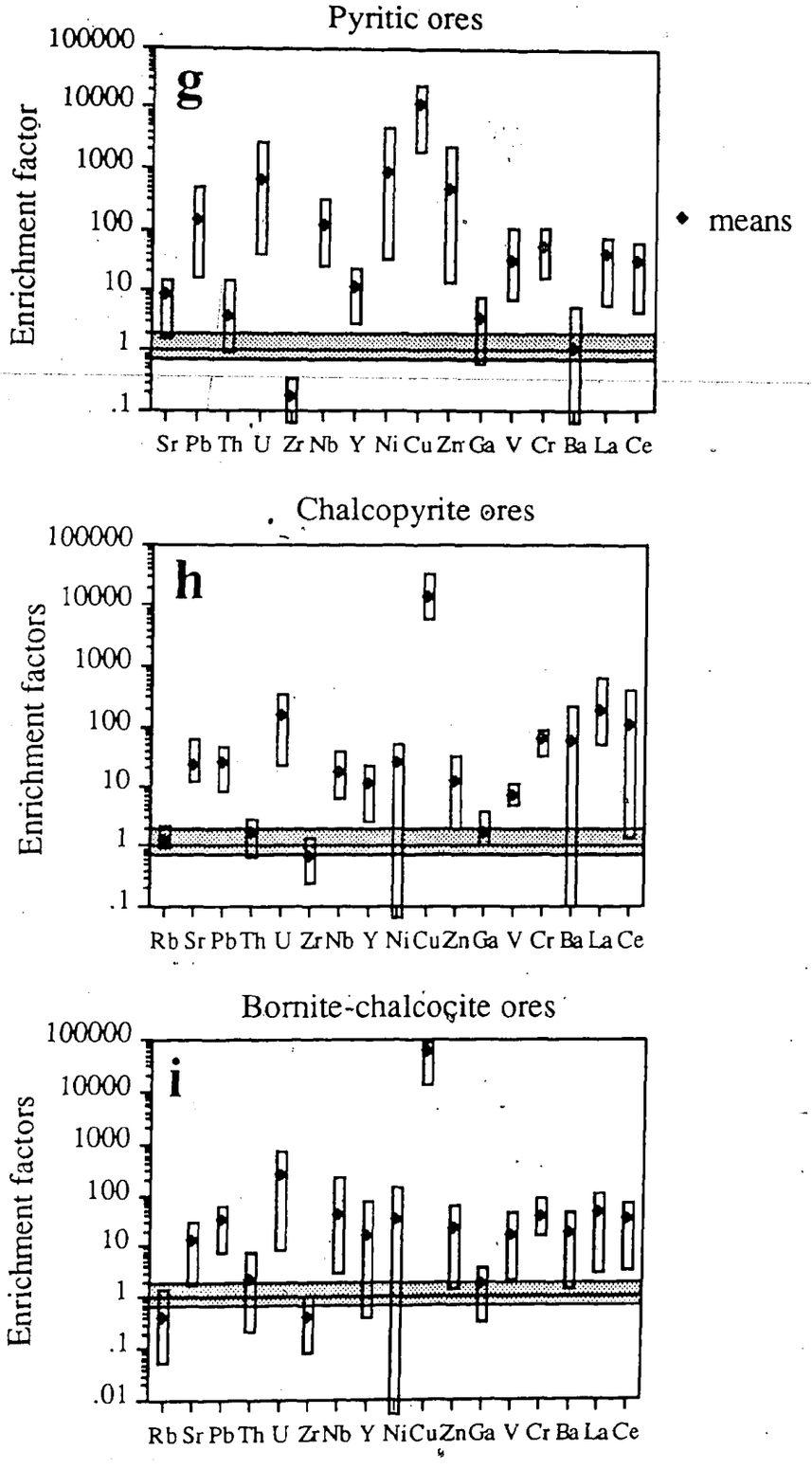

Figure 5.7 continued

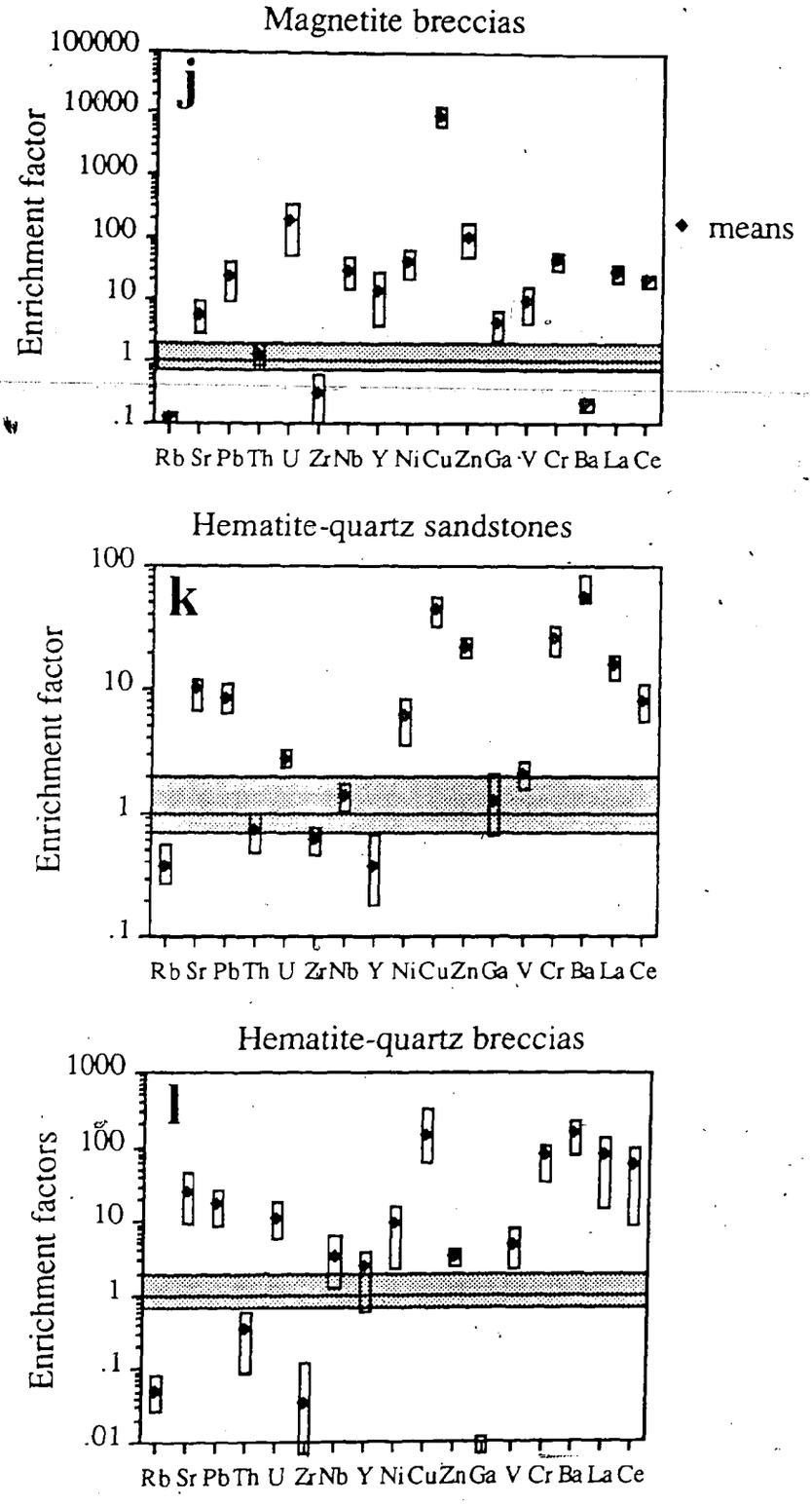

Figure 5.7 continued.

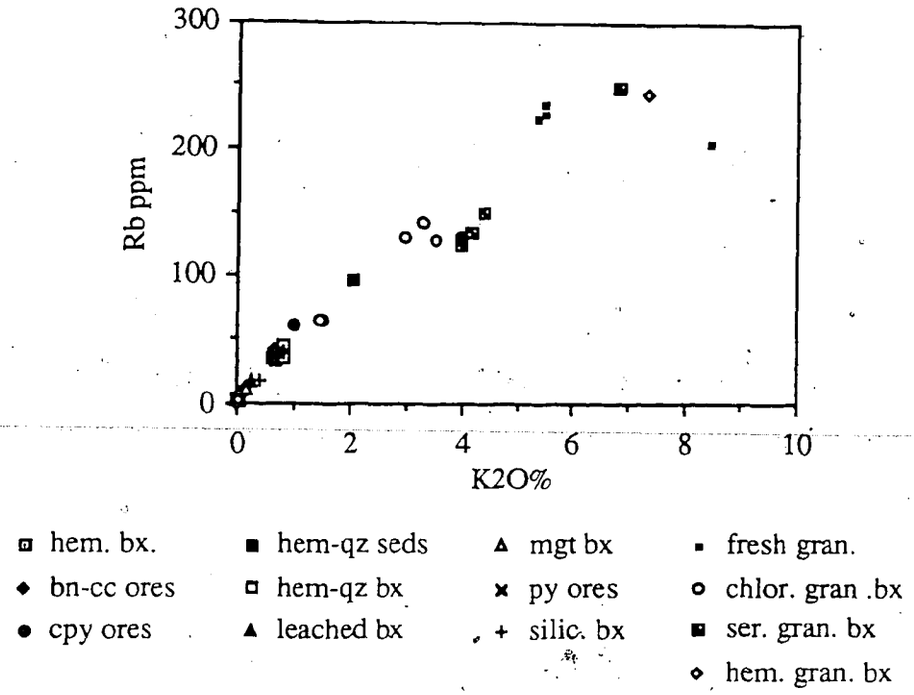

Figure 5.8 Linear correlation between Rb and K_2O indicates that Rb distribution at Olympic Dam is controlled by the occurrence of potassic phases, dominantly sericite.

Strontium continued. strontianite has not been identified in this sample, the high Sr concentration indicates the presence of a Sr-rich mineral.

Sr is also able to substitute for Ba in the solid solution series between barite ($BaSO_4$) and celestine ($SrSO_4$). Figure 5.9b shows that for the Olympic Dam breccias, Sr bears a scattered positive correlation with Ba, with the highest concentrations (except RX4533, see above) occurring in rocks with high modal barite content, e.g. the hematite-quartz

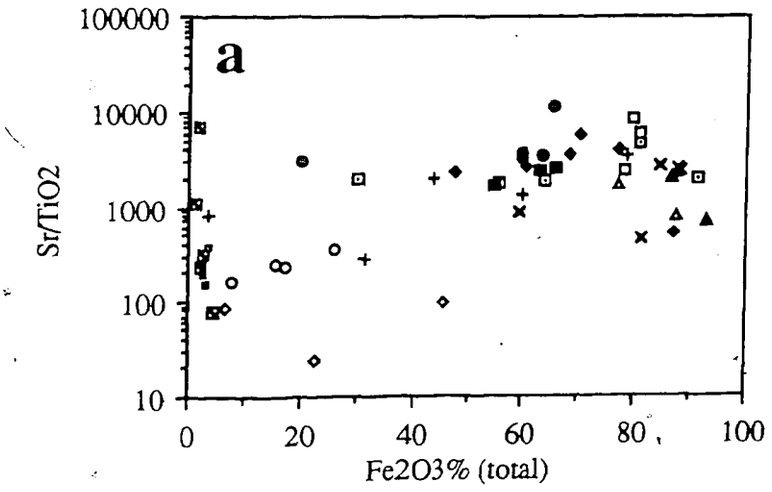

Figure 5.9a. caption overleaf

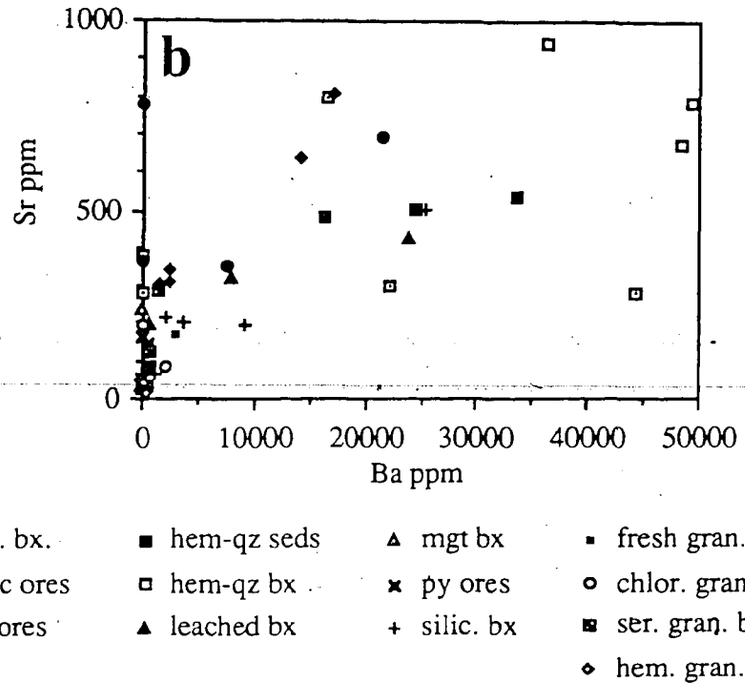

Figure 5.9 a) Scattered increase in Sr/TiO2 with increasing Fe_2O_3 (total) indicates that Sr has been introduced to the deposit. **b)** Sr bears a scattered correlation with Ba, which suggests Sr distribution at Olympic Dam may be controlled by distribution of barite which can accomodate significant amounts of Sr (see text).

---

breccias from the centre of the breccia complex. It is therefore suggested that the dominant control on Sr distribution at Olympic Dam is the occurrence of barite.

Barium. The occurrence of barite clasts and veinlets attests to the mobility of barium during ore genesis at Olympic Dam. Ba concentrations reflect the distribution of barite throughout the deposit (Appendix 2 XRF data; cf. rock descriptions, Appendix 4). Ba is depleted in the hematitised granite- and chloritised granite-breccias (Figure 5.7 a and b), and in two of the sericitised granite breccias (RX4533 and RX3698). This suggests that the Ba observed as enrichments in several of the other rock categories (see Figure 5.7) is at least partially derived from the Roxby Downs Granite.

Lead. The plot of Pb/TiO_2 vs total Fe (Figure 5.10a) shows a positive correlation and these data can be interpreted in three ways: a) Pb was introduced to the deposit during ore genesis; b) Pb is radiogenic, produced by decay of the U introduced during ore deposition; c) Both of the above.

A scattered positive correlation between Pb/TiO_2 and U concentration for most samples, excluding the altered granite breccias (Figure 5.10b), suggests that much of the Pb is radiogenic. However, the fact that the altered granite breccia samples do not conform to this correlation means that the Pb/TiO_2 ratios of these samples are not dominated by

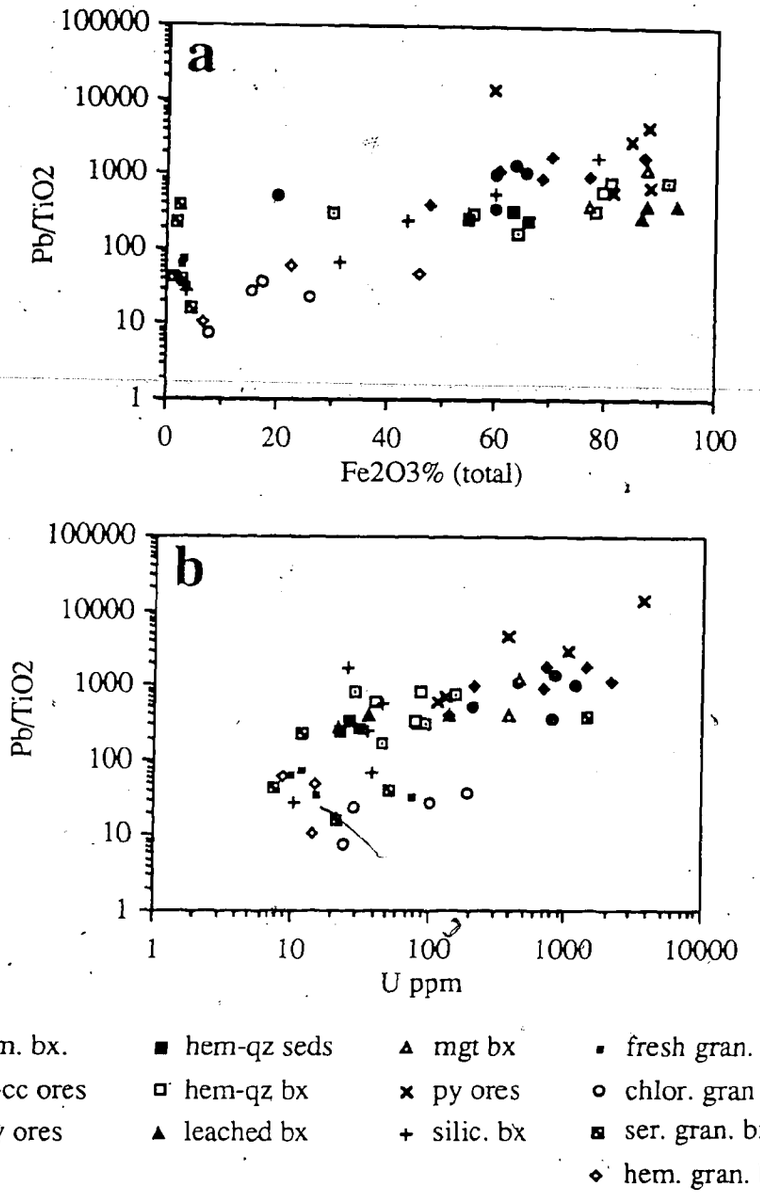

Figure 5.10 a) Pb/TiO_2 increases with total iron which suggests either that Pb was introduced during ore genesis, or that Pb is radiogenic and correlates with Fe_2O_3 (total) because of the higher U content of more iron rich lithologies. The correlation between Pb/TiO_2 and U **b)** suggests that Pb is dominantly radiogenic.

radiogenic Pb. The data for most of the altered granite breccias form a continuation of the trend of Pb/TiO_2 vs total Fe (Figure 5.10a) and this may reflect a primary enrichment in Pb. It therefore appears likely that the present Pb content of the deposit results from both low level enrichment in Pb during ore deposition, and the subsequent accumulation of radiogenic Pb.

Thorium. Thorium has been sparingly mobile at Olympic Dam, as illustrated by the plot of Th/TiO_2 vs total Fe (Appendix 6). However, the flat trend of the data on this plot

suggests that Th was not introduced or removed from the volume of the deposit in an overall sense. It is likely that Th present in the Roxby Downs Granite was remobilised due to the hydrothermal breakdown of minerals such as uranothorite and zircon, and reprecipitated as hydrothermal minerals such as monazite, xenotime and secondary xenotime-zircon. The hematite-quartz breccias are the only sample group to show a systematic depletion in Th (Figure 5.7). All other groups have ranges of enrichment factors which overlap with the "immobile" field (enrichment factors 0.7 to 2).

Zirconium. The Zr/TiO_2 ratio in unaltered Roxby Downs Granite is 880. A plot of Zr/TiO_2 vs total Fe (Appendix 6) shows that this ratio is approximately maintained for samples with total Fe up to 50 wt%, indicating that Zr has been immobile in these samples. For samples containing greater than 50% total Fe, the data scatter to lower Zr/TiO_2 ratios, indicating loss of Zr from these samples. The rock types which include samples that have Zr enrichment factors significantly below 1 are: barren hematite breccias, pyrite-rich ores, chalcopyrite-rich ores, bornite-chalcocite ores, magnetite breccias, hematite-quartz breccias and leached hematite breccias (see Figure 5.7). Hydrothermal rims of a mineral intermediate in composition between zircon and xenotime are observed around granitic zircons in samples of sericite-altered granite breccia (see Section 3.4.2). These provide mineralogical evidence to support the proposition of some Zr mobility in the hydrothermal fluids.

Yttrium. Y/TiO_2 ratios are highly variable over a wide range of total Fe values (Figure 5.11a) attesting to the mobility of Y during ore deposition at Olympic Dam. Most of the samples of Cu sulphide-bearing breccias have higher Y/TiO_2 ratios than the other breccias which indicates that Y enrichment may have accompanied introduction of Cu.

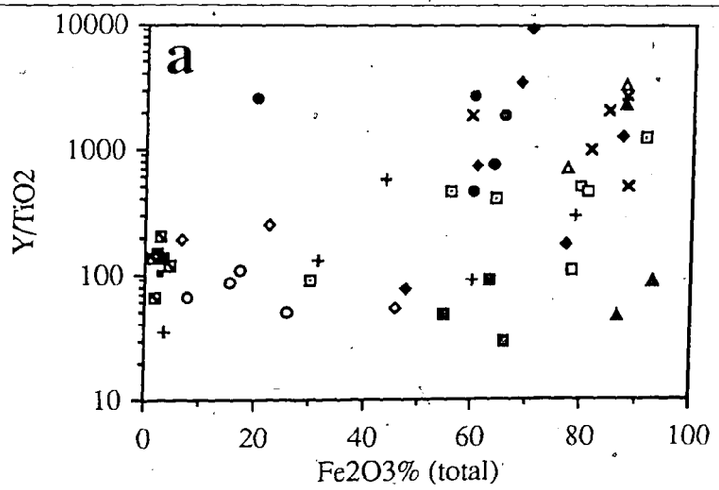

Figure 5.11a. caption overleaf.

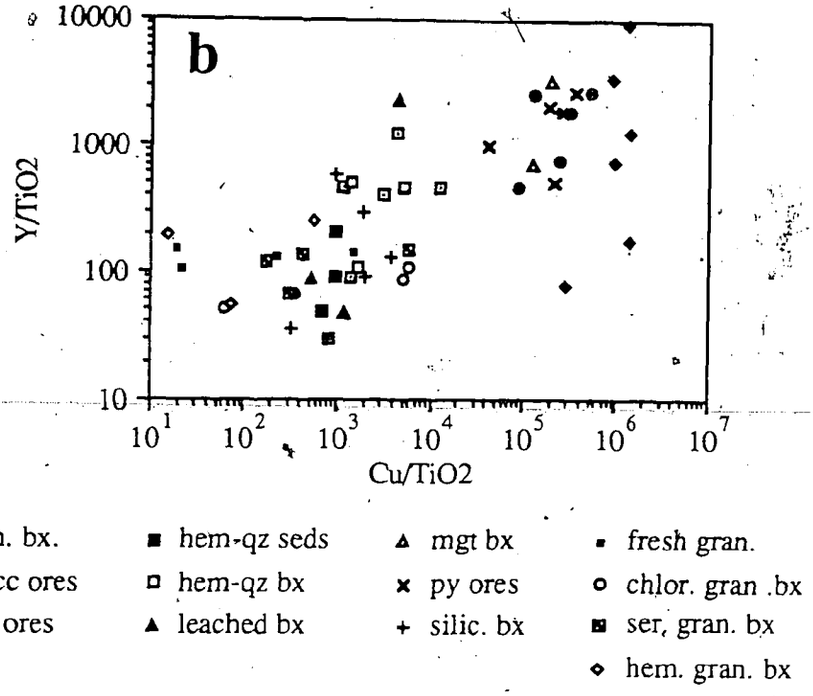

Figure 5.11 The degree of Y enrichment (Y/TiO_2) does not correlate with total iron (**a**) but does bear a scattered correlation with enrichment in Cu. (**b**). This suggests that Y and Cu were deposited by linked processes possibly from the same fluids.

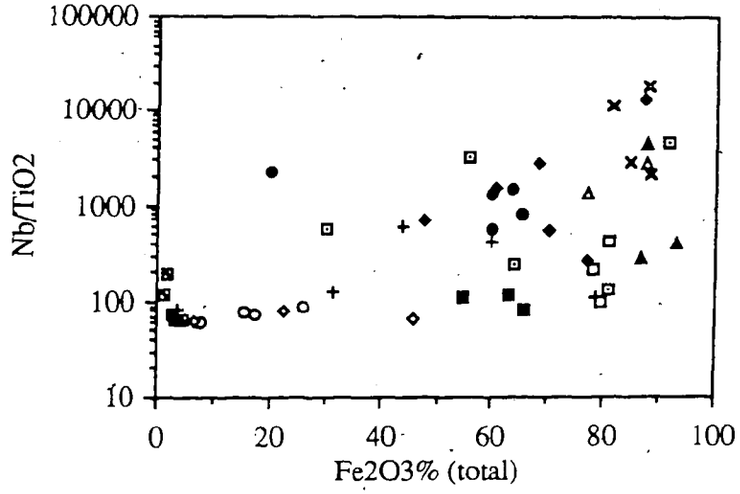

Figure 5.12 The scattered increase in Nb/TiO_2 with increasing total iron indicates that Nb has been introduced to the deposit during hydrothermal activity. The sulphide-bearing breccias have the highest Nb concentrations.

It is significant that Y/TiO_2 ratios do not simply covary with Fe content. This might suggest that three compositional components were involved in ore formation: i) the host granite (low Fe, low Y), ii) the high Fe component (low Y), and iii) a high Y (and Cu) component. The positive correlation displayed on a plot of Y/TiO_2 vs Cu/TiO_2 (Figure 5.11b) supports this interpretation.

Niobium. Fresh Roxby Downs Granite samples contain ~25 ppm Nb (SS-87, RX4523 and RX4524). The highest concentration recorded in this study is 1050 ppm in sample RX4513, a bornite-chalcocite ore from Mine Area DNW. This suggests that Nb was mobile during ore deposition. Further evidence for the same conclusion is provided by the scattered array of data on the plot of Nb/TiO_2 vs total Fe (Figure 5.12) and by the high Nb enrichment factors displayed in Figure 5.7. In a similar manner to the data for Y, the Nb/TiO_2 data indicate three components involved in ore genesis; i) a granitic component, ii) a high Fe-content component which has not introduced Nb, and iii) a distinct high Nb component. The highest Nb enrichments are apparent in the sulphide-bearing breccias (see Figures 5.7 and 5.12).

Lanthanum and Cerium. The introduction of REE during ore deposition is a well documented feature of the deposit (Roberts and Hudson, 1983; Oreskes and Einaudi, 1990; Reeve et al., 1990). Further documentation is provided by the scattered positive trend on a plot of La/TiO_2 vs total Fe (Figure 5.13a). None of the samples analysed in this study are depleted in La relative to the host granite (Figure 5.7). The degree of enrichment in La (as indicated by the La/TiO_2 ratio) is correlated with the degree of enrichment in Cr across the entire spectrum of breccia types (Figure 5.13b). This can be interpreted as suggesting that LREE and Cr were precipitated by linked mechanisms and may have been transported in the same fluid. It is consistent with the source of La and the other LREE having mafic or ultramafic affinities. Stronger evidence in favour of this suggestion is provided by the Nd isotopic systematics discussed in Chapter 7. The discussion of the relationships of La also applies to Ce because there is a linear correlation between La and Ce concentrations for the present sample suite.

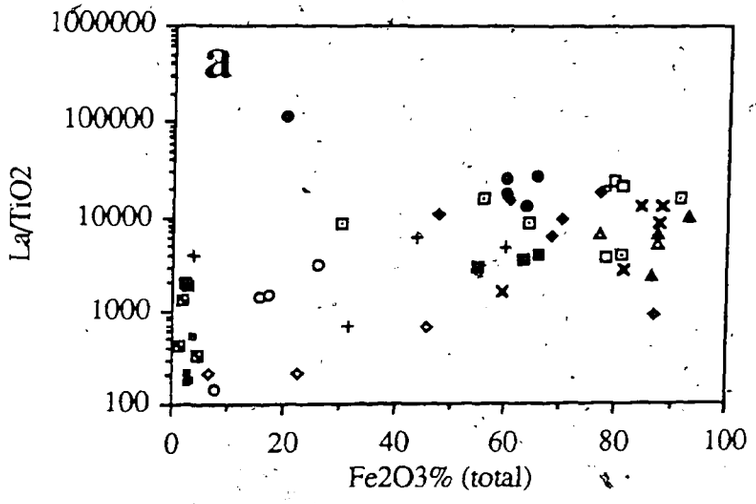

Figure 5.13a. caption overleaf.

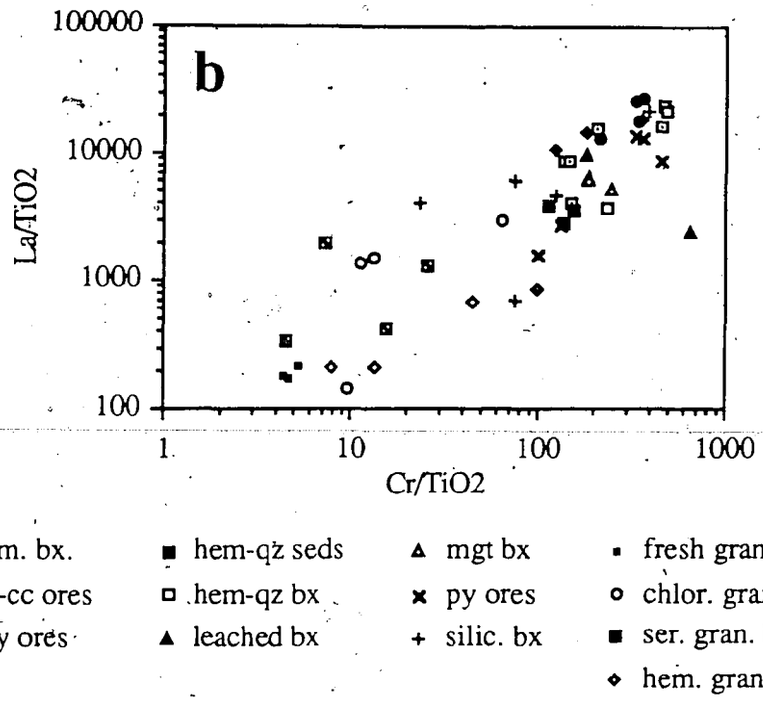

Figure 5.13 **a)** La enrichment increases with increasing total iron, an observation made previously by Oreskes and Einaudi (1990). **b)** The degree of enrichment of La and Cr are correlated, suggesting linked mechanisms of deposition, possibly from the same fluid.

Gallium. In silicate rocks gallium (Ga^{3+}) distribution is usually correlated with Al^{3+} and Ga is concentrated in aluminous phases such as feldspars, micas and amphiboles. However, for the Olympic Dam breccias, a plot of Ga/TiO_2 vs Al_2O_3/TiO_2 (Appendix 6) shows abundant scatter illustrating that Ga and Al_2O_3 have been geochemically decoupled. Ga has been strongly depleted in rocks which show evidence of hematite replacement of aluminous phases e.g. hematitised granite breccias and hematite-quartz breccias, and this feature is consistent with the behaviour of Al_2O_3. Many samples of the sulphide-bearing breccias show enrichments in Ga (Figure 5.7) suggesting that Ga may have been introduced with Cu mineralisation. This is consistent with a relative enrichment of Al_2O_3 observed in these samples (above).

Vanadium. There is a positive correlation between total Fe content and V/TiO_2 ratio (Figure 5.14a), demonstrating that V was introduced during the mineralisation process. The good correlation suggests that V and Fe may have been precipitated by linked mechanisms, possibly redox-controlled reactions. RX4533 (sericitised granite breccia) and RX4522 (hematitised granite breccia) are the only two samples which appear to have been depleted in V relative to the host granite (i.e. they have V enrichment factors significantly below 1; see Figure 5.7).

Chromium. Chromium has been introduced during the mineralisation events as the correlation between Cr/TiO_2 and total Fe (Figure 5.14b) illustrates. This correlation also suggests that Cr precipitation was controlled by redox reactions. Strong Cr enrichment (enrichment factors up to 125; see Figure 5.7) provides clear evidence for the involvement of rocks with mafic or ultramafic affinities in providing metals to the mineralising fluids. Nd isotopic evidence (Chapter 7) leads to the same conclusion.

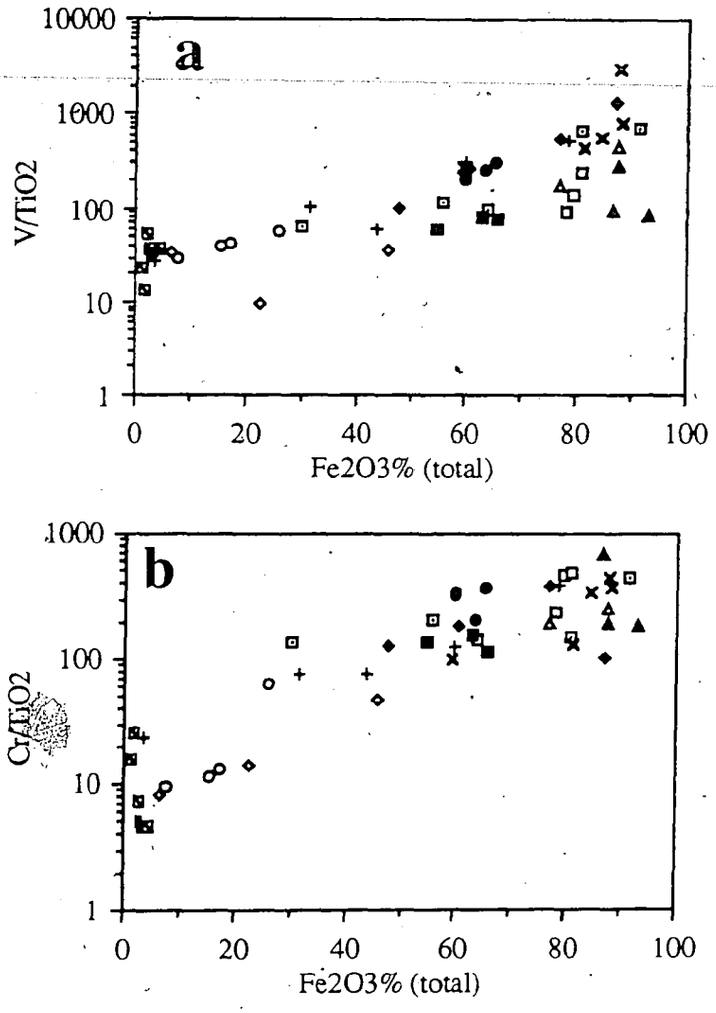

Figure 5.14 Enrichments in V (**a**) and Cr (**b**) are correlated with increasing Fe_2O_3 (total), suggesting that deposition of these elements may be controlled by redox conditions.

Nickel. Ni/TiO_2 ratios bear a scattered correlation with total Fe (Figure 5.15) indicating that Ni has been enriched in Olympic Dam mineralisation. This is consistent with other evidence for a mafic input to the mineralising fluids (Nd isotopes, Cr enrichment). Chloritised granite breccias show a strong enrichment in Ni compared with sericitised granite breccias (Figure 5.7). Considering the evidence from FeO enrichments (above) indicating that the chloritised breccias were altered by a relatively reduced fluid, it seems probable that Ni too was transported in a reduced fluid.

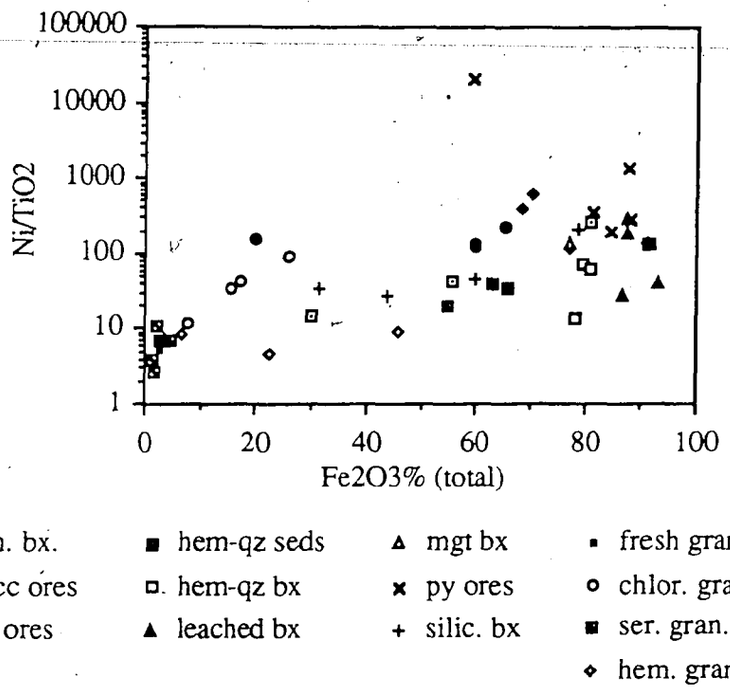

Figure 5.15 Ni/TiO_2 shows an overall increase with increasing Fe_2O_3 (total) indicating that Ni has been introduced to the deposit during hydrothermal activity.

Zinc The Zn/TiO_2 ratio of fresh Roxby Downs Granite is 50. Most of the breccias analysed have Zn/TiO_2 ratios greater than 100 (Appendix 6) illustrating that Zn has been introduced during the mineralising events. The Cu sulphide-bearing breccias have higher levels of Zn enrichment than most of the other samples. This may be due to the introduction of Zn in the same fluids as Cu, or it may be primarily controlled by the propensity of Zn to partition into sulphides. The chlorite-altered granite breccias are more enriched in Zn than the sericite- and hematite-altered granite breccias (Figure 5.7 a, b, c), providing further geochemical evidence of differences between the alteration styles.

5.7 Summary and discussion of major and trace element data

Titanium appears to have been the least mobile element during the hydrothermal processes which formed the deposit. On the basis of field relationships it is believed that

the volume of the deposit was originally occupied by the Roxby Downs Granite. It has therefore been assumed that all TiO_2 measured in most Olympic Dam breccias is granitic in origin and that other elements can be related to TiO_2 to determine their relative mobilities. Enrichment factors were calculated for all elements on this basis.

All of the other elements for which analyses are available appear to have been mobile during mineralisation. MgO and Th were remobilised but neither are enriched or depleted significantly in the spectrum of rock types analysed. The elements which appear to have been significantly depleted relative to the host granite are:

> SiO_2, FeO (largely oxidised to Fe_2O_3), CaO, Na_2O, K_2O, Al_2O_3 and Ga (from barren hematitic rocks), Rb, Zr (weakly), .

The elements which have been added to the volume of the deposit during ore deposition are:

> Fe, MnO, P_2O_5, CaO (to Cu ores and hematite-quartz breccias) Sr, Ba, Cu, U, Y, Nb, LREE, V, Cr, Ni, Al_2O_3 and Ga (to sulphide ores), and Zn.

The most conspicuous element addition is Fe, almost entirely present as hematite. Sm-Nd isotopic evidence (detailed in Chapter 7) indicates that the minor magnetite assemblages are probably cogenetic with the Roxby Downs Granite. Oxygen isotopic data (Oreskes and Einaudi, 1992) indicate that magnetite formed from relatively hot fluids (400°C) which were of deep, possibly magmatic origin. This evidence suggests that Fe was introduced in a hypogene, granite-related fluid. In view of the fact that Fe is only transported in solution as Fe^{2+} (Fein et al., 1992), this fluid must have been relatively reduced and had a high activity of chloride ion (Whitney et al., 1985; Fein et al., 1992). This indicates that one of the key mechanisms of metal precipitation at Olympic Dam was the oxidation of aqueous Fe^{2+}. Several of the elements introduced during mineralisation show enrichments which are well correlated with total Fe concentration, suggesting precipitation mechanisms closely linked with Fe e.g. redox reactions. These elements include Cr, V and Mn. The solubility of these elements is strongly affected by their oxidation state. Cr and V are more mobile in oxidised environments, whereas Mn is more readily transported as a reduced species (Wedepohl et al., 1969). This implies that Mn may have been transported in the same fluids as Fe, whereas Cr and V were probably introduced in an oxidised fluid. Cr has limited mobility in the 3+ oxidation state but is readily soluble as Cr^{6+} (Wedepohl et al., 1969). The most likely sources of Cr in the breccias are the mafic/ ultramafic dykes within the breccia complex, or their extrusive equivalents. These have Cr contents up to 2500 ppm, with Cr now predominantly present in spinels (Chapter 6). Their more evolved variants may have contained Cr-diopside. Both Cr phases contain trivalent rather than hexavalent Cr. Although it is possible that conditions were sufficiently oxidised to convert Cr^{3+} to Cr^{6+} and thereby

enhance Cr mobility, with the source rock Cr levels so high, it may also be possible to transport a relatively small proportion of Cr into the deposit, even with the relatively low solubility of Cr^{3+}.

In contrast with those discussed above, several of the elements added during ore deposition show enrichments do not correlate with total Fe, which suggests that their mechanisms of deposition are not closely linked with the precipitation of Fe. These elements include the main ore metals Cu and U, and La (LREE), Nb, Y, and Ba. This provides further evidence for the input of more than one fluid in ore formation. The critical point in deciding if this represents evidence to support the "two-fluids" model of ore genesis proposed by Haynes et al. (submitted) is whether there are any temporal differences for the input of the separate fluids. If all metal introduction was synchronous then the "two-fluids" model would seem very appealing. The issue of timing of introduction of ore components has been addressed by the use of radiogenic isotopes and is discussed in Chapter 7.

The association of elements apparently transported in a separate fluid from Fe (Cr, V, Nb, LREE, Y, Ba, U) suggests input from mafic-ultramafic source rocks with alkaline petrological affinities.

5.8 Rare Earth Element geochemistry

5.8.1 Introduction

The Olympic Dam deposit is strongly enriched in the REE, particularly the light REE (LREE). La and Ce abundances of ~2000ppm and ~3000ppm are common for mineralised breccias, and the zone of hematite-quartz breccias in the centre of the breccia complex generally contains higher concentrations of LREE than the surrounding hematitic breccias (La and Ce mine assay data). This suggests a deposit-scale REE zonation with the highest concentrations in what Reeve et al. (1990) interpreted as the focus of hydrothermal activity in the deposit. Oreskes and Einaudi (1990) provided a detailed study of the REE mineralogy and geochemistry for a selection of Olympic Dam breccia types. They observed five hydrothermal REE phases: bastnaesite [(Ce, La) $CO_3(F,OH)$], florencite [Ce, $Al_3(PO_4)_2(OH)_6$], monazite (Ce, La, Th)PO_4, xenotime YPO_4, and a U-Y-Si-P phase, possibly a britholite series mineral. The rock types examined by these workers do not include comparisons of the various ore types. They discussed REE distributions in: fresh Roxby Downs Granite, weakly, moderately and strongly sericite altered granite, granite crackle breccias, strongly hematitised granite, heterolithic breccias with a range of proportions of hematite and granite clasts, hematite breccias, hematite-quartz breccias, baritic sediments, and quartz-sericite veins. Their study revealed that total REE abundances and degree of LREE enrichment increased with intensity of sericite alteration of the granite, but more importantly with the proportion of

hematite in the breccias. It was found that the mode of hematite introduction, whether by formation of breccia matrix or by replacement of granitic feldspar, did not control REE distribution. Not all hematitic breccias are equally enriched. Oreskes and Einaudi (1990) concluded that REE concentrations appear to be a function of the degree of Fe metasomatism and proximity to the geographic centre of the breccia complex. REE introduction is accompanied by a reversal in europium anomaly from negative in pristine granite to weakly positive in altered granite and hematitic breccias. They also observed that LREE enrichment increases (higher La/Lu ratio) with total REE.

Thirty two samples of Olympic Dam ores and breccias have been analysed for REE by the Neutron Activation technique in the present study. There is some overlap with the data of Oreskes and Einaudi (1990) particularly with samples of unmineralised granitic, heterolithic and hematitic breccias. However, the comparisons between the various ore types provide new insights into the processes of REE mobility at Olympic Dam.

5.8.2 Ore samples

5.8.2.1 Magnetite-rich breccias

Figure 5.16A is a plot of the REE patterns of two magnetite-rich breccias from Olympic Dam (RX4536 and RX4537) and one from the Acropolis prospect, ~25 km southwest of Olympic Dam (RX4577A). RX4536, a sample of magnetite-siderite-pyrite breccia with significant hematite and chalcopyrite replacement, has a La concentration of ~700X chondrite, and a LREE enriched pattern (La/Lu = 110) which has a consistent decreasing slope from LREE to HREE (except for the negative Eu anomaly), suggesting coherent geochemical behaviour for the whole REE spectrum. The pattern for this sample is very similar to the magnetite ore from the Acropolis prospect (RX4577A), a sample consisting of 77% magnetite, 15% hematite, 5% apatite, lesser quartz and chlorite, and trace chalcopyrite. It is possible that the partially replaced magnetite breccias at Olympic Dam are altered equivalents of the Acropolis-style magnetite-rich mineralisation. RX4537 is a sample of Olympic Dam magnetite-rich breccia which shows considerably more hematite replacement of magnetite, and chalcopyrite replacement of pyrite than is present in RX4536. It is therefore interesting to note the higher LREE content of RX4537 compared to RX4536 (Figure 5.16A). It appears that the replacement of magnetite+pyrite by hematite+chalcopyrite was accompanied by enrichment in LREE.

5.8.2.2 Pyrite and chalcopyrite-rich ores

Figure 5.16B shows that pyrite-rich hematitic ores have LREE enriched patterns with La increasing from ~700X to ~3000X chondrite, and La/Lu increasing from ~100 to ~1300 concomitant with a progressive increase in the amount of chalcopyrite replacement of pyrite (cf. Appendix 4; petrographic descriptions). In contrast to the magnetite ores, the

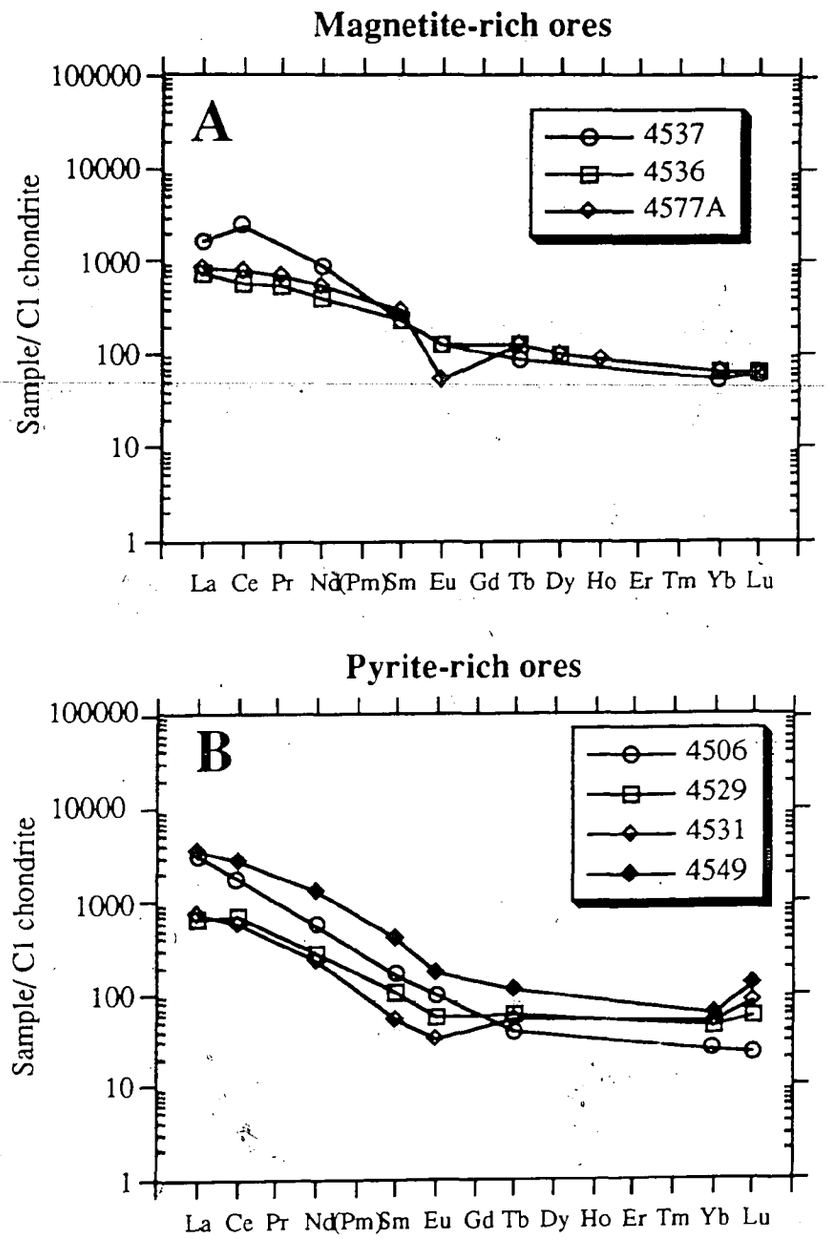

Figure 5.16. Chondrite-normalised REE diagrams of Olympic Dam lithologies. Normalising values of Sun and McDonough (1989).

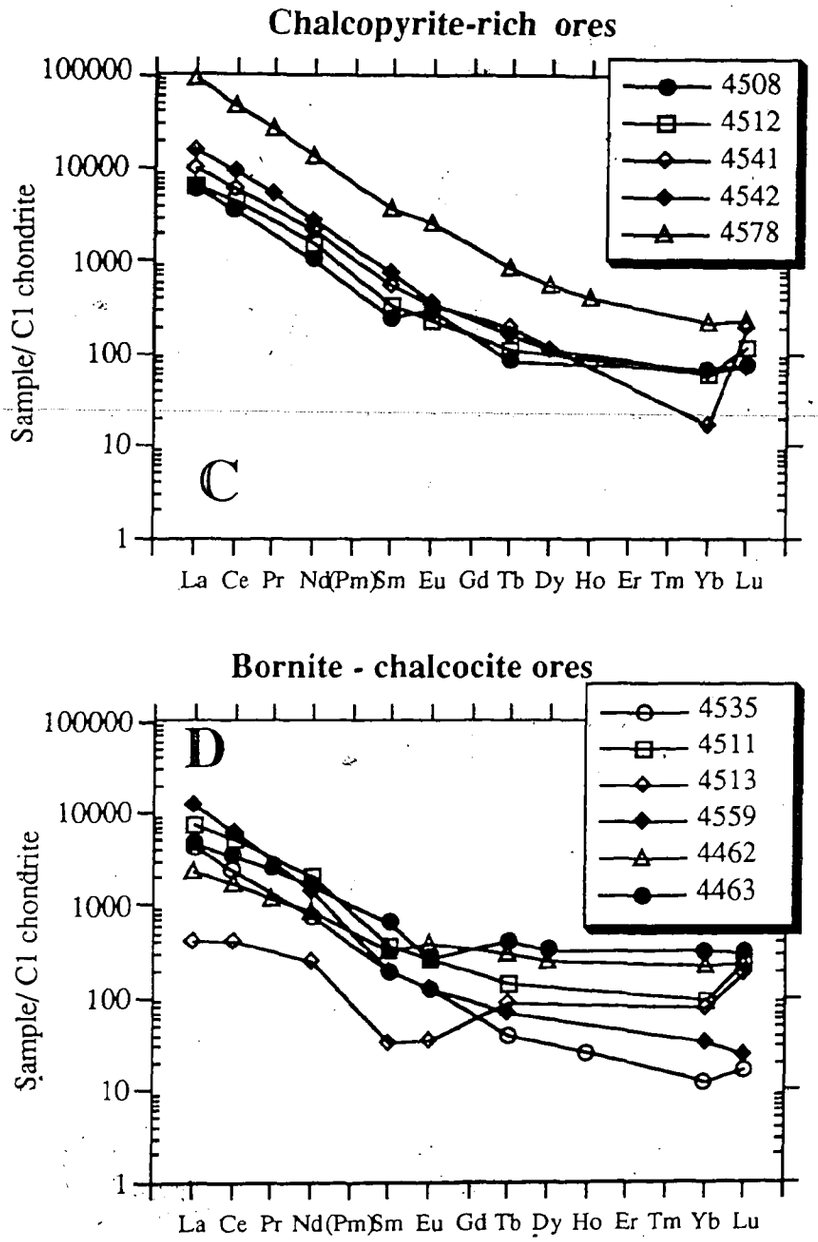

Figure 5.16 continued. Chondrite-normalised REE diagrams of Olympic Dam lithologies. Normalising values of Sun and McDonough (1989).

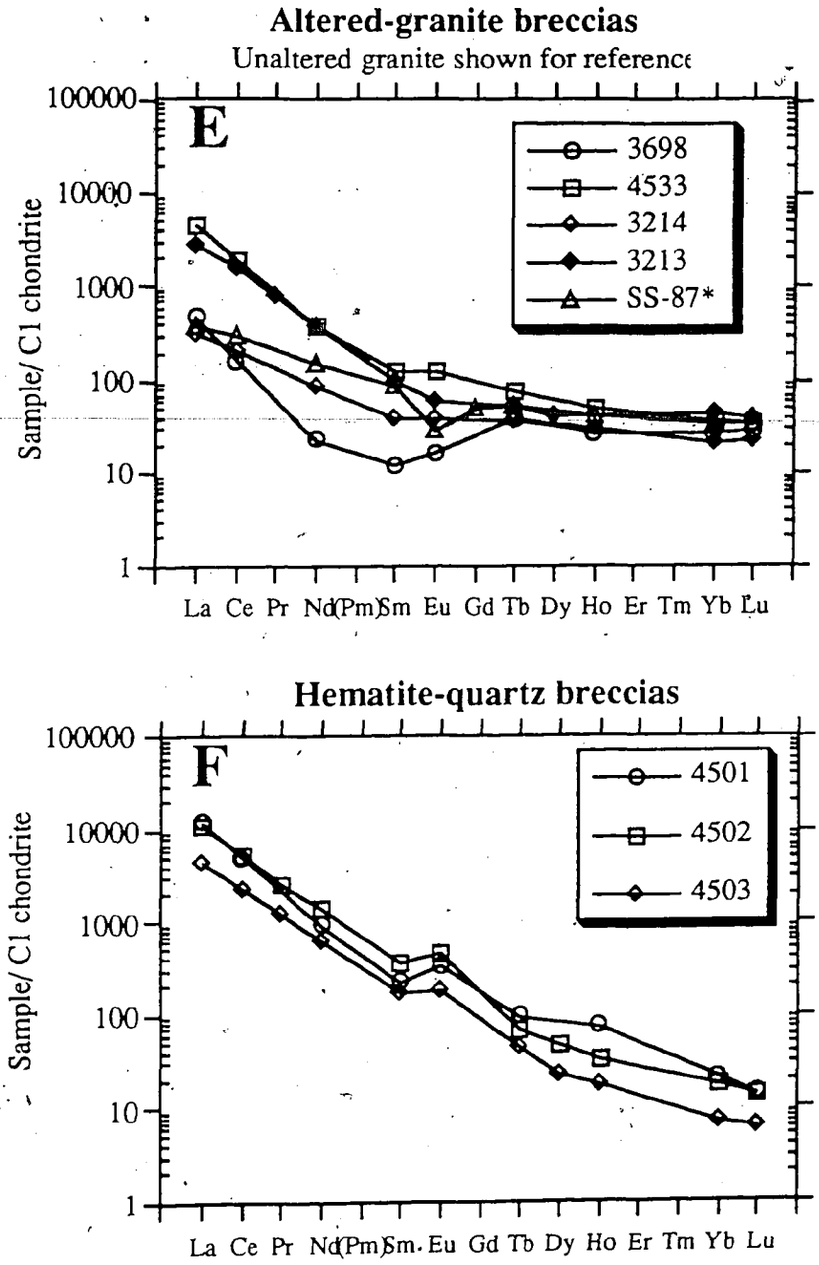

Figure 5.16 continued. Chondrite-normalised REE diagrams of Olympic Dam lithologies. Normalising values of Sun and McDonough (1989).

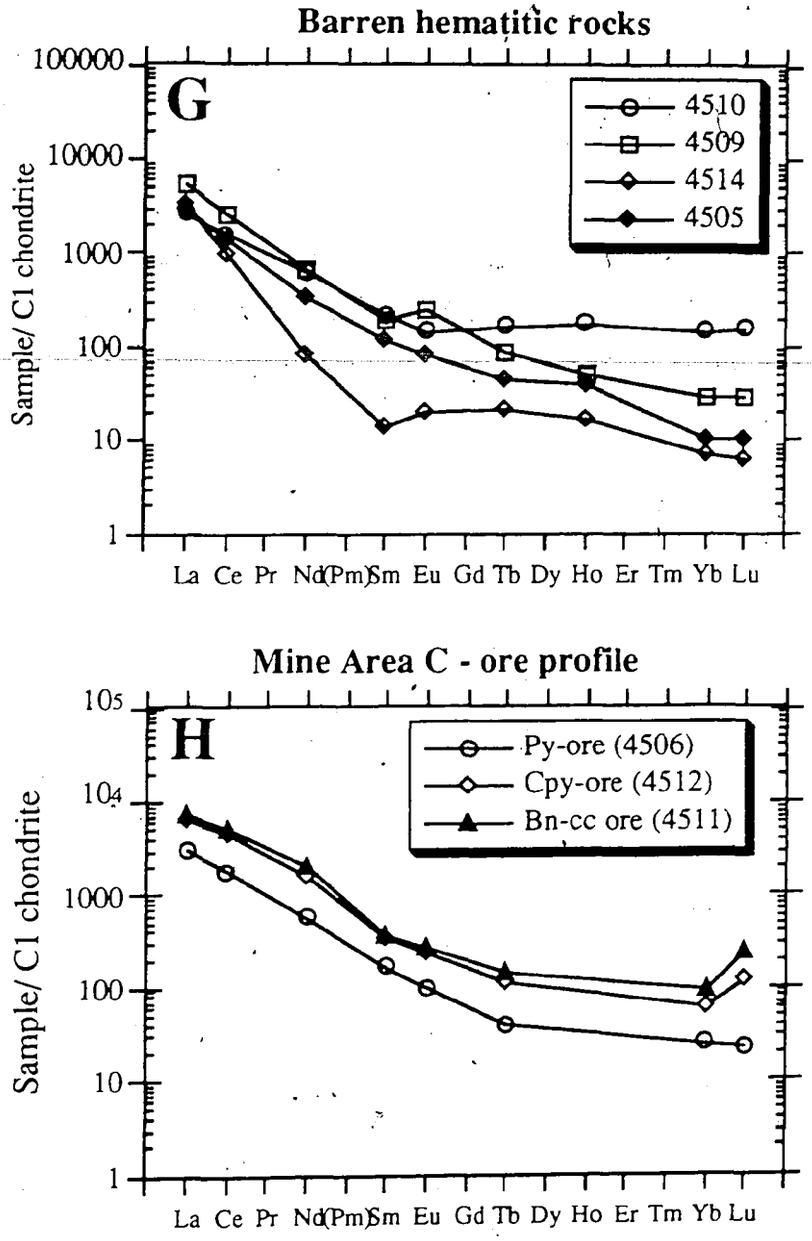

Figure 5.16 continued. Chondrite-normalised REE diagrams of Olympic Dam lithologies. Normalising values of Sun and McDonough (1989).

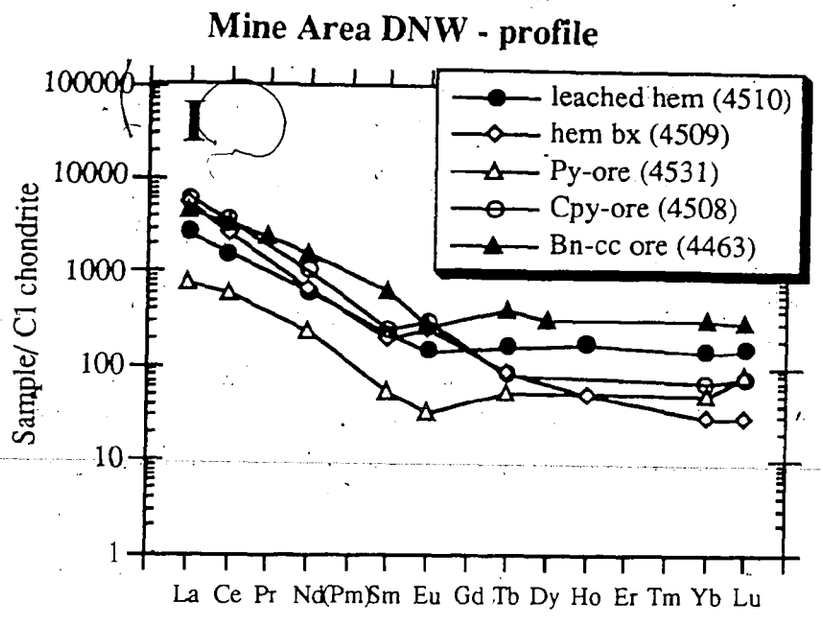

Figure 5.16 continued. Chondrite-normalised REE diagrams of Olympic Dam lithologies. Figures 5.16 H and I represent sampling traverses across the bornite-chalcopyrite interface. Sample localities for I are shown on cross section in Figure 5.18. Normalising values of Sun and McDonough (1989).

REE patterns for these samples have a marked change in gradient towards higher levels of HREE enrichment than would be expected from the steep patterns in the LREE. This suggests that the patterns plotted are the result of superimposing one pattern on another, and this may relate to the replacement of a magnetite-rich by a hematite-rich assemblage. Petrographic observations of sample RX4529 and RX4531 show that the hematite contains very fine-grained inclusions of magnetite suggesting that hematite has replaced magnetite in these samples. RX4529 and RX4530 also contain abundant siderite, a mineral common in the magnetite breccias described above. It is interesting to note that the flat HREE part of the pattern for the pyrite-rich ores (Figure 5.16B) is subparallel to the pattern observed for magnetite-rich breccias (cf.Figure 5.16A). The significance of the inflexions in the REE patterns is discussed further in Section 5.9.1.

In those ore samples where chalcopyrite is the dominant sulphide (Figure 5.16C) the patterns are even more strongly LREE enriched with La values ranging from 5800X to 15500X chondrite, and with a single extreme sample (RX4578) recording the highest REE concentration yet observed at Olympic Dam (La = ~91000X chondrite). With the exception of RX4578, the REE patterns for the chalcopyrite-rich ores also show an inflexion towards flat HREE patterns with abundances of Yb of ~70X chondritic values, again similar to the magnetite breccias. It is apparent from Figures 5.16A, B and C that LREE-rich minerals were precipitated in greater abundance as chalcopyrite replaced pyrite and as hematite replaced magnetite. Figure 5.17 illustrates the correlation between the concentrations of the LREE and Cu for pyrite and chalcopyrite-rich ores. From the REE

patterns, Figure 5.17, and the paragenetic relationships described earlier, it appears likely that Cu and LREE were deposited in higher concentrations relatively late and that they were introduced by linked processes, possibly in the same fluid.

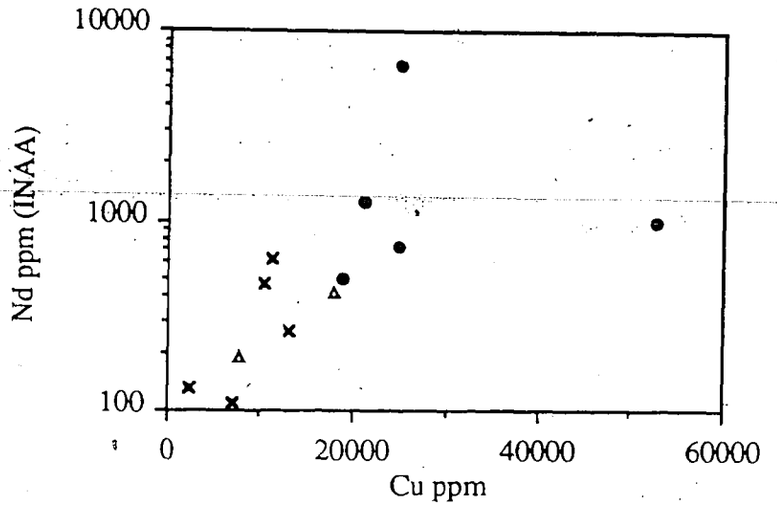

Figure 5.17 Correlation between Nd (and other LREE) and Cu concomitant with chalcopyrite replacement of pyrite. (Pyritic ores = crosses, chalcopyrite ores = dots, magnetite breccias = triangles).

5.8.2.3 Bornite-chalcocite ores

Figure 5.16D shows the REE patterns for the ores which contain bornite, chalcocite or a combination of the two, as the dominant sulphide species. As mentioned in 5.2.3, these ores have been variously interpreted as of primary and supergene (secondary) origin. Without exception, the REE patterns displayed in Figure 5.16D show evidence of being the product of two (or more) superimposed REE signatures. All except RX4513 show the strong LREE enrichment typical of the pyrite-rich and chalcopyrite-rich hematitic ores, and to varying degrees they all show an inflexion toward a flatter, more enriched HREE pattern than is consistent with their respective LREE patterns. There is considerable variation in the HREE concentrations, which range from chondrite normalised values of ~10-30, to ~300. Some of the concentrations of HREE are considerably higher than those observed in the pyrite-rich and chalcopyrite rich ores. REE patterns for samples taken in traverses across the bornite-chalcopyrite interface suggest that there is a systematic increase in HREE concentrations from chalcopyrite ores to bornite-chalcocite ores (Figures 5.16H and I; cf. cross section, Figure 5.18). Interpretations of this enrichment are discussed in Section 5.9.

Figure 5.18 (overleaf) Cross section 586 (marked as A-B on mine-scale plan, Figure 2.1) from Mine Area DNW. Note the location of samples for which REE patterns are compared in Figure 5.16 I.

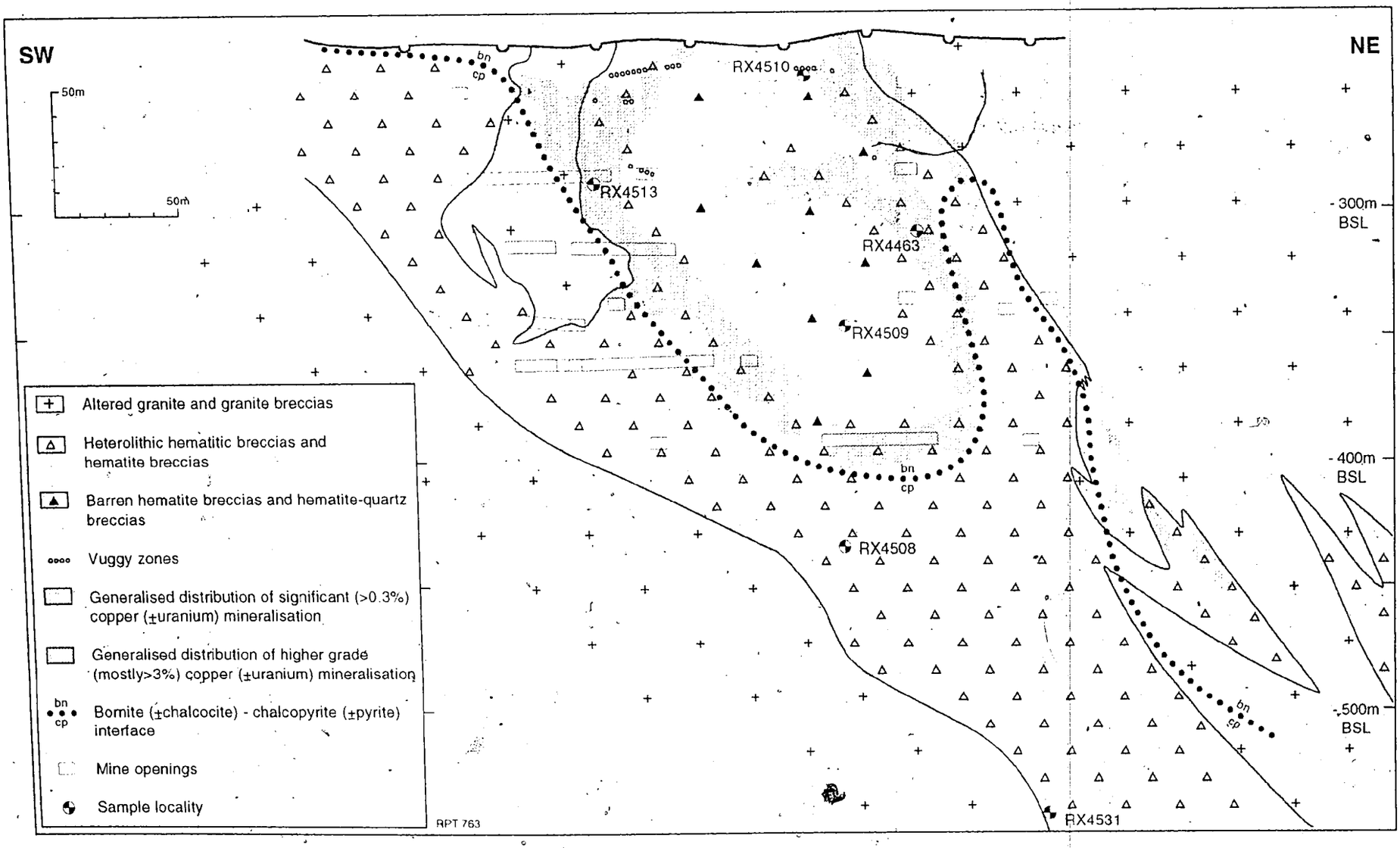
SW
NE
50m
50m
RX4510
RX4513
RX4463
RX4509
RX4508
RX4531
bn
cp
- 300m BSL
- 400m BSL
- 500m BSL
Altered granite and granite breccias
Heterolithic hematitic breccias and hematite breccias
Barren hematite breccias and hematite-quartz breccias
Vuggy zones
Generalised distribution of significant (>0.3%) copper (±uranium) mineralisation
Generalised distribution of higher grade (mostly>3%) copper (±uranium) mineralisation
Bornite (±chalcocite) - chalcopyrite (±pyrite) interface
Mine openings
Sample locality
RPT 763

RX4513 is depleted in LREE relative to any of the other hematite-rich or magnetite-rich breccias analysed. It also has an erratic LREE pattern. This sample has an εNd signature similar to those of the most altered mafic/ultramafic dykes analysed (Section 7.3.2.1 and 7.4.2) which suggests that it may represent a replaced portion of one of the dykes. Although the Ni and Cr concentrations of RX4513 do not support this hypothesis, its elevated V content (101 ppm) is matched only by the dykes (Appendix 2). The concave downward pattern of the LREE in RX4513 is also very similar to the LREE in the least altered dyke sample, RX4548 (Figure 6.13).

5.8.3 Altered granite

Oreskes and Einaudi (1990) observed that as the host granite is progressively sericitised, it becomes more enriched in LREE and loses the negative Eu anomaly found in pristine granite. From this they concluded that the REE were introduced from outside the volume of altered granite, implying that the granite was not the source of the mineralising fluids. Figure 5.16E shows the REE patterns of fresh granite, sericitised granite and chloritised granite samples from the present study. The latter alteration style was not investigated by Oreskes and Einaudi (1990). The two samples of intensely sericitised granite breccia (RX3698 and RX4533, a gold ore) have markedly different patterns (Figure 5.16E). RX4533 has strong LREE enrichment and a slight positive Eu anomaly compared to the fresh granite (SS-87; data of Creaser, 1989), whereas RX3698 is depleted in LREE relative to fresh granite. Similarly, the two samples of chloritised granite show both LREE enrichment (RX3213) and depletion (RX3214) relative to the fresh granite. All samples show HREE patterns sub-parallel to that of the fresh granite, which suggests the HREE have not been mobile during alteration. The small variations in the concentrations of HREE may be primary or may reflect volume changes of the granite during alteration. The variable LREE patterns within the chlorite and sericite alteration categories suggest that generalisations about consistently increasing LREE with alteration (Oreskes and Einaudi, 1990) may be somewhat simplistic.

5.8.4 Unmineralised hematitic breccias and sediments

5.8.4.1 Hematite-quartz breccias

The hematite-quartz breccias in the geographic centre of the breccia complex have been described as having higher LREE concentrations than other hematitic breccias in the deposit (Oreskes and Einaudi, 1990; Reeve et al., 1990). Figure 5.16F shows REE patterns for three samples of hematite-quartz breccias from this study (RX4501, RX4502, RX4503) and these are consistent with the observations of Oreskes and Einaudi (1990), having La concentrations of ~10000X chondrite, positive Eu anomalies

and very high La/Lu ratios (7000). The HREE concentrations are markedly lower than in the magnetite-rich breccias or hematitic ores discussed above.

RX4503 is a sample of strongly silicified hematite-quartz breccia. Quartz occurs interstitial to, and possibly replacing some hematite. The REE pattern is parallel to, but somewhat below, RX4501 and RX4502 suggesting that the introduction of silica into the rock has simply diluted the REE concentration. The absence of any change in the REE trend resultant from silicification suggests that the fluids causing this alteration did not introduce REE, and may be interpreted as an indication that silicification is not related to the principal ore forming fluids.

5.8.4.2 Hematitic breccias and sedimentary rocks

The REE patterns for four hematitic rock units which lack significant economic mineralisation are shown in Figure 5.16G. RX4510, a sample of leached hematitic breccia from Mine Area DNW shows a LREE-enriched pattern but has a very marked inflexion towards high HREE concentrations. This sample is from ~10m below the unconformity, above the bornite-chalcocite ore zone from which RX4513 and RX4463 were taken. It shares the strong HREE enrichment evident in the latter samples, but missing from the underlying pyrite and chalcopyrite ores (cf. ore profile Figure 5.18, Figure 5.16I). This suggests that the observed HREE-enrichment is a feature genetically associated with stratigraphic position. It may be related to the event which caused the leaching in RX4510. However, it might also reflect a coeval but distinct, stratigraphically higher geochemical domain than that in which chalcopyrite ores were deposited.

RX4509 is a barren heterolithic breccia from Mine Area DNW from the same mine cross-section (586-00; Figure 5.18) as RX4510. It shows a steep LREE enriched pattern, a positive Eu anomaly, and a slight inflexion towards higher HREE. Although this sample is also from above the bornite-chalcocite ore zone, it does not show the same leached texture (vuggy hematite, oxidised sulphides), or strong HREE enrichment as RX4510.

RX4505 (Figure 5.16G) is a sample of strongly silicified heterolithic breccia and it has a REE pattern similar to those of the hematite-quartz breccias (cf. Figure 5.16F). RX4514 is a sample of laminated hematite-quartz sandstone. It contains both clastic hematite and finely bladed interstitial hematite, and its finely laminated texture attests to deposition in a relatively quiescent environment. These characteristics have led to the interpretation that this rock unit was deposited in a lacustrine environment in the crater zone of the venting hydrothermal system. Its REE pattern is very different to any yet recorded at Olympic Dam. It is very steep for the LREE and has a convex upward shape for the HREE. A plausible explanation for this pattern is that it was originally similar to the host granite

pattern, underwent a depletion in LREE, and was subsequently exposed to an extremely fractionated (LREE-enriched) fluid.

5.9 Discussion

5.9.1 Two fluids involved in ore genesis: REE evidence

The paragenetic relationships described Section 5.2 provide petrographic evidence that the magnetite-siderite-pyrite assemblage may have been a precursor to hematite-chalcopyrite and hematite-bornite-chalcocite assemblages for many of the ores and breccias. REE patterns for relatively unhematitised magnetite-rich breccias show consistent slopes from LREE to HREE, indicative of formation by a single process or from a single fluid. Samples which have remnant magnetite inclusions within hematite have inflexions in their patterns, with LREE enrichments, but HREE patterns too enriched to be consistent with the slope of the LREE. The HREE patterns are similar to those observed for magnetite-dominant breccias. These inflexions are interpreted to result from the superimposition of two REE patterns.

This superimposition of REE patterns presumably relates to the observed hematite+chalcopyrite replacement of magnetite+pyrite, and it could be produced in several ways. If one assumes that the REE patterns of the whole-rock samples reflect the relative proportions of the REE in hydrothermal fluids (see below for converse case), then the inflected patterns provide evidence for the involvement of two fluids with different REE patterns. Considering the paragenetic relationships, the fluid richer in HREE would be that responsible for magnetite precipitation, and the fluid enriched in LREE would be the more oxidised, precipitating hematite and chalcopyrite. The relatively late precipitation of hematite and chalcopyrite may result from a significant temporal difference in the activity of the two hydrothermal solutions, but could also result from the early dominance of a reduced fluid and late dominance of an oxidised fluid in a two-fluid mixing regime.

It is important to note that it may not be valid to assume that the REE patterns of the rocks reflect the relative proportions of REE in the hydrothermal solutions. There is a strong possibility that precipitation-controlled REE fractionation occurred, governed by the crystallographic properties of the minerals deposited. If this is the case, the inflected REE patterns may simply result from the presence of two distinct REE phases; one enriched in LREE, the other relatively enriched in HREE. Considering the paragenetic relationships, the implication is that the conditions under which hematite and chalcopyrite were deposited stabilised the precipitation of a relatively LREE-enriched phase which had not been precipitated under magnetite-stable conditions, and only a relatively HREE-enriched phase was precipitated under magnetite-stable conditions. The change in

conditions of mineral precipitation from reduced to relatively oxidised presumably relates to the sequential dominance of distinct fluids.

In either of the interpretations above, the inflexions in the REE patterns may reflect the involvement of two fluids in ore genesis. To test which interpretation is the more likely it would be necessary to conduct a detailed study of the variations in REE mineralogy and mineral-chemistry in the different oxide + sulphide assemblages. This would determine whether or not the inflexions in REE patterns are manifestations of the presence of two distinct REE phases. Such a study of REE mineralogy is beyond the scope of this project owing to the relatively late stage in the project at which the whole-rock REE data were acquired.

Many samples of other hematitic breccia types also show LREE enrichments, inflexions in the middle REE, and flat HREE patterns similar to those of the magnetite breccias. This again provides evidence of two superimposed REE patterns, even though there is no visible evidence of remnant magnetite. For the same reasons as discussed above, the inflexions in the REE patterns are therefore regarded as evidence of the involvement of two fluids in ore deposition.

5.9.2. Alternative hypotheses for involvement of two fluids

The involvement of two fluids in the genesis of hematite-chalcopyrite ores at Olympic Dam implies one of the following two general models:

A) That there were two separate hydrothermal events, one which produced the magnetite-siderite-pyrite assemblage, and a later event which oxidised the magnetite to form hematite, and introduced Cu, U and LREE.

B) That the magnetite-rich and hematite-rich assemblages formed in essentially the same event from the mixing of two fluids, one reduced and one relatively oxidised. In this model the paragenetic relationships and degree of replacement observed would be functions of the changing ratios of the two fluids in a variable mixing regime.

It is interesting to consider the REE systematics of the bornite-chalcocite ores in this regard because these require a choice between similar competing models. In Section 5.8.2 (Figures 5.16 A to D) it was established that the bornite-chalcocite ores are more strongly enriched in HREE than the other ore types analysed. The HREE enrichment of the bornite-chalcocite ores relative to chalcopyrite-rich ores can be interpreted in two ways:

1) Bornite-chalcocite ores are secondary and formed by the modification of a pre-existing chalcopyrite-rich ore by a HREE-enriched fluid.

2) HREE enrichment relates to the enhanced precipitation of a HREE-enriched phase in the bornite-stable field of a hydrothermal system where bornite-chalcocite ores and chalcopyrite ores were deposited contemporaneously (i.e. both primary ore types). In this model the two ore types reflect different sets of physicochemical conditions and the sulphide interface represents a geochemical front.

Option 1) may equate to the model of supergene weathering and enrichment origin for the bornite-chalcocite ores proposed by Oreskes and Einaudi (1990). In this model, the bornite-chalcocite ores form as a "blanket" by the downward incursion of oxidised low temperature groundwaters which leached metals from chalcopyrite-rich ores and reprecipitated them at the redox front at the base of their penetration. The presence of clasts of bornite and/or chalcocite and of bornite-chalcocite ore in the breccias is inconsistent with this model. These indicate that bornite and chalcocite were being precipitated during formation of the breccia complex rather than in a weathering environment well after primary Cu-mineralisation. Option 2) above is therefore a more likely explanation of the HREE enrichment in the bornite-chalcocite ores.

Option 2) is directly analogous to model B) presented above for the LREE-enrichment of hematite-chalcopyrite ores relative to magnetite-pyrite ores. The genesis of all three sulphide ore types, and their REE systematics, can be explained by a model wherein they represent coeval precipitation due to the mixing in different proportions of two fluids. In other words, a single mixing event could have generated all of the principal ore assemblages observed in any given breccia body. This is the model proposed by Haynes et al. (submitted) on the basis of geochemical modelling. The alternative to this is a two-, or possibly three-stage model in which a primary magnetite-pyrite producing event is overprinted by a second event producing a hematite-chalcopyrite assemblage; the bornite-chalcocite-rich assemblage may have been coeval with the hematite-chalcopyrite assemblage or may represent a third overprinting event. In this scenario, all three mineralisation types may still represent different stages of the same overall (regional scale) thermal event. The errors associated with the zircon ages determined in Chapter 3 allow as much as ~8 million years for temporally distinct stages of mineralisation to develop (1588 ± 4 Ma for the host granite; 1592 ± 8 Ma for RX3222, the most precise minimum age constraint).

The chronological relationship of the deposit with the Gawler Range Volcanic event and the interpreted subvolcanic setting for mineralisation permit the two-fluids model as proposed by Haynes et al. (submitted). There is abundant field evidence for multiple episodes of brecciation affecting various parts of the breccia complex, e.g. breccias containing clasts consisting of pre-existing breccias. This attests to a variable and

dynamic fluid mixing regime where the hypogene fluid involved in the brecciation meets meteoric waters. The zone of mixing and the proportions of reduced to oxidised fluid could therefore have undergone considerable variation at any given locality as hypogene pulses waxed and waned through time. This provides a plausible means by which to create the sulphide zonation pattern, its convolute morphology, and the paragenetic and REE geochemical relationships observed. However, it must also be recognised that the chronological and geological relationships (above) also allow the possibility of temporally distinct fluids that are manifestations of the same regional thermal event.

5.9.3 Relationship between hematite-quartz breccias and bornite - chalcocite ores: Evidence from zone morphology, REE and other elements

In the centre of the breccia complex the bornite-chalcopyrite interface descends steeply, mimicking the margin of the central hematite-quartz breccia zone (Figure 2.3). This zone has steep margins and although its deepest limit is beyond the levels of current drilling, higher in the deposit its lower boundary has been observed to overly more typical heterolithic breccias. The hematite-quartz breccias are enriched in barite ($BaSO_4$) relative to the rest of the deposit.

The modelling of Haynes et al. (submitted) suggests that the hematite-quartz breccias are the product of the extreme oxidation of hematitic breccias by the relatively late downward incursion of meteoric fluids in the waning stages of the hydrothermal system. The morphology of the central hematite-quartz breccia zone, the virtual absence from it of any silicates other than relict granitic and hydrothermal quartz, and the high concentration of barite, are consistent with an origin due to leaching during the descent of a sulphate-rich fluid. The implication of this interpretation is that the zone now observed in the centre of the breccia complex, truncated above by the unconformity, is effectively a remnant pendant which may be the lowest projection of a previously more laterally extensive zone of hematite-quartz rock types which once overlay much of the deposit. The fact that the bornite-chalcopyrite interface mimics the shape of the present hematite-quartz breccia zone implies that it formed by related processes. It is therefore important to note the complementarity of HREE in the hematite-quartz breccias (low HREE) and the bornite-chalcocite ores (high HREE).

If the supergene enrichment model of Oreskes and Einaudi (1990) is correct, the hematite-quartz breccias would probably represent a zone of weathering in which metals were leached from primary chalcopyrite-rich ores, to be reprecipitated below as bornite-chalcocite ore zones. The low levels in the hematite-quartz breccias of relatively less mobile elements such as Zr and Th, and of the HREE, are consistent with strongly corrosive leaching. If the "two-fluids" model of Haynes et al. (submitted) is correct and the hematite-quartz breccias represent a zone of leaching due to inundation of the meteoric

fluid following downward retreat of a more reduced hypogene fluid. It is inherent in this model that the bornite-chalcocite ore below the hematite-quartz zone represents remobilisation of metals during the late stages of, and as a consequence of, primary mineralisation events. In this scenario, the low levels of HREE and Zr and Th again relate to their enhanced mobility in what would be the depositional environment most dominated by meteoric fluids.

As discussed in Chapter 3, the hematite-quartz breccias are intruded by several diatremes. Both of the above models for the genesis of the hematite-quartz breccias have the same important implication for the date determined on the diatreme tuff (Chapter 3). Both models imply that the bornite-chalcocite ores below the hematite-quartz breccias formed by the same processes as the hematite-quartz breccias. The date determined for diatreme activity (1598 ± 7 Ma) is a minimum age for formation of the hematite-quartz breccias and therefore represents a minimum age for formation of the bornite chalcocite ores. This cannot be reconciled with the supergene model as proposed by Oreskes and Einaudi (1990) who postulated an origin of bornite-chalcocite ores at an age considerably younger than 1400 Ma. If the supergene weathering processes invoked by Oreskes and Einaudi are responsible for formation of these ores, these events occurred shortly after 1590 Ma.

5.9.4 Reversal of Eu anomaly

Introduction of REE to Olympic Dam breccias has affected Eu markedly, relative to the other REE. The negative Eu anomaly observed in fresh Roxby Downs Granite is lessened with alteration of the granite, and a positive Eu anomaly is evident in some of the more hematite-rich breccias and ores. The positive anomaly observed provides a possible insight into the source of the REE for the deposit. In general, REE ions of higher charge form more stable complexes and are preferentially taken into aqueous solution (Bau, 1991). This implies that if Eu is present in the source rock as Eu^{2+} rather than Eu^{3+}, the fluid will tend to develop a negative Eu anomaly relative to the source. If divalent Eu was oxidised to Eu^{3+} during alteration of the source, no anomaly would develop in the fluid. Yet Olympic Dam breccias tend towards positive Eu anomalies. If Eu in the Olympic Dam REE-source was divalent, the only way to achieve the positive anomaly in the ores and breccias is if the REE-source itself had a positive Eu anomaly. Similarly, if present in the source as Eu^{3+}, no anomaly would develop in the fluid unless it was inherited from the REE source. It therefore seems likely that, assuming the Olympic Dam REE were complexed during transport, the positive Eu anomaly observed is a feature inherited from the source, possibly due to the selective breakdown of Eu-enriched minerals (e.g. plagioclase and/or alkali feldspar; cf. Nash and Crecraft, 1985) during alteration. This suggests that the source of the REE contained abundant feldspar, but does not differentiate between a mafic or felsic source rock type.

5.9.5 Aqueous REE speciation

The plausible ligands available for complexing REE in the Olympic Dam ore forming fluids include fluorides, sulphates, phosphates and chlorides. The deposit is enriched in F, SO_4 and P_2O_5, and the fluids were undoubtedly enriched in Cl^- ion to be able to transport abundant Fe (Whitney et al, 1985). The stability constants of REE complexes of fluoride, sulphate and phosphate anions increase with increasing atomic number (Wood, 1990) such that these complexes preferentially take HREE into solution. Therefore, if any of these ligands were the principal transporters of REE at Olympic Dam, it is probable that precipitation of REE minerals involved considerable fractionation of the REE. Without strong precipitation-controlled fractionation it would not be possible to achieve the extremely LREE-enriched patterns observed in the ores and breccias. However, chloride REE complexes have stability constants which decrease with increasing atomic number, such that they fractionate LREE into solution (Wood, 1990). If chlorides were the main transporter of REE it is possible that the observed REE patterns of the ores and breccias could be produced without significant fractionation of the REE during precipitation.

5.10 Conclusions

The main conclusions of this study of the geochemistry of the Olympic Dam breccias are:

1) All elements analysed except TiO_2 and Zr show clear evidence of mobility during ore genesis; in some cases mobility is extreme.

2) Mass transfer was dominated by the addition of Fe.

3) Enrichments of Cr, Ni and V in the breccias suggest the involvement of a mafic/ ultramafic source component in ore genesis. The reversal of the negative Eu anomaly of the host granite to a slight positive anomaly in many breccias suggests a feldspar-rich (possibly plagioclase-rich) source for the mineralising fluids. This is also consistent with derivation of some of the ore metals from a mafic source rock.

4) A saline, relatively reduced fluid is required to transport iron into the breccia complex (as Fe^{2+}). Thermodynamic modelling (Haynes et al., submitted) suggests that such a fluid is unlikely to transport significant U, and the lack of correlation between the enrichments of these elements suggests that they were not transported together. U is mobile in oxidised environments, and the U concentration data correlate with Cu. Both of these ore elements were probably introduced to the deposit in a second fluid during or after Fe introduction.

5) Nb, Y, LREE and Ba enrichments also show no correlation with Fe, which suggests that they too were transported in a separate fluid from iron. Correlation between La and Cr enrichments, and Nd isotopic data (Chapter 7) indicate a contribution from a mafic/ultramafic REE source. This point, combined with the element association indicated as being transported separately from Fe (i.e. Cu, U, Y, Nb, Ba, LREE, Cr, V), suggests that the mafic/ultramafic source component may have had alkaline affinities. Altered, alkaline, mafic/ultramafic dykes are observed within the deposit (Chapter 6).

6) LREE-enrichment accompanied hematite + chalcopyrite replacement of magnetite + pyrite-rich breccias. Bornite-chalcocite ores are enriched in HREE relative to chalcopyrite-rich and pyrite-rich ores. These observations can be interpreted either as evidence for up to three temporally separate stages of ore formation, or as manifestations of a single fluid-mixing system. The alternative interpretations are discussed in Chapter 8 in view of the data presented in Chapters 6 and 7.

6 MAFIC/ ULTRAMAFIC INTRUSIVE ROCKS

6.1 Introduction

Three suites of igneous intrusive rocks are present within the Olympic Dam deposit:

1) Altered porphyritic felsic dykes

2) Relatively unaltered dolerite dykes

3) Altered, aphyric to microporphyritic dykes of mafic/ultramafic affinity (see below).

The petrography and geochemistry of the porphyritic felsic rocks have been discussed by Bradbury (1988) and briefly in Chapter 3. Their U-Pb zircon ages coupled with petrographic and geochemical similarities indicate that these dykes are correlatives of the Gawler Range Volcanics (see Chapter 3). Bradbury (1988) also discussed the dolerites in detail. These are quartz tholeiites which have been interpreted as correlatives of the Gairdner Dyke Swarm (Bradbury, 1988; Creaser, 1989), an extensive suite of north-northwest striking dykes that occur throughout much of the Stuart Shelf. The dolerites are considerably younger than the main mineralisation events at Olympic Dam (500 to 700 million years younger; see Section 7.3.2). They are therefore not relevant to Olympic Dam ore genesis, except perhaps as a heat source for minor remobilisation of ore components. The petrogenesis of the dolerites has not been investigated in this study.

The mafic/ultramafic nature of the altered aphyric/ microporphyritic dykes in the deposit has been documented by Bradbury (1988). These dykes are of special interest because the Nd systematics of the breccias and ores strongly imply that the ore fluids had interacted with a mafic or ultramafic source at 1590 Ma (discussed in Chapter 7). Because primitive mantle-derived rocks are implicated in Olympic Dam ore genesis, it is prudent to examine the petrogenesis of the the mafic/ultramafic rocks intruding the deposit in some detail. Unless otherwise specified, dykes referred to in the remainder of this chapter are the mafic/ultramafic types.

6.2 Field relationships

The mafic/ ultramafic dykes are interpreted to have been emplaced contemporaneously with the late stages of the ore-producing hydrothermal system because they cross cut hematitic breccias but are themselves strongly altered. It is possible that dyke emplacement spanned much or all of the brecciation and mineralisation history of the Olympic Dam Breccia Complex and that only those emplaced relatively late have been preserved. The dykes occur as both coherent and fragmental bodies (Plate 8). The

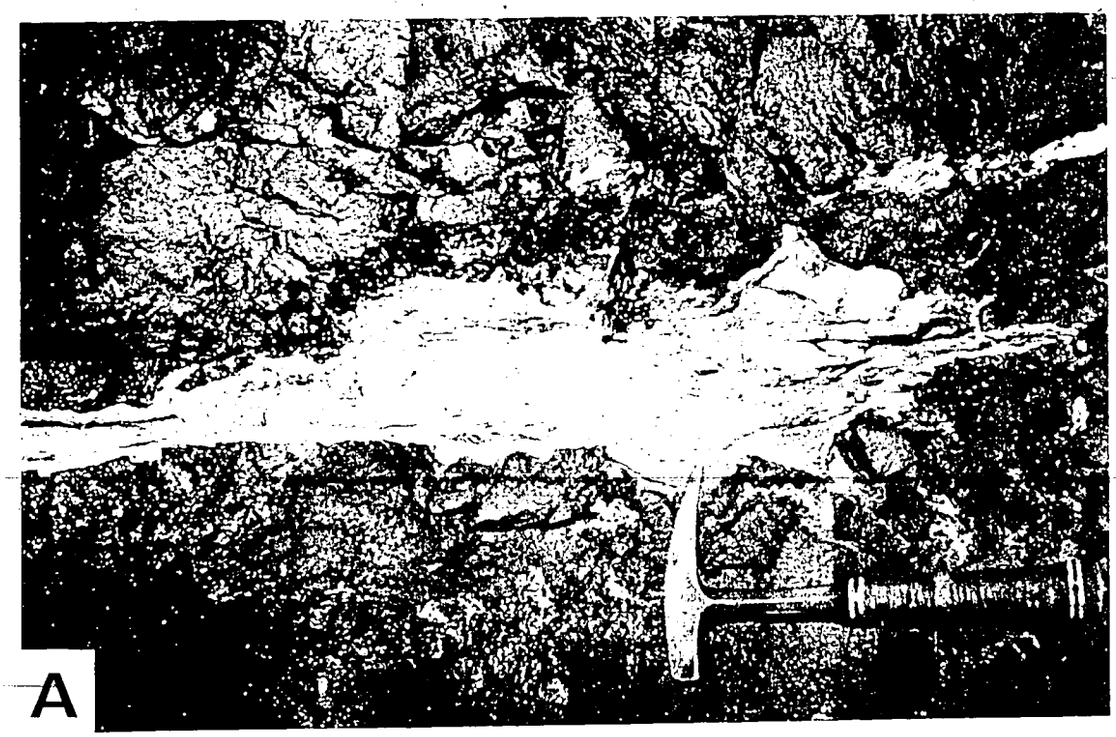

Plate 8. Altered mafic/ultramafic dykes. **A)** Coherent dyke with typically irregular morphology intruding hematitic breccias. Pronounced changes in dyke width over short distances, and fine apohyses exploiting wallrock fractures suggest a low viscosity magma.

B) Fragmental dyke showing hyaloclastite textures, interpreted to result from autobrecciation upon intrusion of the magma into wet unconsolidated breccias. Up left of photograph for A) and B).

morphologies of the coherent dykes are generally irregular. They have very fluidal textures and delicate apophyses where the low viscosity magmas have exploited fractures or unconsolidated zones in the wall-rock. The dykes pinch and swell over very short distances, ranging in width from centimetres to approximately one metre (Plate 8). Partial assimilation of fragments of wall rock is commonly observed, but marginal contact metamorphism is rare. The fragmental dykes occur as wispy tuffisites indicative of emplacement of magma into wet, unconsolidated breccias. Juvenile tuffisite fragments occur within several diatreme zones (see Plate 1; described in Chapter 2). The apparent low viscosity of the magmas is consistent with a mafic/ultramafic character.

6.3 Petrography

The dykes are invariably strongly altered to sericite and chlorite. Petrographically, their general mafic affinity is discerned by the presence of chromian spinels and pseudomorphs after euhedral olivine (Plate 9; also Bradbury 1988).

Six coherent dykes were sampled for this study (RX4539, RX4543, RX4546, RX4547, RX4548, RX4566). The rock textures are variable and it is difficult to discern whether the differences result from magmatic evolution, hydrothermal alteration, deformation, or any combination of these. Primary textures are best preserved in RX4548 (Plate 9). This sample contains abundant chlorite + serpentine+ sericite pseudomorphs after euhedral "hopper" olivine. Olivine crystallised both as phenocrysts (up to 1 mm) and as a groundmass phase. The groundmass contains numerous tabular aggregates of chlorite and sericite that may represent former feldspar and/or clinopyroxene crystals. The remainder of the groundmass consists of fine grained intergrowths of chlorite + sericite + quartz. The only primary minerals present are chromian spinels. These are observed as euhedral inclusions (<5 μm to 10 μm) within former olivine (Plate 9) and within the groundmass. A weak groundmass foliation in this sample is defined by aligned phyllosilicates. The foliation "wraps" around the pseudomorphs after olivine. It is difficult to determine whether it mimics a primary flow alignment of microlites, is a product of weak shearing, or reflects a degree of dissolution and volume reduction during alteration.

RX4543 shows a higher degree of deformation and hematite alteration than RX4548, but has many textural similarities, including pseudomorphs of olivine, feldspar, and possibly clinopyroxene. In many cases sericite + chlorite pseudomorphs after olivine are elongate due to stretching during shearing. The shear fabric is defined by a preferred orientation of the sheet silicates in the groundmass, by hematite alteration along grain boundaries, and by the elongate (former) olivines. Spinel occurs as fine inclusions (5-10 μm) in olivine pseudomorphs and as discrete phenocrysts (30-50 μm).

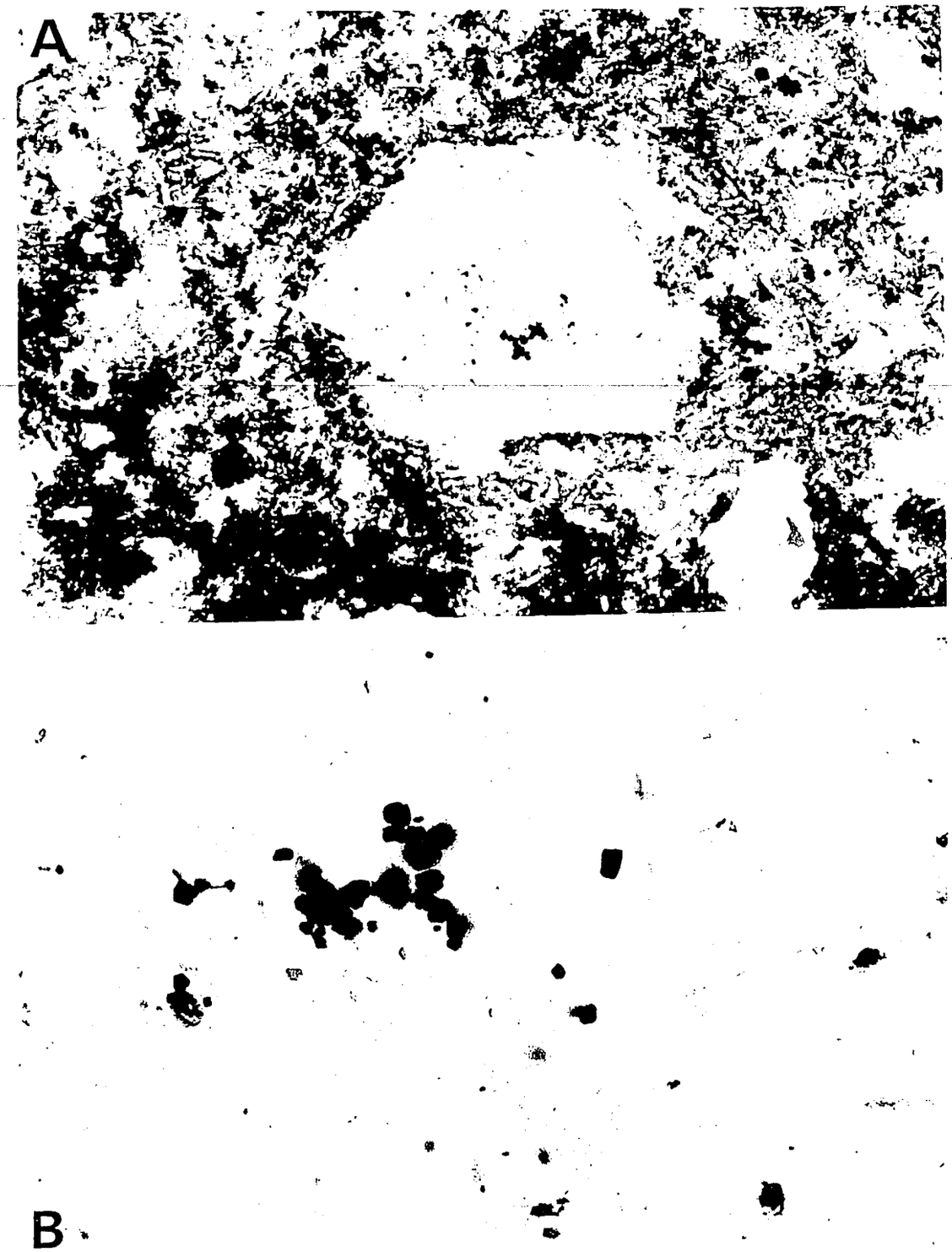

Plate 9. Photomicrographs of dyke sample RX4548. A) Euhedral olivine pseudomorphed by chlorite and serpentine. Note cluster of spinel inclusions in lower centre of grain. Groundmass contains chlorite+sericite pseudomorphs of elongate tabular grains, possibly feldspars and/or clinopyroxenes. The groundmass microlites are weakly aligned. Plane polarised light; width of frame is 1.3 mm.
B) Magnified view of euhedral brown spinels within the pseudomorph of olivine in A). Spinels range in size from 2 to 10 μm. Width of frame is 325 μm.

RX4546 and 4539 both show pseudomorphs after olivine and tabular feldspar/ clinopyroxene in rocks now dominated by quartz and sericite. In RX4546 olivine has been replaced by aggregates of polygonal quartz grains. Spinel inclusions are present within the quartz.

Unlike the other samples, RX4547 and 4566 show no textural evidence for pre-existing olivine. RX4547 is a felted mass of fine grained (<5 μm) sericite. Weakly defined tabular aggregates of sericite may reflect former feldspar microlites. A distinct foliation is defined by aligned phyllosilicates and veinlets of hematite. It is possible that the primary texture has been largely obliterated by deformation.

RX4566 contains many grains of quartz with undulose extinction, probably derived from assimilated granite fragments. The presence of clusters of zircons within sericite is consistent with this observation. No pseudomorphs after olivine were observed. Hematite has almost entirely pseudomorphed abundant euhedral 200 μm magnetite phenocrysts. This suggests the pristine composition of the dyke from which RX4566 was sampled was more evolved than the compositions of those containing Cr-spinel.

6.4 Spinel chemistry

Spinels are the only potentially primary igneous phase preserved in these rocks. The spinel chemistry has been examined in an attempt to place constraints on the compositions and petrogenetic affinities of the parent magmas. Electron probe analyses are tabulated in Appendix 8 which includes unpublished data supplied by Olympic Dam Operations. The range in spinel compositions is illustrated in Figure 6.1. The spinels are rich in Cr_2O_3, typically with 50 to 60 wt% Cr_2O_3 and Cr# (100Cr/[Cr+Al]) >65. They have low TiO_2 concentrations (generally <0.3 wt%). The main compositional variation is in the Mg-Fe^{2+} dimension of the spinel prism (Figure 6.1).

Evans and Frost (1975) documented chromites of metamorphic origin in rocks from Italy and the USA. The only occurrences of spinel with Cr_2O_3 contents as high as the Olympic Dam dykes were in rocks of amphibolite (and higher) metamorphic grade, conditions which are clearly not relevant for the Olympic Dam rocks. It is therefore considered extremely unlikely that the the Olympic Dam spinels are of secondary origin.

When the spinel data are plotted on a diagram of Cr# versus Ti# (100Ti/[Ti+Cr+Al]) a trend of decreasing Cr# and increasing Ti# is evident (Figure 6.2). It is tempting initially to interpret this as a magmatic evolution trend, suggesting that the different dykes were emplaced at different stages of evolution of the parent magma source. The most evolved spinel compositions are from sample RX4546 taken from a dyke within a late stage diatreme (V1 on Figure 2.2). This dyke is therefore one of the latest intrusives in the

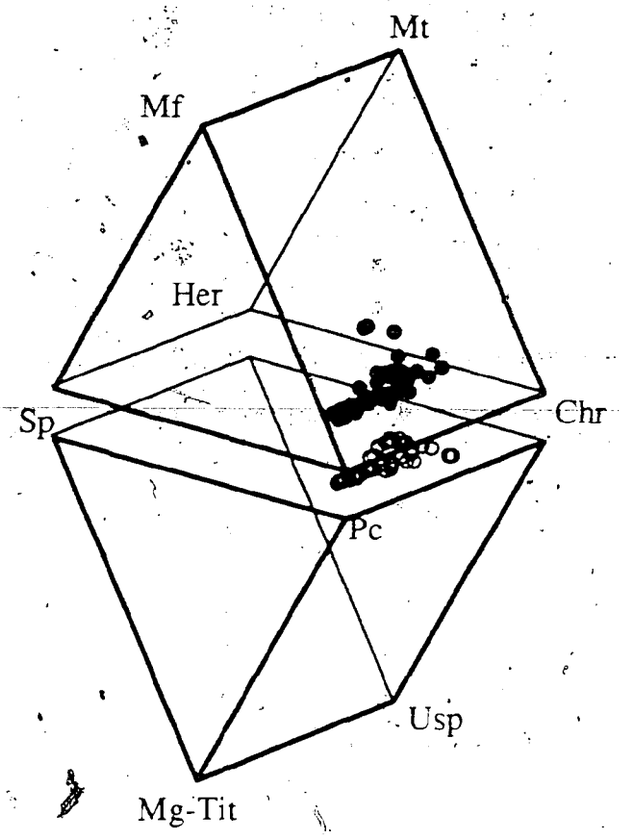

Figure 6.1. Olympic Dam spinel compositions represented on the spinel prism (after Haggerty, 1976). The dominant variation is in the Fe2-Mg dimension.
Chr= chromite ($FeCr_2O_4$); Her= hercynite ($FeAl_2O_4$); Mt= magnetite (Fe_3O_4); Mf= magnesioferrite ($MgFe_2O_4$); Mg-Tit= magnesiotitanite ($MgTiO_4$); Pc= picrochromite ($MgCr_2O_4$); Sp= spinel ($MgAl_2O_4$); Usp= ulvospinel (Fe_2TiO_4)

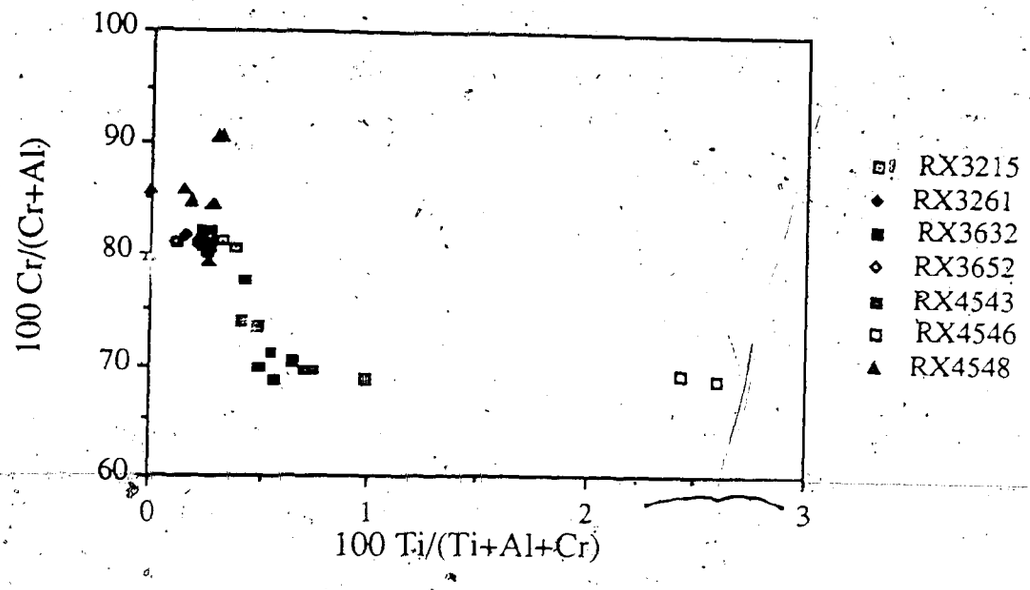

Figure 6.2. Cr# versus Ti# for Olympic Dam spinels, showing a magmatic evolution trend of decreasing Cr# with increasing Ti# (see discussion in text). The trend suggests that the different dykes were emplaced at different stages of evolution of the parent magma chamber.

deposit (excluding the "Gairdner" dolerites mentioned above), so its relatively evolved spinel compositions are consistent with field relationships of the dykes.

Two samples (RX4543 and RX4548) show significant "within-sample" variability of spinel compositions (Figure 6.2). This may be due to heterogeneous reequilibration of spinels, or to hydrothermal alteration. Roeder and Campbell (1985) and Scowen et al. (1991) have demonstrated that subsolidus reequilibration can cause spinels in mafic rocks to become richer in Ti and poorer in Cr content. However Scowen et al. (1991) also suggest that liquidus chromite compositions may be preserved in rapidly quenched materials. The Olympic Dam dykes are rapidly quenched intrusives. The within-sample variability of spinels in RX4543 and RX4548 may also be due to hydrothermal alteration. Kimball (1990) demonstrated that hydrothermal alteration can lead to significant increases in Cr# of spinels by removal of Al, which is taken up by aluminous alteration phases such as chlorite. She described changes in Cr# from ~20 in unaltered spinels to ~80 in altered spinel from the same rock unit. Clearly the relatively minor variability of Cr# in RX4543 and RX4548 could be caused by alteration.

This raises questions about whether the Cr# and Ti# ratios plotted in Figure 6.2 are close to the primary (igneous) values for *any* of the samples. One important factor suggests that most of them are: under most circumstances Ti and Cr are both likely to be relatively immobile and remain as residual elements in spinels during alteration. If this is the case, then alteration of spinel by removal of Al (e.g. Kimball, 1990) should result in a positive correlation between Ti and Cr concentrations. This is not observed. The magmatic

evolution of spinel compositions from high Cr# and low Ti# towards lower Cr# and higher Ti# is a widely observed feature of igneous rocks. Consequently the overall trend in Figure 6.2 is regarded as a primary igneous feature, although alteration may have had minor effects on spinels from some samples.

Cr# and Ti# can therefore be used broadly as indices of magmatic differentiation for the sample suite described here. In unaltered spinels it is expected that increasing magmatic evolution would lead to an increase in Fe2# ($100Fe^{2+}/[Mg+Fe^{2+}]$). A plot of Cr# versus Fe2# (Figure 6.3) shows that these samples do not form the expected negative correlation. This suggests that the variation in Fe2# does not reflect magmatic evolution. Mg and Fe^{2+} are known to exchange between spinels and silicates at subsolidus temperatures (Roeder and Campbell, 1985; Scowen et al., 1991). This suggests that the variation in Fe2# of the Olympic Dam spinels may be a product of post-alteration reequilibration or of the alteration process itself. For this reason Fe2# and Mg# are not used in discussions aimed at identifying primary affinities of the spinels.

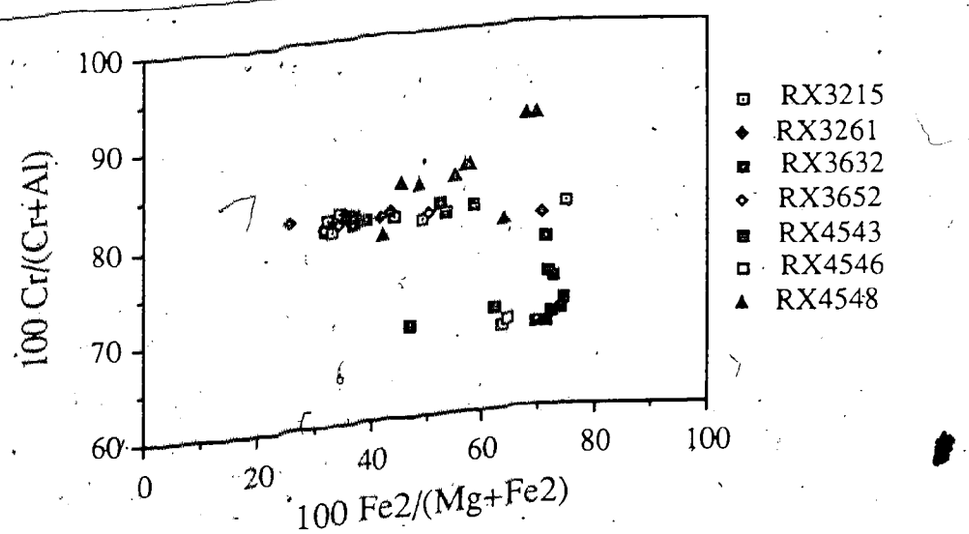

Figure 6.3 Cr# versus Fe2# for Olympic Dam spinels. The absence of correlation suggests that the Mg and Fe2 variations are governed by alteration and not by magmatic differentiation.

The Olympic Dam spinel data are therefore best compared with data for other rock types using a plot of Cr# versus Ti# (Figure 6.4). The more evolved Olympic Dam spinels (RX4546 and RX4543; lower Cr#, higher Ti#) are within the compositional ranges of several mafic rock types e.g. basalts from Hawaii and Vanuatu, Bushveld cumulates, and also the less evolved members of the lamproite field (Figure 6.4). The more primitive Olympic Dam spinels overlap with the compositional fields of spinel inclusions in diamonds, spinels from komatiites, meymechites (alkalic komatiites; Egorov, 1970; Sobolev et al., 1991), and some island arc magmas (boninites and basalts from Vanuatu). The fields for spinels from lamproites and kimberlites have similarly high Cr#, but are

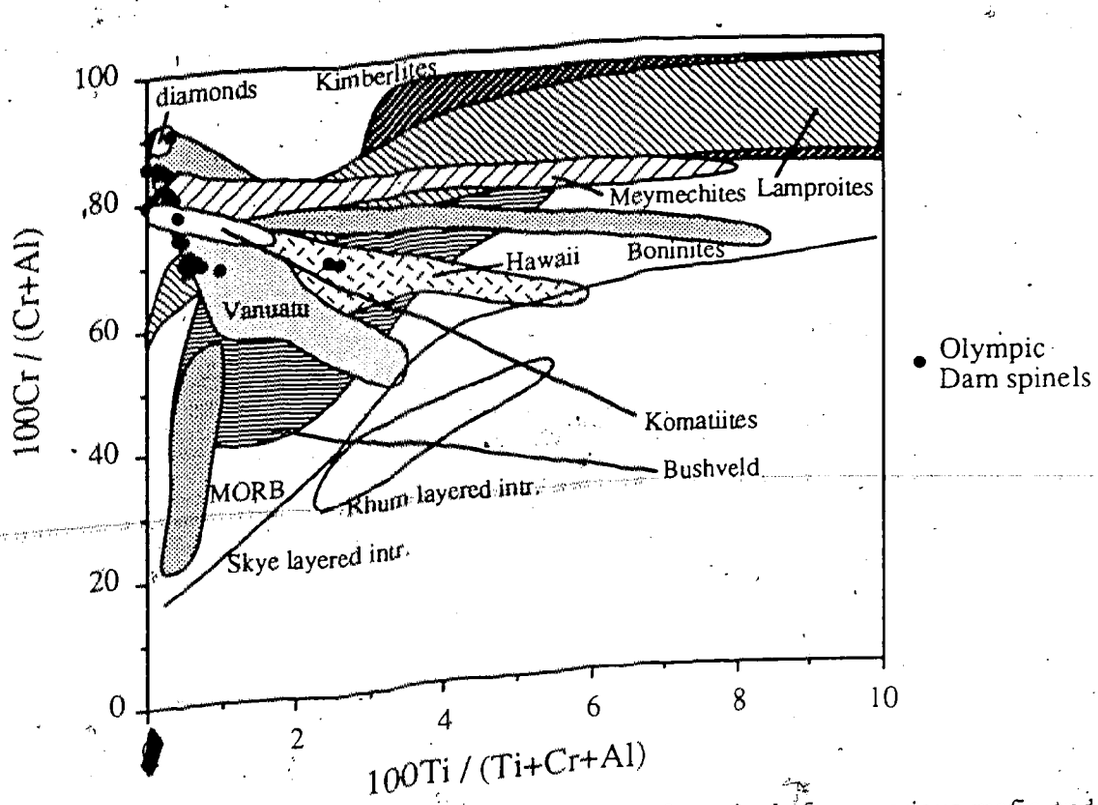

Figure 6.4. Compositional fields (Cr# versus Ti#) for spinels from various mafic and ultramafic rock types, with Olympic Dam spinels plotted for comparison. The closest similarities for the the most primitive Olympic Dam dykes are with spinels from komatiites, boninites, meymechites and possibly low-Ti variants of alkaline rock series (e.g. kimberlites and lamproites). Spinel analyses obtained from: Kimberlites, Mitchell (1986) - 35 analyses; Lamproites, Mitchell and Bergman (1991) - 29 analyses; Meymechites, Bagdasarov et al. (1981) - 33 analyses; Boninites, Brown and Jenner (1989) - 10 analyses, Coish (1989) - 7 analyses, Falloon et al. (1989) - 14 analyses; Diamond inclusions, Meyer and Boyd (1972) - 5 analyses; Hawaii, Bohrson and Clague, (1988) - 13 analyses, Nicholls and Stout (1988) - 11 analyses, Wilkinson and Hensel (1988) - 5 analyses, Dr S Eggins unpublished data - 22 analyses, Scowen et al. (1991) - 41 analyses; Vanuatu island arc basalts, Barsdell (1988) - 12 analyses, Barsdell and Berry (1990) - 9 analyses, Eggins (in press) - 9 analyses, Dr S Eggins unpublished data - 145 analyses; Komatiites, Zhou and Kerrich (1992) - 14 analyses; Bushveld, Cameron (1977) - 65 analyses; Rhum layered intrusion, Henderson (1975) - 26 analyses; Skye layered intrusion, Bell and Claydon (1992) - 15 analyses; MORB, Dr S Eggins unpublished data - 46 analyses, Sigurdsson and Schilling (1976) - 20 analyses.

more enriched in TiO_2 than the Olympic Dam spinels. However, a kimberlitic magma source cannot be ruled out on the basis of spinel composition, as is illustrated by the field for spinel inclusions in diamonds. Meyer and Boyd (1972) suggested that inclusions within diamonds have compositions in equilibrium with deep mantle sources, and have not participated in lower temperature equilibration because they are armoured by the host diamond.

The high Cr_2O_3 content of the spinels suggests that they crystallised from a relatively MgO-rich melt. This could be produced either by high temperature melting in an anhydrous mantle source (>1500°C for spinels of 55-60 wt% Cr_2O_3: Murck and Campbell, 1986) or by lower temperature partial melting of a volatile-rich mantle source.

If sourced from anhydrous mantle, a magma produced above 1500°C would have an MgO content greater than 25 wt% (Campbell and Murck, in press). This high MgO content and temperature are unlikely for Proterozoic melts; the highest MgO content known for post-Archaean melts (estimated for a primary magma) is 22 wt% (Campbell and Griffiths, 1992). It is therefore believed more likely that the implied high MgO of the melts is a function of volatile-rich partial melting (e.g. in a source appropriate for the generation of lamproites, kimberlites, lamprophyres, or subduction-related basalts and picrites). This possibility is discussed further in Section 6.6. The low TiO_2 contents of the spinels suggest crystallisation from a low-Ti melt (< 1.%).

Several spinel samples have elevated ZnO contents, particularly RX3652 (4-6 wt% ZnO; see also 3215, 3261, 3632). The spinels from RX4548 contain significant MnO (up to 2%). Rock (1991) suggested that magmatic spinels with ZnO > 2% and/or MnO > 2% are diagnostic features of lamprophyres. Meyer and Boyd (1972) reported elevated ZnO and MnO in spinel inclusions within a single diamond from Sierra Leone. Given the evidence presented above that the MgO and FeO contents of the spinels have been affected by hydrothermal alteration, the concentrations of the oxides of other divalent cations (e.g. ZnO and MnO) should be interpreted cautiously. For example, the high ZnO of some spinels may be due to the uptake of Zn released from olivine as it was altered to hydrous silicates. Nevertheless, it is possible that ZnO contents as high as ~5 wt % (i.e. RX3652) reflect a lamprophyric affinity.

The Olympic Dam dykes cannot be regarded as close analogues of boninites or island arc basalts because they were emplaced in an intracontinental setting (Giles, 1988). However, one fundamental petrogenetic feature of boninites and some island arc basalts may be comparable: boninites are believed to owe their distinctive compositional characteristics to an origin by hydrous partial melting of a refractory mantle source i.e. a source that was depleted in incompatible elements by a prior partial melting event. The refractory nature of the source coupled with melting under hydrous conditions has been used to explain the high Cr, low Ti nature of the rocks (Crawford, 1989). It is possible that the mantle that sourced the Olympic Dam dykes underwent similar processes, but in an intracontinental environment.

To summarise, the spinel compositions suggest that the Olympic Dam dykes may have magmatic affinities with:

a) a low-Ti variant of an alkaline (kimberlitic or lamproitic) rock series,

b) mafic magma derived from a refractory mantle source (boninitic),

c) ultramafic magmas from an anhydrous source (i.e. komatiites; considered unlikely), or

d) alkalic ultramafic magmas (meymechites).

These options are discussed further (Section 6.6) in the light of the whole-rock geochemical data presented below.

6.5 Whole-rock geochemistry

XRF analyses of the dyke samples are presented in Appendix 2 and INAA analyses in Appendix 3. In Chapter 5 it was observed that Ti and Zr have behaved in a relatively immobile manner during brecciation and alteration of the Roxby Downs Granite. The near-linear relationship between TiO_2 and Zr for the six dyke samples (Figure 6.5a) suggests that these elements have behaved in a similarly immobile manner in these rocks, despite their altered character. Al_2O_3 contents range from 11.3 wt% (RX4548) to 32 wt% (RX4547). Clearly the higher concentrations are extremely unlikely to be igneous values. They must therefore result either from hydrothermal introduction of Al, or from the residual concentration of Al_2O_3 as other elements are removed. In this regard it is interesting to note the near linear correlations of both Ti and Zr with Al_2O_3 (Figure 6.5 b and c). These correlations suggest that Al has been immobile, and that the high concentrations are due to its residual behaviour during mass loss accompanying alteration. This implies very large mass/ volume losses during alteration (up to ~60%) in order to concentrate Al_2O_3 from ~11 wt% to 32 wt%. The only physical evidence that may account for this is the foliation developed in some of the dyke samples (Section 6.3). The residual behaviour of Al_2O_3 means that it can be used in a general way as an index of alteration (higher concentration = greater volume loss, i.e. more altered). However, it is noted that there may have been some variability in primary Al_2O_3 content of the dykes.

Elemental gains and losses during alteration have been investigated by plotting element/TiO_2 ratios against Al_2O_3 (presented in Appendix 9), an analogous method to that used for the breccias (Chapter 5). These plots indicate that Si, Ca, Mg, Mn, Cr, Nb, Cu, Ni, Th, V and Zn have all been lost during alteration (using data from Krcmarov [1987], Bradbury [1988] and this study). The elements that were mobile but which show no consistent trend of gain or loss over the Al_2O_3 range include Na, P, Ba, Pb, Rb, Sr, Y and U. In the case of Na, the lack of consistent trend may be due to its extensive loss during the earliest stages of alteration (cf. Na_2O loss during granite alteration, Chapter 5). Flat element/TiO_2 versus Al_2O_3 trends are displayed by Al, K, La, Ga and Zr (Appendix 9), suggesting that they are residual and that they have been concentrated during alteration.

One sample (RX4548) consistently has TiO_2-normalised element ratios that form the least-altered end-member of the trends mentioned above (see Appendix 9). It forms the end member for the trends of Si, Mg, Ca, Cr, Ni, Cu, Nb, Th, REE and V.

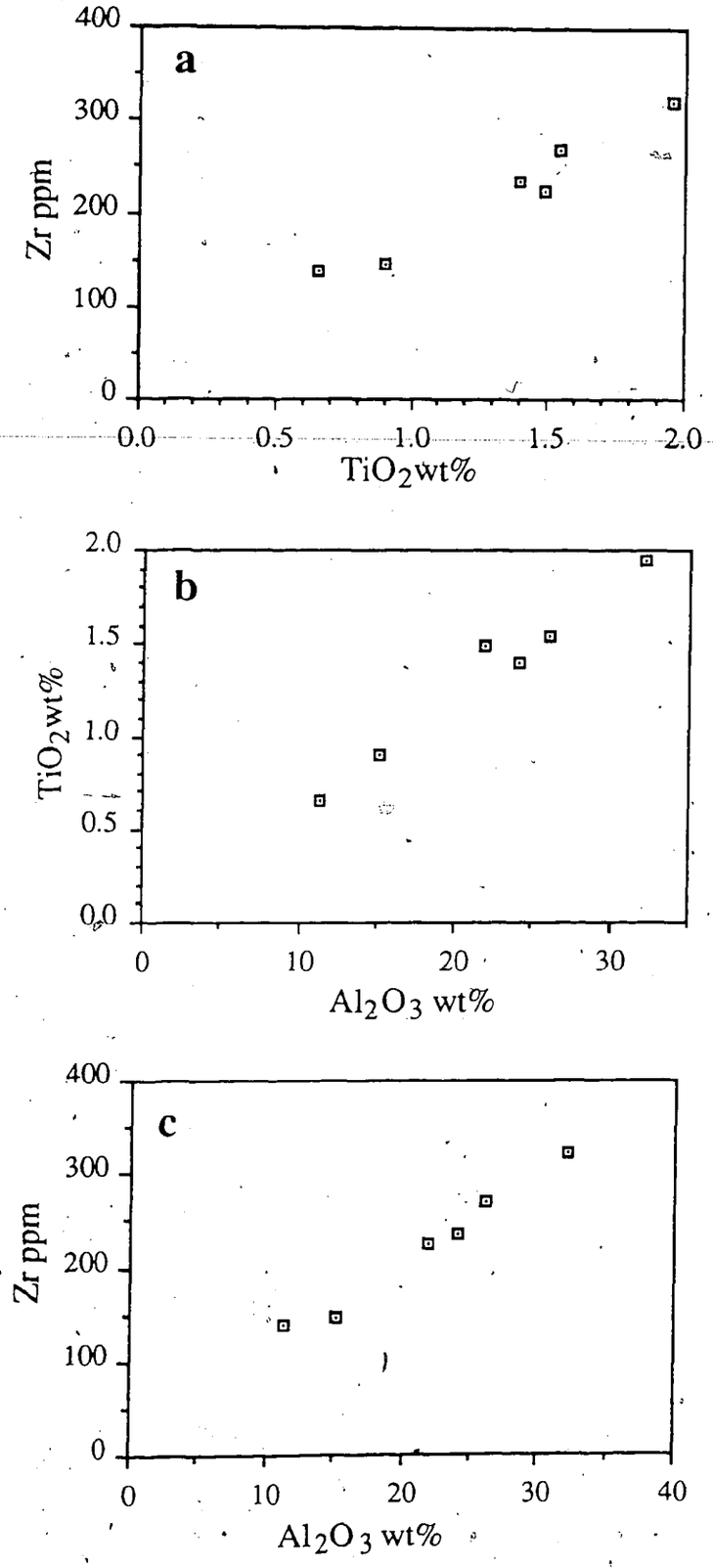

Figure 6.5. Variation diagrams for whole rock samples of Olympic Dam dykes: a) Zr versus TiO_2; b) TiO_2 versus Al_2O_3; c) Zr versus Al_2O_3. The correlations illustrate the relatively immobile behaviour of these elements during alteration.

RX4548 has the lowest concentrations of any of the dykes for many of the incompatible elements represented in Figure 6.6. It also has the best preserved igneous textures of any samples examined in this study (Section 6.3). This sample is therefore considered to be the closest available approximation to the primary composition(s) (i.e. least altered) of the dykes and is used below in geochemical comparisons with various major lithological categories. The composition of RX4548 and the sense of the gain or loss trend for each element are presented in Table 6.1.

6.6 Discussion

It is not possible to confidently determine the magmatic affinities of the dykes using the major element chemistry because even the least altered sample may have undergone significant major element mobility and possibly concentration changes due to volume change. However, it is possible to discern a great deal about magmatic affinities by examining the abundances of the trace elements that show either immobility or a consistent trend of loss with progressive alteration. For the latter, the element abundances may be interpreted as minimum values.

Variation diagrams of elements in Olympic Dam dykes normalised to model primitive mantle are presented in Figure 6.6. The first point to note is the strong enrichment in the incompatible trace elements. In Chapter 5 it was demonstrated that potassium metasomatism is not a feature of Olympic Dam ore genesis. K and Rb were removed from, rather than introduced to, the volume of the deposit. The strong enrichment of K and Rb in RX4548 is therefore believed to reflect high igneous contents of these elements, although primary concentrations may well have differed from present concentrations. One would need to invoke selective metasomatic enrichment of K and Rb in the dykes, compared to the remainder of the deposit, to attribute their high levels to hydrothermal alteration. The high REE content of RX4548 cannot be attributed to either metasomatic introduction of REE or to contamination by assimilation of the hematite breccia wallrocks because its initial Nd isotopic signature ($\varepsilon Nd_{1590} = +3.7$) is in stark contrast to the ore signature ($\varepsilon Nd_{1590} = -2.5$; it is demonstrated in Chapter 7 that the signature of +3.7 is unlikely to result from any later isotopic resetting events). The shape of the REE pattern for RX4548 therefore can be regarded as primary.

In the following discussion the mantle-normalised patterns of RX4548 and various other rock types are compared. The elements of most interest are those which are generally regarded as less mobile (Ti, Zr, Hf, Nb, Ta, REE, Y and Th). These elements have generally smooth and consistent patterns for the less altered Olympic Dam samples (Figure 6.6a), which suggests that they have behaved as a coherent group. This too suggests that the enrichment in incompatibles is a primary feature. If it were due to alteration, the mantle-normalised patterns must represent very uniform alteration and a

Sample No.	RX4548	gain/loss trend	PY1-74
Rock-type	mafic/ ultmaf.dyke		Mount Gunson bas.
SiO_2	54.05	loss	46.99
TiO_2	0.66	constant	0.76
Al_2O_3	11.31	constant	9.53
Fe_2O_3	5.84	variable	5.49
FeO	6.60	variable	5.99
MnO	0.25	loss	0.30
MgO	8.72	loss	12.62
CaO	1.62	loss	8.41
Na_2O	0.25	variable	1.36
K_2O	1.22	minor gain	2.40
P_2O_5	0.35	variable	0.26
SO_3	0.02	-	-
S	0.01	-	-
H_2O^+	4.02	-	-
H_2O^-	0.52	-	-
CO_2	1.27	-	-
LOI	2.29	-	5.25
Cu	0.04	-	-
Rest	0.79	-	-
Total	99.83	-	99.36
Rb	75	variable	89
Sr	25	variable	306
Pb	30	variable	13
Th	25.5	loss	6
U	34	variable	2.5
Zr	139	constant	110
Hf	4.2		
Nb	95	loss	6.5
Ta	5		
Y	51	variable	21
Ni	980	loss	512
Cu	350	loss	15
Zn	745	loss	274
Ga	13	constant	13
V	138	loss	223
Cr	2510	loss	1643
Ba	380	variable	1160
La	116	constant	30
Ce	295	constant	55
Pr	38.4	-	
Nd	175	-	
Sm	40.7	-	
Eu	5.7	-	
Tb	3.1	-	
[illegible]	15.7	-	
Ho	2.75	-	
Yb	8.45	-	
Lu	0.41	-	

Table 6.1. Geochemical data for the least altered Olympic Dam dyke sample RX4548. Behaviour of elements during progressive alteration, as determined by element/TiO_2 vs Al_2O_3 "gain/ loss diagrams", is indicated in column two. Data for one sample of Mount Gunson potassium-rich basalt (Knutson et al., 1992) of similar age to the Olympic Dam dykes given for comparison (discussed in section 6.6). REE, Ta and Hf by INAA.

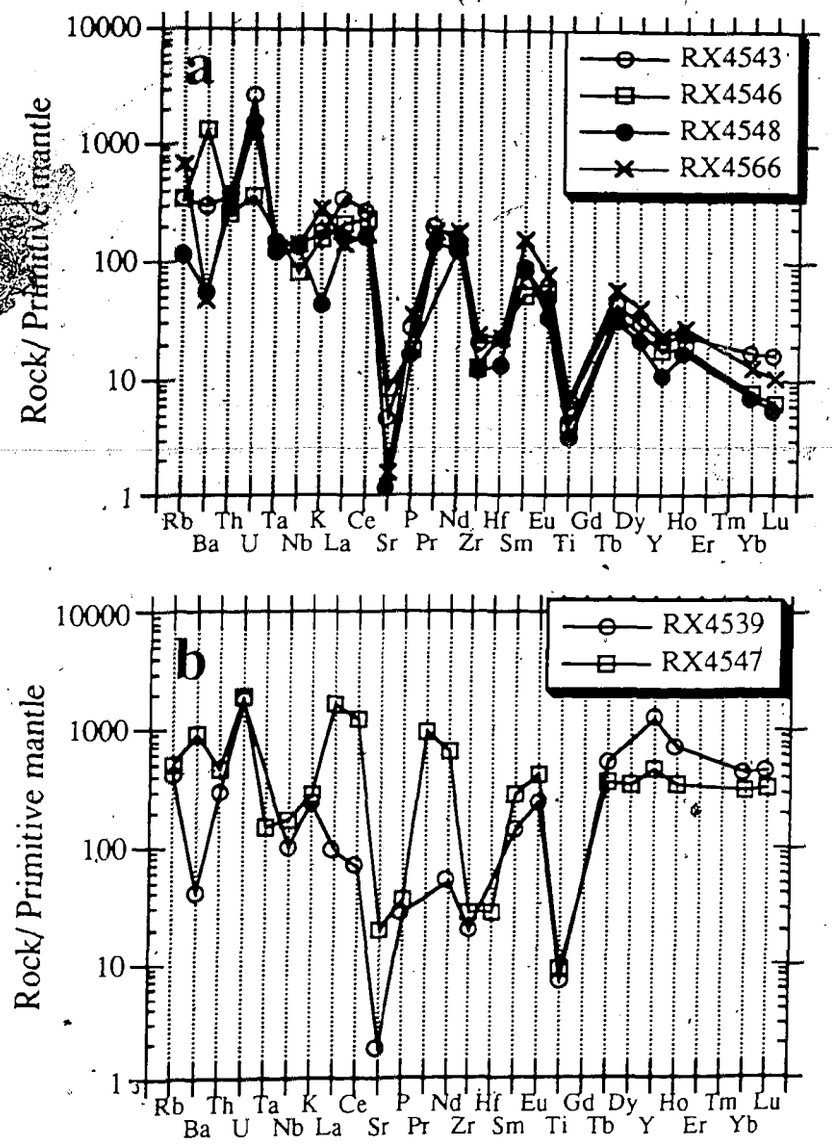

Figure 6.6. Trace element compositions of the Olympic Dam dyke samples normalised to primitive mantle (values of Ringwood, 1991). The patterns in a) show close similarities for samples RX4543, RX4546, RX4548 and RX4566, with the least altered sample (RX4548; see text) having the lowest concentrations for many of the elements. RX4539 and RX4547 (6.7b) have suffered greater degrees of element mobility during alteration, particularly a strong enrichment in HREE.

---

constancy of proportions of elements in the alteration products. If the pattern shapes are interpreted as primary, the differences in absolute abundances can be viewed as a function of volume changes during alteration. The important geochemical features shown by the patterns are:

1) the strong overall enrichment in the incompatible elements,

2) a very pronounced negative Ti anomaly,

3) a pronounced negative anomaly for Zr and Hf, and

4) a weak negative Nb anomaly, in contrast to the Ti anomaly.

The strong negative Ti anomaly implies a low-Ti melt, the same conclusion made on the basis of the low TiO_2 content of the spinels (Section 6.4).

Changes in element concentration due solely to volume changes are likely to be minor in the least altered sample, RX4548; they should be well below a factor of two (corresponding to a volume loss of 50% which is unreasonably high for this sample). At high concentrations such uncertainty can be ignored on the mantle-normalised plots because comparisons are made on a logarithmic scale.

The spinel chemistry (Section 6.4) and the high Cr and Ni content of the least altered sample RX4548 (~2500 ppm Cr and ~1000 ppm Ni), imply that the magma had a high MgO content. It is therefore appropriate to compare the trace element composition of RX4548 with high-MgO rock types such as komatiites. In Section 6.4 the MgO contents implied by the spinel Cr_2O_3 content (if an anhydrous melt) were considered to be unrealistically high for post-Archaean melts. The enrichment of incompatible elements observed in RX4548 is dissimilar to the depleted signatures typically observed in komatiitic rocks (e.g. Campbell and Griffiths, 1992; Sun and Nesbitt, 1978; Grŭau, 1987; Jochum, 1991; Collerson, 1991). This provides further evidence that the possibility of komatiitic affinities is unlikely. It is therefore more likely that the Olympic Dam dykes were sourced from volatile-rich mantle, and a number of enriched mafic/ultramafic rock types are worthy of consideration as possible analogues for the dykes.

The picrites of the Karoo province (South Africa) are among the most enriched known (Campbell and Griffiths, 1992). RX4548 and the Nuanetsi (Karoo) picrites are compared in Figure 6.7. The Olympic Dam dykes are obviously more enriched in most of the the incompatible elements than the Karoo picrites. The other significant differences are the absence of the pronounced negative Ti, Zr and Hf anomalies in the Nuanetsi picrites. Clearly these are not closely analogous to the Olympic Dam dykes.

The only rock types known to have enrichments of incompatible elements (particularly REE) similar to RX4548 are carbonatites, nephelenites and members of Rock's (1991) "lamprophyre clan", e.g. kimberlites, lamproites and lamprophyres. The absence of carbonate-rich dykes and Na- or K-metasomatism associated with the dykes suggests that a direct carbonatitic affinity is unlikely. Figure 6.8 illustrates comparisons between the incompatible element compositions of RX4548 and average compositions for the rocks of the lamprophyre clan (data after Rock, 1991). It is recognised that there is a wide range of compositions for rocks that fall into these categories. However the average compositions are for large numbers of samples (846 lamproites, 550 kimberlites, and 456

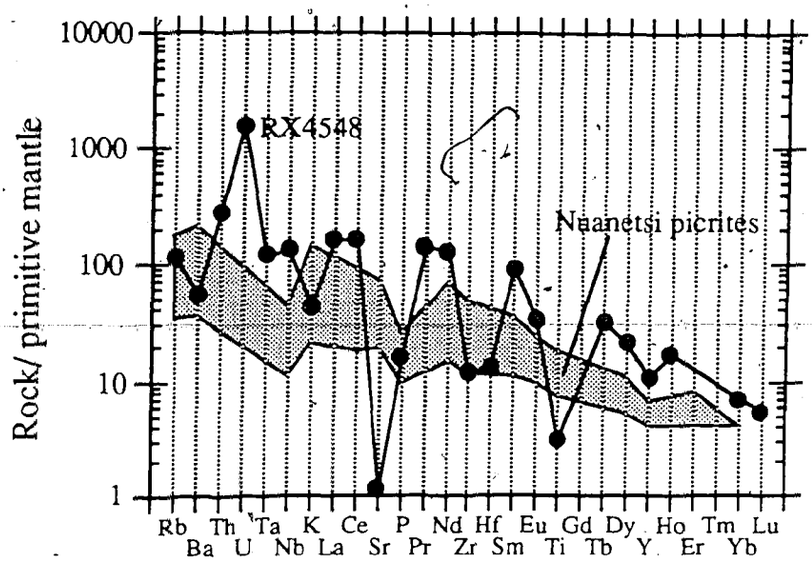

Figure 6.7. Comparison between the incompatible element composition of RX4548 (normalised to primitive mantle) and the range for the Nuanetsi Picrites from the Karoo province in South Africa. The Nuanetsi picrites (data from Ellam and Cox, 1989) are among the most enriched picrites known. RX4548 is significantly more enriched in many of the elements plotted.

ultramafic lamprophyres) and are therefore weighted towards the more common compositions. The average compositions are adequate for the purposes of comparisons of degrees of trace element enrichment. Trace element abundances in RX4548 differ significantly from the average lamproite (Figure 6.8a). In particular, lamproites are more enriched in Rb, Ba, K, La, Ce and P, have a stronger negative Nb anomaly than RX4548, and show no evidence of the pronounced negative Zr, Hf and Ti anomalies observed in the latter. The Olympic Dam dykes therefore are not readily classifiable as lamproites.

There are close similarities between RX4548 and trace element compositions of average kimberlite, ultramafic lamprophyres (Figure 6.8b) and nephelinites (Figure 6.9). Of the elements likely to have been relatively immobile in RX4548, Th, Nb, Y and the REE (reasons for suggesting primary REE patterns given above) are at least as enriched in RX4548 as in kimberlites, ultramafic lamprophyres and nephelinites. These average compositions do not show negative Nb anomalies, but they do show negative anomalies in Ti, Zr and Hf, although these are less pronounced than in RX4548 (see below).

The overall enriched nature of the Olympic Dam dykes is interpreted as evidence that they are strongly alkaline rocks, possibly members of the lamprophyre clan, with close trace element geochemical similarities to kimberlites, nephelinites and ultramafic lamprophyres.

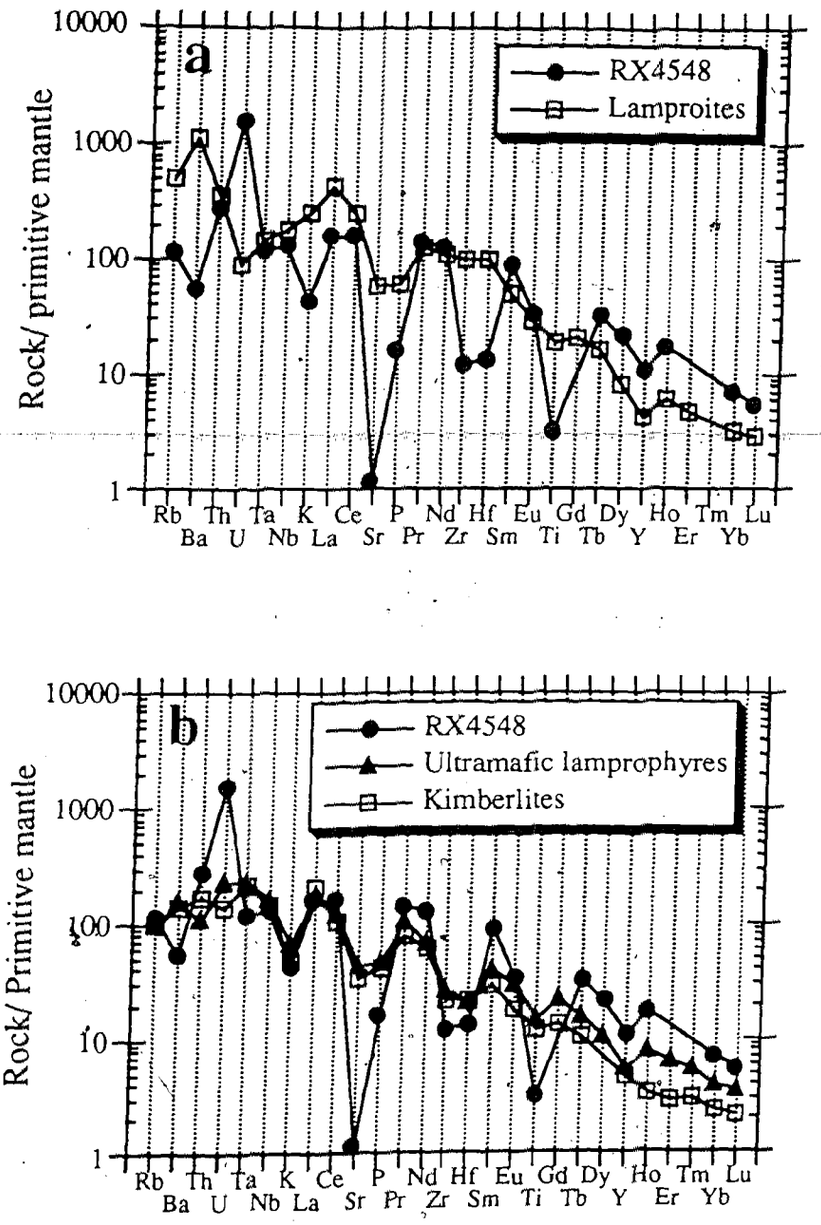

Figure 6.8. RX4548 incompatible elements compared to **a)** an average of 846 lamproite analyses, **b)** an average of 550 kimberlite analyses and an average of 456 analyses of ultramafic lamprophyres (averages after Rock,, 1991). RX4548 shows extreme enrichment, similar to kimberlites and ultramafic lamprophyres, though it is not as enriched in Rb, Ba, K, La and Ce as lamproites. RX4548 has notably lower concentrations of Ti, Zr and Hf (discussed in text) than each of the other categories plotted (data are normalised to primitive mantle values of Ringwood, 1991).

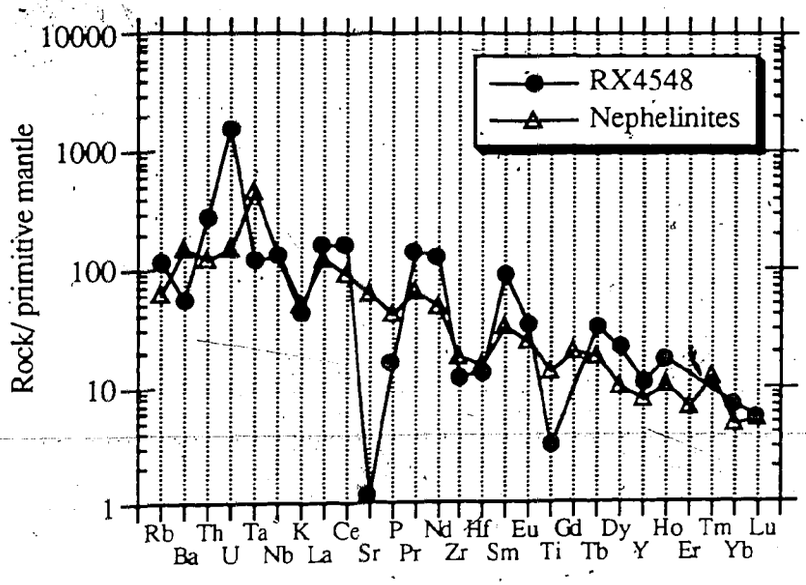

Figure 6.9 Mantle normalised diagram comparing RX4548 with average nephelinite incompatible element composition (Wedepohl and Muramatsu, 1979). RX4548 has similar levels of enrichment for Rb, Th, Nb, K, REE and Y (normalisation values of Ringwood, 1991).

Rock (1991) insists that nephelinites are anhydrous equivalents of monchiquites, a type of alkaline lamprophyre. More general usage suggests that "nephelinite" encompasses alkaline, anhydrous and volatile-rich melts produced by a low degree of partial melting of a mantle source. They are generally regarded as produced from a somewhat greater degree partial melting than is required to produce kimberlites, but less than that required to produce alkali basalts and tholeiites; Wedepohl and Muramatsu, 1979; Bailey, 1984. The broader use of the term is adopted here. The high ZnO content of spinels in RX3652 is consistent with a lamprophyric attribution (Section 6.4; cf. Rock, 1991).

Nd isotopic evidence (initial $\varepsilon Nd = +4$; Chapter 7) indicates that the REE were derived from mantle with a time-averaged LREE depleted signature. This implies that the observed enrichment in incompatible elements occurred either shortly before or, more likely, at the same time as the melting event that produced the dyke magma. The highly fractionated REE patterns (Figure 6.10) combined with the Nd isotopic signature suggest that the enriched melt was produced by a low-degree partial melt of weakly depleted (therefore probably asthenospheric) mantle in the presence of residual garnet. The higher content of HREE in RX4548 than in the average compositions of kimberlites and ultramafic lamprophyres (Figure 6.8b) suggests a lower proportion of garnet for the source of the Olympic Dam dykes than in the source for the other rock categories. This may reflect an origin from shallower depths than kimberlites. Alternatively the relatively high HREE in RX4548 may result from a higher degree of partial melting for the Olympic Dam dyke magmas than for kimberlites and ultramafic lamprophyres. Some

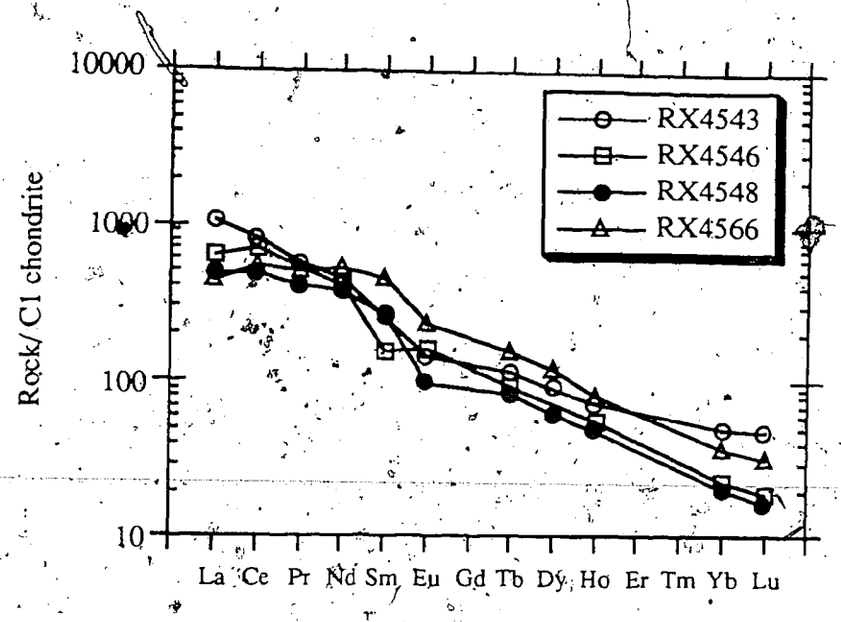

Figure 6.10. Chondrite-normalised REE plot of RX4548 compared to the less altered of the other Olympic Dam dyke samples. The REE are strongly fractionated, implying derivation by partial melting in the presence of residual garnet. The REE pattern of RX4548 is interpreted as primary, rather than reflecting alteration by the ore-forming fluids, because the isotopic composition of εNd_{1590} +3.7 is in contrast to the ores' signature of -2.5 (Chapter 7). It is illustrated in Chapter 7 that the calculated εNd_{1590} value of RX4548 is not influenced by a later isotopic resetting event, but probably represents a primary igneous value.

Ocean Island Basalts (OIB), Group I (basaltic) kimberlites and intracontinental rift magmas (nephelinites and carbonatites) share the characteristics of time-averaged depleted Nd signatures and LREE enrichment (Mitchell, 1986; Nelson, 1987; Sun and McDonough, 1989; Wilson, 1989). In contrast, Group II kimberlites and lamproites have negative εNd signatures (Mitchell, 1986) indicating that enrichment in incompatibles occurred well before production of the erupted melt.

The relatively low concentrations of Ti, Zr, and Hf in RX4548 require explanation. If the dykes were sourced from garnet-stable asthenospheric mantle, the low Ti, Zr and Hf imply that residual minerals in the source preferentially retained these elements during a low percentage partial melting episode. Minerals capable of suppressing the amount of Ti, Zr and Hf available to the melt include rutile, ilmenite, clinopyroxene, titanate minerals, kimzeyitic garnets, and crichtonite series minerals (Mitchell, 1986). Sun and McDonough (1989) noted that among samples of OIB and kimberlites with La >50 ppm, it is common to see decoupling and lowering of Ti and Zr (and by implication Hf) from their REE of corresponding incompatibility. Depletions in Zr and Hf relative to Sm are common in kimberlites (Sun and McDonough, 1989). Figure 6.11 shows that the Newlands kimberlite (Group II; Smith, 1983) in South Africa has pronounced negative anomalies for Ti, Zr and Hf and a weak negative Nb anomaly (data from Muramatsu, 1983; Muramatsu and Wedepohl, 1985). These are attributes shared by RX4548, though

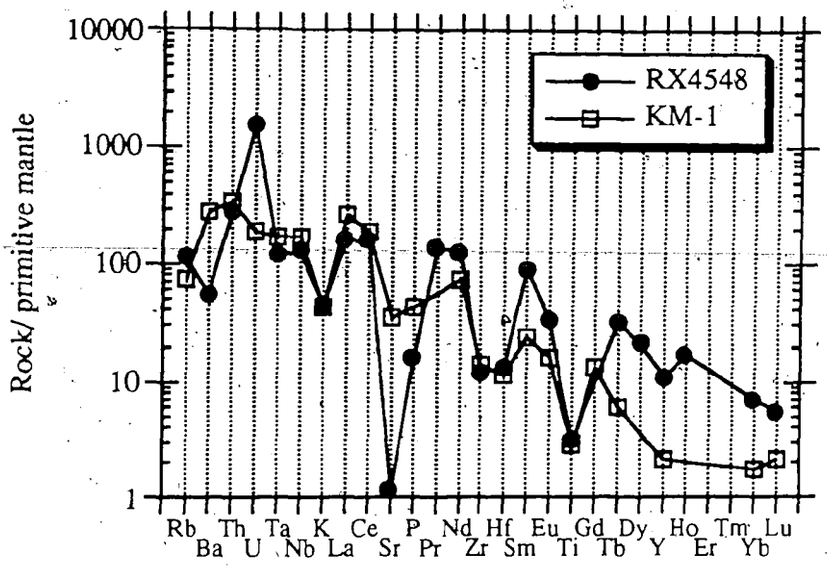

Figure 6.11. Mantle-normalised plot of RX4548 incompatible elements compared to a low-Ti South African kimberlite (Newlands). Note the strong negative Ti, Zr and Hf anomalies in KM-1, similar to those in RX4548. Data from Muramatsu (1983), and Muramatsu and Wedepohl (1985).

to different degrees (Figure 6.11). The depletions of Ti, Zr and Hf in the Olympic Dam dykes are therefore consistent with a kimberlitic affinity.

An alternative interpretation for the low Ti, Zr and Hf is that the magma was derived from shallower depths from "refertilised" refractory (therefore probably lithospheric) mantle. The fluid or melt responsible for the re-enrichment of the refractory source is still constrained to derivation from time-averaged depleted mantle in the presence of garnet and possibly titanate minerals. Such a model evokes comparisons with the petrogenesis of boninites, one of the rock categories implicated by the spinel geochemical comparisons (Section 6.4). Boninites are thought to form when refractory mantle is later enriched by fluids/ melts prior to hydrous melting (Crawford, 1989). Figure 6.12 demonstrates that the concentrations of TiO_2, Zr and Hf in RX4548 are within the range for rocks that have been described as boninitic. Foley and Venturelli (1989) reported ultrapotassic igneous rocks "of similar origin to boninitic rocks" in localities in southeast Spain, the Italian Alps, Tuscany and Algeria. These rocks occur in a post collisional, subduction-related setting. Foley and Venturelli (1989) postulated derivation by hydrous partial melting of peridotitic mantle that had undergone enrichment in LILE after a major depletion event, but before the melting event that produced the ultrapotassic rocks. In this regard it is interesting to note the similarity of the concave downwards LREE patterns for RX4548 and a typical example of the Western Mediterranean lamproites (Figure 6.13; cf. Nixon et al., 1984). These contrast with the more regular patterns of kimberlites. Such

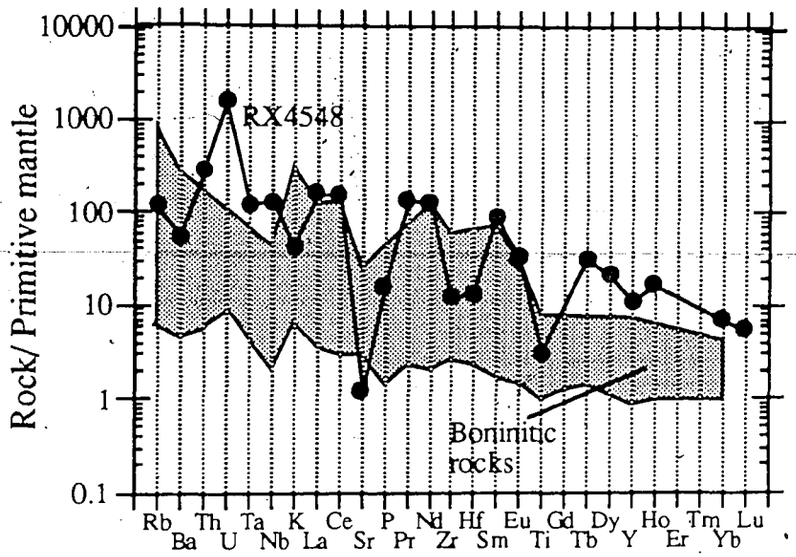

Figure 6.12. RX4548 incompatible elements compared to the broad compositional field for boninitic rocks. The upper bound of this field is defined by data for ultrapotassic boninitic rocks (analysis CL of Foley and Venturelli, 1989); the lower bound is defined by data for a boninite sample from Cape Vogel (analysis 2 of Cameron et al., 1983). Note the pronounced negative Nb anomalies for these analyses, a characteristic of subduction-related magmas. This is not observed for RX4548. The Ti, Zr and Hf concentrations of RX4548 are within the range of boninitic rocks.

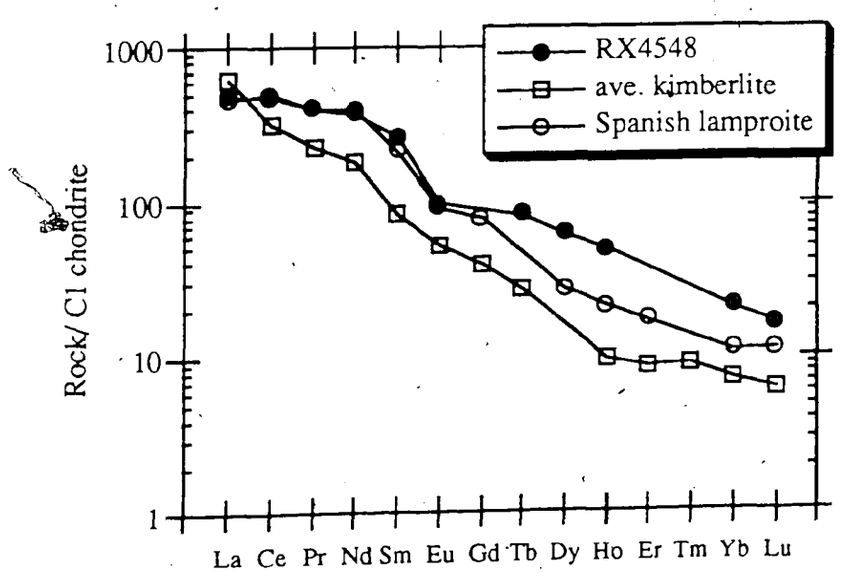

Figure 6.13. Chondrite-normalised REE plot of RX4548 compared to an average kimberlite composition (Rock, 1991) and a representative analysis of ultrapotassic boninitic rocks from southeast Spain (4607 of Nixon et al., 1984; cf. Foley and Venturelli, 1989). RX4548 and the Spanish lamproite have concave downward LREE patterns in contrast to the more fractionated LREE of kimberlites.

similarities might be taken to suggest that the Olympic Dam dykes have been derived by similar processes. However there are significant geochemical and isotopic differences. The analyses used to define the upper and lower bounds of the boninitic field in Figure 6.12 both show more pronounced Nb anomalies than RX4548. Coupled negative Nb and Ti anomalies are a characteristic feature of subduction-related rocks, relative to rocks derived from an OIB-type source. The Western Mediterranean lamproites also have εNd signatures reflecting time-averaged enrichment in LILE (typically εNd = -10; attributed to subducted sediments of continental derivation; Mitchell and Bergman, 1991; Foley and Venturelli, 1989). In contrast, the initial εNd value of +3.7 for RX4548 indicates derivation from time-averaged depleted mantle.

The Olympic Dam deposit and the dykes within it formed as part of the Gawler Range Volcanics event (Chapter 3), an episode of large scale melting of continental crust resulting in bimodal volcanism (dominantly felsic). The regional thermal event has been interpreted as the result of diapiric upwelling of mantle material (i.e. a mantle plume) in an intracontinental setting (Giles, 1988; Creaser, 1989) at 1590 Ma causing incipient rifting. This tectonic setting is inconsistent with derivation of the Olympic Dam dykes by the subduction-related processes of boninite petrogenesis. On the other hand, kimberlitic magmatism in South Africa has been correlated with plume activity by the palaeo-tracks of South Atlantic hotspots, and by comparisons of trace element signatures between kimberlites and their "matching" OIB hotspots (le Roex, 1986). The balance of evidence therefore suggests that boninites, as subduction-related rocks, are not an appropriate analogue for the Olympic Dam dykes, but kimberlites and rocks formed by similar, possibly plume-related processes are. Nephelinites are often associated with intracontinental rifts (eg. East African Rift). As such they too are plausible analogues for the dykes.

6.7 Rock-type: the difficulty in classifying Olympic Dam dykes

The available trace element, Nd isotopic, and spinel chemistry data indicate that, of the possible affinities discussed, the Olympic Dam dykes bear closest similarities to Group I kimberlites and nephelinites. However, they cannot have had kimberlitic major element compositions unless there have been large mass and volume losses accompanying alteration - even for RX4548, the least altered sample. Kimberlites have high MgO and low Al_2O_3 contents (typically 17-30 wt% and 2.5 to 5 wt% respectively; Mitchell, 1986). By comparison RX4548 contains 9 wt% MgO and 11 wt% Al_2O_3. The MgO/TiO_2 versus Al_2O_3 diagram (Appendix 9) shows a trend of MgO loss with increasing alteration. If this trend is extrapolated back to an "unaltered" 5 wt% Al_2O_3 (reasonable for kimberlites), the corresponding MgO content is within the 20-30 wt% range i.e. a plausible kimberlitic composition. If this approximates the pristine

composition, it necessitates approximately 55% mass loss during alteration to increase residual Al_2O_3 to its present concentration. There is no textural evidence in RX4548 to support such a large mass loss. Furthermore, there is no textural evidence of several features characteristic of kimberlites, e.g. megacrysts of ilmenite, diopside or rounded olivine (Mitchell, 1986). The olivine pseudomorphs in RX4548 are euhedral hopper shapes which Mitchell (1986) suggests are "rare in kimberlites but common in lamprophyres, mica peridotites and lamproites". Moreover feldspars, for which there are possible pseudomorphs in RX4548, are absent in kimberlites. It therefore seems that the Olympic Dam dykes cannot be classified as kimberlites, despite the trace element similarities.

The dykes bear trace element similarities to nephelinites. The average nephelinite composition of Wedepohl and Muramatsu (1979) contains 11.64% Al_2O_3, similar to RX4548. It is therefore tempting to suggest that the Olympic Dam dykes may be closely related to nephelinites. However, the SiO_2 content of RX4548 (~54%) is too high to represent a pristine nephelinite composition (~40%; Wedepohl and Muramatsu, 1979). If the dykes are nephelinites, the high SiO_2 of RX4548 must reflect alteration processes. This could result from metasomatic introduction of Si, or its residual concentration as other elements were lost. The gain/loss diagram for SiO_2 (Appendix 9) suggests the latter process is more likely.

An alternative interpretation for the high Al_2O_3 (relative to kimberlites) and high SiO_2 (relative to kimberlites and nephelinites) of the Olympic Dam dykes is that they represent mafic rather than ultramafic melts. In this case the high Cr_2O_3 content of the spinels would reflect a refractory mantle source rather than an ultramafic melt composition. This implies a source in the continental lithospheric mantle. Such a source would require an injection of heat from below to trigger melting, which is consistent with the plume-related tectonic setting (above). Using this model, the time-averaged depleted Nd isotopic signature (εNd +3.7 for RX4548; Chapter 7) coupled with the elevated concentrations of incompatible elements suggests that the lithospheric mantle was enriched by low degree partial melts (and possibly fluids) of asthenospheric origin during the lithospheric melting event. The Olympic Dam dykes could therefore represent hybrid melts, with major element compositions dominated by relatively shallow (lithospheric) mantle, and incompatible trace element compositions dominated by low degree partial melts of garnet-stable asthenosphere.

It is apparent from the above discussion that it is not possible to rigorously classify the Olympic Dam dykes in terms of rock type due to the uncertainty of original mineralogy and major element composition. However, the trace element and isotopic data do place some constraints on the type and origin of the melt.

6.8 Possible correlatives

Alkaline mafic magmatism of comparable age is known elsewhere on the Gawler Craton. Creaser (1989) and Knutson et al. (1992) have reported potassic basalts (referred to as picritic absarokites by Creaser) intercalated with felsic rocks of the 1590 Ma Gawler Range Volcanics at Mount Gunson, 100 km southeast of Olympic Dam. These rocks are less altered than the Olympic Dam dykes and contain phlogopite, relict olivine, clinopyroxene, alkali feldspar, plagioclase and chromian spinel. The spinels are not as Cr-rich as those from Olympic Dam (Cr_2O_3 approx. 20-30 wt%; Cr# 67-82; Creaser, 1989). They have high ZnO and MnO contents which, along with the elevated whole-rock K, Ba, Rb, Th and U, and essential phlogopite, is consistent with a lamprophyric affinity (Rock, 1991). Considering their similarities in age and geochemical affinity, it is possible that the Mount Gunson basaltic rocks are more evolved correlatives of the dykes at Olympic Dam. The composition of the least altered sample from Knutson et al. (1992) is reproduced in Table 6.1 for comparison with RX4548. The two samples show similar concentrations of TiO_2, Zr, P_2O_5, and Ga, but also show many differences. Some of the differences may be primary and others due to alteration (cf Knutson et al., 1992).

6.9 Summary and implications

It is not possible to be specific in classification of the Olympic Dam dykes due to the paucity of primary mineralogy. High Cr and Ni contents indicate that they were high-MgO (ultramafic) melts, or mafic melts derived from refractory mantle. The available evidence indicates that the parent magma had strongly alkaline affinities similar to kimberlites, nephelinites and ultramafic lamprophyres. It was derived from either:

A) a low degree partial melt of asthenospheric mantle in the presence of residual garnet and a mineral that retains Zr, Hf and Ti, possibly a titanate and/ or Ti-rich clinopyroxene, or

B) a refractory lithospheric mantle source that had undergone re-enrichment shortly before or during the melting event that produced the magma (i.e. similar to boninite petrogenesis but in an intracontinental setting). The enriching fluid/melt is constrained to have a similar source to that described in A).

Option A is simpler, and implies that the dykes are closely related to nephelinites (rather than kimberlites; see Al_2O_3, above). Option B is more complex and somewhat ad hoc, but nevertheless cannot be discounted. Both models are consistent with the accepted plume-related tectonic setting of the Gawler Range volcanic event.

Despite the occurrence of the alkalic Mount Gunson basalts (above), the "non-felsic" component of the Gawler Range Volcanics is dominated by tholeiitic basaltic rocks which

Giles (1988) interpreted to be derived from lithospheric mantle at relatively shallow depths (<60 km). These are likely to have been melts produced by the upwelling mantle plume material that is believed to have caused the large scale crustal melting at 1590 Ma. The alkaline mafic/ultramafic intrusives within the Olympic Dam Breccia Complex are not typical of the Gawler Range Volcanics. Indeed it may be that their localised occurrence is essential for the formation of the Olympic Dam deposit. Their spatial association with the deposit provides a potential source for the observed enrichments of REE, Y, Ba, Nb, Cr, Ni, V and of course Cu in the deposit (Chapter 5). The isotopic data presented in Chapter 7 indicate that these rocks have played an important role in Olympic Dam ore genesis. If lamprophyric, these magmas are likely to be volatile-rich and prone to explosive emplacement (e.g. the diatremes within the deposit and possibly the breccia complex itself). Any fluids exsolved from such magmas may also have had the capacity to transport the elements listed above. This model, which invokes a contribution from lamprophyre-derived magmatic volatiles, is in contrast to the "two-fluids" ore genesis model of Haynes et al. (submitted) who suggest that the involvement of mafic (basaltic) rocks dominantly through the leaching of a bimodal volcanic pile. It is important to note that the evidence for the presence of mafic/ ultramafic lamprophyric intrusions within the deposit does not disprove the model of Haynes et al. Although volatile-rich lamprophyric/ kimberlitic magmas are unlikely to form extensive flows within bimodal volcanic complexes, there may have been more typical "Gawler Range-type" basaltic flows above the deposit to provide a leachable source of some of the elements in the deposit. The "two-fluids" model and the possible role of exsolution of volatiles from mafic/ ultramafic lamprophyric magmas are discussed in Chapter 8.

7 RADIOGENIC ISOTOPE GEOCHEMISTRY

7.1 Introduction

In Chapter 3 the age of the hematite-producing hydrothermal system at Olympic Dam was established as ~1590 Ma. Moreover, from the inferred cogenesis of the bornite-chalcocite ores and the hematite-quartz breccias (based on HREE geochemistry and complementary zone morphologies; see Section 5.9.3), the diatreme tuff age of 1597 ± 8 Ma can be interpreted as a minimum age for the bornite-chalcocite ores. This means that the age of all of the major ore types at Olympic Dam is constrained to be ~1590 Ma. With this knowledge it is possible to calculate and compare the initial (1590 Ma) ratios for other radiogenic isotope systems for all of the ore and breccia types, and that is the subject of this chapter. Comparison of initial ratios between the various ores and breccias reveals which rock types may share a common genesis and which have distinct origins.

Another important issue pertinent to Olympic Dam ore genesis models is the source of ore metals. From the range of rock types within the deposit and the surrounding region, the principal candidates for metal sources include the host granite and related rocks of the Burgoyne batholith, the mafic/ultramafic intrusives within the deposit or their plutonic or extrusive equivalents, and a regionally extensive red-bed sandstone (the Pandurra Formation) which unconformably overlies basement rocks over much of the Stuart Shelf to the west of the Olympic Dam deposit. The involvement of a mafic source rock for the metals has been suggested by Roberts and Hudson (1983) and Reeve et al. (1990). Oreskes and Einaudi (1990) invoked a magmatic heat source and dismissed the Roxby Downs Granite as a possible metal source on the basis of contrasting REE patterns for altered and unaltered granite. Oreskes and Einaudi (1992) used fluid inclusion and oxygen isotope data to suggest that the involvement of a surface derived water mixing with a metal-bearing magmatic derived water may have been important to ore genesis, but did not comment on the petrological affinity of the magmatic source. The speculation about possible sources of ore metals is investigated in this chapter by isotopic tracing techniques.

As discussed in Chapter 5, altered and mineralised rocks of the Olympic Dam Breccia Complex are strongly enriched in LREE. This makes the Sm-Nd isotope system ideal for tracing studies, and this system is discussed in parts 7.3 and 7.4 of this chapter. In Chapter 5 it was also established that Sr was introduced to the deposit during ore deposition. For this reason the Rb-Sr isotopic systematics have also been investigated (Section 7.5). The samples analysed are representatives of the lithological categories used for geochemical discussion in Chapters 5 and 6.

7.2 Analytical methods

Rb-Sr and Sm-Nd isotopic compositions were determined for 32 whole-rock samples and one mineral separate. Samples were dissolved using HF and HNO_3 in teflon bombs at 200° C followed by treatment with $HClO_4$. Many Olympic Dam samples were also placed in bombs overnight at 200° C in 6N HCl to dissolve the high concentrations of iron oxide minerals. Samples were spiked using ^{147}Sm-^{150}Nd and ^{85}Rb-^{84}Sr tracers. Samples with very high REE concentrations were diluted before aliquots containing ~2μg Nd were spiked in order to avoid using impracticably large volumes of spike solution. This procedure introduces a potential source of error if the sample is not fully dissolved prior to aliquotting. A clear solution is therefore necessary prior to dilution, and data require careful scrutiny to check that the element concentrations as determined by isotope dilution are in agreement with determinations by independent methods. Sm, Nd and Sr isotopic ratios were measured using a Finnigan MAT 261 multicollector mass spectrometer in static mode with samples loaded on Ta filaments and with Re ionisation filaments. The $^{143}Nd/^{144}Nd$ ratios have been corrected for mass discrimination by normalising to $^{146}Nd/^{144}Nd = 0.7219$. The errors quoted for $^{143}Nd/^{144}Nd$ ratios in Table 7.1 are as measured, and most vary only in the sixth decimal place. However, the reproducibility of the ratio for the standard "nNd-1" over the year in which the analyses of unknowns were carried out was ~± 0.000010 (2σ; n=87), and this figure is therefore regarded as a more realistic estimate of the error. This translates into an error in initial ratios (at 1590 Ma) equivalent to ±0.2 ε units. Measurements of the La Jolla international standard during the period of sample analyses yielded a mean $^{143}Nd/^{144}Nd$ of 0.511884 ± 8 (2σ mean; n=23); the cited error reflects external reproducibility rather than in-run precision. Sample/ blank ratios for Nd were all above 25,000 and most were above 100,000 and consequently have been ignored. Initial $^{143}Nd/^{144}Nd$ ratios are expressed in ε notation (De Paolo and Wasserburg, 1976) as deviations from a model primitive mantle (CHUR) where

$$\varepsilon_{Nd} = \left[\frac{(^{143}Nd/^{144}Nd^{T}_{sample})}{(^{143}Nd/^{144}Nd^{T}_{CHUR})} - 1 \right] X\ 10^{4}$$

and $(^{143}Nd/^{144}Nd)^{T}_{CHUR} = (^{143}Nd/^{144}Nd)^{0}_{CHUR} - (^{147}Sm/^{144}Nd)^{0}_{CHUR} .(e^{\lambda t}-1)$.

T represents any designated point in time. The present day values used for CHUR are: $^{143}Nd/^{144}Nd = 0.51265$, and $^{147}Sm/^{144}Nd = 0.1967$; The decay constant used for ^{147}Sm is $\lambda = 6.54 \times 10^{-12} y^{-1}$. Regression analysis was performed using the program "Isoplot" (Ludwig, 1992).

The Sm-Nd data have been presented previously in conference proceedings (Johnson and Cross, 1991b) with initial ε values calculated using $CHUR_0$ $^{143}Nd/^{144}Nd = 0.512638$ (Wasserburg et al., 1981; Faure, 1986) rather than the value mentioned above. The revised εNd (1590 Ma) values quoted in this study differ by approximately 0.2 ε units from those presented in Johnson and Cross (1991b).

Measured Sr ratios were normalised to $^{86}Sr/^{88}Sr = 0.1194$. The decay constant used for ^{87}Rb is $\lambda = 1.42 \times 10^{-11} y^{-1}$. Rb isotopic ratios were measured using the MSZ mass spectrometer (Clement and Compston, 1972) with sample loaded on Re triple filaments.

7.3 Sm-Nd systematics

7.3.1 Olympic Dam breccias

The Sm-Nd isotopic data for all analyses in this project (including initial $^{143}Nd/^{144}Nd$ ratios expressed in ε units and calculated for an age of 1590 Ma) are listed in Table 7.1 and 7.2. The data are displayed in Figure 7.1, a plot of initial εNd versus copper concentration, which illustrates several important aspects of the genesis of the deposit.

7.3.1.1 The "Ore Envelope"

Most of the hematite-rich rocks analysed have εNd-values in the range -2 to -3 and this field is labelled as the "Ore envelope" in Figure 7.1. The samples within it have a mean εNd value of -2.5 and include four samples of bornite-chalcocite ore, three samples of chalcopyrite-rich ore, two samples of pyrite-rich ore, a leached hematite breccia, a hematite-quartz breccia, and a silicified hematite-quartz breccia. The three chalcopyrite-rich ores, RX4512, RX4542 and RX4508 have initial εNd signatures (-2.4, -2.3 and -2.6 respectively) close to the mean value. The pyrite-rich ore samples RX4529 and RX4531 have values of -3.2 and -2.0, more divergent from the mean εNd value of -2.5 and possible reasons for this are discussed below. The similarity in Nd isotopic compositions within the ore envelope spans a very wide range of copper concentrations (~100 ppm to ~175,000 ppm). It indicates that all of these samples share a common source of LREE and can therefore be interpreted as cogenetic. This has particular relevance to the comparison between Cu ores and hematitic breccias with low Cu concentrations. In Chapter 5 (Figure 5.17) a positive correlation between Nd and Cu was illustrated for pyrite-rich and chalcopyrite-rich ores (including magnetite-rich breccias). This was interpreted to indicate that LREE were precipitated in greater quantity during Cu-mineralisation than during pyrite precipitation. Considering the observation that, on a local scale, Cu minerals are often paragenetically later than hematite, the fact that barren hematite-rich breccias and Cu-mineralised breccias have approximately the same Nd isotopic signature (Figure 7.1) indicates that the LREE introduced during

Table 7.1. Samarium - Neodymium isotopic data.

Sample No.	Lithology	Sm (ppm)	Nd (ppm)	$^{147}Sm/^{144}Nd$	$^{143}Nd/^{144}Nd(t_0)$[a]	$\varepsilon_{Nd(0)}$[b]	ε_{Nd}(1590 Ma)[b]
RX4536	Magnetite breccia	33.57	192.4	0.1055	0.511446 ± 6	-23.5	-4.9
RX4537	Magnetite breccia	34.36	350.5	0.0593	0.511108 ± 6	-30.1	-2.1
RX4529	Pyrite-rich ore	18.41	140.1	0.0794	0.511263 ± 8	-27.1	-3.2
RX4531	Pyrite-rich ore	8.39	84.5	0.0600	0.511120 ± 7	-29.9	-2.0
RX4512	Chalcopyrite-rich ore	42.33	449.3	0.0570	0.511068 ± 8	-30.9	-2.4
RX4542	Chalcopyrite-rich ore	107.95	1275.5	0.0512	0.511014 ± 10	-31.9	-2.3
RX4508	Chalcopyrite-rich ore	42.90	474.7	0.0546	0.511031 ± 7	-31.6	-2.6
RX4511	Bornite-chalcocite ore	51.65	506.3	0.0617	0.511099 ± 7	-30.3	-2.7
RX4513	Bornite-chalcocite ore	6.15	55.4	0.0672	0.511282 ± 9	-26.7	-0.3
RX4559	Bornite-chalcocite ore	40.23	836.5	0.0291	0.510785 ± 8	-36.4	-2.2
RX4462	Bornite-chalcocite ore	47.98	456.9	0.0635	0.511108 ± 7	-30.1	-2.9
RX4463	Bornite-chalcocite ore	95.16	752.1	0.0765	0.511251 ± 9	-27.3	-2.8
RX4510	Leached hem.breccia	40.39	376.9	0.0648	0.511149 ± 10	-29.3	-2.4
RX4509	Heterolithic breccia	35.13	348.5	0.0609	0.511037 ± 6	-31.5	-3.8
RX4514	Hem-qz sandstone	2.50	57.3	0.0264	0.510733 ± 6	-37.4	-2.7
RX4502	Hem-qz breccia	51.02	684.2	0.0451	0.510932 ± 7	-33.5	-2.6
RX4503	Silic.hem-qz breccia	21.59	284.3	0.0459	0.510942 ± 6	-33.3	-2.6
SS-87[d]	Granite - fresh[d]	12.55	72.12	0.1052	0.511437 ± 7	-23.7	-5.0
RX3698	Granite - sericitised	1.83	11.2	0.0988	0.511424 ± 6	-23.9	-4.0
RX4533	Granite - sericitised	21.68	205.9	0.0636	0.511087 ± 7	-30.5	-3.4

Table 7.1 contd.

Sample No.	Lithology	Sm (ppm)	Nd (ppm)	$^{147}Sm/^{144}Nd$	$^{143}Nd/^{144}Nd(t_0)$[a]	$\varepsilon_{Nd(0)}$[b]	$\varepsilon_{Nd}(1590\ Ma)$[b]
RX3213	Granite - chloritised	11.19	117.9	0.0574	0.510981 ± 7	-32.6	-4.2
RX3214	Granite - chloritised	6.49	40.8	0.0961	0.511421 ± 6	-24.0	-3.5
RX4548	Ultramafic dyke	38.22	174.3	0.1325	0.512170 ± 9	-9.4	3.7
RX4566	Ultramafic dyke	61.01	237.7	0.1552	0.512223 ± 6	-8.3	0.1
RX4546	Ultramafic dyke	22.35	177.6	0.0763	0.511417 ± 8	-24.1	0.5
RX4539	Ultramafic dyke	83.14	93.6	0.5374	0.514285 ± 6	31.9	-37.7
RX4543	Ultramafic dyke	33.07	178.2	0.1122	0.511970 ± 8	-13.3	4.0
RX4547	Ultramafic dyke	119.38	894.0	0.0807	0.511444 ± 6	-23.5	0.1
Mineral separates							
RX3184	Hematite	8.05	77.3	0.0629	0.511132 ± 7	-29.6	-2.3
RX3184	Magnetite	30.73	188.4	0.0986	0.511421 ± 8	-24.0	-4.0
Regional lithologies							
RX4570	Pandurra Fmn. sst.	7.22	39.8	0.1096	0.511582 ± 9	-20.8	-3.1
RX4571	Pandurra Fmn. sst.	5.71	31.8	0.1085	0.511866 ± 10	-15.3	2.7
RX4577A	Acropolis magnetite	44.82	288.6	0.0939	0.511407 ± 10	-24.3	-3.3

a. Measured values with 2σ errors, normalised to $^{146}Nd/^{144}Nd = 0.7219$.

b. $\varepsilon_{Nd}(t_0)$ refers to the present day, $\varepsilon_{Nd}(1590Ma)$ calculated at the age of the deposit, 1590 Ma.

c. ε_{Nd} calculated using the following present day values for CHUR: $^{147}Sm/^{144}Nd = 0.1967$ and $^{143}Nd/^{144}Nd = 0.512650$; $\lambda^{147}Sm = 6.54 \times 10^{-12}\ y^{-1}$.

d. Denotes data from Creaser (1989).

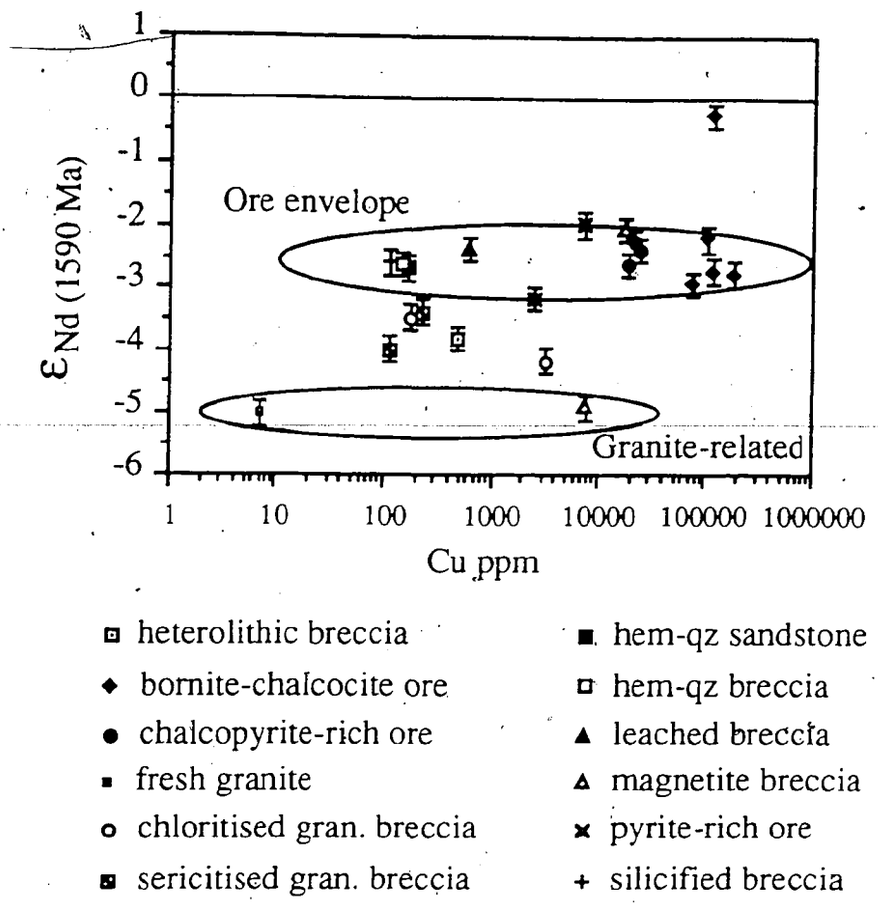

Figure 7.1 εNd, calculated for 1590 Ma, versus Cu concentration. Note the hematitic breccias and ores have similar initial signatures at εNd = ~-2.5 (labelled "Ore envelope"), which indicates a shared source of Nd. The magnetite breccia signature of -4.9 is indistiguishable from the fresh granite signature of -5.0 indicating that the magnetite-rich assemblage is cogenetic with the Roxby Downs Granite or other members of the same batholith, rather than with the hematitic rocks. The contrasting signature of the hematiic breccias and ores demonstrates the contribution of REE from a source more primitive than the host granite during ore genesis.

The data plotting between the "Ore envelope" and "Granite-related" fields have hybrid signatures due to contributions from both the granite and the ore Nd signatures. A single sample of bornite-chalcocite ore has a more positive εNd value (-0.3) than the other samples. Geochemical evidence (high V contents and similar LREE pattern to the mafic/ ultramafic dykes; Chapters 5 and 6) suggest the sample represents hematite replacement of dyke material. This explains the distinct Nd signature. Data for all samples are discussed more fully in the text.

hematite-precipitation are derived from the same source as the LREE introduced in greater concentrations somewhat later during deposition of chalcopyrite. This implies that the sequential deposition of hematite and Cu-sulphides is a manifestation of a single evolving hydrothermal system rather than being evidence of temporally separate overprinting systems.

Four of the bornite-chalcocite ores analysed plot within the ore envelope in Figure 7.1 (RX4462, RX4463, RX4511, RX4559). They have εNd values of -2.9, -2.8, -2.7 and -2.2 respectively. In Chapter 5 two competing models for the origin of the bornite-chalcocite ores (single stage versus multi-stage) were discussed with particular reference to differences in REE patterns between these ores and the chalcopyrite-rich ores. The fact that these ores have Nd isotopic signatures similar to the chalcopyrite ores and other hematitic breccias is readily explained by a single predominant REE source in a single-stage ore genesis. Considering the 1590 Ma age of the bornite-chalcocite ores (mentioned at start of this chapter; see also Section 5.9.3), if the multi-stage (supergene) model is correct, modification of a primary ore must have occurred at an age not resolvably younger (by the present U-Pb zircon methods) than primary ore formation. The REE geochemical evidence (HREE enrichment) and Nd isotopic data indicate that if the multi-stage model is correct, the enrichment event has mobilised HREE and possibly LREE, but without introducing LREE from any exotic source.

A sample of hematite-quartz breccia (RX4502) has an εNd value of -2.7 (Figure 7.1). As discussed in Section 5.9.3, these breccias are interpreted as having formed from heterolithic and hematitic breccias which have undergone leaching from above by a sulphate-rich fluid such that all aluminosilicates have been replaced by hematite, and Cu, U, HREE, Y, Zr, Nb, Ba and Sr have been remobilised downwards. This occurred either during the waning stages of the primary mineralisation events (Haynes et al., submitted) or during a later supergene weathering event (Oreskes and Einaudi, 1990).

The low level of HREE in RX4502 and other hematite-quartz breccias (RX4501, RX4503; cf. Figure 5 of Oreskes and Einaudi, 1990), relative to most of the hematitic breccias analysed, may be the complement of the HREE enrichment observed in the bornite-chalcocite ores which lie below, and mimic in form, the outline of the hematite-quartz breccia zone. This implies that the two rock types formed during the same leaching and reprecipitation processes (Section 5.9.3). Their similarity in Nd isotopic signatures is consistent with the model of Haynes et al. (submitted) which suggests that the hematite-quartz breccias formed as the final stage of primary mineralisation. If the supergene model is correct, the Nd data imply that Nd was not introduced from any exotic source (outside the deposit) during the REE-mobilising leaching event (see discussion of bornite-chalcocite ores, above).

RX4503 is a sample of a hematite-quartz breccia that has undergone silicification; it has an εNd signature of -2.6, the same as that of its unsilicified equivalent, RX4502 (see "silicified breccia", Figure 7.1). This indicates that the silicification process did not remobilise LREE and is consistent with the parallel nature of the REE patterns for these two samples (Figure 5.16 F).

A sample of laminated hematite-quartz sandstone (RX4514) has an εNd value of -2.7 (Figure 7.1). The fact that this signature is identical to those of the ores and other hematitic breccias indicates that these sedimentary rocks are an integral part of the deposit, and is consistent with the interpretation presented in Chapter 3 that they represent the surficial (crater) facies of a venting hydrothermal system.

RX4510 is a sample of leached hematitic breccia from ~10m below the unconformity, and above a bornite-chalcocite ore zone in Mine Area DNW (see cross-section, Figure 5.18). It has an εNd value of -2.4, similar to the Cu ores and other hematitic breccias (Figure 7.1). Its REE pattern shows a steep LREE trend and an inflexion towards strong HREE enrichment (Figure 5.16 G). The leaching which has affected this sample may or may not be related to the HREE enrichment (see Section 5.8.4), but it has apparently not affected the initial εNd value which indicates cogenesis of this rock type with the other hematitic ores and breccias.

7.3.1.2 Granite-related signatures

One sample of unaltered Roxby Downs Granite and four samples of variably altered Roxby Downs Granite are plotted on Figure 7.1. The sample of unaltered granite (SS-87; data from Creaser, 1989) has an initial εNd value of -5, well below the ore envelope. This demonstrates that the host granite cannot have been the sole source of the REE, and therefore of the mineralising fluids, at Olympic Dam.

One sample (RX4536) of the paragenetically early magnetite-siderite-pyrite assemblage, which occurs in a restricted zone on the eastern side of the deposit, has an εNd value of -4.9. This is the same signature within error as the Roxby Downs Granite, suggesting that the magnetite assemblage is derived from fluids in isotopic equilibrium with the granite. However, a second sample of magnetite-rich breccia (RX4537) has an initial εNd value of -2.1. This sample shows more extensive hematite replacement of magnetite and chalcopyrite replacement of pyrite than is observed in RX4536 (Plate 7; see also paragenetic relationships, Section 5.2), and the REE patterns in Figure 5.16.A illustrate that this overprinting has been accompanied by LREE enrichment. It is therefore believed that the Nd isotopic signature of RX4537 reflects the LREE introduced during alteration of the sample. To test this hypothesis, mineral separates of magnetite and hematite were analysed from a single sample (RX3184; the sample was received as prepared mineral

separates and no whole rock analysis has been performed). The hematite separate has an εNd signature of -2.3 (Table 7.1), consistent with the hematitic ores plotted in Figure 7.1. In contrast, the magnetite grains, which unavoidably contained minor secondary hematite, have a lower εNd value of -4.0 (Table 7.1). This value is consistent with the pristine magnetite assemblage in this sample having a Nd signature such as that of RX4536 (~-5), with minor alteration to hematite accompanied by LREE-enrichment causing a shift in isotopic composition towards εNd -2.3. The initial εNd signature of -4.9 for the magnetite-siderite-pyrite breccias indicates that these breccias were in isotopic equilibrium with the Roxby Downs Granite or related plutons, perhaps being derived from magmatic fluids associated with the granite or the other more mafic members of the same suite.

7.3.1.3 Hybrid signatures

The samples of sericite-altered granite (RX3698; RX4533, a gold ore) and chlorite-altered granite (RX3213 and RX3214) have isotopic compositions intermediate between the fresh granite signature and the ore signature. The fact that sericitic and chloritic alteration processes have both moved the Nd isotopic signature from granitic (-5) towards the ore signature (-2.5) suggests that both alteration styles are accompanied by introduction of Nd from the same source. Geochemical evidence presented in Chapter 5 (FeO, Ni and MnO enrichments) suggested that chlorite alteration was effected by different fluids to those responsible for sericitic and hematitic alteration. The Nd data are ambiguous in this regard. They are permissive of, but do not support, models attributing sericite and chlorite alteration to different fluids. If, as suggested in Chapter 5, chlorite alteration was caused dominantly by reduced fluids associated with magnetite precipitation, it is paradoxical that the Nd isotopes demonstrate an input of REE from a source with more positive εNd values than the magnetite (and granite) signature of -5. This may be a function of mixing between a reduced fluid with a relatively low LREE concentration and εNd of -5, and an oxidised fluid with a higher LREE concentration and εNd of -2.5.

A sample of heterolithic breccia (RX4509; see cross-section, Figure 5.18) containing clasts of both granite and hematite has an εNd value of -3.8, intermediate to the end-member granite and hematite signatures and reflecting the mixture of these components.

One of the samples of pyrite-rich ore (RX4529) has an εNd signature of -3.2, the lowest value of the samples grouped in the ore envelope on Figure 7.1. Hematite is the dominant oxide in this sample but within the hematite grains there are many fine inclusions of magnetite (see Plate 7; cf. Section 5.2), suggesting that hematite has replaced magnetite in this locality. Moreover, this sample contains ~25% siderite, a mineral typically associated with the paragenetically early magnetite. It is therefore

suggested that the εNd signature, which is relatively low for a hematite-dominant rock, is a mixed signature due in part to the magnetite-siderite assemblage, but dominated by the overprinting hematitic signature.

A single sample of bornite-chalcocite ore (RX4513) has an initial εNd signature of -0.3. It is one of three samples (the other samples are RX4462 and RX4463) taken from an ore zone in Mine Area DNW that has been suggested to have undergone supergene weathering and enrichment processes (Oreskes and Einaudi, 1990), but the other two samples have more typical ore εNd signatures of -2.9 and -2.8. This sample has the highest vanadium content of any of the breccias analysed (101 ppm) and the only rocks in the present study which overlap with and exceed this concentration are the mafic/ultramafic dykes (see Chapter 6). The dykes (with one exception; see Sections 7.3.2 and 7.4.2) vary in εNd values from +0.1 to +4.0. The Nd signature of RX4513 (-0.3) is therefore intermediate between the ore signature and those of the mafic/ultramafic dykes. Considering its elevated vanadium content and the similar concave downwards LREE patterns of the dykes and RX4513 (cf. Sections 5.8.2.3 and 6.6), it is possible that RX4513 represents an ore which has replaced dyke material, producing a hybrid εNd signature. The Nd isotopic evolution trajectory for this sample (discussed in Section 7.4.2) is consistent with this hypothesis.

RX4531, a pyrite-rich ore, has an εNd signature of -2.0 which is slightly less negative than most other members of the ore envelope. This too may reflect a component of replaced mafic/ultramafic dyke.

In summary, Figure 7.1 allows the identification of two distinct Nd signatures:

a) The hematitic/ ore signature of εNd = -2.5, and

b) The granite/ magnetite signature of εNd = -5.

It also allows the recognition of systematic variations in isotopic composition which are attributable to mixtures of the end-member signatures. The isotopic analyses for the samples of Olympic Dam ores and breccias are plotted on an isochron diagram in Figure 7.2. Most of the samples fit closely to a 1590 Ma reference line (drawn through an initial $^{143}Nd/^{144}Nd$ equivalent to εNd -2.5), and these have have been used to calculate a fourteen point isochron age of 1572 ± 99 Ma (95% confidence; Model 3, MSWD 8.17). The data which lie well off the line (Figure 7.2) and which have been excluded from the age calculation are from samples which have mineralogical and/ or geochemical differences from the hematitic breccias. These include samples with a substantial granite component (RX4533, RX3698, RX3213, RX3214, SS-87, RX4509), and the magnetite and/or siderite-rich samples RX4536 and RX4529. RX4513, a sample of bornite-chalcocite ore which is interpreted to have replaced mafic/ultramafic dyke material (above)

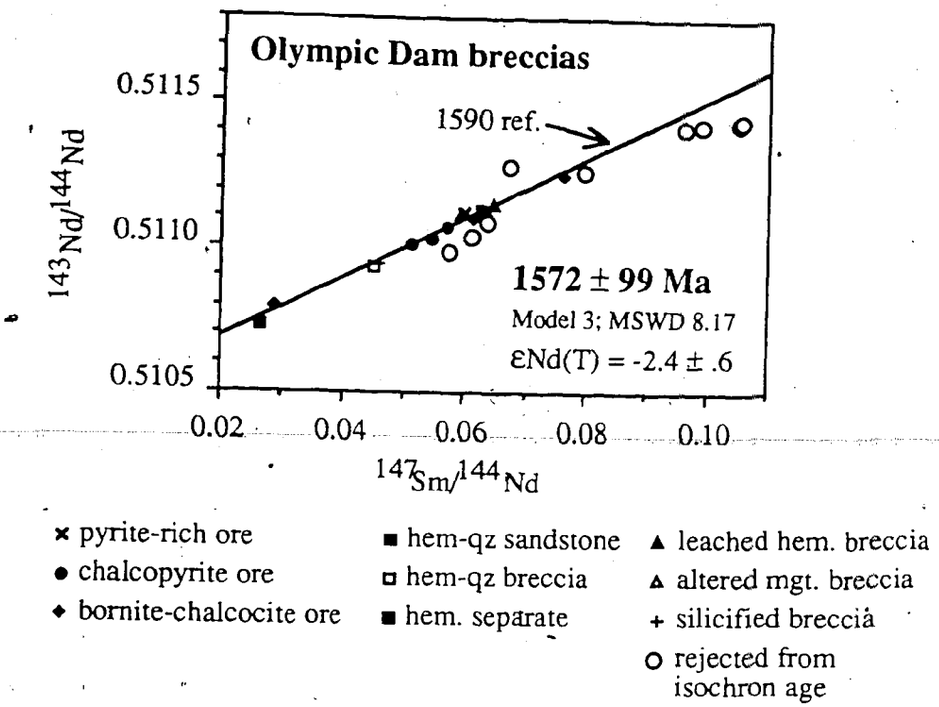

Figure 7.2 Sm-Nd isochron plot for the Olympic Dam hematitic breccias and ores. Most samples fit well to the 1590 Ma reference line. Those which do not (open circles) are samples containing a high proportion of granite or magnetite+siderite, or show geochemical evidence of replacement of a mafic/ ultramafic precursor (RX4513; see text). The remaining samples yield a fourteen point Model 3 isochron age of 1572 ± 99 Ma (95% confidence, MSWD 8.17). Although much less precise, this age is consistent with the age of the breccia complex determined by U-Pb zircon dating (Chapter 3).

has also been rejected from the age calculation. The isochron age of 1572 ± 99 Ma is consistent with the age determined by U-Pb zircon methods (Chapter 3).

7.3.2 Olympic Dam intrusives

7.3.2.1 Mafic/ultramafic dykes

As discussed in Chapter 6, the alkaline mafic/ultramafic dykes which intrude the Olympic Dam Breccia Complex are invariably composed of an alteration assemblage dominated by chlorite, sericite and quartz. The high Cr and Ni contents of the least altered of the sample, RX4548 (2510 and 980 respectively), suggest that the more primitive dykes are ultramafic. Sm-Nd isotopic analyses for the six dyke samples are presented in Table 7.1. RX4539 yielded anomalous isotopic characteristics relative to the other samples, and is therefore discussed separately (Section 7.4.2). The other samples have initial εNd signatures ranging from +0.1 to +4.0. RX4548 was nominated as the least altered dyke sample on the basis of its relatively low Al_2O_3 content (residual Al_2O_3) and its well preserved igneous textures (Chapter 6). This sample has an εNd initial value of +3.7. RX4543, which is deformed and shows geochemical evidence of greater alteration, has a similar signature (+4).

The isotopic data for the dykes sampled in this study and for four samples of mafic/ultramafic clasts from a diatreme zone (analysed by Wawryk, 1989) are presented on a plot of εNd versus 1/Nd in Figure 7.3. The linear array of data for three of the dyke samples (RX4543, RX4548 and RX4566) and three samples from Wawryk (1989; IL, BAS, and LCGS) illustrate that the range in isotopic compositions is a result of mixing of two REE sources.

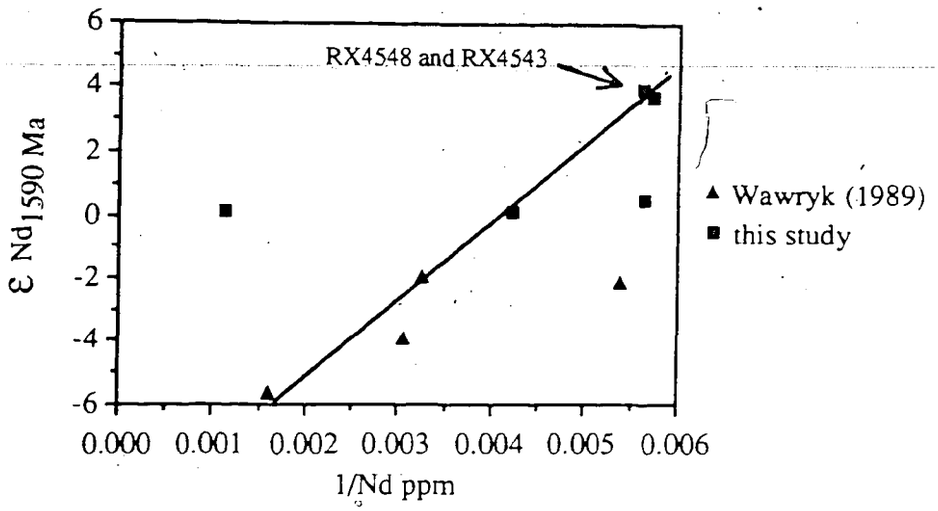

Figure 7.3 εNd_{1590} plotted against inverse Nd concentration for five samples of mafic/ ultramafic dykes from this study (RX4539 omitted due to evidence of isotopic resetting; see 7.4.2), and four samples of mafic/ ultramafic cobbles from an Olympic Dam diatreme zone (Wawryk, 1989). The regular covariation of isotopic composition with Nd concentration for six of the samples indicates mixing of two Nd sources at 1590 Ma. The mixing array is attributed to fluxing of dykes with unaltered signatures of approximately +4 (e.g. RX4548 and RX4543), with fluids in isotopic equilibrium with the host granite or its volcanic equivalents. Those analyses lying off the mixing line may have assimilated varying proportions of wallrock, itself a heterogeneous mixture of hematitic breccias and Roxby Downs Granite, leading to irregular hybrid Nd isotopic signatures and Nd concentrations. The regular variation of most of the samples suggests that the least altered end-member samples, RX4548 and RX4543, have not been isotopically reset after 1590 Ma. The mixing array also indicates that the 1360 Ma four point "isochron age" of Wawryk (1989) has no geological significance.

The upper end-member of the mixing line is defined by the mafic/ultramafic melt composition. The lower end-member has a similar isotopic signature to the Roxby Downs Granite, which suggests that this sample has been extensively fluxed by fluids in isotopic equilibrium with the granite or its cogenetic volcanics. The mixing line is probably the result of hydrothermal alteration rather than wallrock assimilation. In contrast, the samples which lie off the mixing line probably do so because of variable assimilation of wallrock. This could have occurred at depth in the parent magma chamber, or by assimilation of hematitic breccia wallrock.

The regular variation of εNd values calculated for an age of 1590 Ma for six of the samples (Figure 7.3) indicates that the signature of +4 for RX4543 and RX4548 is not the product of isotopic disturbance at a later time and may be close to the magmatic initial value. This signature is in marked contrast to the ore signature of -2.5, indicating that the high REE concentrations in these samples are not a product of alteration, but are a primary igneous feature. The mixing array also demonstrates that the "isochron age" of 1360 Ma calculated by Wawryk (1989) has no geological significance.

The signature of +4 shared by RX4543 and RX4548 is evidence that the parent magma for these dykes was derived from a mantle source with a time-averaged depleted signature. These are the most positive εNd values yet measured for magmas produced in the Gawler Range volcanic event (one basalt sample from the Kokatha area has an εNd_{1590} value of +2.5; S-S Sun, pers. commun.). However, an εNd signature of +4 is not implausibly high. Constraints on the isotopic composition of depleted mantle are provided by analyses of samples of komatiites (of probable Archaean age) from cores drilled near Lake Harris in northern South Australia. These yield εNd_{1590} values of +5 to +7 (M.Fanning, unpublished data).

7.3.2.2 Dolerites

Dolerite is known in drillcore at Olympic Dam but has not been exposed in underground workings. Consequently it is not known from field relations whether the dolerite intersections are from separate dykes or a single plug. The relatively unaltered state of much of the dolerite (dominantly clinopyroxene and plagioclase) and the intrusive relationships observed in drillcore suggest that these rocks are considerably younger than the Olympic Dam Breccia Complex. The dolerites were analysed as part of the isotopic study because of the possibility that they contributed REE during any isotopic resetting of ores and breccias which may have resulted from dolerite emplacement. Creaser (1989) equated the Olympic Dam dolerites with the Gairdner dyke swarm which is known from drillcore and geophysics throughout much of the Stuart Shelf province. Recent Sm-Nd dating of dolerite dykes from the Gairdner dyke swarm reveals that these dolerites have an age of 867 ± 47 Ma, whereas dolerites from the Stuart dyke swarm in the Arunta Inlier and the Kulgera dyke swarm in the Musgrave Inlier have ages of 1076 ± 33 Ma and 1090 ± 32 Ma respectively (Zhao and McCulloch, 1992a). Both of these inliers lie to the north of the Gawler Craton. A three-point Rb-Sr mineral - whole-rock isochron for one dolerite sample from Olympic Dam yielded an age of 1059 ± 60 Ma (Creaser, 1989) and this suggests that the Olympic Dam dolerite is correlated with the mafic magmatic event which produced the Kulgera and Stuart dyke swarms rather than the younger Gairdner swarm.

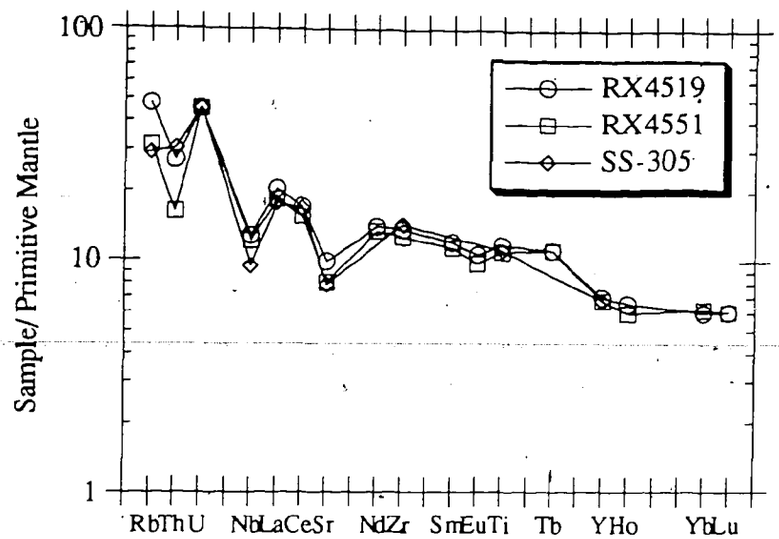

Figure 7.4 Mantle-normalised plot of the incompatible element compositions of dolerite samples from Olympic Dam. The similarity of geochemical signatures indicates that the three samples are from the same generation of dolerite. The "RX" samples are from this study; SS-305 is the sample dated at 1059 ± 60 Ma by Creaser (1989; three-point mineral-whole-rock Rb-Sr isochron). Mantle normalising values of Ringwood (1991).

Two samples of dolerite from Olympic Dam (RX4519 and RX4551) have been analysed for whole-rock Sm-Nd isotopic compositions. RX4551 was taken from a drill intersection adjacent to the sample which yielded the 1060 Ma Rb-Sr isochron, and is therefore effectively a duplicate sample. The geochemical similarity between these samples and RX4519 (Figure 7.4) indicates that they all belong to the same generation of dolerite. The Nd compositions of RX4551 and RX4519 were calculated for an age of 1060 Ma and yielded the same initial εNd signature of +3.8 (Table 7.2). This signature is in contrast to those obtained by Zhao and McCulloch (1992a) for the dolerites of the same age from the Arunta and Musgrave Inliers (εNd values of ~-7 and +0.7 respectively). However, when the initial ratios of the Olympic Dam samples are calculated for an age of 870 Ma they are within the range (+2.5 to +4.1) quoted for the Gairdner dolerites by Zhao and McCulloch (1992a). The preferred interpretation of this surprising result is that the dolerites at Olympic Dam have an age of ~1060 Ma and are related to the same regional thermal event responsible for the emplacement of the Stuart and Kulgera dyke swarms. The differences between the initial εNd signatures of the dolerites from these provinces may be due to different mantle source material and the variable effects of crustal contamination during dyke emplacement.

Table 7.2. Samarium - Neodymium data for younger dolerites.

Sample No.	Sm (ppm)	Nd (ppm)	$^{147}Sm/^{144}Nd$	$^{143}Nd/^{144}Nd(t_0)$[a]	$\varepsilon_{Nd(0)}$[b]	$\varepsilon_{Nd(1060\ Ma)}$[b]
RX4519	6.12	22.5	0.1647	0.512623 ± 9	-0.5	3.8
RX4551	5.77	21.3	0.1639	0.512619 ± 10	-0.6	3.8

a. Measured values with 2σ errors, normalised to $^{146}Nd/^{144}Nd = 0.7219$.

b. $\varepsilon_{Nd}(t_0)$ refers to the present day, $\varepsilon_{Nd}(1060Ma)$ calculated at the age of the dolerites, 1060 Ma.

c., ε_{Nd} calculated using the following present day values for CHUR: $^{147}Sm/^{144}Nd = 0.1967$ and $^{143}Nd/^{144}Nd = 0.512650$; $\lambda^{147}Sm = 6.54 \times 10^{-12}\ y^{-1}$.

Zhao and McCulloch (1992b) propose that the enrichment observed in the isotopic signatures of the Stuart and Kulgera dykes (εNd =-7 to +0.7) is due to partial melting of a metasomatised continental lithospheric mantle rather than due to crustal contamination effects. They cite low values for SiO_2 (average 48%), Zr (average 48 ppm), Nb (average 1.1 ppm), Ti/V (18), and Zr/Y (~2.3), and high values for MgO% (13%), Zr/Nb (average 48), and La/Nb (average 6.5) as features inconsistent with crustal contamination. In contrast the Olympic Dam dolerite samples have higher values for SiO_2 (average ~49.5%), Zr (150 ppm), Nb (9 ppm), Ti/V (~45), Zr/Y (~5), and lower values for MgO (4 to 6 %), Zr/Nb (~17) and La/Nb (1), suggesting that these rocks have undergone crustal contamination. In addition, mineralogical evidence for assimilation of crustal material was found in dolerite samples RX4518 and RX4552 from which 9 very small (50 μm) spheroidal, transparent hyacinth-coloured zircon grains were obtained in heavy mineral separates. The morphology of the zircons is interpreted to result from the partial dissolution of xenocrysts in the dolerite melt. The evidence for crustal contamination is therefore strong and suggests that the uncontaminated εNd signature of the mantle source of the Olympic Dam dolerites must be more positive than +3.8 at 1060 Ma. This means that the source is distinct from that of the contemporaneous dolerites in the Musgrave and Arunta Inliers. The isotopic composition of depleted mantle for the Gawler Craton at 1060 Ma would probably have been in the range εNd = +6.5 to +9.0 (M.Fanning, unpublished data on Lake Harris komatiites; see above). It is therefore possible that the dolerite magmas at Olympic Dam were sourced from depleted mantle and have shifted in isotopic composition towards a more enriched (time-averaged) signature (+3.8) due to the effects of crustal contamination.

7.3.3 Regional units sampled

7.3.3.1 Acropolis prospect

At Olympic Dam the initial εNd values of hematitic ores and magnetite breccias differ markedly (see 7.3.1). The magnetite signature of -4.9 suggests that it is cogenetic with the Roxby Downs Granite, a product of 1590 Ma crustal melting, whereas the hematite signature of ~-2.5 suggests the involvement of a more primitive (mantle-like) component in its genesis. The possible sources of the REE component in the hematitic breccias are discussed more fully below, but the contrasting signature between magnetite and hematite breccias has important implications for ore genesis models and it was therefore thought necessary to further document the isotopic characteristics of the magnetite-rich assemblage. The zone of magnetite-dominant breccias at Olympic Dam measures only ~50m in diameter at the present level of exposure, so testing of geographically separate samples is not possible within the deposit. However, the Acropolis prospect, 25 km southwest of Olympic Dam, is an iron-rich deposit dominated by a magnetite-apatite

assemblage rather than hematite (mentioned in Section 5.8.2.1). Acropolis does not show the high levels of enrichment of Cu, U and LREE observed at Olympic Dam. The magnetite at Acropolis is closely associated with felsic volcanic rocks which have been correlated with the Gawler Range Volcanics on the basis of their age (1591 ± 11 Ma; Creaser, 1989) and geochemical similarities. Apatite intergrown with magnetite has been dated by U-Pb methods at 1602 ± 7 Ma (Mortimer et al., 1988a). If the genetic relationship between magnetite and felsic magmatism (Roxby Downs Granite) indicated by the Nd isotopic data for Olympic Dam were to hold true for similar deposits, the prediction is that the magnetite at Acropolis would have a similar signature to the associated felsic volcanics. The volcanics from Acropolis have not been analysed for Nd isotopes but the regional rocks derived from the 1590 Ma crustal melting event (Hiltaba supersuite granitoids and felsic members of the Gawler Range Volcanics) for which data are available range in isotopic composition from -3.6 to -5.7 (Creaser, 1989; 8 geographically separate samples).

A single sample of Acropolis magnetite (RX4577A) was analysed for this project. It is a sample of massive magnetite with ~15 percent hematite replacement and approximately 5 percent apatite. It has an initial εNd signature of -3.3. This signature is slightly higher than the range for 1590 Ma crustal melts but is well below the Olympic Dam hematite signature, and this is consistent with the pristine magnetite being cogenetic with the felsic volcanics. The value of -3.3 is interpreted as representing a mixture between a more negative εNd signature for unaltered magnetite, and a higher εNd value associated with hematitic alteration. It therefore appears that there is a fundamental difference in genetic models required for the Olympic Dam hematitic breccias and ores, and the magnetite-rich rocks at Olympic Dam and Acropolis. This is discussed further in Section 7.6.

7.3.3.2 Pandurra Formation sandstone

The Pandurra Formation, shown on the regional geological map in Chapter 2 (Figure 2.1), outcrops extensively to the northeast of the Gawler Range Volcanics and forms the basal sedimentary unit over much of the Stuart Shelf to the west and southwest of Olympic Dam. The Pandurra Formation is a fluvial sequence of sandstones, conglomerates and siltstones which locally overlies basalts of the Roopena Volcanics, interpreted to be equivalents of the Gawler Range Volcanics (Chapter 3). Fanning et al. (1983) generated a Rb-Sr whole-rock isochron age of 1424 ± 51 Ma for shale horizons within the Pandurra Formation. However, these workers suggest that this date could be interpreted either as an age of deposition or an age of younger diagenetic effects. It is therefore possible that the Pandurra Formation is only marginally younger than the underlying Roopena Volcanics, and is therefore similar in age to the Olympic Dam deposit. Considering its present position unconformably overlying basement rocks over much of the Stuart Shelf (although not directly above Olympic Dam), the Pandurra

Formation can be considered as a potential source for metals in the Olympic Dam deposit. For this reason two samples of Pandurra Formation sandstone were included in the Sm-Nd isotopic tracing studies. One sample (RX4570) is from the cover sequence above the Acropolis prospect and it has an εNd_{1590Ma} value of -3.1. RX4571 is from the cover sequence above the Oak Dam prospect and it has an εNd_{1590Ma} value of +2.7. The implications of these initial ratios for Olympic Dam metal provenance are considered in the next section.

7.4 Sm-Nd isotopic tracing

7.4.1 REE sources

The isotopic results presented above enable some important constraints to be placed on the possible sources of the mineralising fluids at Olympic Dam. Figure 7.5 shows two histograms which compare the Nd isotopic ratios of the Olympic Dam ores with those of the regional rock units for which data are available (all compositions calculated for 1590 Ma). Data for the Archaean rocks of the Gawler Craton were obtained from Daly and Fanning (1990), C.M. Fanning (pers. commun., 1990) and Cowley and Fanning (1991). The data for the 1590 Ma "Crustal melts" field are from Creaser (1989), and those for the mafic rocks of the Gawler Range Volcanics were kindly provided by K. Stewart (pers.com., 1991) and S-S. Sun (pers.com., 1991). The analyses of the alkaline mafic/ultramafic dykes from within the deposit (this study) have also been included in the latter group for the purposes of Figure 7.5.

Figure 7.5 A shows the data for the samples from Olympic Dam which plot within the "ore envelope" on Figure 7.1, most with an εNd signature of ~-2.5. This signature is well above the field occupied by all but one of the analysed Archaean rocks of the Gawler Craton (Figure 7.5B). A single analysis of an Archaean pillowed basalt has an εNd_{1590} of -0.2, and although this is theoretically a possible source analogue for Olympic Dam REE, it is not thought probable in view of the abundance of Gawler Range Volcanics magmas and rocks of appropriate isotopic composition formed at the same time as ore deposition (see below). Figure 7.5 therefore shows that the majority of the Archaean rocks analysed are unlikely sources for the REE budget at Olympic Dam.

Creaser (1989) analysed two samples of Early Proterozoic granitoids from the Gawler Craton and these have εNd_{1590} values of -5.3 and -5.4. These are lower than the values of the Olympic Dam ores, and therefore Early Proterozoic crust of this type is also an impossible source for the Olympic Dam REE complement.

The field labelled "1590 crustal melts" (Figure 7.5B) represents the felsic rocks of the Gawler Range Volcanics and the Hiltaba supersuite granitoids, and the Olympic Dam ores have εNd values above this field. The Archaean rocks together with the crustal

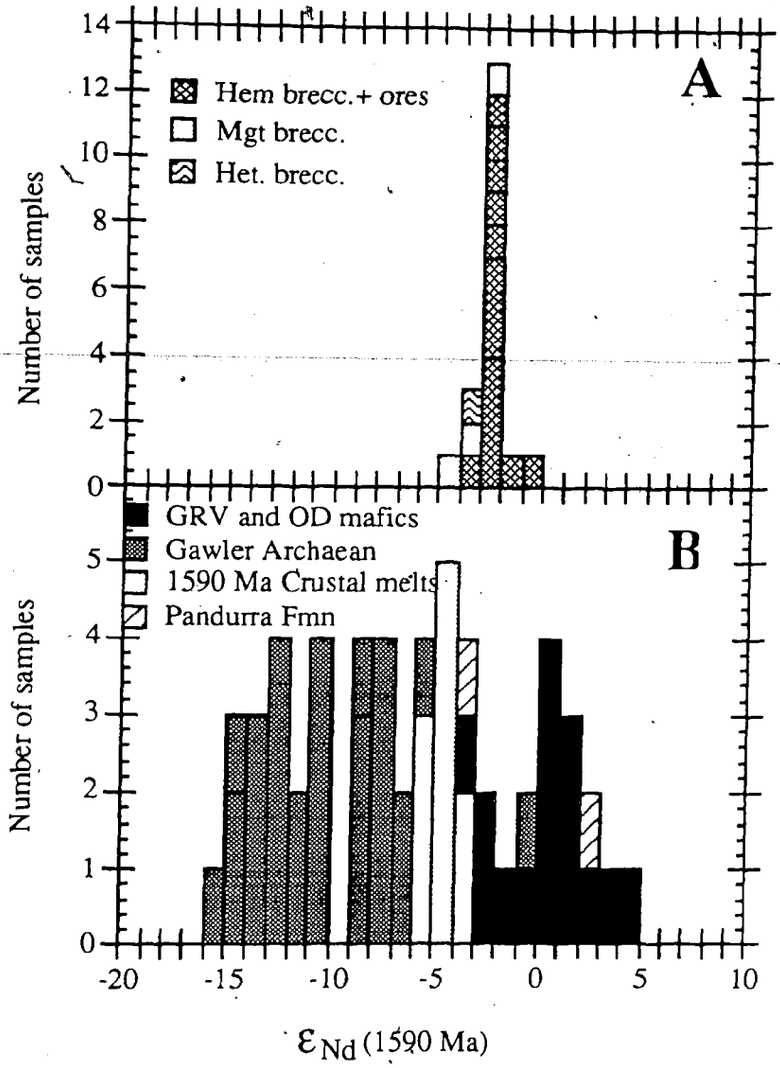

Figure 7.5 Frequency histograms for Nd isotopic compositions calculated at 1590 Ma. **A)** Olympic Dam hematitic breccias and ores, magnetite-rich breccias and heterolithic breccias. **B)** Regional lithologies grouped as: Mafic rocks of the Gawler Range Volcanics and alkaline mafic/ultramafics from Olympic Dam, Archaean rocks of the Gawler Craton, 1590 Ma crustal melts (granites and volcanics), and sandstones of the Pandurra Formation. The Olympic Dam ore signature appears to represent a mixture between pre-existing crustal rocks of the Gawler Craton, and rocks or magmas derived from the mantle at 1590 Ma.

---

melts represent the regional crustal material in existence prior to 1590 Ma. Therefore, on the basis of available Nd isotopic data, pre-existing crust cannot have been the sole source for the REE within the Olympic Dam deposit. Even if a significant proportion of the REE content of the fluids is of crustal origin (discussed below) it is necessary to invoke a contribution from a fluid with a primitive Nd isotopic signature to provide a Nd mixture with an εNd value as high as -2.5.

The range of isotopic compositions for the mafic and ultramafic rocks formed during the Gawler Range Volcanic event encompasses the field of the Olympic Dam ores (Figure 7.5) and these rocks are therefore reasonable source analogues for the REE in the deposit. With their mafic/ultramafic character, these rocks also represent an appropriate source for the Cu, Cr, Ni and V enrichments in the deposit (Chapter 5). The alkaline affinity of the Olympic Dam dykes (Chapter 6) suggests that they are also a plausible source of the Y, Ba and Nb enrichments in the deposit (Chapter 5). Whether or not they could constitute a plausible source of U is open to question. However, the U within the deposit may be derived from felsic rocks. Some felsic variants of the Gawler Range Volcanics have initial εNd values of -2 to -3 and appear to have formed by fractionation from mantle-derived melts at 1590 Ma (Stewart, pers.com., 1991; Sun, pers.com., 1991). Such felsic magmas and rocks are plausible sources for U, and on the basis of their isotopic compositions they should also be considered as potential contributors of fluids and/ or metals to the deposit. Felsic rocks with more negative εNd signatures may also have contributed U and a proportion of REE to the deposit (see Section 7.6).

Two analyses of the regionally extensive Pandurra Formation sandstone are represented on Figure 7.5 B. The isotopic composition of RX4570 (εNd_{1590} = -3.1) borders those of the 1590 Ma crustal melts and the mafic rocks of the Gawler Range Volcanics. The most likely source materials for the quartzo-feldspathic Pandurra Formation sandstones are thought to be the Gawler Range Volcanics and the Hiltaba supersuite granitoids (Fanning et al., 1983), and the available data indicate that these have εNd_{1590} Ma values more negative than -3.6; generally around -5 (Creaser, 1989). Thus there is a more primitive Nd component evident in RX4570. With an initial εNd composition of -3.1 RX4570 is not a feasible sole source of the REE in Olympic Dam. However, the anomalous Nd composition for this sample may be an alteration signature. This raises the possibility that the sandstone originally had a more negative signature but has been exposed to alteration by fluids with a relatively primitive Nd isotopic composition (see below).

RX4571, also a sample from the Pandurra Formation, has a Nd isotopic composition of +2.7 at 1590 Ma which theoretically makes it a plausible source of the Olympic Dam REE. However, this isotopic composition is much more primitive than is consistent with derivation of the sandstone from Gawler Craton Archaean and Early to Middle Proterozoic crustal rocks. Again this can be explained as an alteration signature due to exposure of the sandstone to fluids carrying REE with a relatively primitive Nd signature. Both RX4570 and RX4571 show hematitic alteration, and Fanning et al. (1983) observed that ferruginous alteration is a widespread feature of the Pandurra Formation. The fluids responsible for this alteration may also have modified the Nd isotopic

signature to more positive εNd values. It is therefore possible to interpret the isotopic compositions of RX4570 and RX4571 in two ways:

A) The isotopic compositions are evidence that analogues of the mineralising fluids for Olympic Dam have migrated through this sandstone unit. This interpretation would make the Pandurra Formation a plausible source of U in the deposit, but the REE and probably Cu would still require a separate, more primitive (mafic) source.

B) It is equally possible that a fluid in Nd isotopic equilibrium with overlying mafic volcanics has migrated through the sandstones effecting the widespread ferruginous alteration and superimposing a mafic Nd signature.

Although not present in the drill holes sampled, the basalts of the Beda Volcanics (~1075 Ma) are observed to overly the Pandurra Formation elsewhere on the Gawler Craton (Fanning et al., 1983), and these are a possible source of the mafic Nd component observed in RX4570 and RX4571 (at ~1075 Ma the εNd values of RX4570 and RX4571 are again more primitive than the fields of the Archaean rocks and 1590 crustal melts). The chondrite-normalised REE patterns for RX4570 and RX4571 provide evidence which suggests that the possibility A) is unlikely.

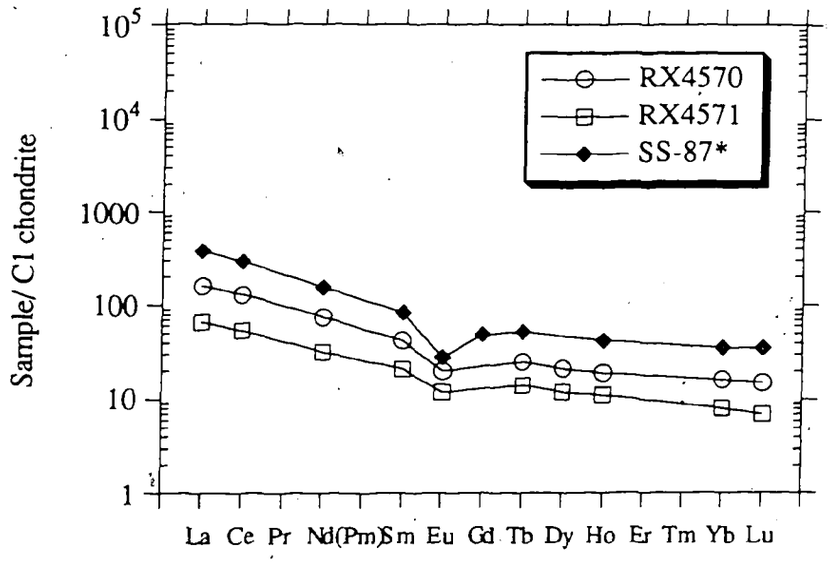

Figure 7.6 Chondrite-normalised REE compositions of two samples of Pandurra Formation sandstones (RX4570 and RX4571), with unaltered Roxby Downs Granite for comparison (SS-87* from Creaser, 1989). The flat patterns and relatively low REE concentrations in the sandstones are inconsistent with having been exposed to fluids such as those producing the mineralisation at Olympic Dam (see text for details). Chondrite normalising values are those of Sun and McDonough (1989).

The REE concentrations of these samples are much lower than any of the altered rocks at Olympic Dam and the patterns are relatively flat (Figure 7.6; cf. Figure 5.16).

If these samples had been altered by the same fluids as introduced REE to Olympic Dam one would expect to see much higher REE concentrations and strongly LREE-enriched patterns, but this is not the case. On the basis of the current (limited) data it appears more likely that the alteration and modification of the Nd isotopic composition of the Pandurra Formation sandstones is unrelated to the mineralising events at Olympic Dam, and a plausible explanation is that alteration was effected by downward percolating fluids in isotopic equilibrium with the basalts of the overlying Beda Volcanics (correlatives of the Gairdner Dyke Swarm; Section 7.3.2.2). This implies that alteration of the sandstone occurred after ~1075 Ma. The Pandurra Formation is therefore regarded as an unlikely source of REE or ore metals at Olympic Dam.

7.4.2 Anomalous samples

Two samples from Olympic Dam have isotopic compositions that are anomalous relative to the samples of macroscopically similar rocks. RX4513 is a sample of bornite-chalcocite ore from the northwest of the deposit and it has an εNd_{1590} value of -0.3, above the values of the other hematitic ores (ε=~-2.5). In Section 7.3.1.3 it was suggested on the basis of vanadium concentrations and LREE patterns that this isotopic composition may represent a mixture between the ore and mafic/ultramafic dyke signatures. Figure 7.7 is a plot of εNd versus time with the isotopic fields of the ores and other key rock types plotted at 1590 Ma, 1060 Ma (the age of dolerite emplacement), and for the present. It also shows the isotopic evolution trajectory for RX4513, which is above the field of the other ores throughout the history of the deposit. This demonstrates that the anomalous initial (1590 Ma) isotopic composition is not simply a product of a later REE fractionation resetting event because, if this were the case, the trajectory would be expected to converge with those of the other ores at the age of the resetting event. The trajectory for RX4513 is intermediate to those of the ores and the mafic/ultramafic rocks from 1590 Ma to the present. This evidence is consistent with the suggestion made in Section 7.3.1.3 that RX4513 is a sample wherein hematite and bornite-chalcocite mineralisation have replaced a portion of a precursor mafic/ultramafic dyke.

The other anomalous sample is RX4539, a strongly sericite-altered mafic/ultramafic dyke. This sample has a present day εNd signature of +31.9 and a calculated signature for 1590 Ma which is impossibly low at -37.7. Its evolution trajectory is plotted on Figure 7.7. Field relationships suggest that the dyke from which RX4539 was sampled is part of the generation of dykes observed throughout the deposit that are interpreted as contemporaneous with mineralisation. The anomalous present day isotopic signature and the negative slope of the evolution trend are therefore probably due to a resetting event

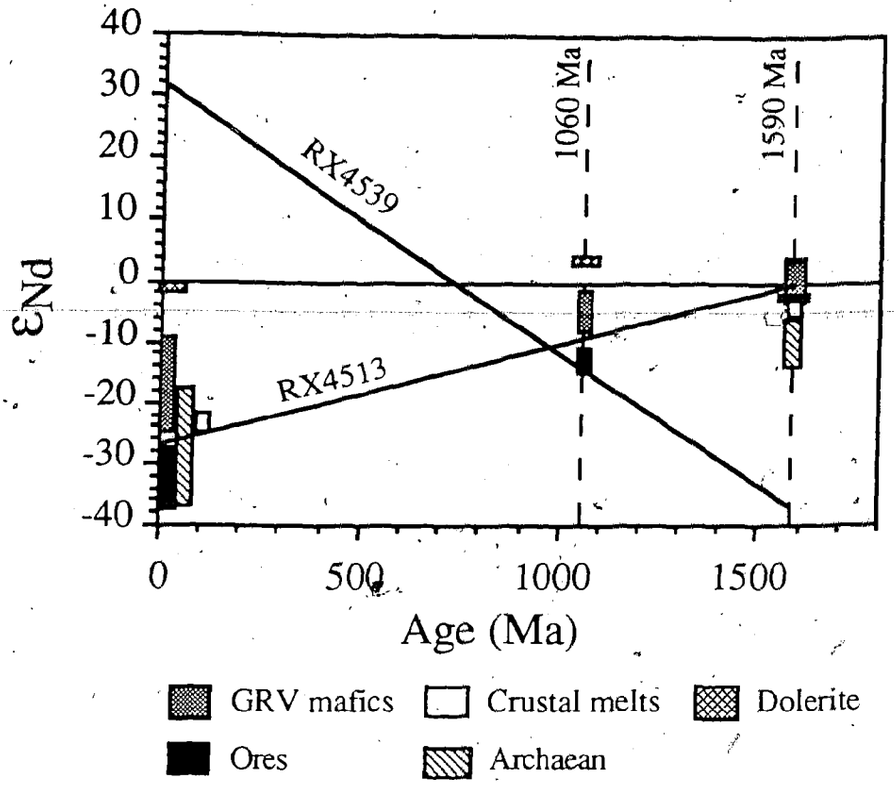

Figure 7.7 εNd versus age showing the isotopic compositional fields of the relevant rock types at 1590 Ma, 1060 Ma - the age of dolerite emplacement, and at present. Note that the trajectory for RX4513 is at values intermediate to the ores and Gawler Range mafics/ ultramafics from 1590 Ma to the present, suggesting that RX4513 may be replaced dyke material. Note also that the evolution trajectory of dyke sample RX4539 has a negative slope which overlaps with the ores signature at ~1060 Ma. This sample may have undergone isotopic resetting, including fractionation of the REE pattern towards HREE enrichment, due to the hydrothermal circulation caused by dolerite intrusion at ~1060 Ma.

which has strongly fractionated the REE in this sample (see HREE-enriched pattern, Figure 6.6b). In this regard it is interesting to note that the isotopic evolution trajectory of this sample overlaps with the field for the ores at ~1060 Ma (Figure 7.7), the age of emplacement of the dolerites within the deposit. It is possible that dolerite intrusion has caused localised hydrothermal remobilisation of REE within the deposit resulting in REE fractionation and isotopic resetting in this sample. Such a hydrothermal event may also have had a modifying influence on some of the ores in the deposit.

7.5 Rb-Sr isotopic systematics

In Chapter 5 it was established that Sr was introduced to the deposit in the ore-forming processes at Olympic Dam. This makes the Rb-Sr system a potentially useful tool for isotopic tracing studies in an analogous manner to that described above for the Sm-Nd system. However, Rb and Sr are generally more mobile than the REE and are therefore more susceptible to post ore-deposition remobilisation effects. If such open system behaviour has affected the Rb-Sr isotopic systematics of the breccias then this system cannot be used for the purposes of isotopic tracing. It is therefore important to assess the Rb-Sr results for any evidence of disturbance of the isotopic system. Possible post ore-formation processes which could have remobilised Rb and/ or Sr at Olympic Dam include:

a) Barite and fluorite veining events which probably occurred in Late Proterozoic or Cambrian times (Sugden, 1989; Sugden and Cross, 1991).

b) The emplacement at ~1060 Ma (and possibly ~860 Ma) of regionally extensive dolerite dyke swarm(s).

c) A regionally extensive Rb-Sr isotopic resetting "event", recognised particularly in the granitoids of the Hiltaba supersuite, which is interpreted by Creaser (1989) to be caused by hydrothermal circulation at ~1500 Ma.

In addition the U-series disequilibrium studies of Guthrie (1990) and the Pb isotopic work described in Chapter 3 indicate that fluids have been circulating through the deposit transporting U and Pb (and therefore possibly transporting Rb and Sr) in recent times. There are therefore many possible means by which the Rb-Sr system may have been disturbed since ore formation at 1590 Ma and this suggests that interpretation of Sr isotopic data requires considerable caution. Despite the ample scope for open system behaviour, the isotopic analyses were made because of the possibility that they would provide useful data.

Isotopic tracing studies require comparison of the initial $^{87}Sr/^{86}Sr$ ratios of the various samples. The Rb-Sr data, including calculated initial Sr ratios, are presented in Table

Table 7.3. Rubidium - Strontium isotopic data.

Sample No.	Lithology	Rb (ppm)	Sr (ppm)	$^{87}Rb/^{86}Sr^{a}$	$^{87}Sr/^{86}Sr(t_0)^{a}$	$^{87}Sr/^{86}Sr$ (1590 Ma)
RX4536	Magnetite breccia	4.9	28.9	0.4863	0.715770 ± 15	0.704664
RX4537	Magnetite breccia	9.5	227.4	0.1206	0.716068 ± 13	0.713314
RX4529	Pyrite-rich ore	0.77	23.6	0.0936	0.718412 ± 12	0.716275
RX4531	Pyrite-rich ore	0.68	42.1	0.0466	0.713877 ± 15	0.712812
RX4512	Chalcopyrite-rich ore	47.9	275.1	0.5030	0.722414 ± 20	0.710928
RX4542	Chalcopyrite-rich ore	1.6	726.9	0.0063	0.717528 ± 12	0.717385
RX4508	Chalcopyrite-rich ore	55.1	551.3	0.2882	0.714147 ± 11	0.707566
RX4511	Bornite-chalcocite ore	30.7	258.5	0.3435	0.723425 ± 12	0.715580
RX4513	Bornite-chalcocite ore	7.1	28.4	0.7180	0.730648 ± 16	0.714253
RX4559	Bornite-chalcocite ore	35.2	602.6	0.1709	0.714664 ± 12	0.710761
RX4462	Bornite-chalcocite ore	41.2	304.3	0.3906	0.716530 ± 13	0.707611
RX4463	Bornite-chalcocite ore	5.3	452.0	0.0337	0.713726 ± 20	0.712956
RX4510	Leached hem.breccia	12.1	235.7	0.1480	0.716435 ± 14	0.713056
RX4509	Heterolithic breccia	87.2	261.0	0.9645	0.714695 ± 17	0.692671
RX4514	Hem-qz sandstone	31.8	460.8	0.1990	0.713507 ± 14	0.708962
RX4502	Hem-qz breccia	9.1	790.0	0.0332	0.708061 ± 11	0.707302
RX4503	Silic.hem-qz breccia	2.0	178.8	0.0325	0.710105 ± 12	0.709364
SS-87*	Granite - fresh[b]	232.4	82.9	8.258	0.891630 ± 20	0.703059
RX3698	Granite - sericitised	126.9	285.6	1.286	0.737221 ± 18	0.707867
RX4533	Granite - sericitised	150.3	5371.0	0.0807	0.710292 ± 15	0.708449

Table 7.3 contd.

Sample No.	Lithology	Rb (ppm)	Sr (ppm)	$^{87}Rb/^{86}Sr$[a]	$^{87}Sr/^{86}Sr(t_0)$[a]	$^{87}Sr/^{86}Sr$ (1590 Ma)
RX3213	Granite - chloritised	85.4	106.7	2.323	0.768920 ± 11	0.715883
RX3214	Granite - chloritised	130.8	84.5	4.501	0.799829 ± 14	0.697050
RX4548	Ultramafic dyke	69.7	24.0	8.508	0.874615 ± 20	0.680346
RX4566	Ultramafic dyke	406.5	30.6	41.26	1.501743 ± 21	0.559618
RX4546	Ultramafic dyke	142.6	133.9	3.088	0.763898 ± 19	0.693384
RX4539	Ultramafic dyke	271.5	40.5	20.03	1.087687 ± 15	0.630324
RX4543	Ultramafic dyke	154.6	98.6	4.574	0.823566 ± 15	0.719109
RX4547	Ultramafic dyke	361.4	418.1	2.504	0.753962 ± 11	0.696787
Mineral separates						
RX3184	Hematite	0.69	53.3	0.0372	0.711838 ± 16	0.710988
RX3184	Magnetite	0.62	31.8	0.0564	0.715352 ± 17	0.714065
Regional lithologies						
RX4570	Pandurra Fmn. sst.	138.4	87.8	4.595	0.811312 ± 18	0.706379
RX4571	Pandurra Fmn. sst.	24.9	75.3	0.9570	0.724005 ± 18	0.702151
RX4577A	Acropolis magnetite	20.4	124.7	0.4732	0.717618 ± 16	0.706812
RX4519	Dolerite	18.6	185.0	0.2896	0.710973 ± 17	
RX4551	Dolerite	20.9	174.6	0.3452	0.709182 ± 17	

a. Measured values with 2σ errors, normalised to $^{86}Sr/^{88}Sr = 0.1194$; $^{85}Rb/^{87}Rb = 2.600$ $\lambda^{87}Rb = 1.42 \times 10^{-11}$ y^{-1}.

b. Denotes data from Creaser (1989).

7.3. One means of assessing the credibility of the calculated initial (1590 Ma) $^{87}Sr/^{86}Sr$ ratio is to plot these values against $^{87}Rb/^{86}Sr$ (Figure 7.8 A, B and C). In groups of samples for which the isotopic systems have remained closed there is no expectation of covariation between these ratios. Figure 7.8 A illustrates that three samples of altered mafic/ultramafic dykes (RX4566, RX4539 and RX4548) which have impossibly low calculated initial $^{87}Sr/^{86}Sr$ ratios (0.5596, 0.6303 and 0.6803 respectively) form a regular trend of decreasing initial ratio with increasing $^{87}Rb/^{86}Sr$. This type of trend in obviously altered rocks indicates either that Sr has been lost or Rb gained since the igneous rock crystallized. The geochemical data presented in Chapter 6 (negative Sr spikes on mantle-normalised diagrams; Figure 6.6) indicate that the mafic/ultramafic rocks have been depleted in Sr during alteration, possibly due to the breakdown of feldspar. Figure 7.8 B shows a more detailed scale for the calculated initial $^{87}Sr/^{86}Sr$ and it is evident that four more samples with relatively high $^{87}Rb/^{86}Sr$ ratios (mafic/ultramafic dyke samples RX4547 and RX4566, heterolithic breccia RX4509, and granite breccia RX3214) have impossibly low calculated initial ratios. There is also a

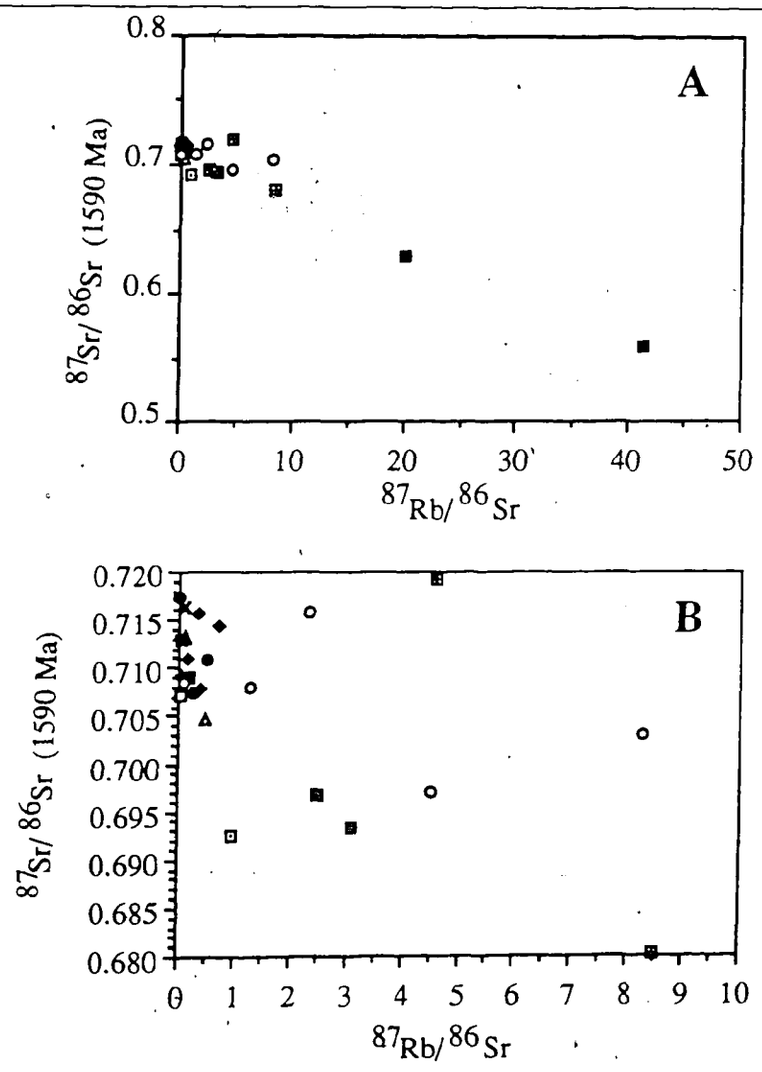

Figure 7.8. caption overleaf

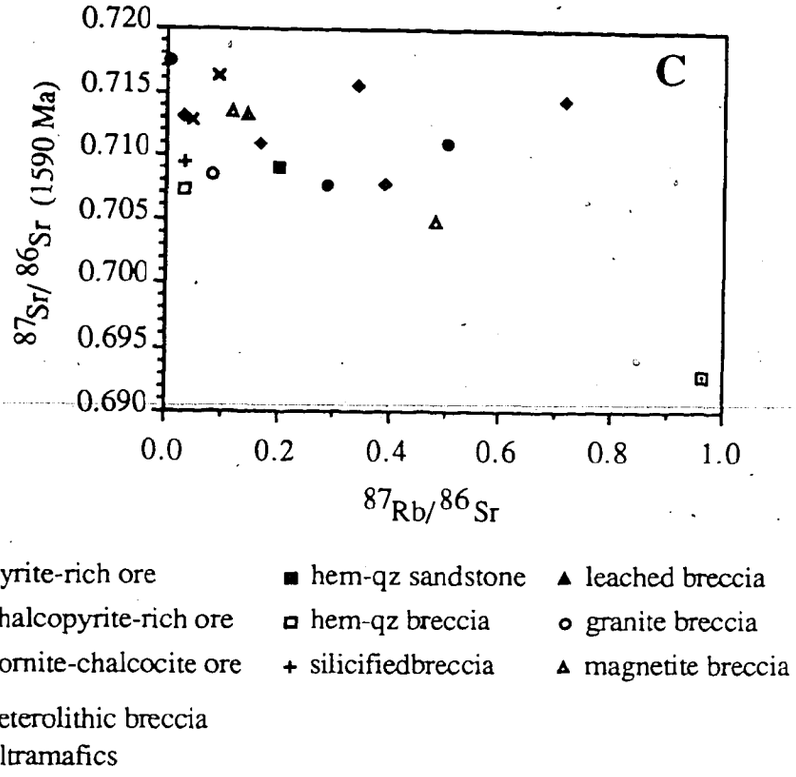

Figure 7.8 Olympic Dam breccias initial (1590 Ma) $^{87}Sr/^{86}Sr$ plotted versus $^{87}Rb/^{86}Sr$ at three different scales for $^{87}Rb/^{86}Sr$. The negative correlations in A) and B) and the impossibly low initial ratios of the samples with higher $^{87}Rb/^{86}Sr$ ratios, suggest that samples have either lost Sr or gained Rb in post-crystallisation disturbance (see text). The initial ratios plotted in C) are plausible (i.e. not impossibly low). Therefore the scattered decrease in $^{87}Sr/^{86}Sr$ initial with increasing $^{87}Rb/^{86}Sr$ evident in C) may result from post-crystallisation disturbance, but may reflect true initial compositons and be caused mixing of two sources; one with high $^{87}Sr/^{86}Sr$ and low $^{87}Rb/^{86}Sr$, the other with converse characteristics.

---

loose inverse correlation between the ratios for these samples. These anomalous "initial" ratios are interpreted as products of disturbance of the Rb-Sr isotopic system. The analyses mentioned above and illustrated in Figure 7.8 A and B are not considered further.

Figure 7.8 C shows the data for the bulk of the ore and Fe-rich breccia samples plotted on the same axes as for Figure 7.8A and B. Although these samples have plausible initial $^{87}Sr/^{86}Sr$ ratios they too show a scattered trend of decreasing initial ratio with increasing $^{87}Rb/^{86}Sr$. This trend can be interpreted in two ways:

a) The trend is caused by later isotopic disturbance as for the samples mentioned above (probably loss of Sr or gain of Rb) such that the $^{87}Rb/^{86}Sr$ ratio is increased, with the result that many of the calculated "initial" ratios are in fact overcorrected and have artificially low values.

b) The "initial" ratios may be real and the trend caused by mixing of two sources; one with low $^{87}Rb/^{86}Sr$ and high $^{87}Sr/^{86}Sr$, and the other with relatively high $^{87}Rb/^{86}Sr$ and low $^{87}Sr/^{86}Sr$.

Option a) is consistent with the regional data of Creaser (1989) who documented a similar negative correlation between $^{87}Rb/^{86}Sr$ and calculated initial $^{87}Sr/^{86}Sr$ for the 1590 Ma granitoids of the region. Creaser attributed this trend to isotopic disturbance caused by low intensity hydrothermal circulation at about 1500 Ma. If the Olympic Dam ore and breccia samples have been affected by open system behaviour of Rb-Sr then they cannot be used to constrain ore genesis models.

On the other hand, Figures 7.8 A and B indicate that it is the rock types which had a significant primary feldspar component which yield calculated initial ratios that are clearly erroneous (i.e. impossibly low), probably due to the loss of Sr from these rocks. It is therefore possible that the rock types consisting predominantly of hydrothermally precipitated minerals, rather than altered igneous minerals, are showing real initial (1590 Ma) $^{87}Sr/^{86}Sr$ ratios. Option b) above is therefore worthy of consideration. If it is assumed that the samples with plausible initial ratios are recording their isotopic compositions at the time of ore deposition (1590 Ma), then it is interesting to examine the relationships between their Sr isotopic signatures and those for Nd which have been used to recognise rocks types of contrasting geneses (Section 7.3).

Figure 7.9 is a plot of the plausible initial $^{87}Sr/^{86}Sr$ ratios (> 0.700) versus εNd_{1590}. The data show considerable scatter suggesting that they result from more than one process, but nevertheless define a loose trend from Sr initial ratios of ~0.703 and εNd of -5 for the granite-related rock units, to Sr initial ratios up to 0.7174 and εNd of ~2.5 for the hematitic breccias and ores. The granitic $^{87}Sr/^{86}Sr$ is unusually low and may be the product of post-1590 Ma loss of radiogenic Sr. On the basis of apatite isotopic compositions, Creaser (1989) suggested that ~0.709 is a more realistic initial value for the granite. Although it is not possible to demonstrate closed system behaviour for Rb and Sr in these samples, the covariation between Nd and Sr isotopic data calculated at 1590 Ma increases the likelihood that most of the samples represented in Figure 7.9 have either not suffered Rb-Sr isotopic disturbance, or have undergone a systematic shift towards lower $^{87}Sr/^{86}Sr$ ratios.

The sample of least altered granite (SS-87) plots with a Sr initial ratio of ~0.703 and an εNd signature of -5. RX4536, the sample of least altered magnetite breccia, has a Sr initial ratio of ~0.705 and, relative to the range of Sr ratios, plots close to the granite sample. The Sr data therefore do not conflict with the interpretation made in Section 7.3.1 that the magnetite-rich breccias are cogenetic with the Roxby Downs Granite particularly considering that the granite initial $^{87}Sr/^{86}Sr$ probably lies in the range 0.703

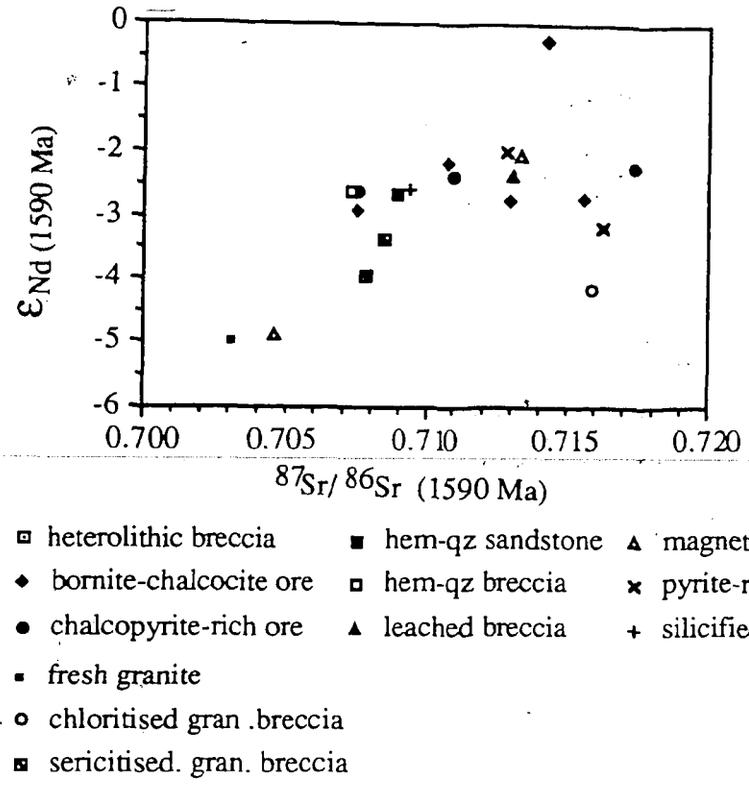

Figure 7.9 εNd_{1590} versus initial $^{87}Sr/^{86}Sr$ for samples of Olympic Dam breccias with plausible initial Sr ratios (>0.700). Two alternative explanations for the scattered positive correlation are given in the text.

to 0.709 (above). Two samples of sericitised granite breccia (RX3698 and RX4533) have $^{87}Sr/^{86}Sr$ values intermediate between the fresh granite and ores (Figure 7.9), again consistent with the Nd isotopic data. RX4533 has an extremely high Sr concentration (~5370 ppm) and, assuming this Sr-enrichment is primary, would therefore have been relatively resistant to isotopic disturbance. The fact that this sample has an isotopic composition intermediate to the apparent granite and ore signatures calculated at 1590 Ma provides further evidence that the other "initial" ratios do approximate the composition at 1590 Ma and are not the result of substantially disturbed isotopic systematics. A chloritised granite breccia sample plotted on Figure 7.9 (RX3213) has an initial $^{87}Sr/^{86}Sr$ value of 0.7159 which is not consistent with the other altered granite samples and lies below and to the right of the overall trend. This may reflect isotopic disturbance after ore deposition or may represent the introduction of more radiogenic Sr to this sample than to the other granitic samples during ore deposition. RX4537, a sample of comparatively hematitised magnetite breccia, has a Sr isotopic composition of 0.7133 in the mid-range of the hematitic ores (Figure 7.9). This suggests that the lower Sr initial ratio of the magnetite has been swamped by the hematite/ ore Sr signature, and this is consistent with the change observed in its Nd signature concomitant with hematitic alteration (cf. Section 7.3.1).

The fact that there is some order in the data in Figure 7.9 warrants investigation, even allowing that there may have been a systematic loss of radiogenic Sr. The trend of the data from low εNd and $^{87}Sr/^{86}Sr$ ratios to high εNd and $^{87}Sr/^{86}Sr$ ratios is the converse of what is generally expected (i.e. most crust and mantle systems show trends of negative slope on Nd-Sr isotopic plots), and the sense of the trend can be explained in two ways. It may be the product of mixing between sources whose Nd and Sr isotopic compositions match the apparent end-members of the trend in Figure 7.9, or it may reflect derivation of Nd and Sr from different sources. The former explanation is considered first.

The highest initial Sr value plotted on Figure 7.9 is for a chalcopyrite-rich ore sample RX4542. This sample has a high Sr content (~725 ppm) and a very low $^{87}Rb/^{86}Sr$ ratio (0.0063) and would therefore have been resistant to isotopic disturbance. Assuming that later Sr-loss would shift the calculated initial ratio to lower values, the initial $^{87}Sr/^{86}Sr$ value of this sample (0.7174) can be regarded as a minimum end-member signature for the ores at Olympic Dam. The question then arises as to what is the origin of the high $^{87}Sr/^{86}Sr$ signature in the ores. Nd isotopic data (Section 7.3) indicates that the rock units contributing REE components to the ore-forming fluids were felsic rocks (Roxby Downs Granite and perhaps its volcanic equivalents) and mafic/ultramafic rocks associated with the Gawler Range Volcanic event. The pristine granitic Sr signature is relatively low (in the range 0.703 to 0.709, above). If there are no other rock types contributing Sr to the ore fluids, the implication is that the high initial $^{87}Sr/^{86}Sr$ ratios of the ores are associated with the mafic/ultramafic component. Such rocks are not usually regarded as being likely to have high initial $^{87}Sr/^{86}Sr$ ratios. However, the Olympic Dam mafic/ultramafic dykes analysed are enriched in Rb and this enrichment is thought to be a primary feature of the rocks (see Chapter 6). The magmas which formed these alkalic mafic/ultramafic rocks were derived from a source which had a time-averaged depletion in Nd relative to Sm (above). However, this source may have been enriched in Rb (i.e. had a high Rb/Sr ratio) for a lengthy period (several hundred million years) prior to the melting event at 1590 Ma if the Rb enrichment process differed from those which would cause concomitant enrichment in LREE (e.g. metasomatism versus introduction of low degree partial melts). If this was the case, melting this source would produce magmas with a high radiogenic Sr content. The alkalic mafics/ultramafics at Olympic Dam are therefore plausible sources for the high $^{87}Sr/^{86}Sr$ component observed in the ores, possibly donating Sr due to the breakdown of feldspar. The same alteration process would have made relatively high concentrations of Eu available to the ore fluids and this may explain the positive Eu anomaly observed in many Olympic Dam breccias (see Chapter 5). Unfortunately it is not possible to verify directly whether the initial Sr isotopic composition of the mafic/ultramafic dykes is similar to or greater than those of the ores because the dyke samples analysed show clear evidence of open system isotopic

behaviour. All except RX4543 ("initial" $^{87}Sr/^{86}Sr$ = 0.7191) have impossibly low calculated initial $^{87}Sr/^{86}Sr$ values (see Table 7.3).

If the mafic/ultramafic rocks are not the source of the radiogenic Sr in the ores, and assuming that the Nd and Sr of the ores were acquired from the same source(s), older crust is the only other plausible source of Sr with $^{87}Sr/^{86}Sr > 0.720$ at 1590 Ma. The metasediments and deformed granites of the Early Proterozoic Hutchison Group and the Archaean rocks of the Gawler Craton have $^{87}Sr/^{86}Sr_{1590\ Ma}$ values in excess of 0.720 (Webb et al., 1986; Creaser, 1989). However if these were the sources of the radiogenic Sr signature in the ores the expectation is that they would cause the ores to have more negative εNd signatures.

An alternative explanation for the data array in Figure 7.9 is that the Sr and Nd in the ores were derived from different source rocks. Sr is more soluble than Nd and is therefore able to be scavenged by hydrothermal fluids from a wider area than Nd, i.e. from the more marginal zones of hydrothermal circulation where fluids are perhaps cooler and less corrosive than in the centre of the system. It is possible that the more corrosive central areas of fluid circulation, which were capable of taking both Nd and Sr into solution, acquired these elements from both felsic and mafic/ultramafic rocks. The marginal zones of circulation, taking only Sr into solution, may have accessed older crust with a more radiogenic Sr signature such as the examples mentioned above. If this occurred, the Sr was probably acquired from outside the observed volume of altered rocks around the deposit: Altered examples of Early Proterozoic and Archaean crust are not observed in close proximity to the deposit. In view of this, and assuming that the Sr data do approximate the true initial ratios of the ores, the preferred interpretation is that the radiogenic Sr component in the ores was derived from the Rb-enriched mafic/ultramafic source.

Because of the ample scope for post ore-deposition disturbance of the Rb-Sr isotopic system, this system cannot be used to place firm constraints on ore genesis models at Olympic Dam. However, the above discussion of the Sr isotopic data illustrate that the calculated initial ratios for most of the ore samples are plausible and that they can be interpreted in a geologically reasonable manner. The data do not conflict with the better constrained interpretations made on the basis of the Sm-Nd isotopic data.

7.6 Discussion and summary

The Sm-Nd isotopic studies have elucidated several important aspects of the genesis of the deposit. Three principal end-member isotopic signatures have been identified:

i) The granite-related signature of εNd -5; this includes the fresh Roxby Downs Granite and the magnetite-siderite-pyrite assemblage.

ii) The hematite-breccia and ore signature of εNd -2.5. These samples yield a 14 point whole-rock isochron age of 1572 ± 99 Ma.

iii) The mafic/ultramafic volcanic rock signature with the most primitive composition yet measured for 1590 Ma volcanic rocks of the Gawler Craton at εNd +4.

Magnetite is the paragenetically earliest Fe oxide in the Olympic Dam breccias and its initial εNd composition of -5 strongly suggests that it is cogenetic with the Roxby Downs Granite. The magnetite could result from a fluid phase exsolved from the granite melt as it crystallized, or it could be related to a fluid derived from a separate perhaps slightly later pluton from the same suite as the Roxby Downs Granite. The evidence that the host granite had solidified and been unroofed prior to brecciation suggests that the latter possibility is more likely.

The signature of εNd ~-2.5 for hematitic breccias and ores is distinct from the magnetite signature (-5) and, assuming both hematite and magnetite were precipitated from solution, this provides isotopic evidence to support the suggestion made in Chapter 5 that ore genesis involved two fluids. If magnetite was a widespread precursor to hematite, the implication is that there was a temporal difference between the activities of the two fluids. If magnetite and hematite are precipitates of different stages of the same mineralisation cycle, the two fluids were circulating and mixing during a single event. These alternative models are considered further in Chapter 8. The hematitic ore Nd signature (εNd -2.5) also indicates that the Roxby Downs Granite cannot have been the sole source of REE and therefore of mineralising fluids at Olympic Dam. The isotopic data indicate that barren hematitic breccias share the same Nd source as the LREE-enriched chalcopyrite ores. This in turn indicates that the fluids responsible for oxidising magnetite to hematite share the same REE source as (i.e. are cogenetic with) the fluids which introduced copper. It is therefore probable that hematite and chalcopyrite were precipitated due to reactions of the same REE-enriched oxidised fluid.

The Sm-Nd data have established that the Archaean crust of the Gawler Craton and the 1590 Ma crustal melts cannot have been the sole source of REE in the deposit, and that ore genesis at Olympic Dam involved a primitive REE component. The available geochronological data, and the isotopic and REE data for the two samples of Pandurra Formation sandstone indicate that it was probably not a source of REE for Olympic Dam. By implication, the Pandurra Formation is also unlikely to be a source of the ore metals. Of the regional rock units for which Nd isotopic data are available, the most likely source of primitive REE components are the mafic rocks of the Gawler Range Volcanics and the alkaline ultramafic/mafic rocks observed within the deposit. These are also suitable sources for Cu.

The range of Sm-Nd isotopic compositions displayed by the mafic/ultramafic rocks in Figure 7.5 may be due to different magma sources, varying proportions of crustal contamination, or in the case of the dykes at Olympic Dam, to varying degrees of hydrothermal alteration (Section 7.3.2). At Olympic Dam the most primitive εNd signature observed is +4. The mixing array shown in Figure 7.3 illustrates that this is the "least altered" signature in an alteration trend towards higher Nd concentrations with lower εNd values. It is therefore reasonable to assume that any unaltered mafic/ultramafic extrusive rocks which may have been leached to provide REE and Cu for the deposit had isotopic compositions of approximately +4. The constancy of the ore signature (εNd -2.5) suggests that this was the signature of the ore fluid that oxidised magnetite to hematite and introduced Cu to the deposit. Isotopic tracing indicates the involvement of a mafic/ultramafic REE source in ore genesis. If the alkaline mafic/ultramafic rocks at Olympic Dam had a pristine signature of εNd +4, then the ore fluid signature must represent a mixture between Nd derived from the mafic/ultramafic rocks and rocks with a more negative εNd signature. The Roxby Downs Granite, comagmatic intrusives, and perhaps its eruptive equivalents are likely sources of the latter REE component. If one assumes that the ore fluid has acquired its REE complement from these two end-members, it is possible to estimate the relative proportions of the rocks involved. Assuming a mafic/ultramafic end-member with εNd of approximately +4 and a Nd concentration of ~175 ppm (as for RX4548 and RX4543), and a granitic/ felsic volcanic end-member with εNd of -5 and a Nd concentration of ~70 ppm (Table 7.1), the rock fraction "*f*" of mafic/ultramafic rock can be calculated using the following mixing equation:

$$\varepsilon_M = \varepsilon_A X_A f + \varepsilon_B X_B (1-f) \,/\, X_A f + X_B (1-f)$$

where ε_M is the isotopic composition of the mixture (-2.5), X is the Nd concentration, and A and B denote the mafic/ultramafic and felsic components respectively (after Faure, 1986 pp 229). Solving for *f* yields an estimate of 0.133 (or approximately 13.5%) for the rock fraction of mafic/ultramafic volcanic/hypabyssal rocks contributing REE to the mineralising fluids. This necessitates that the majority (~86%) of the rock leached to afford REE and other ore metals to the mineralising fluid was the felsic end-member. Such rocks are certainly plausible sources for the uranium within the deposit. If the mafic/ultramafic rocks which contributed REE to the deposit had acquired an εNd signature more negative than +4 due to assimilation of crustal material during magma ascent, their proportional contribution to the Olympic Dam REE must be higher (i.e. a greater proportion of rock leached). Therefore the rock fraction figure of 13.5% given above should be viewed as a minimum contribution for the mafic/ultramafic rocks. It should also be noted that the dykes at Olympic Dam are all altered, and volume reduction and residual behaviour of REE during alteration may have increased the Nd concentration

in these rocks above their igneous levels (see Chapter 6; the Nd isotopic signature of RX4548 and RX4543 precludes the high REE concentrations being of metasomatic origin). If the dyke Nd concentrations were originally lower than the 175 ppm used in calculations, then mixing relationships again dictate that a higher proportion of mafic/ultramafic rocks (relative to felsics) contributed REE to the deposit.

Using the minimum proportion of ~14% mafic/ultramafic rocks contributing metals to the ore fluid, it is possible to use mass balance calculations to test if the rock volumes inferred to be leached are in fact geologically reasonable. The ore resource figures quoted in Table 1.1 indicate that there are ~32 million tonnes of Cu metal within the deposit. The following parameters are assumed for the purpose of calculations:

i) The felsic component (granite and volcanics) contain 15 ppm Cu

ii) The mafic/ultramafic component contains 100 ppm Cu (estimates after Haynes et al., in press)

iii) Mafics/ultramafics have a density of about 3.2; felsics have a density of about 2.6.

It is also assumed that the source rock leached has donated 100% of its contained copper. Clearly this is not a reasonable assumption but it allows the calculation of the minimum rock mass/ volume required to donate metals. The mass balance calculation results in 1.7 x 10^{11} tonnes of mafics/ultramafics and 1.0 x 10^{12} tonnes of felsic material required to be leached. These figures equate to rock volumes of 52 km^3 of mafics/ultramafics and ~390 km^3 of felsic rocks. This can be visualised as a 1 km thick sequence over an area of approximately 20 x 20 km, with 10 to 15% of the volume occupied by mafic/ultramafic rocks and the remainder by felsic rocks. Even allowing for a leaching efficiency of well below 100%, these rock volumes are not unreasonably large, considering that the volume of mineralised rock in the Olympic Dam Breccia Complex is in excess of 35 km^3. This therefore reinforces that the calculated proportions of mafics/ultramafics (14%) and felsics (86%) in the source are reasonable. Similar mass balance calculations for U indicate that only 5 km^3 of mafics/ultramafics and 39 km^3 of felsic rocks are required to contribute the deposit's complement of U (assuming 10 ppm U in the felsic source and 0.6 ppm U in the mafic/ultramafic source, and 100% leaching efficiency). These volumes are very much smaller than the volumes calculated for Cu, and this probably relates to the more resistant nature of the primary minerals that contain high concentrations of U (e.g.zircon, monazite) which would result in much lower leaching efficiencies for U than Cu. The REE content of the deposit can be accounted for from even lower source-rock volumes at 100% leaching efficiency; only ~1 km^3 of mafics/ultramafics and ~7 km^3 of felsic rocks are required to yield the Ce content of the deposit [assuming an average Ce content of 1500 ppm in the breccias of the deposit,

~380 ppm Ce in the mafics/ultramafics as per mean of RX4543 and RX4548, and 150 ppm Ce in the felsic rocks as is indicated for the Gawler Range Volcanics and Hiltaba granitoids from the data of Giles (1988) and Creaser (1989)]. The relatively low solubility of REE and the resistant nature of their primary mineral hosts suggest that they would be leached much less efficiently than Cu and U. It is apparent from these calculations that the limiting factor on the minimum volume of source-rock required is the volume necessary to contribute Cu to the deposit.

In Section 7.5 it was suggested that the mafic/ultramafic rocks represented by the dykes in the deposit are a plausible source of the radiogenic Sr signature of the Olympic Dam ores. If this is the case it has implications for the evolution of the mantle source of the mafic/ultramafic magmas. The dykes (e.g. RX4548 and RX4543) are strongly enriched in LREE but have time-averaged depleted Nd isotopic signatures (up to +4). This combination of features indicates that LREE enrichment to the present highly fractionated levels did not occur long before melting of this source; otherwise the Nd isotopic signature would have evolved to more negative (enriched) values. However, in Section 7.5 it was suggested that the mantle source of the mafic/ultramafic dykes may have been enriched in Rb relative to Sr for several hundred million years prior to melting at 1590 Ma, because this allows time for the accumulation of the radiogenic Sr observed in the ores. This raises the possibility of mantle enrichment events for Rb which do not cause enrichment in LREE. This may relate to the differences between the enriching properties of mantle-derived metasomatic fluids, which perhaps transport alkalis but not REE, and low degree partial melts which would transport all incompatibles. The timing of such hypothetical events cannot be constrained because the pre-enrichment isotopic composition of the source is unknown.

8 SYNTHESIS

8.1 Summary

This chapter reviews the contributions made by this study to the understanding of ore genesis in the Olympic Dam deposit. It also assesses the geological, chronological and geochemical factors which must now be considered by models of ore genesis for this deposit. Two plausible models of ore genesis are then considered in the light of the new data.

One of the most important advances made by this study is in establishing the age of the deposit (Chapter 3). Prior to this geochronological work the age of the deposit was not well constrained. The only published estimate of the age of mineralisation was 1400 Ma (Oreskes and Einaudi, 1990, 1992). However, it is apparent that these workers had taken at face value the upper intercept age estimate of a discordia calculated from the pitchblende analyses of Trueman et al. (1988). In Chapter 4 it is demonstrated that U and Pb have been mobilised from the pitchblendes analysed by Trueman et al. (1988), and from pitchblendes analysed in this study, and that this mobility had taken place over a period spanning one billion years since primary mineralisation was deposited. This open system behaviour of U and Pb clearly violates the requirements of the discordia regression approach adopted by Trueman et al. (1988). The 1400 Ma age calculation is therefore the result of an inappropriate treatment of data, and it has been considerably misleading for ore genesis models for Olympic Dam. This situation highlights the dangers associated with accepting an isotopically determined "age" without investigating how it was derived.

Largely on the basis of the isotopic work of Trueman et al. (1988), the ore genesis model erected by Oreskes and Einaudi (1990) stipulates that mineralisation occurred approximately 200 million years after emplacement of the host Roxby Downs Granite. These workers proposed that a magmatic heat source was necessary to drive hydrothermal circulation, but make no attempt to account for the fact that this requires ore deposition to have occurred at a time for which no magmatism has actually been recorded on the Gawler Craton. If such a large time period did elapse between emplacement of the host rocks and deposition of the ore, then it must be assumed that the tectonic setting indicated by the host rocks does not necessarily bear any relevance to the tectonic setting required for metallogenesis.

The isotopic work presented in Chapter 3 (this study) strongly suggests that Olympic Dam mineralisation is an integral part of the tectonomagmatic history of its host rocks. The U-Pb zircon ages of two felsic dykes and a diatreme tuff presented in Chapter 3 place firm minimum age constraints on brecciation and mineralisation events at Olympic Dam.

The ages calculated are not resolvable from the maximum age constraint provided by the host granite, meaning that the deposit has an age of ~1590 Ma. This age determination therefore enables a confident correlation between ore genesis and the major regional thermal event that produced the Gawler Range Volcanics and the Hiltaba supersuite granitoids. The tectonic setting implied for metallogenesis is one of major crustal melting caused by the emplacement of large volumes of mantle-derived melts into the crust. Giles (1988) interpreted this thermal event to be due to mantle diapirism, and Reeve et al. (1990) suggested it represents an event of incipient intracontinental rifting. The strongly alkaline nature of the mafic/ultramafic dykes within the deposit (Chapter 6) is consistent with styles of magmatism common in continental rift settings such as the East African Rift, where rifting and magmatism are probably associated with mantle plume activity (Griffiths and Campbell, 1991).

A second important result from this study is the recognition (from Sm-Nd isotopic tracing studies; Chapter 7) of a primitive Nd component in the hematitic ores and breccias. Of the regional rock units for which Nd data are available, the most likely sources of the primitive Nd component in the deposit are the mafic and ultramafic rocks produced during the Gawler Range Volcanic event. Such rocks are clearly plausible sources for contributing the Cu, Cr, Ni and V enrichments observed in the breccias (Chapter 5). The ore fluid isotopic signature (εNd -2.5) reflects contributions from granite or felsic volcanic-related sources (εNd -5) as well as mafic/ultramafic sources (εNd +4). Mass balance calculations (Chapter 7) indicate that the ore signature could result from as little as ~15% rock fraction of mafic/ultramafic rocks contributing to the ore fluid. The involvement of mafic/ultramafic rocks in ore genesis effectively rules out models that suggest ore metals were derived *solely* from the host granite or related plutons of the Burgoyne batholith. This is one of the less obvious ways in which Olympic Dam ore genesis is fundamentally different to the genesis of porphyry-copper type deposits.

The geochemical data presented in Chapters 5 and 6, combined with the isotopic data in Chapter 7, have revealed several interesting relationships between various rock types within the deposit, and these are important for the ore genesis models discussed below. The elements that have been introduced to the Roxby Downs Granite to form the deposit include Fe, Mn, P, Sr, Ba, Cu, U, Y, Nb, REE, V, Cr, Ni and Zn (Chapter 5). The chemistry of the altered mafic/ultramafic dykes (Chapter 6; Appendix 9) indicates that during progressive alteration they were depleted in many elements, including Mn, Nb, Cu, Ni, Zn, V and Cr. When one considers that Nd isotopic data implicate these dykes as possible sources of REE for the deposit, it is interesting to note the complementarity of elemental losses from the dykes and elemental gains in the breccias. This observation strengthens the interpretation that the dykes or their plutonic or extrusive equivalents were an important metal source.

The geochemistry of the breccias (Chapter 5) suggests that ore genesis at Olympic Dam could have involved up to three distinct overprinting hydrothermal stages to produce the observed magnetite-pyrite-siderite, hematite-chalcopyrite, and hematite-bornite-chalcocite types of mineralisation. However, the geochronological constraints indicate that *all* of these stages must have occurred within ~8 million years after granite emplacement. The fact that several elemental enrichments in the breccias (including Cu, U, LREE, Nb, Y and Ba) do not correlate with total iron is interpreted to mean that these elements may have been introduced in fluids separate from those which introduced iron. As discussed in Chapter 5, these geochemical relationships could be interpreted as evidence for either a) ore deposition due to mixing of a saline, reduced, Fe-bearing fluid with an oxidised fluid carrying the other elements (e.g. Haynes et al., submitted), or b) an origin by the sequential activity of these contrasting hydrothermal fluids. The contrasting REE patterns of the magnetite-rich breccias (paragenetically early) and the later chalcopyrite-rich hematitic breccias (Chapter 5) permit the same two interpretations. The interpretation of the HREE enrichment observed in the bornite-chalcocite ores (and in some other breccias) relative to the chalcopyrite-rich ores presented in Chapter 5 requires a similar choice between a) models involving fluid mixing events whereby the chemical conditions in the upper levels of the hydrothermal system enhanced the precipitation of bornite, chalcocite and HREE-enriched phases, and b) models involving temporally distinct oxidative overprinting of chalcopyrite-rich ores (supporting a supergene weathering model). The major and trace element geochemical data and apparent paragenetic relationships therefore allow the possibility of one, two or even three stages of ore genesis.

The isotopic data presented in Chapter 7 reduce these options. The similar initial εNd signatures of bornite-chalcocite ores, chalcopyrite-rich ores, pyrite-rich hematitic breccias and barren hematitic breccias indicate that all these rock types share a common Nd source, and are therefore cogenetic (see "ore envelope", Figure 7.1). This suggests that they are products of a single evolving hydrothermal system rather than the result of distinct overprinting events involving fluids of differing provenance. In contrast, the magnetite-rich breccias have the same Nd isotopic signature as the fresh Roxby Downs Granite (εNd -5). This suggests that the magnetite-rich rocks may be products of fluids exsolved from the crystallising granite itself and/or related plutons of the Burgoyne batholith, or from deeply circulated meteoric waters that equilibrated with these rocks alone. The Nd isotopic evidence therefore confirms that two fluids were involved in ore genesis, and limits plausible ore genesis models to those involving only one or two principal stages, namely:

a) those which propose that magnetite-rich breccias may be a distinct first stage produced by granite-related fluids, with Cu-REE enriched oxidised fluids overprinting at a later time, or

b) those which propose that magnetite-rich breccias and hematitic breccias are coeval products of the mixing of reduced Fe-bearing granite-related fluids with oxidised Cu-U-REE enriched fluids.

8.2 Requirements of ore genesis models

The results of this study and the data of previous workers necessitate that any plausible model of Olympic Dam ore genesis must account for the following features:

1) The Olympic Dam Breccia Complex and its zones of economic mineralisation were formed at ~1590 Ma as part of the Gawler Range /Hiltaba volcano-plutonic event. Metallogenesis is therefore believed to be linked to an intracontinental extensional (rifting) tectonic setting that was probably sited above a diapiric upwelling of anomalously hot mantle (Giles, 1988), i.e. a mantle plume.

2) All significant paragenetic stages of sulphide mineralisation (magnetite-pyrite-siderite, chalcopyrite-hematite, bornite-chalcocite-hematite) are constrained to have formed within ~8 million years of emplacement of the host Roxby Downs Granite.

3) Geochemical and Nd isotopic correlations indicate that barren hematitic breccias, pyrite-rich breccias, chalcopyrite-hematite ores, and bornite-chalcocite-hematite ores are all products of the same evolving hydrothermal system rather than products of distinct superimposed systems. The fluids which produced these ores interacted with, and probably acquired ore metals from, rocks or magmas derived from the mantle at ~1590 Ma.

4) Magnetite-rich assemblages are isotopically similar to the Roxby Downs Granite and are isotopically distinct from hematitic breccias.

5) Alkaline mafic/ultramafic magmas were emplaced within and below the Olympic Dam Breccia Complex during its formation.

6) The Nd isotopic signatures of the alkaline mafic/ultramafic dykes within the deposit imply that they are representative of source rocks for at least some of the mineralising fluids. These rocks and their parent plutons/magmas are plausible sources of the enrichments of Cu, Cr, Ni, V, Ba, Nb, Y and REE in the deposit.

7) The deposit overlies a positive magnetic anomaly.

8) Fluid inclusion and oxygen isotopic data (Oreskes and Einaudi, 1992) indicate that at least two sources of fluids of contrasting temperature and composition were involved in ore genesis.

8.3 Ore genesis

There is consensus among previous workers that ore genesis at Olympic Dam probably involved a magmatic heat source driving hydrothermal circulation (Roberts and Hudson, 1983; Reeve et al., 1990; Oreskes and Einaudi, 1990; Haynes et al., submitted). Oreskes and Einaudi (1990) suggested a magmatic heat source but were non-specific about the petrological affinities of the magma involved, or whether metals were introduced from a hypogene source or from above. Oreskes and Einaudi (1992) suggested that ore deposition involved two fluids, one of "deep-seated possibly magmatic origin" from which magnetite-rich assemblages were formed, and a cooler fluid, possibly of surficial origin, responsible for deposition of hematite and probably Cu ores. Although they did not explicitly favour introduction of metals from above, these workers implied that it is possible. Haynes et al. (submitted) most clearly proposed a model involving metals introduced from above. Reeve et al. (1990) suggested that ore deposition involved both a magmatic fluid, possibly associated with mafic magmatism, and meteoric waters. These workers favoured the introduction of metals in hypogene magmatic fluids. All of the above workers agree that metal precipitation involved fluid mixing and redox-controlled reactions. The fundamental differences worthy of closer consideration concern whether metals were primarily introduced from above or below. These contrasting models imply quite different geological controls on ore formation. As such they are of considerable importance for exploration for this type of deposit. The two general models are considered below.

8.3.1 Fluid-mixing model

The fluid mixing model of Haynes et al. (submitted) stems from numerical modelling of the chemistry of hypothetical ore fluids, the compositions of which were constrained by mineralogical, textural, and fluid inclusion data. The model suggests:

1) Ore deposition is due to the mixing of a hot (at least 250°C), relatively reduced, saline (10 wt% NaCl equivalent) hypogene fluid with cooler, saline, more oxidised meteoric water.

2) The hypogene fluid was in chemical and Nd isotopic equilibrium with the Roxby Downs Granite and related granitoids of the Burgoyne batholith. It could have been a magmatic water derived from the granite itself or a deeper related pluton of the Burgoyne batholith, or possibly a "deeply circulated" crustal water which was ultimately of meteoric origin. The reduced fluid is viewed as the medium which transported the large quantities of iron into the deposit.

3) The modelled meteoric fluid is saline (10 wt% NaCl equivalent), oxidised, cooler (150°C), and was the main transporter of Cu, U, Au, and Ag.

4) With the exception of Fe, the dissolved metals were predominantly acquired by leaching of a bimodal volcanic pile. The mafic component of this volcanic sequence contributed the primitive component of the Nd isotopic signature of the hematitic ores. The meteoric fluid therefore transported significant amounts of REE to the deposit.

5) Mineralisation is believed to have occurred through hundreds or perhaps thousands of brecciation cycles and associated fluid-mixing events as pulses of the hypogene fluid were introduced. Metal precipitation was controlled mainly by redox reactions.

6) The different paragenetic stages of mineralisation are interpreted to result from temporal fluctuations in the proportions of the two mixing fluids during any given mineralisation cycle: i) magnetite-siderite-pyrite ores formed when and where the reduced hypogene fluid was dominant, ii) hematite-chalcopyrite and hematite-bornite-chalcocite ores formed as the hypogene fluids became progressively more diluted by the meteoric fluids, and iii) hematite-quartz breccias formed due to the progressive inundation of the breccias by oxidised meteoric waters as the input of hypogene fluids waned.

8.3.1.1 Implications

None of the data from the present study are inconsistent with this model. However, several implications of this model warrant further consideration. Haynes et al. (submitted) state that genesis of an Olympic Dam style deposit does not require "an exotic event or unusual rocks". A Cu-U deposit could be formed from meteoric waters that had access to any sequence of felsic (for U) and mafic (for Cu) source rocks. The Cu-source (bimodal volcanic pile) need not contain strongly alkaline rocks of the type observed at Olympic Dam except to contribute the REE enrichment which characterises this particular deposit. This implies that the unusual alkaline mafic/ultramafic magmatism occurring during ore deposition at Olympic Dam is not a necessary feature for the formation of a Cu-U-Au-Ag deposit, but rather is a local coincidence arising from the tectonomagmatic setting of the deposit.

The model of Haynes et al. (submitted) also requires a specific geomorphological and hydrological setting: It requires a source of saline meteoric waters which were in a somewhat confined hydrological system such that fluids leached bimodal volcanics over an area of at least 20 x 20 km (Chapter 7 mass balance calculations; assuming a volcanic

sequence 1 km thick). Metal-bearing brines must have been focussed into the present approximate lateral dimensions of the deposit, i.e. an areal extent of approximately 3 x 5 km where they mixed with the more reduced granite-related fluid. Haynes et al. (submitted) suggest that a playa lake in an arid environment is the likely setting. These workers also suggest that other Middle Proterozoic Fe-rich deposits, which are generally dominated by magnetite (Acropolis; Great Bear magmatic zone in Canada; Kiruna, Sweden; deposits in southeast Missouri, USA; see Hitzman et al., 1992), formed from the equivalent of the deeply circulated crustal or magmatic fluid, and are not as enriched in Cu, U, Au and Ag as the Olympic Dam deposit because they did not form beneath saline lakes or within zones of oxidised groundwaters which equilibrated with suitable source rocks.

Existing thermodynamic data indicate that it is not possible to transport significant Cu in a 250°C hypogene fluid of the composition of the deep crustal/ magmatic fluid of Haynes et al. (submitted). Their modelled fluid contains only 3 ppm Cu. However, a hypogene source of Cu (and other metals) may be plausible if the parameters used by Haynes et al. (submitted) to model fluid composition are not entirely appropriate. For example, these workers were forced to limit the temperature of their hypothetical hypogene fluid to 250°C and a salinity of 10 wt% NaCl equivalent because at higher levels of both parameters the thermodynamic data are unreliable. However, they recognise that ore formation temperatures indicated from fluid inclusions and oxygen isotopes suggest that the hypogene fluid was significantly hotter (up to 400°C). Measured salinities in fluid inclusions range well above 10 wt% NaCl equivalent. Such increased estimates of temperature and salinity may dramatically increase the solubility of Cu in the hypogene fluid (e.g. Helgeson, 1969). It is therefore necessary to consider the possibilities for hypogene introduction of ore metals raised by Reeve et al. (1990).

8.3.2 Fluids from an alkaline mafic/ultramafic magma

An alternative model worthy of consideration involves the following sequence of events:

1) The Roxby Downs Granite was emplaced at 1590 Ma as a product of large scale crustal melting above a diapiric upwelling of hot mantle.

2) Late-stage fluids exsolved from the crystallising granite, or perhaps from a slightly later pluton of the Burgoyne batholith, may have caused some brecciation, and precipitated magnetite-siderite-pyrite assemblages. This type of mineralisation has analogues associated with similar felsic rocks in comparable tectonic settings (e.g. Acropolis; Kiruna, Sweden; southeast Missouri, USA; Great Bear magmatic zone, Canada). Metal precipitation occurred due to gradients in temperature, pressure and redox conditions consequent upon release of magmatic fluids and mixing with cooler oxygenated groundwaters. The interpretation of the genesis of

the magnetite-rich assemblage is not significantly different to that of previous workers for the same rock type, but the Nd isotopic data presented in this study provide definitive constraints.

3) Alkaline mafic/ultramafic dykes within the deposit imply emplacement of a more substantial body or bodies of this magma type following the emplacement of the Roxby Downs Granite and its associated magnetite-rich mineralisation. The positive magnetic anomaly associated with the deposit may be taken as evidence for the presence of such a pluton.

4) Heat from the alkaline mafic/ultramafic magma may have initiated convective hydrothermal circulation leading to leaching of iron and other elements from granitic country rocks and possibly from the quenched margins of the mafic/ultramafic magma chamber. If these fluids leached granitic rocks only, this may have resulted in further precipitation of magnetite-rich assemblages in Nd-isotopic equilibrium with the Roxby Downs Granite.

5) The mafic/ultramafic magma exsolved a late-stage aqueous phase trapped within a sealed carapace. As crystallisation progressed the fluid phase became enriched in CO_2, H_2O, Cl, F, and incompatible elements e.g. REE, Ba, Nb, Y, Cu (if undersaturated in S) and possibly U. This provides a mechanism which can explain the greater degree of REE-enrichment and LREE fractionation observed in the hematitic ores and breccias compared to the mafic/ultramafic dykes [cf. Chapters 5 and 6]. The Cl-rich fluid may also be capable of transporting large quantities of Fe.

6) When the vapour pressure of the volatile phase exceeded the confining pressure, the cupola ruptured, releasing hot, saline, metal-laden brines upwards. Regional scale faulting may also have triggered fluid release. Explosive release of volatiles would also cause brecciation of the overlying rocks. These fluids may have been focussed by the fractured nature of the granitic and magnetite-rich breccias above. Alternatively fluid flow could have been controlled by regional-scale structures. Metal deposition was presumably controlled by gradients in temperature, pressure and redox conditions upon mixing with groundwaters.

7) Release of pressure from the crystallising magma allowed its upper levels to quench and seal, and the build up of volatiles recommenced. Repetitive release of volatiles may be the cause of the multiple overprinting brecciation episodes which are evident in the deposit.

8) The sulphide zonation in the deposit could have been produced in a similar manner to that proposed by Haynes et al. (submitted), i.e. due to the varying proportions

of mixing between hypogene and meteoric waters, with oxidation conditions acting as an important control on the stability of different sulphide species.

8.3.2.1 Implications

In many respects this model is similar to that proposed by Reeve et al. (1990). Like the fluid-mixing model of Haynes et al. (submitted), this model has specific implications and potential pitfalls:

Nd isotopic constraints indicate that the hematitic ores have an initial composition (εNd -2.5) intermediate between the granitic and mafic/ultramafic dyke end-member signatures (εNd -5 and +4 respectively). If the "alkaline magmatic volatiles" model is correct, the ore isotopic signature suggests that a high proportion of Nd was acquired from the granitic country-rocks after fluids were released from the mafic/ultramafic pluton.

It is implicit in the model that the key factor in forming the ore deposit is the emplacement at high crustal levels of a volatile-rich alkaline mafic/ultramafic magma. The model places great importance on the petrological affinities of the dykes within the deposit, and on a means of focussing the flow of reduced magmatically derived volatiles into a more oxidising environment.

This model suggests that the emplacement of magnetite-rich mineralisation is probably associated with emplacement of the granite. It therefore implies a temporal difference between emplacement of early magnetite-rich mineralisation and later hematite-dominant (Cu-U-enriched mineralisation). However, the field relationships and geochronological evidence suggest that the two styles of mineralisation are products of different evolutionary stages of the same regional thermal event.

Granitic magma and mafic/ultramafic magma were sequentially emplaced at high crustal levels in approximately the same locality. Their spatial coincidence may be controlled by crustal-scale structures (e.g. O'Driscoll, 1985; Sugden and Cross, 1991). Their temporal coincidence is not surprising given the interpreted tectonic setting of the deposit.

The fluid derived from the mafic/ultramafic magma is envisaged to be sufficiently reduced and saline that it is able to transport large quantities of Fe. Such a fluid is unlikely to be capable of transporting U as oxidised U^{6+}. Oreskes (1990) suggested that it is possible to transport U^{4+} as fluoride complexes. On the other hand, U may have been introduced to the deposit as U^{6+} following leaching of U from felsic country-rocks by oxidised meteoric waters.

If the "alkaline magmatic volatiles" model is correct, one would expect a degree of alkali metasomatism associated with the deposit. The geochemical data presented in Chapter 5 indicated that K and Na have been lost from the Roxby Downs Granite during alteration

and ore deposition. Creaser (1989) reported zones of sodic metasomatism in remote parts of the Burgoyne batholith, but the absence of potassic metasomatism in the vicinity of the deposit needs to be explained if this model is to be accepted.

On the basis of the data presented in this study it is not possible to choose the more probable of the two principal ore genesis models discussed. Refinement of plausible models awaits more detailed petrological and geochemical studies.

8.4 Conclusions

This study has made several significant contributions to understanding the genesis of the Olympic Dam deposit. The conclusions that can be drawn from the data presented are:

1) The deposit has an age of 1590 Ma and can be correlated with major regional magmatism, i.e. the Gawler Range/ Hiltaba volcano-plutonic event. A pre-existing age determination (1400 Ma) derived from isotopic analyses of pitchblende is shown to have resulted from an inappropriate treatment of data.

2) The initial Nd isotopic signatures of Olympic Dam hematitic ores and breccias have a primitive Nd component. The most likely source of this component are mafic and ultramafic rocks or magmas produced during the Gawler Range/ Hiltaba volcano-plutonic event.

3) Relative to the precursor Roxby Downs Granite, the Olympic Dam ores and breccias are enriched in many elements, including Cu, Cr, Ni, V, Mn, REE, Y, Nb and Ba. This suite of elemental enrichments is consistent with derivation from an alkaline mafic or ultramafic source.

4) The mafic/ultramafic dykes within the deposit have alkaline petrological affinities. Their incompatible trace element enrichments (interpreted as a primary igneous feature; see Chapter 6) are comparable to those of kimberlites, nephelenites and ultramafic lamprophyres. With increasing degree of alteration, these dykes are progressively depleted in Cu, Cr, Ni, V, Mn and Nb. The trace element and isotopic comparisons between the hematitic ores and the mafic/ ultramafic dykes strongly implicate these dykes or their plutonic or extrusive equivalents as sources of metals for the deposit.

5) Nd isotopic data indicate that magnetite-rich assemblages formed from fluids in isotopic equilibrium with the Roxby Downs Granite. These may have been magmatic fluids derived from the granite or a cogenetic pluton, or fluids which had equilibrated with the granite.

6) The data presented are inconsistent with the ore genesis model of Oreskes and Einaudi (1990), mainly due to their interpretation of the age of the deposit. The new data are

permissive of the model of Haynes et al. (submitted) which suggests that ore genesis is due to the mixing of a hot, saline Fe-bearing magmatic or deeply circulated fluid, with a cooler, saline Cu-U-REE-bearing meteoric fluid. The latter fluid is interpreted by these workers to have leached the metals of economic interest from a bimodal volcanic pile. The data presented also permit a model of ore genesis involving the sequential activity of magmatically derived fluids; firstly, Fe introduction associated with late stage crystallisation of the Roxby Downs Granite or a cogenetic pluton, followed by introduction of Cu, REE and possibly U transported by volatiles exsolved from an alkaline mafic/ultramafic pluton.

REFERENCES

Adler, H.H.,1964. The conceptual uranium ore roll and its significance in uranium exploration: Econ.Geol.: 59, 46-53.

Bagdasarov, E.A., Landa, E.A. and Markovskiy, A.A., 1981, Chemical composition and crystallization conditions of chrome spinels of volcanic ultramafics and other rocks of the mafic-ultramafic series: Int. Geol. Rev., 23, 931-940.

Bailey, D.K., 1984, Kimberlite: "The Mantle Sample" formed by ultrametasomatism: in Kornprobst, J. (ed.), 1984, Kimberlites I: Kimberlites and related rocks, Elsevier, Amsterdam.

Barsdell, M., 1988, Petrology and petrogenesis of clinopyroxene-rich tholeiitic lavas, Merelava Volcano, Vanuatu: J. Petrology, 29, 927-964.

Barsdell, M. and Berry, R., 1990, The petrology and geochemistry of Western Epi: J. Petrology, 31, 747-777.

Bau, M.,1991, Rare earth element mobility during hydrothermal and metamorphic fluid-rock interaction and the significance of the oxidation state of europium: Chem. Geol., 93, 219-230.

Bell, B.R. and Claydon, R.V., 1992, The cumulus and post-cumulus evolution of chrome-spinels in ultrabasic layered intrusions: evidence from the Cuillin Igneous complex, Isle of Skye, Scotland: Contrib. Mineral. Petrol., 112, 242-253.

Blisset, A.H., Parker, A.J. and Scheffler, J., 1989, Gawler Range Excursion Guide: Unpub. Geol. Soc. South Aust. 47p.

Bohrson, W.A. and Clague, D.A., 1988, Origin of xenoliths containing exsolved pyroxenes from Hualalai Volcano, Hawaii: Contrib. Mineral. Petrol., 100, 139-155.

Bradbury, J.,1988, The volcanic and shallow sub-volcanic component of the breccia hosted Olympic Dam U-Cu-Au deposit: implications for breccia pipe development: Unpub. B.Sc.(Hons) thesis, Melbourne, Australia, Monash Univ., 108p.

Brown, A.V. and Jenner, G.A., 1989, Geological setting, petrology and chemistry of Cambrian boninite and low-Ti tholeiite lavas in western Tasmania: in Crawford, A.J. (ed.), 1989, Boninites and related rocks: Unwin Hyman Ltd., London.

Cameron, E.N., 1977, Chromite in the central sector of the Eastern Bushveld Complex, South Africa: Amer. Mineral., 62, 1082-1096.

Cameron, W.E., McCulloch, M.T. and Walker, D.A., 1983, Boninite petrogenesis: chemical and Nd-Sr isotopic constraints: Earth Planet. Sci. Lett., 65, 75-89.

Campbell, I.H. and Griffiths, R.W., 1992, The changing nature of mantle hotspots through time: Implications for the chemical evolution of the mantle: J. Geology, 92, 497-523.

Campbell, I.H. and Murck, B.W., in press, Petrology of the G and H chromitite zones in the Mountain View area of the Stillwater Complex, Monatana: J. Petrology.

Cas, R.A.F. and Wright, J.V., 1987, Volcanic successions, modern and ancient: Allen and Unwin Ltd., U.K., 528p.

Chappell, B.W., 1991, Trace element analysis of rocks by X-ray spectrometry: Advances in X-ray analysis: 34, 263-276.

Chappell, B.W., and Hergt, J.M., 1989, The use of known Fe content as a flux monitor in neutron activation analysis: Chem. Geol., 78, 151-157.

Claoué-Long, J.C., King, R.W., and Kerrich, R., 1990, Archaean hydrothermal zircon in the Abitibi greenstone belt: constraints on the timing of gold mineralisation: Earth Planet. Sci. Lett., 98, 109-128.

Clement, S. and Compston, W., 1972, The design and performance of a new mass spectrometer using ion beam transport theory: Internat. J. Mass Spectrometry Ion Physics, 10, 323-342.

Coish, R.A., 1989, Boninitic lavas in Appalachian ophiolites: a review: in Crawford, A.J. (ed.), 1989, Boninites and related rocks: Unwin Hyman Ltd., London.

Collerson, K.D., Campbell, L.M., Weaver, B.L. and Palacz, Z.A., 1991, Evidence for extreme fractionation in early Archaean ultramafic rocks from northern Labrador: Nature, 349, 209-214.

Collins, W.J., Beams, S.D., White, A.J.R. and Chappell, B.W., 1982, Nature and origin of A-type granites with particular reference to southeastern Australia,: Contrib. Mineral. Petrol., 80, 189-200.

Compston, W., Crawford, A.R. and Bofinger, V.M., 1966, A radiometric estimate of the duration of sedimentation in the Adelaide Geosyncline, South Australia: J. Geol. Soc. Australia, 13, 229-276.

Compston, W., Kinny, P.D., Williams, I.S. and Foster, J.J., 1986 . The age and Pb loss behaviour of zircons from the Isua supracrustal belt as determined by ion microprobe: Earth Planet. Sci. Lett. , 80, 71-81.

Compston, W., Williams, I.S., Kirschvink, J.L., Zichau, Z. and Guogan, M., 1992, Zircon U-Pb ages for the Early Cambrian time-scale: J. Geol. Soc. London, 149, 171-184.

Compston, W., Williams, I.S. and Meyer, C., 1984, U-Pb geochronology of zircons from lunar breccia 73217 using a sensitive high mass-resolution ion microprobe: Proc. Lunar Planet. Sci. Conf. 14th J. Geophys. Res., 89, B525-B534.

Cowley, W.M. and Fanning, C.M., 1991, Low-grade Archaean metavolcanics in the Northern Gawler Craton: Geol. Surv. Sth. Aust. Quarterly Geol. Notes, 119, 2-17.

Crawford, A.J. (ed.), 1989, Boninites and related rocks: Unwin Hyman Ltd., London.

Creaser, R.A., 1989, The geology and petrology of Middle Proterozoic felsic magmatism of the Stuart Shelf, South Australia: Unpub. PhD thesis Melbourne, Australia, La Trobe Univ., 434p.

Creaser and Cooper, (in press), U-Pb geochronology of Middle Proterozoic felsic magmatism surrounding the Olympic Dam Cu-U-Au-Ag and Moonta Cu-Au-Ag deposits, South Australia: Econ Geol.

Cumming, G.L. and Richards, J.R., 1975, Ore lead isotope ratios in a continuously changing Earth: Earth Planet. Sci. Lett., 28, 155-171.

Daly, S.J. and Fanning, C.M., 1990, Archaean geology of the Gawler Craton, South Australia: Extended Abstracts Volume, Third International Archaean Symposium, Perth, 1990.

Dana, E.S., 1898, revised by Ford, W.E., 1932, Dana's textbook of mineralogy: New York, John Wiley and Sons, 851p.

Deer, W.A., Howie, R.A. and Zussman, J., 1966, An introduction to the rock forming minerals: London, Longman, 528p.

DePaolo, D.J. and Wasserburg, G.J., 1976, Nd isotopic variations and petrogenetic models: Geophys. Res. Letters, 3, 249-252.

Eggins, S.M., in press, Origin and differentiation of picritic arc magmas, Ambae (Aoba), Vanuatu: Contrib. Mineral. Petrol.

Egorov, L.S., 1970, Carbonatites and ultrabasic-alkaline rocks of the Maimecha-Kotu region, N. Siberia: Lithos, 3, 341-359.

Einaudi, M.T. and Oreskes, N., 1989, Progress toward an occurrence model for Proterozoic iron-oxide deposits - A comparison between the ore provinces of South Australia and Southeast Missouri. *in* Pratt, W.P. and Sims, P.K. eds., The Midcontinent of the United States- Permissive terrane for an Olympic Dam-type deposit?: U.S. Geol. Survey Bull. no. 1932: 58-69.

Ellam, R.M. and Cox, K.G., 1989, A Proterozoic lithospheric source for Karoo magmatism: evidence from the Nuanetsi picrites: Earth Planet. Sci. Lett., 92, 207-218.

Esdale,D.J., Pridmore,D.F.,Coggan,J.H.,Muir,P.M.,Williams,P.K. and Fritz,F.P., 1987, Olympic Dam deposit-geophysical case history: Bull. Aust. Soc. Explor. Geophys. 18, 47-49.

Evans, B.W. and Frost, B.R., 1975, Chrome-spinel in progressive metamorphism - a preliminary analysis: Geochim. Cosmochim. Acta, 39, 959-972.

Falloon, T.J., Green, D.H. and McCulloch, M.T., 1989, Petrogenesis of high-Mg and associated lavas from the north Tonga Trench: in Crawford, A.J. (ed.), 1989, Boninites and related rocks: Unwin Hyman Ltd., London.

Fanning, C.M., Flint, R.B., Parker,J.A., Ludwig,K.R. and Blisset, A.H., 1988, Refined Proterozoic evolution of the Gawler Craton, South Australia, through U-Pb zircon geochronology: Precamb. Res., 40/41, 363-386.

Fanning, C.M., Flint, R.B. and Preiss, W.V., 1983, Geochronology of the Pandurra Formation: Q. Geol. Notes, Geol. Surv. S. Aust., 88, 11-16.

Faure, G., 1986, Principles of isotope geology: John Wiley and Sons, New York.

Fein, J.B., Hemley, J.J, D'Angelo, W.M., Komninou, A. and Sverjensky, D.A., 1992, Experimental study of iron-chloride complexing in hydrothermal fluids: Geochim. Cosmochim. Acta, 56, 3179-3190.

Fisher, R.V. and Scmincke, H.-U., 1984, Pyroclastic Rocks: Berlin, Springer Verlag, 472p.

Foley, S.F. and Venturelli, G., 1989, High-K2O rocks with high-MgO, high SiO2 affinities: in Crawford, A.J. (ed.), 1989, Boninites and related rocks: Unwin Hyman Ltd., London.

Giles, C.W., 1988, Petrogenesis of the Proterozoic Gawler Range Volcanics, South Australia: Precamb. Res., 40/41, 407-427.

Giles, C.W. and Teale, G.S., 1979, A comparison of the geochemistry of the Roopena Volcanics and the Beda Volcanics: Q. Geol. Notes, Geol. Surv. S. Aust., 71, 7-13.

Grant, J., A., 1986, The isocon diagram - a simple solution to Gresen's equation for metasomatic alteration: Econ Geol., 81, 1976-1982.

Gresens, R.L., 1966, Composition - volume relationships of metasomatism: Chem. Geol., 2, 47-55.

Griffiths, R.W. and Campbell, I.H., 1991, Interaction of mantle plume heads with the Earth's surface and onset of small-scale convection: J. Geophys. Res., 96, 18295-18310.

Gruau, G., Jahn, B.M., Glikson, A.Y., Davy, R., Hickman, A.H. and Chauvel, C., 1987, Age of the Archaean Talgo-Talgo subgroup, Pilbara Block, Western Australia, and early isotopic evolution of the mantle: new Sm-Nd isotopic evidence: Earth Planet. Sci. Lett., 85, 105-116.

Gustafson, L.B. and Compston, W., 1979, Rb-Sr dating of Olympic Dam core samples: Canberra, ACT, Australian National University, Research School of Earth Sciences, unpublished report, 9p.

Guthrie, V., 1991, Determination of recent ^{238}U, ^{234}U and ^{230}Th mobility in granitic rocks: application of a natural analogue to the high-level waste repository environment: Applied Geochemistry, 6, 63-74

Haggerty, S.E., 1976, Opaque mineral oxides in terrestrial igneous rocks. In Rumble, D. (ed.), Oxide Minerals Short Course Notes. Min. Soc. America, 3, 101-300.

Hagni, R.D. and Brandom, R.T.,1988, Comparison of Boss-Bixby, Missouri, and Olympic Dam, South Australia ore deposits, and the potential for these deposits in the midcontinent region, *in* Kisvarsanyi, G. and Grant, S.K., eds., Proc. North American conference on tectonic control of ore deposits and the vertical and horizontal extent of ore systems. Proceedings volume: Rolla, Univ. Missouri-Rolla Press, 333-345.

Hagni, R.D. and Brandom, R.T., 1989, The mineralogy of the Boss-Bixby, Missouri copper-iron-cobalt deposit and a comparison to the Olympic Dam deposit at Roxby Downs, South Australia, *in* Brown, V.M., Kisvarsanyi, E.B. and Hagni, R.D., eds., "Olympic Dam-Type" deposits and geology of the Middle-Proterozoic rocks in the St. Francois Mountains Terrane, Missouri: Soc.Econ.Geologists guidebook series, 4 (series ed. T.B.Thompson), 172p.

Hauck, S.A., 1989, Petrogenesis and tectonic setting of middle Proterozoic iron oxide-rich deposits - an ore deposit model for Olympic Dam-type mineralisation, *in*, Pratt, W.P. and Sims, P.K., eds., The Midcontinent of the United States - permissive terrane for an Olympic Dam-type deposit ?: U.S. Geol. Survey Bull. no.1932, 4-39.

Hauck, S.A. and Kendall, E.W., 1984, Comparison of Middle Proterozoic iron-oxide rich ore deposits, mid-continent USA, South Australia, Sweden and People's Republic of China: 30th Annual Institute on Lake Superior Geology, Wasau, Wisconsin: 17-18.

Haynes, D.W., 1979, Geological technology in mineral resource exploration, *in* Kelsall, D.F. and Woodcock, J.T., eds., Mineral Resources of Australia. Third invitation symposium, Proceedings volume: Adelaide, 1979 Australian Academy of Technological Sciences, Melbourne. 75-95.

Haynes, D.W., Cross, K.W., Bills, R.T. and Reed, M.H., Olympic Dam ore genesis: A fluid mixing model: submitted to Econ. Geol.

Helgeson, H.C., 1969, Thermodynamics of hydrothermal systems at elevated temperatures and pressures: Amer. J. Sci., 267, 729-804.

Henderson, P., 1975, Reaction trends shown by chrome-spinels of the Rhum layered intrusion: Geochim. Cosmochim. Acta, 39, 1035-1044.

Hinthorne, J.R., Andersen, C.A., Conrad, R.L. and Lovering,J.F., 1979. Single grain 207Pb/206Pb and U/Pb age determinations with a 10μm spatial resolution using the ion microprobe mass analyser (IMMA): Chem. Geol., 25, 271-303.

Hitzman, M.W., Oreskes, N. and Einaudi, M.T., 1990, Geologic characteristics and tectonic setting of Proterozoic Olympic Dam (Kiruna)-type deposits: Abstracts , Eighth International Association on the Genesis of Ore Deposits, Ottawa.

Hitzman, M.W., Oreskes, N. and Einaudi, M.T., 1992, Geological characteristics and tectonic setting of Proterozoic iron oxide (Cu-U-Au-REE) deposits: Precamb. Res., 58, 241-287.

Hoeve, J.and Quirt,D.,1987. A stationary redox front as a critical factor in the formation of high-grade, unconformity-type uranium ores in the Athabasca Basin, Saskatchewan, Canada. Bull.Mineral., 110: 157-171.

Ireland, T.R., Compston, W., Williams,I.S., and Wendt, I., 1990, U-Th-Pb systematics of individual perovskite grains from the Allende and Murchison carbonaceous chondrites: Earth Planet. Sci. Lett., 101, 379-387

Jochum, K.P., Arndt, N.T. and Hoffman, A.W., 1991, Nb-Th-La in komatiites and basalts: constraints on komatiite petrogenesis and mantle evolution: Earth Planet. Sci. Lett., 107, 272-289.

Johnson, J.P. and Cross, K.C., 1991a, Geochronological constraints on the genesis of the Olympic Dam Cu-U-Au-Ag deposit, South Australia: S.G.E.G. Ore Fluids Conference Abstracts, Canberra. B.M.R. Record No. 1990/95, 84p.

Johnson, J.P. and Cross, K.C., 1991b, Geochronological and Sm-Nd isotopic constraints on the genesis of the Olympic Dam Cu-U-Au-Ag deposit, South Australia, *in* Pagel, M. and Leroy, J.L., eds., Source,Transport and Deposition of Metals. Proceedings of the 25 Years S.G.A. Anniversary Meeting, Nancy. Rotterdam, Balkema, 841p.

Kimball, K., 1990, Effects of hydrothermal alteration on the compositions of chromian spinels: Contrib. Mineral. Petrol., 105, 337-346.

Kisvarsanyi, G. and Kisvarsanyi, E.B., 1989. Precambrian geology and ore deposits of the Southeast Missouri iron metallogenic province. *in* Brown, V.M., Kisvarsanyi, E.B. and Hagni, R.D., eds., "Olympic Dam-Type" deposits and geology of the Middle-Proterozoic rocks in the St. Francois Mountains Terrane, Missouri: Soc.Econ.Geologists guidebook series, 4 (series ed. T.B.Thompson), 172p.

Knutson, J., Donnelly, T.H., Eadington, P.J. and Tonkin, D.G., 1992, Hydrothermal alteration of Middle Proterozoic basalts, Stuart Shelf, South Australia - a possible source for Cu mineralisation: Econ. Geol., 87, 1054-1077.

Krcmarov, R., 1987, The geology, petrology and geochemistry of the volcanic unit at Olympic Dam, South Australia: Unpub. B.Sc. (Hons.) thesis, Adelaide, Australia, Univ. Adelaide, 32p.

Lalor, J.H., 1984, Olympic Dam South Australia- the discovery history, *in* Geoscience in the Development of Natural Resources, Seventh Australian Geological Convention, Sydney. Geol.Soc.Australia Abstracts no. 12, 321-322.

Lalor, J.H., 1986, Olympic Dam copper-uranium-gold deposit, South Australia, *in* Fourth Circum-Pacific Energy and Mineral Resources Conference, Singapore, 1986, Abstracts, Bull. A.A.P.G., 70: 926.

Le Roex, A.P., 1986, Geochemical correlation between southern African kimberlites and South Atlantic hotspots: Nature, 324, 243-245.

Long, J.V.P. and Hinton, R.W., 1984, The intensity of metal hydride peaks in secondary positive-ion spectra from silicates: Int. J. Mass Spectrom. Ion Proc., 55, 307-318.

Lorenz, V., 1985, Maars and diatremes of phreatomagmatic origin; a review: Trans. Geol. Soc. South Afr., 88, 459-470.

Ludwig, K., 1992, Isoplot: A plotting and regression program for radiogenic-isotope data: U.S.G.S Open-file Report 91-445.

Mason, M.G., Thomson, B.P. and Tonkin, D.G., 1978, Regional stratigraphy of the Beda Volcanics, Backy Point Beds and Pandurra Formation on the southern Stuart Shelf, South Australia: Geol. Surv. South Aust. Q. Geol. Notes, 66, 2-9.

Meyer, C., 1988, Proterozoic ore-forming habitats -tectonic and chemical transitions, *in* Kisvarsanyi, G. and Grant, S.K., eds., Proc. North American conference on tectonic control of ore deposits and the vertical and horizontal extent of ore systems. Proceedings volume: Rolla, Univ. Missouri-Rolla Press, 333-345.

Meyer, H.O.A. and Boyd, F.R., 1972, Composition and origin of crystalline inclusions in natural diamonds: Geochim. Cosmochim. Acta, 36, 1255-1273.

Mitchell, R.H., 1986, Kimberlites: Mineralogy, Geochemistry and Petrology. Plenum Press, New York, 422p.

Mitchell, R.H. and Bergman, S.C., 1991, Petrology of Lamproites. Plenum Press, New York.

Mortimer, G.E., Cooper, J.A., Patterson, H.L., Cross, K.C., Hudson, G.R.T. and Uppill, R.K., 1988a, Zircon U-Pb dating in the vicinity of the Olympic Dam Cu-U-Au deposit, Roxby Downs, South Australia: Econ. Geol., 83, 694-709.

Mortimer, G.E., Cooper, J.A. and Oliver, R.L., 1988b, The geochemical evolution of Proterozoic granitoids near Port Lincoln in the Gawler orogenic domain of South Australia: Precamb. Res., 40/41, 387-407.

Mumpton, F.A. and Roy, R., 1961, Hydrothermal stability studies of the zircon-thorite group: Geochim. Cosmochim. Acta, 21, 217-238.

Muramatsu, Y., 1983, Geochemical investigations of kimberlites from the Kimberley area, South Africa: Geochem. Journal, 17, 71-86.

Muramatsu, Y. and Wedepohl, K.H., 1985, REE and selected trace elements in kimberlites from the Kimberley area (South Africa): Chem. Geol., 51, 289-301.

Murck, B.W. and Campbell, I.H., 1986, The effects of temperature, oxygen fugacity and melt composition on the behaviour of chromium in basic and ultrabasic melts: Geochim. Cosmochim. Acta, 50, 1871-1887.

Nash, W.P. and Crecraft, H.R., 1985, Partition coefficients for trace elements in silicic magmas: Geochim. Cosmochim. Acta, 49, 2309-2322.

Nelson, D.R., 1987, Petrogenesis of alkaline rocks - isotopic constraints: Unpub. PhD thesis, Canberra, Australia, Australian National University.

Nicholls, J. and Stout, M.Z., 1988, Picritic melts in Kilauea - evidence from the 1967-1968 Halemaumau and Hiiaka eruptions. J. Petrology, 29, 1031-1057.

Nixon, P.H., Thirlwall, M.F., Buckley, F. and Davies, C.J., 1984, Spanish and Western Australian lamproites: aspects of whole rock geochemistry: in Kornprobst, J. (ed.), 1984, Kimberlites I: Kimberlites and related rocks, Elsevier, Amsterdam.

Norrish, K. and Hutton, J.T., 1969, An accurate X-ray spectrographic method for the analysis of a wide range of geological samples: Geochimica et Cosmochimica Acta, 33, 431-453.

O'Driscoll, E.S.T., 1985, The application of lineament tectonics in the discovery of the Olympic Dam Cu-Au-U deposit, Roxby Downs, South Australia: Global Tectonics and Metallogeny, 3 (1), 43-57.

Oreskes, N., 1990, Uranium content of Olympic Dam hematite: Implications for fluid chemistry and ore depositional mechanisms: Abstracts, Eighth International Association on the Genesis of Ore Deposits, Ottawa.

Oreskes, N. and Einaudi, M.T., 1990, Origin of rare earth element-enriched hematite breccias at the Olympic Dam Cu-U-Au-Ag deposit, Roxby Downs, South Australia: Econ. Geol., 85, 1-28.

Oreskes, N. and Einaudi. M.T., 1992, Origin of hydrothermal fluids at Olympic Dam: preliminary results from fluid inclusions and stable isotopes: Econ. Geol., 87, 64-90.

Parker, J.A., 1990, Gawler Craton and Stuart Shelf - regional geology and mineralisation, In Hughes F.E (ed.), Geology of the Mineral Deposits of Australia and Papua New Guinea. The Australasian Institute of Mining and Metallurgy: Melbourne, Monograph 14, 999-1008.

Philpotts, J., Tatsumoto, M., Li, X. and Wang, K., 1991, Some Nd and Sr isotopic systematics for the REE-enriched deposit at Bayan Obo, China: Chemical Geology, 90, 177-188.

Pupin, J.A., 1980, Zircon and granite petrology: Contr. Mineralogy Petrology, 73, 207-220.

Preiss, W.V., (Comp.), 1987. The Adelaide Geosyncline: Late Proterozoic stratigraphy, sedimentation, palaeontology and tectonics. Geol. Surv. South Aust. Bull. 53., 438pp.

Rankin, L.R., Flint, R.B. and Fanning, C.M., 1988, The Bosanquet Formation of the Gawler Craton: Q. Geol. Notes, Geol. Surv. S. Aust., 105, 12-18.

Reed, S. J. B., Trueman, N. A. and Long, J. V. P., 1987, Ion microprobe U-Pb dating of pitchblende; in Secondary Ion Microscopy (SIMS VI). Benninghaven, A., Huber, A.W. and Werner, H.W., eds.. Wiley, 1988, 945-948.

Reeve, J.S., Cross, K.C., Smith, R.N. and Oreskes, N., 1990, The Olympic Dam copper-uranium-gold-silver deposit, South Australia, *in* Hughes, F.E., ed., The Australasian Institute of Mining and Metallurgy Monograph.14, 1009-1035.

Richards, J.P., Cumming, G.L., Krstic, D., Wagner, P.A. and Spooner, E.T.C., 1988, Pb isotope constraints on the age of sulfide ore deposition and U-Pb age of late uraninite veining at the Musoshi stratiform copper deposit, Central African Copper Belt, Zaire: Econ. Geol., 83, 724-741.

Ringwood, A.E., 1991, Inaugural Ingerson Lecture: Phase transformations and their bearing on the constitution and dynamics of the mantle: Geochim. Cosmochim. Acta, 55, 2083-2110.

Roberts, D.E. and Hudson, G.R.T., 1983, The Olympic Dam copper-uranium gold-silver deposit, Roxby Downs, South Australia: Econ. Geol., 78, 799-822.

Rock, N.M.S., 1991, Lamprophyres: Blackie and Son Ltd., London.

Roeder, P.L. and Campbell, I.H., 1985, The effect of postcumulus reactions on composition of chrome-spinels from the Jimberlana intrusion.: J. Petrol., 26, 763-786.

Rubin, J.N., Henry, C.D. and Price, J.G., 1989, Hydrothermal zircons and zircon overgrowths, Sierra Blanca Peaks, Texas: Am. Mineralogist, 74, 865-869.

Scowen, P.A.H., Roeder, P.L. and Helz, R.T., 1991, Reequilibration of chromite within Kilauea Iki lava lake, Hawaii: Contrib. Mineral. Petrol., 98, 326-345.

Shimizu, N. and Hart, S. R., 1982, Applications of the ion microprobe to geochemistry and cosmochemistry: Ann. Rev. Earth Planet. Sci., 10, 483-526.

Sigurdsson, H. and Schilling, J.G., 1976, Spinels in Mid-Atlantic Ridge basalts: Chemistry and occurrence: Earth Planet. Sci. Lett., 29, 7-20.

Smith, C.B., 1983, Pb, Sr and Nd isotopic evidence for sources of African Cretaceous kimberlites: Nature, 304, 51-54.

Sobolev, A.V., Kamenetskiy, V.S. and Kononkova, N.N., 1991, New data on Siberian meymechite petrology: Geokhimiya, 8, 1084-1095.

Steiger, R.H. and Jäger, E., 1977, Subcommission on geochronology: Convention on the use of decay constants in geo- and cosmochronology: Earth Planet. Sci. Letters, 36, 359.

Stewart, K., and Foden, J., 1990, The fundamental role of mantle derived magma in the production of a large volume felsic volcanic province, Gawler Ranges, South Australia: Seventh International Conference on Geochronology and Isotope Geology. Geol. Soc. Australia Abstracts, no. 27, 125p.

Streckeisen, 1976, To each plutonic rock its proper name: Earth Sci. Rev., 12, 1-33.

Sugden, T.J., 1989, Characteristics of faults at Olympic Dam and their possible relationship to regional lineaments. *in* Australasian Tectonics, Specialist Group in Tectonics and Structural Geology, Kangaroo Island Conference, Geol. Soc.Aust.Abstr., 24: 143-145.

Sugden, T.J. and Cross, K.C., 1991, Significance of overprinting fault systems in the Olympic Dam Breccia Complex. In: Structural Geology in Mining and Exploration: extended abstracts to accompany conference held in Kalgoorlie, 10-13 October, 1991; p93-98. Publication No. 25, Geology Department (Key Centre) & University Extension, The University of Western Australia.

Sun, S-S. and McDonough, W.F., 1989, Chemical and isotopic systematics of oceanic basalts: implications for mantle composition and processes: in Saunders, A.D. and

Norry, M.J. (eds.), Magmatism in the Ocean Basins, Geol. Soc. Special Publication No. 42, 313-345.

Sun, S-S and Nesbitt, R.W., 1978, Petrogenesis of Archaean ultrabasic and basic volcanics: evidence from rare earth elements: Contrib. Mineral. Petrol., 65, 301-325.

Taylor, S.R. and McLennan, S.M., 1985, The Continental Crust: its composition and evolution: Oxford, Blackwells Scientific Publications.

Thomson, B.P., Daily, B., Coats, R.P. and Forbes, B.G., 1976, Late Precambrian and Cambrian geology of the Adelaide 'Geosyncline' and Stuart Shelf, South Australia: Excursion Guide No. 33A, 25th International Geological Congress, Sydney.

Thornton, C.P., 1989, Lava and lava eruptions, In Bowes, D.R. (ed.) The Encyclopedia of Igneous and Metamorphic Petrology, Van Nostrand Reinhold, New York, p 278.

Trueman, N.A., Long, J.V.P., Reed, S.J.B. and Chinner, G.A., 1988, The lead-uranium systematics, and rare earth element distributions of some Olympic Dam and Stuart Shelf mineralisation: Western Mining Corp. unpub. report K/3143 Adelaide, Australia.

von der Borch, C.C., 1980, Evolution of Late Proterozoic to Early Palaeozoic Adelaide Fold Belt, Australia: comparisons with post-Permian rifts and passive margins: Tectonophysics, 70, 115-134.

Wasserburg, G.J., Jacobsen, S.B., DePaolo, D.J. and McCulloch, M.T., 1981, Precise determination of Sm/Nd ratios, Sm and Nd isotopic abundances in standard solutions: Geochim. Cosmochim. Acta, 45, 2311-2323.

Wawryk, C., 1989, Strontium and Rare Earth Element geochemistry of barite-fluorite mineralisation at Olympic dam, South Australia: Unpub. B.Sc. (Hons.) thesis, Adelaide, Australia, Univ. Adelaide, 31p.

Webb, A.W., Coats, R.P., Fanning, C.M. and Flint, R.B.,1983, Geochronological framework of the Adelaide geosyncline: Geol. Soc. Australia Abstracts, no.10.

Webb, A.W., Thomson, B.P., Blisset, A.H., Daly, S.J., Flint, R.B. and Parker, A.J., 1982, Geochronology of the Gawler Craton, South Australia: S. Aust. Dept. Mines and Energy report 82/86 (unpublished)

Webb, A.W., Thomson, B.P., Blisset, A.H., Daly,S.J., Flint, R.B. and Parker, A.J., 1986, Geochronology of the Gawler Craton, South Australia: Australian J. Earth Sci., 33 (2), 119-143

Wedepohl, K.H., Correns, C.W., Shaw, D.M., Turekian, K.K. and Zemann, J. (eds.), 1969, Handbook of Geochemistry: Springer-Verlag, Berlin.

Wedepohl, K.H. and Muramatsu, Y., 1979, The chemical composition of kimberlites compared with the average composition of three basaltic magma types, in: Kimberlites, Diatremes and Diamonds: Their Geology, Petrology and Geochemistry, F.R. Boyd and H.O.A. Meyer, eds., American Geophysical Union, Washington DC, 300-312, 1979.

Whitney, J.A., Hemley, J.J. and Simon, F.O., 1985, The concentration of iron in chloride solutions equilibrated with synthetic granitic compositions: the sulphur-free system: Econ. Geol., 80, 444-460.

Wilkinson, J.F.G. and Hensel, H.D., 1988, The petrology of some picrites from Mauna Loa and Kilauea volcanoes, Hawaii: Contrib. Mineral. Petrol., 98, 326-345.

Wilson, M., 1989, Igneous Petrogenesis: a global tectonic approach. Unwin Hyman, London, 466p.

Winchell, A.N. and Winchell, H., 1951, Elements of optical mineralogy; an introduction to microscopic petrography: John Wiley and Sons, New York.

Wood, S. A., 1990, The aqueous geochemistry of the rare earth elements and yttrium 2. Theoretical predictions of speciation in hydrothermal solutions to 350 °C at saturation water vapour pressure: Chem. Geol., 88, 99-125.

Wyborn, L.A.I., Page, R.W. and Parker, A.J., 1987, Geochemical and geochronological signatures in Australian Proterozoic igneous rocks, *in* Pharoah, T.C.,.Beckinsale, R.D. and Richard, D. eds., Geochemistry and Mineralisation of Proterozoic Volcanic Suites: Geol.Soc.Australia Special Publication 33, 377-394.

Zhao, J. and McCulloch, M.T., (1992a), Sm-Nd mineral isochron ages of Late Proterozoic dykes swarms in Australia: evidence for two distinctive events of mafic magmatism and ctustal extension: Chem. Geol. (submitted).

Zhao, J. and McCulloch (1992b), Melting of a subduction-modified continental lithospheric mantle (CLM): Evidence from Late Proterozoic mafic dyke swarms in central Australia: Geology (submitted).

Zhou, M-F, and Kerrich, R., 1992, Morphology and composition of chromites in komatiites from the Belingwe greenstone belt, Zimbabwe: Canadian Mineralogist, 30, 303-317.

APPENDIX 1 THE MUSOSHI URANINITE STANDARD

A1.1 Introduction

A reconnaissance ion microprobe study of Olympic Dam pitchblende has been described in Chapter 4. It demonstrated that Pb and U ionic species sputtered from pitchblende are correlated and amenable to internal calibration of Pb/U isotopic ratios. Despite disturbance of the U-Pb isotopic systematics, in many cases Olympic Dam pitchblende retains sufficient radiogenic Pb to yield concordant or near-concordant data. Although open system behaviour requires that geological interpretation of the analyses must be approached with caution, the reconnaissance study was an analytical success. For this reason developmental work on a suitable uraninite standard was commenced and the purpose of this appendix is to document that work.

A uraninite standard should be coarse-grained, free of inclusions, homogeneous, and have concordant U-Pb systematics. A suitable uraninite which fits most of the above criteria has been well-documented by Richards et al. (1988). The sample is from the Musoshi stratiform copper deposit in Zaire where cubic uraninite with few inclusions occurs in veins as undeformed centimetre-sized euhedra and coarse aggregates. The veins also contain dolomite, feldspar, quartz, biotite, molybdenite, rutile, copper sulphides and native copper. Uraninite only occurs in the veins where they have propagated into a relatively reduced shale (Richards et al., 1988) which suggests that reduction of dissolved U^{6+} was the cause of uraninite precipitation. Conventional U-Pb analyses (TIMS) of the Musoshi uraninites are concordant to near-concordant, defining a discordia line with intercepts of 514 ± 2 and 4 ± 82 Ma. A small amount of recent Pb loss can be inferred from these data. Dr J.P. Richards kindly supplied samples of these uraninite grains for selection of a standard for the ion probe. Specimen No. 19 of Richards et al. (1988) was selected because it had yielded a concordant analysis. The data from the conventional analyses of these workers were confirmed by analyses on the same material by Mr M. Fanning at the Australian National University. The data are listed in Table A1.

Fifty-four areas were analysed in two separate ion probe sessions. The analyses consist of four scans through the mass spectrum with the following steps; ^{204}Pb, ^{206}Pb, ^{207}Pb, ^{208}Pb, ^{238}U, $^{248}(ThO)$, $^{254}(UO)$ and $^{270}(UO_2)$. In each scan the uranium species were counted for 1 second, ^{204}Pb, ^{207}Pb and ^{208}Pb for 10 seconds, and ^{206}Pb and ^{248}ThO were counted for 5 seconds. The $^{207}Pb/^{206}Pb$ ratios measured in the first session were consistently higher than the conventional analyses (discussed in more detail below). The sample was re-polished with new pads to eliminate the possibility that the high $^{207}Pb/^{206}Pb$ ratios were caused by contamination with Pb from the polishing pad, which had previously been used to polish Olympic Dam pitchblende, and the second analytical

session was undertaken. The same problem was evident so a third analytical session was made in an attempt to determine whether isobaric interferences were the cause of the problems in measuring Pb isotopic ratios.

Table A1 Thermal ionisation mass spectrometry data for the Musoshi uraninite sample No. 350W-1040(H), Specimen no. 9, of Richards et al. (1988)

	Wt (mg)	$^{*207}Pb/^{206}Pb$	$^{208}Pb/^{206}Pb$	$^{*204}Pb/^{206}Pb$	U %	Pb %	$^{*207}Pb/^{235}U$	$^{*206}Pb/^{238}U$	Age $^{207}Pb/^{206}Pb$
a	13.62	0.05767	0.00034	0.00000	83.67	6.33	0.6604	0.0832	514 ± 3
b	0.0038	0.057610	0.00053	0.00003	67.24	5.03	0.65307	0.08222	514.9 ± 1.2
b	0.0062	0.057636	0.00017	0.00001	81.23	6.03	0.64846	0.08160	516 ± 1.1

a Analysis of Richards et al. (1988)

b Analyses of M. Fanning, Australian National University

* Radiogenic ratio

A1.2 Pb/U calibration

In the ion probe study of Olympic Dam pitchblende (Chapter 4) the covariation of $^{206}Pb^+/UO^+$ and UO_2^+/UO^+ yielded a calibration curve with a lower degree of scatter (10.8 % error) than the curve derived from $^{206}Pb^+/U^+$ and UO^+/U^+ ratios (17.2% error). This is not the case for the Musoshi uraninite. A plot of $^{206}Pb^+/UO^+$ against UO_2^+/UO^+ for the data from session 1 (Figure A1) demonstrates that these ratios are not well-correlated and the data from session 2 have an overall poorly-defined negative correlation (Figure A2). The difference in relative ionic yields between the Olympic Dam pitchblende and the Musoshi uraninite may be attributable to different sputtering conditions caused by the different mineral structures of uraninite (UO_2) and its oxidised and hydrated variant, pitchblende (Winchell and Winchell, 1951).

In contrast the data for Pb^+/U^+ and UO^+/U^+ ratios are well correlated. Figure A3 shows these ratios for the data from session 1 and a curve can be derived which relates the variables by the following quadratic equation:

$$^{206}Pb^+/^{238}U^+ = 0.005239 .(UO/U)^2 + 0.042408 .(UO/U) - 0.32608$$

The data scatter about this curve with a relative standard deviation (uncertainty) of 6.9%. If analyses 1.5 and 2.1 (the two points circled in Figure A3) are deleted as outliers the uncertainty is reduced to 5.0%.

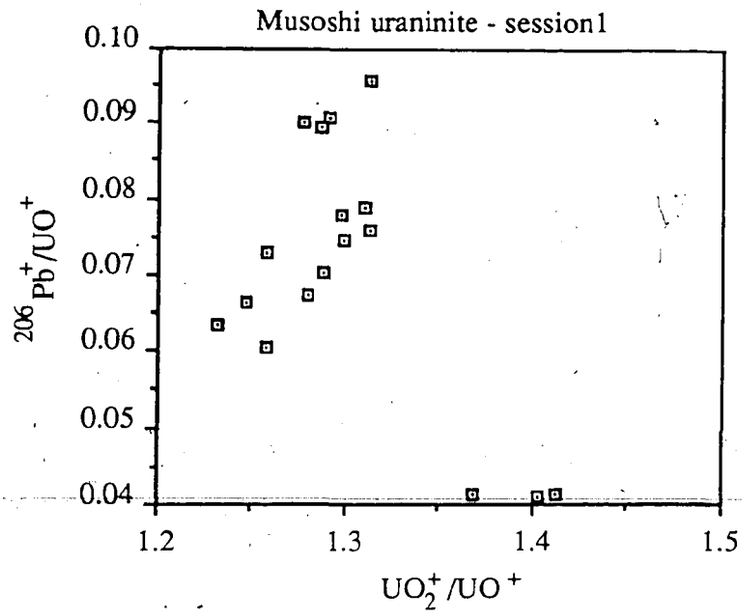

Figure A.1

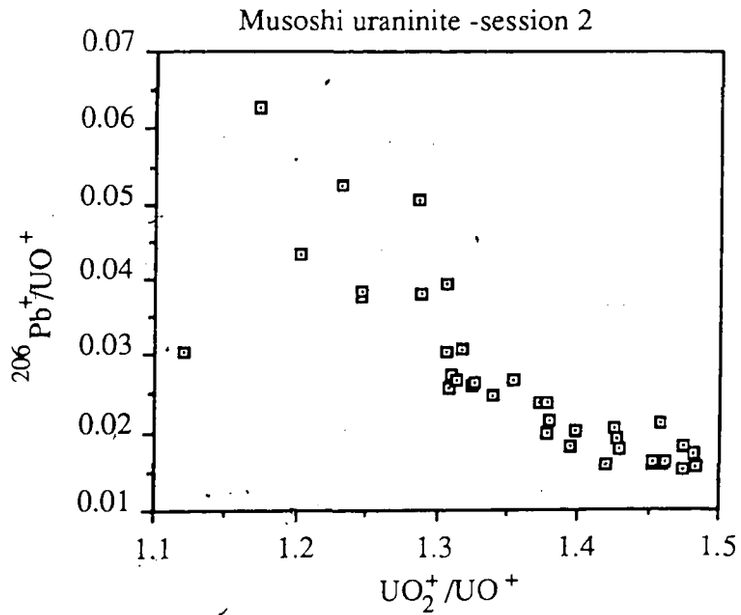

Figure A.2

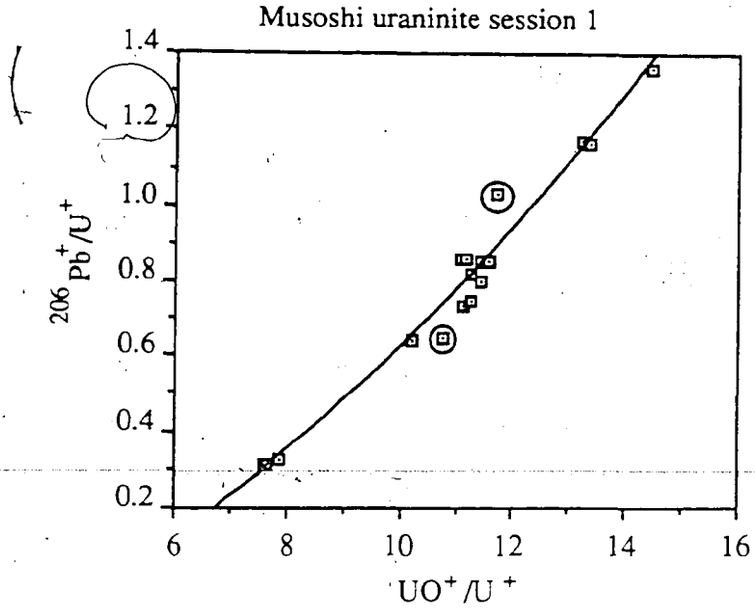

Figure A.3

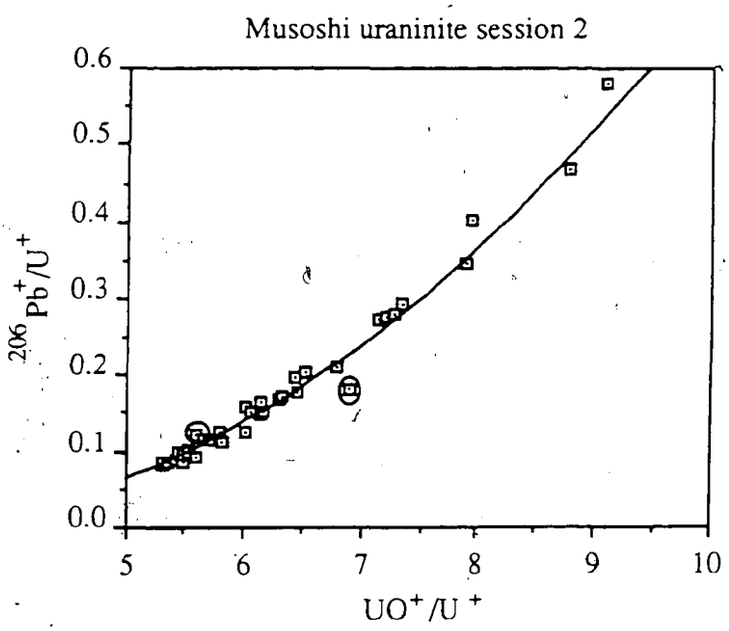

Figure A.4

The data for session 2 yield similar results (Figure A4) with a calibration equation of

$$^{206}Pb^+/^{238}U^+ = 0.01352 .(UO/U)^2 - 0.075439 .(UO/U) + 0.10227.$$

The scatter about the curve equates to a calibration uncertainty of 7.2%. Deletion of analyses 5.2 and 7.1 (circled points in Figure A4) reduces the uncertainty to 5.9%. A

plot of the data from both sessions (Figure A5) shows that the data lie on the same curve, i.e.:

$$^{206}Pb^{+}/^{238}U^{+} = 0.005839 .(UO/U)^2 + 0.027910 .(UO/U) - 0.23816$$

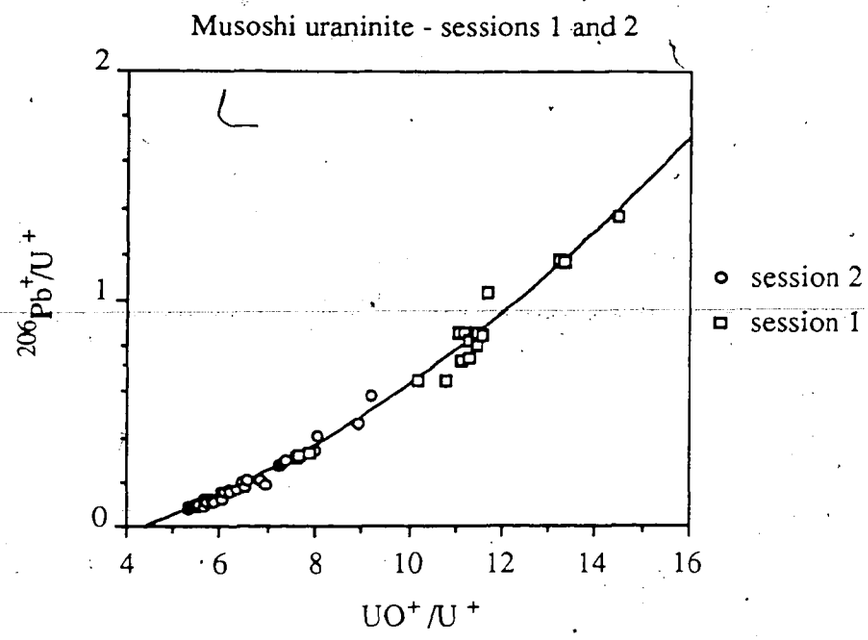

Figure A.5

with an uncertainty of 7.8%. If analyses 5.2 and 7.1 (session 1) and 1.5 (session 2) are deleted as outliers the uncertainty is reduced to 6.6%. The absence of significant drift in calibration between sessions is in contrast to the drift observed for zircon analysis (Compston et al., 1984). Further analytical sessions are necessary to assess the long term reproducibility of the uraninite Pb/U calibration. It is possible that the much greater quantities of Pb and U in uraninite compared to zircon influence the reproducibility. On the basis of the above observations it is appropriate to expect an uncertainty of around 5 to 6% for the $^{206}Pb/^{238}U$ ratios of the standard, larger than the 2 to 2.5% uncertainty for this ratio in a standard zircon (e.g. Compston et al., 1986; Claoué-Long et al, 1990). The uncertainty in the calibration curve is a major component in the precision of Pb/U isotopic ratios quoted for unknowns. The correlations between Pb and U species sputtered from the Musoshi uraninite suggest that it is a suitable standard in terms of Pb/U calibration.

A1.3 Pb Isotopic measurements

The Pb isotopic ratios measured by the ion probe are listed in Table A2. $^{204}Pb/^{206}Pb$ ratios are not reported. The peak measured as mass ^{204}Pb in the first two analytical sessions was subsequently identified as due to an adjacent isobaric interfering species.

Table A2. Ion microprobe data for the Musoshi uraninite

Sample No.	$^{207}Pb/^{206}Pb$	$^{208}Pb/^{206}Pb$	$^{206}Pb^+/^{238}U^+$	$^{206}Pb^+/^{238}UO^+$	UO^+/U^+	UO_2^+/UO^+	ThO^+/U^+	Th/U[a]
Session 1								
1.1	0.05912	0.00040	1.3617	0.0957	14.457	1.313	0.00047	0.00004
1.2	0.05617	0.00050	1.1614	0.0901	13.335	1.277	0.00054	0.00004
1.3	0.05870	0.00042	1.1719	0.0907	13.221	1.291	0.00477	0.00040
1.4	0.05920	0.00018	0.7449	0.0674	11.269	1.279	0.00098	0.00010
1.5	0.05975	0.00022	1.0275	0.0896	11.692	1.286	0.00131	0.00012
1.6b	0.05954	0.00011	0.8587	0.0790	11.160	1.309	0.00155	0.00015
1.7	0.05793	0.00011	0.8201	0.0730	11.269	1.258	0.00084	0.00008
1.8	0.06075	0.00044	0.8540	0.0759	11.452	1.312	0.00131	0.00013
1.9	0.05044	0.00027	0.8593	0.0780	11.047	1.297	0.00076	0.00008
1.10	0.05976	0.00029	0.8499	0.0748	11.568	1.298	0.00120	0.00012
2.1	0.05967	0.00063	0.6452	0.0606	10.769	1.257	0.00715	0.00074
2.2	0.05961	0.00056	0.7996	0.0704	11.453	1.287	0.00091	0.00009
3.1	0.06045	0.00140	0.3253	0.0413	7.876	1.412	0.01318	0.00186
3.2	0.06105	0.00195	0.3107	0.0410	7.617	1.403	0.00865	0.00126
3.3	0.05812	0.00186	0.3144	0.0414	7.646	1.369	0.00914	0.00133
3.4	0.05831	0.00058	0.7340	0.0663	11.097	1.246	0.00281	0.00028
3.5	0.05913	0.00081	0.6432	0.0634	10.195	1.231	0.00216	0.00023
Session 2								
Mus1.1	0.05959	0.00023	0.5793	0.0628	9.221	1.174	0.00117	0.00014
1.2	0.05929	0.00047	0.3459	0.0433	7.982	1.203	0.00322	0.00045
1.3	0.05910	0.00037	0.4669	0.0524	8.911	1.231	0.00166	0.00021
1.4	0.06039	0.00037	0.2760	0.0378	7.292	1.246	0.00136	0.00021
1.5	0.05994	0.00064	0.2812	0.0382	7.354	1.246	0.00658	0.00099
1.6	0.06023	0.00035	0.1645	0.0266	6.189	1.326	0.00129	0.00023
2.1	0.05929	0.00031	0.1699	0.0267	6.362	1.314	0.00089	0.00016
2.2	0.05952	0.00020	0.1689	0.0263	6.355	1.324	0.00052	0.00009
3.1	0.05931	0.00032	0.1792	0.0276	6.497	1.310	0.00044	0.00007
3.2	0.06040	0.00023	0.1567	0.0259	6.053	1.309	0.00106	0.00019
3.3	0.05931	0.00032	0.1253	0.0215	5.817	1.379	0.00153	0.00029
3.3b	0.05931	0.00031	0.1521	0.0249	6.105	1.339	0.00130	0.00024
3.4	0.05969	0.00261	0.1146	0.0200	5.723	1.378	0.03172	0.00615
3.4b	0.05923	0.00270	0.1968	0.0304	6.475	1.307	0.03891	0.00667
3.5	0.05922	0.00048	0.1123	0.0192	5.845	1.427	0.00020	0.00004
3.6	0.05881	0.00032	0.0999	0.0180	5.554	1.429	0.00023	0.00005
4.1	0.05957	0.00077	0.0852	0.0159	5.371	1.452	0.00580	0.00120

Table A2 contd.

Sample No.	$^{207}Pb/^{206}Pb$	$^{208}Pb/^{206}Pb$	$^{206}Pb^+/^{238}U^+$	$^{206}Pb^+/^{238}UO^+$	UO^+/U^+	UO_2^+/UO^+	ThO^+/U^+	Th/U^a
Session 2 contd.								
4.2	0.06163	0.00038	0.0946	0.0172	5.512	1.482	0.00094	0.00019
4.3	0.06297	0.00044	0.1001	0.0183	5.463	1.475	0.00107	0.00022
4.4	0.05968	0.00037	0.0864	0.0157	5.509	1.483	0.00113	0.00023
1.7	0.05861	0.00038	0.2121	0.0309	6.852	1.317	0.00301	0.00049
1.1b	0.05947	0.00018	0.4013	0.0506	8.028	1.285	0.00130	0.00018
1.2b	0.05836	0.00038	0.2737	0.0380	7.210	1.287	0.00249	0.00038
1.3b	0.05725	0.00038	0.2929	0.0395	7.415	1.306	0.00132	0.00020
1.8	0.05965	0.00031	0.1251	0.0207	6.054	1.424	0.00154	0.00028
4.4b	0.05956	0.00029	0.0928	0.0164	5.625	1.453	0.00121	0.00024
4.5	0.05957	0.00049	0.1160	0.0203	5.679	1.398	0.00094	0.00018
4.6	0.05990	0.00036	0.0864	0.0160	5.330	1.420	0.00057	0.00012
4.7	0.05893	0.00072	0.0867	0.0160	5.371	1.460	0.00509	0.00105
4.7b	0.05922	0.00044	0.1026	0.0184	5.547	1.394	0.00398	0.00080
5.1	0.06381	0.00036	0.0876	0.0161	5.433	1.463	0.00040	0.00008
5.2	0.05797	0.00023	0.1205	0.0211	5.622	1.458	0.00069	0.00014
5.3	0.05964	0.00040	0.0822	0.0154	5.321	1.474	0.00067	0.00014
6.1	0.05884	0.00022	0.2041	0.0304	6.572	1.121	0.00096	0.00016
6.2	0.05953	0.00027	0.1497	0.0238	6.193	1.372	0.00046	0.00008
6.3	0.05844	0.00020	0.1511	0.0239	6.212	1.377	0.00056	0.00010
7.1	0.05872	0.00067	0.1821	0.0269	6.966	1.354	0.00685	0.00109

a $Th/U = 1.11 \cdot ThO^+/UO^+$: assumes the relationship observed for zircons (Compston et al., 1984) applies also to uraninite

For the third session a fragment of Pb metal was used to correctly align the spectrum for ^{204}Pb. In this session no ^{204}Pb was detected in the Musoshi uraninite. This is consistent with the $^{204}Pb/^{206}Pb$ ratios measured by conventional analysis (Table A1) and so $^{204}Pb/^{206}Pb$ ratios are not given.

The mean of the $^{207}Pb/^{206}Pb$ ratios for both sessions listed in Table A2 is 0.05920 with an uncertainty of 2.7% (relative standard deviation). This $^{207}Pb/^{206}Pb$ ratio corresponds to an age of ~575 Ma, considerably higher than the age of 514 Ma as determined by TIMS. This discrepancy could not be caused by mass fractionation in the ion probe because this process favours the lighter isotopes and therefore tends to yield lower $^{207}Pb/^{206}Pb$ ratios (Ireland et al., 1990). Scans through the mass spectrum indicate that adjacent peaks, possibly REE molecular species, are fully resolved from the ^{207}Pb peak and are therefore not responsible for the elevated $^{207}Pb/^{206}Pb$ ratio. Elevated $^{207}Pb/^{206}Pb$ ratios may be caused by interference from Pb hydride species, i.e. $^{206}PbH^+$ contributing to the peak at mass 207 as these are not resolved even at the high mass resolution (6500) of SHRIMP (Compston et al., 1992). Long and Hinton (1984) discuss the causes of, and relationships between, different metal hydride species in secondary ion mass spectrometry. They conclude that the most important sources of hydrogen contributing to metal hydrides are:

i) the residual water vapour pressure in the sample chamber,

ii) water in the matrix of the minerals analysed, and

iii) OH within the primary-beam bombarding the sample.

Filtering of the primary ion beam during the course of this work eliminates the presence of OH. However, both i) and ii) are possible causes of a hydride problem. The residual water vapour pressure is minimised by the use of a liquid N_2 cold trap in the source chamber but nevertheless may vary from one day of data accumulation to the next, and for this reason the data for sessions 1 and 2 are considered separately below.

The mean $^{207}Pb/^{206}Pb$ ratio for session 1 is 0.05869 with a relative standard deviation of 4.1%, reflecting the considerable scatter shown by the histogram of $^{207}Pb/^{206}Pb$ values (Figure A6). Variably elevated $^{207}Pb/^{206}Pb$ ratios are not likely to be caused by the water bound within a sample unless the water is distributed heterogeneously. The variation is more likely to be caused by changing water vapour pressure conditions within the sample chamber. The regular variations of subsets of the $^{207}Pb/^{206}Pb$ and $^{208}Pb/^{206}Pb$ ratios through time (Figures A7 and A8) are consistent with this hypothesis. The $^{208}Pb/^{206}Pb$ ratios in particular show wide variation with a relative standard deviation of 90% (mean value 0.00063) Although residual vapour pressure was probably a contributor to the elevated and variable $^{207}Pb/^{206}Pb$ ratios measured during

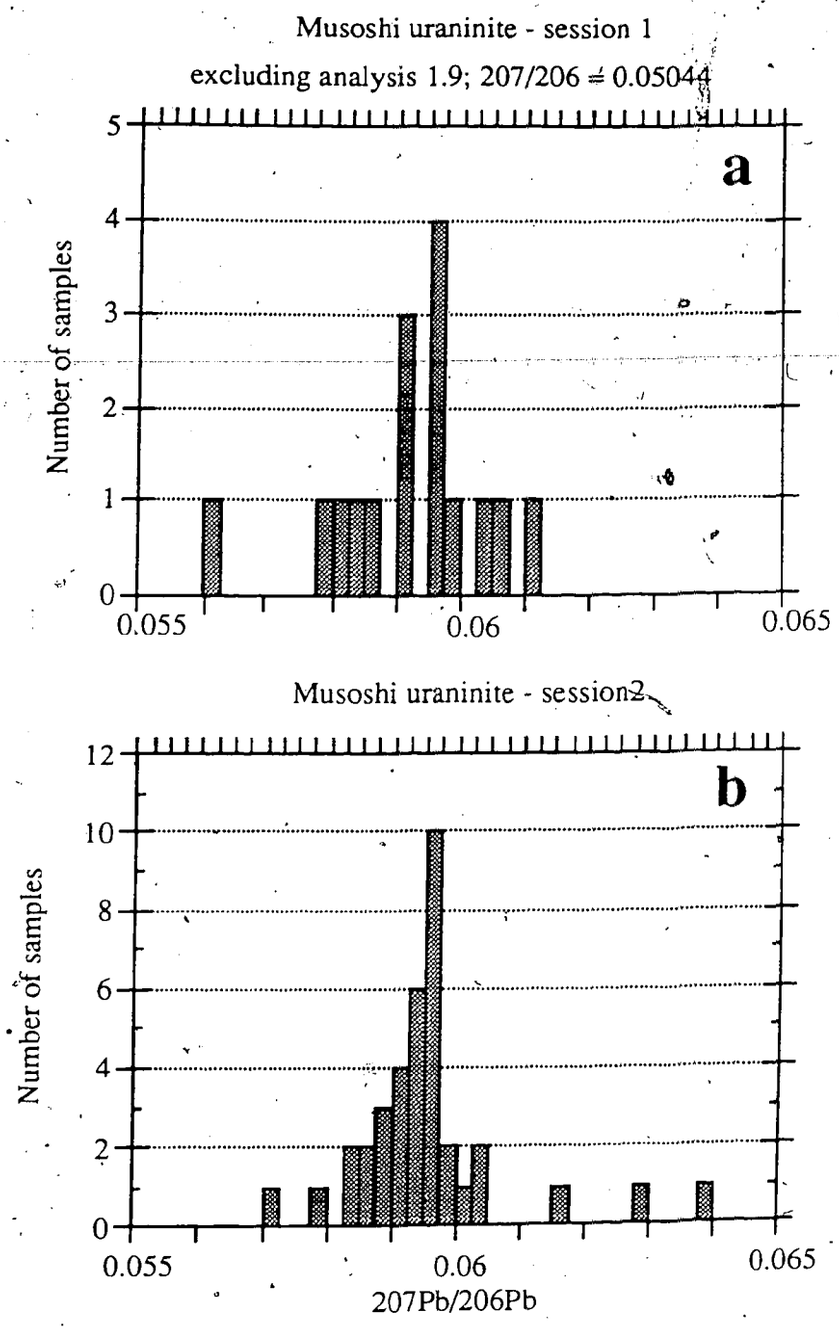

Figure A.6

session 1, the possibility that water within the uraninite was also yielding Pb hydrides cannot be discounted.

The $^{208}Pb/^{206}Pb$ ratios for session 2 are lower than those for session 1, and they do not show the same variability. The data are illustrated in a histogram (FigureA9b) and, with the exclusion of the two outliers with $^{208}Pb/^{206}Pb$ ratios of ~0.0027, yield a mean value of 0.00038 and a relative standard deviation of 38%. From the lower degree of scatter

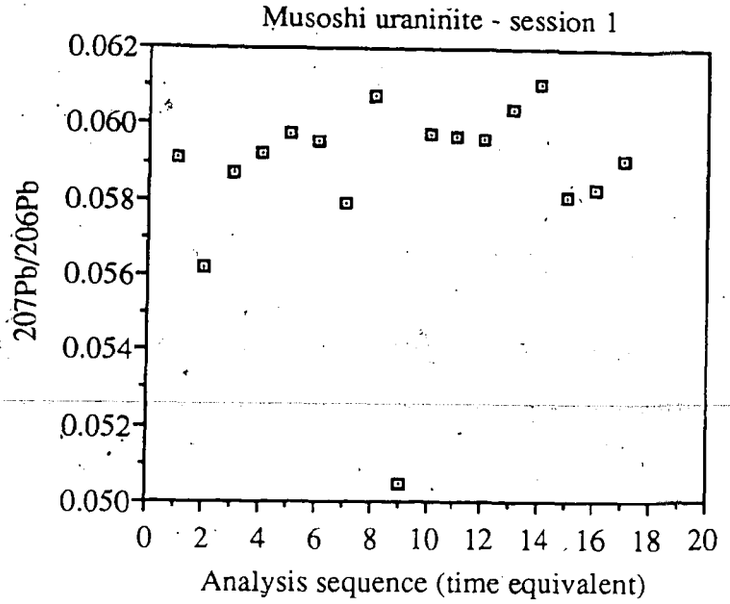

Figure A.7

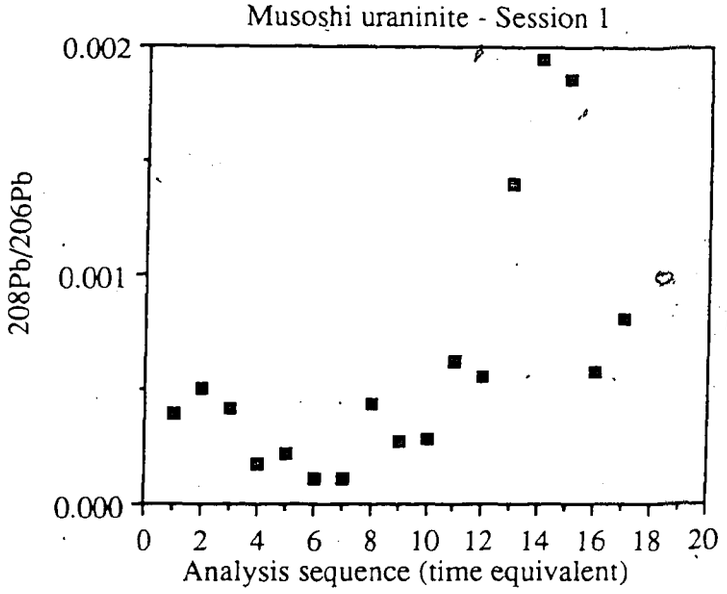

Figure A.8

---

relative to the $^{208}Pb/^{206}Pb$ ratios from session 1 one can infer more consistent, probably lower, residual water vapour conditions during session 2 than in session 1. Nevertheless the $^{207}Pb/^{206}Pb$ ratios measured in session 2 are again erroneously high (0.05957, relative standard deviation = 2.0%) which suggests that Pb hydrides may yet have affected the measurements during this session. The possibility must therefore be considered that both analytical sessions have high $^{207}Pb/^{206}Pb$ ratios because of hydrides generated by water within the uraninite sample, an effect that is not eliminated by the use of a cold trap. An approximation of the maximum hydride proportion may be calculated

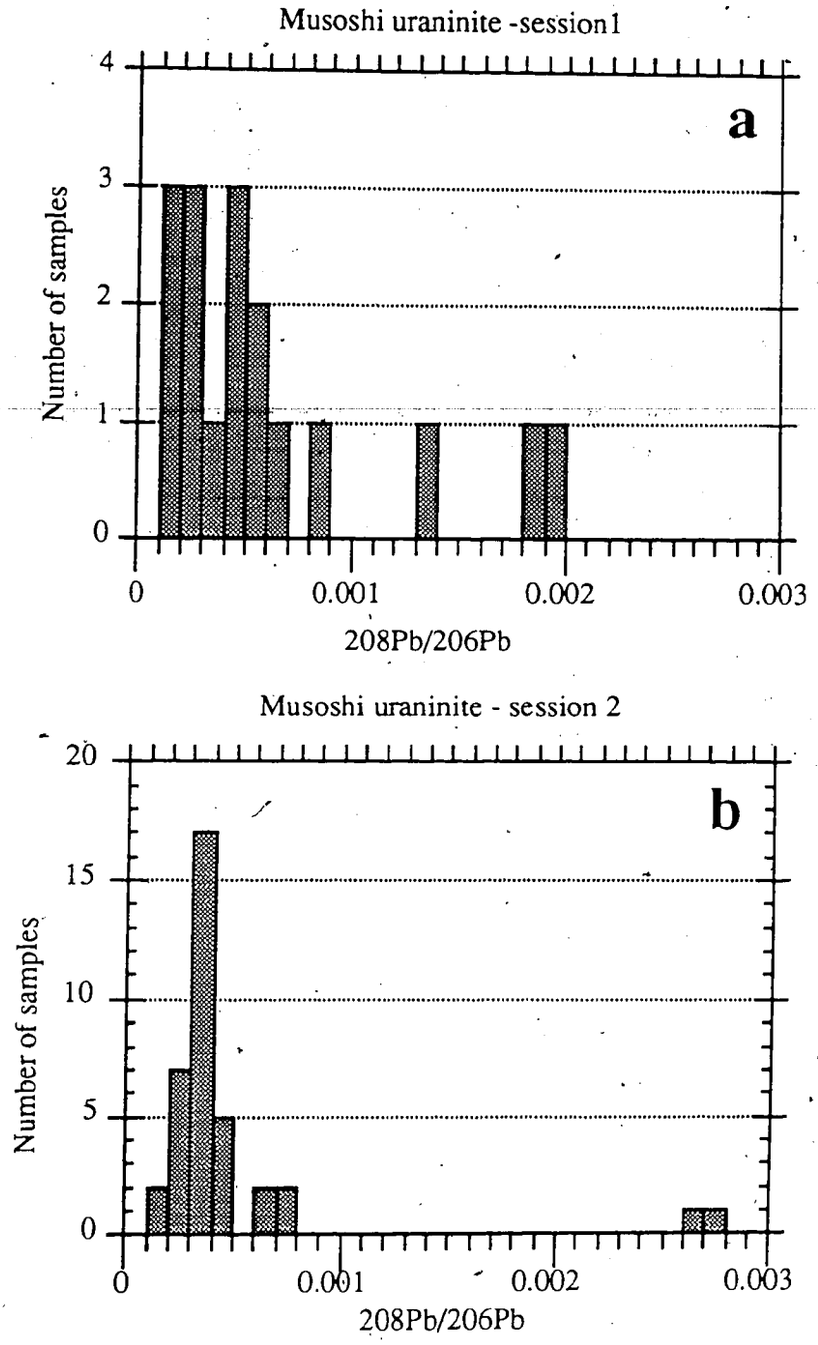

Figure A.9

by determining the $^{208}Pb/^{207}Pb$ ratio and assuming that all of the ions measured at mass 208 are actually ^{207}PbH. This provides a deliberate overestimate of the hydride proportion as there is a small component of real ^{208}Pb in the sample (TIMS data; Table A1). If this estimate is used to correct the raw counts for ^{207}Pb and ^{206}Pb, the corrected $^{207}Pb/^{206}Pb$ ratios are somewhat lower than the true value, 0.0576. This provides further evidence that hydrides are a plausible source of the systematic error in the $^{207}Pb/^{206}Pb$ ratio. Had the deliberate overcorrection for hydrides still yielded high

$^{207}Pb/^{206}Pb$ ratios it would have seemed unlikely that hydrides were the cause of the problem.

Further use of the Musoshi uraninite as a standard requires development of a method for determining the proportion of the Pb peaks attributable to hydride interferences. Hydride interferences can also affect SHRIMP zircon analyses (Compston et al., 1992). The practice used to correct for hydrides in zircon analysis is to assign a hydride proportion to the $^{207}Pb/^{206}Pb$ ratios of the unknowns based on the discrepancy between the measured $^{207}Pb/^{206}Pb$ of the standard zircon (corrected for common Pb) and its true radiogenic value. This assumes that the difference is due totally to Pb hydrides caused by the residual water vapour pressure of the sample chamber. This method is inapplicable to uraninite/ pitchblende dating because it cannot be assumed that there is either negligible or uniform water contents in these minerals; pitchblende may have water contents ranging from -2 to -5 wt % (Winchell and Winchell, 1951). It cannot even be assumed that the water content of the pitchblende in a single sample will be homogeneous. The hydride correction appropriate to a uraninite standard will not be correct for an unknown with a different water content, which means that separate corrections will need to be applied for each analysis of standard and unknowns.

Hydride corrections for uraninite could be made by measuring mass 209 (^{208}PbH; assuming there is no Bismuth in the sample) and using the 209/208 ratio as the hydride fraction by which to adjust the counts of the Pb peaks, or by measuring mass 239 (^{238}UH) and calculating the (approximately constant) relationship between the UH/U and PbH/Pb ratios, a method described by Trueman et al. (1988) based on the experimental work of Long and Hinton (1984). Alternatively, measurements of Pb hydrides could be made directly on the hydride peaks adjacent to ^{206}Pb, ^{207}Pb and ^{208}Pb using a microprobe with sufficiently high mass-resolution to separate hydrides from the Pb peaks. In either case Pb isotopic ratios would need to be recalculated after adjusting the raw counts for the Pb isotopes by the following arithmetic relations;

$$^{206}Pb_{true} = {}^{206}Pb_{meas.} + f.{}^{206}Pb,$$

$$^{207}Pb_{true} = (1+f).({}^{207}Pb_{meas.} - f.{}^{206}Pb), \text{ and}$$

$$^{208}Pb_{true} = (1+f).({}^{208}Pb_{meas.} - f.{}^{207}Pb)$$

where f is the hydride factor PbH^+/Pb^+.

The development of the Musoshi uraninite standard was initiated primarily to enable the rapid dating of many samples from Olympic Dam. The inability to reproduce the true $^{207}Pb/^{206}Pb$ ratio of the Musoshi uraninite with ion probe analyses, probably because of

hydride interferences, was not forseen because the crystalline uraninite was not expected to have a significant water content. The realisation of the hydride problem coincided with an autoradiographic study of the Olympic Dam samples which demonstrated that few of the samples were suitable for ion probe analysis because the pitchblende within most samples was very fine-grained (<< 30μm, the diameter of the ion probe beam). Although the hydride problem could be overcome by further technique development, the work required was deemed to be outside the scope of this project when it became apparent that little progress could be made with the Olympic Dam samples. No further work on the Musoshi uraninite was undertaken.

A1.4 Summary

Ion microprobe analysis of the Musoshi uraninite has indicated that it is a suitable standard with respect to calibration of Pb/U isotopic ratios. However there are some unresolved problems with the Pb isotopic ratios measured, primarily the elevated $^{207}Pb/^{206}Pb$ ratios. The future development of the Musoshi uraninite as a standard for ion microprobe analysis will require that Pb hydride peaks are monitored by either

A) using sufficiently high mass resolution that the hydride peaks are separated from the Pb peaks with which they would otherwise interfere, or

B) measuring hydride peaks where there are no potential interferences from other Pb isotopes e.g. measuring ^{208}PbH at mass 209 or 238UH at mass 239.

If the hydride problem is verified and overcome the Musoshi uraninite will be a viable standard for routine ion probe analysis of uraninite/ pitchblende samples.

APPENDIX 2

Whole-rock geochemical data

XRF data have been recalculated according to the following method:

1) Sufficient sulphur has been allocated as SO_3 to account for the Ba concentration (assuming Ba is present as barite). The remaining sulphur is allocated as S.

2) Loss on ignition has been calculated as:

$$LOI = MLOI + \{(FeO \times 1.11134) - FeO\} - CO_2 - H_2O^+ - H_2O^- - S,$$

where MLOI is measured loss on ignition.

3) Copper percent has been calculated as Cu metal (rather than CuO).

4) For the whole-rock total, the other trace elements are calculated as element oxides and are given as a percentage.

Possible sources of error in whole-rock totals include:

A) The high iron content of the samples; many samples contain >50 wt%.total iron, with some as high as 95 wt%. Despite the 1:1 dilution of the rock powders with pure silica prior to fusion, the iron contents are still well above the range of the calibration standards. This necessitates a large extrapolation in iron determinations, and may contribute to errors in the whole-rock totals.

B) Ba totals; errors in Ba determination cause errors in calculation of SO_3 (above) and therefore in calculation of S and LOI totals. Under ideal conditions, the precision of Ba determinations is ± 1-4% (relative) for Ba > 100 ppm. High Ce contents cause interferences and increase the uncertainty for Ba. Many of the samples have high Ba and Ce concentrations and are therefore prone to errors in whole-rock totals.

C) Self-absorption; elements usually regarded as trace elements and therefore analysed in pressed powder pellets are assumed not to absorb any of the primary X-ray beam. This assumption is not valid at high concentrations (>1%) and will tend to cause underestimates of the concentrations of the elements concerned. This effect therefore may contribute to low whole-rock totals. In the present sample suite the elements which may be of concern are Cu (up to ~15%), Ba (up to ~5%), La and Ce (up to ~2%).

D) All divalent iron has been calculated as FeO. This is not appropriate for rocks containing a high proportion of Cu-Fe- and/or Fe-sulphides. The standard "oxygen equals sulphur" correction may be applied where the sulphide mineral contains sulphur in

a 1:1 molar ratio with Cu and Fe (e.g. where the only sulphide present is chalcopyrite - $CuFeS_2$). However, this correction is not applicable where the sulphide minerals have S:metal ratios which differ from 1:1 (e.g. pyrite -FeS_2, bornite -Cu_5FeS_4, and chalcocite -Cu_2S). The Olympic Dam samples typically contain assemblages of two sulphides of differing S:metal ratio. In many samples the sulphides occur as exsolution intergrowths. The exact proportion of Fe^{2+} in the sulphides is therefore not known, and it would be misleading to attempt to correct for Fe^{2+} attributed as FeO rather than as Fe sulphide. For this reason, Fe^{2+} remains expressed as FeO in the following table, recognising that this will tend to cause whole-rock totals to be erroneously high for samples with high sulphide contents.

From the above points it is apparent that the samples for which the totals are most likely to be in error are the those with high concentrations of Fe, Ba and Ce, and high contents of Cu-Fe sulphides.

Appendix 2 i XRF geochemical data.

Sample RX No.	4501	4502	4503	4504	4505	4506	4507	4508	4509	4510
ANU No.	89-105	89-106	89-107	89-378	89-379	89-374	89-380	89-381	89-382	89-383
Rock type	hem-qz bx	hem-qz bx	silic. hem-qz bx	leached bx	silic. bx	pyrite-rich ore	silic. bx	chalco-pyrite ore	barren hem. bx	leached bx.
SiO_2	5.39	3.87	16.50	0.32	35.59	3.47	60.10	12.76	26.19	5.20
TiO_2	0.13	0.11	0.06	0.22	0.15	0.06	0.24	0.06	0.16	0.14
Al_2O_3	0.40	0.41	0.29	0.18	0.67	1.51	3.07	5.26	2.87	2.68
Fe_2O_3	80.39	79.03	78.23	86.51	59.52	86.38	26.27	64.13	63.49	85.65
FeO	0.36	0.41	0.42	0.26	0.46	1.50	4.81	0.99	0.48	1.68
MnO	0.04	0.04	0.04	0.06	0.02	0.04	0.08	0.02	0.04	0.04
MgO	0.08	0.11	0.04	0.10	0.06	0.18	0.46	0.16	0.12	0.39
CaO	0.10	3.83	0.02	0.02	0.06	0.65	0.48	3.77	0.00	0.10
Na_2O	0.40	0.34	0.39	0.75	0.24	0.26	0.26	0.33	0.39	0.27
K_2O	0.04	0.04	0.00	0.04	0.11	0.02	0.14	1.49	0.67	0.29
P_2O_5	0.36	0.26	0.25	0.14	0.34	0.22	0.14	0.37	0.14	0.37
SO_3	2.87	2.11	0.21	1.39	0.53	0.03	0.06	1.25	1.29	0.46
S	0.28	0.11	0.00	1.04	0.00	3.45	0.10	1.91	0.00	0.03
H_2O^+	0.56	0.18	0.15	0.09	0.16	0.00	0.25	0.21	0.51	0.00
H_2O^-	0.49	0.14	0.12	0.15	0.14	0.00	0.06	0.07	0.17	0.71
CO_2	0.23	0.20	0.22	0.02	0.03	0.05	0.48	0.07	0.46	0.00
LOI	2.13	1.37	0.10	0.00	0.71	0.08	1.39	2.62	0.60	0.81
Cu	0.07	0.01	0.01	0.03	0.03	1.32	0.09	1.90	0.05	0.06
Rest	6.42	4.97	0.82	6.55	1.29	0.39	0.24	3.11	2.95	1.34
Total	100.74	97.55 *	97.87 *	97.87 *	100.11	99.61	98.73 *	100.48	100.59	100.22
Rb	2.5	4.5	1	3	6.5		9	65	33	16
Sr	785	940	202	428	196	142	67	696	298	319
Pb	104	64	104	59	83	41	16	65	26.5	55
Th	8.5	1	28	8.5	28	17.5	17	18	20	48
U	85	41	25.5	22.5	46.5	131	39	438	46	145
Zr	<1	<1	35	<1	98	3	174	43	80	15
Nb	54	11	6.5	60	61	131	30.5	50	40	598
Y	59	57	18	10	14	31	32	115	66	319
Ni	8	8	13	6	7	17	8	14	<1	26
Cu	650	149	114	268	298	13170	880	19027	491	617
Zn	19	18	19	26	22	66	114	80	27	102
Ga	<.5	<.5	3.5	<.5	2.5	14.5	10	3.6	6.6	9.2
V	32	15	31	20	45	49	25	18	16	37
Cr	63	51	23	145	19	22	18	22	23	26
Mn	55	17	39	47	38	62	770	23	16	70
Ba	49300	36200	3680	56340	9050	510	1090	21500	22200	7950
La	2790	2580	1280	510	700	800	168	1650	1380	890
Ce	4580	4140	1660	880	1010	1180	220	2470	2140	1510
INAA	yes	yes	yes	no	yes	yes	no	yes	yes	yes
Sm-Nd	no	yes	yes	no	no	no	no	yes	yes	yes
Rb-Sr	no	yes	yes	no	no	no	no	yes	yes	yes

* See Appendix 2 explanatory notes, page 205.

Appendix 2 ii. XRF geochemical data.

Sample RX No.	4511	4512	4513	4514	4515	4516	4517	4518	4519	4520
ANU No.	89-384	89-385	89-386	89-387	89-388	89-389	89-390	89-365	89-391	89-392
Rock type	bn-chlcite ore	chalco pyrite ore	bn chlcite ore	hem-qz sst.	hem-qz sst.	hem-qz sst.	hem-qz bx	dolerite	dolerite	leached bx
SiO_2	19.48	23.59	0.36	20.10	28.58	23.18	10.37	49.07	51.00	47.82
TiO_2	0.12	0.10	0.08	0.20	0.29	0.22	0.28	2.29	2.55	0.46
Al_2O_3	2.41	3.62	0.92	3.70	7.82	2.96	0.24	15.04	14.34	0.14
Fe_2O_3	55.09	62.32	80.68	63.74	53.90	62.12	77.52	4.24	14.47	45.49
FeO	5.04	1.05	5.89	1.75	0.72	0.74	0.44	9.18	1.75	0.63
MnO	0.04	0.02	0.04	0.04	0.02	0.02	0.10	0.18	0.19	0.16
MgO	0.27	0.23	0.15	1.93	0.58	0.66	0.49	4.53	3.78	0.69
CaO	0.19	0.15	0.06	0.04	0.10	0.16	0.63	9.94	5.21	1.27
Na_2O	0.31	0.31	0.31	0.34	0.40	0.36	0.32	2.66	2.56	0.28
K_2O	0.58	1.02	0.16	0.62	2.07	0.72	0.02	0.38	0.92	0.00
P_2O_5	0.29	0.27	0.04	0.20	0.31	0.30	0.26	0.20	0.22	0.10
SO_3	0.09	0.44	0.02	1.43	0.94	1.95	2.82	0.00	0.01	0.00
S	3.50	1.63	2.34	0.07	0.02	0.10	0.00	0.04	0.03	0.01
H_2O^+	0.33	0.10	0.66	0.48	0.04	0.79	0.30	1.42	1.69	0.75
H_2O^-	0.21	0.23	0.05	0.03	0.26	0.14	0.10	0.33	0.46	0.06
CO_2	0.19	0.10	0.05	0.09	0.06	0.06	0.89	0.30	0.64	1.86
LOI	0.00	0.30	0.00	2.66	2.36	2.10	2.29	0.25	0.02	0.00
Cu	11.47	2.50	11.46	0.02	0.02	0.02	0.05	0.02	0.02	0.00
Rest	1.50	1.81	0.47	3.03	2.17	4.09	5.81	0.15	0.19	0.16
Total	101.11 *	99.78	103.74 *	100.46	100.66	100.69	102.92 *	100.22	100.05	99.88
Rb		60		35	96	39.5		10.5	31	<0.5
Sr	303	351	39	505	483	535	675	206	217	42.5
Pb	130	134	141	48	74	75	93	24	14	21
Th	41	30	75	16	39	27.5	21.5	1.5	2.5	34
U	2180	837	730	22.5	31.5	26.5	80	1	1	15.5
Zr	81	60		82	179	141	24	147	159	369
Nb	179	149	1050	16	33	25.5	60	8.5	9.5	29.5
Y	87	75	101	6	14	20	31	30	33	24
Ni	<1	<1	<1	7	6	9	4	48	59	4
Cu	114692	24950	114560	166	193	204	473	235	230	35
Zn	10.8	30	60	238	302	226	49	124	167	7
Ga	8.1	14.9	9	11.5	26.5	7	<.5	25.5	24.5	0.1
V	31	26	102	15	17	18	26	300	330	16
Cr	22	21	8	23	40	34	65	56	84	21
Mn	122	35	48	134	61	55	660	1370	1290	1170
Ba	1550	7540	280	24500	16200	33500	48300	83	124	2
La	1730	1320	68	780	830	790	1060	11	12	300
Ce	2390	1950	155	750	800	1030	1290	27	26	390
INAA	yes	yes	yes	yes	no	no	no	no	yes	no
Sm-Nd	yes	yes	yes	yes	no	no	no	no	yes	no
Rb-Sr	yes	yes	yes	yes	no	no	no	no	yes	no

* See Appendix 2 explanatory notes, page 205.

Appendix 2 iii XRF geochemical data.

Sample RX No.	4521	4522	4523	4524	4525	4526	4527	4528	4529	4530
ANU No.	89-393	89-394	89-367	89-368	89-395	89-396	89-397	89-398	89-375	89-399
Rock type	silic. bx	hem. altered granite	"fresh" granite	"fresh" granite	chlor. altered granite	hem. altered granite	sericite altered granite	leached breccia	pyrite-rich ore	pyrite-siderite vein
SiO_2	91.32	75.75	70.67	70.27	53.36	68.02	70.47	0.53	5.33	0.29
TiO_2	0.26	0.44	0.45	0.42	0.56	0.50	0.44	0.29	0.06	0.04
Al_2O_3	1.82	0.13	12.96	13.69	9.70	13.17	13.58	0.75	0.18	0.80
Fe_2O_3	3.54	22.61	1.58	1.44	20.43	5.68	2.15	92.58	65.53	43.06
FeO	0.21	0.24	1.50	1.13	5.07	1.00	2.04	0.45	14.34	14.61
MnO	0.01	0.02	0.07	0.04	0.04	0.04	0.05	0.14	0.92	0.66
MgO	0.06	0.02	0.62	0.45	3.70	0.96	0.82	1.02	0.48	0.31
CaO	0.03	0.00	1.02	1.13	0.15	0.22	0.27	1.26	0.44	0.41
Na_2O	0.12	0.17	3.15	3.77	0.20	0.29	0.22	0.35	0.32	0.25
K_2O	0.41	0.03	5.49	5.32	1.47	7.33	6.79	0.00	0.00	0.23
P_2O_5	0.32	0.04	0.07	0.07	0.46	0.06	0.06	0.51	0.32	0.33
SO_3	0.12	0.03	0.04	0.04	0.00	0.02	0.02	0.03	0.00	0.00
S	0.01	0.03	0.08	0.01	0.01	0.00	0.00	0.09	3.34	21.50
H_2O^+	0.44	0.13	0.72	0.56	0.51	1.26	1.91	0.37	2.30	1.37
H_2O^-	0.10	0.02	0.17	0.08	0.22	0.45	0.18	0.11	0.22	0.71
CO_2	0.12	0.03	0.76	0.38	0.15	0.35	0.39	1.44	7.84	9.45
LOI	0.08	0.18	0.22	0.32	3.39	0.38	0.06	0.00	0.00	1.70
Cu	0.01	0.03	0.01	0.00	0.00	0.00	0.01	0.02	0.25	1.04
Rest	0.58	0.17	0.22	0.20	0.59	0.19	0.20	0.92	0.23	0.72
Total	99.56	100.06	99.79	99.33	100.01	99.92	99.67	100.86	102.10 *	97.48 *
Rb	18.5	1.5	227	223	64	243	249	2		
Sr	214	10.5	69	82	194	42	34	197	26	34.5
Pb	7	25	34	26	13	5	7	112	37	570
Th	21	27.5	51	34	95	68	52	19.5	18.5	7.5
U	10.5	9	12	10	29	15	21.5	38	116	3650
Zr	232	412	324	269	407	409	338	267	<1	
Nb	22	34.5	28	25.5	48	30.5	28.5	112	675	
Y	9	107	58	44	28	96	53	25	61	75
Ni	2	2	3	3	51	4	3	12	22	795
Cu	86	252	99	9	35	8	77	151	2460	10360
Zn	12	23	39	30	204	37	69	396	47	385
Ga	6	<.5	18	19.5	24	17.5	18	4	4	1.5
V	7	4	14	12	32	16	16	24	26	11
Cr	6	6	2	2	36	4	2	52	8	4
Mn	3	26	670	330	240	370	370	680	7550	4370
Ba	2040	460	680	740	7	340	350	580	0	12
La	1040	92	82	73	1690	102	151	2830	163	62
Ce	1360	167	152	136	1950	159	240	3120	320	111
INAA	no	no	no	no	no	no	no	no	yes	yes
Sm-Nd	no	no	no	no	no	no	no	no	yes	no
Rb-Sr	no	no	no	no	no	no	no	no	yes	no

* See Appendix 2 explanatory notes, page 205.

Appendix 2 iv XRF geochemical data.

Sample RX No.	4531	4532	4533	4534	4535	4536	4537	4539	4540	4541
ANU No.	89-377	89-400	89-401	89-402	89-403	89-404	89-405	89-407	89-408	89-409
Rock type	pyrite-rich ore	dolerite	ser. alt. gran.bx (Au ore)	barren hem. bx	bn-chlcite ore	magnt. siderite bx	magnt. siderite bx	mafic/ ultmaf. dyke	chlor. altered granite	chalco pyrite ore
SiO_2	4.86	50.25	66.49	2.15	6.29	0.95	6.32	59.80	58.34	16.68
TiO_2	0.02	2.47	0.74	0.00	0.08	0.04	0.14	1.49	0.53	0.10
Al_2O_3	0.79	15.07	18.21	0.57	1.30	0.48	3.15	21.92	14.39	2.17
Fe_2O_3	86.92	13.39	1.32	94.87	69.49	56.54	54.08	2.24	6.19	56.46
FeO	0.87	1.57	0.38	0.34	6.78	27.82	20.80	0.49	8.53	3.06
MnO	0.04	0.17	0.01	0.04	0.04	0.87	0.70	0.02	0.06	0.06
MgO	0.12	4.18	0.37	0.14	0.14	0.54	0.70	0.59	0.76	0.32
CaO	2.23	5.45	0.20	0.12	0.18	0.33	0.80	0.02	0.90	6.06
Na_2O	0.21	2.78	0.58	0.37	0.39	0.23	0.26	0.28	0.21	0.38
K_2O	0.00	1.10	4.39	0.02	0.20	0.00	0.16	6.80	3.30	0.02
P_2O_5	0.06	0.22	0.92	0.37	0.39	0.06	0.26	0.60	0.18	0.60
SO_3	0.00	0.01	0.25	0.00	0.15	0.00	0.00	0.02	0.03	0.00
S	3.14	0.04	0.23	0.07	2.68	2.74	2.78	0.01	0.34	3.77
H_2O^+	0.55	2.20	2.73	0.20	0.30	0.41	1.44	4.13	0.31	0.36
H_2O^-	0.25	0.41	0.42	0.20	0.20	0.11	0.17	0.77	0.60	0.52
CO_2	0.03	0.92	0.07	0.16	0.18	6.67	6.23	0.03	0.12	0.14
LOI	0.00	0.00	0.62	0.17	0.00	1.52	0.00	0.00	3.53	1.80
Cu	0.71	0.02	0.02	0.17	11.00	0.79	1.82	0.00	0.27	5.27
Rest	0.25	0.17	1.54	0.53	0.73	0.29	0.51	1.05	0.41	1.17
Total	101.05	100.41	99.50	100.49	100.50	100.39	100.32	100.27	99.00	98.94
Rb		36.5	150		11		10.5	263	141	
Sr	51	216	5370	281	309	31	238	39.5	126	369
Pb	91	9	168	120	77	46	52	37	14	105
Th	36	3.5	55	16	15.5	10	21.5	26	73	13
U	381	0.5	12	1.83	218	463	397	38.5	102	1160
Zr	6	159	354	11	26	2	68	224	391	31
Nb	365	9	138	24	21	111	185	73	40	129
Y	54	32	50	299	14	132	99	5760	46	274
Ni	27	55	2	13	9	11	19	<1	18	12
Cu	7080	194	224	1680	109950	7900	18180	48	2680	52680
Zn	30	194	17	194	211	273	427	131	318	52
Ga	6.5	25.5	91	8.5	8	10.5	18.5	18.5	22	8
V	61	280	10	80	41	18	23	330	21	22
Cr	9	73	19	270	29	10	26	230	6	33
Mn	29	1270	<2	111	55	6170	5660	14	410	178
Ba	10	117	4340	18	2490	14	64	280	460	24
La	177	10	980	1240	1410	200	870	65	730	2540
Ce	300	27	1170	1660	2090	380	1280	131	950	3660
INAA	yes	no	yes	no	yes	yes	yes	yes	no	yes
Sm-Nd	yes	no	yes	no	no	yes	yes	yes	no	no
Rb-Sr	yes	no	yes	no	no	yes	yes	yes	no	no

* See Appendix 2 explanatory notes, page 205.

Appendix 2 v XRF geochemical data.

Sample RX No.	4542	4543	4544	4546	4547	4548	4549	4550	4551	4552
ANU No.	89-410	89-411	89-369	89-413	89-414	89-415	89-376	89-416	89-417	89-366
Rock type	chalco pyrite ore	mafic/ ultmaf. dyke	ash-fall tuff	mafic/ ultmaf. dyke	mafic/ ultmaf. dyke	mafic/ ultmaf. dyke	pyrite-rich ore	silic. bx (Au ore)	dolerite	dolerite
SiO_2	18.52	32.24	62.10	68.40	41.37	54.05	4.44	47.46	49.10	50.27
TiO_2	0.24	1.40	0.72	0.90	1.95	0.66	0.06	0.25	2.39	2.18
Al_2O_3	5.85	24.15	19.40	15.17	32.07	11.31	0.57	0.79	12.53	13.41
Fe_2O_3	50.25	12.93	2.91	1.03	7.56	5.84	83.78	43.20	3.90	8.63
FeO	8.80	9.01	0.74	0.62	0.00	6.60	0.61	0.52	10.75	5.98
MnO	0.06	0.20	0.02	0.08	0.02	0.25	0.04	0.04	0.20	0.19
MgO	0.75	2.63	0.87	0.75	0.33	8.72	0.20	0.30	6.01	6.10
CaO	3.51	1.05	0.25	0.84	0.02	1.62	2.76	0.21	9.58	8.37
Na_2O	0.35	0.56	0.51	0.36	0.71	0.25	0.43	0.14	2.32	2.14
K_2O	0.02	5.02	5.95	4.49	8.06	1.22	0.04	0.03	0.51	0.26
P_2O_5	1.06	0.58	0.23	0.39	0.75	0.35	0.41	0.53	0.20	0.18
SO_3	0.00	0.12	0.05	0.55	0.38	0.02	0.00	1.48	0.01	0.00
S	1.64	0.00	0.01	0.06	0.00	0.01	3.52	0.00	0.01	0.04
H_2O^+	0.13	4.62	3.20	1.85	4.08	4.02	0.37	0.27	nd	1.12
H_2O^-	0.40	1.19	1.09	0.78	0.36	0.52	0.24	0.02	nd	0.21
CO_2	0.14	0.70	0.06	0.09	0.05	1.27	0.04	0.11	nd	0.20
LOI	3.00	1.25	0.73	1.62	0.57	2.29	0.00	1.68	2.55	0.78
Cu	2.12	0.00	0.02	0.05	0.00	0.04	1.12	0.02	0.03	0.02
Rest	2.13	1.45	0.50	1.37	1.54	0.79	1.38	3.39	0.17	0.15
Total	98.97	99.10	99.37	99.41	99.82	99.83	100.01	100.44	100.25	100.23
Rb		218	370	217	331	75		2	20.5	7
Sr	780	100	269	181	423	25	163	505	176	181
Pb	83	66	41	45	33	30	177	61	3	2
Th	51	33.5	21	23	41	25.5	10	43	1.5	2
U	800	57	48.5	8	42	34	1040	35	1	<0.5
Zr	65	236	231	146	321	139	17	163	148	132
Nb	137	101	15	61	126	95	176	148	9	7
Y	109	99	29	85	2120	51	124	143	32	29
Ni	33	1910	30	65	<1	980	12	7	69	94
Cu	21190	23	236	488	1	350	11160	233	252	210
Zn	166	3230	244	307	48	745	5700	35	88	123
Ga	18.5	40	16.5	14	38	13	9	<0.5	21.5	23.5
V	47	280	104	200	93	138	33	15	320	300
Cr	81	2280	460	250	110	2510	20	19	88	112
Mn	260	1450	83	650	<2	2120	84	105	1580	1490
Ba	25	2010	920	9480	6440	380	40	25400	109	69
La	4320	250	500	124	1070	111	810	1510	13	10
Ce	6170	440	790	420	1880	260	1360	1970	32	26
INAA	yes	yes	no	yes	yes	yes	yes	no	yes	no
Sm-Nd	yes	yes	no	yes	yes	yes	yes	no	yes	no
Rb-Sr	yes	yes	no	yes	yes	yes	yes	no	yes	no

* See Appendix 2 explanatory notes, page 205.

Appendix 2 vi XRF geochemical data.

Sample RX No.	4553	4559	4560	4561	4562	4563	4564	4566	4567	4568
ANU No.	89-418	89-419	89-420	89-421	89-422	89-423	89-424	89-425	89-426	89-427
Rock type	dolerite	bn-chlcite ore	barren hem. bx	barren hem. bx	sericite altered gran. bx	barren hem. bx	barren hem. bx	mafic/ ultmaf. dyke	anorth. gabbro	dacite
SiO_2	49.77	25.66	56.53	38.01	69.73	4.77	3.05	50.78	46.42	62.60
TiO_2	2.62	0.36	0.40	0.21	0.36	0.06	0.06	1.54	1.71	1.21
Al_2O_3	13.52	3.67	3.79	0.98	16.93	3.75	2.84	26.11	19.03	13.80
Fe_2O_3	13.06	38.10	29.91	55.17	1.79	80.48	91.05	2.77	3.01	2.03
FeO	3.03	8.91	0.24	0.29	0.55	0.47	0.24	0.99	6.40	5.54
MnO	0.19	0.02	0.03	0.02	0.01	0.04	0.04	0.02	0.16	0.05
MgO	4.98	0.16	0.19	0.10	0.30	0.14	0.16	0.84	5.18	1.54
CaO	5.96	0.04	0.02	0.06	0.18	0.00	0.08	0.94	10.52	2.12
Na_2O	2.44	0.32	0.14	0.33	0.30	0.37	0.31	0.48	2.32	4.47
K_2O	0.70	0.70	0.83	0.02	4.82	0.81	0.76	8.08	1.92	2.90
P_2O_5	0.22	0.88	1.01	0.71	0.04	0.04	0.12	0.75	0.34	0.33
SO_3	0.00	1.00	0.96	0.00	0.05	2.59	0.04	0.02	0.02	0.02
S	0.02	2.38	0.03	0.03	0.07	0.00	0.01	0.00	0.21	0.05
H_2O^+	1.89	0.74	0.62	0.24	2.38	0.35	0.29	2.63	2.60	1.81
H_2O^-	0.26	0.17	0.11	0.11	0.22	0.08	0.09	1.15	0.14	0.11
CO_2	0.64	0.06	0.03	0.09	0.12	0.02	0.08	0.02	0.13	0.80
LOI	0.71	0.21	1.47	0.40	0.30	1.48	0.28	1.80	0.21	0.39
Cu	0.01	10.62	0.05	0.02	0.21	0.08	0.03	0.00	0.01	0.00
Rest	0.17	3.01	3.08	1.14	0.56	5.11	0.46	0.58	0.17	0.18
Total	100.21	97.01	99.44	97.93	98.92	100.64	99.98	99.50	100.50	99.95
Rb	20.5	42	44.5	3.5		36	34.5	431	79	86
Sr	182	805	800	382	82	283	123	34	316	51
Pb	10	137	124	63	135	45	50	18	10	4
Th	2.5	61	92	63	66	16.5	22	35	<0.5	41.5
U	<0.5	142	95	84	1420	157	29.5	30	1	10.5
Zr	164	107	272	140	312	<1	6	270	37	489
Nb	9	247	229	665		8	274	101	3	29
Y	33	28	37	97	55	28	75	110	13	67
Ni	63	<1	6	9	4	16	8	161	39	<1
Cu	141	106240	535	234	2130	760	262	13	86	7
Zn	170	101	165	14	20	45	81	1860	86	53
Ga	25	22.5	21.5	4	19	3.5	11.5	30	19.5	21.5
V	360	34	26	25	19	41	42	310	240	21
Cr	93	45	55	43	<2	9	27	380	149	2
Mn	1590	48	21	<2	10	35	31	97	1420	380
Ba	85	17100	16400	0	790	44400	650	330	290	360
La	12	3690	3500	3350	750	240	970	91	7	80
Ce	25	5280	5100	4800	1110	380	1440	290	14	149
INAA	no	yes	no	no	no	no	no	yes	no	no
Sm-Nd	no	yes	no	no	no	no	no	yes	no	no
Rb-Sr	no	yes	no	no	no	no	no	yes	no	no

* See Appendix 2 explanatory notes, page 205.

Appendix 2 vii XRF geochemical data.

Sample	4570	4571	4572	4573	4574	4575	4576(i)	4576(ii)	4577A	4577C
RX No.										
ANU No.	89-428	89-429	89-430	89-431	89-432	93-019	93-020	93-020	93-021	93-021
Rock type	sand-stone	sand-stone	amphib-olite	ser. alt. basalt	rhyolite tuff	hem. alt. basalt	ser. alt. basalt	ser. alt. basalt	magnt apatite rock	magnt apatite rock
SiO_2	78.22	90.82	49.93	41.58	72.47	56.05	57.08	56.63	1.19	2.90
TiO_2	0.43	0.13	3.30	1.67	0.36	1.30	1.77	1.75	0.49	0.29
Al_2O_3	9.03	5.55	14.16	16.60	12.19	14.11	17.66	17.55	0.67	0.61
Fe_2O_3	6.93	1.00	8.52	2.01	1.01	10.10	4.06	4.25	68.06	69.61
FeO	0.18	0.14	8.96	11.49	1.11	0.59	2.23	2.29	24.90	25.74
MnO	0.11	0.02	0.11	0.91	0.51	0.07	0.06	0.06	0.10	0.08
MgO	0.35	0.04	3.82	5.03	0.87	3.16	3.53	3.67	0.41	0.29
CaO	0.07	0.00	0.74	4.47	1.84	0.81	0.83	0.85	1.98	0.21
Na_2O	0.19	0.11	0.20	0.19	0.18	0.26	7.77	7.55	0.29	0.29
K_2O	2.67	0.69	4.42	3.16	3.48	10.34	0.58	0.63	0.00	0.00
P_2O_5	0.07	0.01	0.60	0.37	0.11	0.29	0.38	0.37	1.62	0.17
SO_3	0.02	0.00	0.01	0.00	0.01	0.13	0.01	0.01	0.10	0.04
S	0.00	0.00	0.12	0.03	0.01	0.00	0.00	0.00	0.01	0.00
H_2O^+	1.40	1.50	2.97	5.11	1.78	1.49	2.10	2.87	0.02	0.02
H_2O^-	0.47	0.11	0.30	1.12	0.40	0.72	1.46	1.11	0.00	0.08
CO_2	0.02	0.42	0.01	5.90	1.92	0.12	0.04	0.08	0.07	0.05
LOI	0.00	0.00	1.43	0.14	1.36	0.59	0.74	0.58	0.00	0.00
Cu	0.00	0.00	0.08	0.01	0.01	0.00	0.00	0.00	0.04	0.01
Rest	0.14	0.04	0.35	0.17	0.09	0.38	0.14	0.14	0.27	0.16
Total	100.30	100.58	100.02	99.96	99.71	100.51	100.44	100.38	100.22	100.55
Rb	136	25	380	170	158	256	11	10.5	0	0
Sr	80	74	20	16.5	32	74	67	64	156	13
Pb	8	4	19	3	5	6	14	14	13	0
Th	16	8	8.5	2.5	29	7	4.5	4	44	19
U	5.5	2	13	<0.5	5.5	1.5	1	1	5	4.5
Zr	148	74	255	140	201	143	146	144	11	9
Nb	10.5	3.5	15.5	4.5	17.5	6	4.5	4	38	42
Y	23	11	57	25	53	31	33	33	177	45
Ni	25	3	66	65	5	56	54	57	89	69
Cu	18	10	750	116	57	16	5	3	383	119
Zn	74	10	945	273	62	94	194	205	278	318
Ga	12.5	5	24	22	13	10	14.5	14.5	19	18
V	44	5	360	300	9	150	194	203	ND	ND
Cr	28	3	102	74	2	52	95	94	ND	ND
Mn	1070	153	860	7540	4490	660	470	500	ND	ND
Ba	370	41	230	39	107	2250	168	167	1650	740
La	44	19	77	10	27	20	18	19	ND	ND
Ce	91	35	90	22	59	41	34	34	ND	ND
INAA	yes	yes	no	no	no	no	no	no	yes	no
Sm-Nd	yes	yes	no	no	no	no	no	no	yes	no
Rb-Sr	yes	yes	no	no						

Appendix 2 viii XRF geochemical data.

Sample	4578	3222	3223	3212	3213	3214	3697	3698	4462	4463	SS-87°
RX No.											
ANU No.	93-016	89-795	89-794	89-434	89-791	89-433	89-792	89-793	93-017	93-018	
Rock type	chalco pyrite ore	felsic dyke	felsic dyke	ser. alt. grn.bx	chlor. alt. grn.bx	chlor. alt. grn.bx	"fresh" granite	ser. alt. grn.bx	bn-chlcite ore	bn-chlcite ore	"fresh" granite
SiO_2	32.28	69.52	70.65	70.07	56.49	69.43	69.99	75.97	8.31	1.34	71.09
TiO_2	0.19	0.62	0.63	0.41	0.53	0.52	0.45	0.26	0.06	0.19	0.38
Al_2O_3	13.31	15.19	13.91	14.95	14.58	13.51	13.64	14.29	3.64	2.37	13.26
Fe_2O_3	17.99	3.44	5.45	2.18	5.98	2.12	3.25	1.15	60.83	54.06	1.02
FeO	1.70	0.42	0.43	0.32	10.36	4.92	0.33	0.27	8.94	13.11	1.39
MnO	0.02	0.01	0.01	0.01	0.06	0.06	0.01	0.00	0.04	0.06	0.03
MgO	0.26	0.48	0.31	0.29	0.81	0.42	0.23	0.26	0.34	0.23	0.47
CaO	5.83	0.12	0.02	2.30	0.84	0.62	0.27	0.00	2.57	0.21	1.10
Na_2O	0.29	0.29	0.20	0.28	0.24	0.20	0.24	0.23	0.36	0.25	3.35
K_2O	3.96	4.29	4.29	4.15	2.99	3.52	8.47	3.97	0.71	0.10	5.46
P_2O_5	0.34	0.09	0.05	0.09	0.17	0.09	0.07	0.05	0.53	0.66	0.06
SO_3	0.00	0.42	0.19	0.03	0.03	0.12	0.18	0.08	0.15	0.83	0.00
S	1.31	0.00	0.00	0.00	0.38	0.03	0.07	0.02	2.07	5.89	0.02
H_2O^+	2.08	2.65	2.22	1.97	4.05	2.77	1.04	1.99	0.73	0.66	1.13
H_2O^-	0.37	0.47	0.32	0.25	0.19	0.89	0.14	0.22	0.27	0.13	0.53
CO_2	2.00	0.03	0.03	0.12	0.04	0.30	0.06	0.06	0.02	0.03	0.54
LOI	2.20	0.55	0.31	1.18	0.60	0.00	0.40	0.26	0.19	0.00	0.21
Cu	2.50	0.00	0.00	0.04	0.32	0.02	0.06	0.01	7.76	17.65	0.00
Rest	7.10	1.03	0.57	0.39	0.42	0.38	0.54	0.29	0.08	0.45	0.29
Total	93.72	99.62	99.60	99.03	99.08	99.91	99.44	99.38	97.00	98.22	100.24
Rb	129	200	226	134	129	127	204	124	39	8	235
Sr	580	180	62	129	121	83	171	290	337	634	85
Pb	100	16	15	16	20	4	14	11	103	168	13
Th	71	56	51	41	61	29	56	76	3	60	59
U	205	23.6	21	52	188	24.5	75	7.5	1422	696	15.6
Zr	177	590	575	335	332	367	356	251	3	48	336
Nb	431	34	31	30	39	31	28.5	30.5	31	515	28.0
Y	498	27	84	86	57	34	64	36	555	652	58
Ni	30	3	4	3	23	6	3	1	36	72	2
Cu	24964	43	21	376	3160	176	640	110	77617	176546	7
Zn	23	339	353	8	354	105	40	17	124	205	19
Ga	10	31	19.5	16.5	23.5	19.5	17	30	9	4	18.6
V		11	11	15	22	15	15	6			13
Cr		4	4	3	7	5	<2	4			2
Mn		30	50	4	430	480	34	14			240
Ba		7130	3220	570	450	2120	3040	1350	2530	14190	750
La	22340	179	93	800	780	74	240	108	552	1111	82
Ce	29040	250	150	1080	970	120	390	94	1054	2071	176
INAA	yes	no	no	no	yes	yes	no	yes	yes	yes	yes
Sm-Nd	no	no	no	no	yes	yes	no	yes	yes	yes	yes
Rb-Sr	no	no	no	no	yes	yes	no	yes	yes	yes	yes

* See Appendix 2 explanatory notes, page 205.

° Data from Creaser (1989)

APPENDIX 3

INAA Rare Earth Element data (ppm).

Sample	4501	4502	4503	4505	4506	4508	4509	4510	4511	4512
RX No.										
La	2900	2665	1087	690	730	1430	1280	630	1750	1590
Ce	3100	3300	1436	860	1090	2230	1600	970	3130	2850
Pr		242	110				310	290	910	740
Nd	430	656	300	160	260	490	29	32	54	52
Sm	34	53.5	25.3	18	25	37	14	8.3	15	13
Eu	19	26	10.4	4.6	5.5	17	2.8	5.4	4.8	3.7
Tb	3.1	2.28	1.41	1.5	1.3	2.7				
Dy		11.7	5.6				2.8	9.7		
Ho	4.1	1.87	0.99	2.2	4	11	4.8	24	15	10
Yb	3.5	3.07	1.1	1.6	0.56	1.9	0.7	3.9	6	3
Lu	0.35	0.36	0.14	0.26						

Sample	4513	4514	4519	4529	4530	4531	4533	4535	4536	4537
RX No.										
La	97	770	15	165	150	185	1070	1010	178	400
Ce	250	610	32.5	440	710	370	1150	1440	375	1530
Pr									50.8	
Nd	116	37	20	130	465	108	175	340	187	410
Sm	5	2.1	5.5	16	61	8	19	29	34.3	35
Eu	2	1.15	1.84	3.2	5.3	1.9	7.2	7.1	7.07	7.1
Tb	2.8	0.7	1.1	2	2.6	1.7	2.5	1.3	4.11	2.8
Dy									25.3	
Ho		0.9	1.1				2.8	1.4		
Yb	13	1.2	3	7.5	7.5	8.4	6.1	2	10.7	8.6
Lu	4.6	0.15	0.46	1.4	2.4	2.1	0.9	0.4	1.62	1.5

Sample	4539	4541	4542	4543	4546	4547	4548	4549	4551	4559
RX No.										
La	69	2450	3787	249	152	1222	116	830	13.5	2970
Ce	129	3860	5740	498	440	2321	295	1660	29.5	3900
Pr			501	53.1		265	38.4			
Nd	72	990	1267	215	188	911	175	620	19	650
Sm	62	85	113	39.1	24	125	40.7	60	5.2	29
Eu	41	19	20.9	8.33	9.4	69.8	5.67	10	1.68	7.2
Tb	52	6.4	5.35	4.31	3.5	35.5	3.08	3.6	1.1	2.2
Dy			27.6	23		253	15.7			
Ho	118			4.04	3.1	56	2.75		1	
Yb	216	2.6	10.7	8.4	3.9	153	3.45	10	3.1	5.3
Lu	34	4.9	1.78	1.2	0.48	24	0.41	3.2	0.46	0.6

Sample	4566	4570	4571	4577A	4578	4462	4463	3213	3214	3698	SS-87°
RX No.											
La	102	38.9	16.3	209	22340	552	1111	662	77	112	92
Ce	330	80.8	34.3	500	29040	1054	2071	980	126	100	185
Pr	49.1	<20	<20	66.7	2466	105	227	73			
Nd	249	35.4	15	253	6477	393	742	173	40	11	72
Sm	68.8	6.32	3.15	44.5	549	49	96	15	6	1.8	12.7
Eu	13.6	1.13	0.66	2.97	145	21.8	15.3	3.48	2.3	0.93	1.61
Tb	5.74	0.81	0.46	4.16	28.4	9.63	13	1.72	1.2	1.3	1.71
Dy	30.4	5.2	2.9	24.6	138	62	81	10.6			
Ho	4.6	1.05	0.59	4.89	22.7				1.7	1.5	2.37
Yb	6.3	2.66	1.25	10.7	36.1	36.4	52	7.51	3.5	4.5	5.77
Lu	0.8	0.37	0.18	1.56	5.8	5.73	7.64	1.02	0.58	0.7	0.9

° Data for SS-87 from Creaser (1989)

APPENDIX 4

Sample Descriptions

Brief descriptions of the samples are given below. XRD data are also presented where available. Abbreviations: anat = anatase, ap = apatite, ba = barite, bi = biotite, bn = bornite, bst = bastnaesite, cb = carbonate, cc = chalcocite, cpx = clinopyroxene, cpy = chalcopyrite, dg = digenite, dj = djurleite, dol = dolomite, flo = florencite, flt = fluorite, fsp = feldspar, hem = hematite, ilm = ilmenite, kaol = kaolinite, mgt = magnetite, ol = olivine, pitch =pitchblende, plag = plagioclase, py = pyrite, qz = quartz, rut = rutile, ser = sericite, serp = serpentine, sid = siderite.

i) Olympic Dam samples

RX4501 *Hematite - quartz breccia.* Hem clasts 1 to 8 mm, qz clasts to 3 mm, minor ser altered granitic clasts. Hem clasts show varied textures; interlocking hem, fans of hem blades, euhedral pseudomorphs of cb. Matrix of fine tabular hem up to 50 μm long. Disseminated ba and qz grains.

RX4502 *Hematite - quartz breccia* (XRD hem 78%, qz 8%, ba 7%, flt 6%, flo 1%, bst 1%). Red and brown hem clasts up to 5 mm. Qz clasts up to 3 mm. Tabular hem 100 x 50 μm. Hem replaces euhedral, hexagonal grains (?mgt or cb). Qz has weakly undulose extinction and may represent relict granitic qz. Some qz with trace cpy inclusions. Ba as veinlets and disseminated grains. Flt as disseminated grains.

RX4503 *Silicified hematite - quartz breccia* (XRD hem 74%, qz 25%, flo 1%, ba <1%). Fine grained bladed hem 10-15 x 5 μm with interstitial qz.

RX4504 *Hematite - barite breccia* (XRD hem 89%, ba 11%). Soft friable rock. Ba clasts up to 3 mm occur in fine-grained matrix of interlocking hem grains up to 50 μm with interstitial ba.

RX4505 *Silicified heterolithic breccia.* Hem clasts up to 20 mm. Clasts of pre-existing granitic breccias are silicified. Qz occurs as relict granitic material, fine-grained (<20 μm) replacement of ser matrix of earlier ser altered granitic breccia, and as prismatic crystals (up to 1 mm wide) in open vugs. Anastamosing qz veinlets cut hem. Matrix of interlocking hem (~10 μm) with interstitial qz.

RX4506 *Pyrite-rich ore.* Fine grained, equigranular hem-py-cpy-qz-flt-chl. Py up to 0.5 mm across; some grains fractured. Py commonly has replacement selvages of cpy. Py occurs as remnant inclusions where cpy replacement is more complete. Hem as acicular 20-100 μm grains in matrix and as larger euhedral grains up to 0.5 mm. Rare anhedral mgt inclusions up to 10 μm in large hem grains. Chl intergrown with qz and hem in matrix.

RX4507 *Siliceous heterolithic breccia.* Clasts of black hem, brown hem and layered granite in a black hem matrix. Granite clasts consist of qz, ser and minor chl. Hydrothermal qz distinguished by mosaic pattern of fluid inclusion trails which are absent in granitic qz. Hydrothermal qz occurs as large 1mm grains and as aggregates of smaller 100 μm grains. Matrix of hem, ser and chl.

RX4508 *Chalcopyrite-rich ore* (XRD hem 62%, ser 14%, qz 9%, flt 6%, cpy 4%, ba 4%, flo 2%, chl <1%). Cpy mineralised heterolithic breccia. Hem and granitic clasts occur in hem matrix. Cpy in matrix and within clasts of earlier cpy mineralisation. Cpy grains up to 300 μm, commonly contain remnant py. Carollite forms a border between cpy and py. Monomineralic cpy occurs but monomineralic py is absent. Clasts of earlier cpy mineralisation do not contain py remnants. Fine (<10 μm) amorphous pitch is intergrown with some cpy. Matrix hem (30-100 μm) intergrown with ser and chl.

RX4509 *Barren heterolithic breccia* (XRD hem 61%, qz 28%, ser 7%, ba 3%, chl 1%). Clasts include hem, qz and altered granite. Granitic fragments consist of qz, ser and chl. Matrix of fine-grained hem (<50-400 μm) and intergrown qz. Ser and qz stringers may represent disaggregated granite.

RX4510 *Leached hematitic breccia* (XRD hem 85%, qz 4%, chl 7%, ba 2%, flo 1%, ser 1%). Sample has porous, vuggy texture. Hem fragments up to 5 mm in a fine-grained (50-100 μm) hem matrix. Red "earthy" grains up to 1 mm diameter consist of trace cpy and hem boxwork textures in microcrystalline brown earthy intergrowth. These red grains may represent oxidised (leached) cpy. Qz occurs in fragments of chl altered granite and as discrete grains.

RX4511 *Bornite-chalcocite ore* (XRD hem 59%, qz 26%, bn 11%, ser 4%). Clasts of hem and granite in a black hem matrix. Granite fragments are strongly ser altered and partially disaggregated. High proportion of qz grains within granite clasts suggests volume loss. Matrix of intergrown hem (10-300 μm), qz (up to 1 mm) and fine-grained ser (~5 μm). Bn grains up to 1 mm, not intergrown with cc. Bn has fine lamellae (~0.5 μm) of cpy which generally occur in three orientations. Bn veinlets in hem grains, hem and qz inclusions in bn.

RX4512 *Chalcopyrite-rich ore* (XRD hem 63%, qz 26%, ser 5%, cpy 4%, ba 1%, chl 1%). Heterolithic breccia with clasts of hem and ser-altered granite in a hem matrix. Cpy in matrix. Matrix of interlocking bladed hem (up to 0.5 mm), qz, ser and flt. Complex sulphide paragenesis: cpy replacing py (py remnants within cpy); cpy rimming bn; cpy inclusions in bn; oriented cpy lamellae within bn; bn partially rims py remnants within cpy, but bn and py not otherwise in contact. Paragenetic relationships suggest py was precipitated first, followed by coprecipitation of cpy and bn.

RX4513 *Bornite-rich ore* (XRD hem 88%, bn 6%, dg 4%, ser 3%). Steely grey hem with interstitial bn. Hem grain size varies from 100 μm to 2 mm. Many long

hem grains are kinked. Fine (1-5 μm) mgt inclusions in hem. Cc occurs interstitial to hem and as veinlets within hem (XRD indicates dg (Cu_9S_5), but optically it resembles Cc Cu_2S). Bn and cc in vermicular intergrowths. Ser is a minor matrix mineral.

RX4514 *Hematite-quartz sandstone* (XRD hem 63%, qz 22%, chl 7%, ba 5%, ser 3%, flt 1%). Rhythmically layered clastic hem and qz. Upward fining layers of qz vary in thickness from 20 μm to 400 μm. Qz laminae interlayered with hem layers. Hem as clasts (~100 μm across) and as microlaths (~1 μm) suggesting both clastic input and in situ precipitation of hem. Trace clastic cpy. Thin discontinuous laminae of chlorite (150 μm wide). All laminae are disrupted by microfaults with offsets of 0.3-2 mm. Fine laminae suggest quiescent aqueous deposition, probably lacustrine. Chl laminae may represent a minor component of airfall tuff.

RX4516 *Hematite-quartz sandstone*. As for RX4514 except laminae are cut by microveinlets of ba which occupy dilational zones forming fine tension gashes.

RX4517 *Hematite-quartz breccia*. Clasts of hem and qz in a matrix of hem, qz and flt. Hem occurs in interlocking masses with variable grain size (10-400 μm). Qz (~30% by volume) occurs as ragged grains with undulose extinction consistent with derivation from granite. Accessory zircon associated with qz and minor ser. Zircons have optically discontinuous overgrowths which may represent hydrothermal zircon.

RX4518 *Dolerite* - hyaloclastite margin. Holocrystalline, medium grained, subophitic dolerite consisting of equigranular plag and cpx, with lesser mgt (ilm exsolution; originally titanomagnetite). Chl alteration of plag and cpx; ser alteration of some plag.

RX4519 *Dolerite*. Medium grained, holocrystalline dolerite consists of plag, cpx and mgt. Plag extensively altered to ser, and cpx to chl. Mgt contains ilm lamellae along cleavage traces (probably originally titanomagnetite).

RX4520 *Hematitised granite*. Granitic texture; vuggy, friable hem and qz. Hem replaces alkali fsp. Granitic qz is equigranular. Cb veinlets ~200 μm wide.

RX4521 *Silicified granite breccia* (approximately qz 90% and hem 10% by volume). Original granitic texture almost obliterated by silicification. Relict granitic qz up to 5 mm. Aggregates of fine (10 μm) polygonal qz preserve relict outline of coarse grains of alkali fsp. Hem localised in 2-3 mm microbreccia veinlets and as matrix to quartz grains. Rare ser veinlets are ~0.5 mm wide. Local vugs are filled with prismatic qz and hem.

RX4522 *Hematite altered granite breccia*. Granitic texture preserved. Alkali fsp replaced by hem. High proportion of qz suggests volume loss during replacement of fsp. Veinlets (to 100 μm) of polygonal qz (~40 μm). Trace cpy in veinlets.

RX4523 *Roxby Downs Granite*. Holocrystalline, coarse-grained qz, perthitic alkali fsp, plag and minor bi. Chl and ser alteration of plag. Chl alteration of bi. Accessory mgt and zircon. Minor micrographic intergrowths of alkali fsp and qz. Hem dusting imparts brown colour to fsp.

RX4524 *Roxby Downs Granite*. As for RX4523.

RX4525 *Chloritised granitic breccia*. Chl altered granite clasts and hem clasts in a hem matrix. Chl replacement of fsp has destroyed granitic texture. Sample dominated by disaggregated qz and chl. Trace mgt inclusions (<5 μm) within hem.

RX4526 *Hematite- and sericite-altered granite*. Hem and ser alteration of fsp. Granitic texture preserved.

RX4527 *Sericite-altered granite*. Granitic texture modified by alteration. Higher proportion of qz than unaltered granite, suggesting volume loss and textural collapse during alteration of feldspar. Complete ser and chl replacement of plag and alkali fsp.

RX4528 *"Leached" black hematite*. Red and black hem clasts in a black hem matrix. Minor ser and ba in matrix. Texture of hem clasts varies from massive to fine-grained (10 μm). Very few hem grains have mgt inclusions.

RX4529 *Pyrite-rich ore* (XRD hem 61%, sid 25%, qz 8%, py>6%, cpy 1%). Matrix of sid and qz aggregates intergrown with hem. Coarse grained hem (up to 2 mm) and fine acicular hem (20 x 250 μm). Ubiquitous mgt inclusions (0.5-2 μm) in coarse hem suggest hem has replaced mgt. Mgt inclusions absent from fine hem. Py of variable grainsize, 20 μm to 1 mm, intergrown with hem; rare mgt inclusions in py; hem inclusions in py are common. Very few grains of py show cpy replacement. A single large (2mm) grain of monomineralic cpy has hem and sid intergrowths.

RX4530 *Pyrite-siderite vein* - brecciated vein with sid interstitial to py. Py fragments up to 1 cm. Some py rimmed by pitchblende then by cpy. This rock represents the structurally deepest sulphides sampled from the deposit.

RX4531 *Pyrite-rich ore* (XRD hem 83%, qz 6%, py 5%, flt 3%, chl 2%, cpy 1%). Hem clasts in matrix of hem + qz + chl + flt. Fine clastic qz (~200 μm) possibly of granitic origin. Chl intergrown with qz. Hem as interlocking blades and as curving rosettes of grains up to 600 μm long. Py grains as both equant fragments of larger grains and elongate grains interstitial to bladed hem. Many py grains show minor replacement by cpy at margins. Most cpy as monomineralic grains intergrown with hem. Very fine (< 1 μm to 5 μm) mgt inclusions (rarely up to 25 μm) present in hem. Flt is present as matrix grains and veinlets (~20 μm).

RX4532 *Dolerite*. Holocrystalline, medium grained subophitic dolerite. Glomerophenocrysts of plag in groundmass of intergranular plag and cpx grains

(~600 μm). Euhedral 0.5-1 mm magnetite grains. Ser alteration of plag. Chl alteration of plag and cpx.

RX4533 *Intensely sericitised granite breccia* (gold ore) (XRD qz 66%, ser 30%, flo 2%, hem 1%, trace ba). Granitic texture destroyed by ser replacement of fsp and by brecciation. Mantles of recrystallised polygonal qz around granitic qz grains. Matrix of felted ser (<30 μm) and minor hem. Gold (5-10 μm) occurs intergrown with ser matrix, with aggregates of hem, and at qz grain boundaries.

RX4534 *Barren hematitic breccia* - massive fine-grained hem. Hem grains (10-200 μm) generally tabular and interlocking (similar to basaltic texture). Many of the larger hem grains contain fine (<3 μm) inclusions of mgt. Large (1mm) qz grains are probably granitic. Trace native Cu intergrown with dg; grains up to 100 μm generally appear to be polygonal aggregates of smaller grains (1-5 μm) with bluish grey dg(?) rims. Ba veinlets cut across the hem.

RX4535 *Chalcocite-bornite ore*. Hem clasts (1-3 mm) and qz clasts (0.5-1 mm) in a fine-grained (5-25 μm) hem matrix. Larger hem grains (0.5-1mm) appear to be clasts. Vermicular intergrowths of bn and cc/dg occupy ~10% volume of rock. Sulphides are intergrown with hem matrix and typically contain hem inclusions.

RX4536 *Magnetite-siderite-pyrite- breccia* (XRD mgt 39%, hem 24%, sid 27%, py 5%, cpy 2%, chl 2%, trace qz). Euhedral mgt 0.2-1 mm partially replaced by hem. Sid and cpy replacement of mgt also occurs. Py grains 30-300 μm across. Local cpy replacement of py. Sid present as large fragments (~400 μm) and smaller matrix grains (~20 μm). Chl intergrown with sid, qz and hem. Hem generally appears to replace mgt, but small blades (~100 μm) interstitial to larger grains are also observed.

RX4537 *Magnetite-hematite-siderite-pyrite breccia* (XRD hem 40%, mgt 21%, sid 18%, chl 6%, qz 5%, cpy 4%, py 4%, flt 1%, flo 1%). Hem predominantly present as replacement of mgt, but primary hem blades are also present. Martite common. Abundant cpy replacement of py. Euhedral rhombs of sid. RX4537 is a more hem + cpy-altered equivalent of RX4536.

RX4539 *Mafic/ultramafic dyke*. "Basaltic" texture preserved; pseudomorphs of ol and plag. Euhedral "hopper-shaped" olivine phenocrysts replaced by ser and minor chl. Tabular plag(?) laths replaced by aggregates of fine ser. Groundmass of finely intergrown ser and qz. Parallel veinlets of hem crosscut groundmass.

RX4540 *Chloritised granite breccia*. Granitic texture modified by volume change upon chl + ser replacement of fsp. Remnant perthitic texture preserved by selective chl replacement of plag and ser replacement of alkali fsp grains. Ser veining cuts chl-qz mineralogy. Oxides include mgt (up to 1mm) and hem with mgt inclusions. Cpy comprises ~2% by volume.

RX4541 *Chalcopyrite-rich ore*. Equigranular rock with hem 40%, cpy 10%, qz 30% and flt 15%. Qz and flt evenly distributed throughout hem and cpy. Hem as

interlocking bladed and acicular grains which range from <10 μm to 1mm. Mgt inclusions (<5 μm) present in hem grains. Cpy intergrown with hem, commonly with hem inclusions. Minor chl intergrown with qz, flt and hem.

RX4542 *Chalcopyrite-rich ore* (XRD hem 53%, qz 20%, chl 14%, cpy 5%, flt 5%, flo 4%). Abundant qz intergrown with chl, probably represents altered granitic fragments. Tabular hem 20-400 μm long evenly distributed with qz and flt. Red-brown florencite(?) evenly distributed, but commonly associated with chl altered granitic fragments. Cpy is monomineralic (i.e. no remnant py) and varies from 5 μm inclusions in hem, to 1 mm grains with hem inclusions.

RX4543 *Mafic/ultramafic dyke* (XRD ser 35%, chl 48%, hem 11%, dol 6%). Fine grained ser with brown hem dusting; sheared fabric; fragments include clasts of hem wallrock. Porphyritic texture. Pseudomorphs of olivine replaced by chl +serp + ser. Olivine pseudomorphs (up to 650 μm long) are deformed; elongate parallel to the shear foliation. Foliation defined by aligned phyllosilicates, hem alteration along aligned grain boundaries, and elongate olivine pseudomorphs. Groundmass of intergrown chl, ser and hem. Tabular aggregates of ser (40x100 μm), probably after plag, visible where the foliation is less intense. Cr-rich spinels (electron probe data) are abundant within pseudomorphs after olivine. Spinels typically 5-10 μm but range up to 50 μm.

RX4544 *Ash-fall tuff; - from diatreme V1.* (XRD qz 72%, ser 19%, anat 3%, hem 2%, chl 2%, ba 1%, trace flo, trace flt). Tuff consists of angular fragments of qz and volcanic fragments generally 400-800 μm. Abundant unstrained, glassy qz probably of volcanic origin. A lesser proportion of strained qz with undulose extinction and recrystallised, polygonal textures probably of granitic origin. Volcanic fragments consist of ser, chl, hem and qz, but commonly preserve interlocking textures. Oxide (hem?) rims define relict plag crystals. Groundmass between volcanic fragments consists of ser and chl. Zircons (25-100 μm) are observed within volcanic fragments and within interstitial ser.

RX4546 *Mafic/ultramafic dyke* (XRD qz 75%, ser 15%, anat 4%, ba 3%, chl 2%, flt 1%). Porphyritic "basaltic" texture. Interlocking laths of ser after plag (~50 x 400 μm). Olivine phenocrysts (500 μm) pseudomorphed by aggregates of polygonal qz (25 μm). Some olivines replaced by ser + qz intergrowths. Euhedral spinels (commonly hem altered) occur within relict olivines. Many vesicles filled by concentrically banded cb, and less commonly with prismatic qz.

RX4547 *Mafic/ultramafic dyke.* Aphyric texture. Massive fine-grained ser, generally <5 μm. Weakly defined tabular aggregates of ser with margins defined by hem may represent pseudomorphs after plag. No evidence of olivine pseudomorphs or spinel grains. Aligned phyllosilicates and parallel veinlets of hem form a foliation.

RX4548 *Mafic/ultramafic dyke* (XRD qz 59%, ser 11%, chl 22%, hem 3%, cb 5%, 1% unidentified phase). Porphyritic texture. Well preserved outlines of former olivine phenocrysts (up to 1 mm) pseudomorphed by chl + serp + ser intergrowths, in a groundmass of qz + ser + chl. Tabular aggregates of ser ± qz may represent primary plag or cpx. High percentage of qz indicated by XRD is not readily observed. Vermicular cb alteration affects primary olivines and the groundmass phases. Euhedral chromian spinels (<5 to 10 μm) occur as inclusions within pseudomorphs after olivine. Groundmass has weak foliation defined by aligned phyllosilicates which wrap around pseudomorphs after olivine.

RX4549 *Pyrite-rich ore*. Hem clasts in a hem-rich matrix. Hem, qz, py, cpy and chl evenly distributed throughout matrix. Hem grainsize ranges from 10 μm to 500 μm. Hem present as interlocking grains intergrown with qz, chl, py, and cpy. Py and mgt (<5 to 40 μm) inclusions in hem. Discrete (1mm) zones are richer in mgt. Fine interstitial hem blades may also have mgt inclusions. Py as large (1 mm) grains which show variable degrees of cpy replacement.

RX4550 *Siliceous heterolithic breccia* (gold ore). Hand Specimen: Polymict breccia with granite and black hem clasts in black hem matrix. Abundant qz. Approx. 70% qz, 28% hem. Qz as individual clasts with undulose extinction, and as intergrowths with ser in clasts of silicified granite. Qz also as veinlets (100 μm wide). Carbonate veins of similar width. Hem and qz evenly distributed. Hem as fine laths (5 μm to 500 μm).

RX4551 *Dolerite* (XRD plag 42%, cpx 22%, qz 16%, mgt 5%, chl 10%, ilm 4%, hem 1%). Medium grained, holocrystalline, equigranular dolerite. Plag crystals typically ~1 mm, and cpx 0.5-1 mm. Chl and qz veinlets. Plag and cpx altered by ser and chl.

RX4552 *Dolerite*: as for RX4551

RX4553 *Dolerite*: as for RX4551

RX4559 *Chalcocite-rich ore* (XRD hem 49%, qz 34%, ser 7% cc(dj) 5%, flo 3%, ba 2%). Heterolithic breccia with clasts of hem and ser altered granite in a hem matrix. Disaggregated granitic qz clasts are very angular. Hem as interlocking tabular grains. Hem inclusions in cc have cuspate margins suggesting cc replacement of hem. Cc also has qz inclusions. Notable absence of bn intergrowths with cc.

RX4560 *Hematitic breccia* (gold ore). Polymict breccia with hem + granite +qz clasts in a hem matrix. No visible sulphides. Qz as clasts 600 μm wide with undulose extinction, and as intergrowths with ser; probably altered granite clasts. Qz also as aggregates of fine polygonal grains. Barite as disseminated grains to ~400 μm width and as veinlets. Matrix of hem + ser.

RX4561 *Hematitic breccia.* Polymict breccia with granite and black hem clasts in a black hem matrix. Approx. 70% hem, 30% qz. Qz as individual grains up to 2mm wide with undulose extinction; also as polygonal aggregates of recrystallised qz. Hem and qz evenly distributed in matrix; hem from 10 μm to 500 μm long, generally tabular. Clasts of massive hem also present.

RX4563 *Massive hematite.* Massive black hem with barely discernible clasts of black hem in black hem matrix. Clasts of hem up to 1 cm long within matrix of hem+ser+qz+ba. Ser+qz+ba fine-grained intergrowths interstitial to hem. Interlocking bladed hem in both clasts and matrix. In clasts hem is commonly aligned length parallel, also kinked. Hem from ~5 μm to 1mm.

RX4564 *Massive hematite:* Black hem clasts in a black hem matrix. Interlocking bladed hem grains from 10 μm to 1mm. Larger grains commonly pseudomorphing octahedral or rhombohedral shapes, possibly mgt or cb. Mgt inclusions in hem present in some of these pseudomorphs. Cb interstitial to hem. Minor aggregates of fine ser also disseminated throughout.

RX4566 *Mafic/ultramafic dyke.* Approximately qz 40%, ser 50%, hem 10%. Abundant qz grains have undulose extinction, probably granitic in origin. The Groundmass of felted ser. Euhedral grains of hem after mgt contain fine mgt inclusions. Clusters of zircons (10-25 μm) occur within ser and are probably granite-derived. Weak foliation throughout.

RX4578 *Chalcopyrite mineralised heterolithic breccia.* Sample received as rock powder, hence no microscopy was performed. Granite and brown hem clasts in hem matrix. Wispy mafic/ultramafic fragments present. Abundant flt. Cpy mineralised matrix.

RX4462 *Bornite-chalcocite ore* (XRD hem 67%, ser 9%, qz 6%, bn 7%, dg 5%, chl ~4%, flo 2%). Hem clasts in hem-rich matrix. Hem as large grains (0.5 x 1.5 mm) and finer grained in matrix (20 x 5 μm). Qz and ser evenly distributed in matrix. Vermicular intergrowths of bn and cc/dg occur interstitial to bladed hem. Sulphide inclusions in hem have cuspate margins suggesting hem replacement of sulphides.

RX4463 *Bornite-rich ore* (XRD hem 63%, bn 19%, chl 11%, flo 4%, ba 2%, qz 1%). Hem clasts in hem matrix. Bn in matrix. Interlocking tabular hem with grain size ranging from 5 x 20 μm to 100 x 300 μm. Bn occurs without cc in interstices between hem grains, rimming qz and replacing hem. Some bn grains show growth zoning with concentric oxide rings marking hiatuses in growth. Chl, ba and qz are distributed evenly through matrix.

RX3212 *Sericitised Roxby Downs Granite.* Coarse grained holocrystalline equigranular texture. Higher proportion of qz than in fresh granite. Feldspars replaced by ser (XRD: qz 69%, ser 26%, flt 4%, hem 1%, rut <1%). Coarse qz grains (up to 3mm) ranging to 40 μm as discrete grains or polycrystalline aggregates i.e.

recrystallised granitic qz retaining original grain outline. Embayed qz observed with ser infill; possibly corroded. Ser generally fine-grained (<30 μm) although coarser grains (~0.5-1mm) are present. Hem in veinlets with fine-grained qz, and as disseminated grains in ser matrix.

RX3213 *Chloritised granite breccia.* Granitic texture with green chlor+ser replacement of fsp. Higher proportion of qz than in fresh granite possibly due to volume loss during alteration of fsp. Approximate modal composition, qz 50%, chl 40%, hem 5%, ser 5%. Accessory zircons have translucent (hydrated?) mantles.

RX3214 *Chloritised granite breccia.* As for RX3213.

RX3697 *Weakly altered Roxby Downs Granite.* Holocrystalline, coarse-grained, equigranular granite. Modal composition approximately alkali fsp 60%, qz 35%, plag 4%, opaques 1% with accessory zircon and cpy. Alkali fsp is perthitic; texture accentuated by ser alteration along k-fsp lamellae. Minor chl alteration, especially of plag.

RX3698 *Intensely sericitised granite breccia.* Clasts of sericitised granite and qz in a sericite matrix. (XRD: qz 77%, ser 21%, hem 1%, rut 1%). Proportion of qz higher than in fresh granite. Minor flt disseminated through ser. Accessory zircons associated with flt; zircons have dark translucent rims of lower reflectance than zircon cores. Veins of coarser grained ser (~500 μm) cut groundmass of fine (<20 μm) ser.

RX3222 *Felsic peperite dyke.* Sericite altered fragmental porphyritic dyke with phenocrysts of altered plag in a qz-fsp groundmass. (XRD: qz 80%, ser 13%, hem 2%, chl 2%, ba 2%, anat 2%). Ser pseudomorphs of plag phenocrysts in fine-grained groundmass of qz + ser. Hem alteration along traces of cleavage in plag. Accessory zircon and flt present.

RX3223 *Felsic peperite dyke.* As for RX3222, but browner colour due to stronger hematite alteration (XRD: qz 78%, ser 16%, hem 3%, anat 2%, ba<1%).

ii) Regional samples

RX4567 *Anorthositic gabbro - Bill's Lookout prospect.* Holocrystalline coarse-grained inequigranular rock. Pale green plag and dark green to black amphibole with heterogeneous texture due to anorthositic clots. Plag up to 8 mm but typically 3-5 mm, occurring in clots. Coarse ophitic textures suggest amph is replacing cpx. Amph 2 x 5 mm, up to 10 mm. Relict cpx is strongly altered to amph, especially along cleavage traces. Amph alteration is within cpx and as fine (50 x 100 μm) ragged grains around margins of cpx and plag. Chl alteration also present in cpx. Plag extensively altered by ser. Amph alteration within fractures in plag. Mgt grains are partially hematitised. Accessory zircons occur within plag as discrete grains approximately 50 x 30 μm, and within anhedral clusters

of grains 150 x 100 μm. Weak foliation through rock defined by veinlets of secondary amph which cut cpx and plag. Foliation causes kinks in cpx cleavage where they cross-cut at high angles.

RX4570 *Sandstone - Pandurra Formation* (XRD qz 85%, ser 11%, hem 4%). Well sorted sandstone, angular to subangular qz and ser altered fsp. Qz grains of varied texture; clear unstrained qz (may be volcanic), qz with undulose extinction, and qz grains which are composites of smaller polygonal grains.

RX4571 *Sandstone - Pandurra Formation* (XRD qz 86%, ser 3%, kaol 11%, hem 1%, ilm <1%). Similar to RX4570, but grains are more rounded and the fsp are kaol altered. Grainsize ranges from 200 μm to 1 mm (average 400 μm).

RX4573 *Altered basalt - Roopena Station.* Pale green ser + chl altered fine-grained vesicular basalt. Strongly altered; Chl and ser alteration of plag grains up to 400 μm long. Plag pseudomorphs are lath shaped and define an intergranular texture. Opaques and chl occupy interstices between plag pseudomorphs, possibly after primary ferromagnesian minerals. Amygdales filled by chl and zeolites. Cb veins present.

RX4576 *Altered basalt - Roopena Station.* Pale green ser + chl altered fine-grained vesicular basalt.. Intergranular texture. Plag replaced by ser and chl occurs as pseudomorphs up to 250 μm long. Ferromagnesian minerals replaced by chl, serp and hem. Octahedral hem grains probably pseudomorphs of mgt. Elongate tabular aggregates of chl with length parallel trains of hem may represent cpx with hem alteration along cleavage traces.

RX4574 *Rhyolitic tuff - Roopena.* Salmon pink laminated fine-grained rock (XRD: qz 78%, ser 9%, dol 8%, chl 2%, anat 2%). Vitroclastic to eutaxitic texture. Flattened shards are parallel to macroscopic laminations (bedding). Shards are entirely altered to fine intergrowths of ser + qz with concentrated oxide dusting around the rims defining the shard shapes. Shards are typically 500 μm x 50 μm with remnant cuspate shapes despites flattening. Fine grained ser + qz occurs interstitial to shards. Angular fragments of clear, unstrained (volcanic) qz lie length parallel to the remnant shards. The shards are not deformed around the qz grains suggesting the rock has not been heavily compacted. Cb replacement affects some shards. Accessory zircon observed.

RX4577A *Magnetite-apatite rock - Acropolis prospect* (XRD mgt 77%, hem 15%, ap 5%, qz 3%, chl <1%). Massive mgt + ap. Equigranular euhedral mgt ~50 to 400 μm. Minor patchy hem alteration with mgt, but more commonly rimming mgt. Ap is coarse-grained (~400 μm) with rare cpy inclusions.

APPENDIX 5

Appendix 5 is an adjunct to Chapter 5. It consists of tables of enrichment factors for major elements (Appendix 5.1) and trace elements (Appendix 5.2) for the Olympic Dam breccia samples. Enrichment factors are calculated as element/TiO_2 ratio of sample divided by the corresponding ratio in a sample of unaltered Roxby Downs Granite (SS-87; see Appendix 2). This approach relies on the relative immobility of TiO_2 during hydrothermal processes at Olympic Dam. The validity of this assumption is discussed in Chapter 5.

Appendix 5.1. Major element enrichment factors for Olympic Dam breccias.

Sample	SiO_2	Al_2O_3	Fe_2O_3	FeO	MnO	MgO	CaO	Na_2O	K_2O	P_2O5
Barren Hematitic breccias										
RX4509	0.9	0.5	147.8	0.8	3.2	0.6	0.0	0.3	0.3	5.5
RX4560	0.8	0.3	27.9	0.2	0.9	0.4	0.02	0.04	0.1	16.0
RX4561	1.0	0.1	97.9	0.4	1.2	0.4	0.1	0.2	0.01	21.4
RX4563	0.4	1.8	499.8	2.1	8.4	1.9	0.0	0.7	0.9	4.2
RX4564	0.3	1.4	565.4	1.1	8.4	2.2	0.5	0.6	0.9	12.7
Bornite-chalcocite ores										
RX4511	0.9	0.6	171.0	11.5	4.2	1.8	0.5	0.3	0.3	15.3
RX4513	0.02	0.3	375.7	20.2	6.3	1.5	0.3	0.4	0.1	3.2
RX4535	0.4	0.5	323.6	23.2	6.3	1.4	0.8	0.6	0.2	30.9
RX4559	0.4	0.3	39.4	6.8	0.7	0.4	0.04	0.1	0.1	15.5
RX4462	0.7	1.7	377.7	38.1	8.4	4.6	14.8	0.7	0.8	55.9
RX4463	0.04	0.4	134.6	0.0	4.0	1.0	0.4	0.1	0.0	22.0
Chalcopyrite-rich ores										
RX4508	1.1	2.5	398.2	4.5	4.2	2.2	21.7	0.6	1.7	39.0
RX4512	1.3	1.0	232.2	2.9	2.5	1.9	0.5	0.4	0.7	17.1
RX4541	0.9	0.6	210.4	8.4	7.6	2.6	20.9	0.4	0.01	38.0
RX4542	0.4	0.7	78.0	10.0	3.2	2.5	5.1	0.2	0.01	28.0
RX4578	0.9	2.0	35.3	2.5	1.3	1.1	10.6	0.2	1.5	11.3
Hematite-quartz sandstones										
RX4514	0.5	0.5	118.7	2.4	2.5	7.8	0.1	0.2	0.2	6.3
RX4515	0.5	0.8	69.2	0.7	0.9	1.6	0.1	0.2	0.5	6.8
RX4516	0.6	0.4	105.2	0.9	1.2	2.4	0.3	0.2	0.2	8.6
Hematite-quartz breccias										
RX4501	0.2	0.1	230.4	0.8	3.9	0.5	0.3	0.3	0.02	17.5
RX4502	0.2	0.1	267.7	1.0	4.6	0.8	12.0	0.4	0.03	15.0
RX4517	0.2	0.02	103.2	0.4	4.5	1.4	0.8	0.1	0.01	5.9
Leached breccias										
RX4504	0.01	0.02	146.5	0.3	3.5	0.4	0.03	0.4	0.0	4.0
RX4510	0.2	0.5	227.9	3.3	3.6	2.3	0.2	0.2	0.1	16.7
RX4528	0.01	0.1	118.9	0.4	6.1	2.8	1.5	0.1	0.0	11.1
Magnetite breccias										
RX4536	0.1	0.3	526.6	190.5	275.3	10.9	2.8	0.7	0.0	9.5
RX4537	0.2	0.6	143.9	40.7	63.3	4.0	2.0	0.2	0.1	11.8
Pyrite-rich ore										
RX4506	0.3	0.7	536.4	6.8	8.4	2.4	3.7	0.5	0.02	23.2
RX4529	0.5	0.1	406.9	65.5	194.1	6.5	2.5	0.6	0.0	33.8
RX4530	0.04	0.6	401.1	100.1	208.9	6.3	3.5	0.7	0.4	52.2

Appendix 5.1 contd.

Sample	SiO_2	Al_2O_3	Fe_2O_3	FeO	MnO	MgO	CaO	Na_2O	K_2O	P_2O5
Pyrite-rich ore contd.										
RX4531	1.3	1.1	1619.2	11.9	25.3	4.9	38.5	1.2	0.0	19.0
RX4549	0.4	0.3	520.2	2.8	8.4	2.7	15.9	0.8	0.05	43.2
Silicified breccias										
RX4503	1.5	0.1	485.8	1.9	8.4	0.5	0.1	0.7	0.0	26.4
RX4505	1.3	0.1	147.8	0.8	1.7	0.3	0.1	0.2	0.1	14.3
RX4507	1.3	0.4	40.8	5.5	4.2	1.5	0.7	0.1	0.04	3.7
RX4521	1.9	0.2	5.1	0.2	0.5	0.2	0.04	0.1	0.1	7.8
RX4550	1.0	0.1	64.4	0.6	2.0	1.0	0.3	0.1	0.01	13.4
"Unaltered" Granite										
RX4523	0.8	0.8	1.3	0.9	2.0	1.1	0.8	0.8	0.8	1.0
RX4524	0.9	0.9	1.3	0.7	1.2	0.9	0.9	1.0	0.9	1.1
SS-87	1.0	1.0	1.0	1.0	1.0	1.0	1.0	1.0	1.0	1.0
RX3697	0.8	0.9	2.7	0.2	0.3	0.4	0.2	0.1	1.3	1.0
Chloritised Granite										
RX4525	0.5	0.5	13.6	2.5	0.9	5.3	0.1	0.04	0.2	5.2
RX4540	0.6	0.8	4.4	4.4	1.4	1.2	0.6	0.05	0.4	2.1
RX3213	0.6	0.8	4.2	5.4	1.4	1.2	0.5	0.05	0.4	2.0
RX3214	0.7	0.7	1.5	2.6	1.5	0.7	0.4	0.04	0.5	1.1
Sericitised Granite										
RX4527	0.9	0.9	1.8	1.3	1.4	1.5	0.2	0.1	1.1	0.9
RX4533	0.5	0.7	0.7	0.1	0.2	0.4	0.1	0.1	0.4	7.9
RX4562	1.0	1.3	1.9	0.4	0.4	0.7	0.2	0.1	0.9	0.7
RX3212	0.9	1.0	2.0	0.2	0.3	0.6	1.9	0.1	0.7	1.4
RX3698	1.6	1.6	1.6	0.3	0.0	0.8	0.0	0.1	1.1	1.2
Hematitised Granite										
RX4520	0.6	0.01	36.8	0.4	4.4	1.2	1.0	0.1	0.0	1.4
RX4522	0.9	0.01	19.1	0.1	0.6	0.04	0.0	0.04	0.01	0.6
RX4526	0.7	0.8	4.2	0.5	1.0	1.6	0.2	0.1	1.0	0.8

Appendix 5.2. Trace element enrichment factors for Olympic Dam breccias.

Samples	Rb	Sr	Pb	Th	U	Zr	Nb	Y	Ni	Cu	Zn	Ga	V	Cr	Ba	La	Ce
Barren hematite breccia																	
RX4509	0.33	8.3	4.8	0.8	7.0	0.6	3.4	2.7	0.0	167	3.4	0.8	2.9	27	70	40	29
RX4560	0.18	8.9	9.1	1.5	5.8	0.8	7.8	0.6	2.9	73	8.3	1.1	1.9	26	21	41	28
RX4561	0.03	8.1	8.8	1.9	9.7	0.8	43	3.0	8.1	61	1.3	0.4	3.5	39	0.0	74	47
RX4563	0.97	210	22	1.8	64	0.0	1.8	3.1	51	688	150	1.2	20	29	375	19	14
RX4564	0.93	9.2	24	2.4	12	0.1	62	8.2	25	237	27	3.9	21	86	5.5	75	52
Bornite - chalcocite ore																	
RX4511		11	32	2.2	443	0.8	20	4.7	0.0	51885	1.8	1.4	7.6	35	6.5	67	43
RX4513		2.2	52	6.0	222		178	8.3	0.0	77737	15	2.3	37	19	1.8	3.9	4.2
RX4535	0.22	17	28	1.2	66	0.4	3.6	1.1	21	74609	53	2.0	15	69	16	82	56
RX4559	0.19	10	11	1.1	9.6	0.3	9.3	0.5	0.0	16020	5.6	1.3	2.8	24	24	48	32
RX4462	1.1	25	50	0.3	577	0.1	7.0	61	114	70225	41	3.1			21	43	38
RX4463	0.07	14	26	2.0	89	0.3	37	23	72	50442	22	0.4			38	27	24
Chalcopyrite ores																	
RX4508	1.8	51	32	1.9	178	0.8	11	13	44	17215	27	1.2	8.8	70	182	127	1.7
RX4512	0.97	16	39	1.9	204	0.7	20	4.9	0.0	13544	6.0	3.0	7.6	40	38	61	42
RX4541		17	31	0.8	283	0.4	18	18	23	28598	10	1.6	6.4	63	0.1	118	79
RX4542		15	10	1.4	81	0.3	7.7	3.0	26	4793	14	1.6	5.7	64	0.1	83	56
RX4578	1.1	14	15	2.4	26	1.1	31	17	30	7133	2.4	1.1				545	330
Hematite - quartz sandstones																	
RX4514	0.28	11	7.0	0.5	2.7	0.5	1.1	0.2	6.7	45	24	1.2	2.2	22	62	18	8.1

Appendix 5.2 contd.

Sample	Rb	Sr	Pb	Th	U	Zr	Nb	Y	Ni	Cu	Zn	Ga	V	Cr	Ba	La	Ce
Hematite - quartz sandstones contd.																	
RX4515	0.54	7.4	7.5	0.9	2.6	0.7	1.5	0.3	3.9	36	21	1.9	1.7	26	28	13	6.0
RX4516	0.29	11	10	0.8	2.9	0.6	1.6	0.6	7.8	50	21	0.7	2.4	29	77	17	10
Hematite - quartz breccias																	
RX4501	0.03	27	23	0.4	16	0.0	5.6	3.0	12	271	2.9	0.0	7.2	92	192	100	76
RX4502	0.07	38	17	0.1	9.1	0.0	1.4	3.4	14	74	3.3	0.0	4.0	88	167	109	81
RX4517		11	9.7	0.5	7.0	0.1	2.9	0.7	2.7	92	3.5	0.0	2.7	44	87	18	9.9
Leached breccias																	
RX4504	0.02	8.7	7.8	0.2	2.5	0.0	3.7	0.3	5.2	66	2.4	0.0	2.7	125	55	11	8.6
RX4510	0.18	10	12	2.2	25	0.1	58	15	35	239	15	1.3	7.7	35	29	30	23
RX4528	0.01	3.0	11	0.4	3.2	1.0	5.2	0.6	7.9	28	27	0.3	2.4	34	1.0	45	23
Magnetite breccias																	
RX4536		3.5	34	1.6	282	0.1	38	22	52	10722	137	5.4	13	48	0.2	23	21
RX4537	0.12	7.6	11	1.0	69	0.5	18	4.6	26	7049	61	2.7	4.8	35	0.2	29	20
Pyrite - ores																	
RX4506		11	20	1.9	53	0.1	30	3.4	54	11916	22	4.9	24	70	4.3	62	43
RX4529		1.9	18	2.0	47	0.0	153	6.7	70	2226	16	1.4	13	25	0.0	13	12
RX4530		3.9	417	1.2	2223			12	3776	14060	193	0.8	8.0	19	0.2	7.2	6.0
RX4531		11	133	12	464	0.3	248	18	257	19217	30	6.6	89	86	0.3	41	32
RX4549		12	86	1.1	422	0.3	40	14	38	10097	1900	3.1	16	63	0.3	63	49

Appendix 5.2 contd.

Sample	Rb	Sr	Pb	Th	U	Zr	Nb	Y	Ni	Cu	Zn	Ga	V	Cr	Ba	La	Ce
Silicified breccias																	
RX4503	0.03	15	51	3.0	10	0.7	1.5	2.0	41	103	6.3	1.2	15	73	31	99	60
RX4505	0.07	5.8	16	1.2	7.6	0.7	5.5	0.6	8.9	108	2.9	0.3	8.8	24	31	22	15
RX4507	0.06	1.2	1.9	0.5	4.0	0.8	1.7	0.9	6.3	200	9.5	0.9	3.0	14	2.3	3.2	2.0
RX4521	0.12	3.7	0.8	0.5	1.0	1.0	1.1	0.2	1.5	18	0.9	0.5	0.8	4.4	4.0	19	11
RX4550	0.01	9.0	7.1	1.1	3.4	0.7	8.0	3.7	5.3	51	2.8	0.0	1.8	14	52	28	17
"Unaltered" Granite																	
RX4523	0.82	0.7	2.2	0.7	0.6	0.8	0.8	0.8	1.3	12	1.7	0.8	0.9	0.8	0.8	0.8	0.7
RX4524	0.86	0.9	1.8	0.5	0.6	0.7	0.8	0.7	1.4	1.2	1.4	0.9	0.8	0.9	0.9	0.8	0.7
SS-87	1.0	1.0	1.0	1.0	1.0	1.0	1.0	1.0	1.0	1.0	1.0	1.0	1.0	1.0	1.0	1.0	1.0
RX3697	0.73	1.7	0.9	0.8	4.1	0.9	0.9	0.9	1.3	77	1.8	0.8	1.0	0.0	3.4	2.5	1.9
Chloritised.Granite																	
RX4525	0.18	1.5	0.7	1.1	1.3	0.8	1.2	0.3	17	3.4	7.3	0.9	1.7	12	0.0	14	7.5
RX4540	0.43	1.1	0.8	0.9	4.7	0.8	1.0	0.6	6.5	275	12	0.8	1.2	2.2	0.4	6.4	3.9
RX3213	0.39	1.0	1.1	0.7	8.6	0.7	1.0	0.7	8.2	324	13	0.9	1.2	2.5	0.4	6.8	4.0
RX3214	0.39	0.7	0.2	0.4	1.1	0.8	0.8	0.4	2.2	18	4.0	0.8	0.8	1.8	2.1	0.7	0.5
Sericitised.Granite																	
RX4527	0.92	0.3	0.5	0.8	1.2	0.9	0.9	0.8	1.3	9.5	3.1	0.8	1.1	0.9	0.4	1.6	1.2
RX4533	0.33	32	6.6	0.5	0.4	0.5	2.5	0.4	0.5	16	0.5	2.5	0.4	4.9	3.0	6.1	3.4
RX4562		1.0	11	1.2	96	1.0		1.0	2.1	321	1.1	1.1	1.5	0.0	1.1	9.7	6.7
RX3212	0.53	1.4	1.1	0.6	3.1	0.9	1.0	1.4	1.4	50	0.4	0.8	1.1	1.4	0.7	9.0	5.7

Appendix 5.2 contd.

Sample	Rb	Sr	Pb	Th	U	Zr	Nb	Y	Ni	Cu	Zn	Ga	V	Cr	Ba	La	Ce
Sericitised Granite contd.																	
RX3698	0.77	5.0	1.2	1.9	0.7	1.1	1.6	0.9	0.7	23	1.3	2.4	0.7	2.9	2.6	1.9	0.8
Hematitised Granite																	
RX4520	0.00	0.4	1.3	0.5	0.8	0.9	0.9	0.3	1.7	4.1	0.3	0.0	1.0	8.7	0.0	3.0	1.8
RX4522	0.01	0.1	1.7	0.4	0.5	1.1	1.1	1.6	0.9	31	1.0	0.0	0.3	2.6	0.5	1.0	0.8
RX4526	0.79	0.4	0.3	0.9	0.7	0.9	0.8	1.3	1.5	0.9	1.5	0.7	0.9	1.5	0.3	0.9	0.7

APPENDIX 6

Appendix 6 is an adjunct to Chapter 5. It contains variation diagrams in which element/TiO_2 ratios (for SiO_2, MgO, K_2O, Cu, U, Th, Zr, and Zn) are plotted against total iron. These diagrams are used to assess the mobility of the above elements relative to TiO_2. In Chapter 5 it is argued that Ti has been the least mobile element during mineralisation events at Olympic Dam.

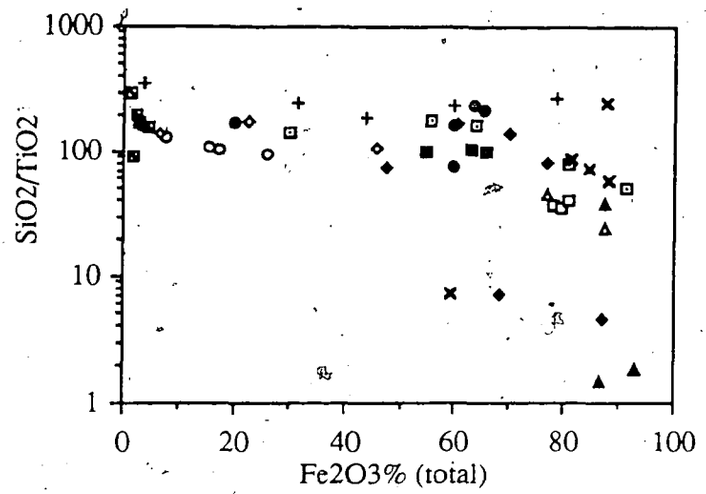

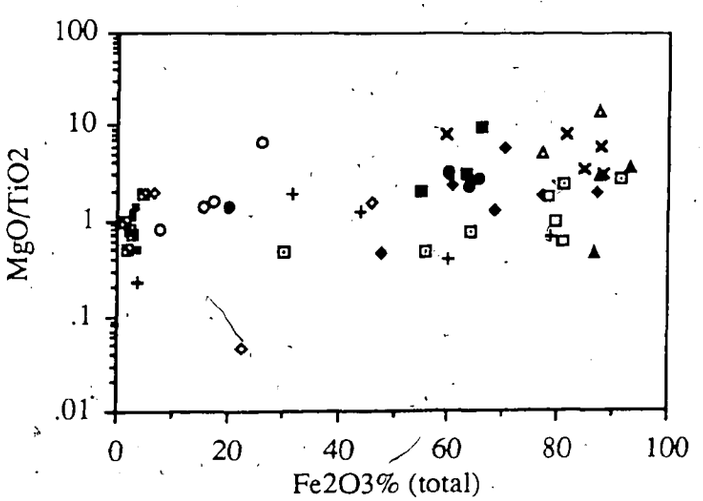

- hem. bx.
- bn-cc ores
- cpy ores
- hem-qz seds
- hem-qz bx
- leached bx
- mgt bx
- py ores
- silic. bx
- fresh gran.
- chlor. gran .bx
- ser. gran. bx
- hem. gran. bx

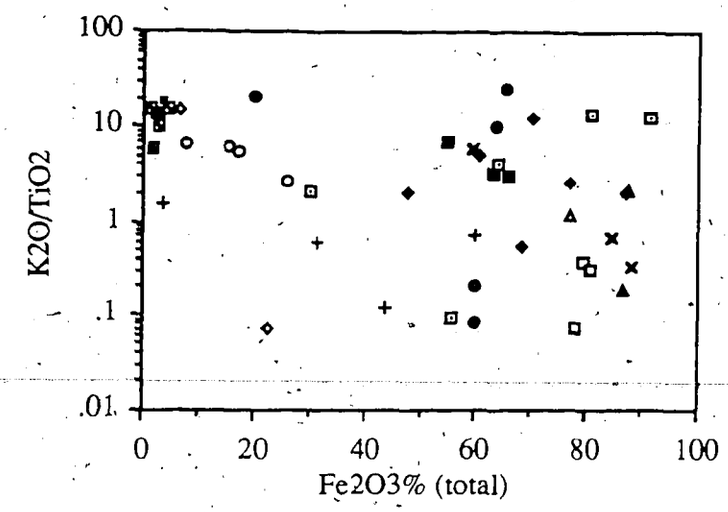

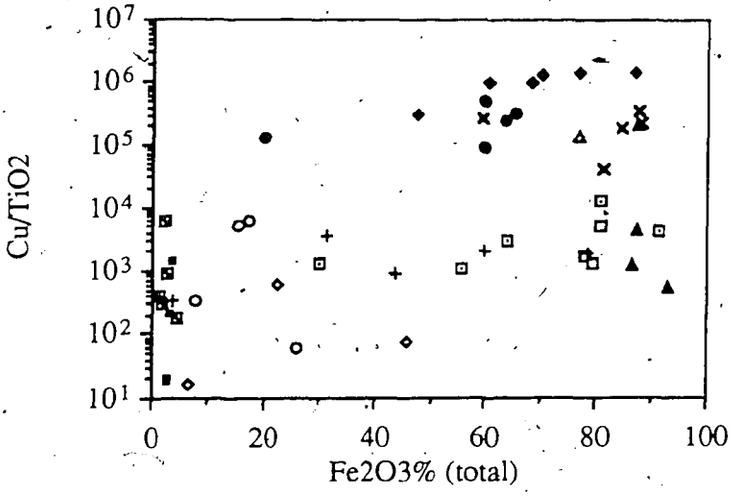

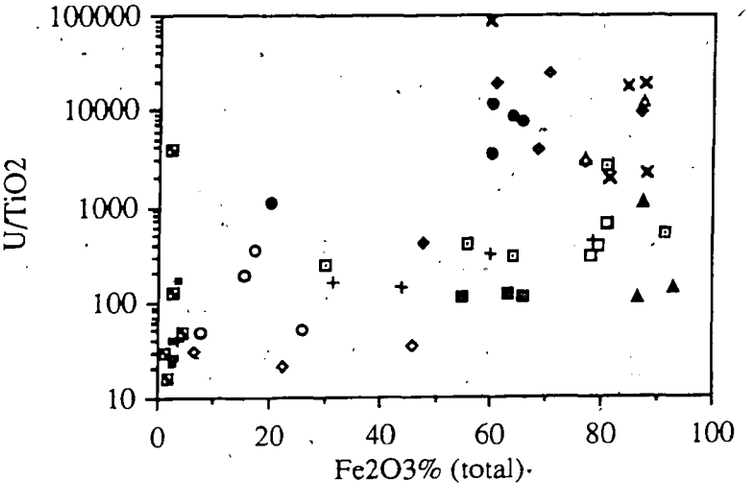

- hem. bx.
- bn-cc ores
- cpy ores
- hem-qz seds
- hem-qz bx
- leached bx
- mgt bx
- py ores
- silic. bx
- fresh gran.
- chlor. gran .bx
- ser. gran. bx
- hem. gran. bx

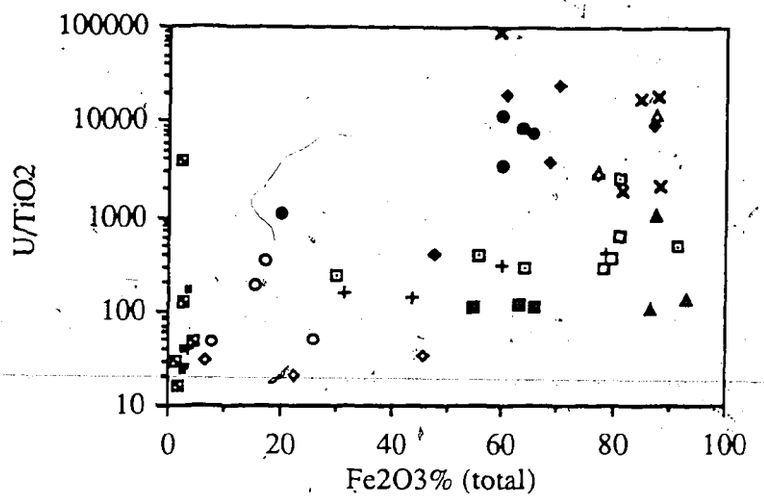

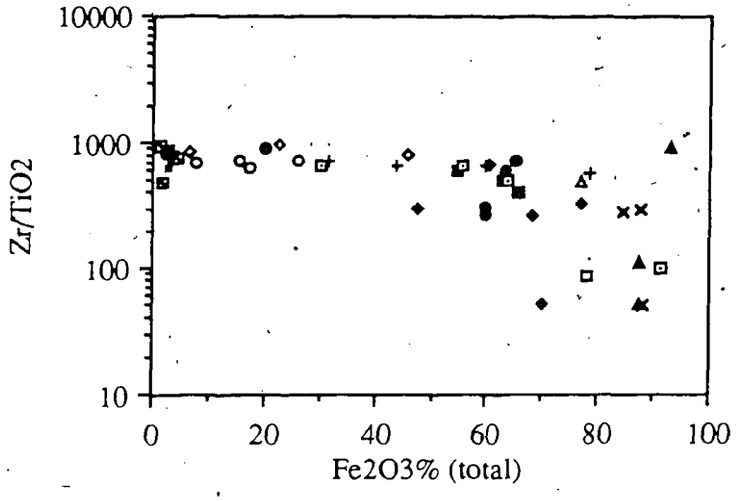

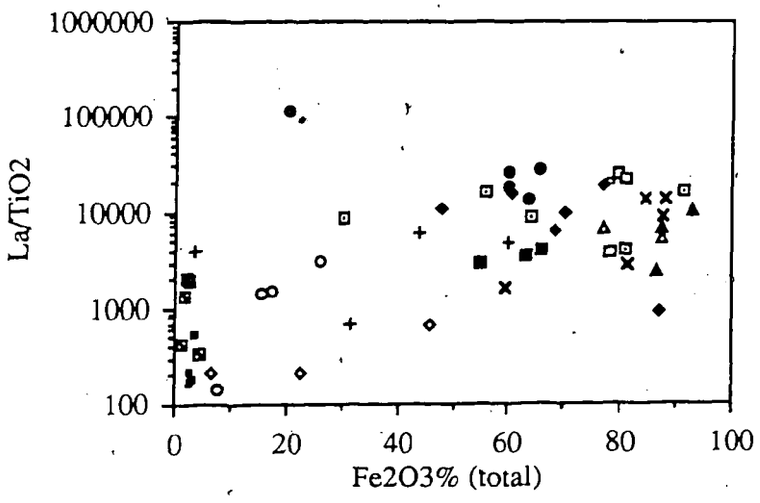

- hem. bx.
- bn-cc ores
- cpy ores
- hem-qz seds
- hem-qz bx
- leached bx
- mgt bx
- py ores
- silic. bx
- fresh gran.
- chlor. gran .bx
- ser. gran. bx
- hem. gran. bx

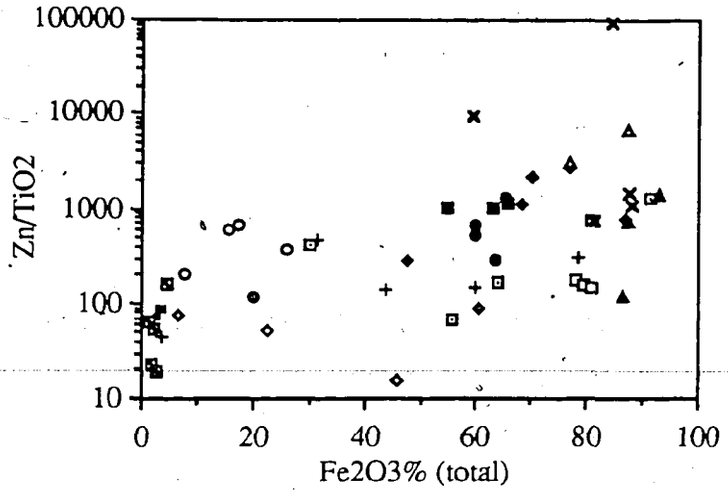

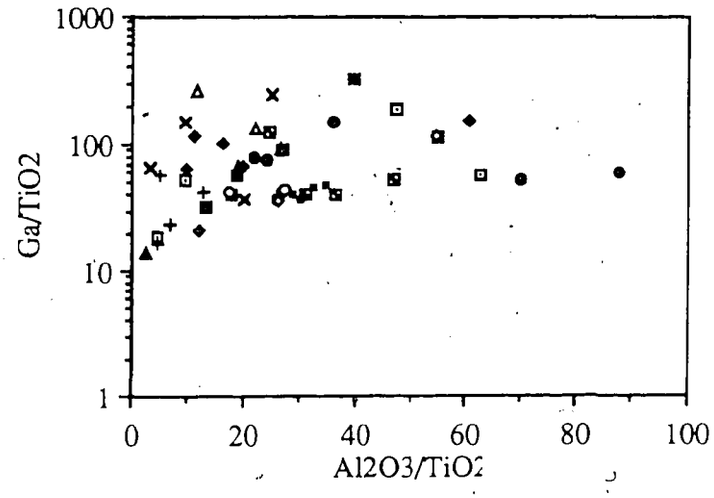

hem. bx.
hem-qz seds
mgt bx
fresh gran.
bn-cc ores
hem-qz bx
py ores
chlor. gran .bx
cpy ores
leached bx
silic. bx
ser. gran. bx
hem. gran. bx

Appendix 7

Sample locations.

Sample Number	ANU#	Locality/ Drill hole#	Hole depth (m)	Mine Coordinates		AMG coordinates		Depth (m) below surface
				Northing	Easting	Northing	Easting	
RX4501	89-105	33MK56W Dr		200604.0	200942.0	6630886.91	680996.05	419
RX4502	89-106	32MJ53 Stck.		200342.0	200867.0	6630614.88	680979.67	427
RX4503	89-107	32MJ54 S Dc		200173.0	200930.0	6630463.57	681077.83	448
RX4504	89-378	Grzly Acc.Inc.		200059.0	200977.0	6630362.48	681148.44	461
RX4505	89-379	26NB56 C.Ac		200674.0	201128.0	6630995.6	681162.44	357
RX4506	89-374	RD44	512-514	200800.6	201000.0	6631091.42	681010.02	513
RX4507	89-380	RD44	588-590	200800.6	201000.0	6631091.42	681010.02	589
RX4508	89-381	RD501	535-537	200944.0	199942.5	6631002.0	679946.59	536
RX4509	89-382	RD501	439-441	200945.8	199944.7	6631004.24	679948.34	440
RX4510	89-383	RU2-314	77-79	200963.7	199931.4	6631018.83	679931.48	344
RX4511	89-384	RU3 653	105-106	200817.0	201019.0	6631111.55	681025.01	386
RX4512	89-385	RU3-653	93.6-94.3	200808.9	201009.6	6631101.6	681017.59	390
RX4513	89-386	RU3-307	24-26	200874.3	199877.0	6630919.75	679897.77	388
RX4514	89-387	RD32	503.8	199206.9	201206.7	6629580.49	681557.52	504
RX4515	89-388	RD32	353.5	199202.2	201200.3	6629574.51	681552.29	353
RX4516	89-389	RD829	422.3	199293.5	201107.0	6629643.40	681441.41	422
RX4517	89-390	RD829	734.3	199282.7	201111.0	6629633.72	681447.65	734
RX4518	89-365	RD160	769.4	200175.2	201466.0	6630581.99	681600.60	770
RX4519	89-391	RD160	693	200177.9	201471.4	6630585.8	681605.28	693
RX4520	89-392	RD602	673.3	199804.1	200397.5	6629987.94	680638.03	673
RX4521	89-393	RD602	640	199804.1	200397.5	6629987.94	680638.03	640
RX4522	89-394	RD781	329.4	199898.6	200396.0	6630079.86	680616.07	329
RX4523	89-367	RD161	736.4	197579.2	202798.9	6628336.92	683464.91	736
RX4524	89-368	RD161	955.8	197571.4	202802.2	6628330.02	683469.83	956
RX4525	89-395	RD602	563.1	199804.4	200398.0	6629988.34	680638.45	563
RX4526	89-396	RD478	882	202394.3	201206.2	6632691.91	680865.60	882
RX4527	89-397	RD478	892.3	202394.3	201206.4	6632691.96	680865.79	892
RX4528	89-398	RD77A	654.4	199996.5	201010.0	6630308.63	681194.22	654
RX4529	89-375	RD16W1	1142.1	200046.8	200794.8	6630311.05	680973.23	1142
RX4530	89-399	RD16W1	1236.65	200046.8	200794.8	6630311.05	680973.23	1237
RX4531	89-377	RD96W1	644.8	200999.3	200005.4	6631069.63	679995.99	644
RX4532	89-400	RD160	703.6	200177.5	201470.6	6630585.23	681604.59	705
RX4533	89-401	RU2-275	21-23	199824.8	201179.0	6630177.67	681396.44	387
RX4534	89-402	RU33-59	72.4	200460.1	201013.3	6630761.91	681096.87	383
RX4535	89-403	RU33-59	102-104	200440.7	200995.2	6630739.04	681083.41	368

Appendix 7 continued

Sample Number	ANU#	Locality/ Drill hole#	Hole depth	Mine Coordinates		AMG coordinates		Depth (m) below surface
				Northing	Easting	Northing	Easting	
RX4536	89-404	38NG52 S.Dc		200250.0	201695.0	6630704.69	681807.92	483
RX4537	89-405	38NG52 S.Dc		200250.0	201695.0	6630704.69	681807.92	482
RX4539	89-407	38NG52 S.Dc		200198.0	201697.0	6630654.36	681821.15	481
RX4540	89-408	39NH51SE.Dc		200175.0	201730.0	6630639.06	681858.36	489
RX4541	89-409	39NH51SE.Dc		200162.0	201734.0	6630627.24	681865.08	490
RX4542	89-410	39NH51SE.Dc		200165.0	201733.0	6630629.95	681863.45	488
RX4543	89-411	33MK56W Dr		200598.0	200911.0	6630874.33	680967.09	417
RX4544	89-369	33NB53W Dr		200465.0	200860	6630733.43	680946.16	418
RX4546	89-413	33NB53W Dr		200465.0	200860.0	6630733.43	680946.16	419
RX4547	89-414	33MK56W Dr		200598.0	200853.0	6630861.75	680910.47	418
RX4548	89-415	RU3-739	47.6	200648.0	200851.7	6630910.28	680898.36	417
RX4549	89-376	RD545	568-569	200733.7	200994.7	6631024.96	681019.36	568
RX4550	89-416	RU4-144	134-136	199413.8	201350.8	6629813.72	681653.31	470
RX4551	89-417	RD222	756-758	197587.2	203637.8	6628526.71	684282.11	757
RX4552	89-366	RD268	753.6	200231.2	201337.3	6630608.74	681462.81	754
RX4553	89-418	RD271	681-683	200099.0	201473.0	6630509.12	681623.96	682
RX4558	89-370	RU3-898	45.3	200451	201101.9	6630772.19	681185.34	409
RX4559	89-419	RU3-401	64-65	199860.5	201085.8	6630192.31	681297.71	404
RX4560	89-420	RU3-401	69-70	199860.4	201081.4	6630191.25	681293.44	402
RX4561	89-421	RU3-402	3.5	199862.4	201144.0	6630206.79	681354.12	428
RX4562	89-422	RU3-751	25-26	201050.3	199948.6	6631107.10	679929.48	423
RX4563	89-423	RU3-751	77.1	201019.0	199913.9	6631069.01	679902.40	445
RX4564	89-424	RU3-898	8.3	200425.9	201076.4	6630742.21	681165.89	418
RX4566	89-425	32MJ54S Dc.		200250.0	200898.0	6630531.8	681029.89	450
RX4569	89-372	29Green 3 Nth		200847	199883	6630894.38	679909.57	390
RX4578	93-016	RU3-923	14-15	200737.4	199987.5	6630810.08	680035.36	404
RX4462	93-017	RU3-769	38	201054.7	199908.5	6631102.69	679889.38	413
RX4463	93-018	RU3-321	130	200959.1	199970.2	6631022.75	679970.35	410
RX3222	89-795	RD32	364-367	199202.5	201200.5	6629574.85	681552.42	366
RX3223	89-794	RD647	474-478	199103.8	202102.4	6629674.14	682454.26	470
RX3212	89-434	32LK58NW D		201061.0	199945.0	6631116.76	679923.65	413
RX3213	89-791	39NH51SE Dc		200173.5	201731.0	6630637.82	681859.66	490
RX3214	89-433	40LJ57 L.Lp		200745.0	199847.0	6630787.02	679896.53	495
RX3642	89-373	37Green5U/cut		200770	199910	6630825.07	679952.63	463
RX3700	89-371	RD783	675	201500	199700	6631492.12	679589.28	675
RX3697	89-792	36DC Blue Ex		200540.0	200105.0	6630642.87	680192.86	453

Appendix 7 continued

Sample Number	ANU#	Locality/ Drill hole#	Hole depth	Mine Coordinates		AMG coordinates		Depth (m) below surface
				Northing	Easting	Northing	Easting	
RX3698	89-793	29NB49S Dr		199854.0	201193.0	6630209.21	681403.77	380
Regional Samples								
RX4567	89-426	BLD-1	694.6			6636900	712800	695
RX4568	89-427	BLD-1	713.5			6636900	712800	714
RX4570	89-428	ACD15	565.2			6610238	670899	565
RX4571	89-429	AD20	439.6			6570375	714455	440
RX4572	89-430	WRD17	650.1			6608767	685913	650
RX4573	89-431	Roopena DDH6	113.5			6376657	724793	113.5
RX4574	89-432	Roopena DDH6	93.7			6376657	724793	94
RX4575	93-019	Roopena Station				6376657	724793	surface
RX4576	93-020	Roopena Station				6376657	724793	surface
RX4577	93-021	ACD7	637.7			6612400	670620	638

Appendix 8

Spinel mineral-chemistry data

Analysis	4548	4548	4548	4548	4548	4548	4548	4548	4548 -	4546A	4546A
RX No.	- 5	- 5B	- 5C	- 6	- 8	- 10	- 11	- 12	13	- 8	- 8B
SiO_2	<.09	0.17	0.18	0.13	0.09	0.51	0.10	<.09	<.09	<.09	<.09
TiO_2	0.19	0.21	0.21	0.20	0.10	<.09	<.09	0.13	0.21	1.61	1.51
Al_2O_3	3.83	7.31	7.46	9.67	6.64	7.87	5.93	7.10	4.09	12.06	11.85
V_2O_3	<.10	<.10	<.10	<.10	<.10	<.10	<.10	<.10	0.12	0.27	0.20
Cr_2O_3	53.58	58.42	59.12	54.72	58.46	45.46	52.66	58.06	57.10	39.44	39.71
Fe_2O_3(a)	11.77	5.02	3.51	7.51	4.44	15.88	12.82	5.77	8.95	15.99	15.95
FeO	22.36	16.14	17.01	15.45	20.15	21.28	19.77	18.98	23.44	23.71	23.69
MnO	0.77	0.55	0.58	0.46	<.23	2.01	0.40	<.23	0.37	<.19	0.25
MgO	5.91	10.73	10.08	11.68	8.17	6.78	8.36	8.69	5.61	7.59	7.34
ZnO											
CaO	<.06	<.06	<.06	<.06	<.06	<.06	<.06	0.63	0.38	<.06	<.06
Total	98.41	98.55	98.15	99.83	98.05	99.79	100.04	99.36	100.27	100.66	100.50
Cations calculated on the basis of 4 oxygens and Fe^{3+}/Fe^{2+} partitioning assuming 3 cations											
Si	0.000	0.006	0.006	0.004	0.003	0.018	0.003	0.000	0.000	0.000	0.000
Ti	0.005	0.005	0.005	0.005	0.003	0.000	0.000	0.003	0.006	0.040	0.038
Al	0.161	0.291	0.299	0.374	0.271	0.319	0.239	0.285	0.169	0.474	0.467
V	0.000	0.000	0.000	0.000	0.000	0.000	0.000	0.000	0.003	0.007	0.005
Cr	1.512	1.559	1.589	1.421	1.602	1.235	1.424	1.561	1.581	1.039	1.051
Fe^{3+}	0.316	0.128	0.090	0.186	0.116	0.411	0.330	0.148	0.236	0.401	0.402
Fe^{2+}	0.668	0.456	0.484	0.424	0.584	0.612	0.566	0.540	0.687	0.661	0.663
Mn	0.023	0.016	0.017	0.013	0.000	0.059	0.012	0.000	0.011	0.000	0.007
Mg	0.315	0.540	0.511	0.572	0.422	0.347	0.426	0.441	0.293	0.377	0.366
Zn											
Ca	0.000	0.000	0.000	0.000	0.000	0.000	0.000	0.023	0.014	0.000	0.000
Cr#	90.37	84.28	84.17	79.15	85.52	79.49	85.63	84.58	90.35	68.69	69.21
Ti#	0.30	0.29	0.28	0.27	0.14	0.00	0.00	0.18	0.32	2.60	2.44
Fe2#	67.97	45.77	48.64	42.59	58.04	63.78	57.02	55.06	70.09	63.66	64.42
Fe3#	15.89	6.45	4.54	9.38	5.82	20.90	16.56	7.41	11.88	20.95	20.92

Analysis	4543	4543	4543	4543	4543	4543	4543	4543	4543	3215	3215
RX No.	- 2B	- 3	- 5	- 5B	- 6	- 6B	- 7C	- 9B	- 13C	- 1	- 2
SiO_2	0.43	0.12	0.13	<.10	<.10	<.10	<.10	0.25	0.30	0.16	0.33
TiO_2	0.40	0.55	0.37	0.44	0.52	0.50	0.75	0.31	0.36	0.19	0.27
Al_2O_3	13.30	14.27	14.58	15.36	14.39	14.43	15.07	12.56	12.74	9.17	9.45
V_2O_3	<.10	0.12	0.15	<.11	0.11	<.11	<.11	<.11	<.11	0.00	0.00
Cr_2O_3	48.63	48.71	50.35	50.00	48.89	51.02	49.43	52.83	52.42	56.35	57.76
Fe_2O_3(a)	4.06	3.88	1.60	2.74	18.64	3.27	4.28	2.08	2.30	4.69	4.37
FeO	26.48	26.06	26.47	26.03	11.65	22.84	25.90	25.73	25.96	17.39	11.67
MnO	0.26	<.21	<.22	<.22	<.22	<.22	<.22	<.23	0.38	0.19	0.00
MgO	5.16	5.64	5.22	5.87	7.36	7.75	6.37	5.72	5.44	10.00	13.93
ZnO										0.59	0.81
CaO	<.07	<.07	<.07	<.07	<.07	<.07	<.07	<.07	0.08	0.00	0.00
Total	98.72	99.35	98.86	100.44	101.56	99.83	101.80	99.49	99.97	98.73	98.59
Cations calculated on the basis of 4 oxygens and Fe^{3+}/Fe^{2+} partitioning assuming 3 cations											
Si	0.015	0.004	0.004	0.000	0.000	0.000	0.000	0.008	0.010	0.005	0.011
Ti	0.010	0.014	0.009	0.011	0.012	0.012	0.018	0.008	0.009	0.005	0.007
Al	0.535	0.566	0.581	0.600	0.538	0.562	0.581	0.501	0.506	0.363	0.364
V	0.000	0.003	0.004	0.000	0.003	0.000	0.000	0.000	0.000	0.000	0.000
Cr	1.311	1.297	1.347	1.310	1.226	1.332	1.277	1.413	1.397	1.498	1.493
Fe^{3+}	0.104	0.098	0.041	0.068	0.445	0.081	0.105	0.053	0.058	0.119	0.107
Fe^{2+}	0.755	0.734	0.749	0.721	0.309	0.631	0.708	0.728	0.732	0.489	0.319
Mn	0.008	0.000	0.000	0.000	0.000	0.000	0.000	0.000	0.011	0.005	0.000
Mg	0.262	0.283	0.263	0.290	0.348	0.382	0.310	0.289	0.273	0.501	0.679
Zn										0.015	0.020
Ca	0.000	0.000	0.000	0.000	0.000	0.000	0.000	0.000	0.003		0.000
Cr#	71.04	69.60	69.85	68.59	69.50	70.34	68.75	73.83	73.41	80.49	80.40
Ti#	0.55	0.74	0.49	0.57	0.70	0.65	0.98	0.41	0.48	0.27	0.38
Fe2#	74.22	72.16	73.99	71.32	47.04	62.31	69.52	71.61	72.81	49.39	31.96
Fe3#	5.34	5.01	2.07	3.45	20.14	4.12	5.36	2.70	2.97	6.01	5.45

Appendix 8 contd. Spinel mineral-chemistry data

Analysis	3215	3215	3215	3215	3215	3261	3261	3261	3261	3261	3632
RX No.	- 3	- 4	- 5	- 6	- 7	- 1	- 2	- 3	- 6	- 7	- 1
SiO_2	0.34	0.16	0.34	0.13	0.19	0.17	0.06	0.11	0.17	0.06	0.14
TiO_2	0.22	0.17	0.21	0.18	0.18	0.22	0.11	0.18	0.19	0.18	0.21
Al_2O_3	8.43	9.20	9.84	8.67	8.95	9.19	8.73	9.19	9.05	8.93	9.57
V_2O_3	0.00	0.00	0.00	0.00	0.00	0.00	0.00	0.00	0.00	0.00	0.00
Cr_2O_3	53.74	58.05	58.78	58.26	58.78	57.75	57.26	58.57	58.76	52.84	58.68
Fe_2O_3(a)	4.43	4.04	2.99	5.33	5.15	5.06	5.50	4.80	5.07	5.91	4.93
FeO	25.56	16.00	12.30	12.72	11.94	15.42	15.85	12.38	9.61	23.81	13.76
MnO	0.10	0.00	0.00	0.00	0.00	0.15	0.01	0.07	0.09	0.47	0.00
MgO	4.78	11.33	13.77	13.41	13.91	11.90	11.32	13.71	15.35	5.52	13.06
ZnO	0.41	0.26	0.46	0.06	0.51	0.08	0.00	0.02	0.13	0.30	0.42
CaO	0.00	0.00	0.00	0.00	0.00	0.00	0.00	0.00	0.00	0.00	0.00
Total	98.01	99.21	98.69	98.76	99.61	99.94	98.84	99.03	98.42	98.02	100.77
Cations calculated on the basis of 4 oxygens and Fe^{3+}/Fe^{2+} partitioning assuming 3 cations											
Si	0.012	0.005	0.011	0.004	0.006	0.006	0.002	0.004	0.006	0.002	0.010
Ti	0.006	0.004	0.005	0.004	0.004	0.005	0.003	0.004	0.005	0.005	0.005
Al	0.350	0.359	0.378	0.336	0.343	0.355	0.343	0.354	0.346	0.368	0.360
V	0.000	0.000	0.000	0.000	0.000	0.000	0.000	0.000	0.000	0.000	0.000
Cr	1.497	1.521	1.516	1.516	1.510	1.498	1.509	1.512	1.509	1.462	1.497
Fe^{3+}	0.117	0.101	0.073	0.132	0.126	0.125	0.138	0.118	0.124	0.156	0.120
Fe^{2+}	0.754	0.444	0.336	0.350	0.325	0.424	0.442	0.339	0.261	0.698	0.372
Mn	0.003	0.000	0.000	0.000	0.000	0.004	0.000	0.002	0.002	0.014	0.000
Mg	0.251	0.560	0.670	0.657	0.674	0.582	0.563	0.667	0.743	0.288	0.628
Zn	0.011	0.006	0.011	0.001	0.012	0.002	0.000	0.000	0.003	0.008	0.010
Ca	0.000	0.000	0.000	0.000	0.000	0.000	0.000	0.000	0.000	0.000	0.000
Cr#	81.05	80.90	80.04	81.86	81.49	80.84	81.48	81.03	81.35	79.89	80.61
Ti#	0.32	0.21	0.26	0.22	0.22	0.27	0.16	0.21	0.27	0.27	0.27
Fe2#	75.02	44.22	33.40	34.76	32.53	42.15	43.98	33.70	26.00	70.79	37.20
Fe3#	5.96	5.10	3.71	6.65	6.37	6.32	6.93	5.95	6.27	7.85	6.07

Analysis	3261	3261	3261	3261	3632	3632	3632	3632	3632	3632	3632
RX No.	- 2	- 3	- 6	- 7	- 1	- 2	- 3	- 4	- 5	- 6	- 7
SiO_2	0.06	0.11	0.17	0.06	0.14	0.11	0.29	0.15	0.18	0.31	0.16
TiO_2	0.11	0.18	0.19	0.18	0.21	0.20	0.08	0.22	0.20	0.30	0.15
Al_2O_3	8.73	9.19	9.05	8.93	9.57	9.12	9.25	8.70	9.04	10.15	9.04
V_2O_3	0.00	0.00	0.00	0.00	0.00	0.00	0.00	0.00	0.00	0.00	0.00
Cr_2O_3	57.26	58.57	58.76	52.84	58.68	59.35	58.40	58.71	60.41	52.13	56.82
Fe_2O_3(a)	5.50	4.80	5.07	5.91	4.93	4.31	4.29	4.03	3.66	4.87	4.12
FeO	15.85	12.38	9.61	23.81	13.76	13.52	14.29	18.95	13.43	24.58	18.98
MnO	0.01	0.07	0.09	0.47	0.00	0.00	0.00	0.13	0.00	0.14	0.11
MgO	11.32	13.71	15.35	5.52	13.06	12.85	12.39	9.59	13.38	5.63	9.24
ZnO	0.00	0.02	0.13	0.30	0.42	0.70	0.58	0.31	0.09	0.57	0.19
CaO	0.00	0.00	0.00	0.00	0.00	0.00	0.00	0.00	0.00	0.00	0.00
Total	98.84	99.03	98.42	98.02	100.77	100.16	99.57	100.79	100.39	98.68	98.81
Cations calculated on the basis of 4 oxygens and Fe^{3+}/Fe^{2+} partitioning assuming 3 cations											
Si	0.002	0.004	0.006	0.002	0.010	0.004	0.001	0.005	0.006	0.011	0.005
Ti	0.003	0.004	0.005	0.005	0.005	0.005	0.002	0.005	0.005	0.008	0.004
Al	0.343	0.354	0.346	0.368	0.360	0.350	0.357	0.340	0.345	0.413	0.360
V	0.000	0.000	0.000	0.000	0.000	0.000	0.000	0.000	0.000	0.000	0.000
Cr	1.509	1.512	1.509	1.462	1.497	1.527	1.514	1.538	1.545	1.423	1.517
Fe^{3+}	0.138	0.118	0.124	0.156	0.120	0.106	0.106	0.101	0.089	0.127	0.105
Fe^{2+}	0.442	0.339	0.261	0.698	0.372	0.369	0.392	0.526	0.364	0.711	0.537
Mn	0.000	0.002	0.002	0.014	0.000	0.000	0.000	0.004	0.000	0.004	0.003
Mg	0.563	0.667	0.743	0.288	0.628	0.624	0.605	0.474	0.645	0.290	0.465
Zn	0.000	0.000	0.003	0.008	0.010	0.017	0.014	0.008	0.002	0.015	0.005
Ca	0.000	0.000	0.000	0.000	0.000	0.000	0.000	0.000	0.000	0.000	0.000
Cr#	81.48	81.03	81.35	79.89	80.61	81.35	80.92	81.90	81.75	77.51	80.82
Ti#	0.16	0.21	0.27	0.27	0.27	0.27	0.11	0.27	0.26	0.43	0.21
Fe2#	43.98	33.70	26.00	70.79	37.20	37.16	39.32	52.60	36.08	71.03	53.59
Fe3#	6.93	5.95	6.27	7.85	6.07	5.35	5.36	5.10	4.50	6.47	5.30

Appendix 8 contd. Spinel mineral-chemistry data

Analysis	3632	3652	3652	3652
RX No.	- 8	- 1	- 3	- 8
SiO_2	0.05	0.14	0.30	0.16
TiO_2	0.21	0.14	0.15	0.09
Al_2O_3	8.67	9.37	9.62	8.91
V_2O_3	0.00	0.00	0.00	0.00
Cr_2O_3	56.58	58.39	59.15	55.88
Fe_2O_3(a)	4.96	2.81	2.84	3.97
FeO	20.52	10.94	10.64	14.88
MnO	0.11	0.12	0.01	0.21
MgO	8.25	11.53	12.67	8.10
ZnO	0.28	5.02	4.26	6.21
CaO	0.00	0.00	0.00	0.00
Total	99.63	98.46	99.64	98.41
Cations calculated on the basis of 4 oxygens and Fe^{3+}/Fe^{2+} partitioning assuming 3 cations				
Si	0.002	0.005	0.010	0.006
Ti	0.005	0.004	0.004	0.002
Al	0.346	0.369	0.371	0.361
V	0.000	0.000	0.000	0.000
Cr	1.514	1.544	1.523	1.520
Fe^{3+}	0.126	0.071	0.070	0.103
Fe^{2+}	0.581	0.306	0.292	0.429
Mn	0.000	0.003	0.008	0.006
Mg	0.416	0.575	0.619	0.415
Zn	0.007	0.124	0.103	0.158
Ca	0.000	0.000	0.000	0.000
Cr#	81.40	80.71	80.41	80.81
Ti#	0.27	0.21	0.21	0.11
Fe2#	58.27	34.73	32.05	50.83
Fe3#	6.34	3.58	3.56	5.19

APPENDIX 9

Appendix'9 is an adjunct to Chapter 6. It contains element enrichment/depletion diagrams for the mafic/ultramafic dykes discussed in that chapter. Increasing Al_2O_3 concentrations correspond to increasing degree of alteration of the dykes due to the residual behaviour of Al during alteration. Ti has also behaved in a relatively immobile manner (see Chapter 6) By plotting element/TiO_2 ratios versus Al_2O_3 it is possible to monitor which elements were lost, which were gained, and which were immobile with increasing degree of hydrothermal alteration. There is an apparent complementarity between losses from the dykes and gains in the Fe-rich breccias (cf. Chapter 5 and Appendix 6) for several elements, e.g. Cr, Cu , Mn, V, Ni, Zn.

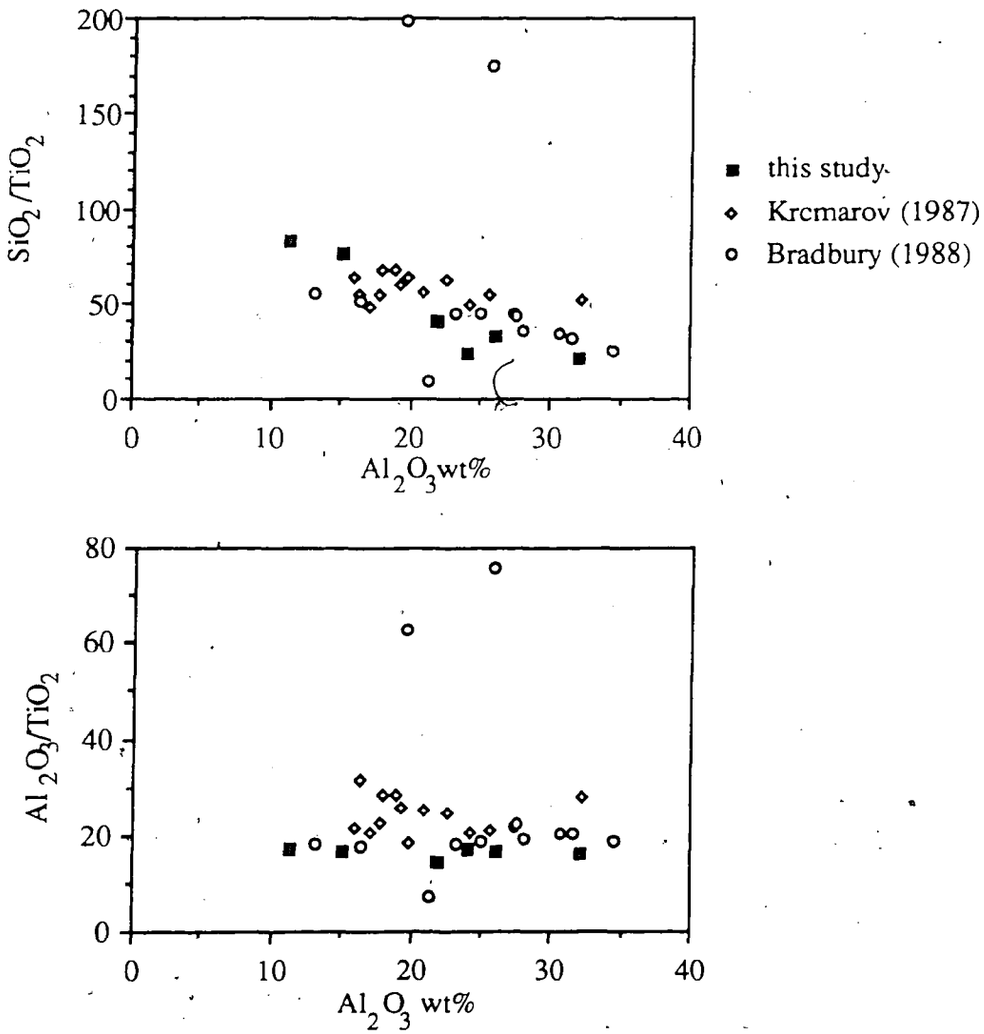

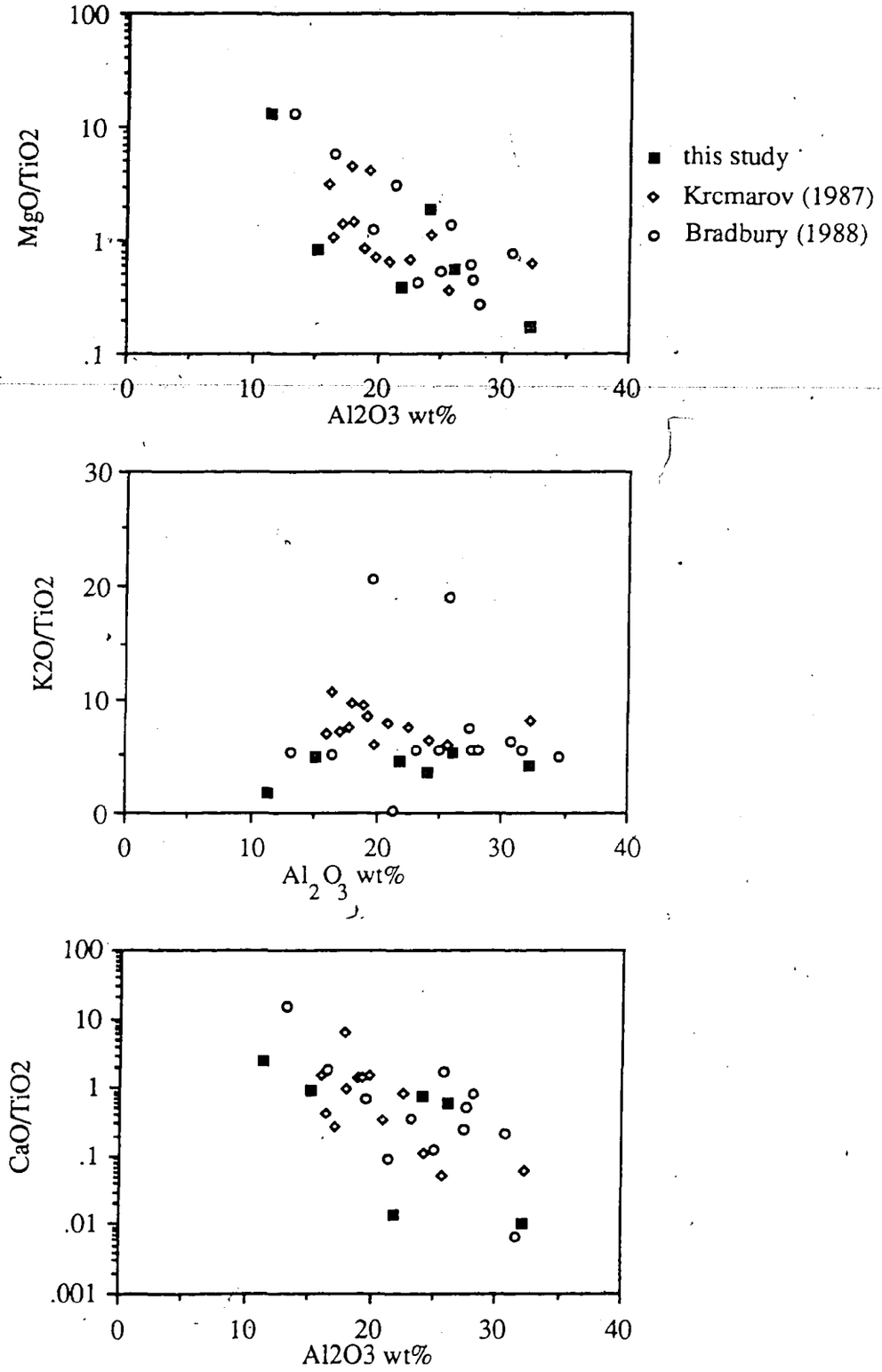

Appendix 9 continued.

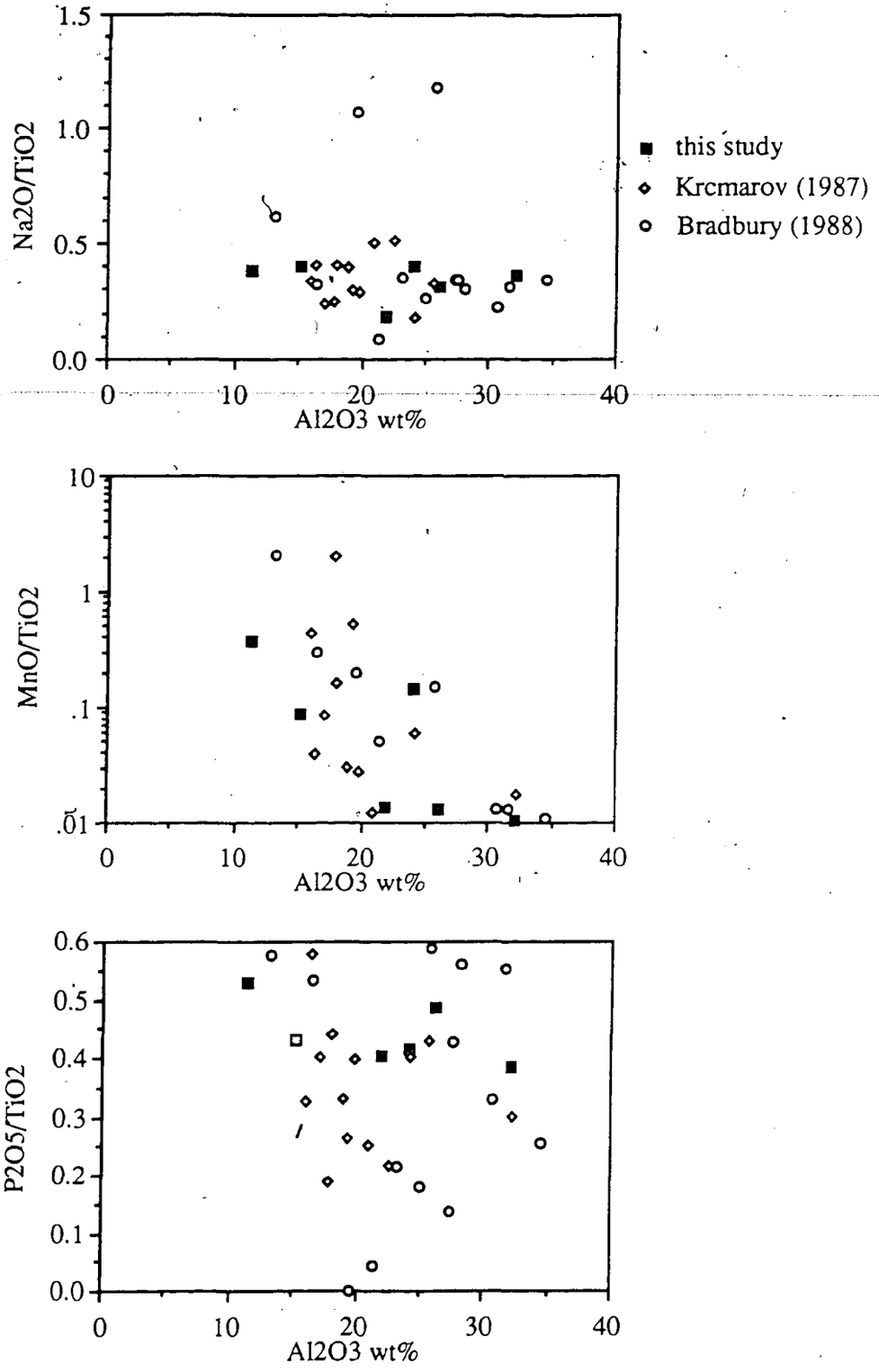

Appendix 9 continued.

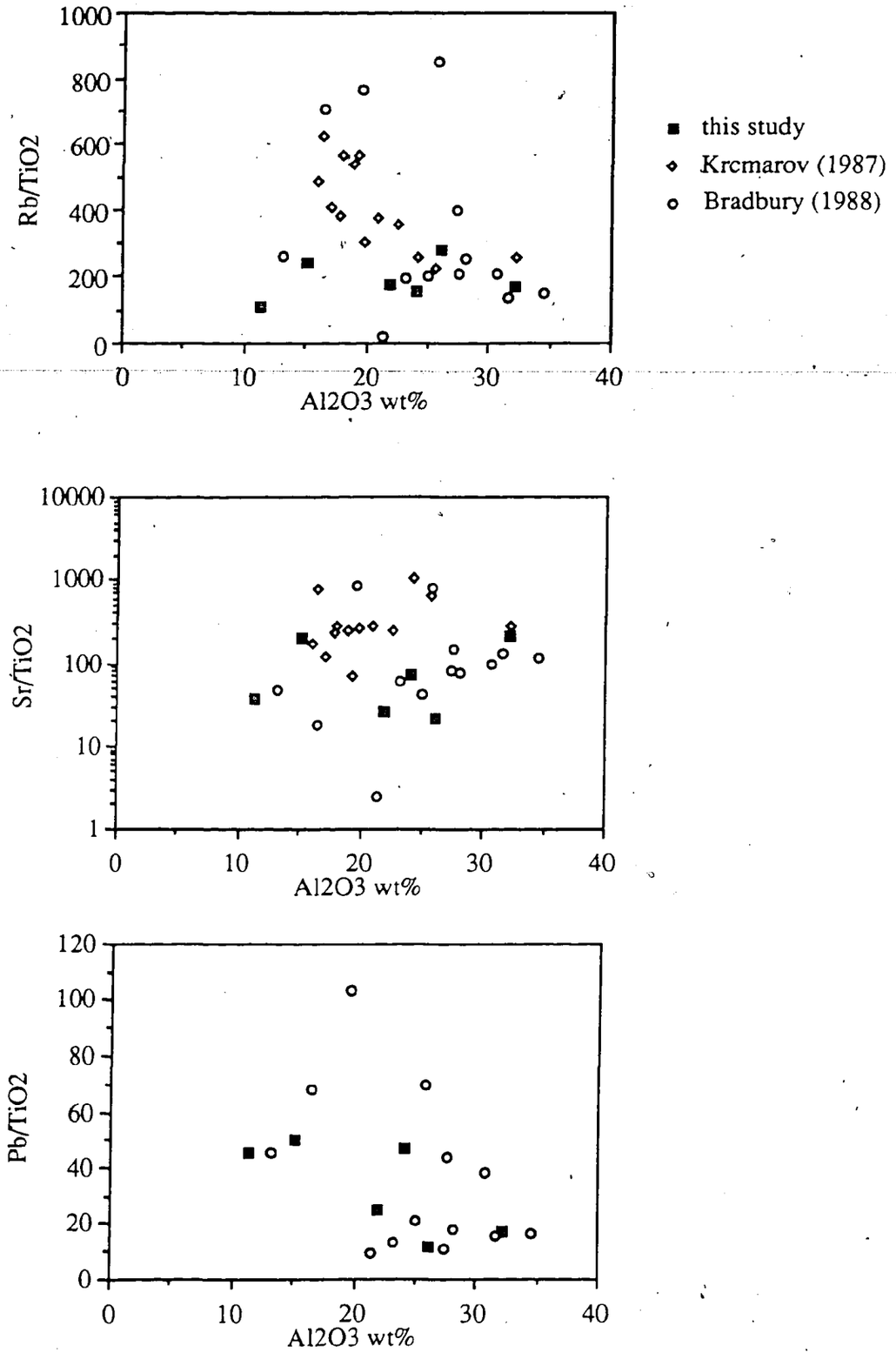

Appendix 9 continued.

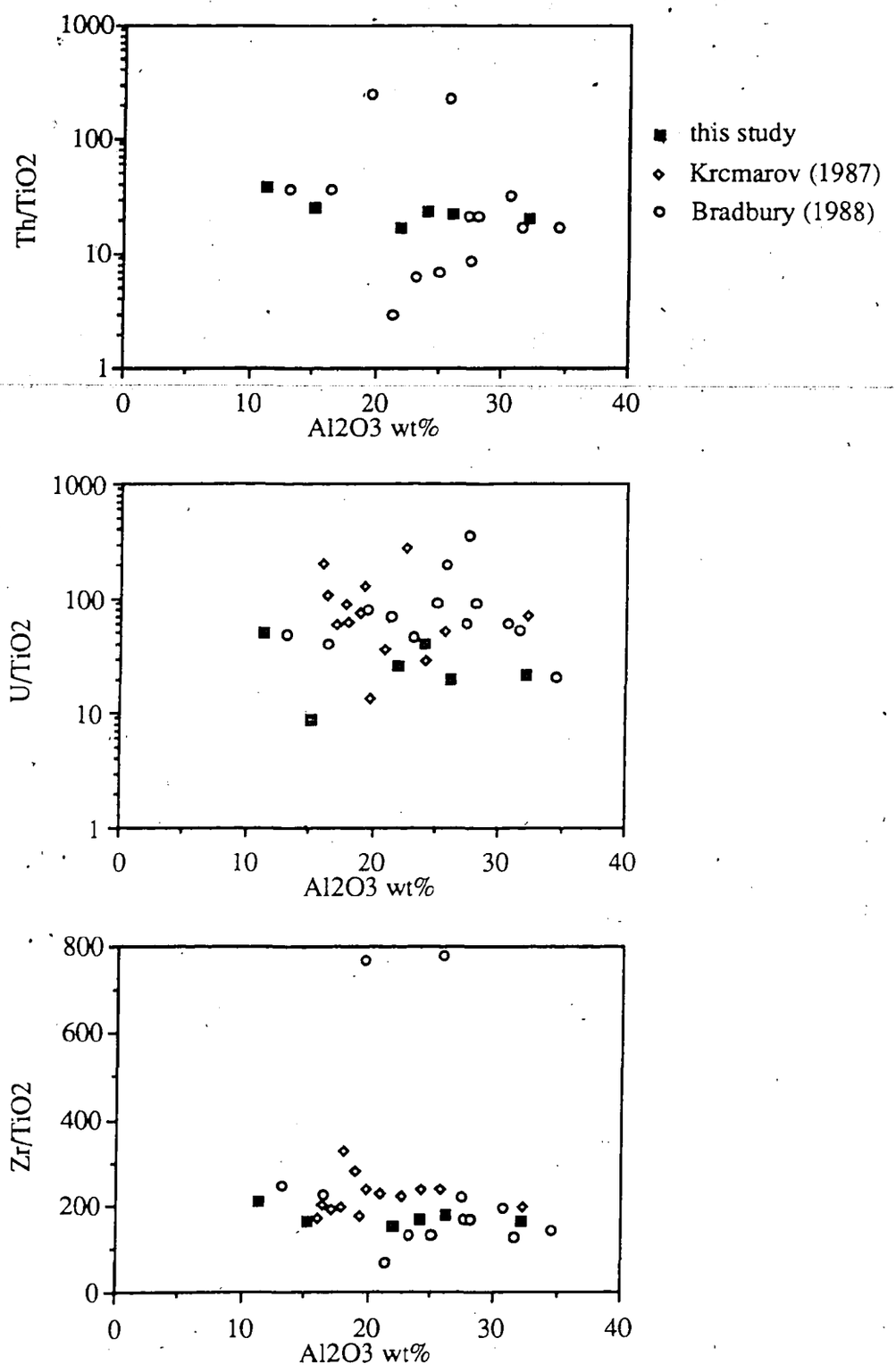

Appendix 9 continued.

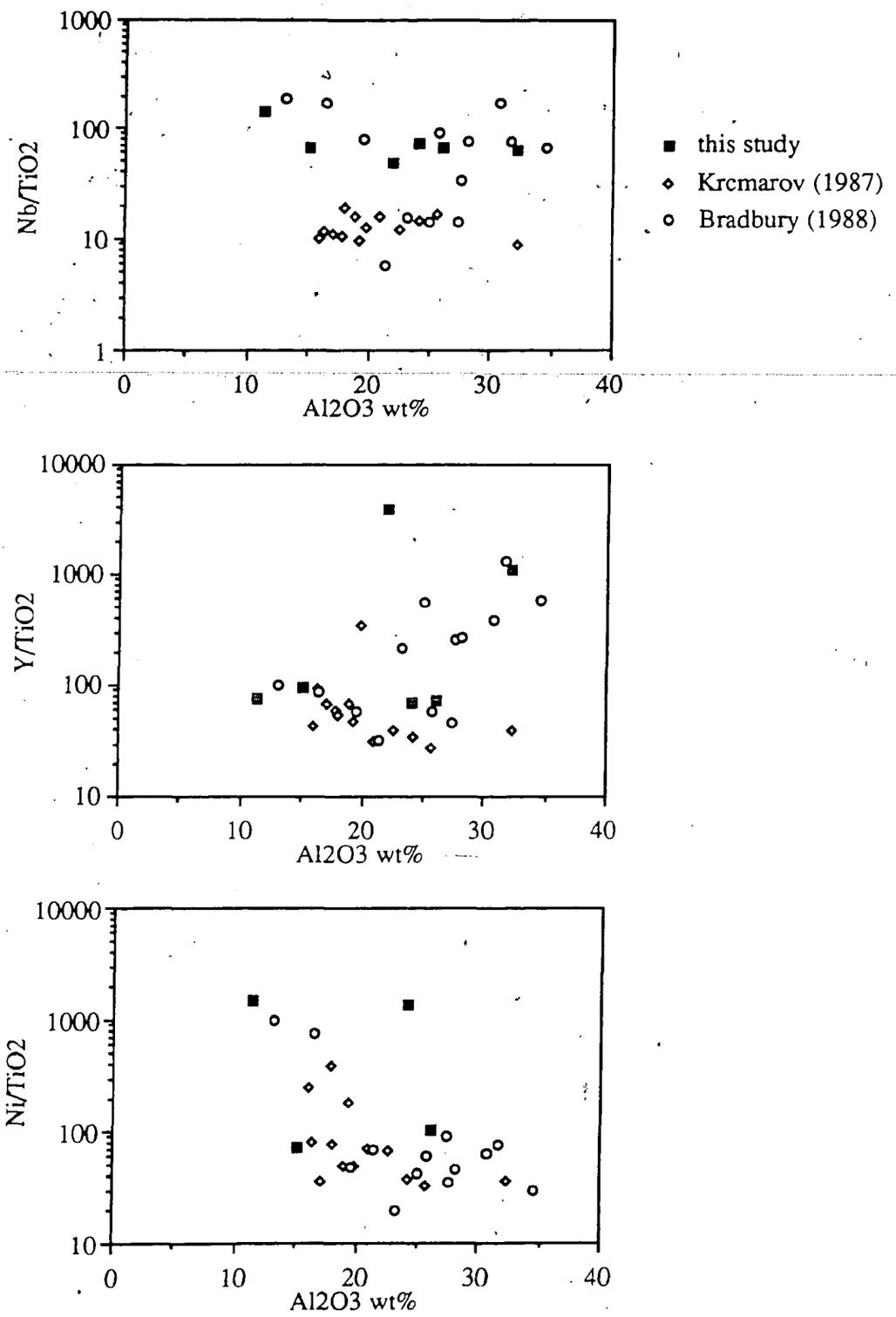

Appendix 9 Continued.

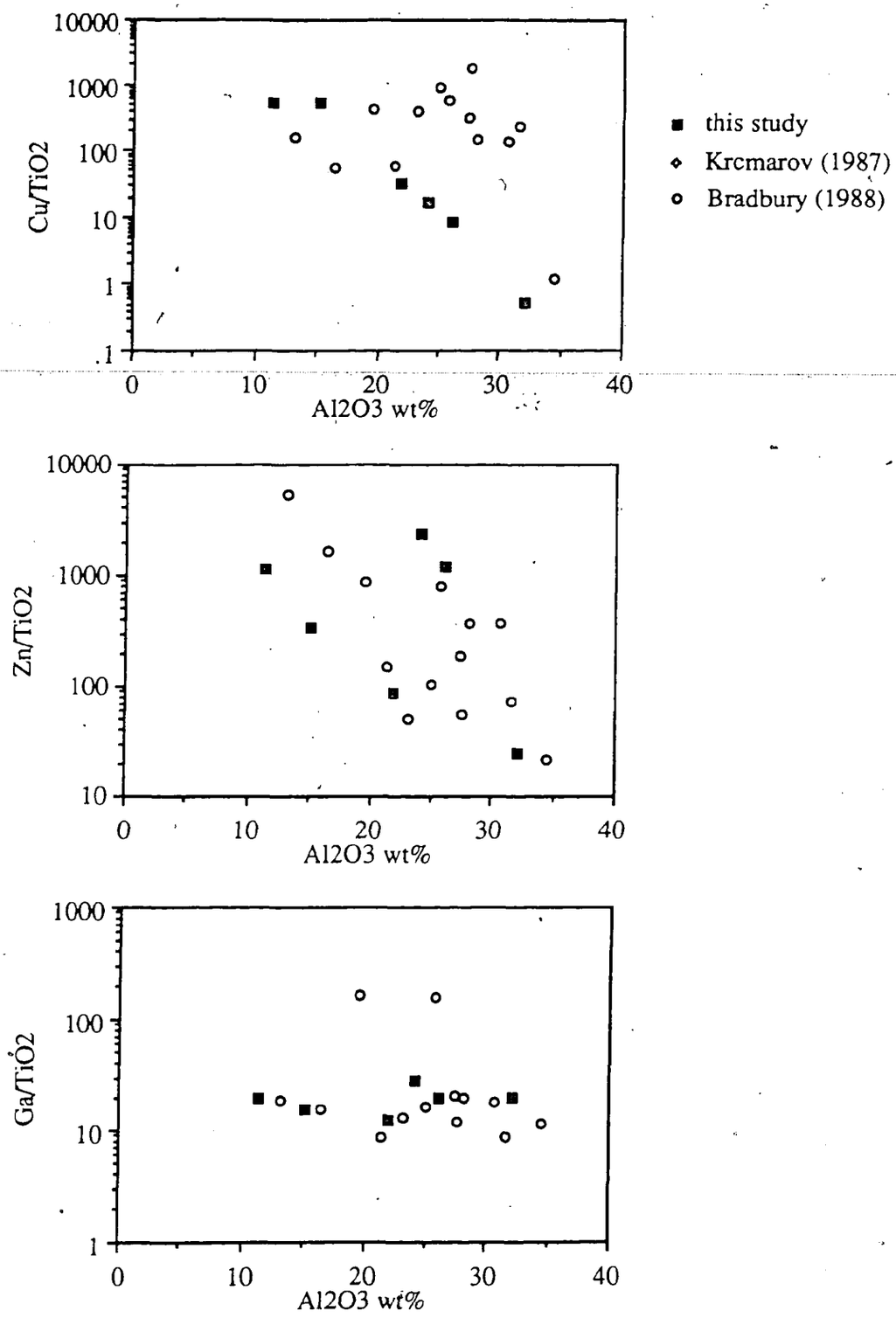

Appendix 9 continued.

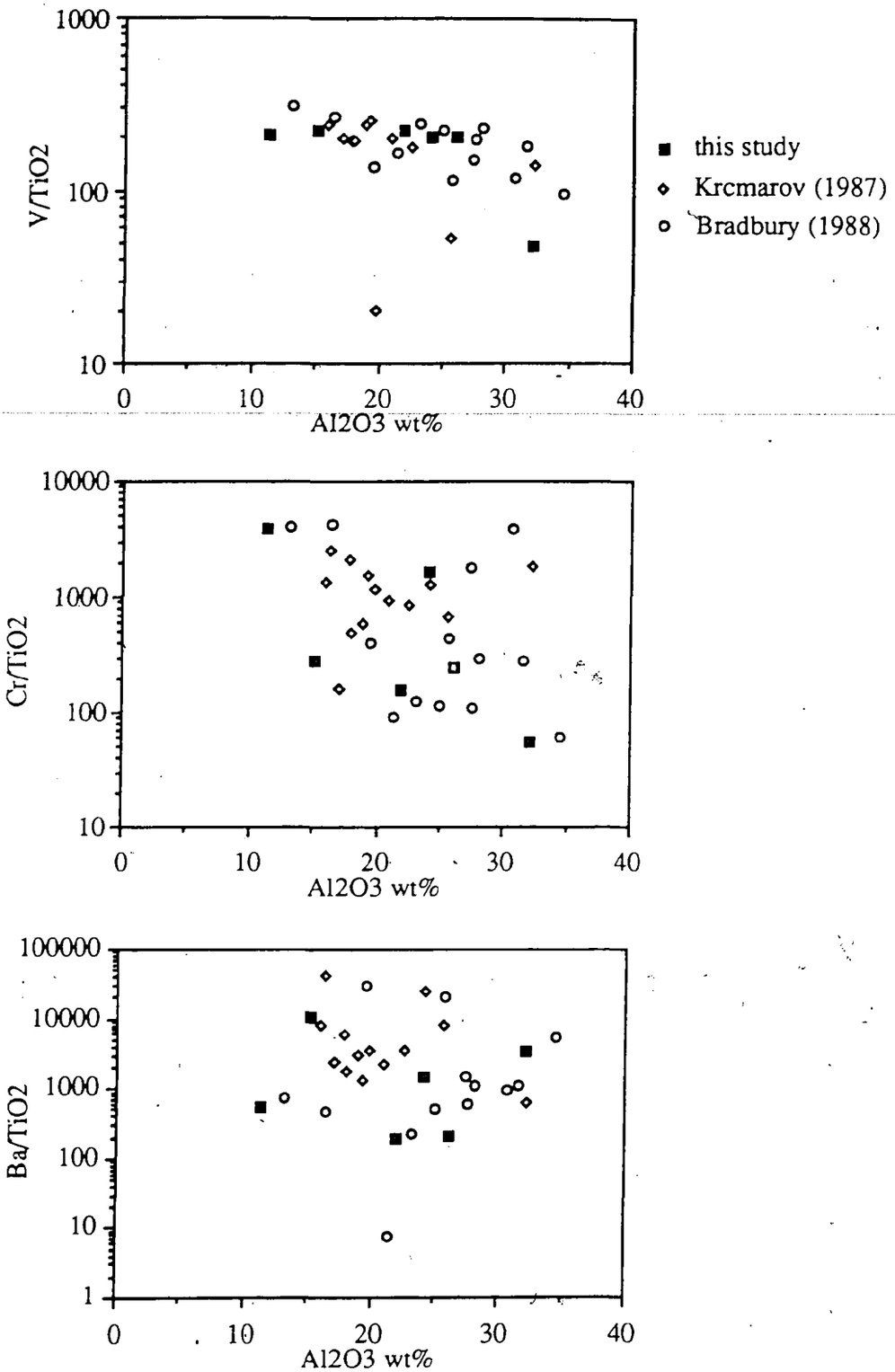

Appendix 9 continued.

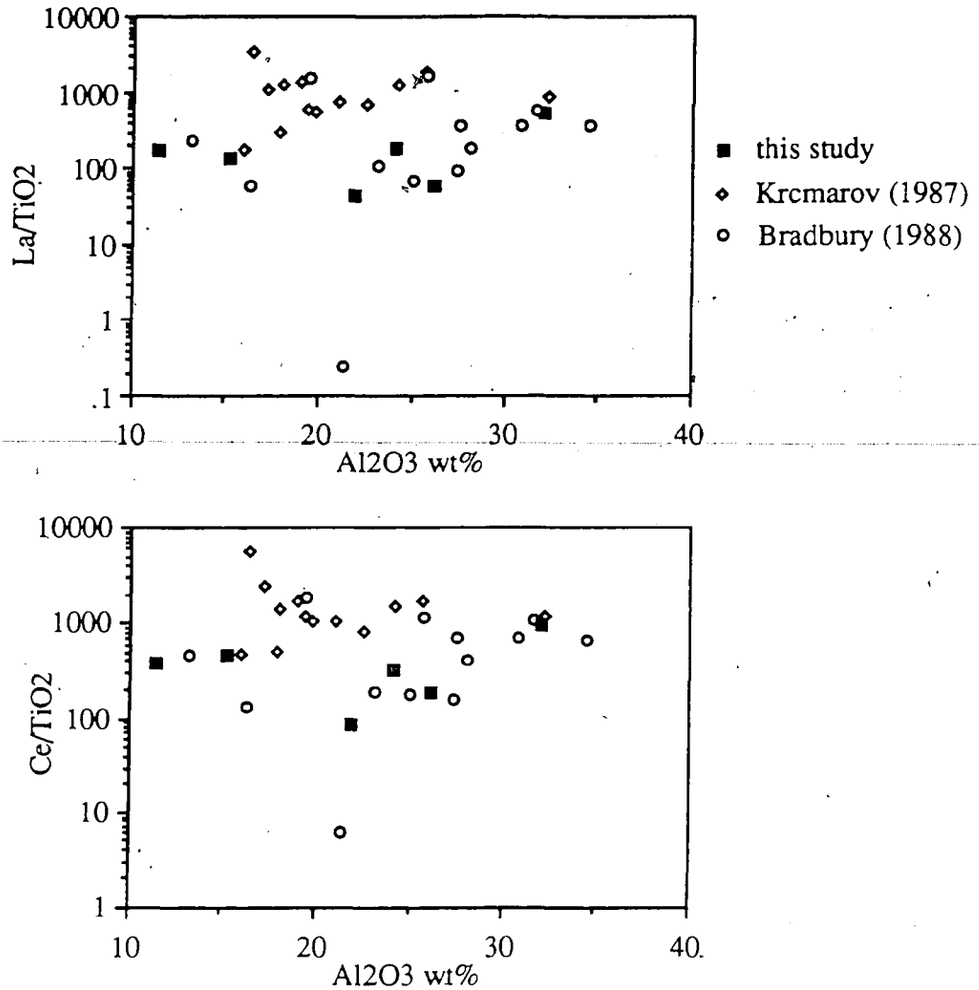

Appendix 9 continued.